IMPERIAL COLLEGE LONDON

ROYAL SCHOOL OF MINES

DEPARTMENT OF EARTH SCIENCE AND ENGINEERING

A THESIS PRESENTED FOR THE DEGREE OF DOCTOR OF PHILOSOPHY

Using magnetic techniques to calibrate lateral hydrocarbon migration in basin modelling: A Case Study from the Lower Tertiary, UK Central North Sea

Sijibomioluwa Adesope Badejo

Supervised by

Dr. Adrian Muxworthy (Imperial College London)

Prof. Alastair Fraser (Imperial College London)

March 2019

Declaration of Originality

I hereby declare that this thesis “Using magnetic techniques to calibrate lateral hydrocarbon migration in basin modelling: A Case Study from the Lower Tertiary, UK Central North Sea”and the work reported here originated entirely from me. Information derived from the published and unpublished work of others has been acknowledged in the text and references are given in the bibliography.

Sijibomioluwa Adesope Badejo (2019)

Copyright Declaration

The copyright of this thesis rests with the author and is made available under a Creative Commons Attribution Non-Commercial No Derivatives licence. Researchers are free to copy, distribute or transmit the thesis on the condition that they attribute it, that they do not use it for commercial purposes and that they do not alter, transform or build upon it. For any reuse or redistribution, researchers must make clear to others the licence terms of this work.

Abstract

Pyrolysis experiments and calculated thermostability diagrams show that iron bearing minerals can be produced inorganically during oil formation in the 'oil-kitchen' or be precipitated in the reservoir via alteration or replacement of existing minerals. This study applies a novel use of this observation to identify a magnetic proxy for hydrocarbon migration pathways. This is addressed by examining the Tertiary Tay Fan in the Western Central Graben in the Central North Sea. In order to constrain potential migration pathways in the Tay, petroleum systems modelling was carried out in the Western Central Graben, an area well constrained by existing borehole and 3D seismic data. The results demonstrate initial downwards migration from a mature Jurassic (Kimmeridge Clay) source in the Central Graben to the east into an underlying Fulmar Formation carrier followed by vertical migration into the overlying Tertiary sandstones of the Tay and Forties Sandstone Member via structural focus zones. Importantly, the Jurassic source rock is shown to be immature in the west and central study area, requiring long distance lateral migration of at least 30 km as the charge mechanism for the existing Tertiary fields in the west.

Importantly, mineral magnetic analysis identified an increasing presence of ferrimagnetic iron sulphides in core samples along the identified lateral hydrocarbon migration pathway (east to west). This is likely caused by increasingly lower reservoir temperatures and resulting biodegradation leading to the precipitation of iron sulphides. Alternatively, it could be caused by iron sulphides precipitated during early mature oil generation traveling with the oil to the traps in the west. These observations suggest magnetic techniques could be an efficient alternative method for identifying the severity of biodegradation or maturity of oil in core samples which can then be used to calibrate petroleum systems models. Results also hint at the potential for high resolution aeromagnetic surveys to identify shallow subsurface migration pathways. Rock magnetic techniques also identified an enhancement of magnetisation at the hydrocarbon-fluid contacts. The magnetic enhancement is due to the precipitation of new nanometric iron oxide (magnetite) and iron sulphide (greigite) phases. This observation has the potential to be used to identify paleo-hydrocarbon-fluid contact in dry wells or map tilted contacts, which could then be used to infer fill history of a basin or calibrate petroleum systems models.

Acknowledgement

I would like to thank petroleum technology development fund (PTDF) for partly funding this PhD and my main supervisors Dr Adrian Muxworthy, Prof. Alastair Fraser and Martin Neumaier for providing guidance and advice thought out my PhD.

I would like to show my gratitude to Richard Salway, Anna Paget and Sue Nicholson for helping provide vital data for this PhD. I thank PGS and TGS for provision of 3D seismic data. I am appreciative of Tracey Gallagher and Scott Renshaw and the staff at the BGS core stores at Keyworth, England for allowing me access to cores from the North Sea UK. Thank you to Dana Petroleum for the provision of oil samples for this PhD.

For the experimental work, I would like to thank the Institute of Rock magnetism (IRM) at the University of Minnesota, USA for awarding me two visiting fellowship positions, which allowed me to conduct the majority of the magnetic experimentation. Especially I am indebted to Dario Bilardello and Pete Solheid for their time and patience during my visits. My appreciation also goes to Graham Stevenson for his help with imagining, Ruth Davey for her help with geochemical experiments and Mike Jackson for their help with experiments during my PhD. In addition, I would to thank Dr Mahmoud Ardakani within the department of Materials at Imperial College London who trained and guided me on the SEM equipment.

During the 4 years of my PhD I have made good friend in the department who have made the years fly by. I would like to thank you all especially Pete Gordon, Bailey Lathrop, Francesco Palci, Melissa Gray, Ashkan Kavei, Alex Griffiths, Charlie Penny, Jay Shah, Al Boyce, Thomas Berndt, Aike, Miguel Valdez-Grijalva, Isaac Odeh, Chris Ogden, Ikenna Okwara, Joe Perkins, Maryam Abdulkarim, Nan Wu, Lewis Jones and so many more.

Most importantly, I would like to show my appreciation to my family for their constant support during my PhD. I appreciate my parents for provision of funds during the first year of my PhD and for always believing in me. Lastly, I would like to thank my girlfriend Lucie KBidy for her constant support throughout this process.

Contents

Abstract 3
Acknowledgement 4
Contents 5
List of Figures 10
List of Tables 22
List of Publications 24
List of Abbreviations 25
Chapter 1: Introduction 27
1.1 Brief Introduction to Thesis 28
1.1 Review of Magnetisation 30
1.1.1 Fundamentals of Magnetism 30
1.1.2 Domain Theory 33
1.1.3 Identifying domain states using First-order Reversal Curve diagrams 35
1.2.4 Magnetic Remanence 38
1.2.5 Magnetic Mineralogy 39
Review of Hydrocarbons and Magnetism 42
1.1.4 Chemical and Microbial Processes Responsible for Anomalous Magnetisation in Hydrocarbon Seepage Zones. 42
1.3.2 Hydrocarbon Accumulation Identification through Rock Magnetic Techniques 46
1.3.3 Magnetic mineral formation and Remagnetisation 47
Chapter 2: Introduction to the Geology of the Central North Sea 51
2.1 Introduction 52
2.2 Structural Evolution of the Central Graben 53
2.2.1 Pre-Triassic 53
2.2.2 Triassic 54
2.2.3 Jurassic 56
2.2.4 Cretaceous 59
2.2.5 Tertiary 59
2.3 Stratigraphy 60
2.3.1 Montrose Group 62
2.3.2 Moray Group 63
2.3.3 Stronsay Group 63
2.4 Hydrocarbon Plays in the Central Graben 64

2.4.1 Source Rocks in the Central Graben 64
2.4.2 Hydrocarbon Migration in the Central Graben 67
2.4.3 Reservoirs in the Central Graben 68
2.4.4 Traps 71
2.5 Fields of Interest 71
2.5.1 Selkirk Field 72
2.5.2 Gannet Complex – Pilot Field 72
Chapter 3: 2D Petroleum Systems Modelling 75
3.1 Introduction 76
3.2 Depth Conversion 76
3.2.1 Travel Time Equations 78
3.2.2 Velocity model errors 79
3.3 2D Basin Modelling and Input data 80
3.3.1 Stratigraphic Model 80
3.3.2 Structural Model 85
3.3.3 Thermal Boundary Conditions 88
3.3.4 Source Rock Properties 88
3.3.5 Modelling Migration Methods 90
3.4 Results and Discussion 92
3.4.1 Model Calibration 92
3.4.2 Base-Case Model 93
3.4.2.1 Source Rock Maturation, Hydrocarbon Generation and Expulsion 93
3.4.2.2 Hydrocarbon Migration and Accumulations 95
3.4.3 Testing parameter space: Sensitivity check 99
3.4.3.1 Lack of Injectites 99
3.4.3.2 Varying Initial TOC 100
3.4.3.3 Using Darcy flow and Flowpath Migration 102
3.4.3.4 Open Faults 103
3.5 Conclusions 105
Chapter 4: 3D Petroleum Systems Modelling 107
4.1 Introduction 108
4.2 Modelling and Input Data 108
4.2.1 Stratigraphic Model 108
4.2.1.1 Facies Model 110

4.2.2 Structural Model 114
4.3 Results and Discussion 115
4.3.1 Source Rock Generation and Expulsion 115
4.3.2 Hydrocarbon Migration and Accumulation 116
4.3.2.1 Carrier Beds and the Importance of the Salt Diapir 116
4.3.2.2 Timing of Hydrocarbon Migration into the Reservoirs 117
4.3.2.3 Vertical and Lateral Migration within the Tay Sandstone Member 124
4.3.3 Testing Parameter Space: Sensitivity Check 125
4.3.3.1 Varying Initial TOC 125
4.3.3.2 How important are the injectites? 128
4.3.3.3 Using Combined Darcy flow with Flowpath Migration Method 129
4.3.3.4 Importance of faults on the base-case model 131
4.3.3.5 Tay Accumulation Test 132
4.3.3.6 Alternative Facies Models 133
4.4 Conclusions 136
Chapter 5: Identifying Magnetic Proxies for Hydrocarbon Migration 137
5.1 Introduction 138
5.2 Sampling and Methodology 139
5.2.1 Sampling 139
5.2.2 Magnetic Measurements 141
5.2.2.1 Magnetic Hysteresis Measurements 141
5.2.2.1 Low-temperature measurements. 142
5.2.2.3 High-temperature Measurements 142
5.2.2.4 Room-Temperature (RT) Susceptibility 143
5.2.3 Scanning Electron Microscopy (SEM) 143
5.2.4 Geochemical Experiments 143
5.3 Results 145
5.3.1 Magnetic Hysteresis Parameters and Susceptibility 145
5.3.2 Magnetic Mineral Identification 150
5.3.2.1 Hydrocarbon Wells Core Samples 150
5.3.2.2 Background Sample Behaviour 163
5.4 Discussion 166
5.4.1 Variations in coercivity and susceptibility along the migration pathway 166
5.4.2 Origin of Background and Source Signal 168

5.4.2.1 Origin of Titanohematite and Goethite 168
5.4.2.2 Origin of Magnetite and Maghemite 168
5.4.2.3 Origin of Siderite 169
5.4.2.4 Origin of Greigite 169
5.4.3 Variation of Magnetic Minerals along the Fill Spill Chain 170
5.4.4 Limitations to magnetic data interpretation 174
5.5 Conclusions 175
Chapter 6: Is there a Magnetic Proxy for Hydrocarbon Migration? 177
6.1 Identifying a Proxy for Hydrocarbon Migration 178
6.2 Implications for Hydrocarbon Perspectivity 185
6.3 Conclusions 187
Chapter 7: Identification of magnetic enhancement at hydrocarbon/water contacts 189
7.1 Introduction 190
7.2 Methodology 192
7.2.1 Sample Collection and Magnetic Measurements 192
7.3 Results 193
7.3.1 Oil Samples 193
7.3.2 Core Samples 194
7.4 Discussion 199
7.4.1 Can magnetic minerals be carried in the oil? 200
7.4.2 Are the magnetic minerals authigenic, detrital or do they migrate? 200
7.4.3 Unravelling the magnetic signature: End-member analysis. 201
7.4.4 Magnetic enhancement at the hydrocarbon-fluid contacts 204
7.5 Conclusions 208
Chapter 8: Conclusions 209
8.1 Petroleum Systems and Basin Modelling 210
8.1.1 Future Research- Basin Modelling 211
8.2 Identifying a Magnetic Proxy for Hydrocarbon Migration 212
8.2.1 Future Research- Magnetic Proxy 213
8.3 A New Magnetic Technique for Identifying Hydrocarbon Fluid Contacts 214
8.3.1 Future Research- Fluid Contacts 214
List of References 216
Appendices 233
Appendix 1 234

1.1 Acquisition and processing parameters....234
1.2 Synthetics used for interpretation....236
1.3 Time and depth maps of interpreted surfaces....237
1.4 Time depth relationships for wells used in the velocity model....248
Appendix 2....249
2.1 Lithology Logs....249
Appendix 3....273
3.1 Hysteresis, FORC, LT experiment and Susceptibility vs Temperature....273
Appendix 4....320
4.1 Measured hysteresis parameters for all wells, with gas and oil water contacts highlighted. The contacts were identified using composite logs....320

List of Figures

Figure 1.1. Gross depositional environment (GDE) of the Tay fan across the North Sea. Study area is highlighted in green and available 3D data obtained from PGS and TGS is highlighted by the red polygon. GDE map obtained from OGA data release. 29

Figure 1.2. Classification of magnetic mineral properties which also shows the spin alignment in ferromagnetism. Modified from Tauxe (2010). 31

Figure 1.3. M vs H relationship for a) diamagnetic and paramagnetic materials and b) ferromagnetic materials- hysteresis loop measure for s63595 from well 21/25-04 in the study area. M_s- Saturation magnetisation, M_{rs}- saturation remanence and H_c- coercivity.....32

Figure 1.4. Diagrams showing a) single domain structure b) pseudo-single domain structure and c) multi domain structure. The dashed line represents the domain wall and the arrow show the direction of M_s in the domains. 34

Figure 1.5. Coercivity vs particle size for equal grains. Image modified from (Dunlop, 1981) using threshold values calculated by Dunlop and Özdemir (1997), Roberts et al. (2011) Nagy (2016) and Valdez-Grijalva et al. (2018b). 34

Figure 1.6. Illustration of construction and interpretation of FORC a) FORC measurement starts at H_r, with magnetization measurements along the FORC represented by M (H_r, H) en route back to positive saturation at the saturating field, H_{sat}. b) Illustration of how the FORC distribution ρ(H_r, H) is calculated at a point P using measurements from consecutive FORCs c) FORC diagram on H_b, H_a axis for s63615 from well 22/21-03 in the study area. d) FORC diagram rotated to the H_c, H_u axis for s63615 from well 22/21-03 in the study area. Smoothing factor (SF)=3. Figs. a and b were modified from Roberts et al. (2014). 36

Figure 1.7. FORC diagrams suggesting the presence of a) non-interacting SD and SP grains. b) interacting SD grains. c) Interacting SD grains with multi axial anisotropy or vortex behaviour d) SD and vortex structure (PSD) e) MD grains f) relatively bigger MD grains. Image modified from Roberts et al. (2018b). 37

Figure 1.8. Backscattered SEM images showing a) Authigenic Pyrrhotite plates in early Miocene marine sediments from Sakhalin, Russia. Image obtained from Weaver et al. (2002). b) fine grained greigite with coarser grained pyrite from early Pleistocene marine sediments from Crostolo River, Italy. Image obtained from Roberts and Weaver (2005). 40

Figure 1.9. Processes required for the alteration of magnetic minerals to other phases. Diagram obtained from work done by Dekkers (1989a), Butler (1992), Dunlop and Özdemir (1997), Dekkers et al. (2000) and Pan et al. (2000). 42

Figure 1.10. a) A plot of saturation remanent magnetization (M_s) versus pyrolysis temperature and b) a plot of the magnetic coercivity (B_c) against pyrolysis temperature for the Kimmeridge Clay, Oxford Clay and Blue Lias. Image obtained from Abubakar et al. (2015). 44

Figure 1.11. Magnetic susceptibility (•) and S- Ratio (+) ($IRM_{-0.03T}/IRM_{+2T}$) vs depths from producer wells a) GF -1X and b) GF-2X and non-producer well c) GF -13X. Image obtained from Costanzo-Alvarez et al. (2000). 46

Figure 1.12. model for the formation of magnetic minerals in shale under burial conditions. The left column represents the concentration of the newly formed minerals. The central column is a sedimentary column from surface to 10 km. the right Colum shows the unblocking temperature spectra of chemical remanent magnetization (CRM) and thermoviscous remanent magnetization (TVRM). After Aubourg et al. (2012). 49

Figure 2.1. Map showing the principal structure of the North Sea Rift Basin. The green rectangle is the study area. Image modified from Koša (2007) using data from OGA's data release. 52

Figure 2.2. Effects of salt on the basin evolution of Western trough central graben modified from Hodgson et al. (1992). 55

Figure 2.3. Map of subcrop to Base-Jurassic unconformity. The results suggest a concentric to elliptical area of uplift and erosion. Image obtained from Underhill and Partington (1993). 58

Figure 2.4. Generalised Central North Sea stratigraphic column showing depositional facies, tectonic history, source rock, possible reservoirs, seal and timing of hydrocarbon migration. Useful stratigraphic/seismic horizons are identified. Note: Evaporites above the Permian is as a result of halokinesis 61

Figure 2.5. Lithostratigraphic column showing the Central North Sea Graben lithostratigraphic nomenclature of Knox & Holloway (1992). 62

Figure 2.6 Kimmeridge Clay identified by high gamma ray response. Kimmeridge Clay varies in depth form 4150m in the east to about 1700m in the west. Inset highlights the location of the wells in the study area. 66

Figure 2.7 .Well-log correlation of Tay and Forties sandstone members. Both sandstone members are interbedded with mudstones. The Forties sandstone thins to the wast. Inset is showing the location of the wells in the study area. 69

Figure 2.8 Location of the fields in the area. The study was done with cores from 19 oil/ gas wells, 1 dry well and cuttings from two dry wells. The red polygon represents the 3D data available. 71

Figure 2.9. Diagram showing the Tay fan system modified from Jones et al. (2003). The box highlights the study area. Black arrows represent areas of vertical migration in to the Tay and the green arrows represent areas of lateral hydrocarbon migration within the Tay. 73

Figure 3.1. The workflow used for seismic depth conversion. A velocity model for the 3D cube is generated using the interpreted seismic horizons and well tops. The selected velocity model can then be used for a domain conversion (milliseconds to metres). Checkshot surveys

measure the travel time from a datum to a known depth. See Appendix 1 for the TDR for the wells 77

Figure 3.2 Location map showing wells used to generate a velocity model (red circles), wells used to test the velocity model (green circle) and 2D line (red) used in basin modelling. 77

Figure 3.3. Errors for the velocity models. a) velocity model using linvel for all the zones b) velocity model using adlinvel for all the zones and c) velocity model using a linvel for the first four zones and adlinvel for the last two zones. 79

Figure 3.4. Composite west-east of regional seismic line across the study area. showing structural geology of the CNS. 13 key horizons are interpreted highlighting how the salt affects the overlying structure. The red-box is the location of Figure 3.5 a. The green-box is the location of Figure 3.5 b. KM= Kimmeridge Clay. Insert showing location of seismic line. Faults are marked on in black. Seismic data courtesy of TGS and PGS. See Appendix 1 for the acquisition and processing information of the seismic data. 83

Figure 3.5. Seismic data showing sandstone intrusions (injectites- coloured yellow) seen in the west of the study area. a) is located in the red box highlighted in Figure 3.4 and b) is located in the green box highlighted in Figure 3.4. 84

Figure 3.6 Picture showing injectites observed in the Tay sandstone in well 28/09-03 22 km from the study area. a-b) small scale injectite c) large scale injection breccia. Pictures were taking from core stored in the BGS core repository in Keyworth, Nottinghamshire. 85

Figure 3.7 Present day structural and lithology model input to PetroMod. Red lines represent hydrocarbon wells while black lines represent dry wells. Insert shows the location of the 2D line in the study area. 87

Figure 3.8 Heat flow used in the basin model. Image modified from Scotchman et al. (2000) 88

Figure 3.9 Changes in TR and HI with time demonstrating the ability of equations 4.2 to estimate initial HI value. Black line shows an increase in TR from 0 to 10% while the red line shows the HI drop from an initial value 588 mgHC/gTOC to the present-day value of 530 mgHC/gTOC shown in the geochemistry report for well 21/25-12.....89

Figure 3.10 2D profile of the top of the Kimmeridge Clay showing the relationship between TR line map (black line) and present-day TOC line map (blue line) across the 2D profile. Uniform initial day TOC line map value of 15 % (red line) was obtained from Cayley (1987). 90

Figure 3.11. Examples of model calibration for wells: 21/29a-08: a) temperature and b) porosity); 21/25-02: c) temperature and d) porosity 22/22b-04: (e) temperature and f) R_0 obtained from Barnard and Bastow (1991) and 21/28a-02: g) temperature and h) R_0 obtained from well geochemistry report. Well locations are shown in Figure 3.7. The crosses represent the measured properties. Temperature data was obtained from the OGA and porosity was estimated using wire line logs from IHS. 93

Figure 3.12 Thermal maturity and hydrocarbon generation & expulsion patterns across the 2D section. a) Present day TR across the 2D section. TR vs time (black line), generation mass of gas vs time (dashed red line), generation mass of oil vs time (dashed green line), expulsion mass of gas vs time (red line) and expulsion mass of oil vs time (green line) at b) 57 km mark, c) 42 km mark d) 35 km mark and e) 31 km mark along the 2D profile. 94

Figure 3.13. Temperature vs time extract from the Top Tay sandstone member in well 22/22b-04 (blue line) which is located in the east and 21/28a-02 (red line) which is located in the west. Plot shows a rapid increase in temperature from the start of the Pliocene which is indicative of rapid burial and is responsible for the present-day overpressure seen in the CNS. Location of two wells are shown in Figure 3.7. 95

Figure 3.14. Hydrocarbon accumulation and migration as a function of time: a) 70 Ma- onset of migration, b) 30 Ma- migration into the Fulmar, c) 5*2* Ma-migration into base Chalk, d) *22* Ma- migration through chalk, e) *19* Ma- migration into the Forties and up salt diapir, f) 1*8* Ma-migration into the Tay, g) *7* Ma- continued migration into Tay and Forties, h) *7-3* Ma- onset of lateral migration in the Tay and Forties, I) 0 Ma- present day accumulation and migration. Note: all faults are toggled off. 98

Figure 3.15 Comparison of model with a) injectites in the east and b) no injectites in the study area which shows the lack of hydrocarbon in the Tay sandstones located in the east. 99

Figure 3.16. Modelled variation in present day TOC along the 2D profile with an initial TOC of 8 % (red line) and with an initial TOC of 20%. 100

Figure 3.17. Model simulated with initial TOC of a) 8 % showing a less accumulation in the reservoirs and b) 20 % showing similar accumulations in the Tay sandstone seen in the base case model (Figure 3.14 i) while greater accumulation is notices in the Forties sandstone.101

Figure 3.18. Model simulated using D+FP migration methods which differs to the base case model (D+IP). Both models were simulated with an initial TOC of 15 % 103

Figure 3.19. comparison of a) base case model with closed faults to b) the same model with open faults. Initial TOC of 15 % was used for both models. Faults property appears to have very little influence on the accumulation location and most of the accumulation volumes. 104

Figure 4.1 . Cross line 1438 from the 3D cube showing the poor seismic quality in the lower half of the section and lack of well penetration in the below the Kimmeridge Clay. Interpretation of seismic was guided by the formation tops (white boxes in wells 21/29a-06, 21/29a-08 and 21/28a-05). Seismic data courtesy of PGS 109

Figure 4.2. Amplitude extractions of the Tay and Forties sandstone members (a and c) used to obtain the lateral variation of facies in the Tay and Forties sandstone member (b and d) for input into PetroMod. The Sele facies model (e) was generated by mapping out locations of injectites in the survey area. RMS-Root Mean Square. 111

Figure 4.3. Cross line 1386 showing the presence of large scale injectites (orange lines) from the top of the Maureen formation in the W. This interpretation along with the injectites from the Forties sandstone member (Figure 3.5) were used to build the Sele formation facies model in Figure 4.2. 112

Figure 4.4 Ma.p showing the wells the Fulmar Formation has been interpreted (black circles) by the OGA and its thickness variation (coloured circles) across the study area. Map modified from OGA's data release maps. Red polygon is the study area. 112

Figure 4.5. Interpretation of near top Fulmar Formation across salt draped over the regional fault. a) 3D salt time map showing interpretation of Top Fulmar (black line) showing areas where the Fulmar is laterally consistent from e to w. b & d) examples on seismic where it is laterally consistent and c & e) examples on seismic where it broken up by a diapir or salt wall. 113

Figure 4.6. Present day facies model for the Fulmar Formation facies showing areas where salt pierced the Fulmar and the location of faults cutting through the Fulmar. 114

Figure 4.7. a) TR of the Kimmeridge Clay; expulsion of oil of oil only occurs at TR > 20 % (black line). Plots showing the total 116

Figure 4.8. Fulmar and top salt facies maps showing a) Areas of IP lateral migration of oil and gas in the Fulmar and areas of migration (mostly vertical) of oil through the chalk (red arrows) b) Darcy migration in the Base Chalk (marl) showing migration of oil to the west along with build-up of oil on structural highs which leads to vertical migration through the chalk (red arrow). This figure also demonstrates the oil can either bypass the salt diapir by moving around it or migrate up the diapir. 117

Figure 4.9. Location of present-day accumulations for a) Tay Sandstone Member b) Forties Sandstone Member c) Fulmar Formation. Note: The Fulmar faults are toggled off (not displayed). 119

Figure 4.10. Hydrocarbon mass versus time, depicting the timing of hydrocarbon migration into the Fulmar Formation in the study area. Note: The Fulmar faults are toggled off (not displayed). 120

Figure 4.11. Hydrocarbon mass versus time, showing the timing of hydrocarbon migration into the Forties Sandstone Member in the study area. Note: The Fulmar faults are toggled off (not displayed). 121

Figure 4.12. Hydrocarbon mass versus time showing timing of hydrocarbon migration into the Tay Sandstone Member in the study area. Note: The Fulmar faults are toggled off (not displayed). 122

Figure 4.13. West –East 2D line extracted from the 3D model (Figure 4.9). This line is similar to the 2D profile in Figure 3.14 enabling comparison of the two. 124

Figure 4.14. Map showing areas of vertical (red arrows) and lateral migration (green dots) of oil within the Tay SM. Vertical migration is prominent in the east while lateral migration is

prominent in the west. Areas of vertical migration in the west correspond to underlying Fulmar accumulations. Note: the red arrows on the top left appear horizontal because of a 3D modelling edge effect. 125

Figure 4.15. Location of present-day accumulations for a) Tay Sandstone Member b) Forties Sandstone Member c) Fulmar Formation with an initial TOC of 10%. Note Fulmar faults are toggled off. 127

Figure 4.16. Location of Present-day accumulations for a) Tay Sandstone Member b) Forties Sandstone Member c) Fulmar Formation with an initial TOC of 8%. Note Fulmar faults are toggled off. 128

Figure 4.17. Base case model simulated with no injectites. Results show an incomplete migration of oil into the Tay SM. 129

Figure 4.18. Present-day accumulations using D+FP migration method for a) Tay Sandstone Member b) Forties Sandstone Member c) Fulmar Formation. Note Fulmar faults are toggled off. 130

Figure 4.19. Modelled present-day accumulations for a base-case simulation with faults in the Fulmar FM acting as fluid for a) Tay Sandstone Member b) Forties Sandstone Member c) Fulmar Formation. Faults are represented by the red line. 131

Figure 4.20. Testing undrilled prospect by changing facies to the west to sandstone (see Figure 4.2 c for base case input facies) and running simulations with present day TOCs of a) 15 % and b) 10%. 133

Figure 4.21. Input facies models for simulations run with horizontal variation of facies for a) Mid Tay SM, b) Near-base Tay SM, c) Mid Forties SM and d) Near-base Forties SM. 134

Figure 4.22. Modelled present day accumulations for simulation run with a more detailed facies input (Figure 4.21) for a) Tay SM with an initial TOC of 15 % b) Forties SM with an initial TOC of 15 % c) Tay SM with an initial TOC of 10 % and d) Forties SM with an initial TOC of 10 %. Note: the model predicts oil accumulation in the mudstone in the Forties SM, this is actually accumulation in the mid–base Forties Sandstone facies below the mudstone. 135

Figure 5.1. Example of composite logs (UK well 21/27a-06) used to identify the presence or absence of hydrocarbon in the Tay sandstone member and if the reservoir unit was cored and recovered or not. The increase in resistivity suggests the presence of hydrocarbon and can be used to identify fluid contacts. Formation density and neutron porosity logs are used to identify the presence of gas. This well is only an oil well and contains no gas. Composite logs were obtained from IHS. ROP is the Rate of Penetration. Depth is measured from the top of the rotary table. 140

Figure 5.2. Picture comparing water wet sandstone to the oil stained sandstones in UK well 21/25-06. 141

Figure 5.3. Column chromatography set up used to separate the aliphatic constituents from the organic matter extracts. 144

Figure 5.4. a) Representative hysteresis loop showing a strong ferromagnetic behaviour within the sample. Sample S63594 from well 21/25-04. b) Representative noisy hysteresis loop showing a strong paramagnetic behaviour within the sample. Sample S63598 from well 21/25-04.....145

Figure 5.5. Plot comparing the M_s and M_{rs} values in oil stained sandstones (green), water wet sandstones (blue), sandstones in the gas cap (red) and siltstones (grey). Wells are arranged from east to west with predominantly vertical migration in the east and lateral migration in the west. Note: high M_s and M_{rs} values observed at the hydrocarbon contacts are not shown in the plot.....148

Figure 5.6. Plot comparing the H_c values in oil stained sandstones (green), water wet sandstones (blue), sandstones in the gas cap (red) and siltstones (grey). Wells are arranged from east to west with predominantly vertical migration in the east and lateral migration in the west. Note the various scale ranges on the vertical axes. 148

Figure 5.7. Plot comparing the susceptibility values in oil stained sandstones (green), water wet sandstones (blue), sandstones in the gas cap (red) and siltstones (grey) for two different frequencies. Wells are arranged from east to west with predominantly vertical migration in the east and lateral migration in the west. Note: high susceptibility values observed at the hydrocarbon contacts are not shown in the plot and the various scale ranges on the vertical axes. 149

Figure 5.8. Plot comparing the χ_{FD} (FDF)in oil stained sandstones (green), water wet sandstones (blue), sandstones in the gas cap (red) and siltstones (grey). Wells are arranged from east to west with predominantly vertical migration in the east and lateral migration in the west. 149

Figure 5.9. Representative samples from well 21/29a-08 showing an abundance of siderite relative to Iron sulphides. a) LT and HT experiments suggests the presence of siderite, magnetite and iron sulphides, b) LT and HT experiments suggests the presence of siderite, magnetite and some iron sulphides, c) LT and HT experiments suggests the presence of siderite and magnetite and d) LT and HT experiments suggests the presence of siderite and magnetite. No FORC diagram available as samples were very weak with high levels of noise with a significant paramagnetic signal. Samples were heated in argon. 152

Figure 5.10. Representative samples from well 21/28a-04 showing an almost even mixture of siderite and Iron sulphides with probably more siderite. a) LT and HT experiments suggests the presence of siderite, magnetite and iron sulphides, b) LT and HT experiments suggests the presence of siderite, magnetite and some iron sulphides, c) LT and HT experiments suggests the presence of siderite, magnetite and iron sulphides and d) LT and HT experiments suggests the presence of siderite, magnetite and iron sulphides. No FORC diagram available as samples were very weak with high levels of noise with a significant paramagnetic signal. Samples were heated in argon.....153

Figure 5.11. Representative samples from well 21/28a-03 showing an almost even mixture of siderite and Iron sulphides with probably more Iron sulphides. a) LT and HT experiments suggests the presence of iron sulphides, some siderite and magnetite. FORC diagram suggest the presence of PSD gains. b) LT and HT experiments suggests the presence maghemite and iron sulphides. FORC diagrams suggests the present of SD grains with vortex structure and multiaxial anisotropy c) LT and HT experiments suggests the presence of siderite, magnetite and iron sulphides. FORC diagram suggest the presence of SP greigite and SD grains d) LT and HT experiments suggests the presence of maghemite and iron sulphides. VARIFORC parameters (Egli, 2013) for smoothing FORCs are $s_{c,0} = 2$, $s_{c,1} = 4$, $s_{b,0} = 3$, $s_{b,1} = 4$ and $\lambda_c = \lambda_b = 0$, measuring time= 200 ms. Samples were heated in argon. PSD= pseudo single domain, SD= Single domain and SP = Superparamagnetic (see Chapter 1).....154

Figure 5.12. Representative samples from well 21/27a-06 showing an abundance of Iron sulphides relative to siderite a) LT and HT experiments suggests the presence of iron sulphides and magnetite. The noisy FORC diagram suggests the presence of SP grains. b) LT and HT experiments suggests the presence magnetite and iron sulphides. FORC diagrams suggests the present of SP grains. c) LT and HT experiments suggests the presence of iron sulphides. FORC diagram suggest the presence of SP greigite and SD grains with vortex structure or multiaxial anisotropy. d) LT and HT experiments suggests the presence iron sulphides. FORC diagram suggest the presence of SP greigite and SD grains with vortex structure or multiaxial anisotropy. VARIFORC parameters (Egli, 2013) for smoothing FORCs are $s_{c,0} = 4$, $s_{c,1} = 4$, $s_{b,0} = 5$, $s_{b,1} = 5$, and $\lambda_c = \lambda_b = 0$,measuring time= 200 ms. Samples were heated in argon for susceptibility measurements. Ani = Multiaxial anisotropy or single vortex structure, SD = Single domain and SP = Superparamagnetic. 155

Figure 5.13 Representative samples from well 21/24-03 showing an abundance of Iron sulphides relative to siderite a) LT and HT experiments suggests the presence of iron sulphides and magnetite. The FORC diagram suggests the presence of SP and SD grains. b) LT and HT experiments suggest the presence maghemite and iron sulphides. c) LT and HT experiments suggest the presence of iron sulphides and magnetic. FORC diagram suggests the presence SD grains with vortex structure or multiaxial anisotropy. d) LT and HT experiments suggest the presence iron sulphides. FORC diagram suggests the presence of SP greigite and SD grains with vortex structure or multiaxial anisotropy. VARIFORC parameters (Egli, 2013) for smoothing FORCs are $s_{c,0} = 2$, $s_{c,1} = 3$, $s_{b,0} = 3$, $s_{b,1} = 3$, and $\lambda_c = \lambda_b = 0.1$, , measuring time= 200 ms. Samples were heated in argon for susceptibility measurements. Ani = Multiaxial anisotropy or single vortex structure, SD = Single domain. 156

Figure 5.14. A goethite test on samples a) s72399 from well 21/25-A1 and b) s63605 from well 21/25-04. The drop-in remanence at 300 K suggests some of the remanence in the sample is carried by goethite. M goethite is the percentage drop in remanence at room temperature. 158

Figure 5.15. HT-susceptibility heating and cooling in argon for a) s63605 from well 21/25-04 in CNS, and b) natural pyrite from Imperial College mineral repository.....159

Figure 5.16. (a-b) HT susceptibility curves with heating in argon, compared with thermomagnetic curves heated in vacuum at 100 mT (c-d) for sample s65311 from well21/28a-08 and S65328 for well 21/27-04. Both samples are oiled stained sandstone. Note the increase in magnetisation at 720 °C on cooling in s65311 (c) is due to the MPMS delaying to cool down the sample after the maximum temperature was reached. All curves suggest the presence of greigite. 160

Figure 5.17. SEM Images showing a) Greigite (G) or pyrite (Py) crystals in s65329 b) Two fused coarse-grained euhedral pyrite framboids surrounded by possibly smaller cubic greigite crystals in s65328 c) likely elongated greigite framboid in s65311 d) evidence of bioturbation in s63594 highlighted with a "B", and e) evidence for bioturbation in s65328, also highlighted with a "B". Images a-c are backscattered electron images obtained with a Phenom SEM while images d-e are backscattered electron images obtained with a Leo SEM. 162

Figure 5.18. Mass chromatograph of aliphatic hydrocarbon fractions in samples from dry well core 21/28b-07 a) s70402, b) s70403, c) s70404.....163

Figure 5.19. Samples from dry well 21/28b-07 a) s70402- LT and HT experiments suggests the presence of magnetite with a MD grain size b) s70403- LT experiments suggest the presence of magnetite and possibly monoclinic pyrrhotite and biogenic magnetite. The FORC diagram suggests the presence of a high H_c phase and c) s70404- LT and HT experiments suggest the presence of magnetite and siderite. VARIFORC parameters (Egli, 2013) for smoothing FORCs are $s_{c,0} = 3$, $s_{c,1} = 3$, $s_{b,0} = 4$, $s_{b,1} = 3$ and $\lambda_c = \lambda_b = 0.1$, measuring time= 200 ms. HT susceptibility measurements were heated in argon. BT - Besnus transition, BM - biogenic magnetite and M - magnetite, and MD – Multidomain. 165

Figure 5.20. Plot comparing the susceptibility values measured at 990 and 6000 Hz in oil stained sandstones (green), water wet sandstones (blue), and sandstones in the gas cap (red) Wells are arranged from east to west with predominantly vertical migration in the east and lateral migration in the west. Note: high susceptibility values observed at the hydrocarbon contacts are not shown in the plot. 167

Figure 5.21. Distribution of siderite and iron sulphides (predominantly greigite) in **oil-stained sandstones** in the Tay fan. Areas with predominantly one behaviour are grouped together in coloured ellipses. The abundance of iron sulphides increases along the lateral migration pathway. Background image is RMS amplitude map of Tay Fan. Insert shows the location of the map. 172

Figure 5.22. Distribution of siderite and iron sulphides (predominantly greigite) in **water-wet sandstones** in the Tay fan. Siderite is the most abundant mineral in the water wet sandstones. Background image is RMS amplitude map of Tay Fan. Insert shows the location of the map. 173

Figure 5.23. Distribution of siderite and iron sulphides (predominantly greigite) in the **siltstones** in the Tay fan. The abundance of iron sulphides increases along the lateral migration pathway and the siltstones are generally iron sulphide rich. Background image is RMS amplitude map of Tay Fan. Insert shows the location of the map. 173

Figure 5.24 Distribution of siderite and iron sulphides (predominantly greigite) in **all the core samples** (average of Figure 5.21 to Figure 5.23) in the Tay fan. The abundance of iron sulphides increases along the lateral migration pathway. Some well names are included are reference. Background image is RMS amplitude map of Tay Fan.Insert shows the location of the map. Note: 21/27-03 is a well with evidence for oil. 174

Figure 6.1. Schematic of the magnetic results plotted on a 2D slice of the 3D model shown in Figure 4.9. This figure shows the siderite rich signal in areas dominated with vertical migration and an increasing presence of greigite along the lateral migration pathway. Diagram is not drawn to scale. 178

Figure 6.2 Map showing the variation of API gravity in the Tay fan. API generally reduces from east to west. The red line denotes the Tay fan, the black is the 3D data coverage and red circles are the locations of the wells used to generate the contour plot. API data was obtained from purchased geochemical reports from IHS. Some well names are included for referencing. Insert shows the location of the map. 180

Figure 6.3. Plots of temperature (blue line) and liquid mass of oil (black line) vs time in the top Tay reservoir for wells a) 21/28-04 b) 21/29a-08 c) 21/29a-06 and d) 21/24-03. An increase in liquid mass suggests charging of the well while a reduction indicates loss of oil, because it has moved along the fill spill chain or it has leaked to the surface. Location of the wells are shown in Figure 6.2 and Figure 5.24. Plots are extracts from the PetroMod model shown in Figure 4.9. 181

Figure 6.4. Simplified sketch illustrating the time-line (a to d) of magnetic mineral formation, and oil migration and maturity. The total time period is 30 Myrs. Black layer is the Kimmeridge Clay, the dotted layer is the Tay Sandstone member and the white layers are the carrier beds and seal a) downward migration of early mature oil into the Fulmar FM which migrates west b) capillary failure in the west leads to vertical migration of early mature oil into the Tay SM while downwards and upwards migration of mid-late mature oil occurs in the east c) expulsion of more mature oil leads to replacement of early mature oil with mid-late mature oil in the west traps in the Fulmar FM and mid-mature oil in the E traps in the Tay SM. d) continued vertical migration of mid- late mature oil and gas leads to a mixture of early mature oil and mid- late mature oil in some traps in the Tay SM. 183

Figure 6.5 Petromod 3D model output highlighting timing of oil formation and its eventual the accumulation. Most of the early mature oil migrated west as predicted in Figure 6.4. Tay sandstone has been greyed out for enhanced visibility. Insert showing location of survey. Note: only the oil accumulations that were sampled in the core store are shown in this image. 184

Figure 6.6. PetroMod 3D image showing the locations of oil seepage from 1 Ma to present day. Leakages of oil in the east leads to magnetite leaking to the surface while leakages of oil in the west would lead to magnetite and greigite leaking to surface. This would correspond to

an increase in wave number from the east to the west provided the background signal has been accurately subtracted and the minerals do not alter at shallower depths. 186

Figure 7.1. Wireline logs for well 21/25-04. GR- gamma ray log, ILD- Deep induction log used to determine formation resistivity, RHOB- density log and NPHI- neutron porosity Log. A decrease in resistivity indicates a change from hydrocarbons to formation water.....191

Figure 7.2. Cycling cooling/warming curves and FC/ZFC curves for a) pure Kaolinite clay- noisy signal, b) oil sample from well 21/24-02- cycling and warming curves suggest the presence of magnetite and possibly monoclinic pyrrhotite in the sample. c) oil sample from well 21/29a-08 - cycling cooling and warming curves suggest the presence of magnetite in the sample. 193

Figure 7.3. M_s (green line), M_{rs} (black line), susceptibility measured at 990 Hz (red line) and 6000 Hz (blue line) for samples from wells 21/25-A1 (a and d), 21/25-04 (b and e) and 21/29a-09 (c and f). Distinct peaks are noticed at the GOC (red dashed line) and OWC (blue dashed line). GOC and OWC depths were obtained from wireline logs. All depths are below mean sea level. Measured hysteresis parameters for other wells are shown in Appendix 4. 194

Figure 7.4. LT experiments (cycling cooling, cycling warming, FC and ZFC), HT susceptibility experiments and FORC diagrams for samples in well 21/25-04. S63594; a) LT experiments suggest the presence of titanohematite or goethite and magnetite, b) HT experiment suggests a siderite rich sample and c) FORC diagram suggests a mixture of SP grains with multi axial anisotropy or a vortex structure and PSD grains. S63596 at the GOC; d) LT experiments suggest the presence of titanohematite or goethite and magnetite, e) HT experiment suggests a siderite rich sample with some iron sulphides and f) FORC diagram suggests a mixture of SD grains with multi axial anisotropy or vortex structure and PSD grains. S63598; g) LT experiments suggest the presence of titanohematite or goethite and magnetite, h) HT experiment suggests a siderite rich sample and i) FORC diagram suggests a mixture of SP grains with multi axial anisotropy or a vortex structure and PSD grains. S63599 at the OWC; j) LT experiments suggest the presence of hematite, siderite and magnetite, k) HT experiment suggests a siderite rich sample and l) FORC diagram suggests the presence of SD grains. S63600; m) LT experiments suggest the presence of titanohematite or goethite and magnetite, n) HT experiment suggests a siderite rich sample and o) FORC diagram suggests the presence of SP grains. VARIFORC parameter (Egli, 2013) for FORC smoothing are $s_{c,0}$ = 1.2, $s_{c,1}$ = 3, $s_{b,0}$ = 3, $s_{b,1}$ = 5, and λ_c = 1 λ_b = 1. For the HT susceptibility measurements, the samples were heated in argon.....195

Figure 7.5 LT experiments (cycling cooling, cycling warming, FC and ZFC), HT susceptibility experiments and FORC diagrams for samples in well 21/25-A1. S72396; a) LT experiments suggest the presence of titanohematite or goethite and magnetite, b) HT experiment suggests a siderite rich sample and c) FORC diagram suggests the presence of SP grains with multi axial anisotropy or a vortex structure. S72397 at the GOC; d) LT experiments suggest the presence of titanohematite or goethite and magnetite, e) HT experiment suggests a mixture of siderite and iron sulphides and f) FORC diagram suggests a mixture of SP and SD grains with multi axial

anisotropy or vortex structure. S72399; g) LT experiments suggest the presence of titanohematite or goethite, siderite and magnetite, h) HT experiment suggests the presence of siderite and iron sulphides and i) FORC diagram suggests the presence of SP grains with multi axial anisotropy or vortex structure. S72403 at the OWC; j) LT experiments suggest the presence of titanohematite or goethite and magnetite, k) HT experiment suggests the presence of siderite and iron sulphides and l) FORC diagram suggests the presence of SD greigite grains. S72406; m) LT experiments suggest the presence of titanohematite or goethite and magnetite, n) HT experiment suggests an iron sulphide rich sample and o) FORC diagram suggests the presence of SP grains. VARIFORC parameter (Egli, 2013) for FORC smoothing are $s_{c,0}$ = 1.2, $s_{c,1}$ = 3, $s_{b,0}$ = 3, $s_{b,1}$ = 5, and λ_c = 1 λ_b = 1. For the HT susceptibility measurements, the samples were heated in argon. 196

Figure 7.6 SEM images on the Phenom desktop SEM a) s63597 EDX confirms FeS Framboid. SEM images on the LEO SEM; b and c) s63598 from well 21/25-04, and d) s63600 from well 21/25-04. Py- pyrite, M- magnetite and G- greigite. 199

Figure 7.7. FORC-PCA for well 21/25-04. a) principal-component space, b) end member 2 represents SD particles with multi axial anisotropy, c) end member 1 represents thermally relaxing SD particles and d) proportions of EM1 and EM2 as a function of depth showing an increase in proportion of EM2 at the GOC and OWC. VARIFORC parameter (Egli, 2013) for FORC PCA smoothing are $s_{c,0}$ = 1.2, $s_{c,1}$ = 3, $s_{b,0}$ = 3, $s_{b,1}$ = 5, and λ_c = 1 λ_b = 1. 202

Figure 7.8. FORC-PCA for well 21/25-A1. a) principal component plane, b) end member 1- thermally relaxing SD particles, c) end member 2- thermally relaxing SD particles with multi axial anisotropy, d) end member 3- stable SD greigite particles and e) proportions of EM1, EM2 and EM3 as a function of depth showing an increase in proportion of EM3 at the GOC and OWC. VARIFORC parameter (Egli, 2013) for FORC PCA smoothing are $s_{c,0}$ = 1.2, $s_{c,1}$ = 3, $s_{b,0}$ = 3, $s_{b,1}$ = 5, and λ_c = 0 λ_b = 0. 203

Figure 7.9 A schematic detailing the formation of SD grains at the GOC and OWC: a) formation of SD grains at the top of the oil during early reservoir filling, b) oil has filled to the spill point and the precipitation of SD grains occur at a stable OWC, c) the reservoir is charged with gas which dissolves in the oil, and the OWC is still stable which results in continued precipitation of SD grains, and d) a gas cap is formed displacing oil and the SD grains formed at the top of the oil column down to the GOC. 206

Figure 7.10. Plots of temperature (blue line) and liquid mass of oil (black line) vs time in the top Tay reservoir for wells a) 21/25-04 b) 21/25-A1. An increase in liquid mass suggests charging of the well while a reduction indicates loss of oil, because it has moved along the fill spill chain or it has leaked to the surface. Plots are extracts from the PetroMod model shown in Figure 4.9. 206

Figure 7.11. A schematic of the authigenic ferromagnetic magnetic mineral grain sizes as a function of depth within the reservoir. 207

List of Tables

Table 1.1. Magnetic properties of minerals important to this study. T_c is the Curie temperature while LT B (low-temperature behaviour) comments on the mineral's low temperature crystallographic transition temperature or describes its behaviour on cooling. Table modified from Tauxe (2010).....41

Table 1.2 Changes observed in minerals as they get buried deeper. LTS, MTS and HTS denote total sulphur levels. The magnetic contrasts are shown relative to background levels, an increase (+) or a decrease (-). U=unstable, S=Stable; or replaced by MAG=magnetite, SID=siderite, PY=pyrite, PYR=pyrrhotite and HEM=hematite. HC= hydrocarbon. Red box highlights the conditions closest to the reservoir conditions in the Tay sandstone member. Greigite was not included in these calculations. Table modified from Burton et al. (1993). .43

Table 3.1. Table showing wells with well tops for the different horizons. A tick means well tops were available while crosses indicate there were no well tops. Note: Not all horizons had well tops as some wells did not penetrate that horizon or the horizon was not identified on the composite log.....78

Table 3.2. Depth conversion errors for 10 wells distributed across the 3D cube. Errors were calculated by subtracting the horizon depth converted surface from its measured depth in the well logs. Negative errors mean the converted depth surfaces are deeper than well tops. For some surfaces well, tops were not available for error estimations. 80

Table 3.3. The 2D model's stratigraphic input data showing timing of deposition of horizons along with their lithology as well as timing of erosion (including amount of erosion) and hiatus events obtained from composite logs and study by Cayley (1987) and Underhill and Partington (1993).....82

Table 3.4. Table showing the timing of facies replacement caused by diapirism. Timing was estimated with the aid of PetroMod's burial reconstruction feature.....86

Table 3.5 Modified permeability parameters for selected layers. Permeability values obtained from Megson and Hardman (2001), *Mallon and Swarbrick (2008a)* Mallon and Swarbrick (2008b) and Kilhams et al. (2012).....87

Table 3.6. Hydrocarbons encountered in the wells on the 2D line (Figure 3.7). This information was used to calibrate the location of hydrocarbon accumulation in the 2D models. Information on the oil or gas shows was obtained from composite logs. × means no hydrocarbon accumulation was observed in the sandstone member or formation. 92

Table 3.7. Reservoir accumulation volumes as a function of initial TOC at location highlighted in Figure 3.17. The table shows the differences between accumulation volumes observed in base case model (15 % initial TOC) and accumulation volumes observed when an initial TOC of 8 and 20 % is used. The location of position a-d are shown in Figure 3.17. 101

Table 3.8 Reservoir oil accumulation volumes in MMbbls at locations highlighted in Figure 3.18 102

Table 3.9 Reservoir oil accumulation volumes in MMbbls at locations highlighted in Figure 3.19. F- Faults.....104

Table 4.1. Timing of facies replacement caused by diapirism. Timing was estimated with the aid of PetroMod's burial reconstruction feature. 115

Table 4.2. Table showing the total accumulation of oil in the Fulmar FM, Forties SM and Tay SM shown in Figure 4.9. Note these numbers cannot be compared to published data as PetroMod typically over estimates volume calculations (Hantschel and Kauerauf, 2009)...118

Table 4.3. Total accumulation volumes of oil and gas in the reservoirs when the initial TOC is changed to 10 or 8 %. The table also shows the differences from the base-case model (BC) shown in Table 4.2. 126

Table 4.4. Total accumulation volumes of oil and gas in the reservoirs when no injectites are modelled. The table also shows the differences from the base case model (BC) shown in Table 4.2. A negative difference means the accumulation volumes are greater than the base case model. The additional oil in the Forties is to be expected given the removal of the easy vertical migration pathway provided by the injectites. 129

Table 4.5 Total accumulation volumes of oil and gas in the reservoirs when D + FP migration method is used. The table also shows the differences from the base case model (BC) shown in Table 4.2. A negative difference means the accumulation volumes are greater than the base case model. 130

Table 4.6. Total accumulation volumes of oil and gas in the reservoirs when the Fulmar FM faults are acting as fluid conduits. The table also shows the differences from the base case model (BC) shown in Table 4.2. A negative difference means the accumulation volumes are greater than the base case model. 132

Table 4.7. Total accumulation volumes of oil and gas in the reservoirs when a more detailed facies model is used with initial TOC's of 15 and 10%. The table also shows the differences from the base case model (BC) shown in Table 4.2. A negative difference means the accumulation volumes are greater than the base case model 135

Table 5.1. Mean and median of measured M_s, M_{rs} and susceptibility (χ) in wells in the study area. All measured sample types are included in the calculation as the samples in the gas cap, oil stained samples, water wet samples and siltstones typically have similar values as shown in Figure 5.5, Figure 5.6 and Figure 5.7. Hydrocarbon wells are roughly arranged from east to west. Note: The last 3 wells are dry. Only well 21/28b-07 is cored, the other two wells (21/25-11 and 21/25-12) are cuttings. n is the number of samples 146

Table 5.2. Groups of magnetic minerals belong to background and source signals. Background signals are minerals that are likely present prior to the invasion of oil, while the source signal refers to minerals precipitated or introduced after the charging of the well by oil. 170

List of Publications

Berndt, T. A., Chang, L., Wang, S., & Badejo, S. 2018. Time-Asymmetric FORC Diagrams: A New Protocol for Visualizing Thermal Fluctuations and Distinguishing Magnetic Mineral Mixtures. Geochemistry, Geophysics, Geosystems, 19, 1- 28. doi:10.1029/2018GC007669.

Badejo, S. A.,Muxworthy, A. R., Fraser, A., Stevenson, G. R., Zhao, X. and Jackson, M. 2019. Identification of magnetic enhancement at hydrocarbon/water contacts. Paper ready for submission in AAPG Bulletin

Badejo, S. A.,Muxworthy, A. R., Fraser, A., Neumaier, M., Stevenson, G. R. and Davey, R 2019 Using magnetic techniques to calibrate lateral hydrocarbon migration in petroleum systems modelling: A Case Study from the Lower Tertiary, UK Central North Sea. Paper in preparation.

Badejo, S. A.,Muxworthy, A. R., Fraser, A., Neumaier, M., 2019 3D Petroleum Systems Modelling as an exploration tool in mature basins: A case study from the Central North Sea, UK. Paper in Preparation.

List of Abbreviations

Magnetic terminology

Curie temperature (T_c)

Néel temperature (T_N)

Frequency-dependent susceptibility factor (χ_{FD})

Saturation magnetisation (M_s)

Saturation remanence (M_{rs})

Coercive force (H_c)

Single-domain (SD)

Pseudo-single domain (PSD)

Multi domain (MD)

Isothermal remanent magnetisation (IRM)

Saturation isothermal remanence magnetization (SIRM)

Thermoremanent magnetisation (TRM)

Chemical remanent magnetisation (CRM)

Viscous remanent magnetisation (VRM)

Methodology terminology

Scanning Electron Microscope (SEM)

Energy Dispersive X-ray (EDX)

Gas Chromatography – Mass Spectroscopy (GC-MS)

Field cooling curves at 2.5 T (FC)

Zero-field cooling curves (ZFC)

Room-temperature (RT)

Low-temperature (LT)

High-temperature (HT)

Variable-Field Susceptibility Meter (VFSM)

Chapter 1

Introduction

1.1 Brief Introduction to Thesis

The use of rock magnetic methods for the prospecting of hydrocarbon accumulations is a relatively underutilised field. Studies have suggested low-altitude aeromagnetic surveys may be a complimentary method to conventional exploration techniques in remote areas (Donovan et al., 1984; Foote, 1984; Saunders and Terry, 1985). These studies related the presence of magnetic anomalies (short wavelength) at shallow depths to the tertiary migration (or seepage) of hydrocarbons from the reservoir below. The reducing conditions generated by hydrocarbons at shallow depths has been shown to cause the chemical alteration of iron bearing minerals to authigenic iron oxides and/or iron sulphides (e.g. Reynolds et al., 1990; Machel and Burton, 1991a;1991b; Reynolds et al., 1991; Burton et al., 1993; Machel, 1995; Emmerton et al., 2012). Magnetic minerals such as magnetite, pyrrhotite and greigite are typically precipitated, while hematite is replaced or dissolved (e.g. Reynolds et al., 1991; Costanzo-Alvarez et al., 2000; Emmerton, 2013; Abubakar et al., 2015); I discuss these magnetic minerals in detail in Section 1.3. Non-magnetic iron-rich minerals, such as pyrite and siderite, can also be precipitated (Burton et al., 1993; Machel, 1995; Emmerton et al., 2012). The resulting balance of magnetic and non-magnetic iron-rich minerals depends on the local environment, which can lead to positive or negative magnetic, anomalies, but can also lead to no contrast (Elmore et al., 1987; McCabe et al., 1987; Elmore et al., 1993a).

Studies on shallow sediments and reservoir core samples have found higher magnetic susceptibility and magnetic hysteresis parameters (see section 1.2) in zones invaded by hydrocarbons relative to non-invaded zones (the background signal) in the same area (Costanzo-Alvarez et al., 2000; González et al., 2002; Liu et al., 2006; Guzmán et al., 2011; Emmerton et al., 2012). The higher signal has been attributed to the presence of fine grained authigenic magnetic minerals. These minerals are not necessarily precipitated in the reservoirs or seepage zones; Abubakar et al. (2015) demonstrated the formation of authigenic fine grained (< 100 nm) magnetite, greigite and pyrrhotite in the oil kitchen, which are small enough to form complexes with the oil and travel through the pore throats of the carrier beds and reservoir (Nealson, 2009).

Very few studies have attempted to find a correlation between magnetic mineralogy and hydrocarbon migration and accumulation in the reservoir. In his PhD thesis at Imperial College

London, Rabiu Abubakar (2016) hinted at the increasing presence of magnetite along the migration pathway in core samples from the Wessex Basin, UK, however, the tectonic history of the Wessex Basin is very complicated, and the magnetic findings were inconclusive.

To better understand this link between hydrocarbon migration and magnetic mineralogy, I will examine an area with relatively simple, well constrained geology to verify the concepts hinted at by Abubakar (2016). For this purpose, this thesis concentrates on the Tertiary Tay fan in the Western Central Graben, North Sea, UK (Figure 1.1). The Tay sandstone member has been selected for the reasons listed below:

- The Tay sandstone member is not deformed (other than some gentle salt doming), is laterally continuous with long-distance lateral migration of up to 50 km for oil and 32 km for gas (Cayley, 1987; Kubala et al., 2003).
- The Tay sandstone member is a good quality reservoir with high porosity and permeability (Banner et al., 1992).
- High quality 3D seismic data is available over most of the study area.
- There are a high number of wells in the area with good core coverage.

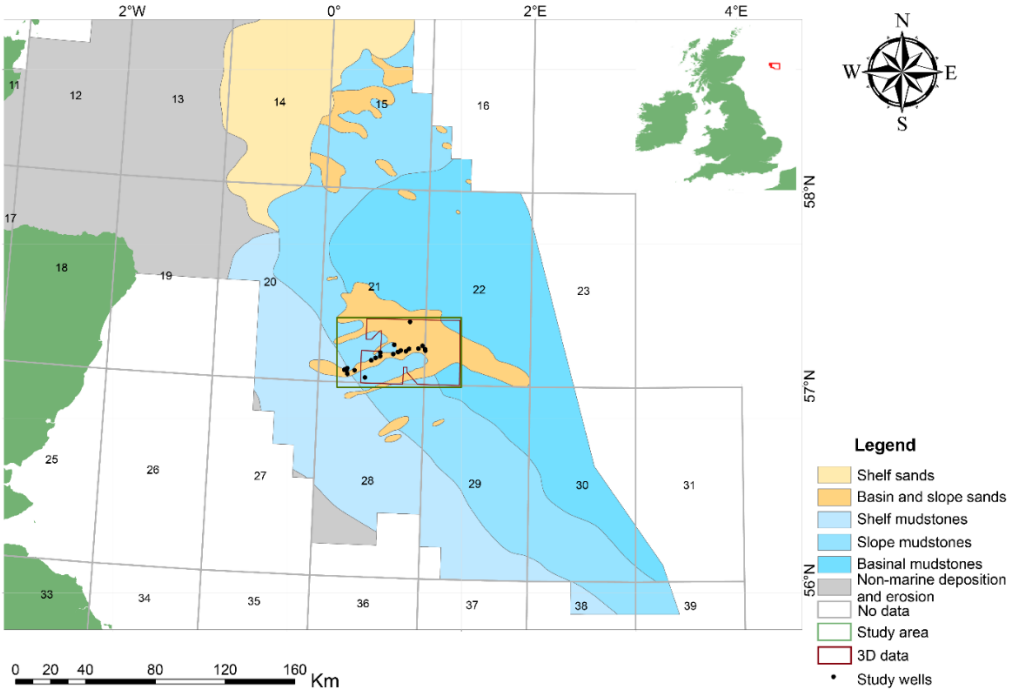


Figure 1.1. Gross depositional environment (GDE) of the Tay fan across the North Sea. Study area is highlighted in green and available 3D data obtained from PGS and TGS is highlighted by the red polygon. GDE map obtained from OGA data release.

Planned Research

This thesis has two main routes of investigation: 1) determining the hydrocarbon migration pathways within the Tay fan using petroleum systems modelling, and 2) understanding the magnetic mineralogy of hydrocarbon bearing sediments within the Tay fan. Rock magnetic techniques are used to determine the morphology, abundance, mineralogy and size of the magnetic minerals in core samples from the Tay fan. This information is synthesised to answer the following questions:

1. Which magnetic minerals are authigenic products of diagenetic changes caused by the infiltration of hydrocarbons?
2. Are the minerals precipitated in the reservoir or do they travel from the source?
3. Are there any obvious differences between the oil-stained samples, samples in the gas column and water wet samples?
4. How do the magnetic minerals change across the hydrocarbon fluid contacts?
5. Can magnetic minerals be used as direct hydrocarbon indicators?
6. Is there a link between biodegradation and magnetic mineralogy?
7. Can magnetic techniques be used to calibrate petroleum systems models?

1.1 Review of Magnetisation

1.1.1 Fundamentals of Magnetism

Magnetisation and Magnetic susceptibility

Magnetisation **M** is the net magnetic moment (**m**) per unit volume, it has dimensions A/m. The external magnetic field **H** and **M** are related by (Butler, 1992) :

$$\mathbf{M} = \mathbf{M_0} + \chi\mathbf{H} \qquad \text{Equation 1.1}$$

where M_0 is the net magnetisation in the absence of the field, $\chi\mathbf{H}$ is the induced magnetisation where χ is the magnetic susceptibility (Butler, 1992). The magnetic response to an applied field can be normalised by volume or by mass. This response varies depending on the magnetic mineral.

Classes of Magnetic Minerals

The magnetic property of a material is described by the spin and orbital motion of its electrons, electron interactions and its response to magnetic fields (Butler, 1992). These magnetic behaviours are classified into five categories: diamagnetism, paramagnetism, ferromagnetism, antiferromagnetism or ferrimagnetism. The magnetic properties of solids are described in Figure 1.2:

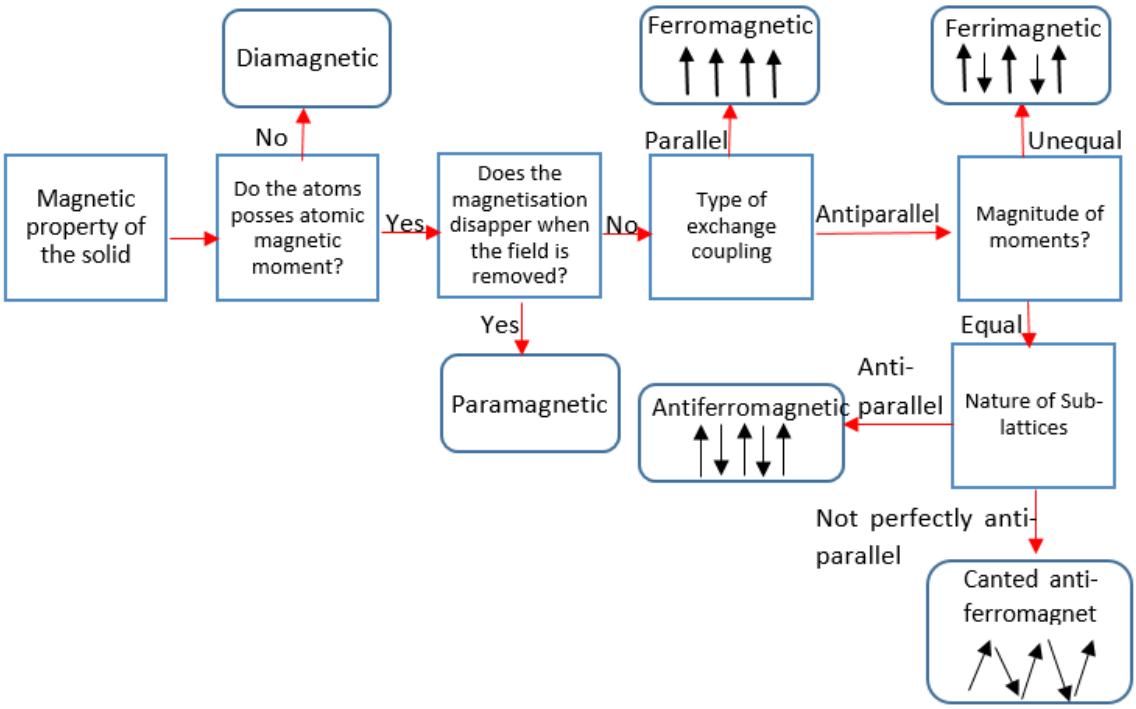


Figure 1.2. Classification of magnetic mineral properties which also shows the spin alignment in ferromagnetism. Modified from Tauxe (2010).

Diamagnetism (Figure 1.2) is the fundamental property of all matter but is very weak. In diamagnetic materials the atoms have no net magnetic moment (Butler, 1992), however, in the presence of a field a negative magnetisation is produced via Lenz's Law; the susceptibility is negative (Figure 1.3 a). Water and quartz are examples of common diamagnetic materials.

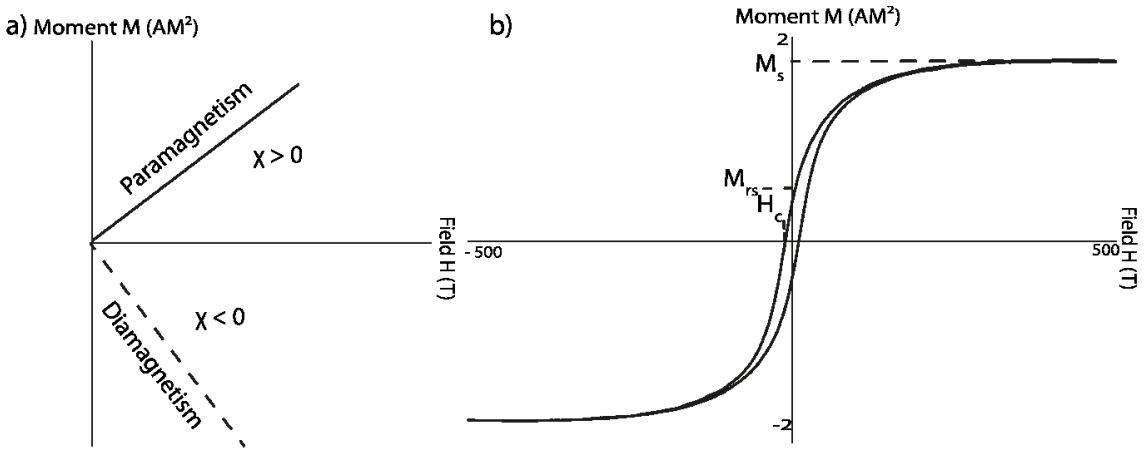


Figure 1.3. M vs H relationship for a) diamagnetic and paramagnetic materials and b) ferromagnetic materials- hysteresis loop measure for s63595 from well 21/25-04 in the study area. M_s- Saturation magnetisation, M_{rs}- saturation remanence and H_c- coercivity.

In paramagnetic and ferromagnetic moments (*sensu lato)* materials (Figure 1.2), atoms consist of unpaired electrons via Pauli's exclusion principle (Tauxe, 2010), giving rise to a net magnetic moment for each atom (Evans and Heller, 2003). If there is no ordering of these moments, then in the absence of an applied field, the net magnetisation is zero, and the system is said to be paramagnetic (Evans and Heller, 2003). If a field is applied to paramagnetic material the atomic moments align with the field, giving rise to a positive susceptibility (Figure 1.3 a), however, on removing the field the magnetisation returns to zero due to thermal fluctuation effects. Pyrite (FeS_2) is a common paramagnetic mineral found in sediments.

In ferromagnetic materials *(sensu lato)*, the atomic moments align due to quantum mechanical exchange coupling (Tauxe, 2010). The coupling interaction can be parallel or antiparallel alignment depending on the crystal structure (Butler, 1992). Ferromagnetic minerals *(sensu lato)* have net magnetisations even in the absence of a magnetic field, giving rise to a spontaneous magnetisation that has net non-zero value even in the absence of an applied field. Such materials can retain a memory of the applied field, that results in features like hysteresis (Fig. 1.2b). On heating, the thermal energy eventually overcomes the exchange coupling and produces a randomising effect. This occurs at the Curie temperature (T_C); below this temperature the material is ordered, above it is disordered (paramagnetic) (Tauxe, 2010).

In ferromagnetic materials (*sensu stricto)* the coupling is positive, and the atomic magnetic moments are parallelly aligned (Figure 1.2). In antiferromagnetic materials (Figure 1.2)

antiparallel coupling is observed between neighbouring spins of equal magnetic moments resulting in a zero net moment (Butler, 1992). Canted antiferromagnetism (Figure 1.2) is observed if the neighbouring spins are tilted at an angle resulting in very small net magnetisations (Dunlop and Özdemir, 1997). Hematite has a canted antiferromagnetic ordering (Butler, 1992). In ferrimagnetic materials (Figure 1.2) antiparallel coupling is observed between neighbouring spins, but negative coupling is asymmetric and there is a resultant net magnetisation (Tauxe, 2010). Macroscopically these materials are very similar to ferromagnets (*sensu strictu*). An example of a ferrimagnetic mineral is magnetite.

1.1.2 Domain Theory

For small particles it is energetically favourable for the magnetisation to be magnetically uniform (Figure 1.4 a), termed single domain (SD) (Dunlop and Özdemir, 1997). As the particles become larger, to reduce magnetic flux leakage and the overall magnetostatic energy (e_m), it becomes favourable to break the magnetisation up into areas that are uniform, termed domains, separated by narrow high-energy domain walls. Such systems are termed multidomain (MD) (Butler, 1992) (Figure 1.4c). For magnetite the SD to MD transition is approximately 100 nm (Dunlop and Özdemir, 1997).

Large SD grains (Figure 1.4a) are magnetically stable with high coercivity (Figure 1.5), where the coercivity is a measure of stability. When measuring a hysteresis loop, the applied field reaches a sufficient level, where the material is saturated, i.e., it has a saturation magnetisation (M_s). Removing this field gives a remanent saturation magnetisation (M_{rs}). To reduce the magnetisation to zero a reverse field (coercive force, H_c) is applied. Very small SD grains (< 30 nm for magnetite at room-temperature) are unstable due to thermal fluctuations and are termed superparamagnetic (SP). The SP/SD transition depends on temperature, measurement time and mineralogy, so it is hard to define, and the term SP is frequently used to describe thermally relaxing behaviour on laboratory time-scales. For example, a simple tool to identify SP grains is to measure AC susceptibility at different frequencies. In SP grains the measured susceptibility vary with frequency; larger grains, i.e., > 40 nm, are essentially invariant to frequency (Muxworthy, 2001).

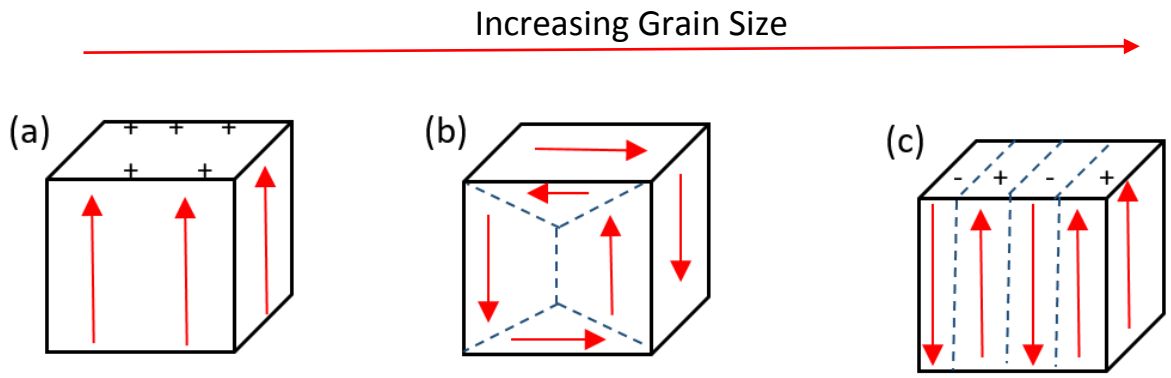


Figure 1.4. Diagrams showing a) single domain structure b) pseudo-single domain structure and c) multi domain structure. The dashed line represents the domain wall and the arrow show the direction of M_s in the domains.

Multi-domain grains (MD) are grains bigger than SD grains with multiple domain walls (Figure 1.4 c). They are magnetically unstable with low-remanences and coercivity (Figure 1.5). Pseudo-single domain grain (PSD) are small MD grains with SD like characteristics (Figure 1.4 b). PSD grains have high coercivity (Figure 1.5) and high remanence, and are bigger than SD grains, but smaller than MD grains. The PSD to MD transition is not sharply defined, but is of the order of 3 µm for magnetite (Nagy, 2016).

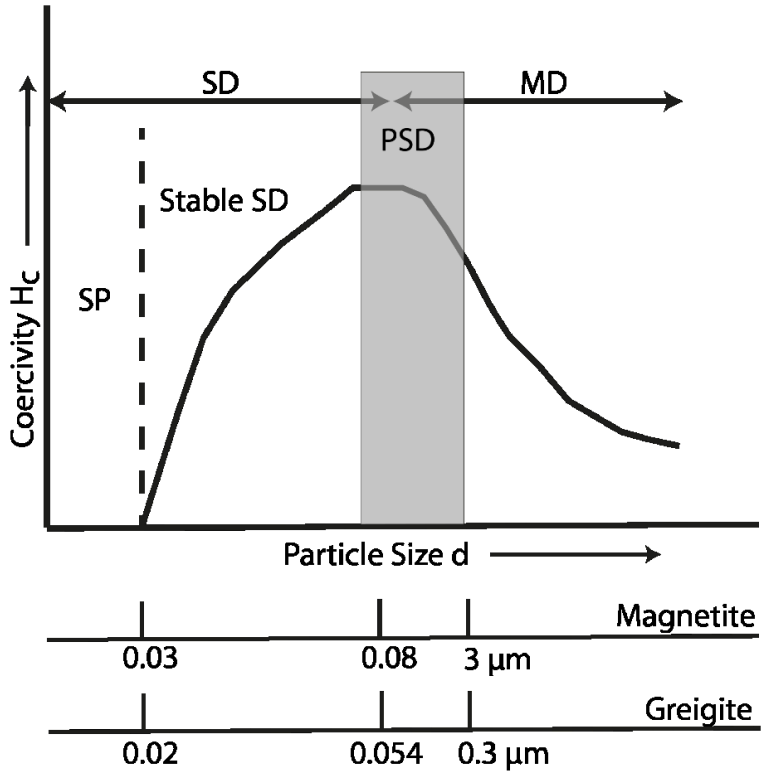


Figure 1.5. Coercivity vs particle size for equal grains. Image modified from (Dunlop, 1981) using threshold values calculated by Dunlop and Özdemir (1997), Roberts et al. (2011) Nagy (2016) and Valdez-Grijalva et al. (2018b).

Magnetic hysteresis parameters (Figure 1.3c) can be used to infer magnetic mineral grain sizes, via coercivity estimates, however, as can be seen from Fig. 1.4, this can give rise to non-unique solutions.

The coercivity of remanence (H_{cr}) is the negative field required to get the sample to have zero remanence. Plotting M_{rs}/M_s vs. H_{cr}/H_c (Day plot) (Day et al., 1977) is typically used to determine domain states but can lead ambiguous diagnosis (Roberts et al., 2018a). In this thesis, first-order reversal curves (FORCs) diagrams are used to identify grain sizes (see the next section).

1.1.3 Identifying domain states using First-order Reversal Curve diagrams

First-order reversal curve (FORC) diagrams (Pike et al., 1999; Roberts et al., 2000) provide information about the magnetic response of the minerals in a sample in terms of the coercivity (Figure 1.5) and magnetic interactions of the magnetic particle (x and y axis of the FORC diagram respectively). This section contains a brief introduction of FORC diagrams and describes typical interpretations of FORC diagrams. See Roberts et al. (2014) for a more detailed overview of FORC diagrams.

What are FORC Diagrams?

A FORC is a partial hysteresis loop (Figure 1.6a), which is measured by saturating a sample in a large positive field (H_{sat}), this field is then decreased to a reversal field H_r, and a FORC measured. A FORC is defined as the magnetisation curve observed when the field is increased from H_r to H_{sat} (Roberts et al., 2000). The magnetization at any field **H** with reversal field H_r is denoted as $M(H_r, H)$ as shown in Figure 1.6a. Multiple FORCs measured for a range of H_r values are needed to obtain gridded magnetisation measurements (Figure 1.6b) used to create a FORC distribution. The FORC distribution is the mixed second derivative of the magnetisation in field space; the FORC diagram is a contour plot of this distribution (Figure 1.6c). FORC diagrams are typically rotated counter clockwise by 45° from the (H_a, H_b) for aesthetic purposes as shown in Figure 1.6c, to the x-y Cartesian axes (H_c, H_i) shown in Figure 1.6d.

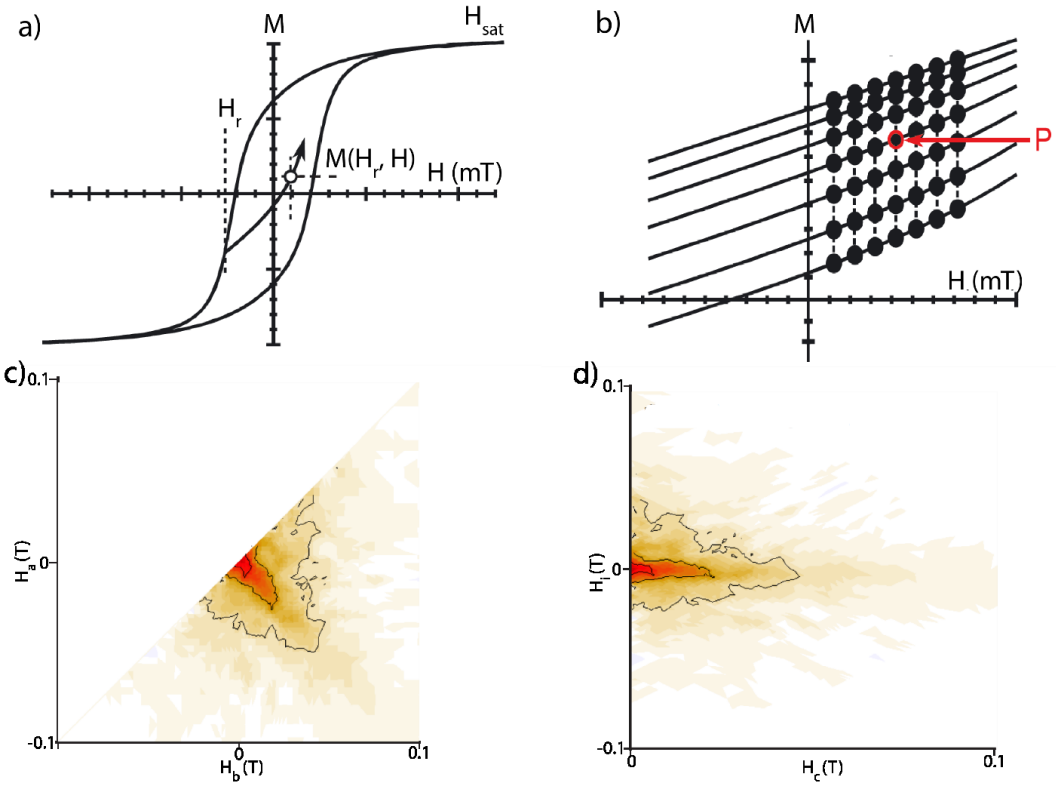


Figure 1.6. Illustration of construction and interpretation of FORC a) FORC measurement starts at H_r, with magnetization measurements along the FORC represented by M (H_r, H) en route back to positive saturation at the saturating field, H_{sat}. b) Illustration of how the FORC distribution ρ(H_r, H) is calculated at a point P using measurements from consecutive FORCs c) FORC diagram on H_b, H_a axis for s63615 from well 22/21-03 in the study area. d) FORC diagram rotated to the H_c, H_u axis for s63615 from well 22/21-03 in the study area. Smoothing factor (SF)=3. Figs. a and b were modified from Roberts et al. (2014).

In this thesis, a slope-corrected hysteresis loop for each sample was used to generate irregular-spaced FORC measurement grids with the aid of the experimental protocol (xFORC) designed by Zhao et al. (2015). This protocol is preferred to the conventional measurement protocol, because it has been proven to reduce measurement time and improve signal-to-noise ratios (Zhao et al., 2015).

Interpretation of FORC Diagrams

FORC diagrams for different domain states are shown in Figure 1.7. Interpretations for these domain states are described below:

- FORC diagrams containing a ridge like distributions along the H_c axis (Figure 1.7 a) suggest the presence of non-interacting SD grains (Pike et al., 1999).
- FORC diagrams containing a concentric peak with vertical spread on the H_i axis (Figure 1.7 b-d) suggest the presence of interacting SD grains (Roberts et al., 2000). A negative peak below the H_i = 0 axis(Figure 1.7b-c) is also indicative of SD mineral assemblages (Muxworthy et al., 2004).

- A positive peak below the $H_i = 0$ axis (Figure 1.7a) suggests the presence of thermally relaxing single domain grains (SP grains) (Roberts et al., 2014).
- PSD is expressed as a positive lobe (Figure 1.7d) in the lower half of the FORC diagram at $H_c < 100$ mT (Roberts et al., 2017).
- Multiaxial anisotropy is expressed on the FOROC diagram as a steeply dipping negative region to the right of the B_u axis (Harrison and Lascu, 2014; Valdez-Grijalva and Muxworthy, 2019) as seen in Figure 1.7c. This feature may also be due to SD vortex behaviour (Lascu et al., 2018; Valdez-Grijalva et al., 2018a)
- Vertical spread on the H_i axis (Figure 1.7e-f) suggests the presence of MD grains (Roberts et al., 2000).

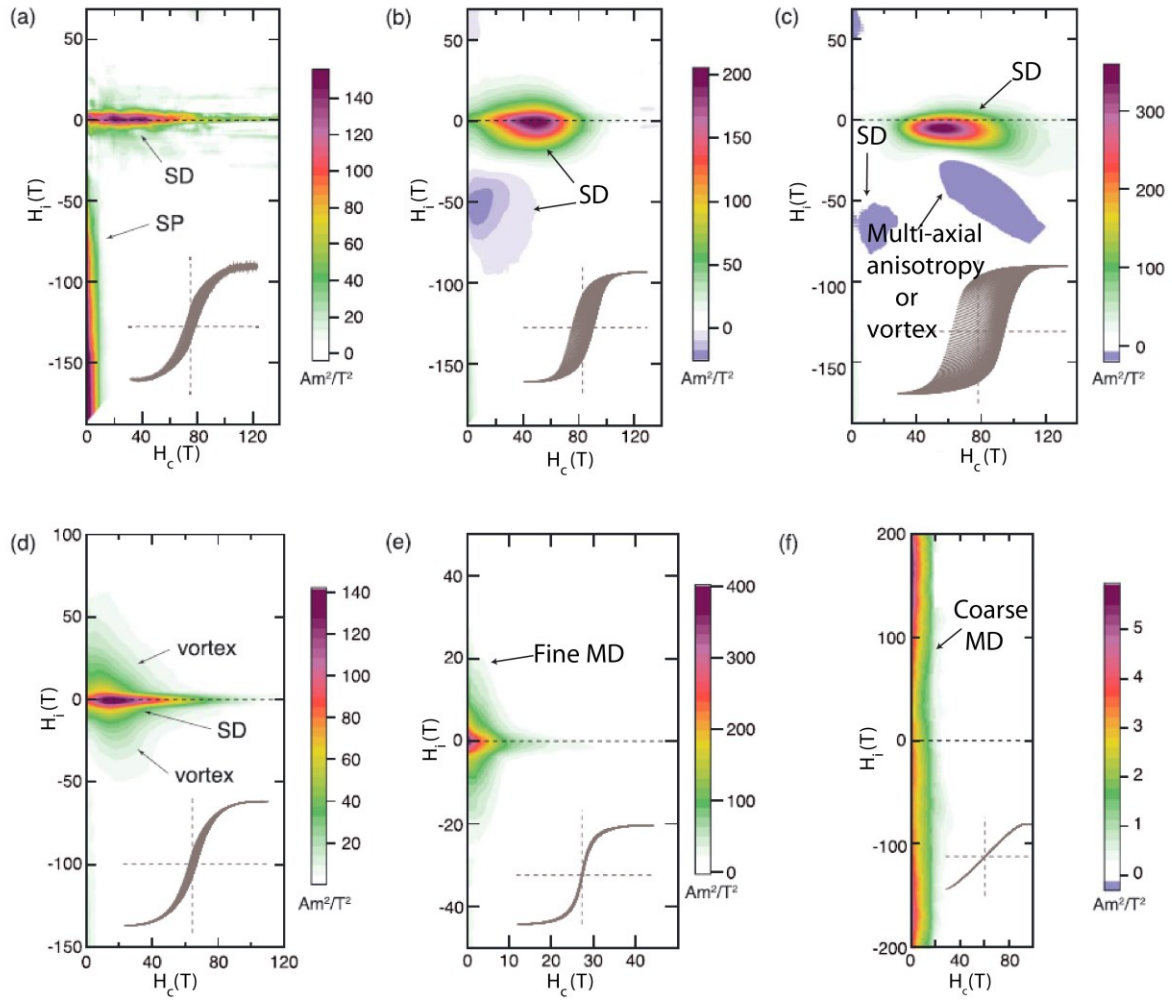


Figure 1.7. FORC diagrams suggesting the presence of a) non-interacting SD and SP grains. b) interacting SD grains. c) Interacting SD grains with multi axial anisotropy or vortex behaviour d) SD and vortex structure (PSD) e) MD grains f) relatively bigger MD grains. Image modified from Roberts et al. (2018b).

1.2.4 Magnetic Remanence

Some of the magnetic remanences seen in nature and the laboratory are described below:

Natural Remanent Magnetisation (NRM)

The NRM is the magnetisation in a sample before any experiments. It is dependent on the geomagnetic field imparted by geological processes during rock formation and during its history (Dunlop and Özdemir, 1997). The NRM is typically composed of two or more components; primary and secondary. The primary component is acquired during the rock formation while the secondary components are acquired during the rock history and can obscure or alter the primary component (Butler, 1992). Most palaeomagnetic studies investigate the primary NRM component.

Thermoremanent magnetisation (TRM)

This is the NRM acquired by cooling from a temperature above the Curie temperature (T_c). This is common in igneous and metamorphic rocks. TRM is stable over geological time periods, because it is acquired at high temperatures where energy barriers are low and stabilises on cooling to lower temperatures where energy barriers are relatively higher (Tauxe, 2010).

Chemical Remanent Magnetisation (CRM)

This is acquired when chemical changes form or alter ferromagnetic minerals below their blocking temperature in the presence of a magnetic field (Dunlop and Özdemir, 1997). The chemical changes are either growth of new minerals or chemical alteration of existing minerals.

Isothermal Remanent Magnetisation (IRM)

This is acquired when a rock/sample is exposed to a strong magnetising field at a constant temperature for a short amount of time. If the sample is saturated (i.e. M_s in Figure 1.3b) it is referred to as an SIRM (Saturation Isothermal Remanent Magnetisation) (Tauxe, 2010). It can be acquired naturally by lightning strikes (Butler, 1992).

1.2.5 Magnetic Mineralogy

In natural magnetic systems we are primarily interested in the presence of ferromagnetic (*sesnu lato*) iron oxides, sulphides and oxyhydroxides plus non-magnetic iron-rich phases than can act as source of iron for ferromagnetic minerals, e.g., pyrite and siderite.

Iron Oxides

Magnetite (Fe_3O_4 or $Fe^{2+}Fe_2^{3+}O_4$) is abundant on earth and magnetically strong. It occurs in igneous, sedimentary and metamorphic rock. Magnetite is a ferrimagnetic mineral with a cubic inverse spinel structure. At 125 K the crystal structure is distorted to a monoclinic structure; this is called the Verwey transition (T_V) (Verwey, 1939). This transition is typically accompanied by a sharp drop-in remanence and is used to identify the presence of magnetite in natural samples. Magnetite can also be identified by its Curie temperature (T_c) at 580 ^oC (Dunlop and Özdemir, 1997).

When magnetite is fully oxidised at room temperature it becomes **maghemite** (γ-Fe_2O_3) (Dunlop and Özdemir, 1997). It is magnetically similar to magnetite and has an inverse spinel structure with a T_c of about 645 ^oC and no T_V. It is difficult to estimate the T_c of maghemite because between 250 and 750 ^oC it inverts to weakly magnetic **hematite** (α-Fe_2O_3). Hematite is a canted-antiferromagnetic mineral with a Néel temperature (T_N) and T_c of 675 ^oC (Butler, 1992); above T_N it becomes paramagnetic. Below 250 K the canted antiferromagnetism becomes a perfect antiferromagnetic, this is called the Morin Transition (Morin, 1950).

Titanohematite (Fe_y^{2+} $Fe^{3+}_{2-2y}Ti_y^{4+}O_3^{2-}$) has magnetisation similar to hematite as its antiferromagnetic with weak ferromagnetism (Sprain et al., 2016). The Néel/Curie temperature of titanohematite varies from 300^oC to room temperature, decreasing linearly with Ti substitution (Burton et al., 2008; Sprain et al., 2016). Titanohematite found in sedimentary rocks are typically weathering products of metamorphic rocks (Kennedy, 1981; Ozima et al., 1992). **Titanomagnetite** is also abundant in metamorphic rocks, specifically TM60 ($Fe_{2.4}Ti_{0.6}O_4$) (Tauxe, 2010), which is the magnetic phase common to Mid-Ocean Ridge Basalts (MORBs). Single-phase titanomagnetites $Fe_{3-}Ti_xO_4$ ($0 \leq x \leq 1$) are inverse spinels, increasing the substitution of titanium (x) weakens the exchange coupling and decreases the Curie temperature (Dunlop and Özdemir, 1997).

Iron Sulphides

Iron sulphides constitute a diverse group of solids that play important roles in sedimentary systems. Magnetic iron sulphides can have biogenic, diagenetic, hydrothermal or detrital origins (Horng and Roberts, 2006; Roberts et al., 2011; Chang et al., 2014; Rudmin et al., 2018). **Greigite** (Fe_3S_4) is typically found in anoxic sulphate-reducing sedimentary environments. In this environment it is known to form as a precursor to paramagnetic **pyrite** (FeS_2) (Berner, 1984; Kao et al., 2004). Greigite can also be produced by anaerobic bacteria in natural environment (Mann et al., 1990). Greigite has a thiospinel structure, is strongly ferrimagnetic and can be identified in sediments by its T_c and T_N of about 330 ^oC (Dunlop and Özdemir, 1997).

Pyrrhotite ($Fe_{1-x}S$) has a range of crystal structures, magnetic properties and compositions ($0< x< 0.13$); monoclinic pyrrhotite (Fe_7S_8) is ferrimagnetic while hexagonal pyrrhotite (Fe_9S_{10}) is antiferromagnetic at room temperature (Dekkers, 1989b). Monoclinic pyrrhotite is typically detrital in origin as it is unable to grow fast enough to be a diagenetic product. Monoclinic pyrrhotite can be identified in samples by its low- temperature transition at 34 K or its T_c at 330 ^oC (Dekkers, 1989b; Rochette et al., 1990). Unlike monoclinic pyrrhotite, hexagonal pyrrhotite is typically a diagenetic product. Its formation has been linked to the anaerobic oxidation of methane and formation of gas hydrates (Roberts, 2015). It has no low temperature transition but can be identified in samples by its T_c of 265 ^oC (Dekkers, 1989b). Magnetically it can be hard to distinguish between pyrrhotite and greigite, however, optically they are quite distinct. Pyrrhotite typically has a needle/ sheet like crystal suture (Figure 1.8a) in backscattered SEM images while greigite (Figure 1.8b) typically has a cubic structure (Roberts, 2015).

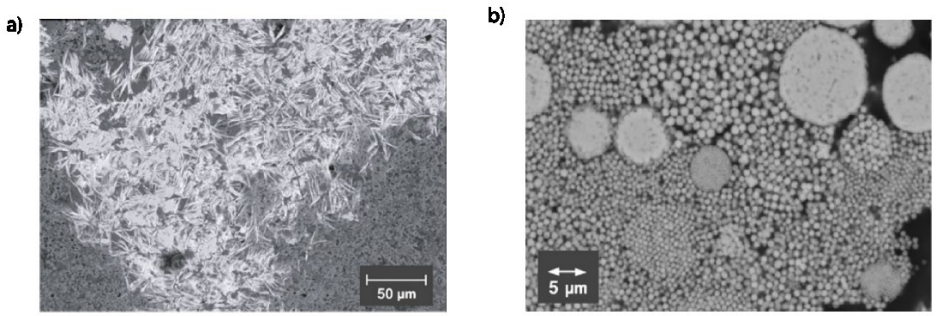


Figure 1.8. Backscattered SEM images showing a) Authigenic Pyrrhotite plates in early Miocene marine sediments from Sakhalin, Russia. Image obtained from Weaver et al. (2002). b) fine grained greigite with coarser grained pyrite from early Pleistocene marine sediments from Crostolo River, Italy. Image obtained from Roberts and Weaver (2005).

Iron Carbonates and Iron Oxyhydroxides

Siderite ($FeCO_3$) is an iron-bearing carbonate of authigenic origin, is common in sedimentary settings and it is typically precipitated in anoxic environments (Larrasoaña et al., 2007). It is paramagnetic at room temperature but is ferromagnetic in the presence of a field (at temperatures < 40 K) with a Néel Temperature of 38 K (Jacobs, 1963; Frederichs et al., 2003). **Goethite** (α FeOOH) is common in soil and sediments, is antiferromagnetic but the spin component is imperfect, allowing a small net moment (Banerjee, 1970). Goethite has a Néel/Curie temperature of 120^{o}C (Dunlop and Özdemir, 1997; Evans and Heller, 2003). It is important to this study as it can be a weathering product of iron bearing minerals (Dunlop and Özdemir, 1997).

In this thesis magnetic minerals are usually identified by their Curie temperature or low temperature behaviour. The properties for the minerals important to this study are summarised in Table 1.1.

Table 1.1. Magnetic properties of minerals important to this study. T_c is the Curie temperature while LT B (low-temperature behaviour) comments on the mineral's low temperature crystallographic transition temperature or describes its behaviour on cooling. Table modified from Tauxe (2010).

Mineral	Composition	Magnetic order	T_c (°C)	LT behaviour (K)
Magnetite	Fe_3O_4	Ferrimagnetic	580	120
Titanohematite	$Fe_y^{2+}Fe^{3+}_{2-2y}Ti_y^{4+}O_3^{2-}$	Ferrimagnetic	150-200	Increase in remanence on cooling
Maghemite	γFe_2O_3	Ferrimagnetic	unstable	Hump noticed on cooling
Hematite	αFe_2O_3	Canted antiferromagnetic	675	250
Goethite	αFeOOH	Antiferromagnetic	120	Increase in remanence on cooling
Greigite	Fe_3S_4	Ferrimagnetic	330	none
Monoclinic Pyrrhotite	$Fe_{1-x}S$	Ferrimagnetic	320	34
Hexagonal Pyrrhotite	$Fe_{1-x}S$	Antiferromagnetic	265	none
Siderite	$FeCO_3$	Paramagnetic	none	34 K in the presence of a field

Diagenesis of magnetic minerals

Minerals form under a set of conditions which can subsequently change, e.g., an. increase in temperature or surface weathering. When this occurs, the minerals start to alter in order to come into equilibrium with the new conditions (Figure 1.9).

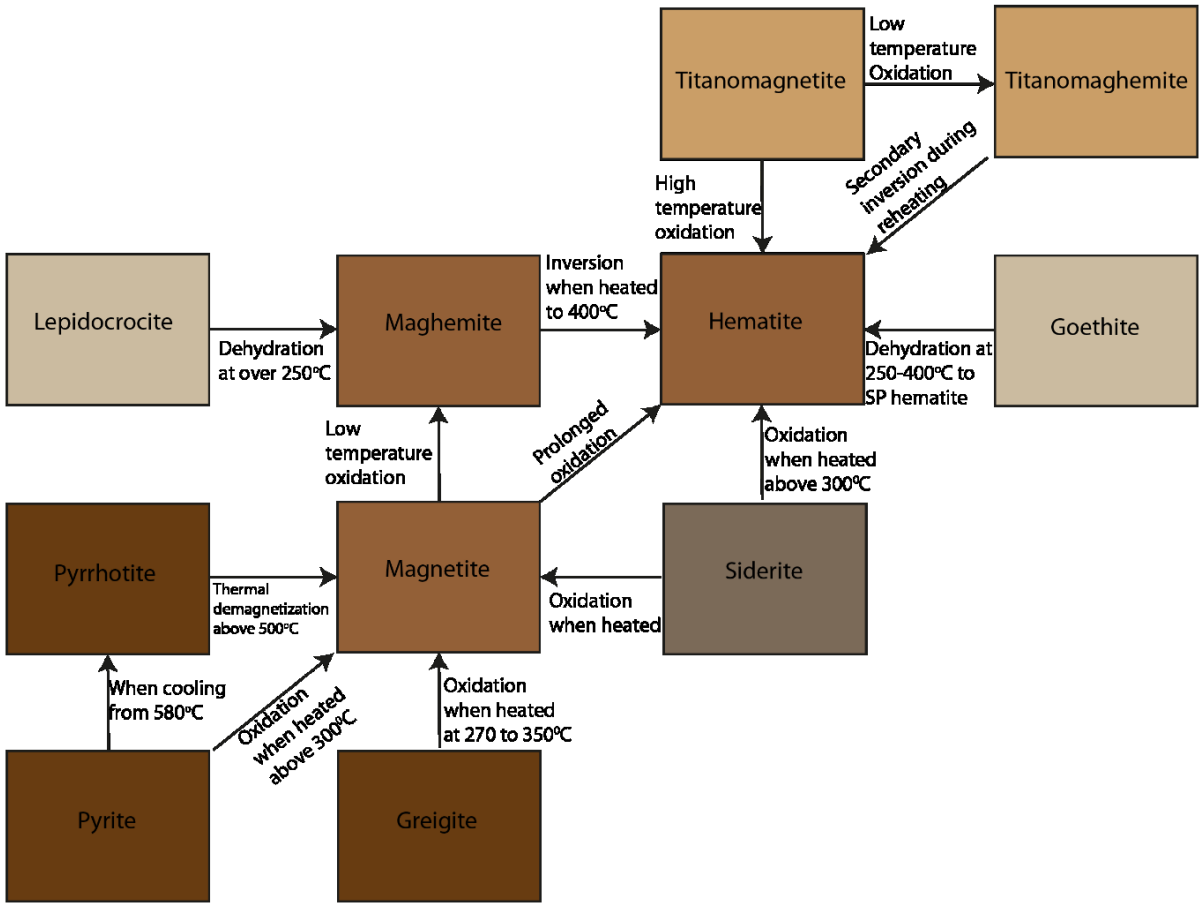


Figure 1.9. Processes required for the alteration of magnetic minerals to other phases. Diagram obtained from work done by Dekkers (1989a), Butler (1992), Dunlop and Özdemir (1997), Dekkers et al. (2000) and Pan et al. (2000).

Review of Hydrocarbons and Magnetism

This section describes the chemical and microbiological processes that are relevant to the formation and destruction of magnetic minerals in reducing conditions generated by hydrocarbons.

1.1.4 Chemical and Microbial Processes Responsible for Anomalous Magnetisation in Hydrocarbon Seepage Zones.

Vertical and lateral infiltration of oil into a reservoir or its migration through the overlying beds in cases of seal failure, results in diagenetic changes which can lead to an increase in

dissolved sulphur and metal content (Miiller et al., 1987). This along with changes in temperature, pressure, dissolved inorganic carbon, pore water Ph and Eh will affect the stability of certain magnetic minerals (Machel and Burton, 1991a; Machel, 1995).

Burton et al. (1993) used thermodynamic models to predict the stability of magnetic minerals present in near surface to deep burial (6000m) digenetic environments caused by hydrocarbon seepage. Twelve phase diagrams were generated and the results are summarised in Table 1.2. The table shows the stability of iron bearing minerals with increasing burial and their proximity to hydrocarbon seepages (zero, low and high concentrations).

Table 1.2 Changes observed in minerals as they get buried deeper. LTS, MTS and HTS denote total sulphur levels. The magnetic contrasts are shown relative to background levels, an increase (+) or a decrease (-). U=unstable, S=Stable; or replaced by MAG=magnetite, SID=siderite, PY=pyrite, PYR=pyrrhotite and HEM=hematite. HC= hydrocarbon. Red box highlights the conditions closest to the reservoir conditions in the Tay sandstone member. Greigite was not included in these calculations. Table modified from Burton et al. (1993).

		No HC Plume			Distant from HC Plume				Near HC Plume			
		Hem	Mag	Pyrrh	Hem	Mag	Pyrrh	+/-	Hem	Mag	Pyrrh	+/-
25 °C 1 bar	LTS	S	U	U	Mag/Sid	S/Sid	U	+/-	U	U	U	-
	MTS	S	U	U	Py	U	U	-	U	U	U	-
	HTS	S	U	U	Py	U	Py	-	U/Py	U	U	-
50 °C 150 bar	LTS	S	U	U	Mag/Sid	S/Sid	U	+/-	U	U	U	-
	MTS	S	U	U	Py	S/Sid	U	-	U/Py	U	U	-
	HTS	S	U	U	Py	U	S	+	Py	U	S	+/-
100 °C 300 bar	LTS	S	U	U	Mag	S/Sid	U	+/-	U	U/Sid	U	-
	MTS	S	U	U	Mag	S/Sid	U	+/-	Py	U/Sid	U	-
	HTS	S	U	U	Py	S/Pyrrh	S	+	Py	U	S	+/-
200 °C 600 bar	LTS	S	U	U	Mag	S/Sid	U	+/-	Mag	S/Sid	U	+/-
	MTS	S	U	U	Mag	S/Sid	U	+/-	Mag	S/Sid	U	+/-
	HTS	S	U	U	Mag	S/Pyrrh	S	+	Mag/Pyrrh	S/Pyrrh	S	+

The results presented in Table 1.2 suggests magnetic minerals are more likely to alter in close proximity to the hydrocarbon seepage. This alteration also increases with burial. The red box in Table 1.2 highlights the burial and levels of sulphur expected in the Tay sandstone member (the area of study in this thesis, see Chapter 2); moderate to high sulphur levels, near the hydrocarbon plume at temperatures between 50 and 100 °C. At these depths, hematite tends to alter to pyrite, magnetite is unstable or alters to siderite while pyrrhotite is only stable in high concentrations of sulphur.

To investigate possible chemical processes responsible for the precipitation of magnetic minerals in hydrocarbon reducing conditions, Abubakar et al. (2015) carried out pyrolysis experiments on immature type II Jurassic source rock samples from southern England (Kimmeridge Clay, Oxford Clay and Blue Lias). To simulate burial conditions, the samples were heated to required temperatures at a rate of 15^{o}C per minute with an applied pressure of 100 bar. On heating, an increase in magnetic hysteresis parameters was observed (Figure 1.10) suggesting magnetic minerals are inorganically precipitated during the onset of hydrocarbon generation. Transmission electron microscopy hinted at the presence of < 100 nm sized magnetite, pyrrhotite and greigite grains (Abubakar et al., 2015). The size of the magnetic minerals reported suggests they can form coordinate bonds with oil and migrate through carrier beds in a basin (Nealson, 2009); however, the sizes of magnetic minerals observed in the study of Abubakar et al. (2015) are likely not indicative of the grain sizes expected in nature. This is because in nature the source would have been heated at a much slower rate (typically 2 ^{o}C per Myr), which could lead to the generation of much larger grains (Pepper and Corvi, 1995). Additionally, the experiments reported by Abubakar et al. (2015) were also carried out at higher temperatures than would occur in nature, to facilitate realistic laboratory timescales. These higher temperatures would likely have led to different mineralogies having formed.

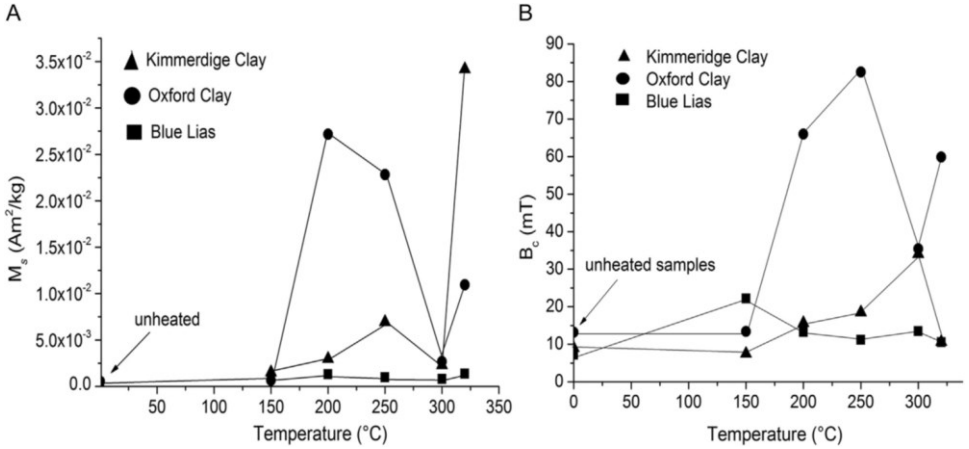


Figure 1.10. a) A plot of saturation remanent magnetization (M_s) versus pyrolysis temperature and b) a plot of the magnetic coercivity (B_c) against pyrolysis temperature for the Kimmeridge Clay, Oxford Clay and Blue Lias. Image obtained from Abubakar et al. (2015).

The presence of microbes complicates the thermodynamic models summarised in Table 1.2 and affects the stability of the magnetic minerals generated in the source. Microbes can promote the formation or destruction of magnetic minerals which are thermodynamically

unstable or stable respectively (Machel, 1995). For example, anaerobic bacteria could generate a thermodynamic disequilibrium by producing magnetite (extracellularly) in conditions where magnetite is unstable. This disequilibrium would likely continue until the conditions become inconducive to the bacteria. In oil fields the most common microorganisms are the anaerobic bacteria (Magot et al., 2000), their contributions to magnetic mineral assemblages are listed below:

- Anaerobic iron reducing bacteria (e.g. GS-15) can produce fine grained extracellular magnetite via the oxidation of certain organic compounds in hydrocarbons (Lovley et al., 1987; Brown et al., 1995).
- Anaerobic nitrite reducing bacteria can produce extracellular magnetite via the oxidation of Fe^{2+} (Chaudhuri et al., 2001).
- Iron reducing bacteria are not important to the formation of hematite but may contribute to its dissolution (Machel and Burton, 1991a; Bose et al., 2009).
- Anaerobic sulphate reducing bacteria (e.g. prokaryotes) generate reduced sulphur (such as H_2S) which combines with iron to produce iron sulphides like greigite and pyrrhotite (Morse et al., 1987; Mann et al., 1990). Some of these bacteria can also synthesis intracellular greigite or pyrrhotite (Mann et al., 1990).
- Some species of sulphate reducing bacteria (e.g. RS-1) can precipitate intracellular nanometric magnetite particles while also synthesising extracellular iron sulphide in hydrocarbon environments (McCabe et al., 1987; Sakaguchi et al., 1993). The distribution and importance of these organisms are unknown.

It is important to note that these microbes reduce the oil quality (biodegradation) and can only survive at temperatures < 80 ^{o}C (Head et al., 2003). Very few studies have attempted to find a link between magnetisation and biodegradation. One study by Emmerton et al. (2013) attempted to identify a connection between magnetic mineralogy and oil biodegradation within oil-bearing sedimentary units from Colombia, Canada, Indonesia and the UK. The less biodegraded oil contained PSD magnetite while MD magnetite and hematite were noticed in the heavily biodegraded oil sand samples. The suggestion that biodegraded oil shows an increase in the proportion of hematite is intriguing as some other research suggest it likely gets reduced/dissolved by anaerobic bacteria and can be unstable in the chemical conditions

generated by hydrocarbons (Machel and Burton, 1991a; Machel, 1995). This thesis will attempt to verify these concepts by analysing core samples from non-biodegraded to biodegraded reservoirs units in the Tay fan.

1.3.2 Hydrocarbon Accumulation Identification through Rock Magnetic Techniques

The majority of the research into the use of magnetics as a direct hydrocarbon indicator has been focused on the differences between oil producing wells and dry wells (Costanzo-Alvarez et al., 2000; Díaz et al., 2000; Liu et al., 2006; Guzmán et al., 2011; Emmerton et al., 2012). Costanzo-Alvarez et al. (2000), Aldana et al. (2003) and Guzmán et al. (2011) analysed drill cuttings between 100–1500m above possible hydrocarbon accumulations from 24 wells in Venezuela and Columbia. Two magnetic susceptibility anomalies were identified, named anomalies A and B. Anomaly A (Figure 1.11 a and b) was found only in producing wells and was linked to the presence of Fe-rich spherical aggregates and low coercivity magnetic phases of authigenic origin, most likely magnetite. Anomaly B (Figure 1.11 c) was observed in both producing and non-producing wells and was linked to the presence of quartz, kaolinite, magnetite and hematite. It was concluded that anomaly A was due to the reducing conditions generated by the underlying reservoir while anomaly B most likely reflected changes in lithology (Costanzo-Alvarez et al., 2000).

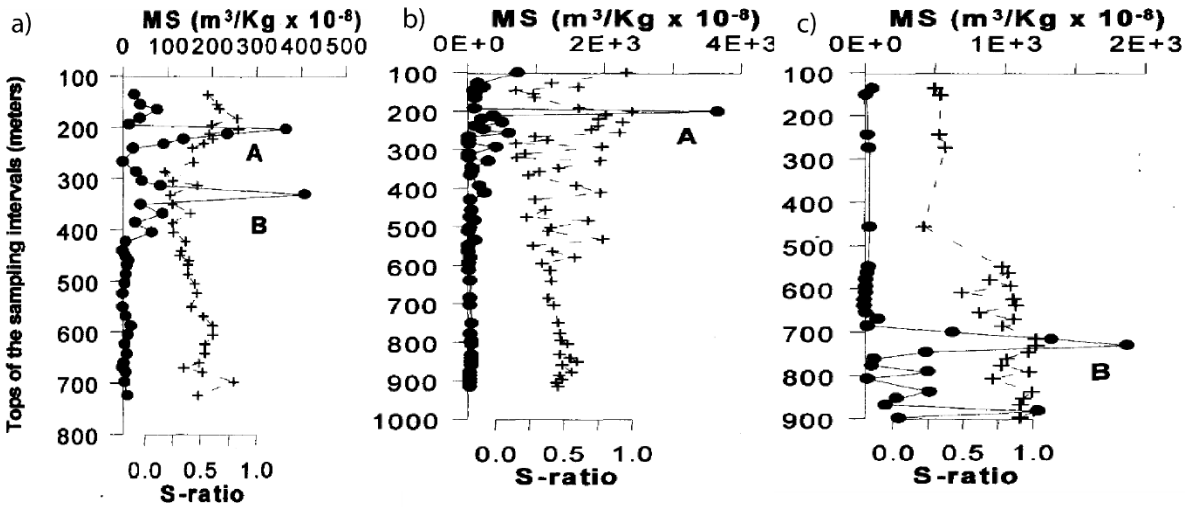


Figure 1.11. Magnetic susceptibility (•) and S- Ratio (+) ($IRM_{-0.03T}/IRM_{+2T}$) vs depths from producer wells a) GF -1X and b) GF-2X and non-producer well c) GF -13X. Image obtained from Costanzo-Alvarez et al. (2000).

Research has attempted to verify the presence of anomaly A in reservoirs themselves, not just above reservoirs (Liu et al., 2006; Emmerton et al., 2012; Emmerton, 2013). One study by Emmerton et al. (2012) on oil sands from the Wessex Basin, UK, compared the magnetic properties of oil stained sand to their cleaned counterpart. They showed the oil-stained sands to have higher mass normalised magnetic susceptibility, M_s and M_{rs}, than their cleaned counterpart. The higher magnetic susceptibility, M_s and M_{rs} was attributed to the presence of 200 nm – 45 µm sized magnetite and hematite spherical clusters or framboids in the oil-stained sands. Similarly, Liu et al. (2006) showed samples from oil wells in China to have 24 to 36 times higher magnetic susceptibility, M_s and $M_{rs,}$ than the corresponding formation in a dry well. Liu et al. (2006) linked the increase in magnetic properties in the oil wells to the presence of authigenic fine grained (~ 25 nm) magnetite and maghemite while the coarser magnetic grains (~ 30 µm) were considered to be detrital.

Others studies have attempted to establish a relationship between extractable organic matter (EOM) and magnetic susceptibility. Emmerton et al. (2012) observed a decrease in magnetic susceptibility with increasing percentage of EOM in oil-bearing sedimentary units from Colombia, Canada Indonesia and the UK. Emmerton et al. (2012) suggested that this relationship was due to biodegradation of the oil. In contrast, Guzmán et al. (2011) study on oil-bearing sedimentary units from eastern Venezuela found a positive correlation between magnetic susceptibility and EOM in samples at depths where biodegradation occurred. This discrepancy maybe due to the microbes present in the different study areas. It is possible that different microbes can promote or hinder the precipitation of certain magnetic minerals which can lead to a positive or negative magnetic contrast depending on the background signal (Machel, 1995).

1.3.3 Magnetic mineral formation and Remagnetisation

Some diagenetic events give rise to the formation of new magnetic phases; these are commonly referred to as “remagnetisation” processes in the palaeomagnetic literature, as they can overprint and reset the NRM (Dunlop and Özdemir, 1997). They can be used to date the diagenetic events (McCabe and Elmore, 1989; Butler, 1992). Remagnetisation is normally considered to be chemical remagnetisation, formed due to fluid interactions (orogenic fluids, hydrocarbons etc), or burial diagenetic processes such as the maturation of organic matter

and clay diagenesis. Below, I describe two common mechanisms for chemical remagnetization, but other mechanisms exist:

Chemical Remagnetisation due to Alternative Fluids

Different fluids types (apart from hydrocarbon already discussed) that cause remagnetisation in sediments are described below:

1. *Orogenic fluids:* They are a common source for chemical remagnetisation (McCabe and Elmore, 1989; Stamatakos et al., 1996; Elmore et al., 2001; Elmore et al., 2012; Wilkinson et al., 2017). Orogenesis can trigger the migration of basinal fluids laterally through aquifers and vertically through faults or fractures resulting in localised remagnetisation and magnetic mineral alteration (Elmore et al., 2012). This process has been proposed as an explanation for regional and localised trends in authigenic magnetite and hematite (McCabe et al., 1989; Saffer and McCabe, 1992; Elmore et al., 1993b).
2. *Mineralising fluids:* Studies have linked these fluids to ore magnetisation in host rocks (Lewchuk and Symons, 1995; Symons et al., 2005). Migration of mineralising fluid into host rocks is typically triggered by tectonic activity and has been linked to the precipitation of authigenic pyrrhotite and magnetite (Symons et al., 1996; Leach et al., 2001; Pannalal et al., 2004).
3. *Weathering fluids:* Several studies present evidence that weathering fluids can cause remagnetization resulting in the precipitation of authigenic hematite and goethite (Johnson et al., 1984; Loucks and Elmore, 1986; Franke et al., 2010).

Other Chemical Remagnetisation processes due to Burial

Several studies have presented evidence for the precipitation of magnetite, greigite, pyrrhotite and possibly goethite during burial conditions (80 ^{o}C to 300 ^{o}C) relevant to this study (Cairanne et al., 2004; Moreau et al., 2005; Aubourg et al., 2008; Aubourg and Pozzi, 2010; Aubourg et al., 2012; Kars et al., 2014). One study by Aubourg et al. (2012) heated shales sampled from the Swiss Jura thrust belt in laboratory conditions from 50 ^{o}C to 250 ^{o}C. The results (Figure 1.12) suggest the precipitation of greigite from temperatures < 50 ^{o}C to 170 ^{o}C, pyrrhotite from temperatures greater than 200 ^{o}C and magnetite from 50 ^{o}C to 250 ^{o}C.

However, the study of Aubourg et al. (2012) failed to truly recreate natural burial conditions by heating in the presence of air and not applying pressure during heating; the results shown in Figure 1.12 are a simplification of natural processes. Under anoxic burial conditions it is highly likely that the greigite, magnetite and pyrrhotite may not be stable (Burton et al., 1993) over the range of temperatures predicted by Aubourg et al. (2012). Aubourg and Pozzi et al (2010) heated similar shale samples to the ones used by Aubourg et al. (2012) from 150 °C to 250 °C under burial conditions. The results suggest the abundance of pyrrhotite reduces with increasing temperature which correlates to an increase in the abundance of magnetite.

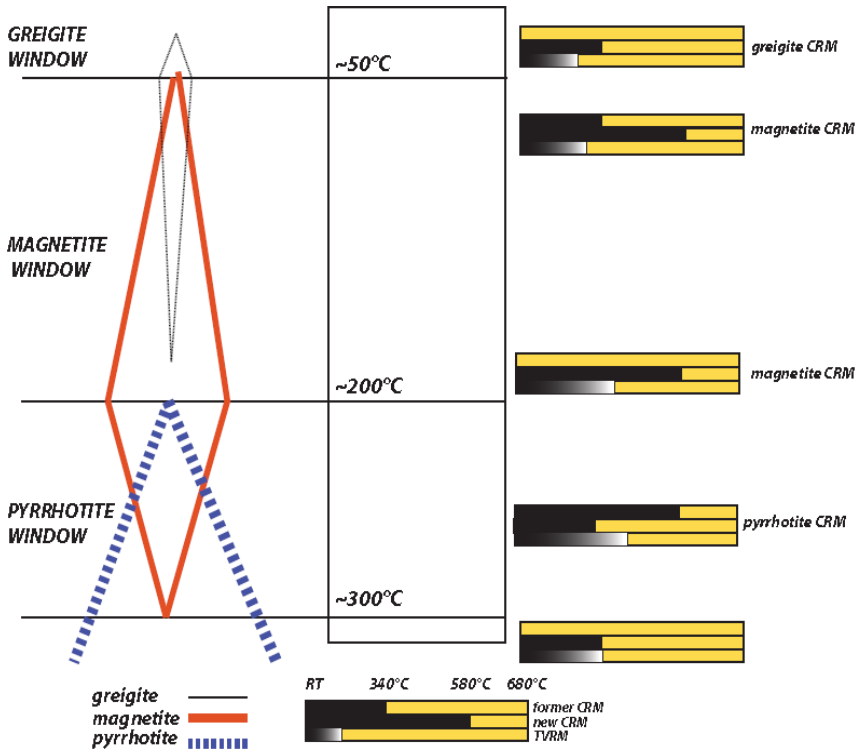


Figure 1.12. model for the formation of magnetic minerals in shale under burial conditions. The left column represents the concentration of the newly formed minerals. The central column is a sedimentary column from surface to 10 km. the right Colum shows the unblocking temperature spectra of chemical remanent magnetization (CRM) and thermoviscous remanent magnetization (TVRM). After Aubourg et al. (2012).

The literature has demonstrated that there is complex relationship between existing magnetic minerals in hydrocarbon reducing environments and the alteration of magnetic minerals due to chemical and microbial processes. The studies appear to be specific to the environment investigated with often contradictory findings, and no consistent trends found. Through a systematic study this thesis attempts to unravel the complex origin of the magnetic minerals in hydrocarbon reducing environments while trying to establish a use for rock magnetic techniques in petroleum systems analysis.

Chapter 2

Introduction to the Geology of the Central North Sea

2.1 Introduction

The North Sea basin comprises a trilete Jurassic rift system with upwards of 10 km of syn and post rift sediments (Cayley, 1987). The three rift arms are the Viking Graben (VG), the Inner and Outer Moray Firth (IMF, OMF) and the Central Graben (CNS) (Erratt et al., 1999). The NW-SE trending Central Graben forms the southern branch of the rift system (Figure 2.1), is located about 240 km east of Aberdeen, Scotland and comprises the focus of this research. The Central Graben differs from the other two rift arms in being underlain by a Permian salt basin. This has the effect of modifying structural styles and wavelength. Most obviously salt tectonics are extensive in the area (Hodgson et al., 1992).

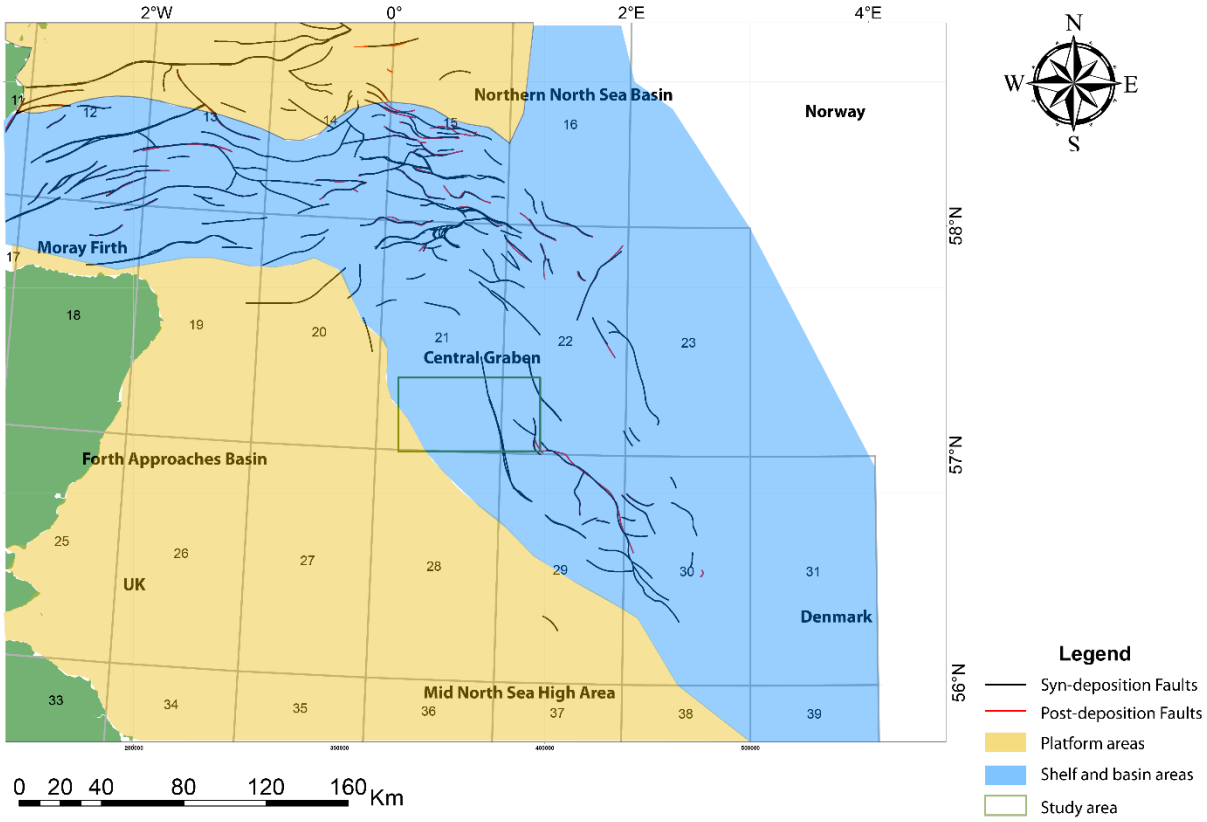


Figure 2.1. Map showing the principal structure of the North Sea Rift Basin. The green rectangle is the study area. Image modified from Koša (2007) using data from OGA's data release.

It is widely accepted that extension across the Northern North Sea started during the Triassic (Cayley, 1987), although Erratt et al. (1999) suggest it is difficult to determine the onset of extension in the CNS because of the overprint of salt tectonics and a decoupling of basement and cover deformation. Multiple phases of extension occurred from the Triassic to the Early Cretaceous with the most widespread extension occurring in the Late Jurassic (Fraser et al.,

2003). Fault control of sedimentation during syn-rift deposition resulted in fault bounded sub-basins such as the East Central Graben and West Central Graben, which are separated by the elevated Forties-Montrose Ridge (Erratt et al., 1999).

The year 1969 marked the first discovery of oil in the Central Basin (Graben) of the North Sea in the Chalk reservoirs at Valhall and Ekofisk and soon after oil was discovered in the Palaeocene sandstones at Montrose and Forties (Cayley, 1987). The main exploration targets have been Upper Jurassic shallow marine sandstones and Tertiary deep-water sandstones with the Kimmeridge Clay as the main source rock. The CNS has a wide variety of hydrocarbon traps due to the deposition of the thick Permian evaporate sequence which were buried and loaded resulting in halokinetic effects (Cayley, 1987).

The Lower Tertiary reservoir systems of the North Sea is the focus of this study, because they facilitate long distance lateral migration which will calibrated using 3D petroleum system modelling in Chapter 4. The earliest discovery of oil in the Tertiary deep marine play was in 1969 in the Arbroath and Montrose field. The massive Forties Field was discovered in 1970, which initiated further exploration in this play (McKie et al., 2015). Since then, reservoirs within the post rift Palaeogene strata have produced significant hydrocarbons amounting to approximately 14% of all discovered North Sea Basin reserves, making it the 3rd most economically successful petroleum play in the North Sea after the pre rift Lower/ Middle Jurassic and syn rift Upper Jurassic system (Robertson, 2013).

2.2 Structural Evolution of the Central Graben

2.2.1 Pre-Triassic

Gowers and Sæbøe (1985) showed that metamorphic rocks of Caledonian age form the basement rock of the area. Some studies suggest extension started in the Permian (Gowers and Sæbøe, 1985; Cayley, 1987), but I believe there is very little evidence for this due to the lack of well data or high resolution seismic data in the pre-Permian basinal areas of the Central Graben.

The Permian Zechstein deposits can be divided into two types; halite dominated basinal facies and a thin shallow-marine carbonate marginal facies. The evaporite deposits are up to 1800m thick and were formed by conditions of restricted marine influx, arid climate and rapid

subsidence in a widespread intermontane trough lying between the Caledonian mountains to the north and the Variscan fold belt to the south (Cayley, 1987). Mapping the top of the Zechstein salt shows three patterns: areas where there is no evidence of mobile Zechstein, areas with evidence of mobile evaporites but no diapirism, and areas with clear evidence of diapirism (Glennie et al., 2003). The movement of the Zechstein salt drastically affects the thickness and facies of the overlying sediments. Figure 2.2 shows the effects of the salt on the structural evolution of the central graben.

2.2.2 Triassic

During the Triassic the loading of the Zechstein salt along with extension gave rise to basins, salt pillows and salt withdrawal (Figure 2.2). The extension of the Zechstein salt resulted in subsidence of sediment packages into synforms which controlled the Triassic deposition (Hodgson et al., 1992). The Triassic strata are non-marine, sedimentation occurred in a playa lake environment with fine-grained thinly-bedded sandstones found within the mud and siltstone deposits (Cayley, 1987). The thickness and deposition of the sediments are highly variable due to erosion, salt displacement and angular unconformities. The sequence in some areas have a thickness of over 3500m post erosion, whilst in others it is completely removed by erosion (Gowers and Sæbøe, 1985). The salt withdrawal in most cases is accompanied by basement faulting resulting in withdrawal troughs with the salt forming semi-continuous ridges above the faults (Cayley, 1987). Erratt et al. (1999) show that the Triassic is thinner in the graben compared to the platform on the east of the rift, the facies and thickness patterns indicate the locus of the coexisting rifting is to the east of the Jurassic rift.

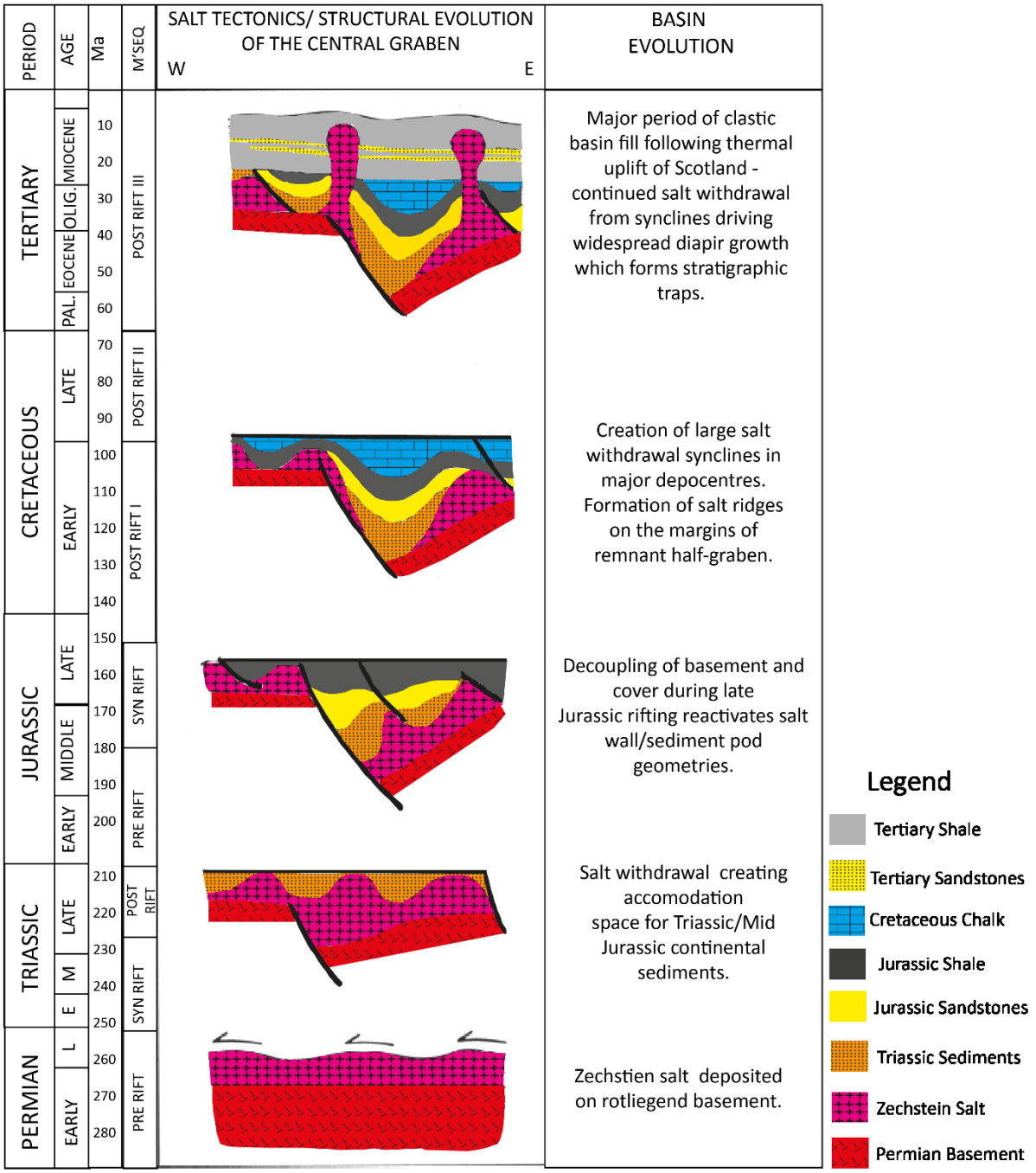


Figure 2.2. Effects of salt on the basin evolution of Western trough central graben modified from Hodgson et al. (1992).

The erosion, thermal doming and rifting in the Jurassic means the CNS only retains a partial record of Triassic sedimentation (Erratt et al., 1999). The Triassic sequence does not have the potential to be a source rock in the West Central Graben and Cayley (1987) suggests reservoir sandstones may be present in the youngest Triassic. This is observed in the Marnock Field located in the East Central Graben (Swanson et al., 2000).

2.2.3 Jurassic

A chronological gap between the Triassic and Middle Jurassic means the Early Jurassic section in the Central North Sea is absent either by non-deposition and/or erosion with a few exceptions in the East and Southeast (Hodgson et al., 1992). The absence of an Early Jurassic section is likely caused by erosion due to doming in the Early-Mid Jurassic (Leeder, 1983). It is also possible that the thermal bulge in the Western Trough separated the Central Graben from its clastic source areas which starved the basin resulting in the lack of preservation of the Early Jurassic sediments in the subsiding sediment packages (Hodgson et al., 1992).

Using high resolution biostratigraphy, Underhill and Partington (1993) mapped the spatial and temporal stratigraphic relations below and above the Base Jurassic unconformity. The results of the map of the subcrop to the unconformity (Figure 2.3) clearly showed that the erosion caused progressive truncation of the beds throughout the North Sea domain resulting in a series of elliptical subcrop patterns with the youngest beds subcropping in the outer region getting older towards the central region near the triple junction. This anomaly has a diameter of >1250km to the maximum extent of the basinward shift in facies and > 900 km diameter across to the correlative conformities. This observation supports the existence of the Central North Sea rift dome, this domal uplift is due to the intruding plume head at the base of the lithosphere (Husmo et al., 2003). According to Underhill and Partington (1993) the doming may have begun in the Toarcian and archived maximum elevation (probably less than 500 m) in the Aalenian, differential deflation started before the Bathonian-Callovian volcanism and early Kimmeridgian rifting.

The Bajocian to Bathonian is represented by delta-plain mudstones, coals and carbonaceous fluvial sandstone comprising the Pentland formation (Vail et al., 1977). During this time tilted fault blocks started to develop, the effects of this movement on the crest of the faults block is difficult to determine as they are typically obscured by the effects of greater tilting and faulting during the main rift movement in the Late Jurassic (Husmo et al., 2003).

The Middle Jurassic has proven to be a prolific hydrocarbon play due to the large tilted fault block traps that are easily defined but the CNS has the least complete Lower-Middle Jurassic sequence and is rich in volcanic rocks (Cayley, 1987; Husmo et al., 2003). The sediment packages of the Middle Jurassic are usually very thick (> 365 m) in the southeast part of the

Central Graben and contain medium to coarse grained sandstones (interbedded with mudstones and coals) which can be good quality reservoirs if the connectivity between the stacked channel sandstones is very high (Hodgson et al., 1992).

In the CNS the Late Jurassic depocentres form a series of five N-S en echelon sub-basins (Erratt et al., 1999). The tectonic pattern in the Upper Jurassic is different from the pattern in the Triassic. The Central Graben was flooded due to rapid subsidence, this marked the return to marine sedimentation which persists to the present (Cayley, 1987; Rattey and Hayward, 1993). According to Johnson et al. (1986) this transgression resulted in the deposition of the Fulmar Formation, which comprises a series of prograding shoreline sequences and forms a major exploration target. The variable subsidence rates, lack of coarse clastics and complex paleogeography means the reservoir distribution is complex both spatially and temporarily (Husmo et al., 2003).

The rapid subsidence was controlled by large N-S oriented normal faults meaning the Late/Upper Jurassic sequence was preserved within grabenal areas of the rift, where it attains a thickness of 3000m. It contains deposits of mudstone with some turbiditic sandstones seen in the Heather Formation in the basinal areas (Cayley, 1987; Fraser et al., 2003). The play is generally defined by two contrasting reservoirs: costal-shelf sandstones (Fulmar Formation) and submarine-fan sandstones (Heather Formation) (Fraser et al., 2003).

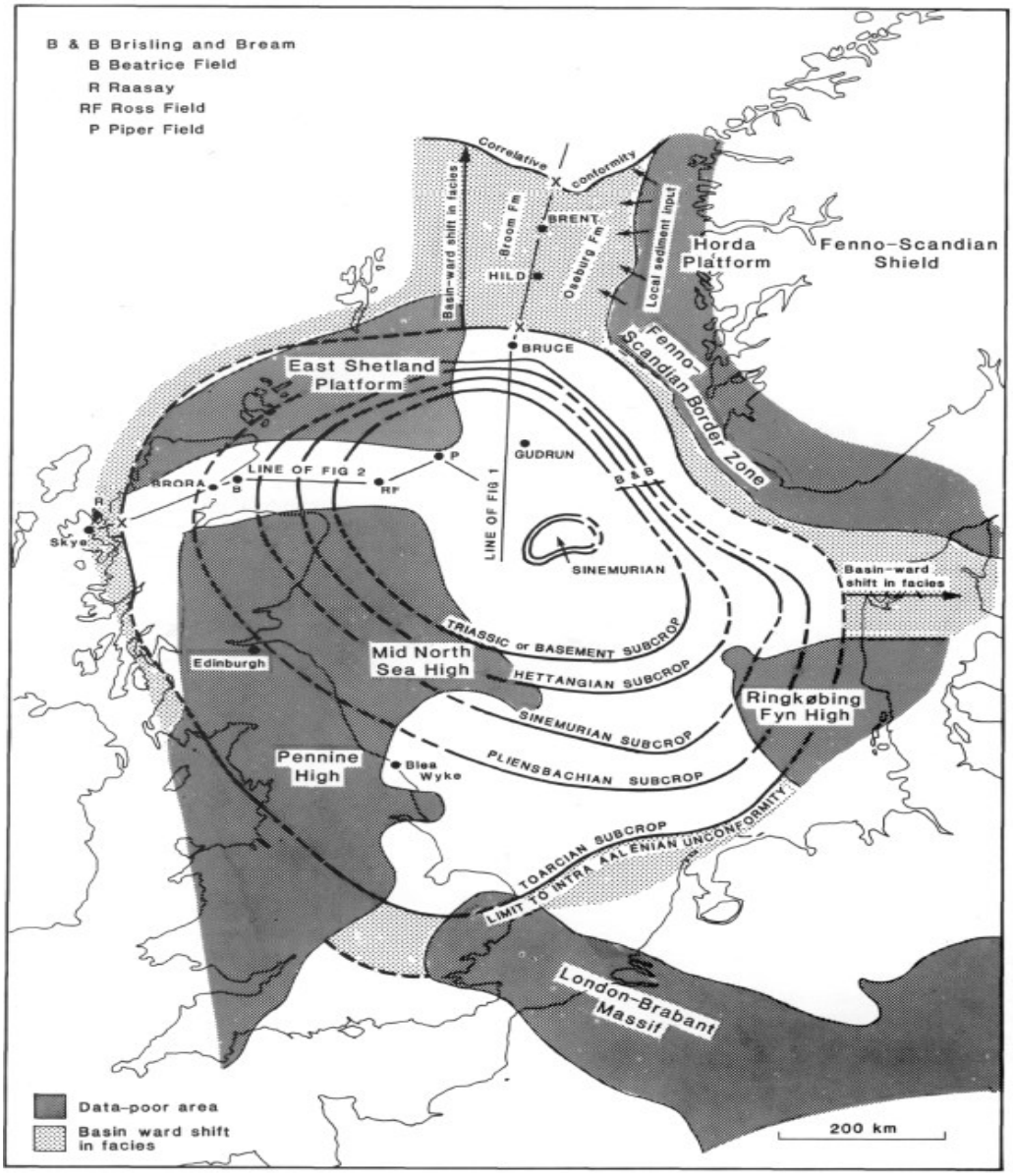


Figure 2.3. Map of subcrop to Base-Jurassic unconformity. The results suggest a concentric to elliptical area of uplift and erosion. Image obtained from Underhill and Partington (1993).

The Late Jurassic can be regarded as the most important time in the structural evolution of the North Sea petroleum system for the following reasons:

1. This was when the Kimmeridge Clay Formation was deposited. During this time anoxic conditions were present with a stratified water column and that allowed the widespread deposition and preservation of world class type II organic rich mudstones (Barnard and Bastow, 1991).
2. Halokinesis is responsible for the formation of most of the traps. These traps preserved hydrocarbon accumulation not only in the Late Jurassic but also in the

Middle Jurassic reservoir rocks (Cayley, 1987; Fraser et al., 2003). This accounts for 80% of the reserves discovered in the North Atlantic Margin (Fraser et al., 2003).

3. It may still contain most of the undiscovered reserves in stratigraphic traps or in a combination of structural and stratigraphic traps (Cayley, 1987). This is addressed in Chapter 4.

2.2.4 Cretaceous

The base of the Lower Cretaceous (Base Cromer Knoll Group) marks the upwards change in facies from the dark organic rich mudstones of the Kimmeridge Clay Formation deposited in anoxic conditions to mudstones and carbonates deposited under oxic conditions; this is termed the Base Cretaceous Unconformity (Hancock, 1990). Regional flooding from the Albian to the Cenomanian resulted in the deposition of the marls of the Cromer Knoll Group which can act as seals in some fields in the Central Graben (Oakman, 2005).

The Cenomanian to the Danian was the time of chalk sedimentation. The chalk deposition was influenced by intra chalk erosion, halokinesis (salt diapirs, domes, pillows and ridges) and fault controlled subsidence (Gowers and Sæbøe, 1985). This resulted in some chalk reservoirs like the Machar Field in the East Central Graben (Brown et al., 1999). The uplift of Scotland in the Early Tertiary introduced Paleocene siliciclastic sediments to the basin, ending the deposition of chalk in the North Sea during the Danian (Surlyk et al., 2003).

2.2.5 Tertiary

During Tertiary times, the Central Graben formed a bathymetric low subject to continuing thermal subsidence from the Cretaceous (Gowers and Sæbøe, 1985; Cayley, 1987). This period of high rates of thermal subsidence was also characterised by high sediment influx and enhanced halokinetic activity (Hodgson et al., 1992).

Development of the Iceland plume marked the beginning of the NE Atlantic Ocean spreading resulting in the large scale thermal uplift and periodic SE titling of the northern British Isles during the Danian (Anderton, 1993; Den Hartog Jager et al., 1993). Western Scotland was raised by 2 to 3 km and eastern Scotland was raised by 0.5 to 1 km (White and Lovell, 1997).

Uplift of Scotland, coupled with eustatic sea-level fall, led to the erosion of the exposed land mass. This led to the deposition of clastic deltas and turbidites in the Central North Sea via

the Outer Moray Firth (Ahmadi et al., 2003). Delivery of siliciclastics into the basin continued throughout the Palaeocene and Eocene resulting in a series of submarine sandstone deposits thinning south-eastwards away from Scotland, becoming increasingly buried and encased in mud (Eldrett et al., 2015). The thinning of sandstone units away from Scotland suggest there was little sediment input from the Norwegian land mass (Ahmadi et al., 2003). The Palaeocene Fan (e.g. Forties sandstone member) originates from the NW shelf trending SE or from the western shelf trending SE while the Eocene fan (e.g. Tay Sandstone Member) originates from the western shelf and trends ESE.

Continental rupture and initiation of sea floor spreading in the NE Atlantic took place around 55-54 Ma (Palaeocene–Eocene boundary) and is marked by the deposition of the ash of the Balder Formation (Knox and Holloway, 1992; Ahmadi et al., 2003). During the Eocene, the sedimentation patterns changed to widespread prograding deltas from the dominantly submarine fan deposits of the Palaeocene as the basin progressively infilled (Jones et al., 2003). The maximum thickness of the Eocene is over 800m (Armstrong et al., 1987). The samples used in this study are from the Eocene Tay sandstone member.

The Eocene surface is similar to the Palaeocene beneath it. They both continue the pattern of the post- rift subsidence and depositional settings controlled by the pre-existing Mesozoic structures (Jones et al., 2003). Up to 2750m of uncompacted mudstones have been deposited in the basin since the Eocene, they serve as the regional seal (Cayley, 1987).

2.3 Stratigraphy

A representative stratigraphic column for the CNS is presented in Figure 2.4. Eocene and Palaeocene stratigraphy are the prime focus of this thesis. This thesis uses the Palaeogene lithostratigraphic nomenclature scheme of Knox and Holloway (1992). The Tay sandstone member is in the Horda Formation within the Stronsay Group (Figure 2.5).

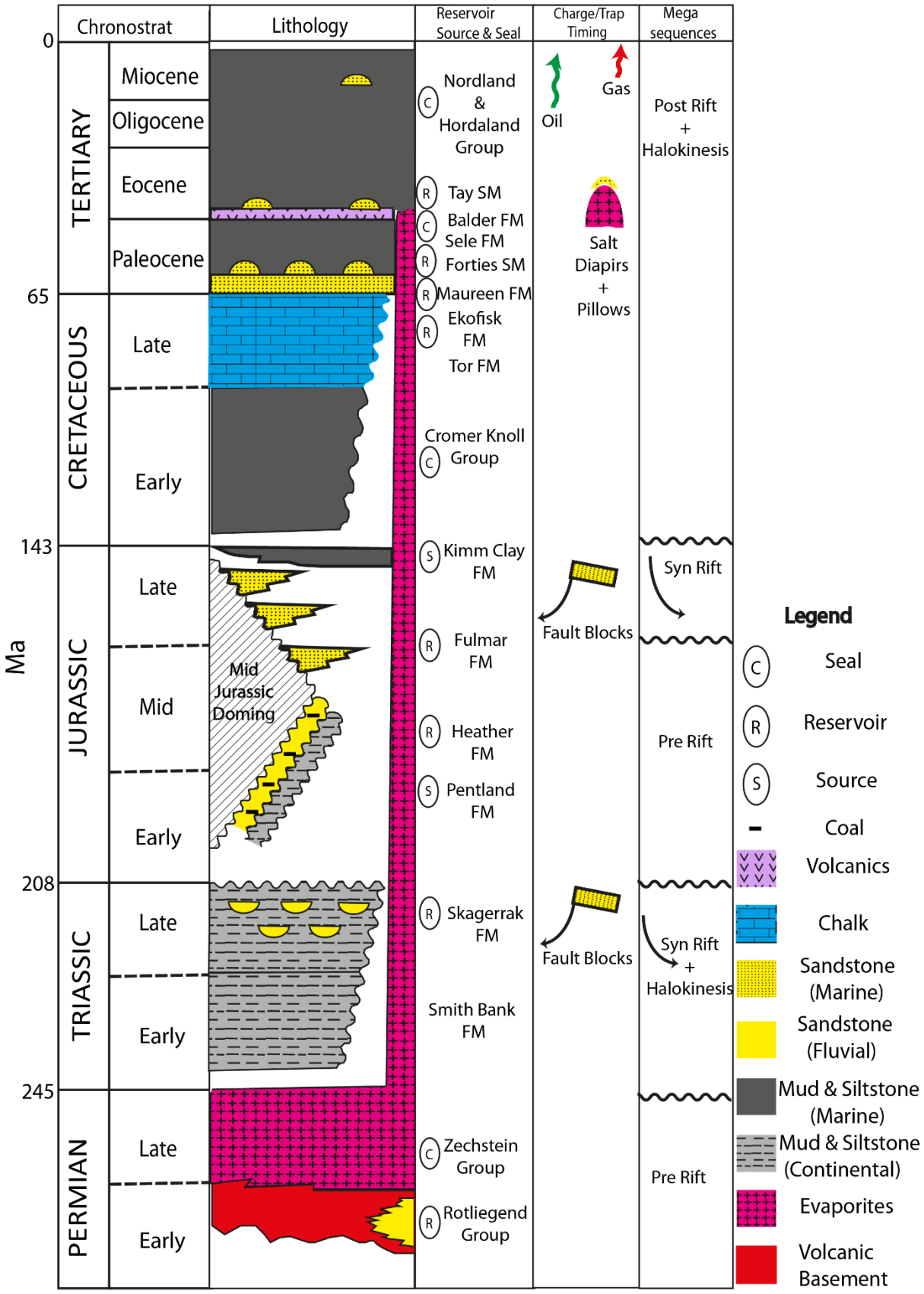


Figure 2.4. Generalised Central North Sea stratigraphic column showing depositional facies, tectonic history, source rock, possible reservoirs, seal and timing of hydrocarbon migration. Useful stratigraphic/seismic horizons are identified. Note: Evaporites above the Permian is as a result of halokinesis

2.3.1 Montrose Group

In the Central North Sea, the Montrose Group (Figure 2.5) comprises Palaeocene aged sediments of the Maureen and Lista formations (Mudge and Copestake, 1992). The Maureen Formation at the base of the Montrose Group is the laterally equivalent of the Ty and Vale Formations which are composed of high- and low-density, gravity-flow, sediment deposits of sandstones interbedded with siltstone, mudstones, basinal marl and basinal limestones (Knox and Holloway, 1992; Ahmadi et al., 2003). The Lista Formation sits at the top of the Montrose Group and is represented by an upwards transition from dark silty mudstones to dark green-grey finer grained mudstone interbedded with sandstones at the base (Knox and Holloway, 1992). The Montrose Group is regionally extensive in the North Sea, reaching thicknesses of at least 600m in the Outer Moray Firth Basin (Knox and Holloway, 1992).

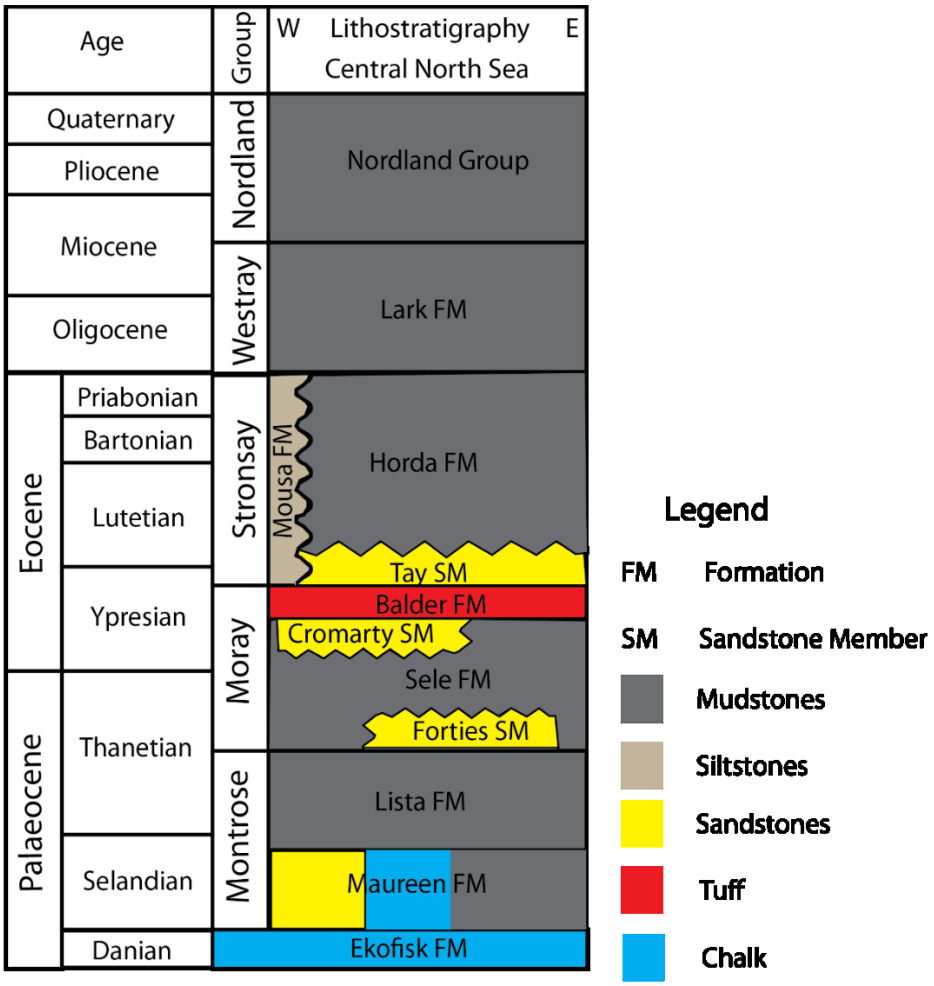


Figure 2.5. Lithostratigraphic column showing the Central North Sea Graben lithostratigraphic nomenclature of Knox & Holloway (1992).

2.3.2 Moray Group

In the Central North Sea, the Moray Group (Figure 2.5) comprises Eocene and Palaeocene aged sediments of the Sele and Balder Formations (Knox and Holloway, 1992). It is located in between the Stronsay Group and the Montrose Group. The Sele and Balder Formations are characterised by a basinal succession dominated by hemipelagic mudstones and sandstones (Mudge and Copestake, 1992). The basinal sandstones of the Cromarty and Forties sandstone member are within the Sele formation at the base of the Moray Group while the top of the Moray Group is characterised by the regionally extensive tuffaceous Balder Formation (a widespread stratigraphic marker across the Northern North Sea) while the base is represented by the Sele Formation (Ahmadi et al., 2003). The tuffs are a product of the intense volcanism to the west of Britain and easterly prevailing winds. The Moray Group varies in thickness across the North Sea. It can vary from 500m in the Outer Moray Firth Basin to 30 m in the southern Central Graben (Knox and Holloway, 1992).

2.3.3 Stronsay Group

The Stronsay Group defined by Knox and Holloway (1992) is located between the overlying Westray Group of the Oligocene and the Moray group (Figure 2.5). Knox and Holloway (1992) have divided this group into two formations based on their depositional facies. The Mousa Formation is characterised by sandstone and siltstone dominated shelf facies while the Horda Formation is characterised by mudstone dominated basinal facies with some deep-water sandstone. The Horda Formation contains the Grid and Tay sandstone members (there is no Grid sandstone member in the study area). The Mousa Formation is commonly 200-300 m thick and the easternmost progradational limit of the Eocene shelf system is marked by its eastern boundary (Jones et al., 2003).

The Stronsay Group can be seen throughout the North Sea and attains a thickness of about 700 m in some areas due to its relatively large time span of approximately 19 Myr when compared to the combined time span of the Montrose and Moray Groups which is about 9 Myr (Knox and Holloway, 1992; Robertson, 2013).

2.4 Hydrocarbon Plays in the Central Graben

This section will describe the petroleum system in the CNS and briefly review the characteristics of the possible source rocks, reservoirs and describe the parameters controlling the migration from Upper Jurassic Source rocks into Jurassic and Tertiary Reservoirs.

2.4.1 Source Rocks in the Central Graben

A source rock is an organic rich rock (usually shale) capable of expelling petroleum compounds if the right temperature and pressure conditions are met. The coal measures of the Upper Carboniferous are the oldest source rocks in the Central Graben area. According to Cayley (1987) they are not important for the following reasons:

- The distribution of the Coal Measures is highly limited and difficult to predict,
- The Coal Measures have largely been eroded and the remnants overly the pre-rift Devonian on structural highs
- The rocks will be gas-prone but are on the margin of the Graben and are still immature.

Cayley (1987), Cornford (1990) and Kubala et al. (2003) also identified other source rocks, which are described below:

1. Kupfershiefer sequence at the base of the Zechstein transgression; Organic rich shale with a Total Organic Carbon (TOC) value between 6% and 1%, contains oil-prone organic matter. It is in the lower limits of the maturity range but has a thickness of only 3m, so it is of minor importance.
2. Other source rocks in the Zechstein (Figure 2.4) found within dolomitized algal laminate facies, but like the Kupfershiefer they are very thin beds
3. Triassic red beds; they are oxidised so have no source rock potential.
4. Algae rich coals in the Mid Jurassic Pentland Formation (Figure 2.4); they are discontinuous with thickness between 1-9 m. With an average TOC value of 4 %, they are gas-prone only when buried to depths of 4900 m. This hinders their potential to be adequate source rocks.
5. The Heather Formation of the Late Jurassic transgression. These marine mudstones are composed of gas-prone organic matter and have an average TOC of 3% with

thicknesses greater than 914 m. Its lateral equivalents are the Haugesund, Egersund and Lola Formations. They are all grouped as the Heather unit (Figure 2.4). The Heather unit is a locally important source rock but has the same maturity limitations as the Mid Jurassic source rocks.

6. The Kimmeridge Clay Formation (Figure 2.4) deposited during the Late Jurassic; this has TOC values of up to 15% with an average value of 8% (Cayley, 1987). Organic facies contain amorphous marine kerogen. The TOC value varies with lithology across the area.
7. The North Sea Tertiary sediments are poor source rocks because of their low maturity.

In the UK sector of the Central Graben, the Kimmeridge Clay Formation has been identified as the main source rock (Cayley, 1987; Fraser et al., 2003). On well logs the Kimmeridge source is marked by a high gamma ray response (Figure 2.6). From the Kimmeridgian to Berriassian times, the combination of the following factors have resulted in the production of this petroliferous source rock (Irwin, 1979; Cornford, 1990):

- Rapid transgressive shoreline due to strong eustatic rise.
- Restricted circulation due to isolation from the world ocean causing density stratification. This widespread anoxic epicontinental seaway extends throughout the North Sea, Mid Norway, Barents Sea and West Siberia and is attributed to closure of the Newfoundland-Iberia gateway to the south.
- Mid-water oxygen minimum due to possible plankton productivity.

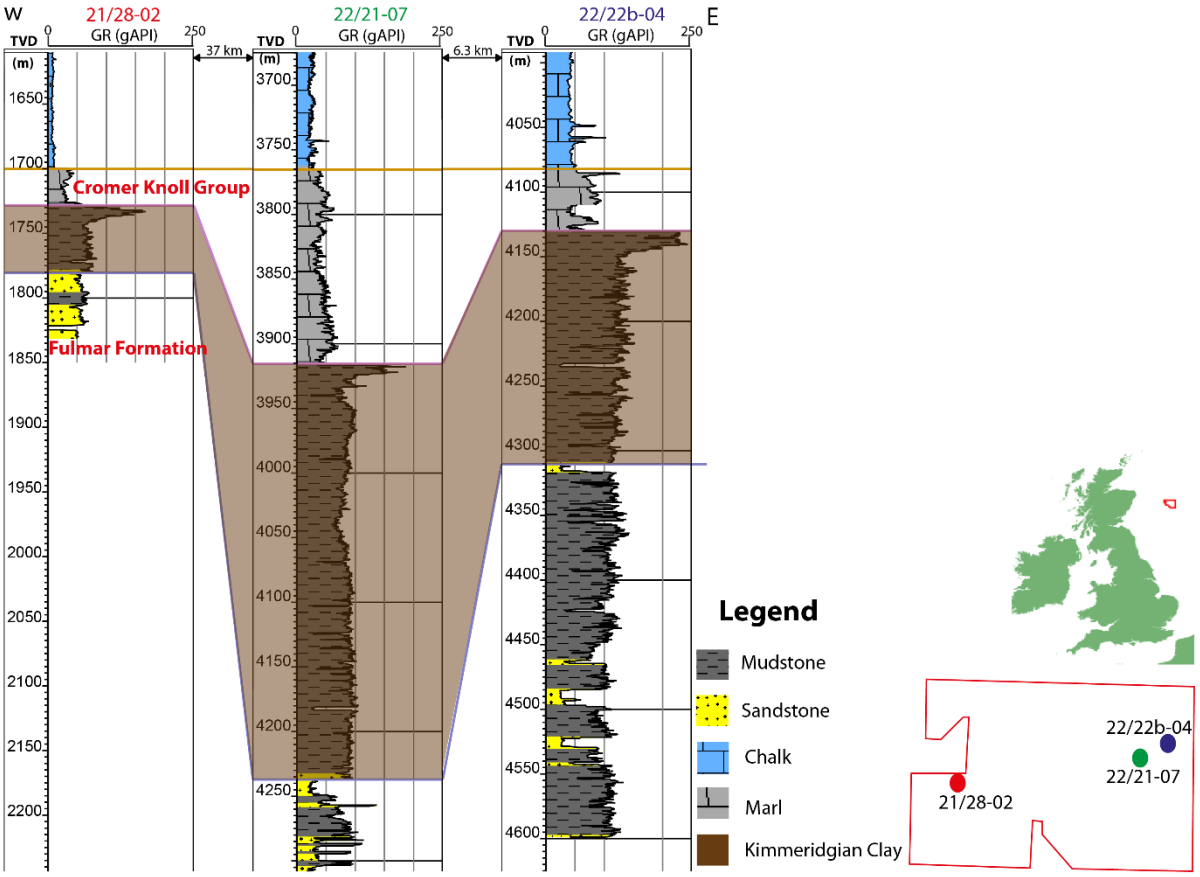


Figure 2.6 Kimmeridge Clay identified by high gamma ray response. Kimmeridge Clay varies in depth form 4150m in the east to about 1700m in the west. Inset highlights the location of the wells in the study area.

Cayley (1987) analysed 22 crude oil samples from the Central graben; the results showed the Kimmeridge Clay Formation was the common source rock in the reservoirs and that the non-biodegraded crude oil was expelled from a mature marine source rock. A similarity was also noticed between the oil and source rock extracts suggesting that the crude oil was expelled and migrated as a bulk phase into the reservoirs.

In terms of maturity, the top of the Kimmeridge Clay Unit is mature for oil generation over most of the Central Graben area with burial depths greater than 3000m (Kubala et al., 2003). In axial zones of the Central Graben the Kimmeridge Clay Unit is mature for significant gas generation while on the platforms and fringes the shales are generally immature to early mature for oil generation (Cayley, 1987; Kubala et al., 2003). This is tested in Chapter 4.

2.4.2 Hydrocarbon Migration in the Central Graben

Migration can be split up into three phases:

(1) Primary migration is defined as expulsion of petroleum from the source rock,

(2) Secondary migration is the migration of petroleum from source rock to trapped reservoir beds via carrier beds.

(3) Tertiary migration is the leakage of petroleum from reservoir (Allen and Allen, 1991).

Where hydrostatic pressure is observed oil and gas move freely due to buoyancy and under this condition lateral migration can be observed, but if there is an increase in abnormal pore pressure, lateral migration is restricted and vertical migration would occur due to the high fluid pressure gradient (Isaksen, 2004).

Migration into Jurassic sandstones and Tertiary sandstones

The Fulmar formation is the main conduit for the migration of hydrocarbon (also common called petroleum) out of the source rock into the Jurassic strata of the Central Graben (Kubala et al., 2003). The source rock lies directly above this formation with downward migration preferentially occurring in synclinal areas. This short-distance migration is an ideal migration model. The efficiency of this is affected by the discontinuous nature of the Fulmar sandstones and its highly fractured nature (Cayley, 1987). Also, the internal depositional geometries of the Fulmar sandstones are strongly influenced by halokinesis and its associated faulting (Hodgson et al., 1992).

Cayley (1987) notices a retention of abnormally high pore pressure in the deep Central Graben; this is due to the presence of a good seal, high temperatures and rapid Late Tertiary burial rates. This suggests the Jurassic strata is a closed aquifer system that prevents hydrocarbon from migrating into some structures. Cayley (1987) also noted this is not the case everywhere and anomalies do occur such as in the western Central Graben (Robertson, 2013).

The salt diapirs as well as regional faulted Cretaceous caprock have been a means for vertical migration out of the Jurassic strata (Cayley, 1987; Kubala et al., 2003). This mechanism has

not been fully explained in the past and is explored in Chapters 3 and 4. The reservoirs in the area of maximum Tertiary burial of Upper Jurassic source rock contain the lightest oil and condensates which suggests migration has mostly been vertical (Parsley, 1990).

Unlike the Jurassic strata the Tertiary sandstones are only mildly deformed, they are laterally continuous and are characterised by a normal aquifer system (Kubala et al., 2003). The lateral migration direction is determined by the regional dip with oil migrating up-dip. Migration in the Tertiary sandstones is not constrained by its proximity to the source rock with lateral migration occurring at distances of 50 km for oil and up to 32 km for gas (Cayley, 1987; Kubala et al., 2003). Lateral migration within the Tertiary Tay Sandstone Member is addressed in Chapter 5.

2.4.3 Reservoirs in the Central Graben

Below I describe the reservoirs considered in this study area.

Fulmar Formation (Upper Jurassic)

The Fulmar Formation (Figure 2.5) is represented by a sequence of moderate to well sorted fine to medium grained sandstones of Oxfordian to Late Kimmeridgian age (Kuhn et al., 2003). The sandstones are typically 150-335 m thick, heavily bioturbated and were deposited in a shallow marine environment (Johnson et al., 1986). The sandstones display good reservoir quality with porosities in the range 25-35 % and permeabilities in the range 1000-10000 mD (Johnson et al., 1986).

Forties Sandstone member (FSM) (Palaeocene)

The Central Graben serves as the main depocentre for the FSM (Figure 2.4 and Figure 2.5). The late Thanetian-aged sandstone is generally moderately to poorly sorted, fine to coarse grained with locally pebbly areas (Ahmadi et al., 2003). Most of the sandstones are homogeneous with soft deformation and dewatering structures observed along with sandstone intrusions (Knox and Holloway, 1992).

The FSM is restricted to the Central Graben and is usually thicker than 150 m along a NW-SE depositional axis (Knox and Holloway, 1992). The sandstone thins towards the west (Figure 2.7) where it onlaps on the Lista Formation (Eldrett et al., 2015). Biostratigraphic

characterisation of the FSM shows it lies beneath the *Apectodinium* biomarker and its lower part contains the *Bathysiphon* biomarker (Knox and Holloway, 1992).

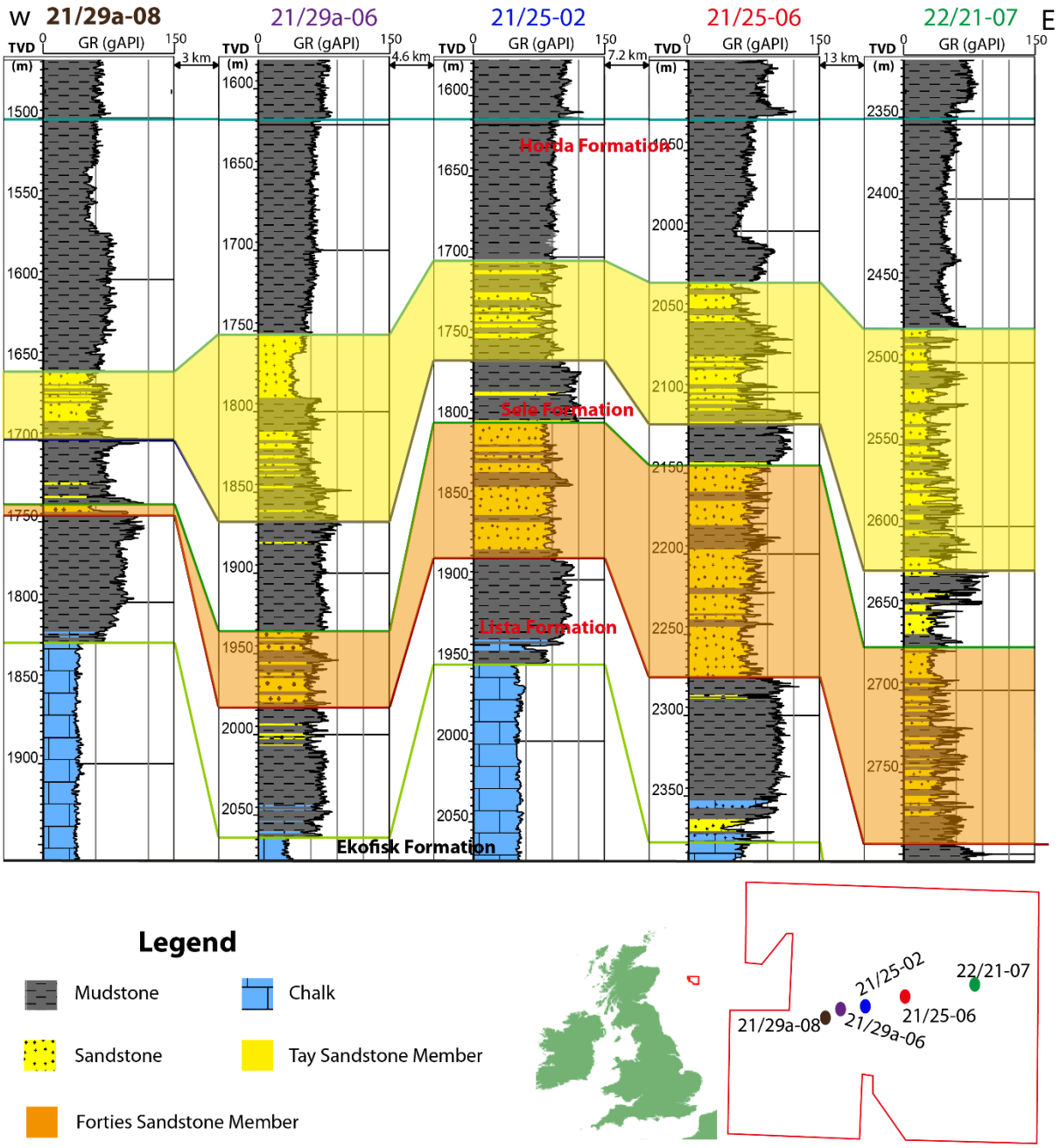


Figure 2.7 .Well-log correlation of Tay and Forties sandstone members. Both sandstone members are interbedded with mudstones. The Forties sandstone thins to the wast. Inset is showing the location of the wells in the study area.

Tay Sandstone Member (TSM) (Eocene)

The Tay sandstone Member (Figure 2.4 and Figure 2.5) of the Horda Formation was deposited during the Eocene (early-mid); its name comes from the River Tay in Eastern Scotland (Knox and Holloway, 1992). The TSM is not only restricted to UK Quadrants 22 and 21, it can be seen

in northern parts of UK Quadrant 28 and extending East towards UK Quadrant 29 (Robertson, 2013). The Tay fan was deposited in a broad WNW-ESE trending topographic low from the Middle Ypresian to the Early Lutetian (Den Hartog Jager et al., 1993). According to Den Hartog Jager et al. (1993) most of sediments were fed in to the basin from the NW and other feeder channels from a W-WSW direction which were active at different times, with the sediments bypassing the slopes to get to the basin-floor fans. The Tay sands occasionally found in depositional slope settings are highly channelized features deposited within submarine canyons (Armstrong et al., 1987). Den Hartog Jager et al. (1993) showed that the TSM developed from basin-floor fans into slope fans while progressively retreating westwards and that the sediments became increasingly sandier and more channelized by evolving from their previous sheet-like geometries into mounded geometries. The depositional setting has mostly been controlled by Mesozoic Graben faults with salt induced structural highs controlling the syndepositional sand accumulation (Armstrong et al., 1987).

Knox and Holloway (1992) described the lithology of the TSM as a clean to argillaceous, fine to medium grained sandstone which can be thinly or thickly bedded, interbedded with silty, fissile, green-grey to grey siltstones and mudstone. From my visit to the BGS core store in Keyworth, Nottinghamshire the Tay sandstones are very friable and typically have no preserved sedimentary structures. The net sand thickness of the Tay sandstone is generally less than 15 m, but a large build-up of sediments greater than 150 m is observed in the slope margin.Other variations in thickness are due to syn-sedimentary salt movement (Den Hartog Jager et al., 1993; Robertson, 2013). In the Gannet B field the salt-induced highs greatly affect flow pathways and sediment accumulation (Armstrong et al., 1987). From looking at the well data, the top of the TSM (Figure 2.7) is characterised by a decrease in gamma-ray values and usually an increase in velocity indicating a possible change from the grey-green to grey siltstones or mudstone to clean sandstone. The seismic data in the study area shows the base of the TSM rests disconformably over sediments in the Balder, Sele or Lista Formation. Towards the east thr TSM rests conformably on the mudstones in the Horda Formation (Knox and Holloway, 1992). The mud prone intervals in the Tay reservoir unit are discontinuous within the sandstone (Figure 2.7). This affects fluid flow and fluid distribution, which can either focus or hinder fluid movement as seen in Gannet A (Lynn et al., 2015). Biostratigraphic

characterisation of the TSM shows it lies beneath the *S.spectabilis* biomarker and it lower part contains the *S.linaperta* biomarker (Knox and Holloway, 1992).

2.4.4 Traps

The common trapping configurations in the CNS are salt cored four way dip closures, salt fland onlaps and pinchouts, large scale sand injection complexes, isolated channels surrounded by shale and lateral fan pinch out onto basin highs (McKie et al., 2015). The traps are sealed by thick mudstone layers of the Horda Formation, Lark Formation and Nordland Group (Figure 2.5).

2.5 Fields of Interest

The selected fields and wells used for this study are shown in Figure 2.8. The fields are described below.

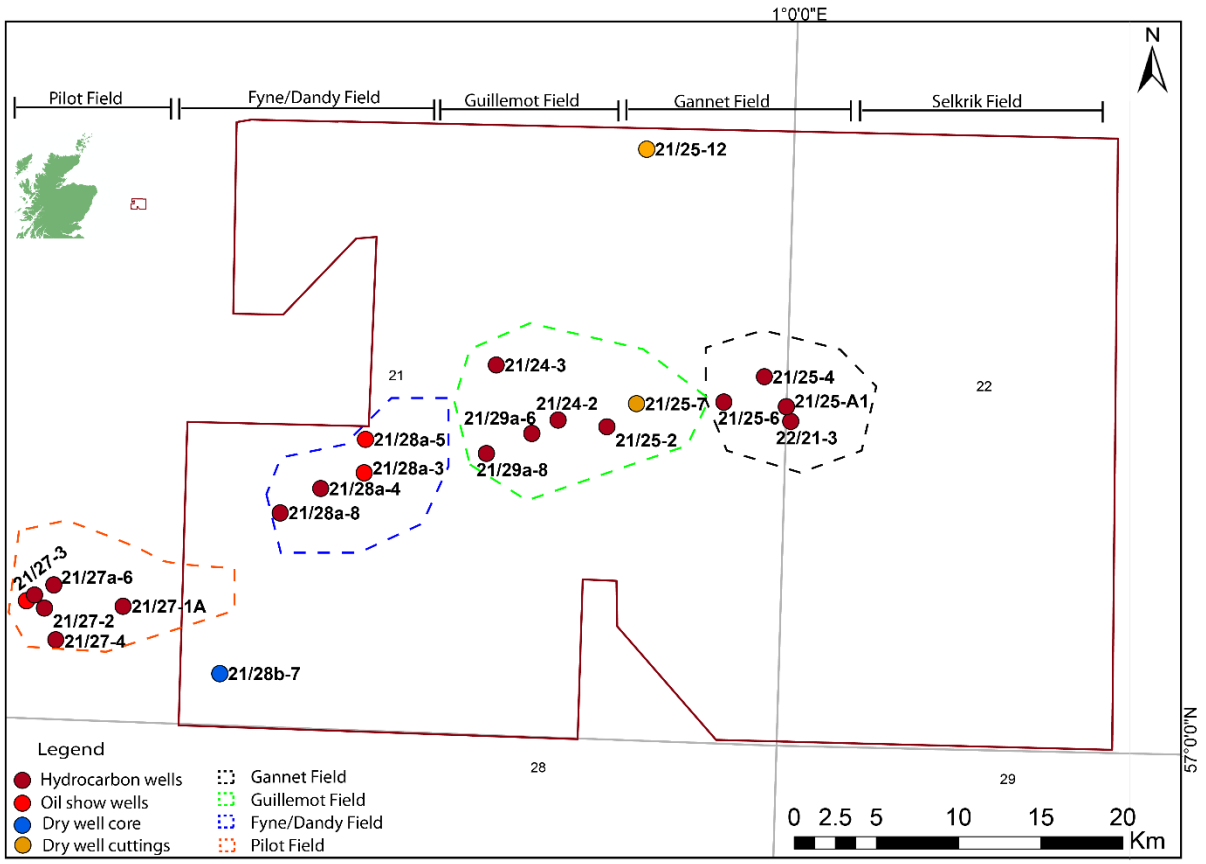


Figure 2.8 Location of the fields in the area. The study was done with cores from 19 oil/ gas wells, 1 dry well and cuttings from two dry wells. The red polygon represents the 3D data available.

2.5.1 Selkirk Field

The Selkirk field lies in Block 22/22b (Figure 2.8). Selkirk has a complex geology with a combination of structural and stratigraphic traps but there is very little literature on this field. The main information about this field was obtained from a relinquishment report by Centrica Energy in August 2013 (Centrica, 2013). As of 2012 the recoverable resource was estimated to be 6.7 mmboe (Centrica, 2013). The main producing well is 22/22b-5Z. In March 2013 the partnership decided to relinquish the licence and made plans to plug and abandon the well. Technical studies in the field showed no potential for any undiscovered recoverable volumes and the field was no longer a viable economic development.

The reservoir is Upper Jurassic Kimmeridgian turbidite sandstones, (J63/J64 in age) according to the biostratigraphic analysis. As at the time of the relinquishment report the younger, overlying strata such as the Cretaceous chalk or Tertiary sands had no significant untested remaining potential remaining: indicating the Tay sandstone is likely to be water wet.

2.5.2 Gannet Complex – Pilot Field.

In the Gannet complex commercial hydrocarbon accumulations have been found in three reservoir levels; Upper Jurassic Fulmar Sands, Palaeocene Forties Sands and Eocene Tay Sands with hydrocarbon-in-place estimates of 800 mmbbls of oil & condensate and 1 tcf of wet gas (Armstrong et al., 1987). In the Guillemot complex hydrocarbon accumulations are found in the Palaeocene Forties Sands and Eocene Tay Sands (Banner et al., 1992). In the Fyne & Dandy and Pilot fields hydrocarbon accumulations are found in the Eocene Tay Sands. According to Enegi Oil Plc, the Guillemot complex has at least 60 mmbbls of recoverable reserves, Fyne and Danny has at least 9.9 mmbbls proved plus probable reserves and the Pilot field has an initial stock-tank oil-in-place estimate of 250 mmbbls.

The Tay Sandstone member is commonly referred to as the Tay fan (Figure 2.9). The Gannet complex (Figure 2.8) comprises of the following fields: Gannet A-G fields. Wells sampled in this project are in Gannet A and Gannet B which covers parts of blocks 22/21b and 21/25 respectively. The Guillemot complex comprises of the following fields: Guillemot north, Guillemot north west, Guillemot west and Guillemot A. Wells sampled in this project are in the Guillemot west, Guillemot north and Guillemot A fields; located in parts of blocks 21/24,

21/25 and 21/29a. The Fyne & Dandy field is in block 21/28a and the Pilot field is in block 21/27a.

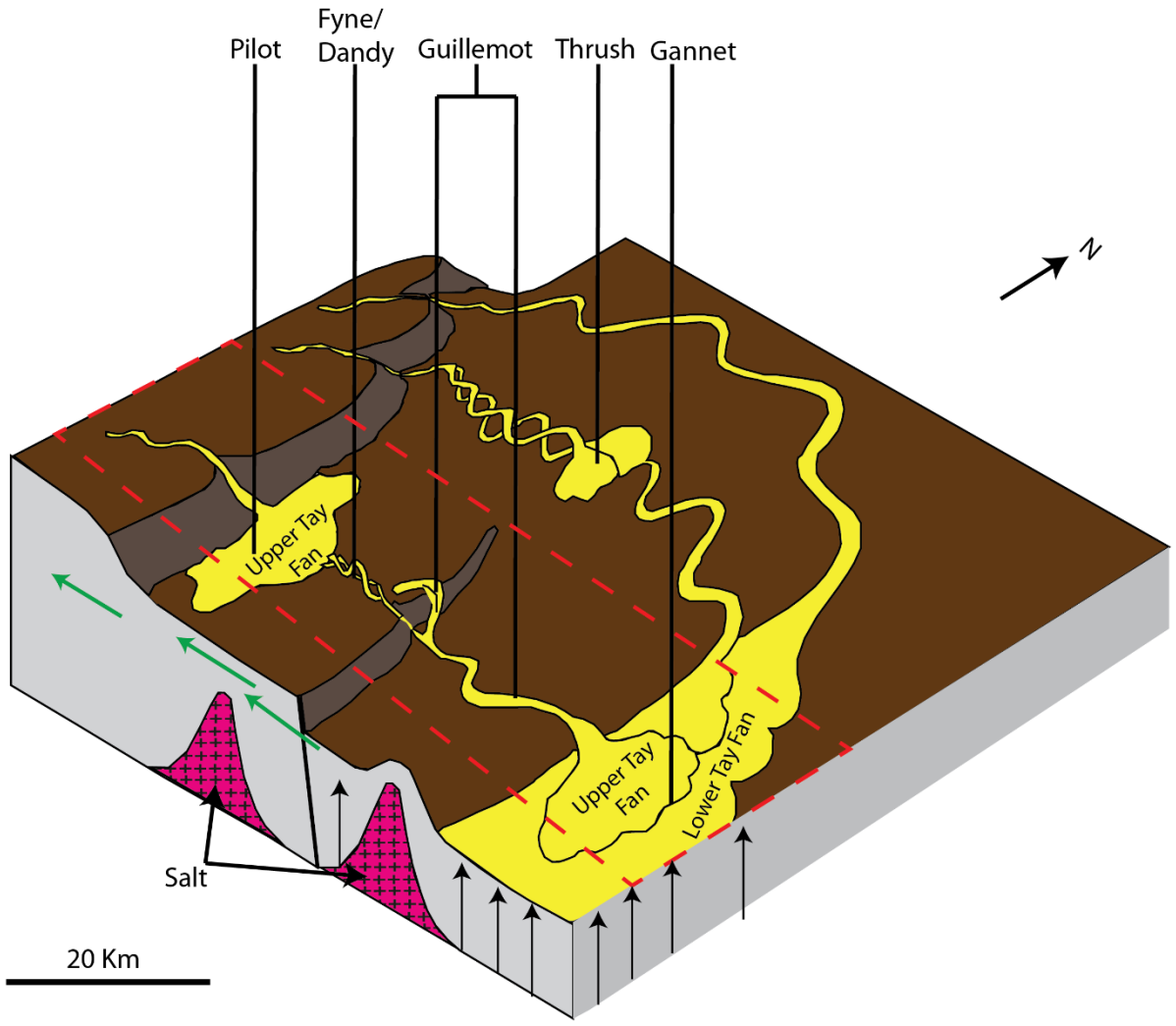


Figure 2.9. Diagram showing the Tay fan system modified from Jones et al. (2003). The box highlights the study area. Black arrows represent areas of vertical migration in to the Tay and the green arrows represent areas of lateral hydrocarbon migration within the Tay.

Armstrong et al. (1987) and Jones et al. (2003) have divided the Tay fan (T50-T92 age assignment) into three fan bodies which are described below:

1. Lower Tay fan Sands (T50): this represents the first phase of deep-water sand deposition probably supplied from the south-west. The radial fans have a relatively small diameter of 5-10 km and have limited areal extent. Evidence of fan progradation is seen by the crude coarsening and thickening upward sequence at the base. The rapidly fining and thinning-upward sequence at the top indicates abandonment.

2. Middle Tay fan sands (T60-T70): these sands are laterally more extensive than the underlying Lower Tay fan sands. They are submarine fan deposits with initial clastic sourcing from the north-west. Evidence of a major phase of fan lobe progradation is seen by the large-scale coarsening and thickening upward sequence. The fan lobes had minimal clastic input from the South-West.
3. Upper Tay fan sands (T84-T92): this unit represents the final phase of fan sedimentation within the Pilot-Gannet depositional system. It consists of thin turbiditic sandstones with finely laminated grey-green shales. The clastic materials are sourced from the south-west via the easterly prograding Eocene slopes. In the case of the Pilot discovery, the sands comprise toe-of-slope fans deposited during a widespread sea-level transgression. In the case of the Fyne, Dandy, Guillemot and Gannet discoveries, the deposits comprise an elongated mud rich turbidite system.

According to Jones et al. (2003) there have been two major pulses of hydrocarbon migration into the fans; the first happened in the Miocene due to basinal flexing and halokinetic effects, the second is occurring at present due to a combination of eastward regional tilting and halokinetic effects which breached the regional Cretaceous seal at the border of Block 21/24 and 21/25. This is analysed and discussed in Chapters 3 and 4 of this thesis. Some wells show evidence of being charged by the two migration events, showing similar migration paths from the deep basin to the traps (Jones et al., 2003). This is explored in Chapter 4 and 6. The local Kimmeridge Clay Formation source rocks are immature indicating the Tay Fan accumulations in this fields must be sourced by lateral migration from deeper parts of the basin in the East (Cayley, 1987; Parsley, 1990; Jones et al., 2003). Although Banner et al. (1992) suggest there is a possibility of having locally mature source rocks in the Gannet F area. If so long-distance lateral migration from the East of the Central Graben may not be needed to explain the charging of the fans. This will again be discussed later in Chapter 4.

Chapter 3

2D Petroleum Systems Modelling

3.1 Introduction

Petroleum systems modelling is a tool used to reconstruct the thermal and geological history of a basin (Welte and Yalçin, 1988). This helps us to quantify the timing of hydrocarbon generation, migration and accumulation in basins (Schneider and Wolf, 2000; Rodrigues Duran et al., 2013; Al-Balushi et al., 2016; Baniasad et al., 2016). This project uses both 2D and 3D petroleum systems modelling to demonstrate how hydrocarbons migrate vertically from the Jurassic source rocks to the Tertiary sandstone carrier/reservoir before migrating laterally up dip in the Central North Sea Basin. Identifying areas in the basin where hydrocarbons move laterally or vertically into the Tay sandstones is crucial to understating the results from the rock magnetic experiments. Basin modelling was carried out in four stages: 1) building the model, 2) populating the model with realistic parameters to accurately model the thermal and structural evolution of the basin, 3) simulating and iteratively calibrating the model to accurately measured data of porosity, temperature, vitrinite reflectance (R_0), total organic carbon (TOC) and hydrogen index (HI) and 4) testing the robustness of the model by exploring parameter space.

This chapter details the construction of a 2D basin model across UK Quadrants 22 & 21 and documents the timing of hydrocarbon generation and explosion in the source rock. This chapter also explores potential pathways and timing for hydrocarbon migration to the Tay sandstone member. 2D and 3D models were constructed using PetroMod (Schlumberger; version 2017). Petrel (Schlumberger; version 2017) was used for seismic interpretation. Chapter 4 documents the construction and results of the 3D model.

3.2 Depth Conversion

All petroleum systems models work in depth. Therefore, the 3D seismic data had to be converted from two-way-time (TWT) in milliseconds to metres bmsl (below mean sea level) prior to 2D petroleum systems modelling. Figure 3.1 shows a work flow for depth conversion. Six horizons were identified from ten composite well-log data (Figure 3.2): (1) Pliocene, (2) Upper Miocene, (3) Tay, (4) Chalk, (5) Kimmeridge Clay and (6) salt (shown in Appendix 1 along with the synthetics generated to aid horizon interpretation). These data were used to generate a velocity model for the entire 3D grid which was used to generate 2D depth surfaces for basin modelling.

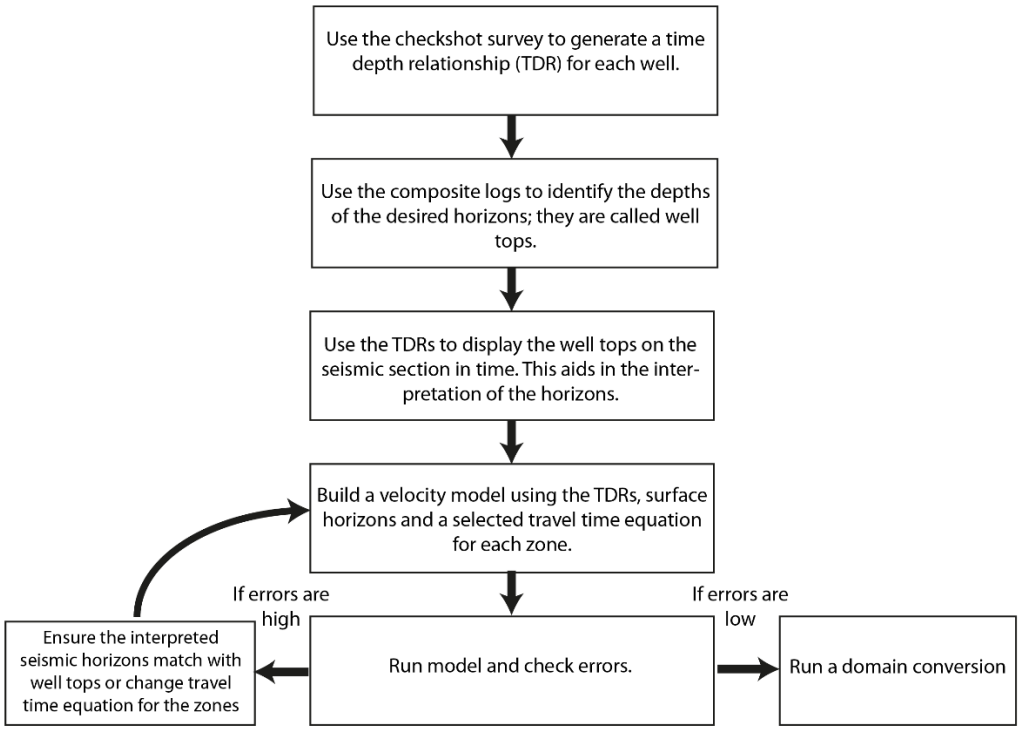


Figure 3.1. The workflow used for seismic depth conversion. A velocity model for the 3D cube is generated using the interpreted seismic horizons and well tops. The selected velocity model can then be used for a domain conversion (milliseconds to metres). Checkshot surveys measure the travel time from a datum to a known depth. See Appendix 1 for the TDRs for the wells used to build a velocity model.

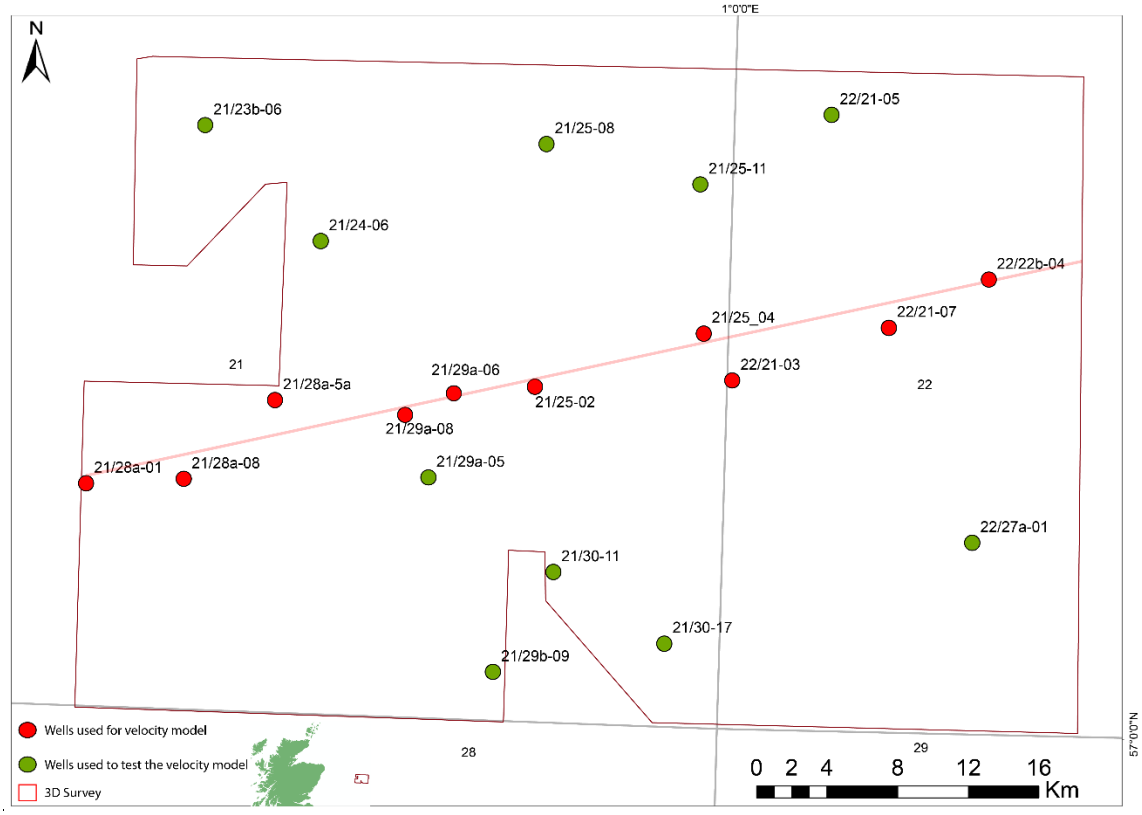


Figure 3.2 Location map showing wells used to generate a velocity model (red circles), wells used to test the velocity model (green circle) and 2D line (red) used in basin modelling.

3.2.1 Travel Time Equations

Two different travel time equations were used for the depth conversion. They are defined below:

1. Linear velocity equation (Linvel): This uses the equation $V= V_o + kZ$ to determine the change in velocity with depth by a factor of k (Baerg, 1991). V_o represents the velocity at the datum (top of the shallowest horizon) while Z is the distance from the datum.
2. Adlinvel equation: This uses the equation $V= V_o + k (Z- Z_0)$ to determine the change in velocity with depth by a factor of k (Schlumberger; version 2017). V_o represents the initial velocity at the surface. This is also a linear velocity equation like Linvel, the difference is the term $(Z- Z_0)$, which represents the distance from a point below the surface to the top of a surface.

V_0 and k were estimated from the wells' time depth relationship (TDR); checkshot survey measures the travel time from the top of the well to a known distance which gives the TDR. For the salt layer V_0 was not obtained from the wells' TDRs, it was assumed to be 4500 ms^{-1} which is consistent with estimated velocities of the Zechstein salt (van Dalfsen et al., 2006; Harding and Huuse, 2015).

Table 3.1 shows the well tops (also called formation tops) identified in the wells used to generate the velocity model (Figure 3.2).

Table 3.1. Table showing wells with well tops for the different horizons. A tick means well tops were available while crosses indicate there were no well tops. Note: Not all horizons had well tops as some wells did not penetrate that horizon or the horizon was not identified on the composite log.

Wells	Pliocene	Upper Miocene	Tay	Chalk	Kimm Clay	Salt
21/28a-01	×	✓	✓	✓	×	×
21/28a-08	×	×	✓	✓	×	×
21/28a-5a	✓	✓	✓	✓	×	×
21/29a-08	×	×	✓	✓	✓	×
21/29a-06	×	×	✓	✓	×	×
21/25-02	✓	✓	✓	✓	✓	✓
21/25-04	×	×	✓	×	×	×
22/21-03	✓	✓	✓	✓	×	×
22/21-07	×	×	✓	✓	✓	×
22/22b-04	×	×	✓	✓	✓	×

3.2.2 Velocity model errors

Three Velocity models were calculated using Linvel (Figure 3.3 a) for all horizons, Adlinvel (Figure 3.3 b) for all horizons and a combination of Linvel & Adlinvel (Linvel for the Pliocene to Chalk horizons and Adlinvel for the Kimmeridge Clay and Salt horizons) as shown in Figure 3.3 c. Model errors were obtained by comparing the horizon depth calculated by the model to the depth of the identified well top. The errors are relatively larger in the wells located in the deepest (easterly) part of the basin (Figure 3.3), and the errors are also larger in the deeper horizons (Top Chalk to Km clay horizons). The lowest errors for most of the horizons were obtained using a combination of Linvel & Adlinvel (Figure 3.3 c) e.g. <100 m for the KM clay and < 60 m for the Chalk. This model (Figure 3.3 c) was used for domain conversion.

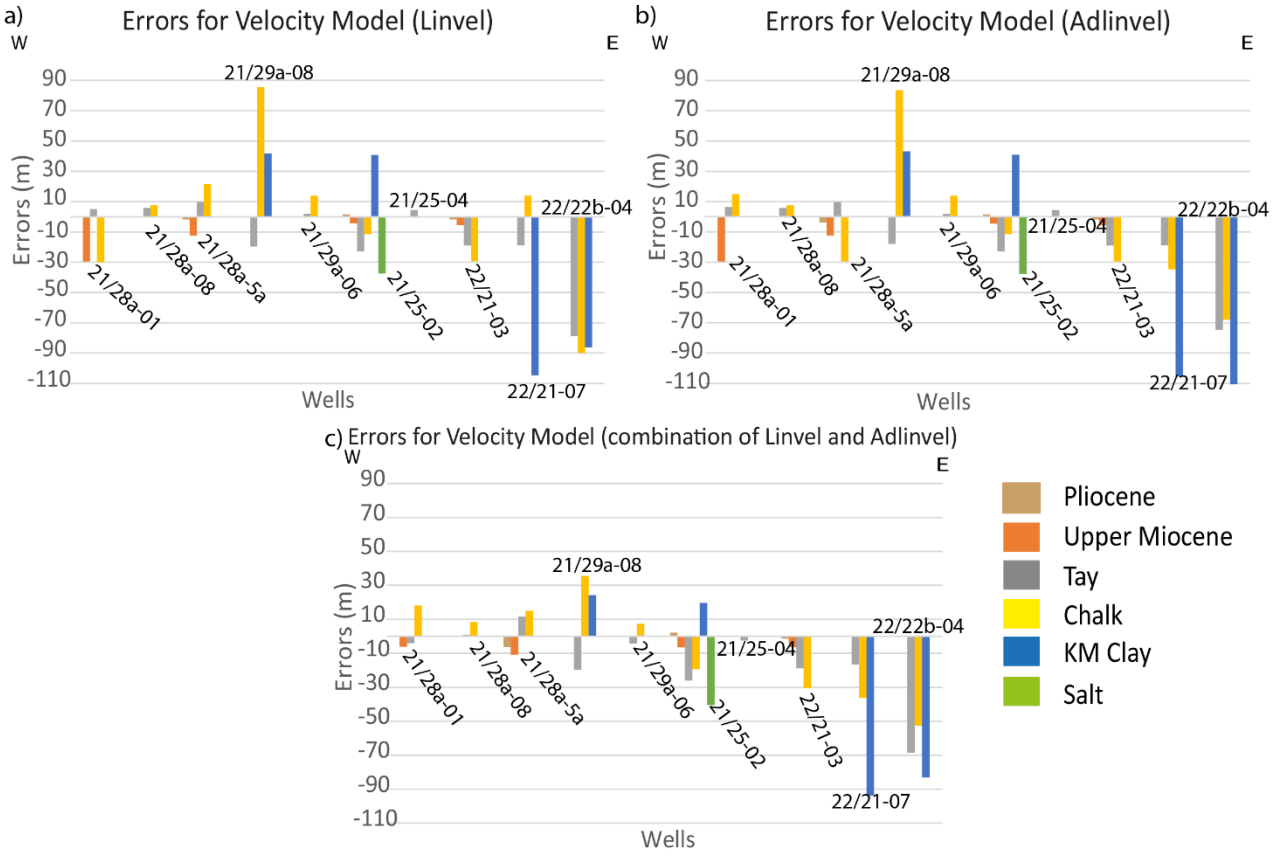


Figure 3.3. Errors for the velocity models. a) velocity model using linvel for all the zones b) velocity model using adlinvel for all the zones and c) velocity model using a linvel for the first four zones and adlinvel for the last two zones.

Most of the wells used to generate the velocity model are arranged diagonally along the centre of the 3D dataset (Figure 3.2). Ten other wells (Figure 3.2) located close to the profile were used to test the velocity model. To do this, 3D surfaces were converted to depth using the model (Figure 3.3 c) which were then compared to the measured depths on the composite

logs. Domain conversion depth errors were worked out for the horizons particularly important to this project (Table 3.2). The largest error was observed in the Kimmeridge clay (± 118 m) and is acceptable for detailed basin modelling.

Table 3.2. Depth conversion errors for 10 wells distributed across the 3D cube. Errors were calculated by subtracting the horizon depth converted surface from its measured depth in the well logs. Negative errors mean the converted depth surfaces are deeper than well tops. For some surfaces well, tops were not available for error estimations.

	Errors (m)					
Wells	Tay	Sele	Forties	Lista	Chalk	KM Clay
21/30-17	30	10	5	-14	8	
22/27a-1		24	24	32	28	107
22/21-05	10	13		-66	-29	
21/23b-06	-59	-44		-49	18	
21/24-06		-45		-80	-39	-64
21/29b-09	29	-7		-49	-3	
21/29a-05		-14		20	-73	-99
21/30-11		17	-7		-2	
21/25-08	-25	-44		-92	-54	
21/25-11	38	13	3	-52	-11	118

3.3 2D Basin Modelling and Input data

The main input data are present day depths of the main horizons, lithologies, erosion times and amounts, hiatus times, past and present heat flow, palaeo- water depth and sediment water interface temperature. The choices for these input parameters are described below.

3.3.1 Stratigraphic Model

Thirteen key horizons were interpreted on the selected 2D line (Figure 3.4). These horizons were depth converted for input into PetroMod. Using the information from wells in the area the following layers were split to represent multiple formations:

1. The Lista formation was split into two layers: The top 80% was attributed to the Lista formation while the bottom 20% was attributed to the Maureen formation.
2. The Chalk was split into two layers: The top 70% was attributed to the Chalk (Chalk Group) while the bottom 30% was attributed to the Base Chalk (Cromer Knoll Group).

3. The Fulmar formation was split into two layers: The top 60% was attributed to the Fulmar formation while the bottom 40% was attributed to the Base Jurassic (Pentland formation).
4. The facies of the bottom 10% of the Tay sandstone member was changed from sandstone to a mixture of 70% mud, 25% sandstone and 5% tuff to represent the Balder Formation.

For simplicity the lithologies of most of layers were not interpreted to vary laterally. Ages, erosion events, hiatus events and lithologies used in the model are shown in Table 3.3. The lithologies of the intervals between horizons were obtained from composite logs.

Table 3.3. The 2D model's stratigraphic input data showing timing of deposition of horizons along with their lithology as well as timing of erosion (including amount of erosion) and hiatus events obtained from composite logs and study by Cayley (1987) and Underhill and Partington (1993).

Age (Ma)	Event Name	Lithology
0	Sea Bed	Shale
2.58	Pliocene	Shale
5	U Miocene	Shale
41.2	Top Tay	Sandstone
47.8	Top Sele	Shale
49.8	Forties Formation	Sandstone
56	Lista Formation	Shale
62.8	Maureen formation	Mixture of shale, sandstone and chalk
66	Top Chalk	Chalk
113.2	Erosion_154_Top	-30 m
129.2	Base chalk	Marl
145	KM clay	Shale
160	Fulmar Sands	Sandstone
168	Erosion_98_Top	-300 m
182	Base Jurassic	Siltstone
195	Hiatus_96_Top	
201	Triassic	Siltstone
252	Salt	Salt
272	Rotliegend	Sandstone overlaying volcanics
300	Model Base	

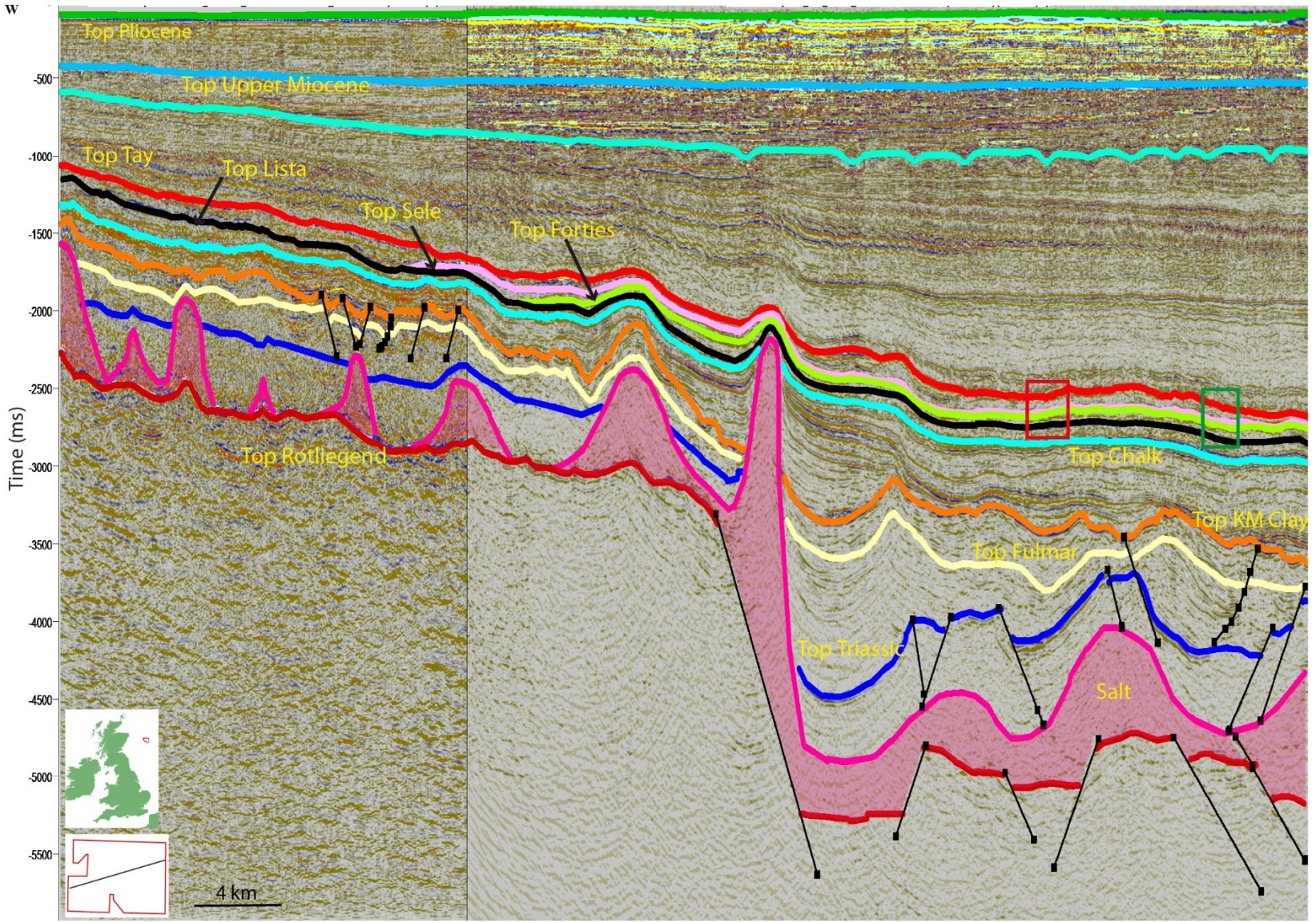


Figure 3.4. Composite west-east of regional seismic line across the study area. showing structural geology of the CNS. 13 key horizons are interpreted highlighting how the salt affects the overlying structure. The red-box is the location of Figure 3.5 a. The green-box is the location of Figure 3.5 b. KM= Kimmeridge Clay. Insert showing location of seismic line. Faults are marked on in black. Seismic data courtesy of TGS and PGS. See Appendix 1 for the acquisition and processing information of the seismic data.

Sandstone intrusions (injectites) have been identified as important elements of the Palaeogene play of the Central and Northern Sea where they form potential reservoirs, waste zones or fluid migration pathways through mudstones (Huuse and Cartwright, 2004; Huuse et al., 2005). Hydrocarbon migration into the sealed sandstones along with differential compaction caused by the rapid burial of these sandstones beneath low-permeability shales would lead to substantial overpressure (Huuse et al., 2005; Jackson, 2007). This build-up of overpressure along with a catastrophic event such as a large magnitude earthquake or a bolide impact is required to trigger a basin wide injection of sand into the overlying layers (Stewart, 1999; Huuse et al., 2005; Jackson et al., 2011). A series of large earthquakes related to the North Atlantic tectonic movement such as the plate reorganisation in the Mid Cenozoic or the regional uplift in the Neogene (both described by Doré et al. (1999)) could be triggers for sand injection into the Eocene strata. Some evidence of wing like sandstone intrusions are seen in the dataset as shown in Figure 3.5. The facies of the Sele formation in the model was changed to sandstone in the areas where the injectites were interpreted.

Injectites (Figure 3.6) were observed in core samples of the Tay sandstone member in the Catcher field which is located 22 km south of the study area. Figure 3.6 a-b shows small injectites < 10 cm most likely originated from the Forties sandstone member while relatively larger scale breccia injectites > 1.5 m (Figure 3.6 c) likely originated from the sandstones in the Maureen Formation. For the injectites to be resolved on seismic data they would have to be thicker than 18 m; assuming a dominant frequency of about 40 Hz (Yilmaz, 2001).

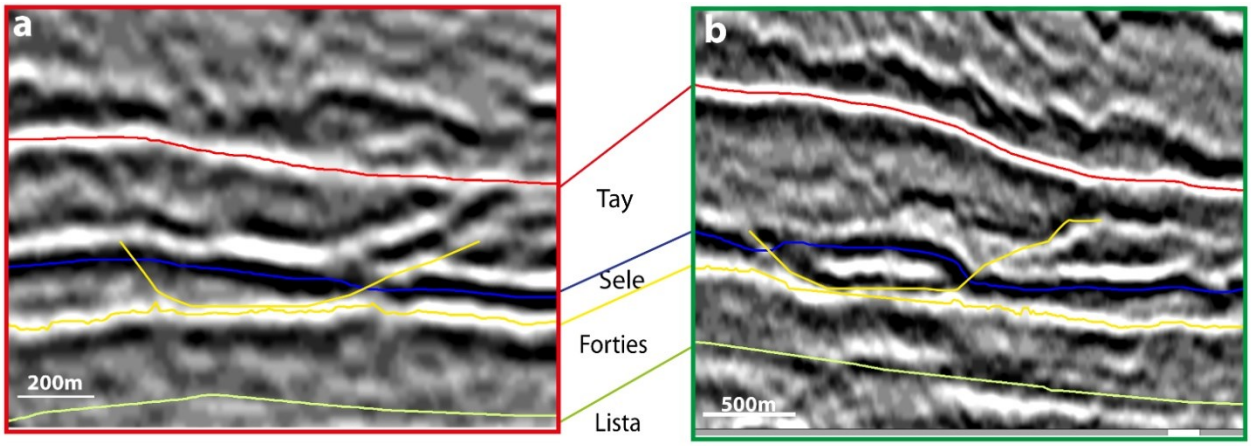


Figure 3.5. Seismic data showing sandstone intrusions (injectites- coloured yellow) seen in the west of the study area. a) is located in the red box highlighted in Figure 3.4 and b) is located in the green box highlighted in Figure 3.4.

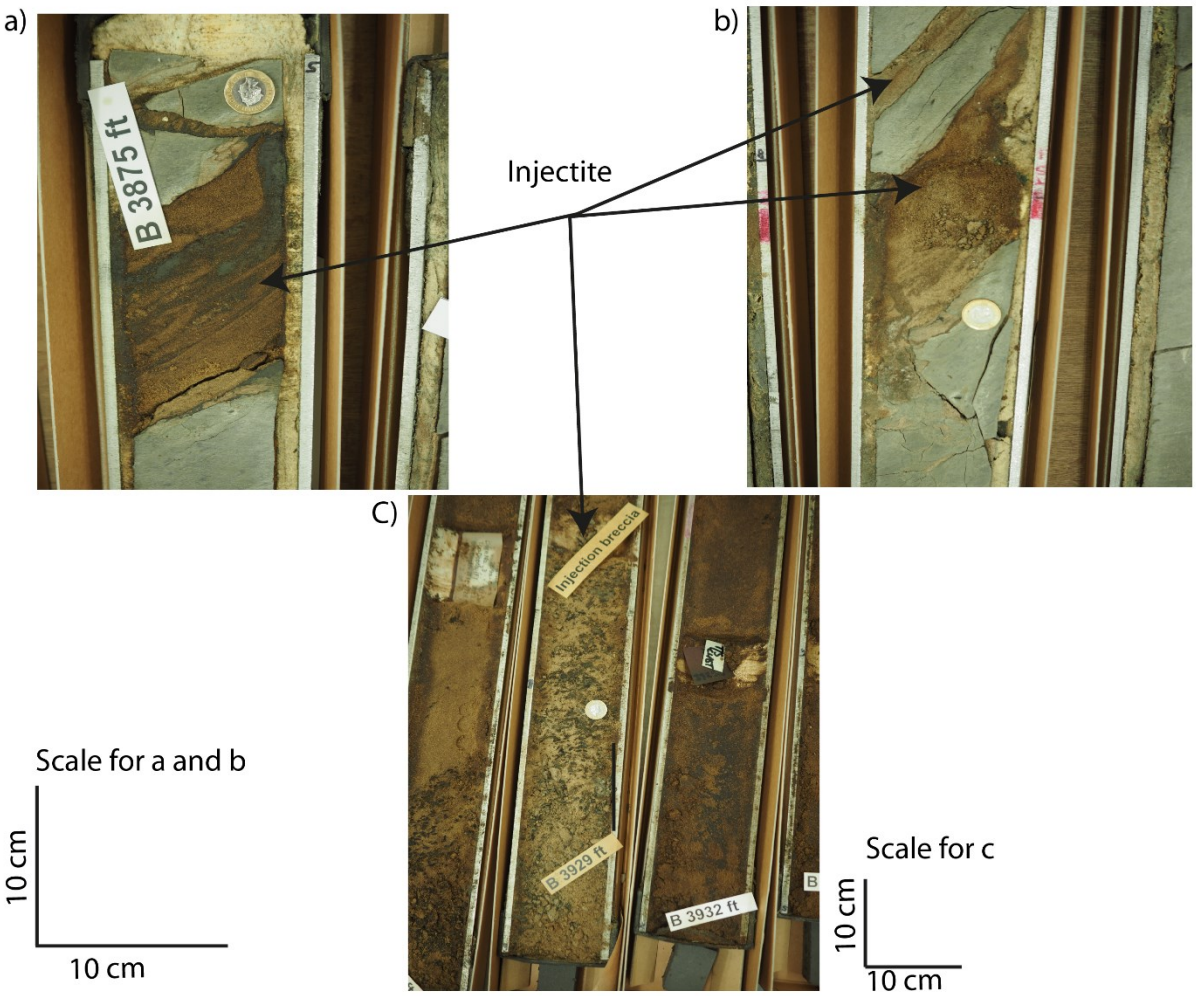


Figure 3.6 Picture showing injectites observed in the Tay sandstone in well 28/09-03 22 km from the study area. a-b) small scale injectite c) large scale injection breccia. Pictures were taking from core stored in the BGS core repository in Keyworth, Nottinghamshire.

3.3.2 Structural Model

Palaeo-water depths were obtained from Barton and Wood (1984). The timing of the erosion and hiatus event (Table 3.3) were obtained from the work done by Cayley (1987) and Underhill and Partington (1993).

Salt Movement

The movement of the salt through time must be considered when reconstructing the evolution of the basin. The 1860 m of salt was assumed to have deposited uniformly until the initiation of movement at 245 Ma (Cayley, 1987). Over time the layer facies were changed to salt in the areas that were pierced by the diapirs. Table 3.4 shows the timing of facies replacement by salt. The palaeo-movement of the diapir was estimated using seismic data

and PetroMod's reconstruction of layer geometries. The seismic data suggests the salt in the area stopped moving during the Pliocene

Table 3.4. Table showing the timing of facies replacement caused by diapirism. Timing was estimated with the aid of PetroMod's burial reconstruction feature.

Facies replaced by Salt	Time of Replacement (Ma)
Maureen Formation	40
Chalk	57
Base Chalk	70
Kimm Clay	130
Fulmar Formation	140
Base Jurassic	142
Triassic	145

Faults

In this model all the faults were treated as fluid barriers, i.e., closed. Fisher and Knipe (2001) have demonstrated that extensional faulting in the CNS produced cataclasites and clay smears, this along with deep burial results in fault permeability ranging from 0.00001 to 0.2 mD. No evidence of inversion was noticed in the 3D cube, so it is unlikly the fault permeability would have increased in recent times.

Layer Permeabilities

Studies have shown that relatively high sedimentation rates along with compaction disequilibrium during the Cretaceous and Tertiary caused overpressure in Jurassic reservoirs which led to capillary seal failure (Cayley, 1987; Isaksen, 2004). This greatly improved the prospectively of the Tertiary sandstones as the hydrocarbons migrated vertically form the Jurassic strata, with the chalk acting as a conduit. To model this correctly, the permeability of the layers above the source rock was increased from their default values to values consistent with measured permeability of the Lista formation shales, chalks and marls in the Central North Sea (Megson and Hardman, 2001; Mallon and Swarbrick, 2008a; Kilhams et al., 2012); see Table 3.5.

Table 3.5 Modified permeability parameters for selected layers. Permeability values obtained from Megson and Hardman (2001), *Mallon and Swarbrick (2008a)* Mallon and Swarbrick (2008b) and Kilhams et al. (2012).

Layer	Lithology	Porosity (%)	Permeability (log (mD))
Base chalk	Marl	1	-1.9
		25	-1
		50	-0.5
Chalk	Limestone (Chalk)	1	-5
		25	-0.5
		70	1
Maureen	Mixture of shale, sandstone and chalk	1	-6.1
		25	-1.0
		41	0.7
Lista	Shale	1	-2
		25	1.2
		70	2

The interpreted 2D seismic line (Figure 3.4) coupled with the modelling input shown in Table 3.3. Table 3.3 and Table 3.5 were used to produce a present-day structural model for input to PetroMod (Figure 3.7).

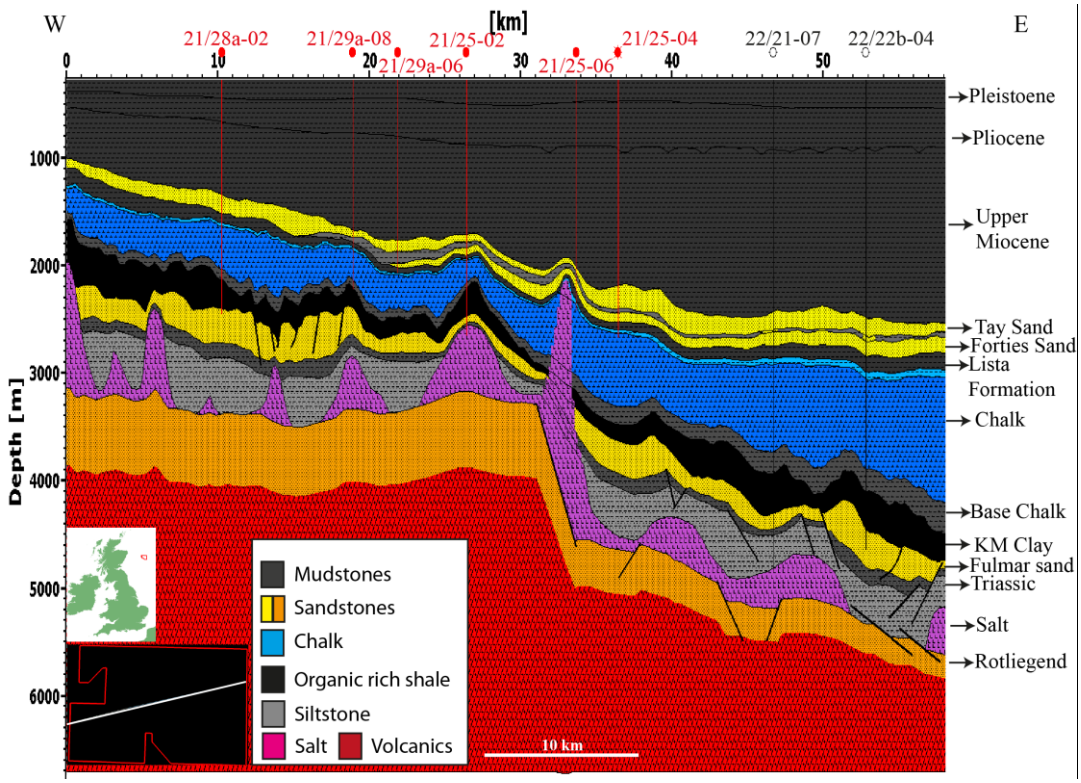


Figure 3.7 Present day structural and lithology model input to PetroMod. Red lines represent hydrocarbon wells while black lines represent dry wells. Insert shows the location of the 2D line in the study area.

3.3.3 Thermal Boundary Conditions

The sediment-water interface temperature (SWIT) and basal heat-flow variations with time are needed to reconstruct the thermal evolution of the basin. SWIT varied between 2 and 25 ^{o}C based on the time-latitude chart defined by Wygrala (1989). Scotchman et al. (2000) calculated the heat flow variation through time in the Central Graben by using the tectonic history from 1D modelled wells. The results were calibrated using R_o data. The palaeo-basal heat flow used is shown in Figure 3.8. This heat flow is from well 20/20a-1 which is located 14 km north of the study area.

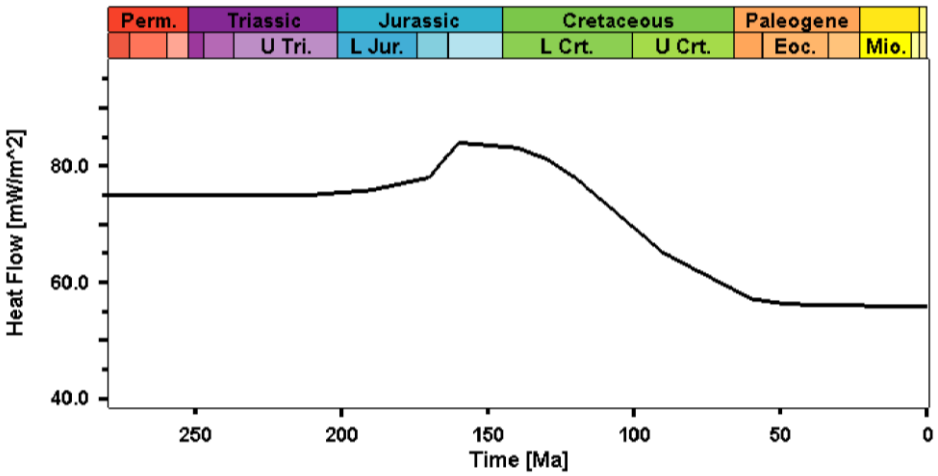


Figure 3.8 Heat flow used in the basin model. Image modified from Scotchman et al. (2000)

3.3.4 Source Rock Properties

Hydrocarbon generation in the Kimmeridge Clay source rock was modelled using the 14 component predictive phase kinetics (TII Kimmeridge clay crack) of di Primio and Horsfield (2006). Estimates of initial HI (hydrogen index) and TOC are needed to accurately simulate hydrocarbon generation. Present day HI is used to back calculate initial HI input for the models. The formula below is used to back calculate HI (Hantschel and Kauerauf, 2009):

$$HI_{\text{in}} = \left(\frac{HI}{1-TR}\right) \times 100 \qquad \text{Equation 3.1}$$

Where HI_{in} is the initial HI, HI is the present-day HI and TR is the transformation ratio. TR measures the effectiveness of the kerogen to generate hydrocarbon (Tissot and Welte, 1984). The geochemistry report from well 21/25-12 (North of 21/25-11 in Figure 3.2) showed the present-day HI of the Kimmeridge Clay to be 530 mgHC/gTOC. The 1D basin model of well

21/25-12 shows the TR to be 10% as indicated in Figure 3.9 (black line). Using these values in Equation 3.1 gives an initial HI estimate of 589 mgHC/gTOC. This is tested by running another 1D basin model with the HI_{in} calculated. The result shown in Figure 3.9 (red line) demonstrates a gradual drop of HI_{in} to a present-day HI of 530 mgHC/gTOC. This is considered to be an acceptable value as HI for immature type II source rocks has been reported to be between 200 and 645 mgHC/gTOC (Isaksen, 2004; Jarvie, 2012).

Present-day TOC of the Kimmeridge clay in the Central North Sea has been reported to be as high as 15% and averaging 8% (Cayley, 1987). These measurements were likely carried out on immature Kimmeridge Clay samples. They would be used as uniform initial TOC inputs in the model. The relationship between TOC and TR is shown in Figure 3.10. A uniform initial TOC of 15 % (red line in Figure 3.10) was applied across the 2D area and a simulation was carried out. It is noticed that the present-day TOC (Blue line in Figure 3.10) is less in areas with higher TR (Black line in Figure 3.10). The present-day TOC varies from 8% in areas with TR higher than 90 % to 15 % in areas with TR less than 20 % (Figure 3.10).

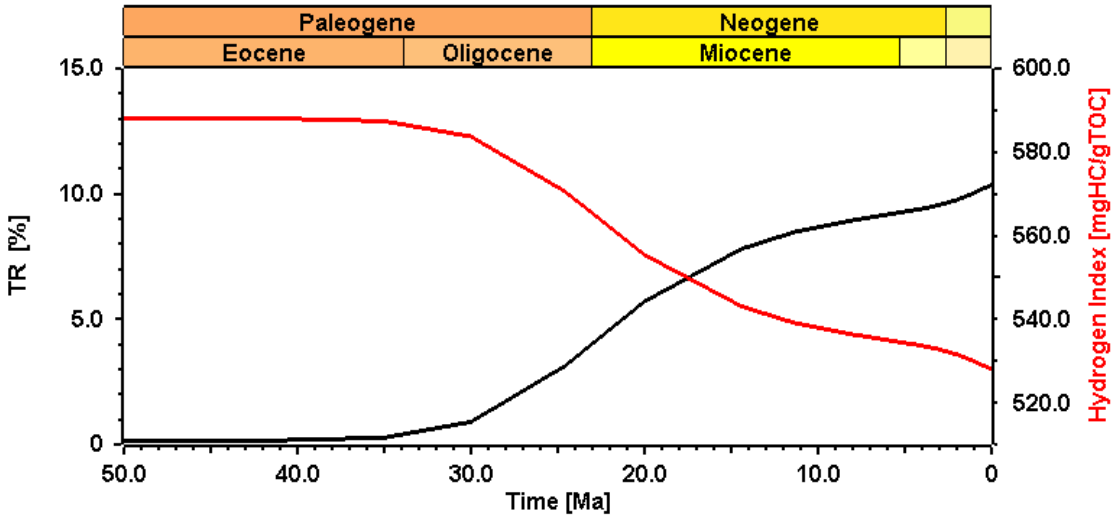


Figure 3.9 Changes in TR and HI with time demonstrating the ability of equations 4.2 to estimate initial HI value. Black line shows an increase in TR from 0 to 10% while the red line shows the HI drop from an initial value 588 mgHC/gTOC to the present-day value of 530 mgHC/gTOC shown in the geochemistry report for well 21/25-12.

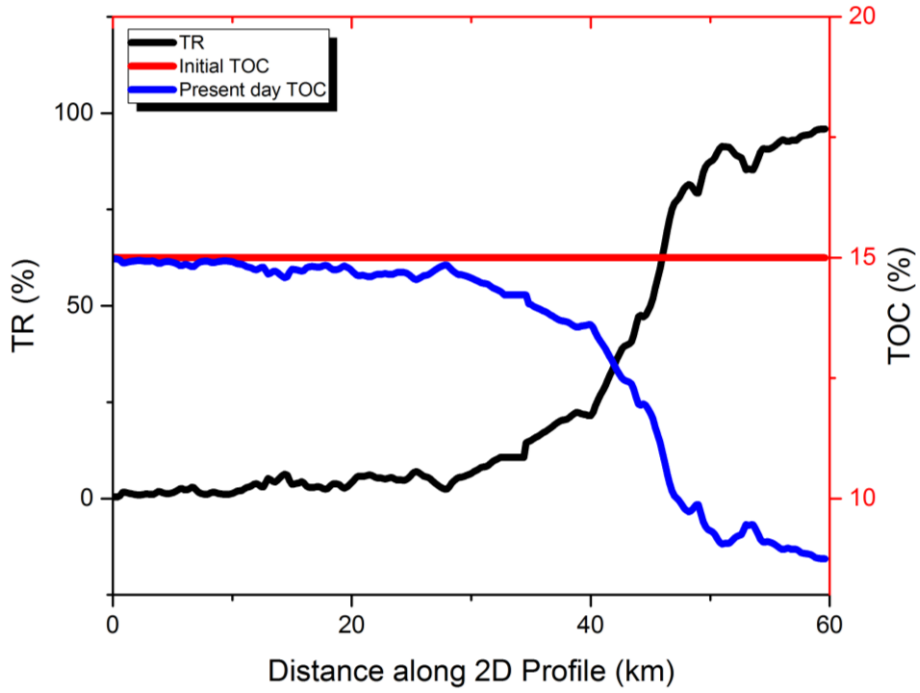


Figure 3.10 2D profile of the top of the Kimmeridge Clay showing the relationship between TR line map (black line) and present-day TOC line map (blue line) across the 2D profile. Uniform initial day TOC line map value of 15 % (red line) was obtained from Cayley (1987).

3.3.5 Modelling Migration Methods

Three different methods are commonly used to migrate fluids through porous media in PetroMod. They are summarized below:

1. Multi-phase Darcy Flow (D): Darcy's law (Darcy, 1856) has been modified by Hubbert (1956) to describe petroleum flow as a function of the effective permeability of the rock matrix for two phase fluid flow, petroleum viscosity and petroleum migration potential over an interval length with a cross-sectional area. PetroMod modifies Hubbert's equation (Hubbert, 1956) to include differential terms for multi-phase fluid flow (Hantschel and Kauerauf, 2009).

   Multi-phase Darcy Flow works effectively in low permeability cells (e.g. shale source rock) but requires multiple iterations before convergence occurs in high permeability cells (e.g. sandstone reservoir) because the model struggles to migrate large amounts of petroleum rapidly (Baur and Katz, 2018). Therefore, multi-phase Darcy Flow is typically used to model primary migration.
2. Flowpath (FP): This migration method models fluid flow as a purely geometrical problem (Hantschel et al., 2000). It is applied to highly permeable cells or carrier beds while the low permeability cells act as seals. In a permeable layer buoyancy is the

driving force for migration (Sylta, 2004). When this happens petroleum moves upwards until higher capillary entry pressure is encountered resulting in the filling of a trap followed by spilling in the steepest direction upwards within the reservoir (Hantschel and Kauerauf, 2009).

FP migration is the only migration method that uses a high resolution geometry to calculate accumulation column heights in the permeable layer (Hantschel et al., 2000). This results in the most accurate estimate of the volume of petroleum trapped in the reservoir, but FP migration alone ignores timing of vertical migration to the reservoir and lateral migration in low permeability regions.

3. Invasion Percolation (IP): This uses the permeability, buoyancy and capillary entry pressure gradients for each model cell to determine flow direction (Wilkinson and Willemsen, 1983). This is regarded as an over simplification of the natural system but is accepted in modelling for fluid flow in highly permeable layers. To better simulate complex migration patterns in a basin, a degree of anisotropy (± 10%) is added to the capillary entry pressure for each model cell (Hantschel and Kauerauf, 2009; Baur and Katz, 2018). Vasseur et al. (2013) has shown that the introduction of anisotropy results in migration patterns consistent with laboratory experiments. IP can easily handle complex geological structures and facies distribution resulting in very few geologically unreasonable artefacts (Baur and Katz, 2018)

Accurately solving the modified Darcy flow equations in high permeability cells leads to longer simulation times (roughly takes double the time). In order to save computation time multi-phase Darcy flow is usually combined with either the FP or IP migration method. In a combined migration method, multi-phase Darcy flow is used in low permeability zones (primary and secondary migration) while either FP or IP is used in high permeability zones (migration within the reservoir and tertiary migration in the case of IP). PetroMod uses a threshold of 2.01 (log) mD to distinguish the two zones (Hantschel and Kauerauf, 2009). In this project, migration methods combining multi-phase Darcy flow with Flowpath are called D+FP (termed “hybrid” in PetroMod), while migration methods combining multi-phase Darcy flow with Invasion Percolation are termed D+IP.

3.4 Results and Discussion

Table 3.6 shows the type of hydrocarbon accumulation in the wells across the 2D line (Figure 3.7). This information was used to calibrate the modelling results.

Table 3.6. Hydrocarbons encountered in the wells on the 2D line (Figure 3.7). This information was used to calibrate the location of hydrocarbon accumulation in the 2D models. Information on the oil or gas shows was obtained from composite logs. × means no hydrocarbon accumulation was observed in the sandstone member or formation.

Well Name	**Reservoir**		
	Tay	Forties	Fulmar
21/28-02	Oil	×	×
21/29a-08	Oil	×	×
21/29a-06	Oil	×	×
21/25-02	Oil	Oil	Oil
21/25-06	Oil	×	×
21/25-04	Oil and Gas	×	×
22/21-07	×	×	×
22/22b-04	×	×	×

.

3.4.1 Model Calibration

Corrected well temperatures and R_o data were used to calibrate the thermal maturity of the basin while the porosity data from wireline logs were used to calibrate the lithology compaction. Corrected temperature data for wells 21/29a-08, 21/25-02, 22/22b-04 and 21/28-02 (Figure 3.11 a, c, e and g respectively) were obtained from the Oil & Gas Authority (OGA) website. R_o data for well 22/22b-04 (Figure 3.11 e) was obtained from measurements carried out by Barnard and Bastow (1991) while R_o data for well 21/28a-02 (Figure 3.11 h) was obtained from the well's geochemistry report carried out by ExxonMobil. Porosity for wells 21/29a-08 and 21/25-02 (Figure 3.11 b and d respectively) were estimated using wireline logs obtained from IHS. The calibration results (Figure 3.11) suggest the palaeo-heat flow, amount of erosion and lithology compaction parameters used in the model can accurately model the thermal and structural evolution of the basin.

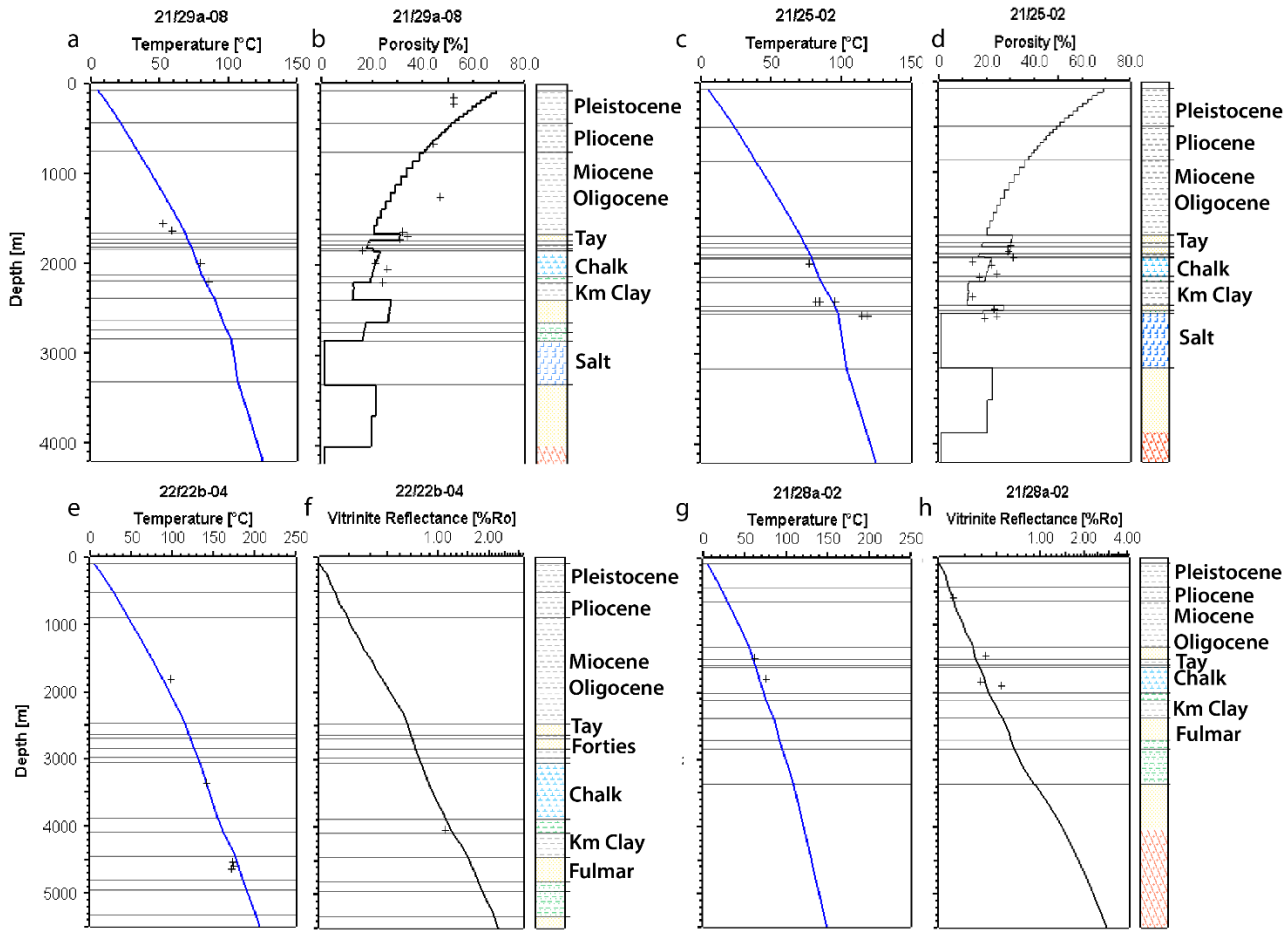


Figure 3.11. Examples of model calibration for wells: 21/29a-08: a) temperature and b) porosity); 21/25-02: c) temperature and d) porosity 22/22b-04: (e) temperature and f) R_0 obtained from Barnard and Bastow (1991) and 21/28a-02: g) temperature and h) R_0 obtained from well geochemistry report. Well locations are shown in Figure 3.7. The crosses represent the measured properties. Temperature data was obtained from the OGA and porosity was estimated using wire line logs from IHS.

3.4.2 Base-Case Model

A base-case model was simulated using the D+IP migration method with an Initial TOC of 15% and initial HI of 589 mg/g TOC. The modelling outputs are described below.

3.4.2.1 Source Rock Maturation, Hydrocarbon Generation and Expulsion

The modelled transformation ratio pattern across the 2D profile is shown in Figure 3.12 a. As expected only the Kimmeridge Clay is mature. Figure 3.12 b-e shows the modelled timing of expulsion and generation of oil from the Kimmeridge Clay at different locations on the 2D profile. The results suggest significant generation and expulsion of hydrocarbons from the source rock occurs only in the deeper, eastern part of the study area (Figure 3.12 a-c; 40-58 km mark). The source rock is mature for oil in the east at burial depths of 3500-4500 m (burial depths) and only reaches the early stages of maturity for gas at the eastern edge at

depths greater than 4600 m. This observation is consistent with work carried out by Isaksen (2004). Generation of oil (Figure 3.12 b; 57 km mark) slowly started in the Early Cretaceous (around 130 Ma) and in the Early Oligocene (around 30 Ma) for the generation of gas (Figure 3.12 b; 57 km mark). This is similar to estimates made by Barnard and Bastow (1991). A noticeable increase in TR (Figure 3.12 b-e; 31-58 km mark) is noticed between the Oligocene and Miocene, this is likely caused by continued burial (temperature extracts from the top of the Tay in Figure 3.13 shows the main increase in burial rate was during the Pliocene). This was accompanied by an increase in generation of oil (Figure 3.12 b-c; 57 and 42 km mark) and triggered generation of some gas at the eastern edge (Figure 3.12 b; 57 km mark).

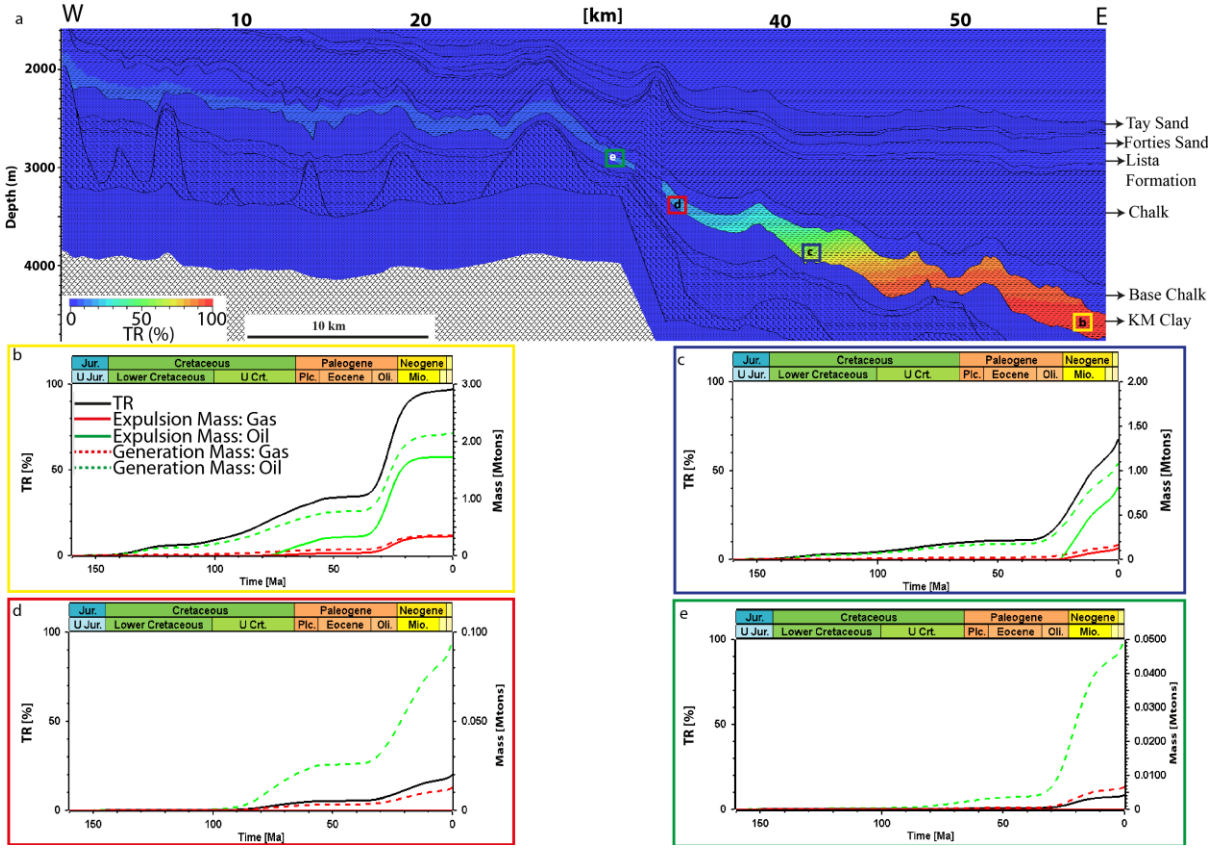


Figure 3.12 Thermal maturity and hydrocarbon generation & expulsion patterns across the 2D section. a) Present day TR across the 2D section. TR vs time (black line), generation mass of gas vs time (dashed red line), generation mass of oil vs time (dashed green line), expulsion mass of gas vs time (red line) and expulsion mass of oil vs time (green line) at b) 57 km mark, c) 42 km mark d) 35 km mark and e) 31 km mark along the 2D profile.

Expulsion of oil slowly started during the Late Cretaceous (around 75 Ma) in the east (Figure 3.12 b; 57 km mark). Increased generation of hydrocarbons (Figure 3.12 b-c; 57 and 42 km mark) during the Oligocene to Miocene triggered another noticeable expulsion of oil (Figure 3.12 b-c; 57 and 42 km mark) and expulsion of some gas (Figure 3.12 b; 57 km mark) in the eastern edge of the study area. There was no expulsion of oil or gas modelled in the west (Figure 3.12 d-e; 35 and 31 km mark) as very little to no generation of hydrocarbons occurred.

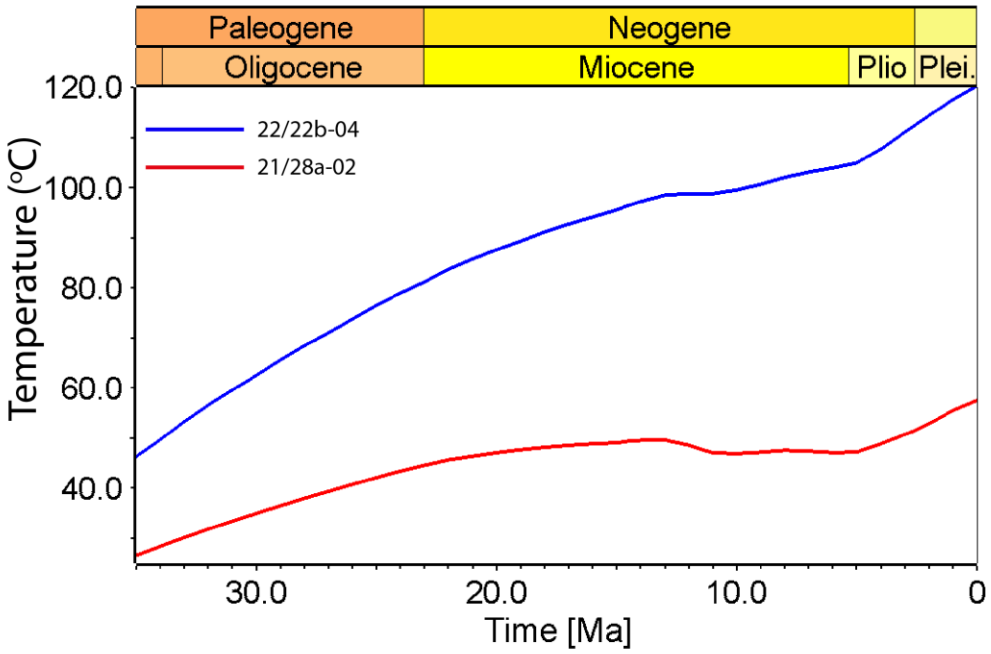


Figure 3.13. Temperature vs time extract from the Top Tay sandstone member in well 22/22b-04 (blue line) which is located in the east and 21/28a-02 (red line) which is located in the west. Plot shows a rapid increase in temperature from the start of the Pliocene which is indicative of rapid burial and is responsible for the present-day overpressure seen in the CNS. Location of two wells are shown in Figure 3.7.

3.4.2.2 Hydrocarbon Migration and Accumulations

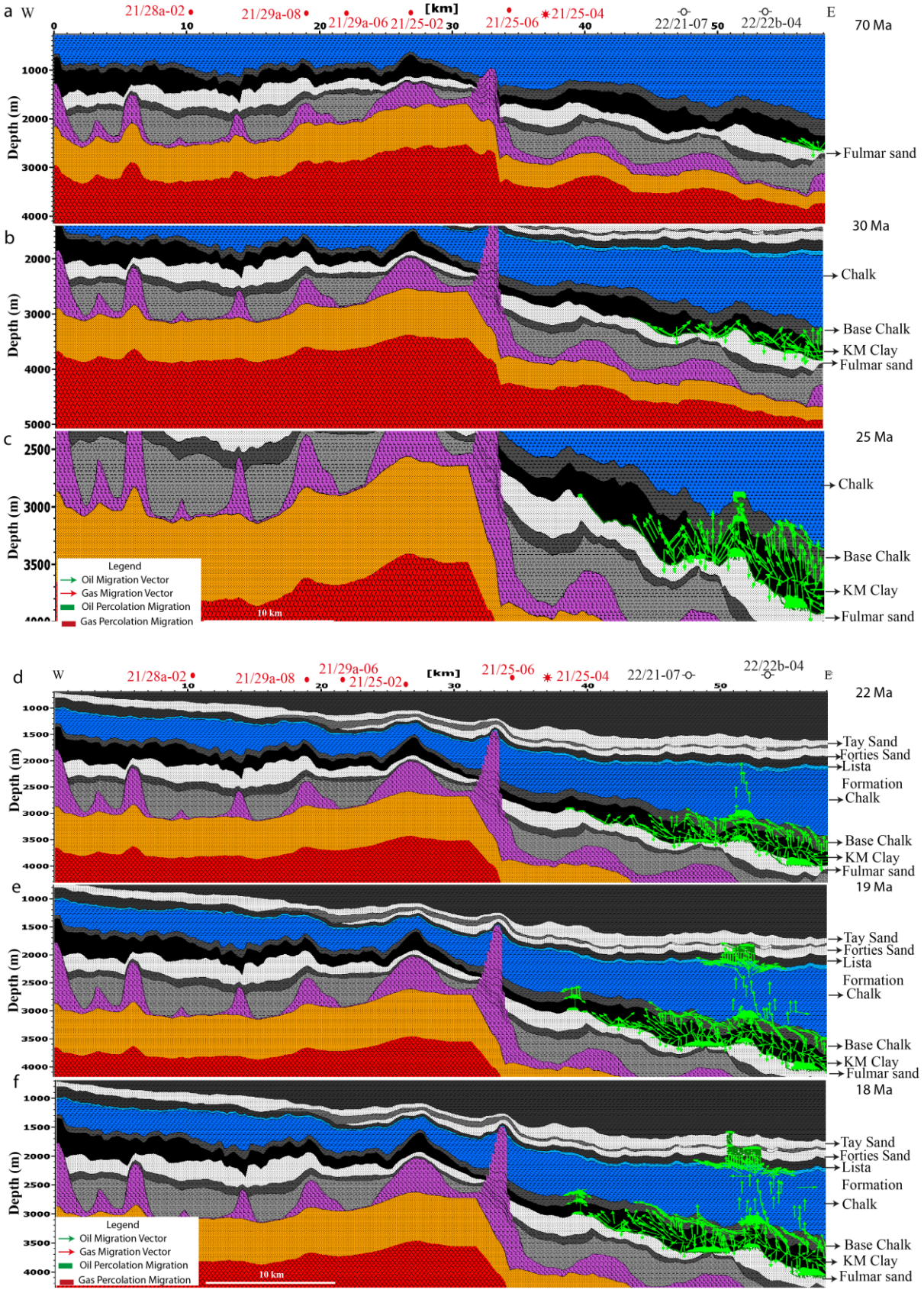
The modelled timing of the primary migration, secondary migration and migration within the reservoirs (Fulmar formation, Forties and Tay sandstone member) are shown in Figure 3.14. Downward expulsion of oil into the Fulmar sandstone begins around 70 Ma (Figure 3.14 a). This continues until about 30 Ma (Figure 3.14 b) where both downwards and upwards expulsion of oil occurs. Oil reaches the top of the base Chalk at about 25 Ma (Figure 3.14 c) and takes about 3 Myr to reach the top of the Chalk (Figure 3.14 d). At the same time the oil migrates up dip, mostly along the regional dip to the west, following a fill to spill chain in the Fulmar sandstone (Figure 3.14 d).

At 19 Ma (Figure 3.14 e) oil reaches the Forties sandstone via vertical migration through the Chalk in the east. With the aid of injectites the oil migrates vertically into the Tay sandstones in the east at about 18 Ma (Figure 3.14 f). This agrees with the Jones et al. (2003) estimate of migration into the Tay Fan. From 18 Ma to 7 Ma (Figure 3.14 g) traps are filled in the east and the oil starts to migrate up dip in both the Tay and Forties sandstone. While this is happening the capillary entry pressure at the base of the Chalk forces some oil to migrate laterally within the base Chalk till it reaches the salt which aids vertical migration into the Forties and Tay sandstones in the centre of the basin (Figure 3.14 g-h). Around 3 Ma (Figure 3.14 h) oil

migrating up dip from the east in the Tay and Forties sandstones mixes with the oil accumulation above the salt diapir and continues moving to west. Also, at this time gas being expelled from the deepest part of the source rock reached the top of the Tay in the east. This continues until present day as shown in Figure 3.14i.

The following key observations in the base case model (Figure 3.14i) are listed below:

- Oil is migrating into the Tertiary sandstones at present day (Figure 3.14i), agreeing with estimates of Jones et al. (2003).
- The injectites and salt diapirs are vital for migration into the Tay sandstones.
- The injectites are required to migrate oil into the Tay sandstones in the east (Figure 3.14 i). Without the injectites vertical migration of oil into the Tay would be incomplete.
- The salt diapir acts as a salt wall in 2D space which stops migration in the marl (base Chalk) and forces vertical migration through the chalk (Figure 3.14g-h). The salt diapir also creates a trap above its crest which results in sufficient build-up of oil in the Forties to initiate seal capillary failure and breakthrough into the Tay (Figure 3.14h).
- Wells 22/21-07 and 22/22b-04 are dry wells (Table 3.6), but due to a 2D artefact the model suggests hydrocarbon accumulation at their locations (Figure 3.14i). In this 2D model oil and gas can only move east to west, accumulations of oil and gas can occur in areas where the oil and gas would spill to the north or south in reality.
- Model seems to predict the accumulation of oil in the Base Chalk (Figure 3.14i), this is a migration artefact. Once the model has switched from Darcy flow to IP it cannot switch back to Darcy flow even if that oil leaks into low permeability cells (Baur and Katz, 2018). In this model IP migration was used during migration in the Fulmar sandstones and as it escaped from the traps into the overlying strata (Figure 3.14).
- Running a more sophisticated 3D model with a facies model (shown in Chapter 5) should remove the 2D artefacts and test the importance of the salt and injectites for the vertical migration of oil into the Tay Sandstones.


a
W
21/28a-02
21/29a-08
21/29a-06
21/25-02
[km]
21/25-06
21/25-04
22/21-07
22/22b-04
E
70 Ma
Depth (m)
Fulmar sand
b
30 Ma
Chalk
Base Chalk
KM Clay
Fulmar sand
c
25 Ma
Chalk
Base Chalk
KM Clay
Fulmar sand
Legend
Oil Migration Vector
Gas Migration Vector
Oil Percolation Migration
Gas Percolation Migration
10 km
d
W
21/28a-02
21/29a-08
21/29a-06
21/25-02
[km]
21/25-06
21/25-04
22/21-07
22/22b-04
E
22 Ma
Depth (m)
Tay Sand
Forties Sand
Lista
Formation
Chalk
Base Chalk
KM Clay
Fulmar sand
e
19 Ma
Tay Sand
Forties Sand
Lista
Formation
Chalk
Base Chalk
KM Clay
Fulmar sand
f
18 Ma
Tay Sand
Forties Sand
Lista
Formation
Chalk
Base Chalk
KM Clay
Fulmar sand
Legend
Oil Migration Vector
Gas Migration Vector
Oil Percolation Migration
Gas Percolation Migration
10 km

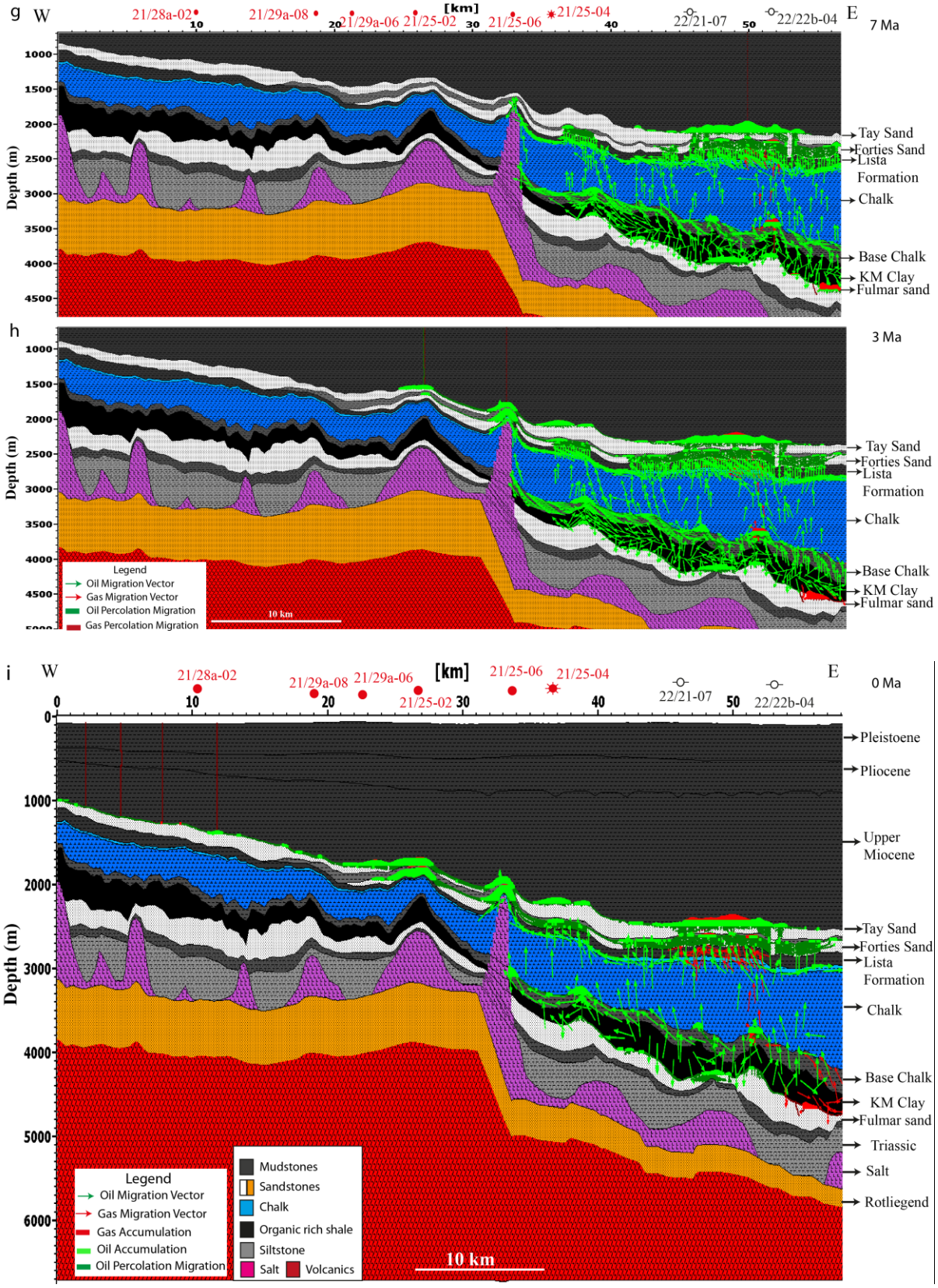


Figure 3.14. Hydrocarbon accumulation and migration as a function of time: a) 70 Ma- onset of migration, b) 30 Ma- migration into the Fulmar, c) 52 Ma-migration into base Chalk, d) *22* Ma- migration through chalk, e) *19* Ma- migration into the Forties and up salt diapir, f) 1*8* Ma- migration into the Tay, g) *7* Ma- continued migration into Tay and Forties, h) *7-3* Ma- onset of lateral migration in the Tay and Forties, I) 0 Ma- present day accumulation and migration. Note: all faults are toggled off.

3.4.3 Testing parameter space: Sensitivity check

The sensitivity of the model was tested by varying initial TOC, migration method and layer and fault properties. Differences from the base model are measured by comparing migration vectors, accumulation location and volume of oil.

3.4.3.1 Lack of Injectites

To test the importance of injectites the facies of the Sele Formation was changed to a uniform layer of mud in the base case model (Figure 3.14 i). The differences are highlighted in Figure 3.15. Without the injectites there would be no migration of oil into the Tay sandstones in the east as demonstrated by the lack of oil in well 21/25-04 (37 km mark in Figure 3.15 b). Most of the oil stays in the Forties sandstones and migrates vertically into the Tay sandstones at the 33 km and 27 km mark (Figure 3.15 b). See Chapter 4 for a discussion on the importance of the injectites (in 3D) in the study area.

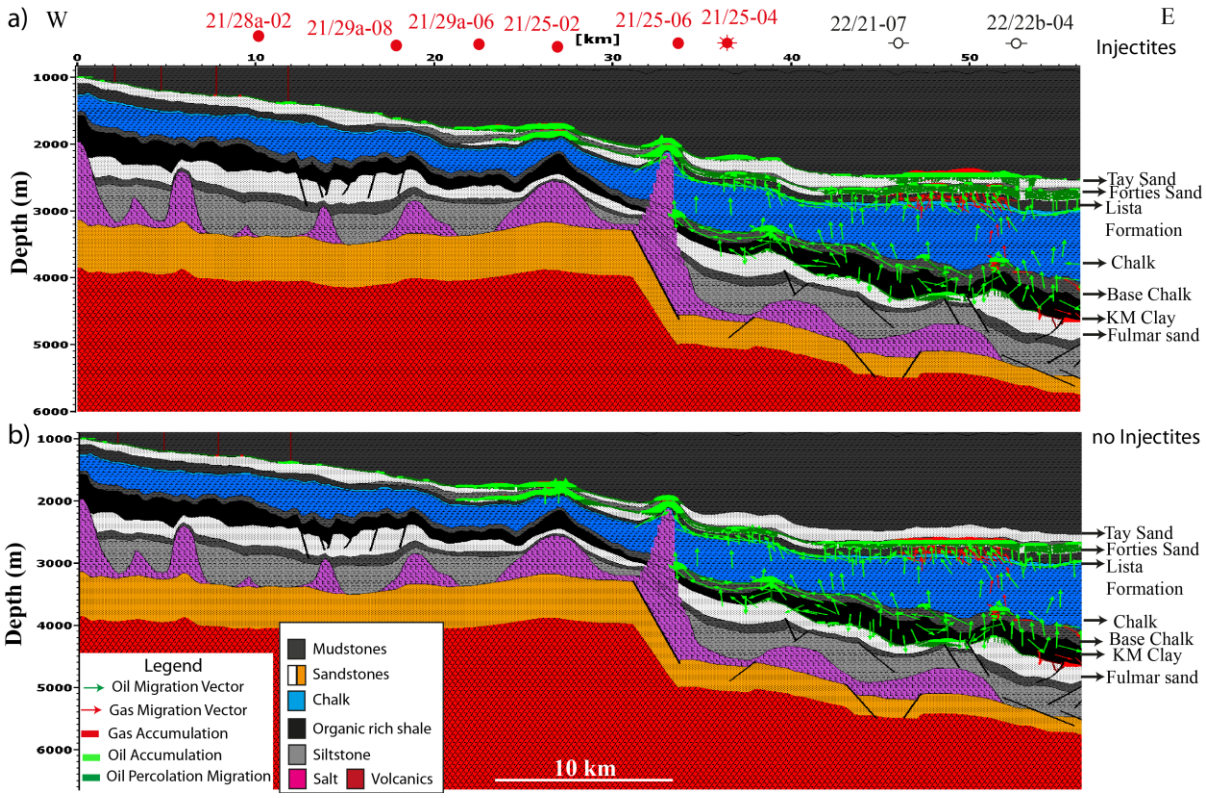


Figure 3.15 Comparison of model with a) injectites in the east and b) no injectites in the study area which shows the lack of hydrocarbon in the Tay sandstones located in the east.

3.4.3.2 Varying Initial TOC

Alternative TOC scenarios were explored using uninform initial TOC of 8 % and 20 % across the Kimmeridge Clay. Modelling with an initial TOC of 8 % results in a present-day TOC varying from 5 % to 8 % (red line in Figure 3.16) while a variation from 13 % to 20 % present-day TOC (blue line in Figure 3.16) is observed with an initial TOC of 20 %.

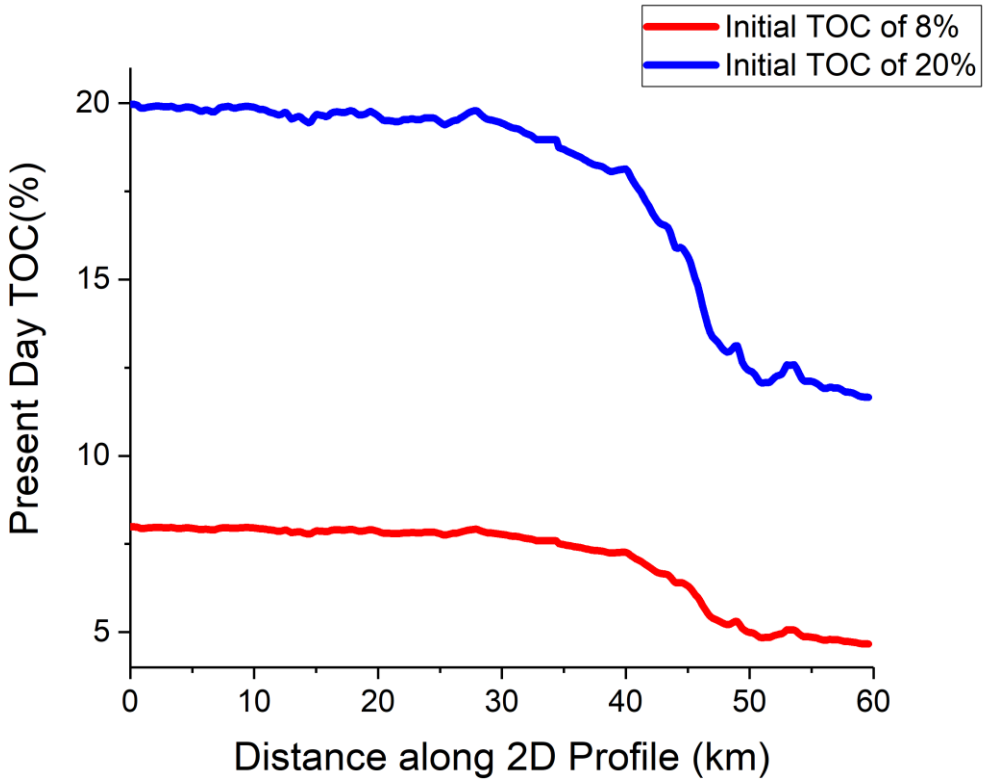


Figure 3.16. Modelled variation in present day TOC along the 2D profile with an initial TOC of 8 % (red line) and with an initial TOC of 20%.

As expected, the TOC is proportional to the hydrocarbons generated by the source (Figure 3.17). Table 3.7 highlights the differences in oil accumulation volume when the initial TOC is changed to 8 or 20%. Using an initial TOC of 8 % results in insufficient lateral migration of oil in the Tay sandstones (Figure 3.17 a) while using an initial TOC of 20 % (Figure 3.17 b) results in similar accumulation in the Tay sandstones and an increase in accumulation in the Forties sandstone (Table 3.7 d). An initial TOC of 20 % results in a 59 % increase in accumulation within the Forties sandstones between well 21/25-02 and 21/29a-06 (Figure 3.17 b and d in Table 3.7). An initial TOC of 20 % generates more gas which accumulates in well 22/22b-04 (Figure 3.17 b) which leads to a 9 % decreases in the accumulation volume of oil relative to the base model (Table 3.7 a).

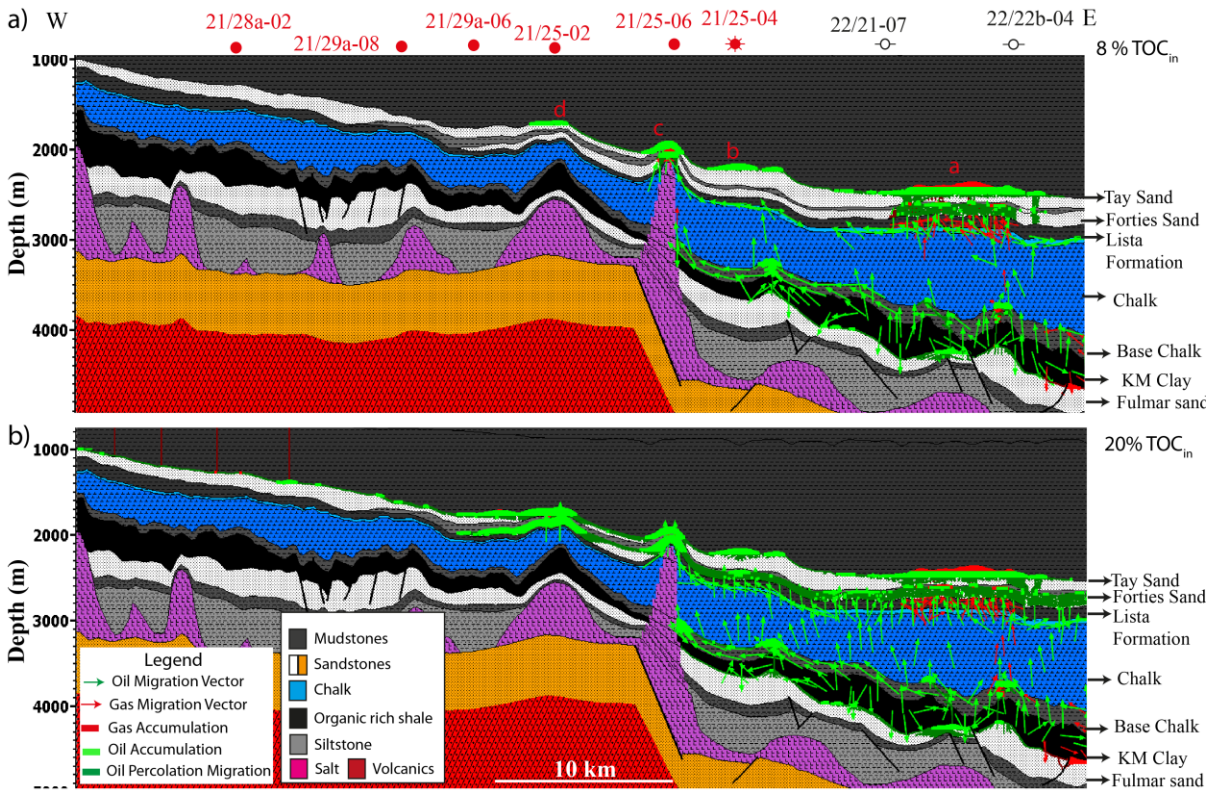


Figure 3.17. Model simulated with initial TOC of a) 8 % showing a less accumulation in the reservoirs and b) 20 % showing similar accumulations in the Tay sandstone seen in the base case model (Figure 3.14 i) while greater accumulation is notices in the Forties sandstone.

Table 3.7. Reservoir accumulation volumes as a function of initial TOC at location highlighted in Figure 3.17. The table shows the differences between accumulation volumes observed in base case model (15 % initial TOC) and accumulation volumes observed when an initial TOC of 8 and 20 % is used. The location of position a-d are shown in Figure 3.17.

		Accumulation Volume (MMbbls)				
Position	Reservoir	15% TOC	8% TOC	Difference	20 % TOC	Difference
a	Tay	477	504	-27	433	44
a	Fulmar	30	23	7	37	-7
b	Tay	126	120	6	126	0
c	Tay	137	139	-2	137	0
c	Forties	239	45	194	239	0
d	Tay	387	52	335	389	-2
d	Forties	306	0	306	488	-182

3.4.3.3 Using Darcy flow and Flowpath Migration

The base case model in Figure 3.14i (D+IP) was simulated using an alternative migration method (D+ FP). Most of oil that reaches the Forties sandstone through the chalk in the east moved vertically into the Tay sandstones via the injectites (Figure 3.18b). The accumulation volume of oil at the 50 km mark (highlighted by the letter a in Figure 3.18) in the Tay sandstones is about 305 MMbbls less than the accumulation volume noticed with the D+IP migration method with no gas cap (a in Table 3.8). The biggest differences are seen in the Forties where the most oil accumulated in the Forties at the 27 km and mark migrates laterally instead of vertically (due to capillary failure) into the Tay sandstones resulting in a 141 % increase in Forties accumulation (d in Table 3.8 and Figure 3.18b). The D+ FP migration also shows no accumulation against the salt diapir and less oil appears to be trapped in the Tay reservoirs (Figure 3.18). The complexity of the model (injectites, salt, two sand bodies separated by thin shale and injectites) is likely the reason why the D+FP migration method gives a different result as it ideally used in simple scenarios (Hantschel and Kauerauf, 2009).

Table 3.8 Reservoir oil accumulation volumes in MMbbls at locations highlighted in Figure 3.18

		Accumulation Volume (MMbbls)		
Position	Reservoir	D+IP	D+FP	Difference
a	Tay	477	172	305
a	Fulmar	30	232	-202
b	Tay	126	0	126
c	Tay	137	105	32
c	Forties	239	158	81
d	Tay	387	367	20
d	Forties	306	739	-433

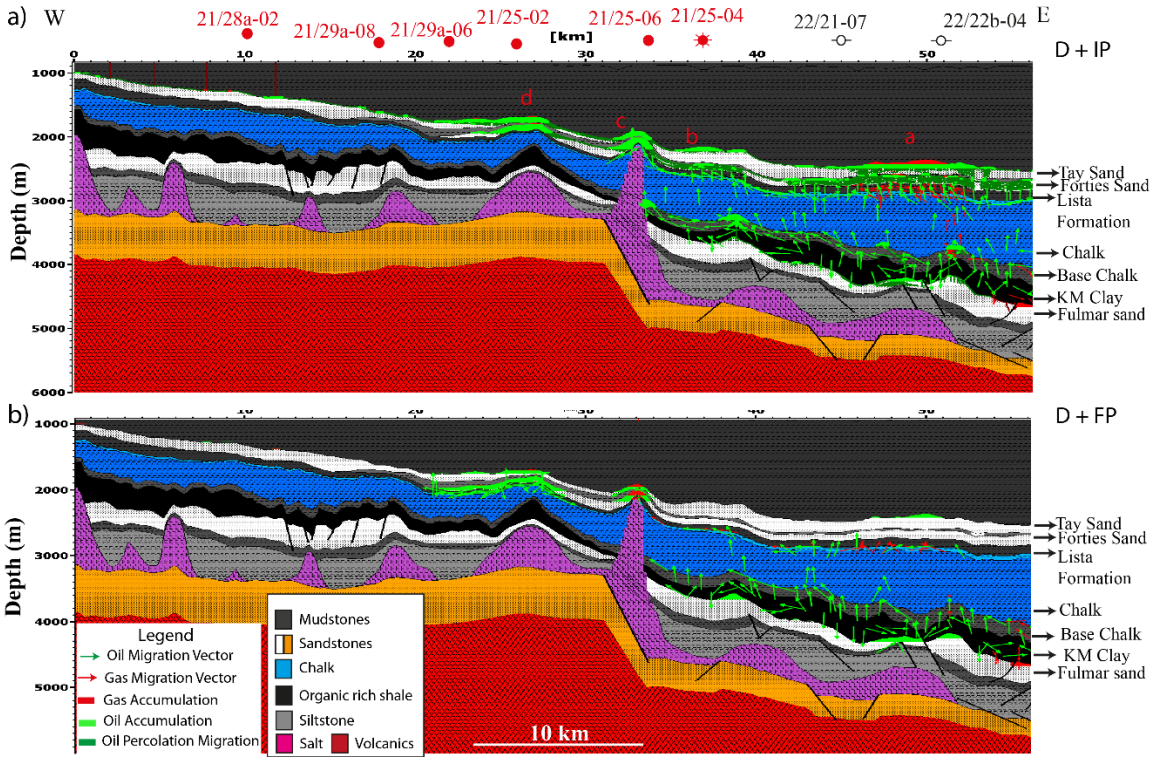


Figure 3.18. Model simulated using D+FP migration methods which differs to the base case model (D+IP). Both models were simulated with an initial TOC of 15 %

3.4.3.4 Open Faults

The base case model (Figure 3.19 a) was run with the faults acting as fluid conduits (Figure 3.19 b). The comparison of both models (Figure 3.19 and Table 3.9) suggest the fault properties have very little effect on the accumulation location of oil in the Tay and Forties traps. The accumulation volume at most of the traps is similar (Table 3.9). The only major difference is noticed in the Tay sandstone at the 50 km mark (location a in Figure 3.19). At this location the base case model (Figure 3.19a) has a larger gas cap when compared to the model with open faults (Figure 3.19b). This results in an 18 % increase in oil accumulation relative to the base case model (Figure 3.19b and position a in Table 3.9).

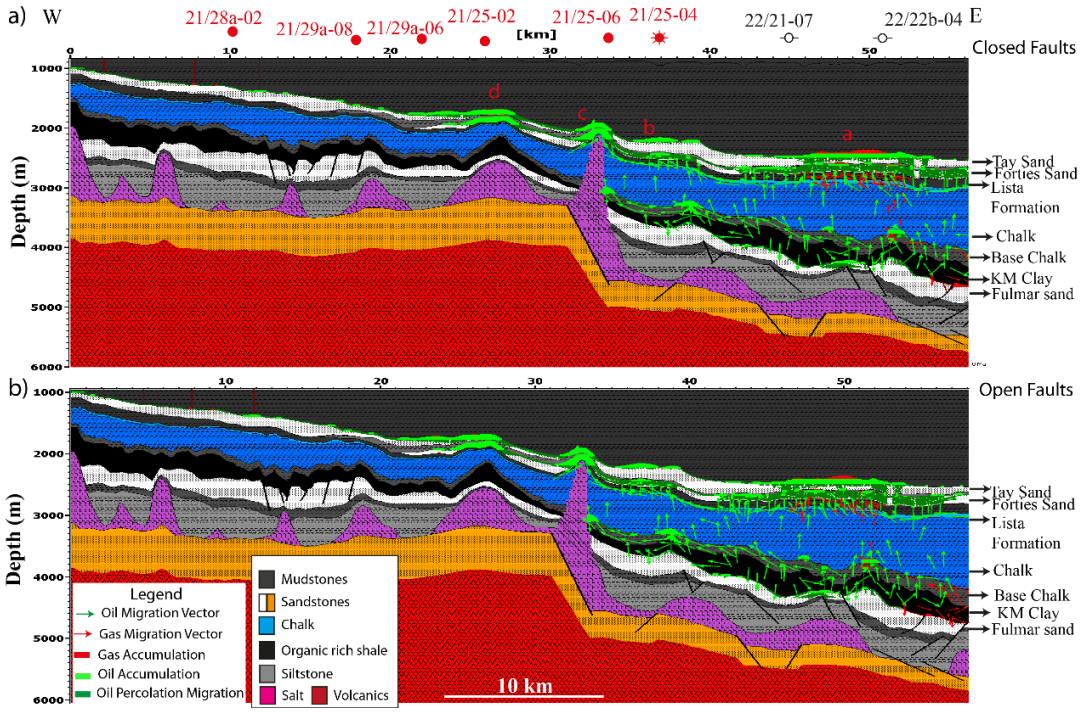


Figure 3.19. comparison of a) base case model with closed faults to b) the same model with open faults. Initial TOC of 15 % was used for both models. Faults property appears to have very little influence on the accumulation location and most of the accumulation volumes.

Table 3.9 Reservoir oil accumulation volumes in MMbbls at locations highlighted in Figure 3.19. F- Faults

		Accumulation Volume (MMbbls)		
Position	Reservoir	Closed F	Open F	Difference
a	Tay	477	562	-85
a	Fulmar	30	30	0
b	Tay	126	126	0
c	Tay	137	137	0
c	Forties	239	238	1
d	Tay	387	389	-2
d	Forties	306	296	10

3.5 Conclusions

The integration of seismic interpretation, well data, geochemical data and 2D petroleum system modelling was carried out to quantify the timing of hydrocarbon generation, expulsion, fluid migration and to determine the lateral and vertical migration pathways (particularly in the Tay sandstone) in the Central North Sea, UK (Figure 3.14I is the preferred simulation). The following observations were made from all the models run in section 3.4:

- The Kimmeridge Clay is the main source rock in the area. The source rock is only mature for oil in the east and early mature for gas in the eastern edge (Figure 3.12).
- Hydrocarbon generation commenced in the Early Cretaceous (Figure 3.12b and Figure 3.14b).
- Hydrocarbon expulsion (Figure 3.12b-e) occurred in 2 phases; initially in the Late Cretaceous and again in the Oligocene (Figure 3.12b).
- Maximum rate of burial was in the Pliocene (Figure 3.13)
- Oil reached the Tertiary sandstones in the Miocene (Figure 3.14e).
- The injectites provide a vital vertical hydrocarbon migration pathway into the Tay sandstones in the east of the study area (Figure 3.14 f). The traps formed by the salt diapir may also increase oil charge into the Tay sandstones from the Forties sandstone (Figure 3.14 g).
- Lateral migration via a Tay sandstone fill-to-spill chain is required to fill traps in the west as the Kimmeridge Clay is immature in this area (Figure 3.12 and Figure 3.14).
- 2D artefacts led to the trapping of oil against the diapir and accumulation of oil in trap that were dry (Figure 3.14).

3D basin and petroleum systems modelling is required to further investigate the lateral and vertical migration attributes of the petroleum system and test the importance of the injectites and salt. This will be described in the following Chapter.

Chapter 4

3D Petroleum Systems Modelling

4.1 Introduction

Accurately identifying areas in the basin where hydrocarbons move laterally or vertically into the Tay sandstones is important to finding a possible magnetic proxy for hydrocarbon migration. 2D petroleum systems modelling carried out in Chapter 3 showed the Kimmeridge Clay to be only mature in the east with the injectites and salt diapir aiding vertical migration into the Tay sandstones (Figure 3.12 and Figure 3.14). The 2D basin modelling in Chapter 3 was carried out on a simplified facies model and with salt diapirs acting as vertical salt walls in 2D models.

With a more sophisticated facies model in 3D space it is entirely possible that the oil will migrate differently. This chapter details the construction of a 3D basin model across UK blocks in the Central North Sea (CNS) (22/22, 22/21, 22/27, 21/23, 21/24, 21/25, 21/27, 21/28, 21/29 and 21/30), identifies the migration pathways within the Tay and Forties sandstone member and documents any deviations from the 2D basin model in Chapter 3. Building, running and calibrating (Figure 3.11) a 2D model first means the 3D model can be populated with the same parameters used to model the thermal and structural evolution of the basin (Section 3.3 and Figure 3.11). Any parameter deviations from the 2D model are clearly stated below.

4.2 Modelling and Input Data

Inputs of depositional events, erosion times & amounts, hiatus times, layer permeabilities, palaeo-heat flow, palaeo-water depth and sediment water interface temperature from the 2D model are used to build the 3D model (section 3.3). The inputs particular to building a 3D basin model are described below.

4.2.1 Stratigraphic Model

Sea bed, top Pliocene, top Miocene, top Tay, top Sele, top Forties, top Lista, top Chalk, top Kimmeridge Clay, top Salt and top Rotliegend shown in Figure 3.4 were interpreted across the 3D grid. The top Fulmar and top Triassic were not interpreted as the seismic data is poor below the Kimmeridge Clay (Figure 4.1); amplitudes are low and very few of the available wells penetrate the horizons so not enough well tops (also called formation tops) were available to generate an accurate interpretation. The Forties (Figure 2.7) and Sele layers are not laterally continuous in the study area; the wells were used to identify the locations where both horizons were absent. Seismic data showed the top Forties and Sele reflections onlapping on the top Lista formation in the west as shown in Figure 4.1.

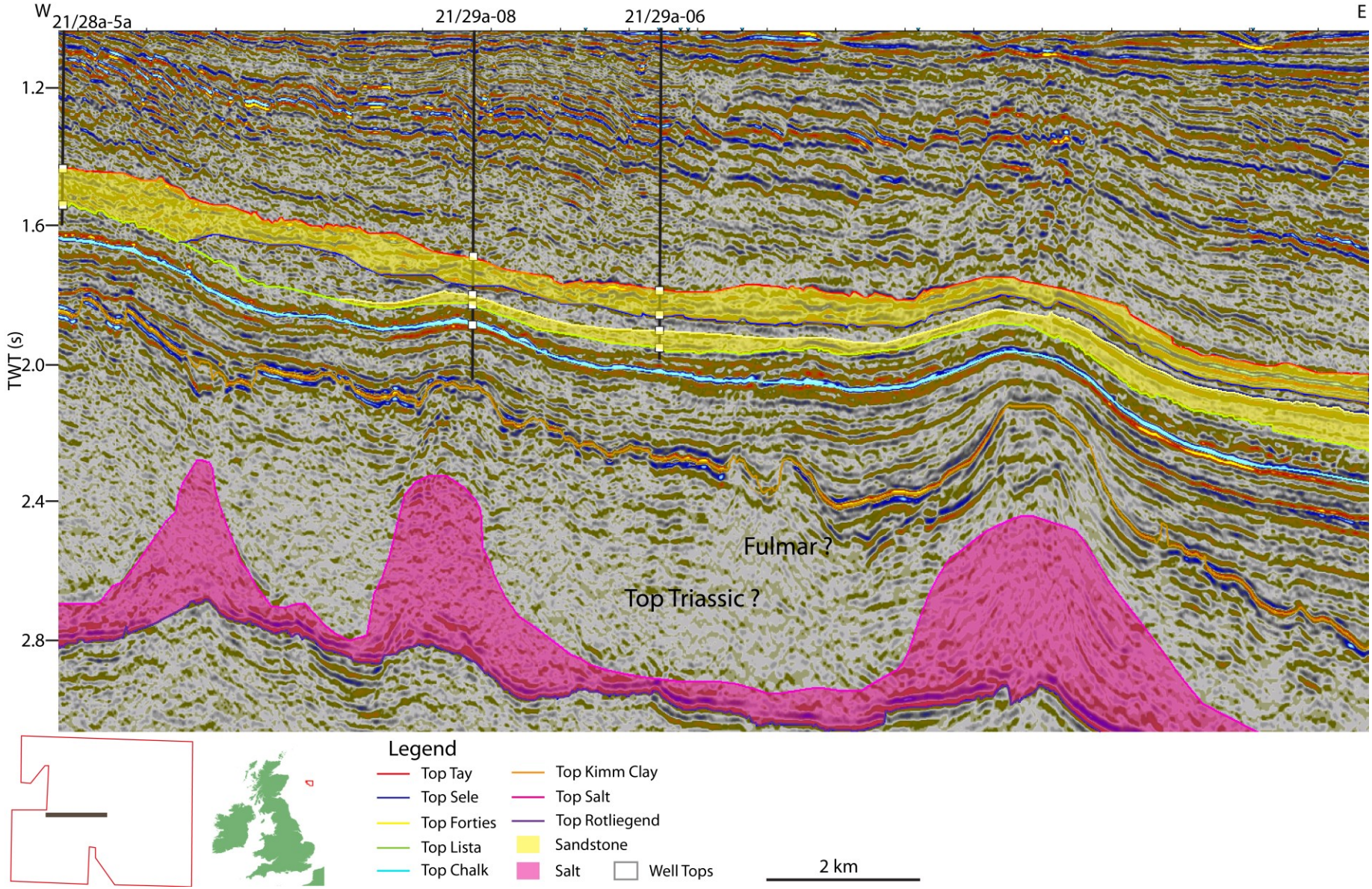


Figure 4.1 . Cross line 1438 from the 3D cube showing the poor seismic quality in the lower half of the section and lack of well penetration in the below the Kimmeridge Clay. Interpretation of seismic was guided by the formation tops (white boxes in wells 21/29a-06, 21/29a-08 and 21/28a-05). Seismic data courtesy of PGS

Using the information from wells in the area, the following layers were split:

5. The Lista formation was split into two layers: The top 80% was attributed to the Lista formation while the bottom 20% was attributed to the Maureen formation.
6. The Chalk was split into two layers: The top 70% was attributed to the Chalk (Chalk Group) while the bottom 30% was attributed to the Base Chalk (Cromer Knoll Group).
7. The Kimmeridge Clay layer was split into four layers: The top 25% was attributed to the Kimmeridge Clay the next 30% was attributed to the Fulmar Formation (FM) the next 10% was attributed to the Base Jurassic (Pentland FM). The bottom 35% was attributed to the Triassic (Skagerrak to Smith bank FM).
8. The facies of the bottom 10% of the Tay SM (sandstone member) was changed from sandstone to a mixture of 70% mud, 25% sandstone and 5% tuff to represent the Balder Formation.

4.2.1.1 Facies Model

RMS (root mean square) amplitude extractions (from Petrel) of the interpreted top Tay and Forties (Figure 4.2 a and c respectively) were used to build a detailed facies model (in PetroMod); higher amplitudes are indicative of a sandstone lithology while the lower amplitudes are indicative of a mudstone lithology (Ahmadi et al., 2003; Jones et al., 2003; Jackson, 2007). The facies model used for the Tay and Forties SM (Figure 4.2b and d respectively) are similar to the gross depositional environment maps drawn by Jones et al. (2003) and Eldrett et al. (2015).

The amplitude extraction for the top Sele FM was not used to generate a facies model because it is very thin in some areas, e.g., in the east of Figure 4.1, and the amplitudes of the base Tay or Top Forties interfere with the extractions which led to bright amplitudes in areas where well data suggested the top Sele was shale. A mudstone lithology was used for majority of the Sele layer, the lithology changed to sandstone in areas with possible injectites identified on the seismic data (Figure 3.5 and Figure 3.6). Most of the injectites were originally interpreted in the east but the rock magnetic signal showed a change in mineralogy in the west that suggested a possible vertical migration pathway (see Chapter 6). This led to the discovery of larger scale injectites from the top of the Maureen formation in the west (Figure 4.3).

For a complete the facies model for all the layers; interpolation of data was carried across data gaps (dashed black box in Figure 4.2 a and c). The gaps were caused by either lack of data or a mute applied to the data during in processing by PGS.

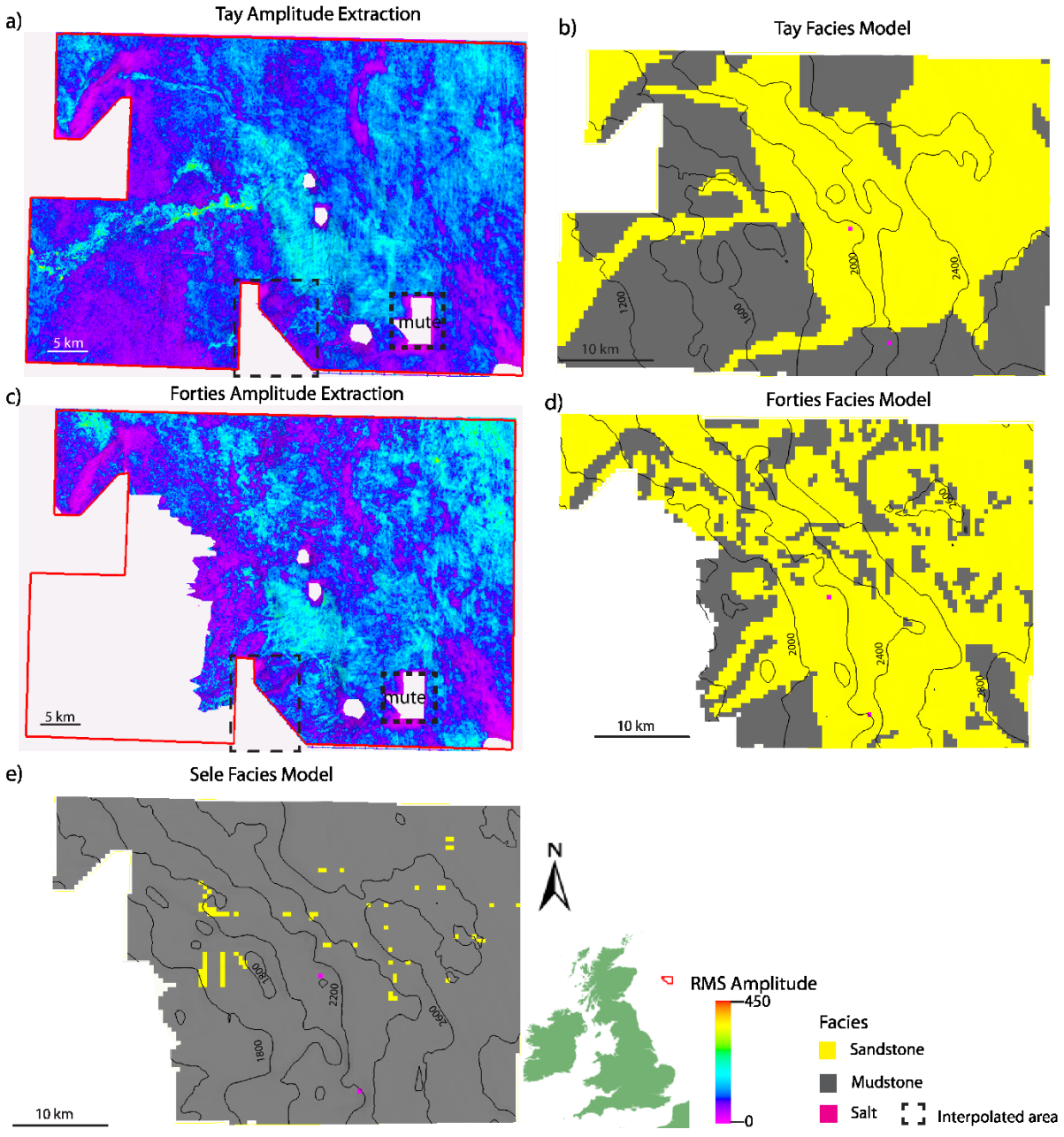


Figure 4.2. Amplitude extractions of the Tay and Forties sandstone members (a and c) used to obtain the lateral variation of facies in the Tay and Forties sandstone member (b and d) for input into PetroMod. The Sele facies model (e) was generated by mapping out locations of injectites in the survey area. RMS-Root Mean Square.

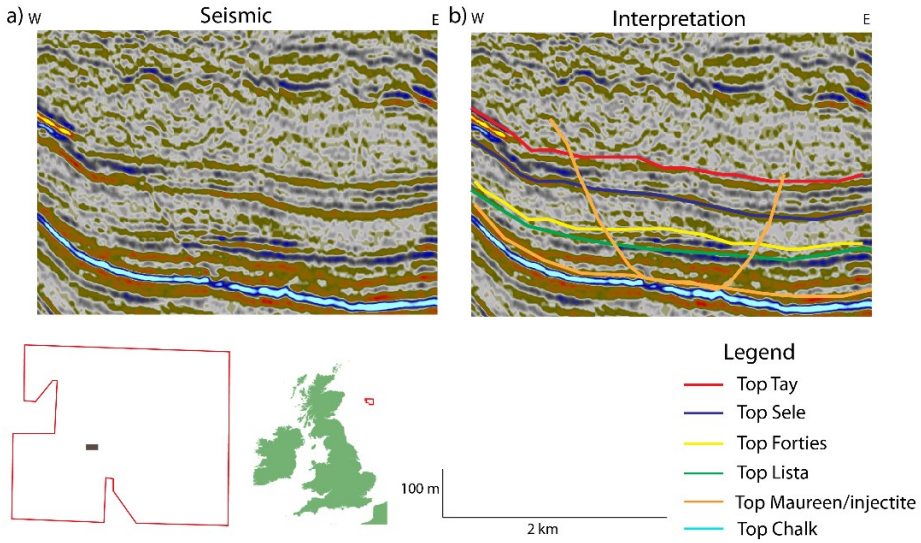


Figure 4.3. Cross line 1386 showing the presence of large scale injectites (orange lines) from the top of the Maureen formation in the W. This interpretation along with the injectites from the Forties sandstone member (Figure 3.5) were used to build the Sele formation facies model in Figure 4.2.

As the top Fulmar Formation was not interpreted due to poor imaging and stratigraphic complexity, its facies and layer thickness had to be inferred from well data and regional studies. Composite logs showed the Fulmar Formation to be composed of sandstones. The OGA (Oil and Gas Authority, UK) interpreted the Fulmar Formation to be present across the whole study area with thicknesses varying from 100-200 m in the east to 25-100 m in the west (Figure 4.4). In this model an average thickness of 150 m was used for the Fulmar sandstone in the east and thickness of 50 m in the west.

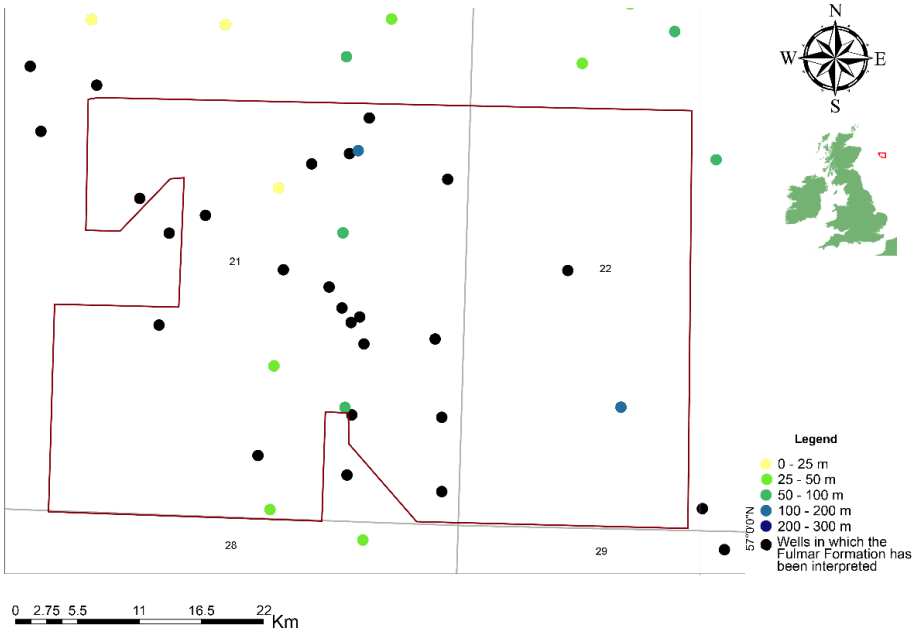


Figure 4.4 Ma.p showing the wells the Fulmar Formation has been interpreted (black circles) by the OGA and its thickness variation (coloured circles) across the study area. Map modified from OGA's data release maps. Red polygon is the study area.

A large N-S trending salt body was formed by lateral salt movement in the hangingwall of a regional fault cutting through the Rotliegend in the centre of the study area (Figure 3.4). This evolved into a series of offset salt walls and diapirs which disrupt the lateral continuity of the Fulmar sandstones. The 3D seismic was interpreted (Figure 4.5) to identify possible areas where the Fulmar was pierced by the diapir or salt wall, e.g., Figure 4.5c and d, and where it is probably unperturbed by halokinesis, e.g., Figure 4.5b and e. This interpretation (Figure 4.5) was used to build the present-day facies model shown in Figure 4.6.

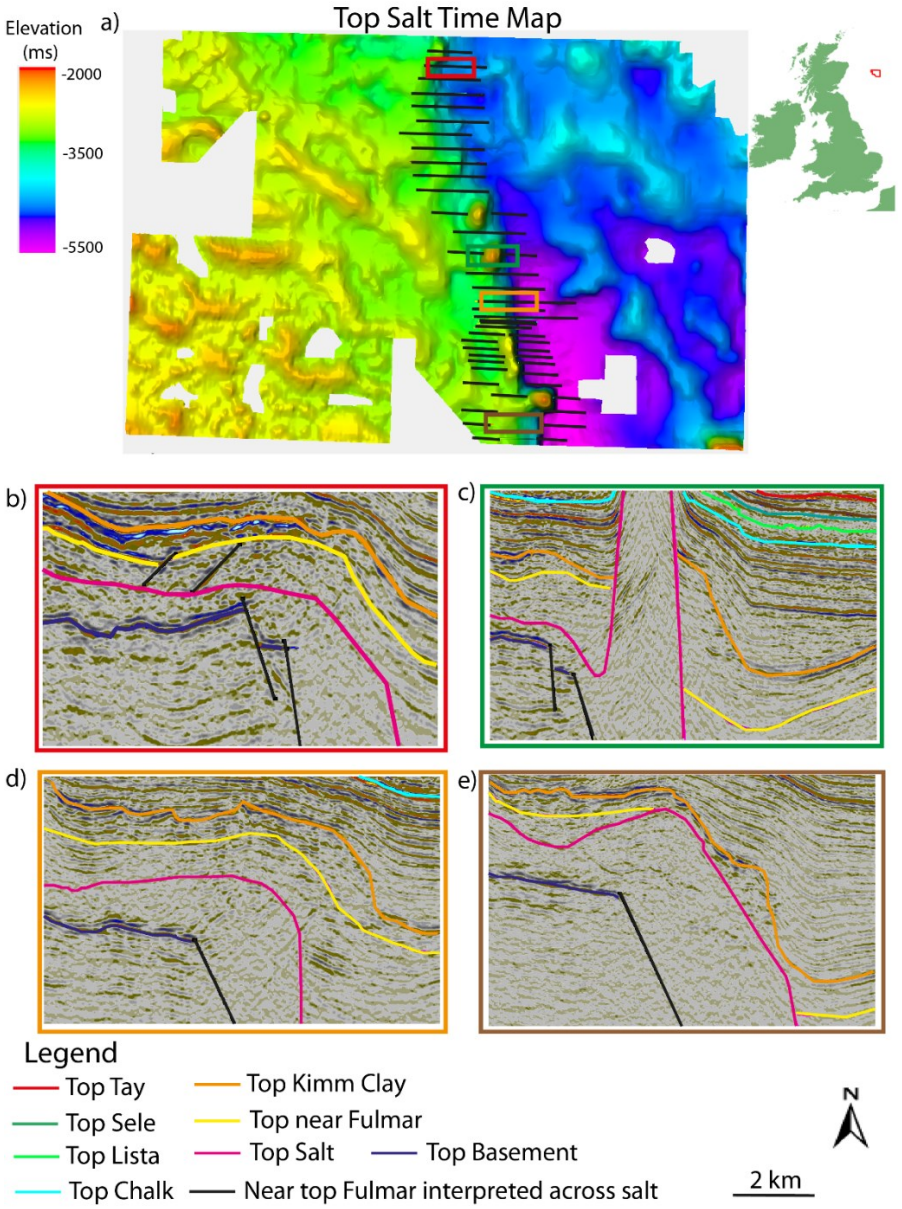


Figure 4.5. Interpretation of near top Fulmar Formation across salt draped over the regional fault. a) 3D salt time map showing interpretation of Top Fulmar (black line) showing areas where the Fulmar is laterally consistent from e to w. b & d) examples on seismic where it is laterally consistent and c & e) examples on seismic where it broken up by a diapir or salt wall.

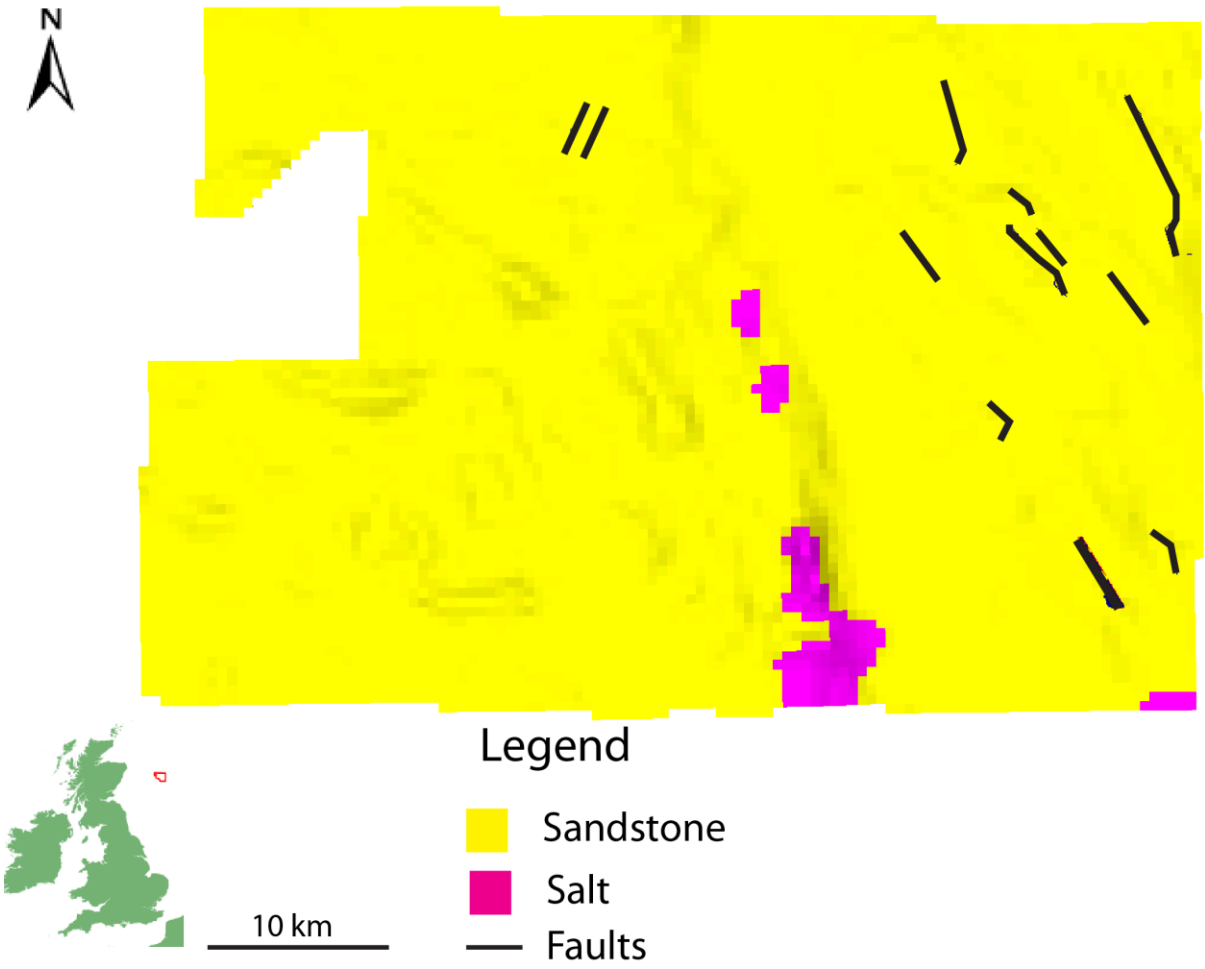


Figure 4.6. Present day facies model for the Fulmar Formation facies showing areas where salt pierced the Fulmar and the location of faults cutting through the Fulmar.

4.2.2 Structural Model

Faults

Only Faults that cut through the Fulmar FM (formation) (Figure 4.6) are included in the 3D model. The 2D model shown in Figure 3.19 suggests having the faults acting as fluid barrier (closed) or fluid conduits (open) has very little effect on hydrocarbon accumulation and volume (Table 3.9). The base case model (shown in section 4.3.1 and 4.3.2) was run with the faults acting as fluid barriers.

Salt Movement

The salt movement through time was modelled as described in Section 3.3.2. Table 4.1 shows the timing of facies replacement by salt for all the diapirs interpreted in the 3D model (Figure 4.5 a).

Table 4.1. Timing of facies replacement caused by diapirism. Timing was estimated with the aid of PetroMod's burial reconstruction feature.

Facies replaced by Salt	Time of Replacement (Ma)
Base Oligocene	30
Tay Sandstone Member	35
Forties Sandstone Member	36
Sele Formation	40
Lista Formation	45
Maureen Formation	52
Chalk Group	57
Base Chalk	70
Kimm Clay	130
Fulmar Formation	140
Base Jurassic	142
Triassic	145

4.3 Results and Discussion

For comparison with the 2D base-case model, the 3D base-case model was simulated using the D+IP migration method (Section 3.3.5) with an Initial TOC of 15% and an initial HI of 589 mg/g TOC. The modelling outputs are described below.

4.3.1 Source Rock Generation and Expulsion

The Transformation Ratio (TR) of the Kimmeridge Clay (Figure 4.7a) suggests it is immature over the majority of the study area, and the oil is only mature in the east and mature for gas at the eastern edge; entirely consistent with the 2D model as expected. Expulsion of hydrocarbon only occurs when the TR > 20 % (Figure 4.7a). Timing of the generation (during the Cretaceous) and expulsion (during the Oligocene) of hydrocarbon (Figure 4.7b-c) is consistent with the 2D model Figure 3.12. Unlike the 2D model (Figure 3.12a), the 3D model (Figure 4.7b-c) does not predict the expulsion of oil during the upper Cretaceous. This expulsion event only occurs at the eastern edge of the 2D study area (Figure 3.12 a), so it is likely smoothed out in the 3D model. This expulsion would have been shown in the model if more data was available to the east of the study area. The model predicts 96 Bbbls of oil was

generated by the source rock while 50 Bbbls of oil was expelled (Figure 4.7b). The model also predicts 83 TCF of generated gas and 41 TCF of expelled gas (Figure 4.7c). The modelling of the source rock (Figure 4.7a), importantly demonstrates the need for lateral migration to charge the Tertiary traps in the west (Cayley, 1987; Kubala et al., 2003).

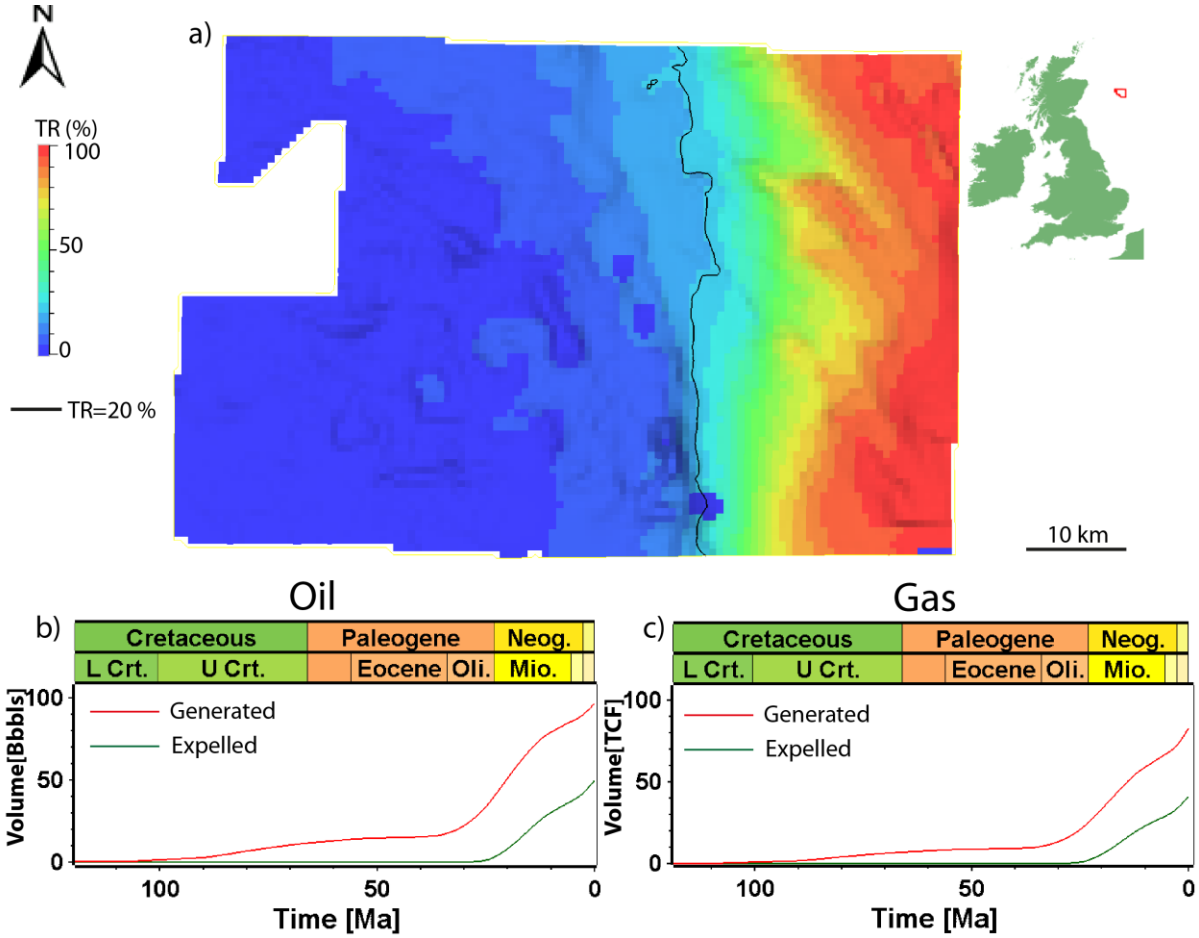


Figure 4.7. a) TR of the Kimmeridge Clay; expulsion of oil of oil only occurs at TR > 20 % (black line). Plots showing the total amount of b) oil and c) gas generated and expelled by the Kimmeridge Clay. Note: the amount of hydrocarbon generated and expelled is dependent on the initial TOC and HI.

4.3.2 Hydrocarbon Migration and Accumulation

4.3.2.1 Carrier Beds and the Importance of the Salt Diapir

In common with the 2D model (Figure 3.14), the 3D model predicts the Fulmar sandstones (Figure 4.8a) and the Base Chalk (Figure 4.8b) to be lateral carriers of oil to the west; oil typically accumulates on the structural highs formed by halokinesis (in both the Fulmar or Base Chalk) until capillary pressure is reached and the oils moves vertically through the chalk, this is accompanied by spilling of some oil to the west. The model also predicts the salt assists

vertical migration into the Tertiary sandstones (Figure 4.8). Oil migrating in either the Fulmar sandstones or Base Chalk typically takes two pathways when it reaches a diapir; some of it bypasses the diapir while some of it moves up the diapir into the overlying Tertiary sandstone (as highlighted in Figure 4.8 a and b).

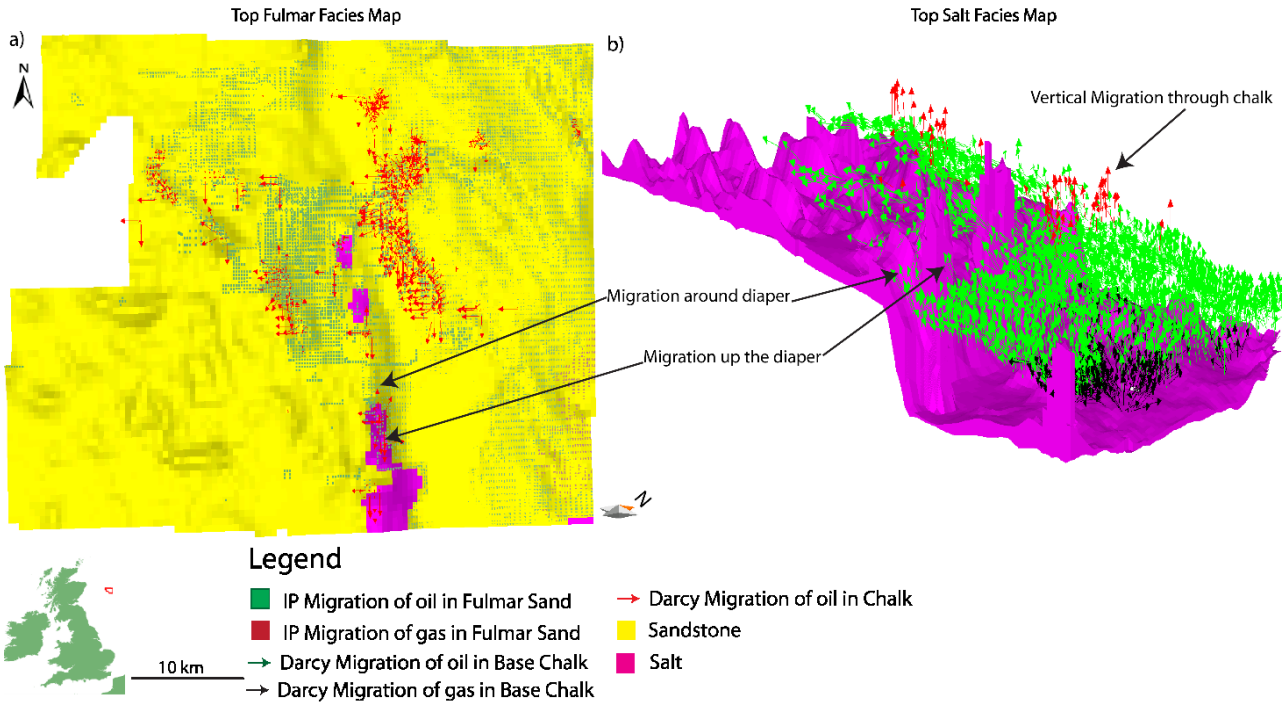


Figure 4.8. Fulmar and top salt facies maps showing a) Areas of IP lateral migration of oil and gas in the Fulmar and areas of migration (mostly vertical) of oil through the chalk (red arrows) b) Darcy migration in the Base Chalk (marl) showing migration of oil to the west along with build-up of oil on structural highs which leads to vertical migration through the chalk (red arrow). This figure also demonstrates the oil can either bypass the salt diapir by moving around it or migrate up the diapir.

4.3.2.2 Timing of Hydrocarbon Migration into the Reservoirs

The model predicts a total of 8.1 Bbbls and 1.2 Mm^3 of gas is accumulated in traps in the study area (Table 4.2), suggesting the limited gas expelled (Figure 4.7c) by the source rock is most likely dissolved in the oil (note: the oil and gas in place are typically overestimated by the model). The location of present-day hydrocarbon accumulations in the reservoirs are shown in Figure 4.9.

The accumulation locations are calibrated against available wireline log data from wells in the area. The hydrocarbon accumulation in the Fulmar FM (Figure 4.9c) roughly coincides with wells were hydrocarbons have been identified. Some accumulations in the south occur in areas with no wells, supporting Cayley's (1987) claim of undiscovered reserves in the Late

Jurassic sandstones; as the top Fulmar was not interpreted across the 3D seismic it is unclear if the model has predicted undrilled hydrocarbon prospects. The accumulation of oil in the Forties SM mostly correlates with well data apart from wells 21/29b-01 and 21/29b-02 (Figure 4.9 b). In these wells the model predicts an accumulation of oil, but the wells turned out to be dry. This discrepancy could be due to the presence of small scale injectites (< 18 m) facilitating vertical migration out of the Forties SM, seal failure that was not predicted by the model or as a result of using a high TOC. One discrepancy was noticed in the Tay SM (Figure 4.9 a); well 21/30-10 which is a dry well, but the model predicts an accumulation which is likely caused by errors in the top salt interpretation. Wells 22/22-04 and 22/21-08 showed the Tay SM to contain oil (Figure 4.9 a), but they are at the edge of a big accumulation of oil that has not been tested (see Section 4.3.3.5). It is possible that the model has predicted a potentially undrilled hydrocarbon prospect.

Wells 21/24-03, 21/25-A1 and 21/25-06 have gas caps (Figure 4.9 a), but the model predicts zero gas. This is likely due to data limitations as the Kimmeridge Clay is mature for gas generation to the east of the study area (Barnard and Bastow, 1991) It is possible gas may have migrated from east to west into the study area. The alternative explanation is the gas in these wells could also be biogenic, which can only be modelled using D+FP migration method. Unfortunately, the 2D model has shown the study area is too complicated to be modelled using D+FP (Figure 3.18).

Table 4.2. Table showing the total accumulation of oil in the Fulmar FM, Forties SM and Tay SM shown in Figure 4.9. Note these numbers cannot be compared to published data as PetroMod typically over estimates volume calculations (Hantschel and Kauerauf, 2009).

	Accumulation volume	
Reservoir	Gas (Mm^3)	Oil (Bbbls)
Tay	0	3.9
Forties	0	2.6
Fulmar	1.2	1.6
Total	1.2	8.1

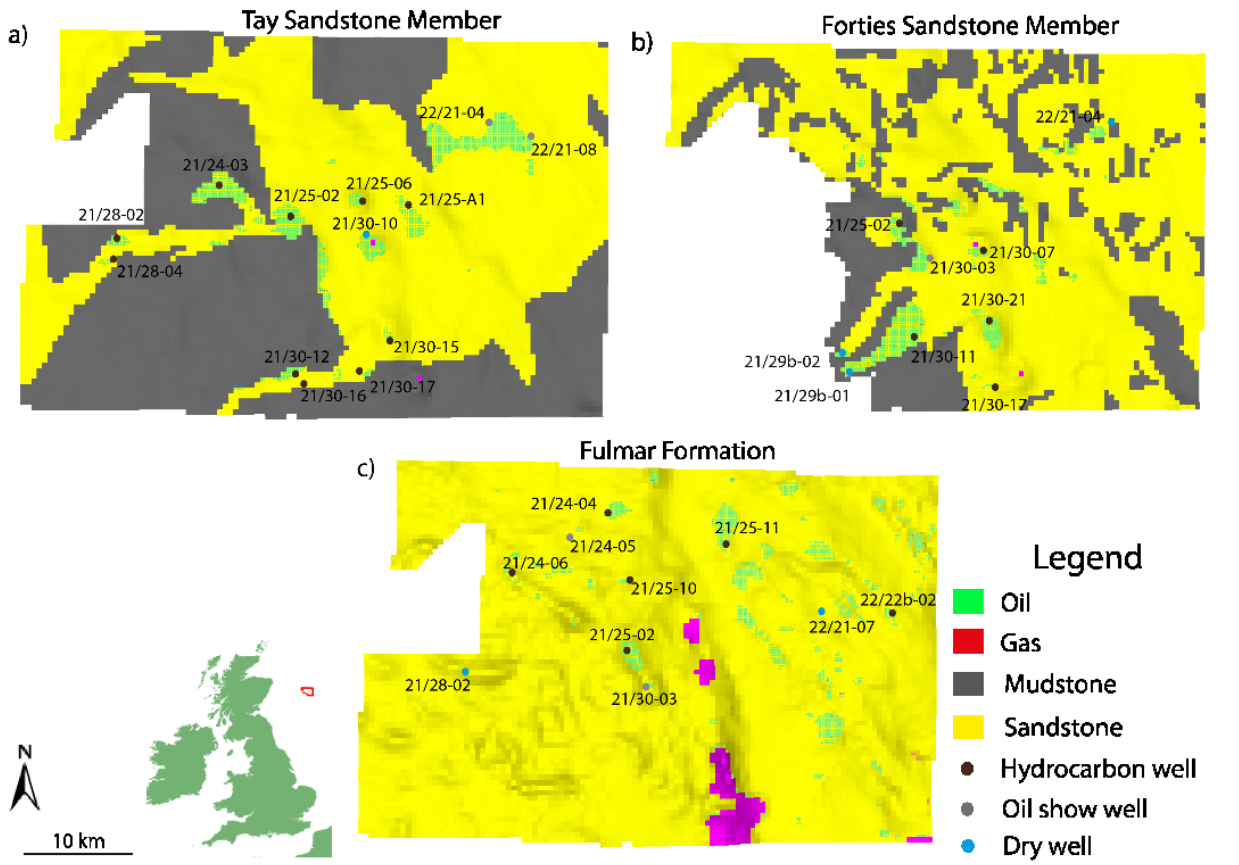


Figure 4.9. Location of present-day accumulations for a) Tay Sandstone Member b) Forties Sandstone Member c) Fulmar Formation. Note: The Fulmar faults are toggled off (not displayed).

The timing of hydrocarbon charge in the Fulmar FM, Forties SM and Tay SM are shown in Figure 4.10, 11 and 12 respectively.

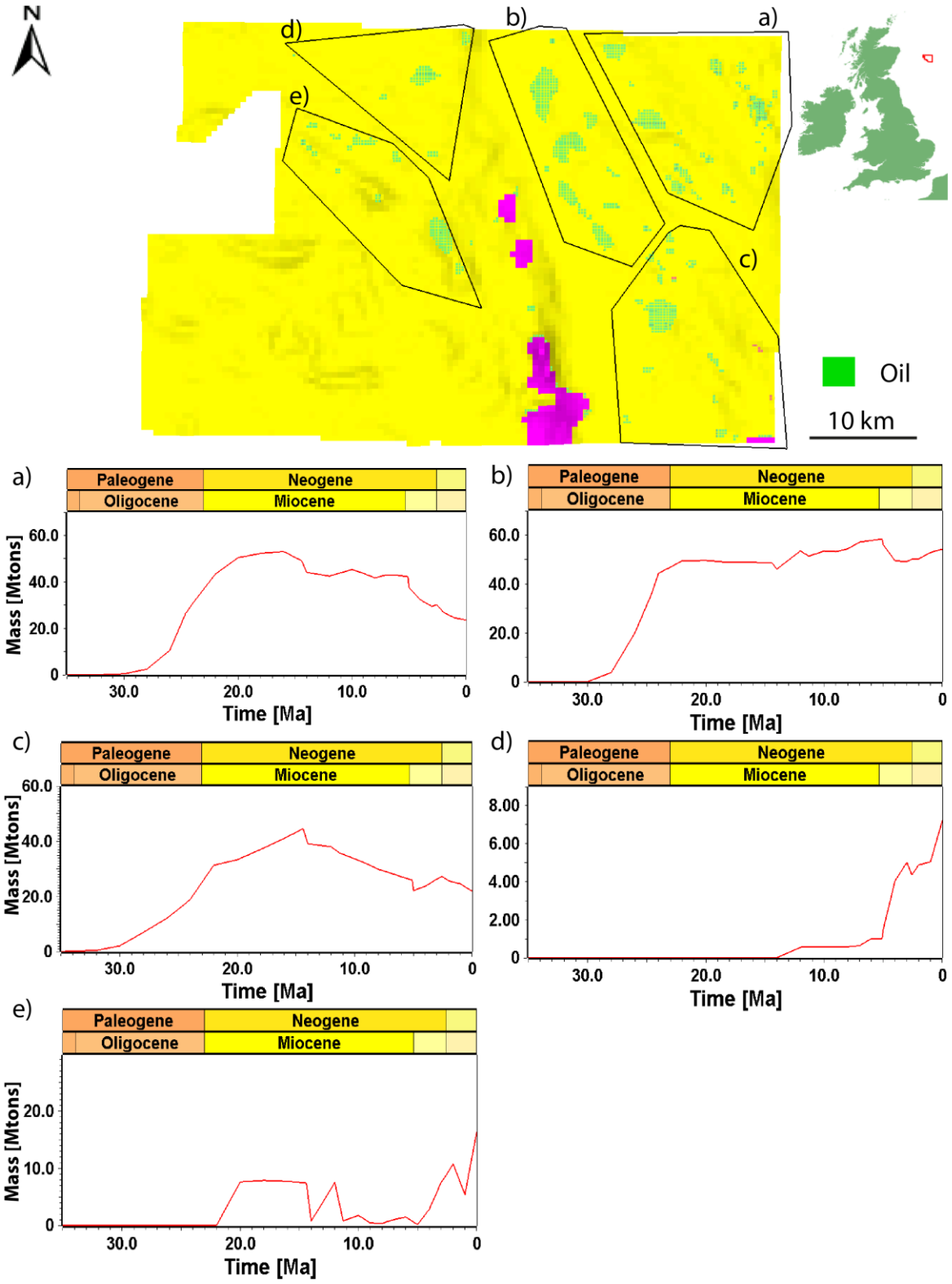


Figure 4.10. Hydrocarbon mass versus time, depicting the timing of hydrocarbon migration into the Fulmar Formation in the study area. Note: The Fulmar faults are toggled off (not displayed).

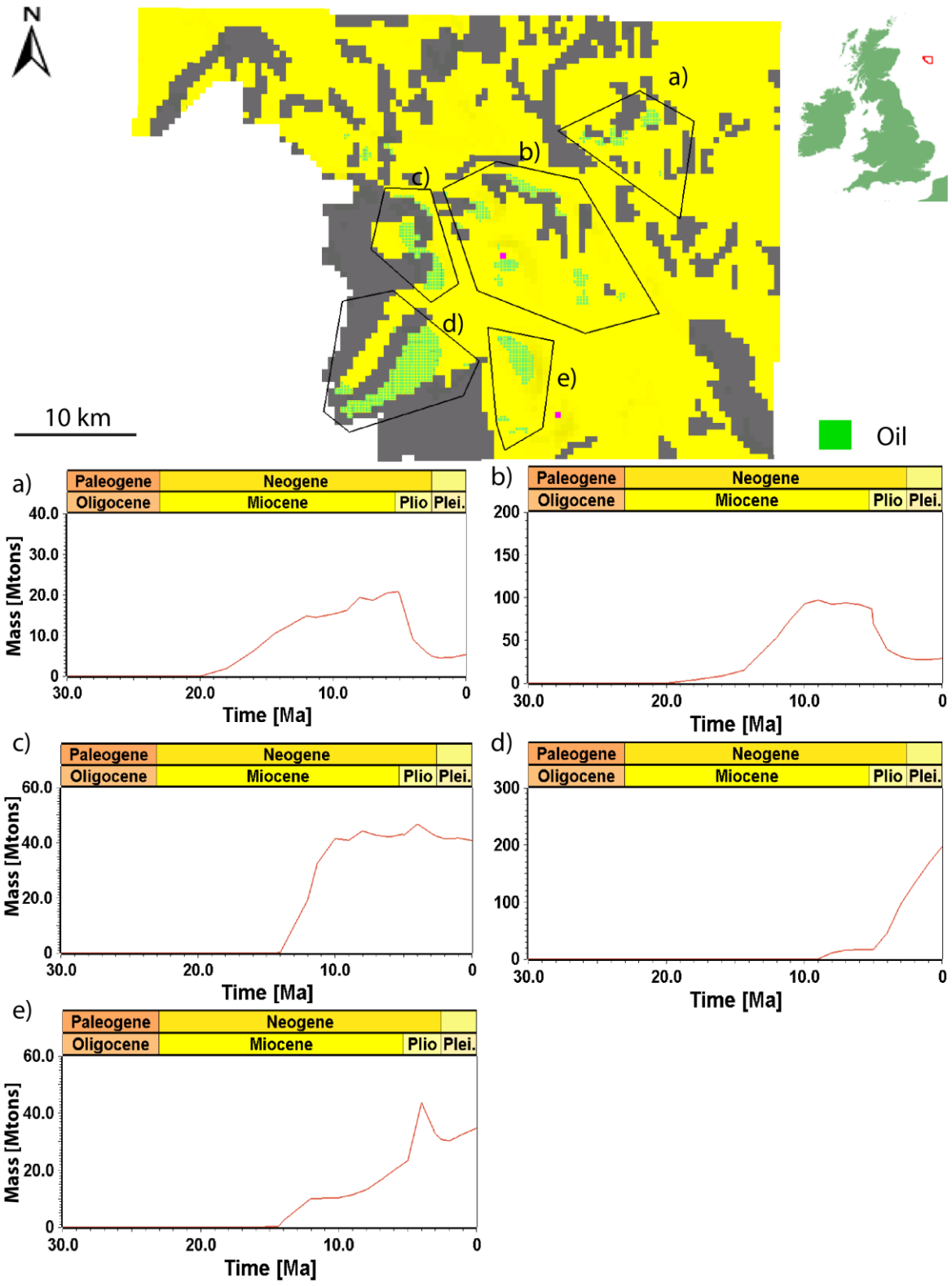


Figure 4.11. Hydrocarbon mass versus time, showing the timing of hydrocarbon migration into the Forties Sandstone Member in the study area. Note: The Fulmar faults are toggled off (not displayed).

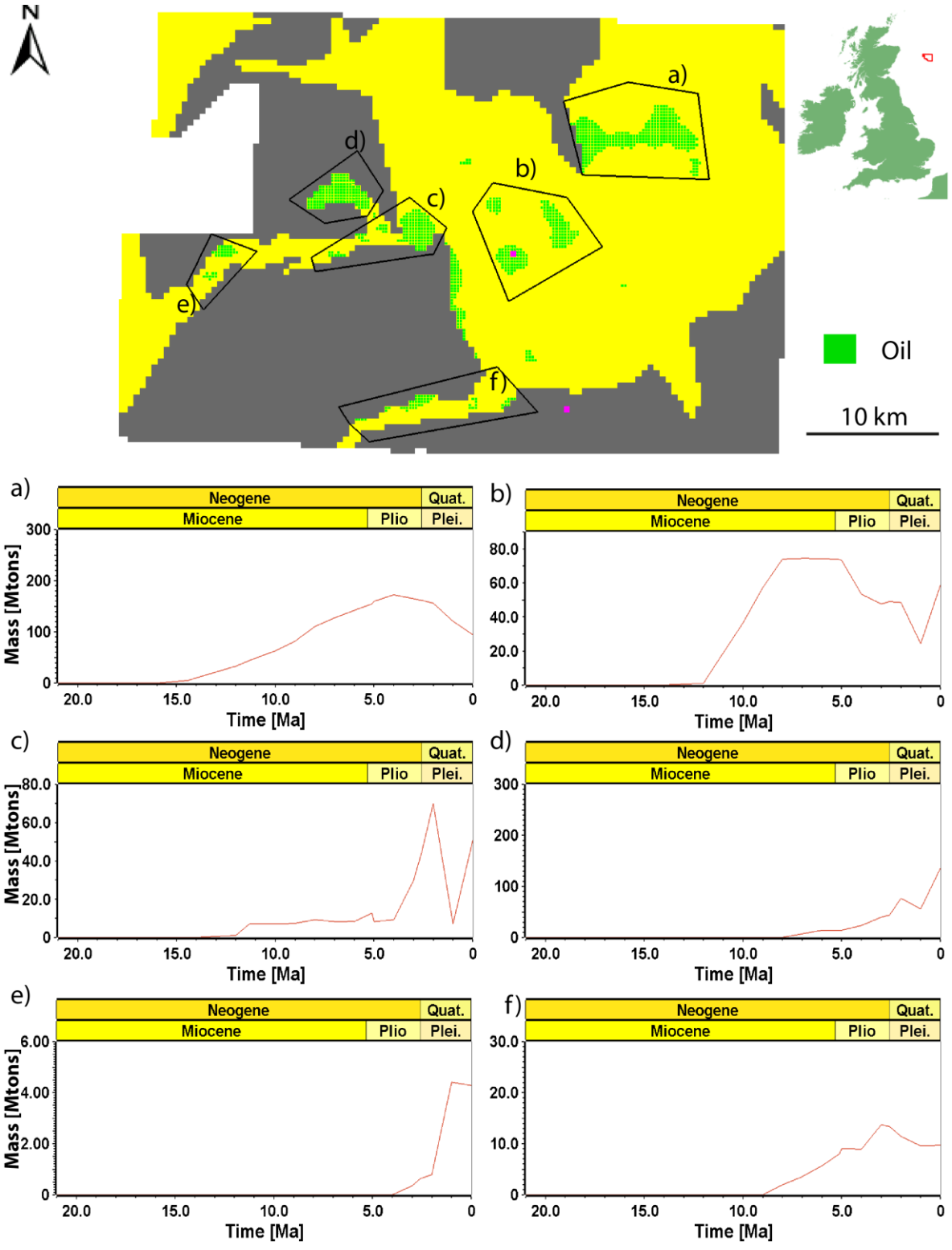


Figure 4.12. Hydrocarbon mass versus time showing timing of hydrocarbon migration into the Tay Sandstone Member in the study area. Note: The Fulmar faults are toggled off (not displayed).

The following observation are made from the hydrocarbon mass versus time plots for the Fulmar FM, Forties SM and Tay SM (Figure 4.10, 11 and 12 respectively):

- Downward migration of oil into the Fulmar FM in the east occurred around 30 Ma (Figure 4.10 a-c) agree with the estimates made by the 2D model (Figure 3.14 b).
- Oil migrating in the Fulmar FM from the east reached the north-west traps at around 14 Ma (Figure 4.10 d) and the north-south traps at 22 ma (Figure 4.10 e).
- Loss of hydrocarbon mass seen in the Fulmar FM (Figure 4.10 a, b, c and e) is likely due to vertical hydrocarbon leakage to the Tertiary strata.
- Oil Migrates vertically into the Forties SM around 20 Ma in the east (Figure 4.11 a-b) and between 14 and 9 Ma in the west (Figure 4.11 c-d). These estimates are similar to the 2D model's predictions (Figure 3.14 e).
- The reduction in hydrocarbon masses observed in the Forties SM in Figure 4.11a, b, c and e are likely due to hydrocarbon leakage caused by capillary failure in the mudstones of the Sele FM or hydrocarbon leakage via injectites (Figure 3.5).
- Oil migrates vertically into the Tay SM in the east at 15 Ma (Figure 4.12 a) and at 12 Ma in the centre (Figure 4.12b and c). This is about 3 Myr later than predicted in the 2D model (Figure 3.14 f).
- Oil migrates vertically or laterally into the Tay SM in the west between 8 and 4 Ma (Figure 4.12 d-e) while oil reaches the channel in the south at around 9 Ma (Figure 4.12 f).
- Drops in hydrocarbon mass seen in Figure 4.12a, b and f are likely due to filling and spilling of traps to the west.
- The rapid drop in hydrocarbon mass observed in Figure 4.12 c is a PetroMod bug, which exaggerates the amount of oil spilled west and oil leaking due to capillary failure.

A 2D extraction was carried out on the 3D model; this line is similar to the profile used for the 2D basin model (Figure 3.4). The 2D extraction shown in Figure 4.13 is quite different to the 2D modelling results in Figure 3.14. In the 3D model (Figure 4.13) there is a lot less oil accumulated within the 45-55 km mark in the Tertiary strata. This suggests the oil accumulated there in the 2D model (Figure 3.14) spilled north or south out of the plane of the

2D section. There is also some accumulation of oil in the Fulmar FM at the 26 km in the 3D model (Figure 4.13), this is not predicted in the in the 2D model (Figure 3.14) because the oil can only migrate around the salt in a 3D space (Figure 4.8 a). The oil is not trapped by the salt diapir in the 3D model (Figure 4.13) unlike in the 2D model (Figure 3.14). The differences between the 3D model and 2D model highlights the superiority of a 3D model with a detailed facies model to a simplistic 2D model in complex geological settings (Figure 4.13).

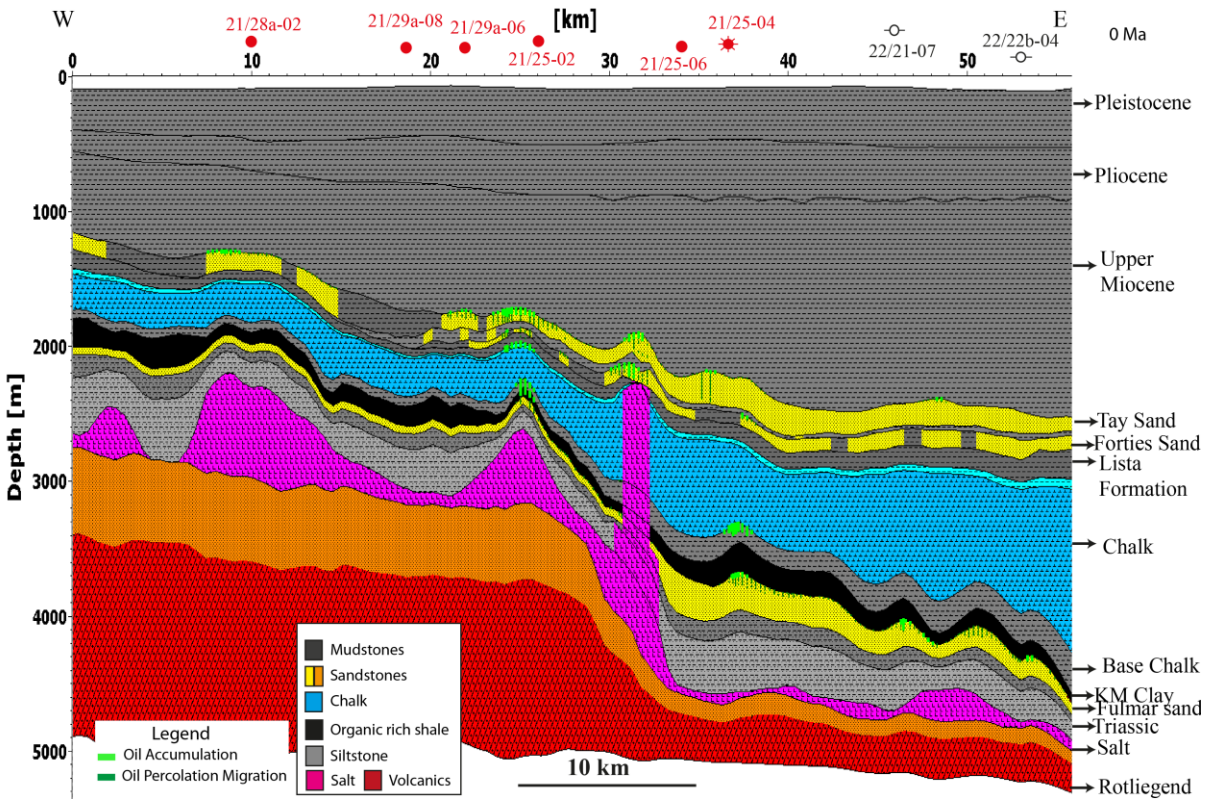


Figure 4.13. West –East 2D line extracted from the 3D model (Figure 4.9). This line is similar to the 2D profile in Figure 3.14 enabling comparison of the two.

4.3.2.3 Vertical and Lateral Migration within the Tay Sandstone Member

The influence of the salt, Fulmar sands and Chalk means vertical migration into the Tertiary sandstones is not limited to the area where the Kimmeridge Clay is mature (Figure 4.8 and Figure 4.14). Areas of vertical migration into the Tay sandstones in the west typically correlate with underlying Fulmar accumulations (comparing Figure 4.9 c to Figure 4.14). The model results suggest the Gannet field is mostly charged vertically, the Guillemot field is charged both vertically and laterally, while the Fyne/Dandy and Pilot fields are charged laterally (Figure

4.14). From my calculations, long distance lateral migration of at least 30 km is needed to charge the Pilot field with oil; the Pilot field is about 15 km west of the Fyne/Dandy field.

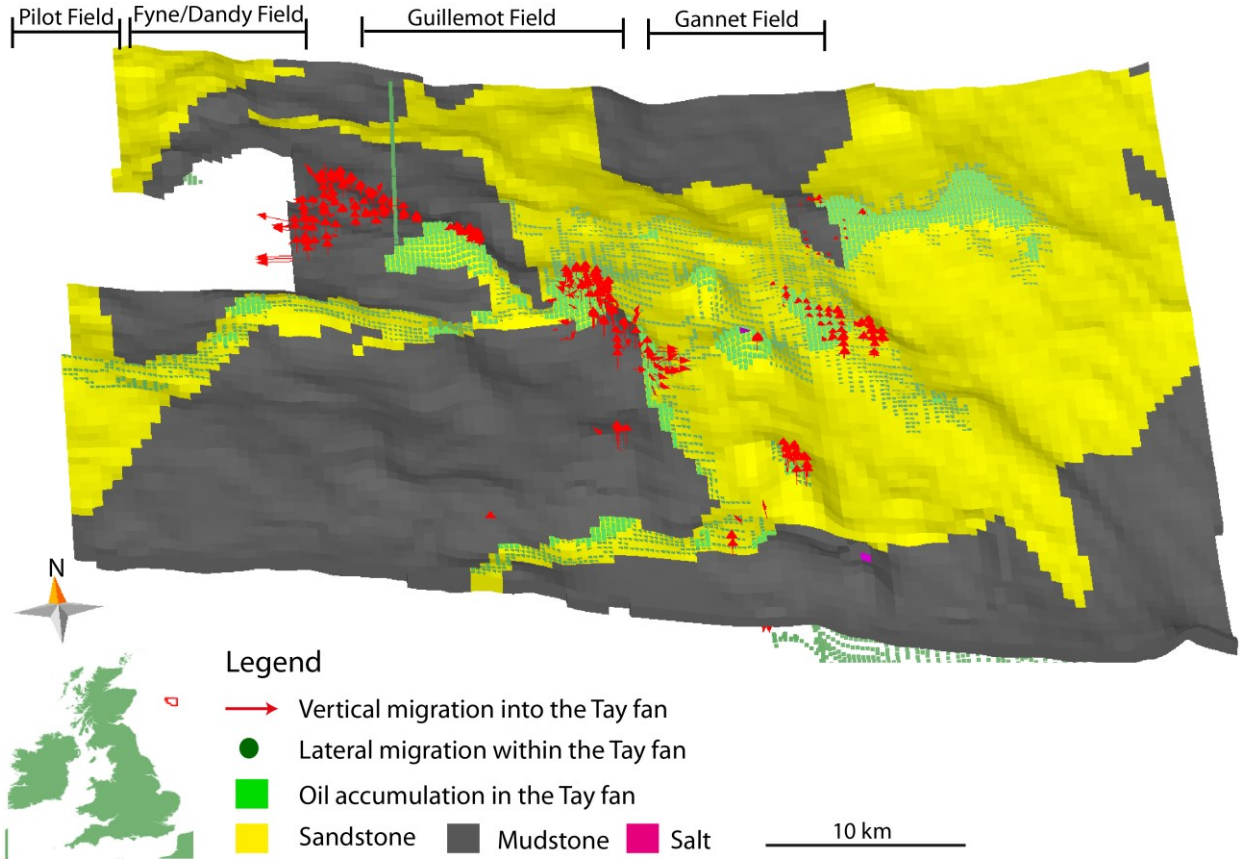


Figure 4.14. Map showing areas of vertical (red arrows) and lateral migration (green dots) of oil within the Tay SM. Vertical migration is prominent in the east while lateral migration is prominent in the west. Areas of vertical migration in the west correspond to underlying Fulmar accumulations. Note: the red arrows on the top left appear horizontal because of a 3D modelling edge effect.

4.3.3 Testing Parameter Space: Sensitivity Check

4.3.3.1 Varying Initial TOC

Results of the 2D model (Section 3.4.3.2) suggest using an initial TOC of 15 or 20 % is needed to fill the traps. The different values have no significant effect on the accumulation location and little effect on the accumulation volume (Figure 3.17 and Table 3.7). 3D modelling does a better job of determining column height so an initial TOC less than 15 % should be able to fill the traps in the Fulmar FM, Forties SM and Tay SM. To test this, the base case model (Figure 4.9) was simulated with uniform initial TOCs of 10 and 8%.

Using an initial TOC of 10% (Figure 4.15) results in very similar accumulation location and volume of oil in the Tay SM and Fulmar FM (Table 4.3). Gas caps are also formed in wells 21/24-03 and 21/25-02 in the Tay SM (Figure 4.15 a). No gas caps were observed in the Forties SM and there is a 31 % decrease in the accumulation of oil is noticed (Figure 4.15b and Table 4.3). This results in less oil accumulation in the south-west Forties feeder channel and no accumulation in well 21/29b-02 which matches the well's wireline log data.

Table 4.3. Total accumulation volumes of oil and gas in the reservoirs when the initial TOC is changed to 10 or 8 %. The table also shows the differences from the base-case model (BC) shown in Table 4.2.

	TOC 10				**TOC 8**			
	Accumulation volume		Difference from BC		Accumulation volume		Difference from BC	
Reservoir	Gas (Mm^3)	Oil (Bbbls)	Gas (Mm^3)	Oil (Bbbls)	Gas (Mm^3)	Oil (Bbbls)	Gas (Mm^3)	Oil (Bbbls)
Tay	1.3	3.7	-1.3	0.2	0.4	3.1	-0.4	0.8
Forties	0	1.8	0	0.8	0	1.5	0	1.1
Fulmar	1.2	1.4	0	0.2	1.1	1	0.1	0.6
Total	2.5	6.9	-1.3	1.2	1.5	5.6	-0.3	2.5

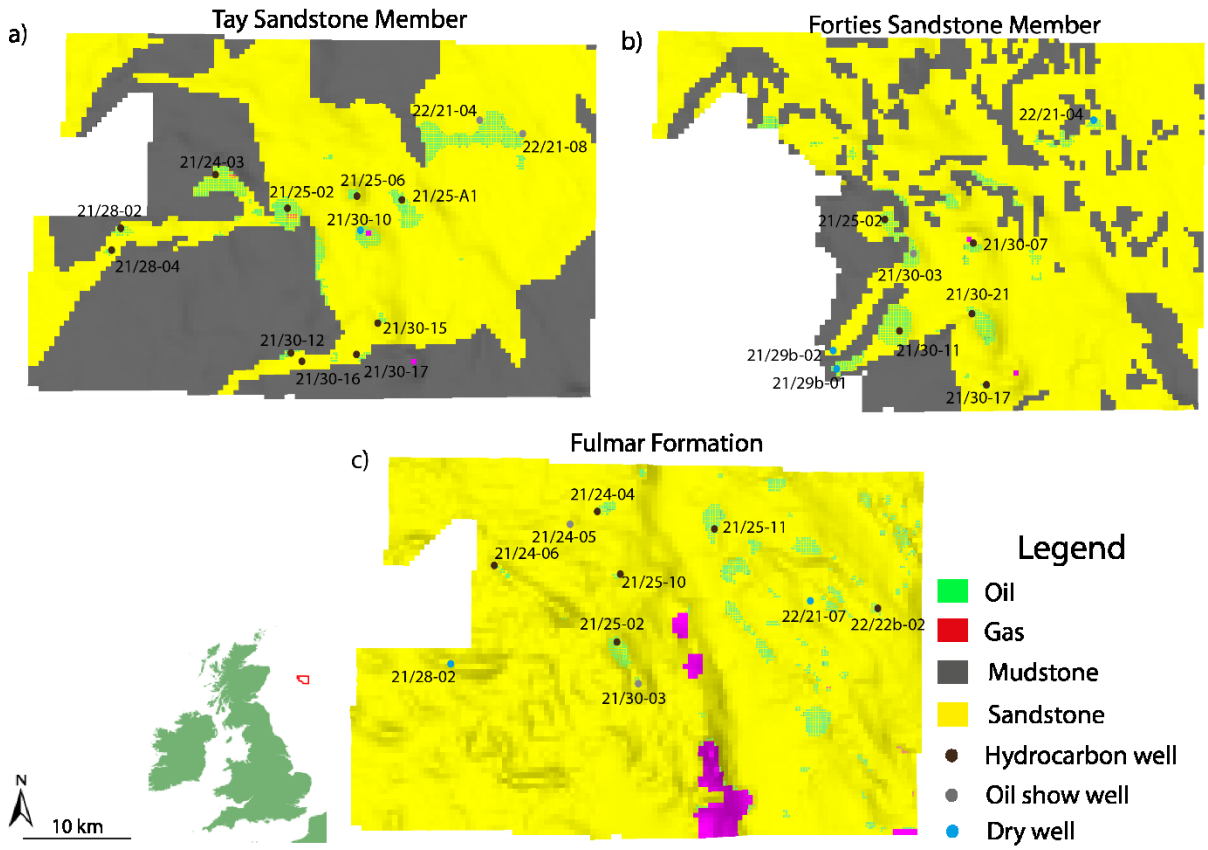


Figure 4.15. Location of present-day accumulations for a) Tay Sandstone Member b) Forties Sandstone Member c) Fulmar Formation with an initial TOC of 10%. Note Fulmar faults are toggled off.

Using an initial TOC of 8 % results in less accumulation of oil in the Fulmar FM, Forties and Tay SM (Figure 4.16 and Table 4.3). Importantly this results in no accumulation of oil in the southern Tay channel (Figure 4.16 a). For this dataset to achieve complete migration/accumulation of oil in the Tay channel the initial TOC must be greater than 8 % and less than 10 %. In reality the average TOC over the study area may be less than the range proposed because the Kimmeridge Clay is mature for oil and gas generation to the east of available data (Barnard and Bastow, 1991) and oil (and gas as mentioned in section 4.3.2.2) could migrate into the study area via mechanisms shown in Figure 4.8.

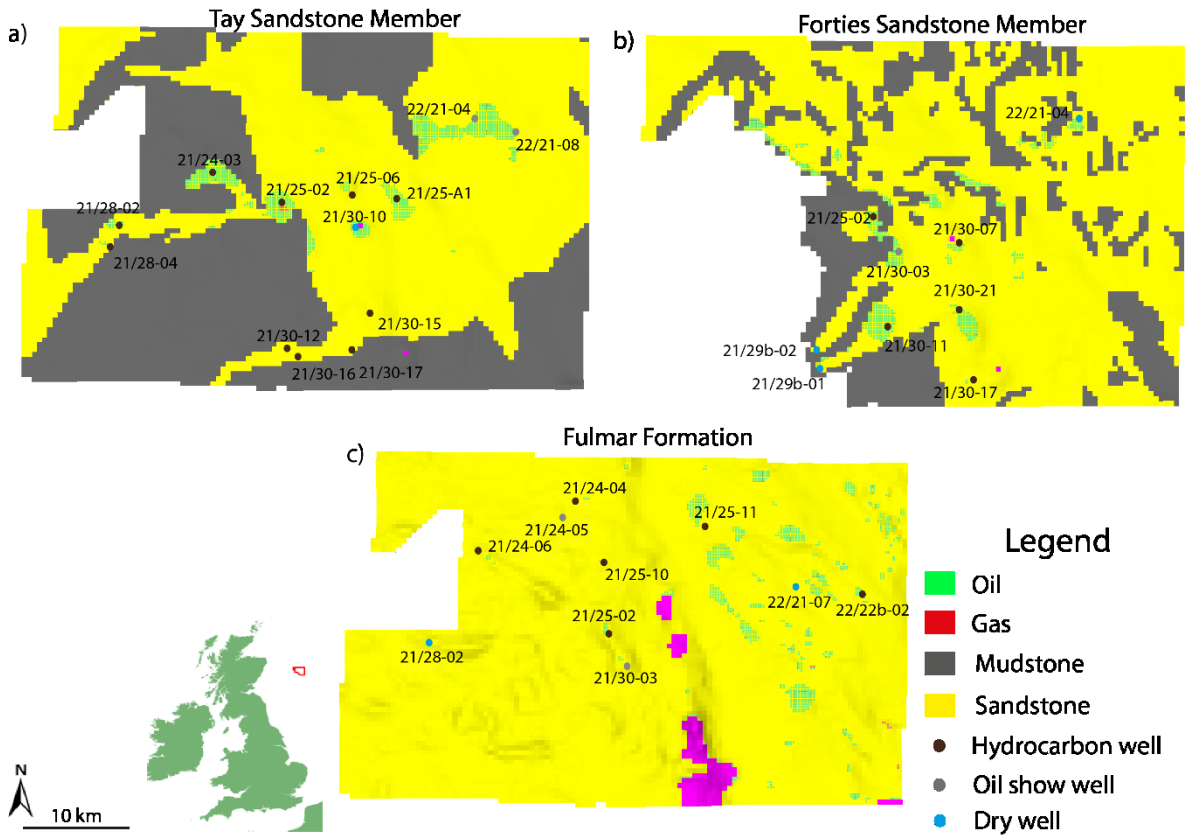


Figure 4.16. Location of Present-day accumulations for a) Tay Sandstone Member b) Forties Sandstone Member c) Fulmar Formation with an initial TOC of 8%. Note Fulmar faults are toggled off.

4.3.3.2 How important are the injectites?

The base-case model (Figure 4.9) was re-simulated, but this time with no injectites, i.e., the Sele FM facies in Figure 4.2 e was changed to mudstone. The present- day accumulation is shown in Figure 4.17. Without injectites there is a 55 % decrease in total oil accumulation volume in the Tay SM, which corresponds to a 119 % increase in total oil accumulation volume in the Forties SM (Table 4.4). This results in no accumulation in well 21/25-06, 21/28-04 in the Tay SM (Figure 4.17). This simulation also demonstrates the need for injectites in the Guillemot Field area for complete lateral migration of oil to the Fyne/Dandy and Pilot fields in the west (Figure 4.17).

Table 4.4. Total accumulation volumes of oil and gas in the reservoirs when no injectites are modelled. The table also shows the differences from the base case model (BC) shown in Table 4.2. A negative difference means the accumulation volumes are greater than the base case model. The additional oil in the Forties is to be expected given the removal of the easy vertical migration pathway provided by the injectites.

	Accumulation volume (No injectites)		**Difference from BC**	
Reservoir	Gas (Mm^3)	Oil (Bbbls)	Gas (Mm^3)	Oil (Bbbls)
Tay	0	2.1	0	1.8
Forties	0	5.7	0	-3.1
Fulmar	1.2	1.6	0	0
Total	1.2	9.4	0	-1.3

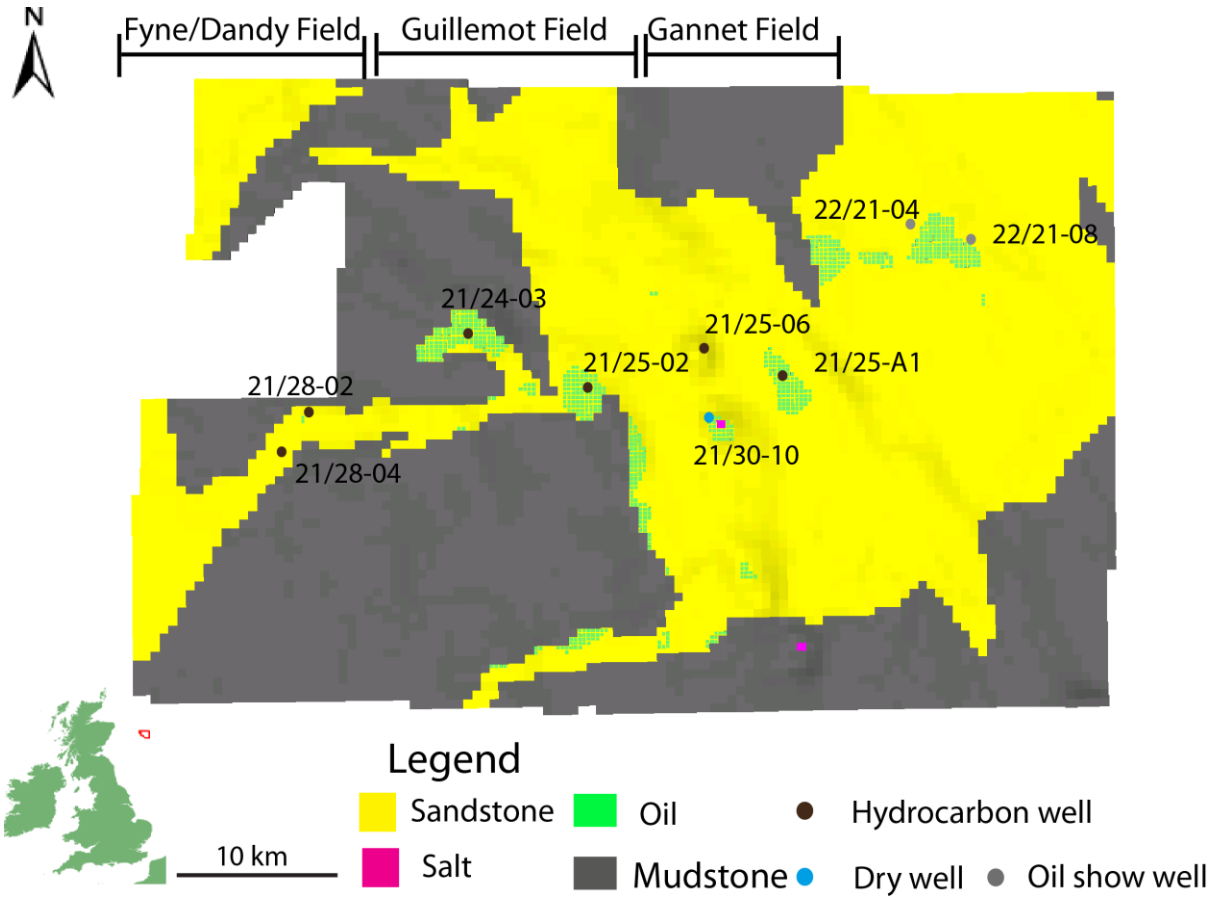


Figure 4.17. Base case model simulated with no injectites. Results show an incomplete migration of oil into the Tay SM.

4.3.3.3 Using Combined Darcy flow with Flowpath Migration Method

The base-case model in Figure 4.9 (D + IP) was simulated using an alternative migration method (D + FP). The D + FP migration (Figure 4.18) produced a completely different result to the D + IP migration (Figure 4.9). D + FP migration method results in larger gas caps in both the Tay and Forties SM (Table 4.5, Figure 4.18 a and b). It is unclear why the two different

migration methods have large differences in gas cap volume (Table 4.5). The accumulation locations observed (Figure 4.18) do not tie with wells in the area. For example, there is no accumulation in the Tay SM in known hydrocarbon wells 21/25-06 and 21/25-A1 (Figure 4.18 a). The D + FP migration method is also not able to predict long distance lateral migration as there are no accumulations in the Tay SM in the west. The results support Baur and Katz (2018) who claim that D + FP migration is not ideal for models with complex geology.

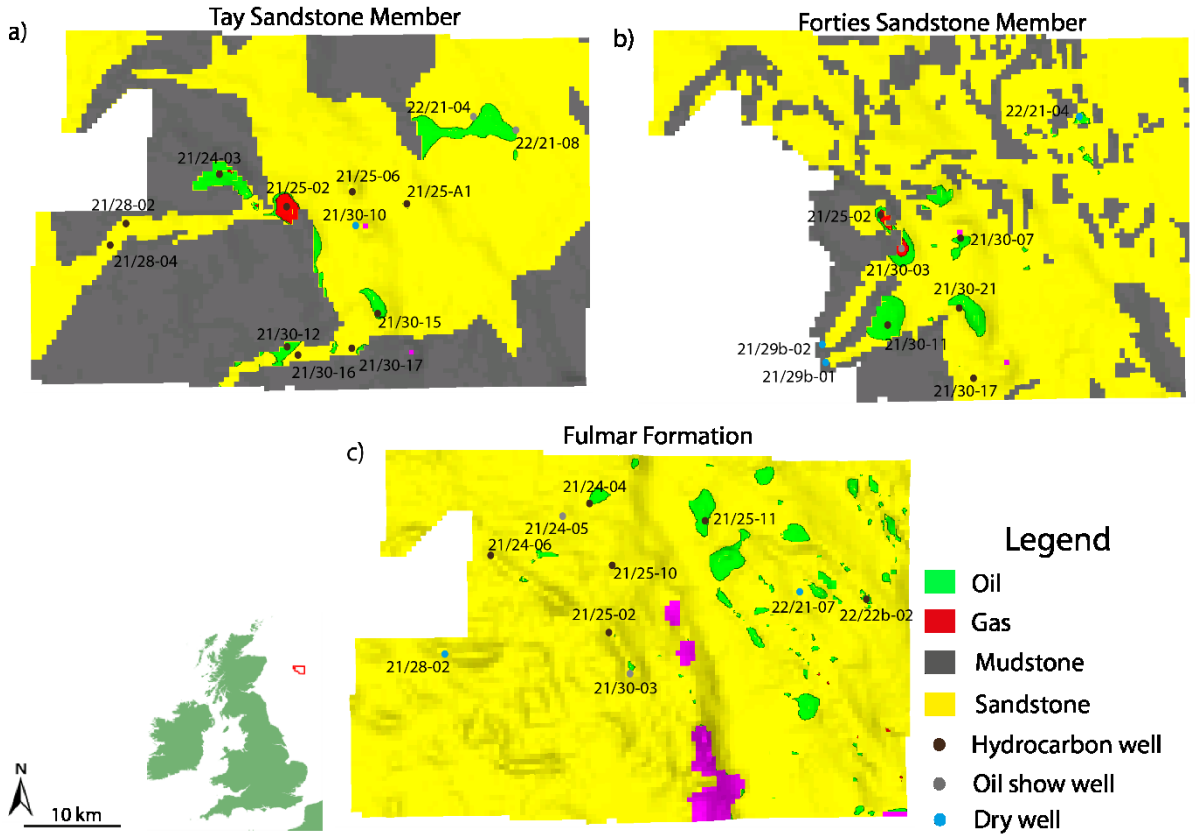


Figure 4.18. Present-day accumulations using D+FP migration method for a) Tay Sandstone Member b) Forties Sandstone Member c) Fulmar Formation. Note Fulmar faults are toggled off.

Table 4.5 Total accumulation volumes of oil and gas in the reservoirs when D + FP migration method is used. The table also shows the differences from the base case model (BC) shown in Table 4.2. A negative difference means the accumulation volumes are greater than the base case model.

	Accumulation volume (D+FP)		**Difference from BC**	
Reservoir	Gas (Mm^3)	Oil (Bbbls)	Gas (Mm^3)	Oil (Bbbls)
Tay	44.6	3.3	-44.6	0.6
Forties	10.5	1.9	-10.5	0.7
Fulmar	0.6	1.1	0.6	0.5
Total	55.7	6.3	-54.5	1.8

4.3.3.4 Importance of faults on the base-case model

Faults which cut through the Fulmar FM (Figure 4.6) were modelled as fluid conduits and a simulation was run with an initial TOC of 15 %. Results of this simulation are shown in Figure 4.19 and Table 4.6. The results show virtually no difference in accumulation location and volumes in the Tay and Forties SM (Figure 4.19a-b and Table 4.6). Making the faults fluid conduits affects the accumulation volume of oil and gas in the Fulmar FM. A 13 % decrease is noticed in the total accumulation volume of oil in the Fulmar FM while a 75 % decrease in the total accumulation volume of gas is observed (Table 4.6). Running this model suggests the faults have little effect on migration of oil and gas into the Tay and Forties SM but results in less accumulation of hydrocarbons in the Fulmar FM (Figure 4.19 and Table 4.6). Hydrocarbon volumes lost from the Fulmar formation most likely reached fill to spill traps in the Tay and Forties SM and spilled off the sides of the model, hence no increase in accumulation was observed.

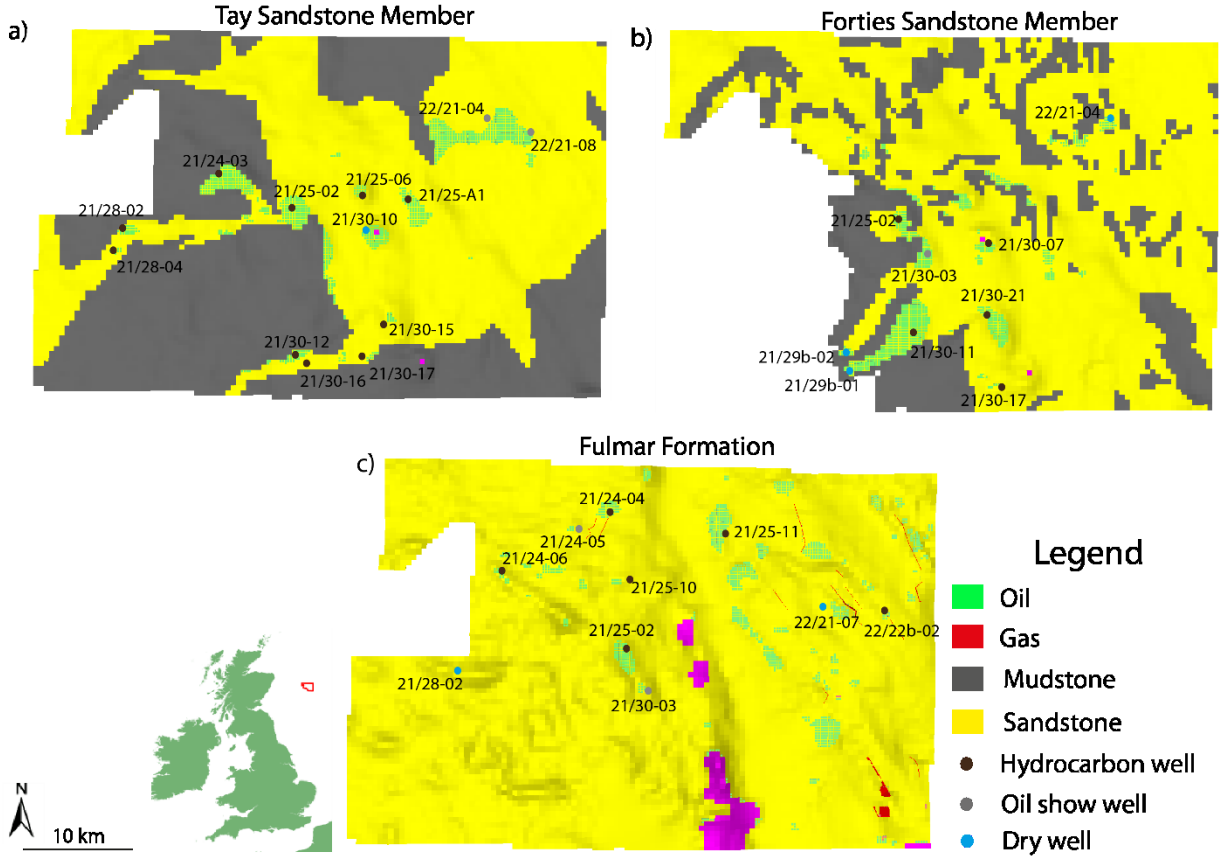


Figure 4.19. Modelled present-day accumulations for a base-case simulation with faults in the Fulmar FM acting as fluid for a) Tay Sandstone Member b) Forties Sandstone Member c) Fulmar Formation. Faults are represented by the red line.

Table 4.6. Total accumulation volumes of oil and gas in the reservoirs when the Fulmar FM faults are acting as fluid conduits. The table also shows the differences from the base case model (BC) shown in Table 4.2. A negative difference means the accumulation volumes are greater than the base case model.

Reservoir	Gas (Mm^3)	Oil (Bbbls)	Gas (Mm^3)	Oil (Bbbls)
Tay	0	3.9	0	0
Forties	0	2.6	0	0
Fulmar	0.3	1.4	0.9	0.2
Total	0.3	7.9	0.9	0.2

4.3.3.5 Tay Accumulation Test

Accumulation A in Figure 4.12 is an undrilled hydrocarbon prospect that has been identified by 3D basin modelling. This prospect was missed by wells 22/21-08 and 22-21/04 (Figure 4.9 a). These wells were drilled in the late 80s to early 90s, and located on 2D data which may have given an inaccurate location of the structural highs. The undrilled hydrocarbon prospect (Polygon a in Figure 4.12) is trapped against an interpreted shale facies (Figure 4.2a and b) to its west. This potential accumulation might be due to the input facies model for the Tay SM. To test this, the facies to the west of this prospect was changed to sandstone and two simulations were run; one with an initial TOC of 15 % (Figure 4.20a) and the other with an initial TOC of 10 % (Figure 4.20b). Petromod estimated the oil accumulation volume of the undrilled prospect (UP) to be 0.9 Bbbls (Polygon a in Figure 4.12), changing the facies to its west to sandstones caused a drop in accumulation volume to 0.4 Bbbls in both models (Figure 4.20 a and b). The results suggest the undrilled prospect (UP a in Figure 4.20 a and b) is likely not a modelling artefact and may contain commercial volumes of hydrocarbons. The second undrilled prospect (UP b in Figure 4.20 a and b) is at the edge of the fan, which was identified by 3D amplitude extraction (Figure 4.2 a) highlighting the importance of 3D data in assessing hydrocarbon prospectively.

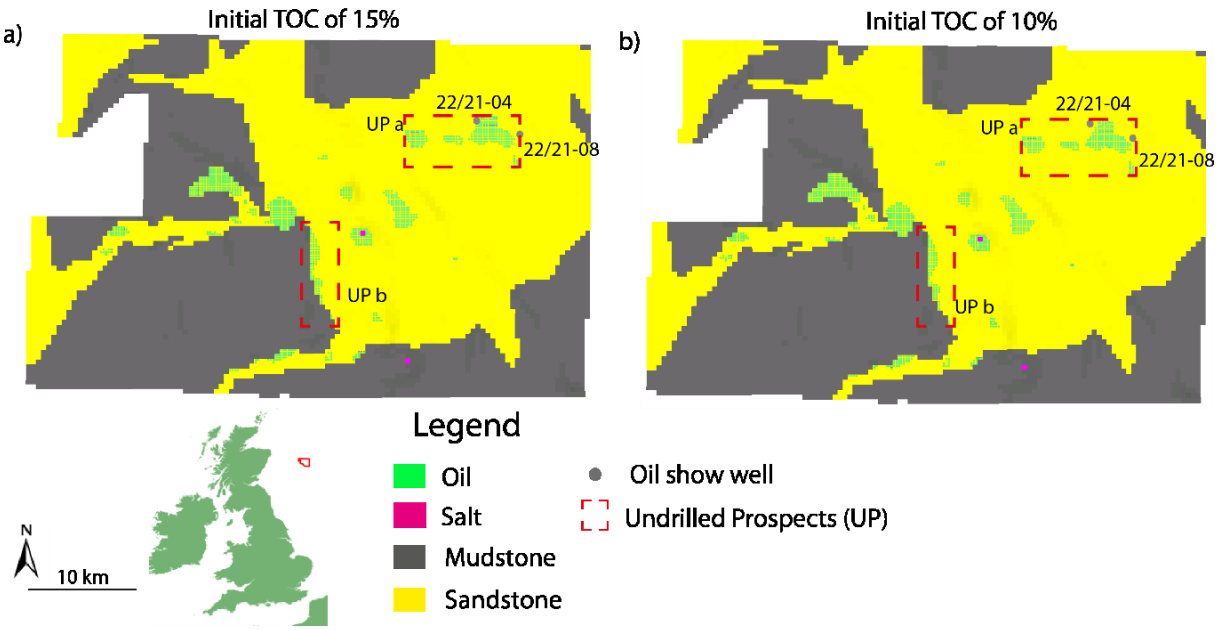


Figure 4.20. Testing undrilled prospect by changing facies to the west to sandstone (see Figure 4.2 c for base case input facies) and running simulations with present day TOCs of a) 15 % and b) 10%.

4.3.3.6 Alternative Facies Models

This section attempts to build a more realistic model my including horizontal facies variations in the Tay and Forties layers. To do this, the following steps were carried out:

1. Amplitude extractions were obtained from the mid and near base Tay and Forties layer in Petrel.
2. High amplitudes are classed as sandstones while lower amplitudes are classed as mudstones as done in Figure 4.2.
3. The Tay and Forties SM are split into 3 sublayer groups in PetroMod.
4. The top third is attributed to the input facies shown in Figure 4.2b and d. The middle third is attributed to the amplitude extraction result from the mid Tay and Forties (Figure 4.21 a and c respectively). The bottom third is attributed to the amplitude extraction result from the near base Tay and Forties (Figure 4.21 b and d respectively).

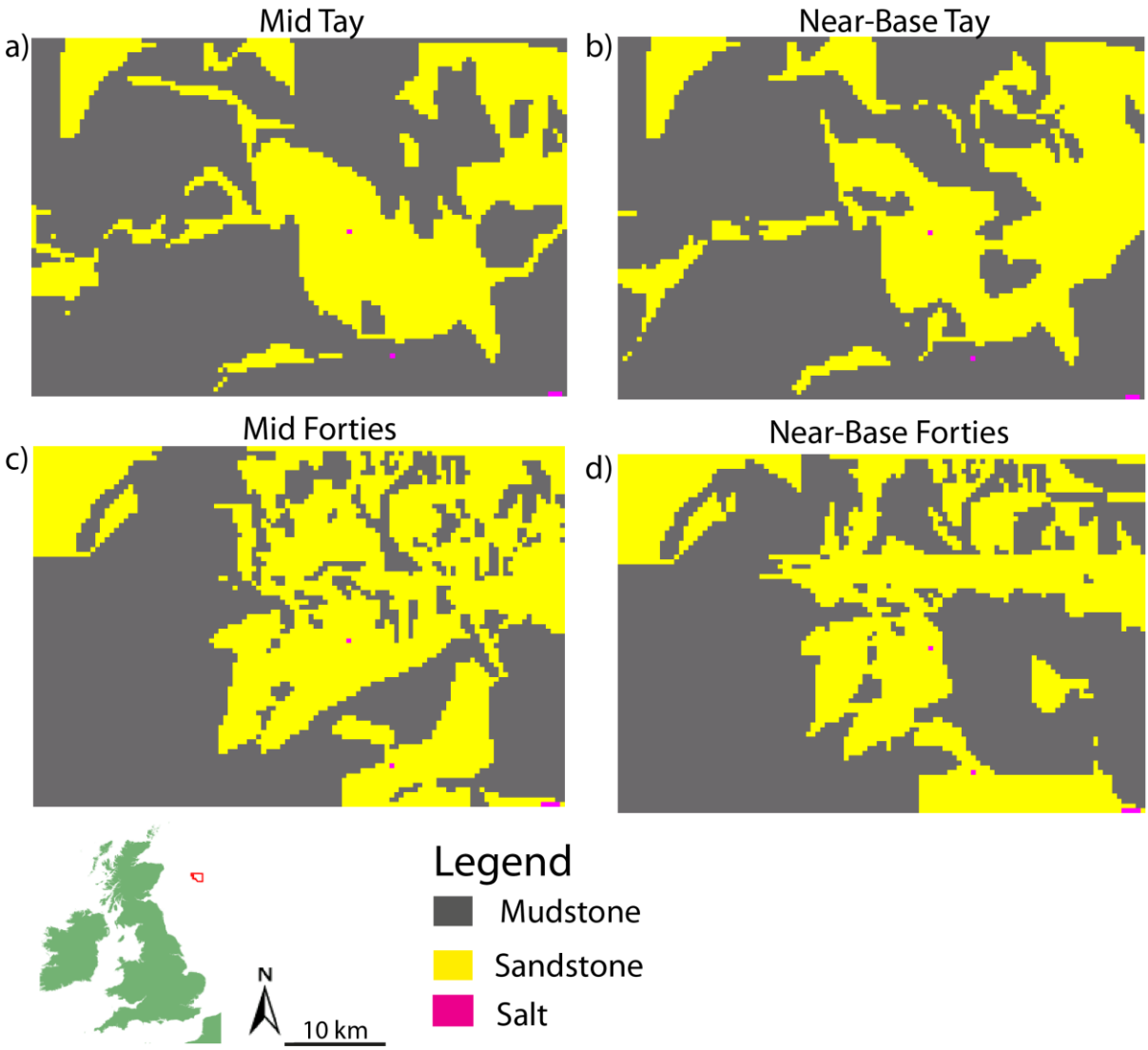


Figure 4.21. Input facies models for simulations run with horizontal variation of facies for a) Mid Tay SM, b) Near-base Tay SM, c) Mid Forties SM and d) Near-base Forties SM.

Two simulations were run with the input facies (Figure 4.21); the first using an initial TOC of 15 %, while the second uses an initial TOC of 10 % (Figure 4.22). The first simulation resulted in similar accumulation locations and volumes within the Tay sandstone (Figure 4.22a and Table 4.7). A difference in accumulation locations is observed in the Forties; a potential undrilled accumulation is observed in the north-west and there is no accumulation in known oil well 21/25-02 (Figure 4.22 b).

The first simulation and the second simulation show similar accumulation locations and volumes within the Forties SM (Figure 4.22 b and d respectively). The major difference is noticed in the Tay SM with the second simulation showing a 25 % decrease in accumulation volume resulting in a lack of charge in the southern channel and in wells 21/25-06, 21/28-02

and 21/28-04. These observations suggest that a TOC > 10 % may be needed for this model to have complete migration in the Tay SM when with lateral and horizontal facies model is used. A more detailed facies model using well data coupled with amplitude extractions may result in different observations.

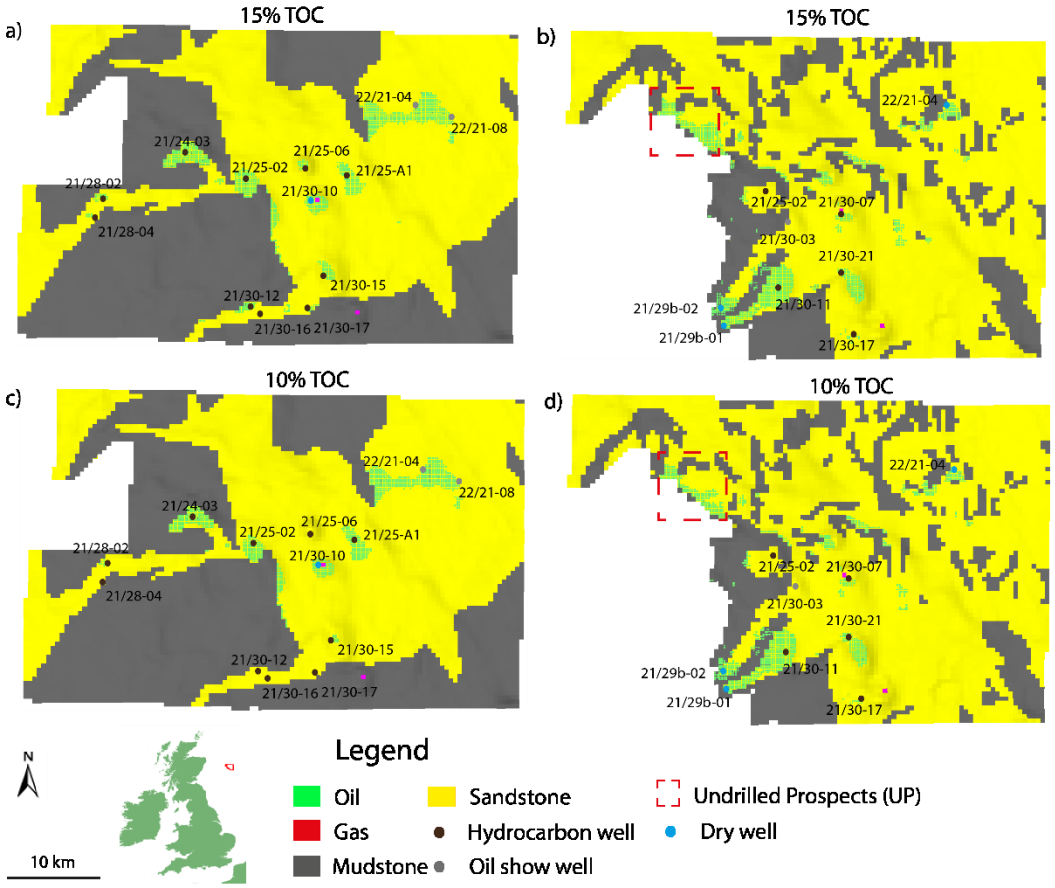


Figure 4.22. Modelled present day accumulations for simulation run with a more detailed facies input (Figure 4.21) for a) Tay SM with an initial TOC of 15 % b) Forties SM with an initial TOC of 15 % c) Tay SM with an initial TOC of 10 % and d) Forties SM with an initial TOC of 10 %. Note: the model predicts oil accumulation in the mudstone in the Forties SM, this is actually accumulation in the mid–base Forties Sandstone facies below the mudstone.

Table 4.7. Total accumulation volumes of oil and gas in the reservoirs when a more detailed facies model is used with initial TOC's of 15 and 10%. The table also shows the differences from the base case model (BC) shown in Table 4.2. A negative difference means the accumulation volumes are greater than the base case model

	TOC 15				**TOC 10**			
	Accumulation volume		Difference from BC		Accumulation volume		Difference from 10 % TOC (Figure 4.15)	
Reservoir	Gas (Mm^3)	Oil (Bbbls)	Gas (Mm^3)	Oil (Bbbls)	Gas (Mm^3)	Oil (Bbbls)	Gas (Mm^3)	Oil (Bbbls)
Tay	0	3.7	0	0.2	0	2.8	1.3	0.9
Forties	0	2.3	0	0.3	0	2.1	0	-0.3
Total	0	6	0	0.5	0	4.9	1.3	0.6

4.4 Conclusions

The integration of seismic interpretation, well data, geochemical data and 3D petroleum system modelling was carried out to quantify the timing of hydrocarbon generation, expulsion, fluid migration and to determine the lateral and vertical migration pathways (particularly in the Tay sandstone) in the Central North Sea, UK (Figure 3.14 I). The following key observations were made from all the models ran in section 4.3:

- The Kimmeridge Clay is only mature in the east (Figure 4.7 a). Hydrocarbon generation commenced in the Cretaceous while the main expulsion of hydrocarbons occurred in the Oligocene (Figure 4.7 b and c). Expulsion of oil occurred in areas with a TR > 20 % while gas was only expelled at the eastern edge with TR > 95 % (Figure 4.7 a).
- Vertical migration of oil into the Tertiary strata does not only occur in the east where the source rock is mature but can occur in the west as the Fulmar FM and Base Chalk (marl of the Cromer Knoll Group in Figure 2.4) layers can act as lateral carriers of oil (Figure 4.8).
- An initial TOC of between 8 % and 10 % is needed for complete migration within the Tay SM (4.3.3.1). In reality, this may be smaller because the study area does not include all the mature Kimmeridge Clay to the east
- Injectites and salt diapirs play important roles for the migration of oil into the Tay SM from the underlying Forties SM (Figure 4.17 and Figure 4.8b)
- In the Tay SM vertical migration of oil is dominant in the Gannet Field area while a mixture of vertical and lateral migration of oil is observed in the Guillemot Filed area and lateral migration is needed to charge the Fyne/Dandy and Pilot Field (Figure 4.14). This observation is vital in identifying a magnetic proxy for lateral hydrocarbon migration which will be discussed in the following Chapter.
- The use of 3D seismic amplitude extractions to obtain a more detailed facies model has led to the discovery of potential hydrocarbon prospects in the Tay and Forties SM (Figure 4.20 and Figure 4.22 respectively).

Chapter 5

Identifying Magnetic Proxies for Hydrocarbon Migration

5.1 Introduction

Interpretation of processed seismic data is the most valuable tool in hydrocarbon exploration, however, acquisition of such data is expensive and does not always fully resolve the geology. As such, there is a need for complementary less expensive techniques that can aid in oil recovery and yield. This chapter focuses on the possible use of mineral magnetic methods as a potential indicator for hydrocarbon presence and migration.

There have been several studies that have focused on the magnetic minerals formed near to hydrocarbon accumulations and plumes (e.g., Reynolds et al., 1990; Machel and Burton, 1991a;1991b; Burton et al., 1993; Machel, 1995; Costanzo-Alvarez et al., 2000; Díaz et al., 2000; Aldana et al., 2003; Guzmán et al., 2011). For example, Costanzo-Alvarez et al. (2000), Aldana et al. (2003) and Guzmán et al. (2011) analysed the magnetic susceptibility of drill cuttings above possible hydrocarbon accumulations from 24 wells in Venezuela. They observed high magnetic susceptibility values over hydrocarbon bearing wells, which was linked to the presence of authigenic magnetite and iron sulphides. The studies saw a positive correlation between extractable organic matter (EOM) and organic-matter-free radical concentrations (OMFRC), and these magnetic anomalies for hydrocarbon bearing wells. These studies concluded the increase in magnetic susceptibility is likely due to the leakage of hydrocarbon from the reservoir (Díaz et al., 2000; Guzmán et al., 2011).

In contrast, only a few studies have been carried out on samples from the reservoir itself (e.g., Liu et al., 2006; Emmerton et al., 2012; Emmerton et al., 2013; Emmerton, 2013; Abubakar, 2016). Liu et al. (2006) and Emmerton et al. (2012) found that magnetic susceptibility and magnetic hysteresis parameters that are mass dependent, e.g., saturation magnetisation and remanent saturation magnetisation, are higher in oil producing samples compared to dry well or oil-cleaned samples from the same formation, i.e., the “background signal”. The increase of saturation magnetisation and remanent saturation magnetisation in the oil producing formations was attributed to the presence of fine-grained magnetite particles (< 50 nm), while only larger particles (~30 μm) were observed in the dry formations. In addition to the nanoparticles found in the hydrocarbon-rich samples, larger micron-sized iron-oxide framboids that are made up of many nanoparticles, have also been observed in hydrocarbon reservoirs along with iron sulphides, e.g., greigite, pyrrhotite, pyrite and siderite (Benthien

and Elmore, 1987; Elmore et al., 1987; Kilgore and Elmore, 1989; Elmore and Crawford, 1990; Reynolds et al., 1991; Elmore et al., 1993a; Emmerton et al., 2012; Abubakar, 2016).

This chapter builds on current research, by attempting to identify a magnetic proxy or set of magnetic proxies that can be used to trace hydrocarbon migration pathways by determining the morphology, abundance, mineralogy and size of the magnetic minerals present in reservoirs. To test for the potential use of magnetic proxies the hydrocarbon migration pathways identified in Tay fan in Chapters 3 and 4, are used to calibrate the rock magnetic results.

5.2 Sampling and Methodology

5.2.1 Sampling

Well cores were sampled from the British Geological Survey core repository in Keyworth, UK. The composite logs, e.g., Figure 5.1, were used to determine if the accumulation of hydrocarbon is in the Tay formation and if the core recovery was successful. Wire-line logs were used to identify the presence of gas and/or oil in the Tay sandstones. A total of 203 samples were collected from 26 wells.

At the British Geological Survey (BGS) core repository samples were selected based on geological observation, i.e., water wet sandstone, oil stained sandstone, siltstones and shale (Figure 5.2). Samples taken were typically 2 cm chips. Sedimentary logs were drawn for each well, detailing the sedimentary structures observed in the core section. Most of sandstones were very fine to fine grained, with very few sedimentary structures as seen in Figure 5.2. Complete lithology logs are included in Appendix 2.

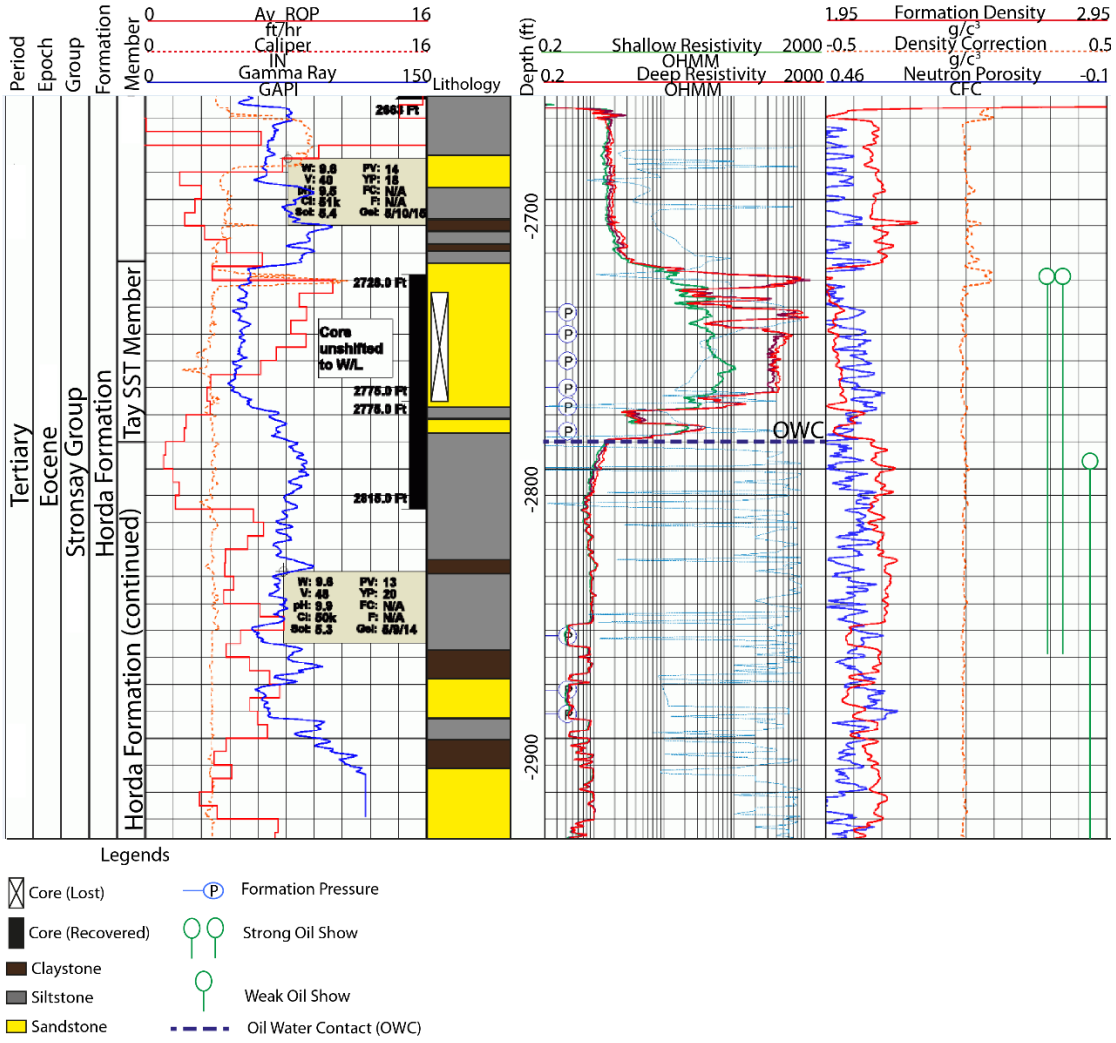


Figure 5.1. Example of composite logs (UK well 21/27a-06) used to identify the presence or absence of hydrocarbon in the Tay sandstone member and if the reservoir unit was cored and recovered or not. The increase in resistivity suggests the presence of hydrocarbon and can be used to identify fluid contacts. Formation density and neutron porosity logs are used to identify the presence of gas. This well is only an oil well and contains no gas. Composite logs were obtained from IHS. ROP is the Rate of Penetration. Depth is measured from the top of the rotary table.



Figure 5.2. Picture comparing water wet sandstone to the oil stained sandstones in UK well 21/25-06.

5.2.2 Magnetic Measurements

Magnetic measurements were carried out to determine the morphology, mineralogy and size of the magnetic minerals present in the samples. The magnetics techniques used are described below.

5.2.2.1 Magnetic Hysteresis Measurements

Room-temperature measurements on a vibrating sample magnetometer VSM were done at Imperial College London. Saturation magnetisation (M_s), remanent saturation magnetisation (M_{rs}) and coercivity (H_C) were estimated from the measured hysteresis loops.

First-order reversal curves (FORC) diagrams are used to identify the domain-state distributions within a sample (Roberts et al., 2000; Roberts et al., 2014). A FORC diagram is calculated from a class of partial-hysteresis curves (Roberts et al., 2000). As a first approximation the x-axis represents the coercivity distribution while the y-axis describes the magnetic-interaction distribution within the sample (Roberts et al., 2000). The 'irregular' measurement protocol by Zhao et al. (2015) was used for all the FORCs in this thesis.

5.2.2.1 Low-temperature measurements.

Low-temperature (LT, 10 – 300 K) experiments were carried out on a Magnetic Property Measurement System (MPMS2) at the University of Minnesota's Institute for Rock Magnetism in Minneapolis. These measurements help to identify the magnetic minerals present in the samples based on mineral-specific crystallographic transitions, e.g., the Verwey transition in magnetite at 125 K (Verwey, 1939), the Morin transition in hematite at 263 K (Morin, 1950), the Besnus transition in monoclinic pyrrhotite at 30-34 K (Besnus and Meyer, 1964; Dekkers et al., 1989) and to identify nanometric particles (< 30 nm) that are difficult to detect at room-temperature due to high thermal energy, i.e., particles that are said to be superparamagnetic at room temperature and are effectively "magnetically transparent".

The following experiments were carried out on selected samples to identify possible magnetic transitions:

1. Low-temperature demagnetisation: the samples were induced with a saturation isothermal remanent magnetisation (SIRM) at room-temperature (field = 2.5 T) and then cooled to 20K and warmed back to 300 K in zero-field. This generates two curves called cycling cooling and cycling warming curves.

2. Field cool (FC) – Zero-field cool (ZFC) warming curves: Induce a SIRM at 10 K (field = 2.5 T) and warm in zero field to 300 K. In the ZFC scenario, the sample is first cooled to 10 K in zero field, in the FC scenario in a field a 2.5 T. This sequence helps to detect siderite (Jacobs, 1963; Frederichs et al., 2003) and nanometric particles (< 30 nm).

5.2.2.3 High-temperature Measurements

High-temperature (HT) susceptibility experiments were carried out on a KLY-2 KappaBridge AC Susceptibility Bridge in Imperial College London. Susceptibility was measured as the samples were heated from room temperature to 700^{o}C in an argon atmosphere. This is used to help determine the mineralogy of the samples based on their Curie temperature and thermomagnetic behaviour (Dunlop and Özdemir, 1997). Curie temperatures were also determined for a small number of samples (S65311 and S65328) by measuring magnetisation as a function of temperature (30 °C to 726 °C) in a field of 100 mT on the MPMS3 located at Quantum Design, Darmstadt. These are called thermomagnetic curves.

5.2.2.4 Room-Temperature (RT) Susceptibility

A Magnon Variable-Field Susceptibility Meter (VFSM) was used to measure the magnetic susceptibility at room temperature over a wide range of frequencies (30 Hz – 10 kHz) at a field of 300 Am^{-1} at Imperial College London. The frequency-dependent susceptibility factor (χ_{FD}) is calculated using the formula below, where χ_{lf} is the susceptibility at low frequency and χ_{hf} is the susceptibility at high frequency (Dearing et al., 1996) :

$$\chi_{FD} = 100\left(\frac{\chi_{lf}-\chi_{hf}}{\chi_{lf}}\right) \quad \text{Equation 5.1}$$

Grains that are near the stable single-domain/superparamagnetic grain size at room-temperature, display superparamagnetic behaviour at the lower frequency, but stable single-domain behaviour at the higher frequency, i.e., this method can detect particles that are near the superparamagnetic/stable-single-domain transition size at room-temperature, i.e., 25- 35 nm for magnetite at room temperature (Muxworthy, 2001).

5.2.3 Scanning Electron Microscopy (SEM)

SEM was carried out for imaging of the magnetic minerals present in the samples. As the abundance of magnetic minerals was much less than 1%, magnetic extraction was needed to increase the magnetic mineral abundance for imaging. To do this samples were ground to an even grain size, and a passed through a Frantz electromagnet magnetic separator three times to reduce the abundance of non- magnetic materials following the protocol developed by Chang et al. (2012).

Samples were grounded and coated in either gold or carbon for imaging energy dispersive X-ray (EDX) analysis on the Zeiss LEO Gemini 1525 scanning electron microscope (SEM) at the Dept. of Materials, Imperial College London. The EDX analysis had a spot size of about 1 µm. Some uncoated samples were also imaged on a Phenom Pro X desktop SEM (Dept. of Earth Science and Engineering, Imperial College London).

5.2.4 Geochemical Experiments

Geochemical experiments were introduced to determine if the dry core samples had ever been impregnated with oil. Samples from dry wells may appear water wet as the formation water would replace the leaked oil, but the oil could leave behind some organic residue

(residual oil) in the samples that can be extracted (Tyson, 2006). Core samples s70402, s70403 and S70404 from dry well 21/28b-07 were selected for column chromatography (Rowland and Revill, 1995). The samples were water wet, very fine to medium grained sandstones with no sedimentary structures. The cuttings from the other dry wells were not used as the samples were covered in drilling mud and stored in plastic bags which contaminates the samples. Organic extraction was carried out before column chromatography. To do this a mixture of dichloromethane (DCM) and methanol (97:3) was added to the ground samples (5-10g). The mixture was sonicated for 5 minutes then placed in a centrifuge at 1500 rpm (revolutions per minute) for 5 minutes. The process was repeated until the solvent was clear. A rotary evaporator was used at 50 °C to increase the concentration of organic extracts in the solvent. The fractions were transferred into clean sample vials using a pipette (cleaned with DCM). This was left to dry leaving behind organic matter extracts.

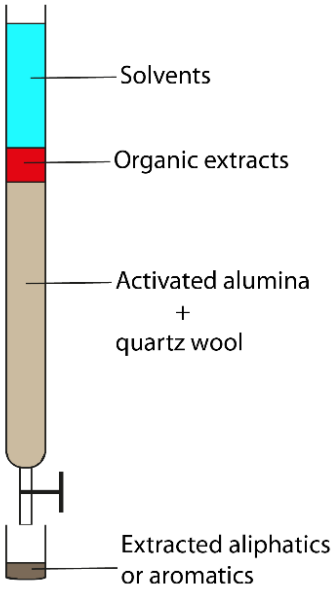


Figure 5.3. Column chromatography set up used to separate the aliphatic constituents from the organic matter extracts.

The set-up for the column chromatography is shown in Figure 5.3. This procedure allows the separation of aliphatic and aromatic constituents of the organic extracts for Gas Chromatography–Mass Spectroscopy (GC–MS) on an Agilent 6890 System (Rowland and Revill, 1995). The constituents were extracted in the following way:

- Alumina was activated in an oven for 1 hr at 150 °C.
- The column was plugged with the activated alumina and small amounts pre-extracted using quartz wool.

- Small amounts of pre-extracted quartz wool were added to the sample vial, stirred with a clean spatula and left to dry. The dry mixture was added to the top of the column.
- Hexane was used to elute the aliphatic fraction while DCM was used to elute the aromatic fraction. The fractions were collected in a test tube.
- The volume of the fractions were reduced to < 1 ml under a stream of nitrogen.
- Fractions were transferred into clean vials and allowed to dry completely.

The fractions were placed in the GC-MS for compound detection and identification. The results would be able to predict any paleo-accumulation of hydrocarbons in the dry core samples.

5.3 Results

5.3.1 Magnetic Hysteresis Parameters and Susceptibility

Mass-normalised room-temperature hysteresis loops, e.g., sample s63594 (Figure 5.4) and susceptibility were measured for all samples. The samples were generally weak and most of the hysteresis loops had a low SNR (signal-to-noise ratio) with a strong paramagnetic behaviour. Mean and median of measures M_s, M_{rs}, H_c and susceptibility values of all the wells used in this study are shown in Table 5.1. M_s, M_{rs} and H_c are similar to the values Emmerton (2013) observed in oil stained and oil-free samples from Colombia, Canada, Indonesia and UK.

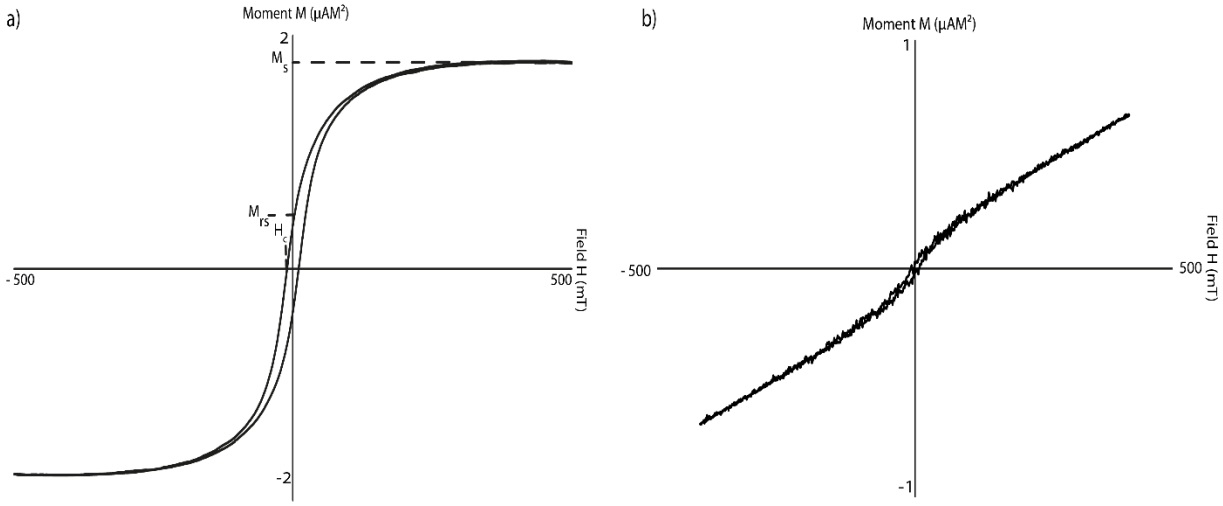


Figure 5.4. a) Representative hysteresis loop showing a strong ferromagnetic behaviour within the sample. Sample S63594 from well 21/25-04. b) Representative noisy hysteresis loop showing a strong paramagnetic behaviour within the sample. Sample S63598 from well 21/25-04.

Table 5.1. Mean and median of measured M_s, M_{rs} and susceptibility (χ) in wells in the study area. All measured sample types are included in the calculation as the samples in the gas cap, oil stained samples, water wet samples and siltstones typically have similar values as shown in Figure 5.5, Figure 5.6 and Figure 5.7. Hydrocarbon wells are roughly arranged from east to west. Note: The last 3 wells are dry. Only well 21/28b-07 is cored, the other two wells (21/25-11 and 21/25-12) are cuttings. n is the number of samples

Well	Mean M_s (10^{-3} Am^2Kg^{-1})	Median M_s (10^{-3} Am^2Kg^{-1})	Mean M_{rs} (10^{-3} Am^2Kg^{-1})	Median M_{rs} (10^{-3} Am^2Kg^{-1})	Mean H_c (mT)	Median H_c (mT)	Mean χ (10^{-3} m^2Kg^{-1})	Median χ (10^{-3} m^2Kg^{-1})	n
21/25-04	2.1	1.0	0.4	0.2	11.9	8.8	2.2	1.1	16
22/21-03	112.2	8.3	24.6	1.1	8.9	8.1	226.8	15.2	9
21/25-A1	1.0	0.9	0.1	0.1	8.9	7.0	0.1	0.1	15
21/25-06	6.0	1.0	1.3	0.1	9.0	7.6	24.5	3.8	26
21/25-02	4.6	1.3	1.8	0.1	35.0	14.9	11.3	13.9	6
21/24-02	1.2	1.2	0.2	0.2	16.9	17.0	0.1	0.1	7
21/24-03	2.1	2.0	0.3	0.3	11.6	11.0	0.3	0.2	11
21/29a-08	1.6	1.5	0.1	0.1	15.6	10.4	36.0	28.3	10
21/29a-06	0.4	0.3	0.1	0.1	15.8	14.2	1.8	0.0	8
21/28a-05	1.0	1.0	0.1	0.1	8.9	6.9	1.5	1.4	6
21/28a-03	39.1	2.6	6.9	0.4	23.9	11.7	75.1	21.3	8
21/28a-04	1.2	1.0	0.1	0.1	17.4	12.4	9.7	3.3	7
21/28a-08	2.9	1.8	0.6	0.4	20.2	13.1	12.5	10.0	8
21/27-1A	6.5	4.5	1.1	0.6	9.8	8.4	11.9	6.9	8
21/27-04	1.2	1.1	0.3	0.2	18.5	15.9	9.3	5.5	7
21/27a-05	1.0	1.0	0.1	0.0	17.4	13.8	6.5	5.7	4
21/27-02	3.5	3.2	0.4	0.4	7.5	7.2	5.1	4.3	4
21/27-03	1.2	0.9	0.2	0.1	16.7	10.9	3.4	1.2	7
21/27a-06	1.8	1.7	0.3	0.3	10.5	11.0	0.1	0.1	7
21/28b-07	2.3	1.6	0.4	0.3	14.4	15.8	0.2	0.2	5
21/25- 12	6.3	6.6	0.7	0.8	10.4	10.9	2.9	1.5	4
21/25- 11	14.5	10.2	1.5	1.2	9.4	8.8	9.0	7.5	3

Given the amount of data, six representative wells (out of 19 hydrocarbon wells) have been selected to demonstrate the variation in M_s, M_{rs}, H_c and susceptibility in the different sample types and along the migration pathways identified in chapters 3 and 4 (Figure 5.5, Figure 5.6 and Figure 5.7 respectively). Measured M_s and M_{rs} values cannot be used to distinguish the four different rock types, i.e., oil stained sandstone, water-wet sandstone, sandstone in the gas cap and siltstone, as they have similar values (Figure 5.5). The siltstones sometimes have higher M_s and M_{rs} values compared to the other rock types as seen in wells 21/28a-04 and 21/27-04 (Figure 5.5 e and g). A similar relationship is noticed when comparing the susceptibility of the different sample types (Figure 5.7). Most of the oil stained samples, water wet samples and samples in the gas cap have a χ_{FD} (calculated using a low frequency of 600 Hz and a high frequency of 6000 Hz) greater than 10 %, while the siltstone samples are generally less than 15 % (Figure 5.8). This suggests the siltstones contain relatively larger grains (Muxworthy, 2001). Peaks in M_s, M_{rs} and susceptibility were noticed at hydrocarbon fluid contacts, this is discussed in detail in Chapter 7. There is not a lot of difference in the H_C of the different sample types within a well (Figure 5.6), suggesting that the magnetic mineralogy and grain size is not significantly different or the differences are not detectable with this parameter.

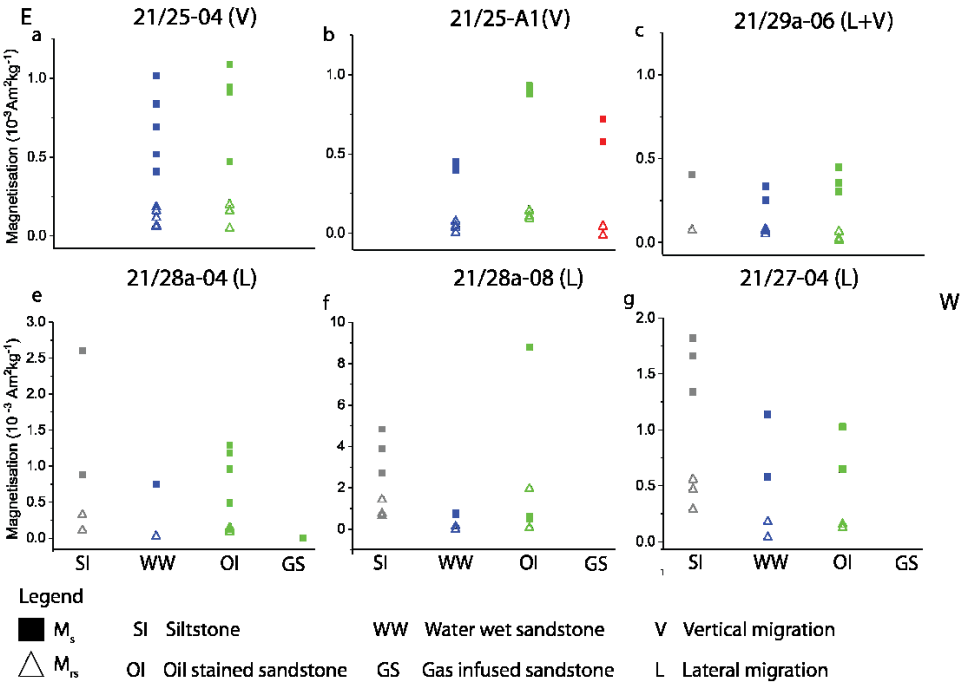


Figure 5.5. Plot comparing the M_s and M_{rs} values in oil stained sandstones (green), water wet sandstones (blue), sandstones in the gas cap (red) and siltstones (grey). Wells are arranged from east to west with predominantly vertical migration in the east and lateral migration in the west. Note: high M_s and M_{rs} values observed at the hydrocarbon contacts are not shown in the plot.

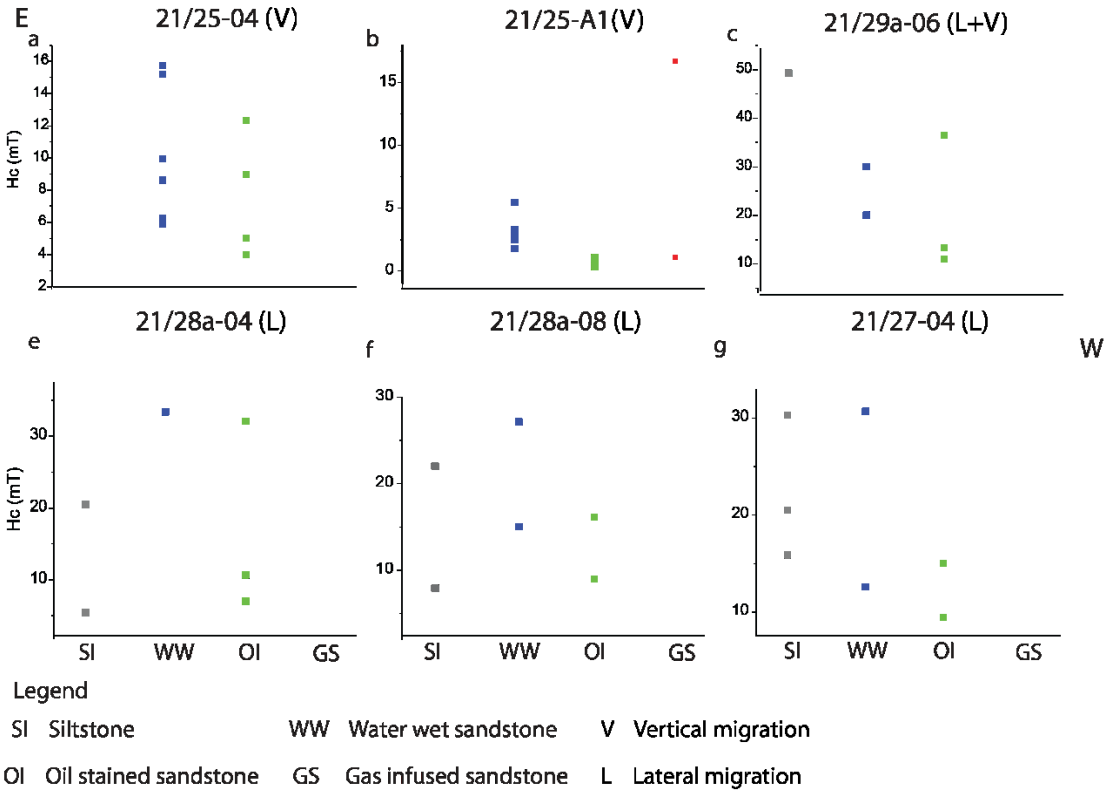


Figure 5.6. Plot comparing the H_c values in oil stained sandstones (green), water wet sandstones (blue), sandstones in the gas cap (red) and siltstones (grey). Wells are arranged from east to west with predominantly vertical migration in the east and lateral migration in the west. Note the various scale ranges on the vertical axes.

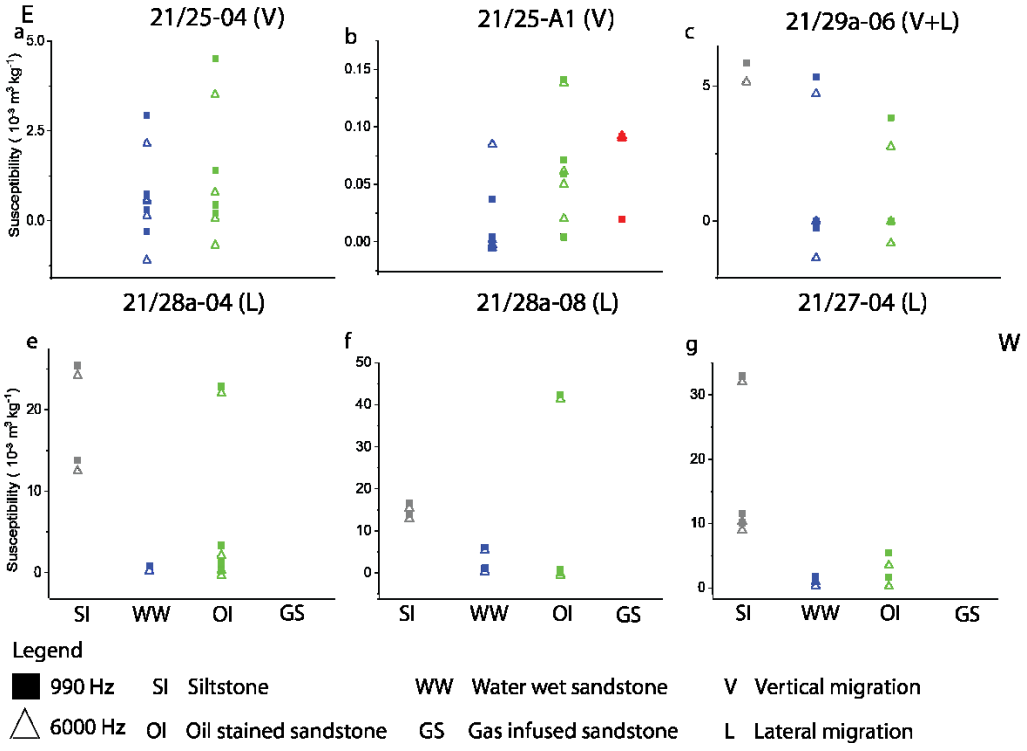


Figure 5.7. Plot comparing the susceptibility values in oil stained sandstones (green), water wet sandstones (blue), sandstones in the gas cap (red) and siltstones (grey) for two different frequencies. Wells are arranged from east to west with predominantly vertical migration in the east and lateral migration in the west. Note: high susceptibility values observed at the hydrocarbon contacts are not shown in the plot and the various scale ranges on the vertical axes.

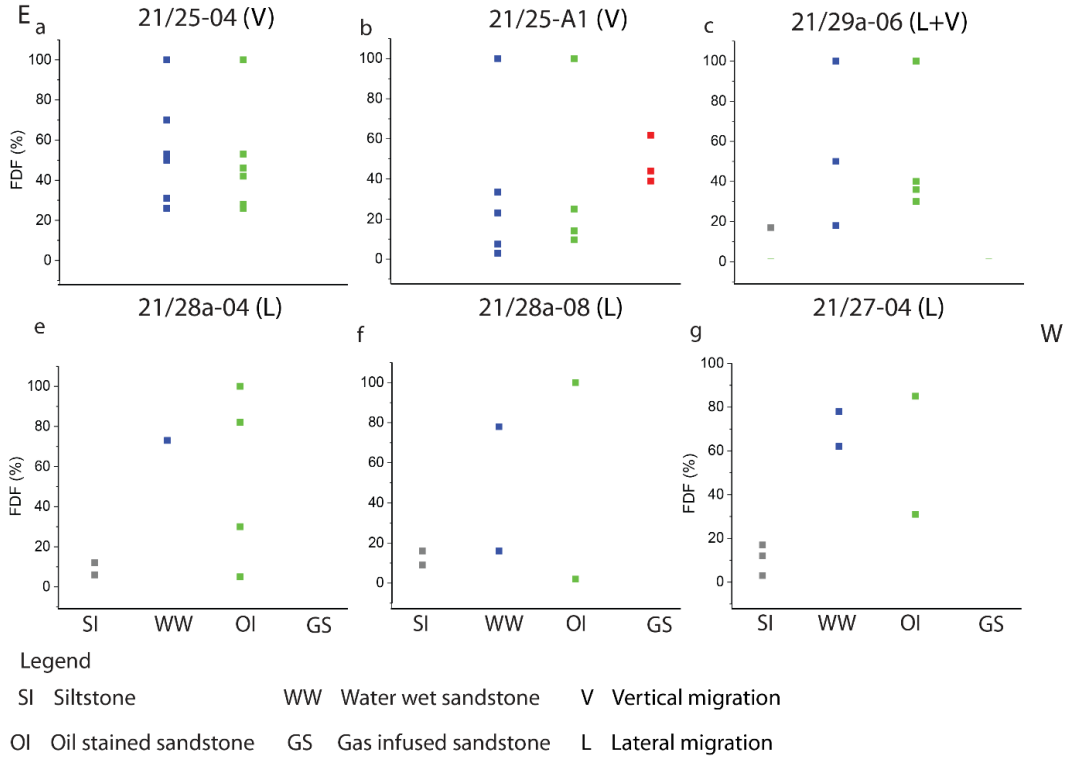


Figure 5.8. Plot comparing the χ_{FD} (FDF)in oil stained sandstones (green), water wet sandstones (blue), sandstones in the gas cap (red) and siltstones (grey). Wells are arranged from east to west with predominantly vertical migration in the east and lateral migration in the west.

No relationship was noticed between M_s and M_{rs} and the hydrocarbon migration pathway (E-W in Figure 5.5). H_c appears to be lower (< 15 mT) in areas with vertical migration as noticed in wells 21/25-04 and 21/25-A1 (Figure 5.6 a-b). This is likely caused by magnetic phases of authigenic origin (Costanzo-Alvarez et al., 2000). The higher H_c noticed in wells charged laterally; wells 21/29a-06, 21/28a-04, 21/28a-08 and 21/27-04 (Figure 5.6 c-g) could be due to the increasing presence of iron sulphides (Horng, 2018). The susceptibility is generally lower in wells that were charged vertically (wells 21/25-04 and 21/25-A1; Figure 5.7 a-b) compared to wells charged laterally (wells 21/28a-04, 21/28a-08 and 21/27-04; Figure 5.7 e-g). This is not surprising as magnetic mineral formation due to the presence of hydrocarbon has been shown to produce either a negative or positive magnetic anomaly, which can lead to a noticeable increases or decreases in relative susceptibility along the profile (Burton et al., 1993; Machel, 1995). For example, a positive magnetic anomaly would be observed if

magnetite was precipitated in a layer with pyrite and/or hematite present prior to the invasion of oil while a negative anomaly would be observed if the invasion of oil led to the precipitation of siderite.

5.3.2 Magnetic Mineral Identification

LT and HT experiments were carried out to determine the magnetic minerals in the samples while the FORC diagrams were used to infer the grain size of the magnetic minerals present in the samples. RT, LT and HT experiments, for all the wells are shown in Appendix 3.

5.3.2.1 Hydrocarbon Wells Core Samples

A drop in remanence around 120 K in the cycling cooling curves was used to confirm the presence of magnetite in all the oil-stained sandstone samples (Figure 5.9, Figure 5.10, Figure 5.11, Figure 5.12 and Figure 5.13). A hump is recorded in some of the cycling cooling curves, e.g., samples s72392, s65305, s65307 and s65300 (Figure 5.9b, Figure 5.10b-c and Figure 5.11d respectively), which is indicative of maghemite (Özdemir and Dunlop, 2010).

A pronounced drop in remanence between 10 and 40 K in the FC experiment was used to identify the presence of siderite as shown in samples s72392, s65302, s65307 and s65297 (Figure 5.9 a, Figure 5.10 a &b and Figure 5.11c respectively). Siderite is paramagnetic at room temperature, but in the presence of a field it acquires a large thermal remanence on cooling below its Néel temperature (~37 K) (Jacobs, 1963; Frederichs et al., 2003). The “zero-field” state in the MPMS is not always truly nulled as some magnetic field can be trapped inside the magnets on zeroing. This is of the order of two to three times the Earth’s field; the more modern version of the MPMS system that I used, has a more sophisticated field zeroing options and can reduce the “zero-field” to < 1% of the Earth’s field. Because the “zero-field” state is non-zero, this can lead to a noticeable increase in remanence at 40 K on the cycling cooling curve and a noticeable drop in remanence between 10 and 40 K on cycling warming curve in samples with a high concentration of siderite, for example, samples s63651, s72392 and s65302 (Figure 5.9a-b and Figure 5.10 a respectively).

In the absence of ZFC and FC experiments, the heating and cooling behaviour of susceptibility seen in samples s63654, s65305, s65308 and s72417 (Figure 5.9c, Figure 5.10b and d and Figure 5.13a) has been attributed to the presence of siderite (Housen et al., 1996). When

heating samples with a high concentration of siderite in argon (e.g. s72392 in Figure 5.9b), the initial susceptibility is very low on heating from room temperature to about 400 °C where the susceptibility increases. A sharp drop is typically noticed around 570 °C, suggesting alteration of siderite to magnetite. On cooling from 700 °C the susceptibility rapidly increases between 570 and 545 °C to values much higher that the susceptibility during heating (at least 50% higher) indicating the continued formation of magnetite. A Hopkinson-like peak on cooling is typically observed (e.g. s63656 in Figure 5.9 d).

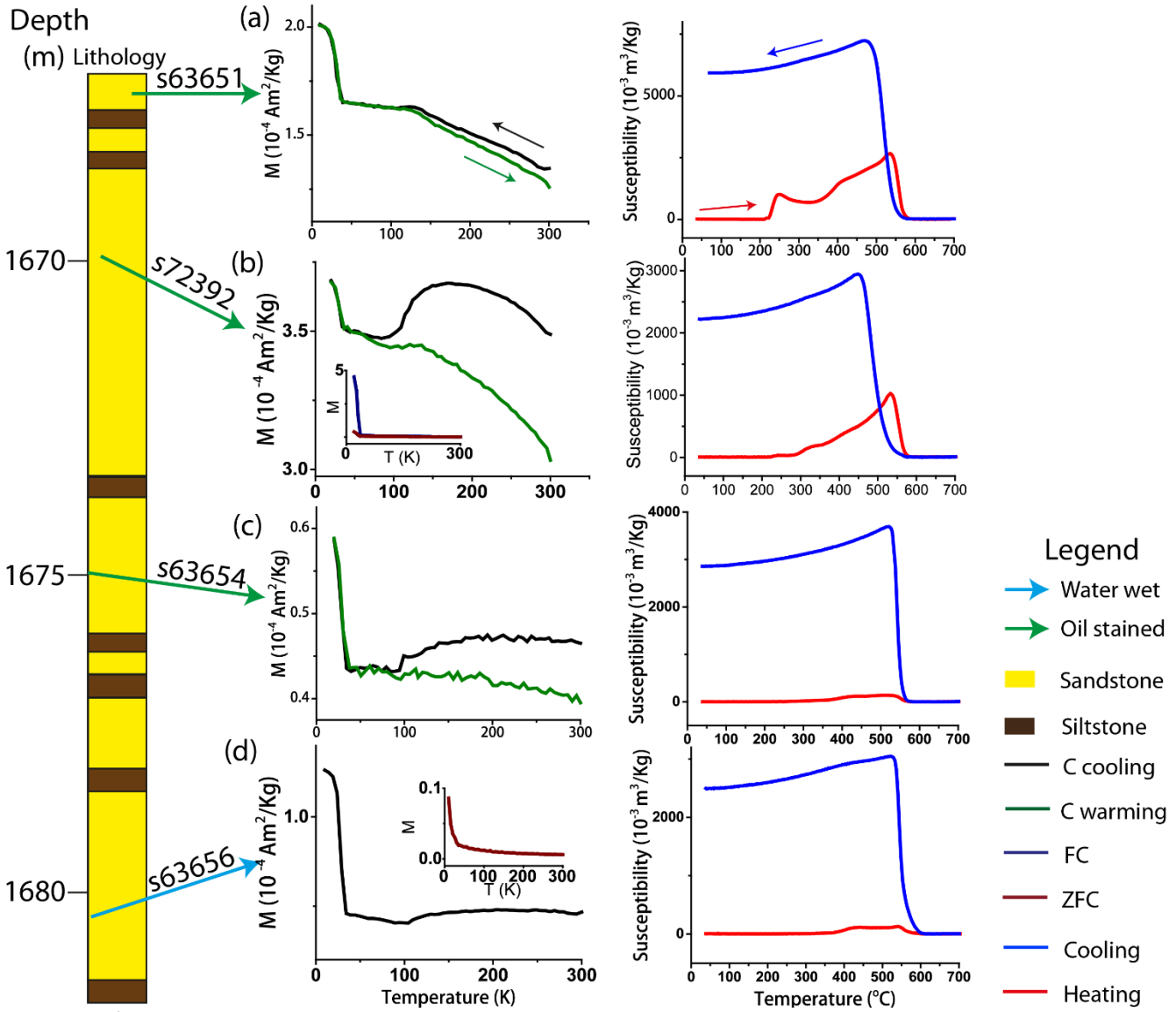


Figure 5.9. Representative samples from well 21/29a-08 showing an abundance of siderite relative to Iron sulphides. a) LT and HT experiments suggests the presence of siderite, magnetite and iron sulphides, b) LT and HT experiments suggests the presence of siderite, magnetite and some iron sulphides, c) LT and HT experiments suggests the presence of siderite and magnetite and d) LT and HT experiments suggests the presence of siderite and magnetite. No FORC diagram available as samples were very weak with high levels of noise with a significant paramagnetic signal. Samples were heated in argon.

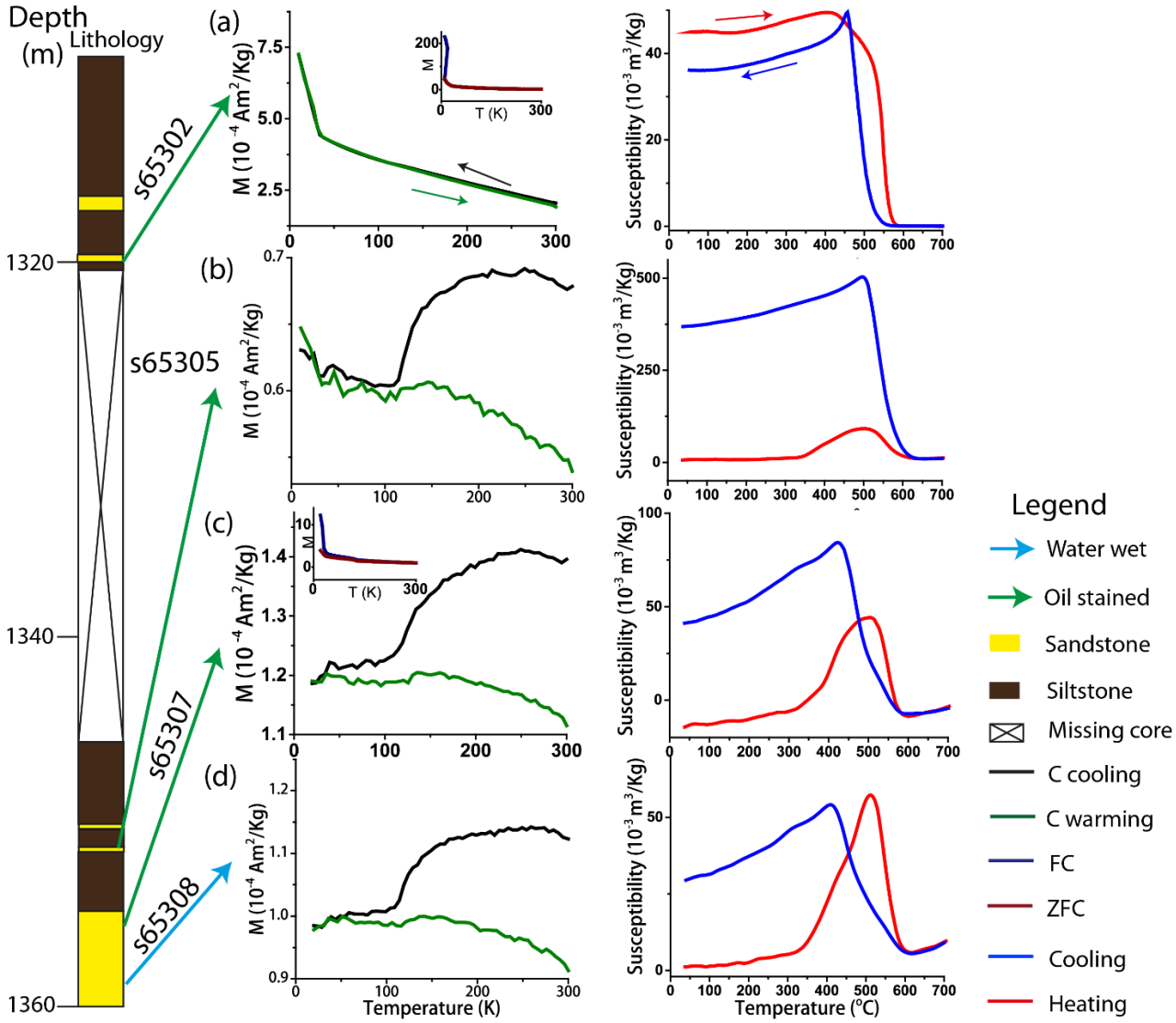


Figure 5.10. Representative samples from well 21/28a-04 showing an almost even mixture of siderite and Iron sulphides with probably more siderite. a) LT and HT experiments suggests the presence of siderite, magnetite and iron sulphides, b) LT and HT experiments suggests the presence of siderite, magnetite and some iron sulphides, c) LT and HT experiments suggests the presence of siderite, magnetite and iron sulphides and d) LT and HT experiments suggests the presence of siderite, magnetite and iron sulphides. No FORC diagram available as samples were very weak with high levels of noise with a significant paramagnetic signal. Samples were heated in argon.

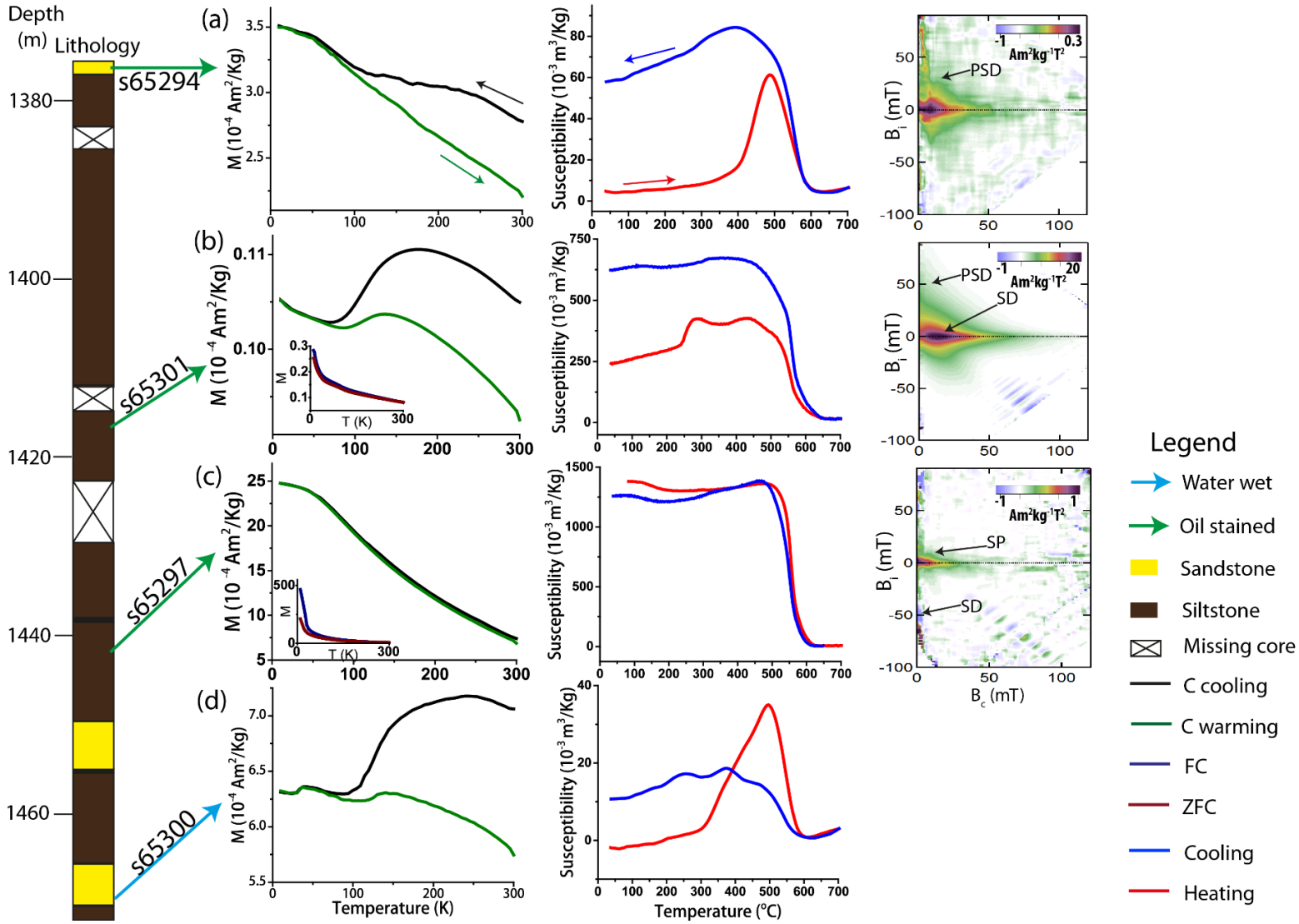


Figure 5.11. Representative samples from well 21/28a-03 showing an almost even mixture of siderite and Iron sulphides with probably more Iron sulphides. a) LT and HT experiments suggests the presence of iron sulphides, some siderite and magnetite. FORC diagram suggest the presence of PSD gains. b) LT and HT experiments suggests the presence maghemite and iron sulphides. FORC diagrams suggests the present of SD grains with vortex structure and multiaxial anisotropy c) LT and HT experiments suggests the presence of siderite, magnetite and iron sulphides. FORC diagram suggest the presence of SP greigite and SD grains d) LT and HT experiments suggests the presence of maghemite and iron sulphides. VARIFORC parameters (Egli, 2013) for smoothing FORCs are $s_{c,0} = 2$, $s_{c,1} = 4$, $s_{b,0} = 3$, $s_{b,1} = 4$ and $\lambda_c = \lambda_b = 0$, measuring time= 200 ms. Samples were heated in argon. PSD= pseudo single domain, SD= Single domain and SP = Superparamagnetic (see Chapter 1).

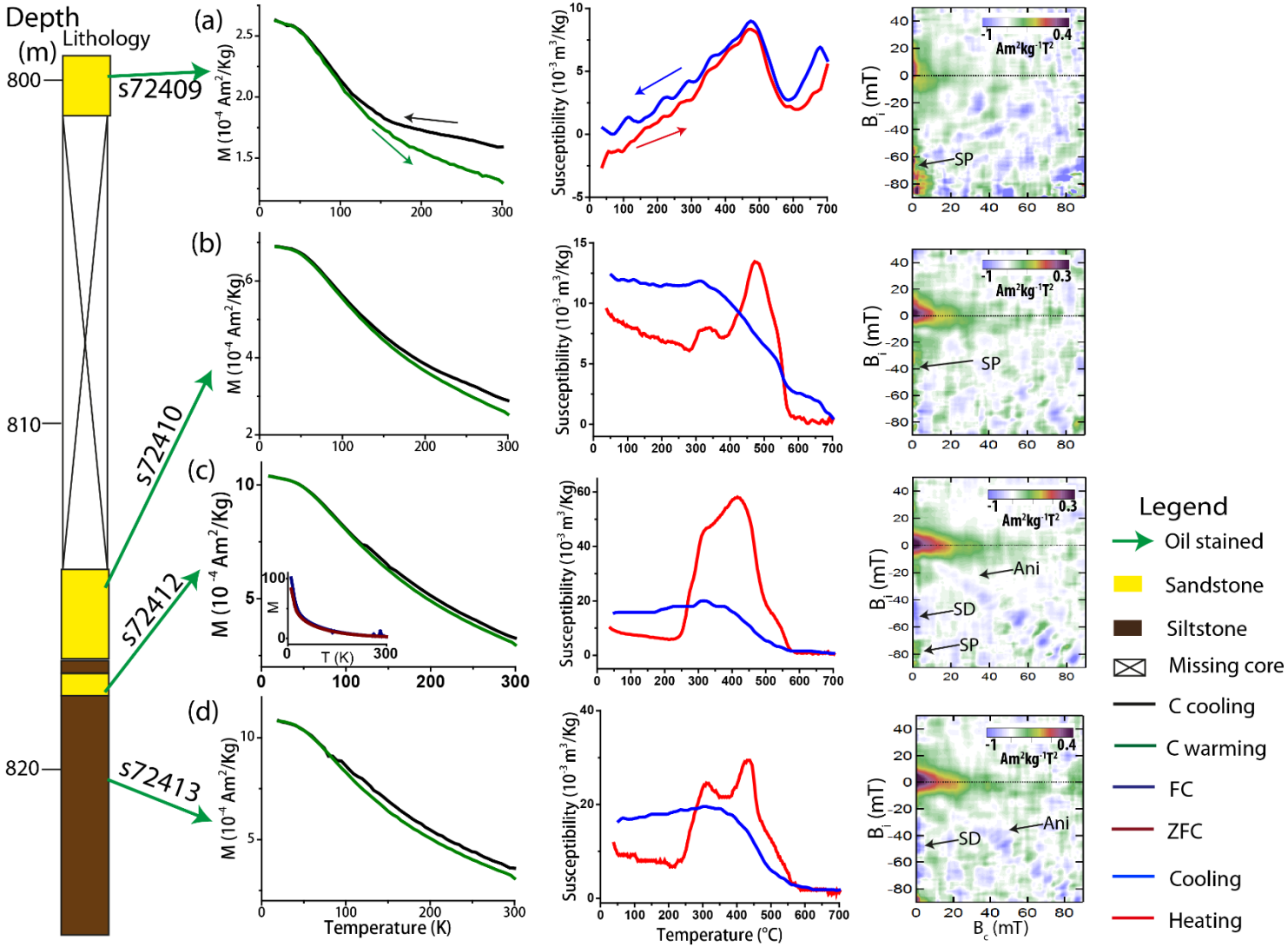


Figure 5.12. Representative samples from well 21/27a-06 showing an abundance of Iron sulphides relative to siderite a) LT and HT experiments suggests the presence of iron sulphides and magnetite. The noisy FORC diagram suggests the presence of SP grains. b) LT and HT experiments suggests the presence magnetite and iron sulphides. FORC diagrams suggests the present of SP grains. c) LT and HT experiments suggests the presence of iron sulphides. FORC diagram suggest the presence of SP greigite and SD grains with vortex structure or multiaxial anisotropy. d) LT and HT experiments suggests the presence iron sulphides. FORC diagram suggest the presence of SP greigite and SD grains with vortex structure or multiaxial anisotropy. VARIFORC parameters (Egli, 2013) for smoothing FORCs are $s_{c,0} = 4$, $s_{c,1} = 4$, $s_{b,0} = 5$, $s_{b,1} = 5$, and $\lambda_c = \lambda_b = 0$,measuring time= 200 ms. Samples were heated in argon for susceptibility measurements. Ani = Multiaxial anisotropy or single vortex structure, SD = Single domain and SP = Superparamagnetic.

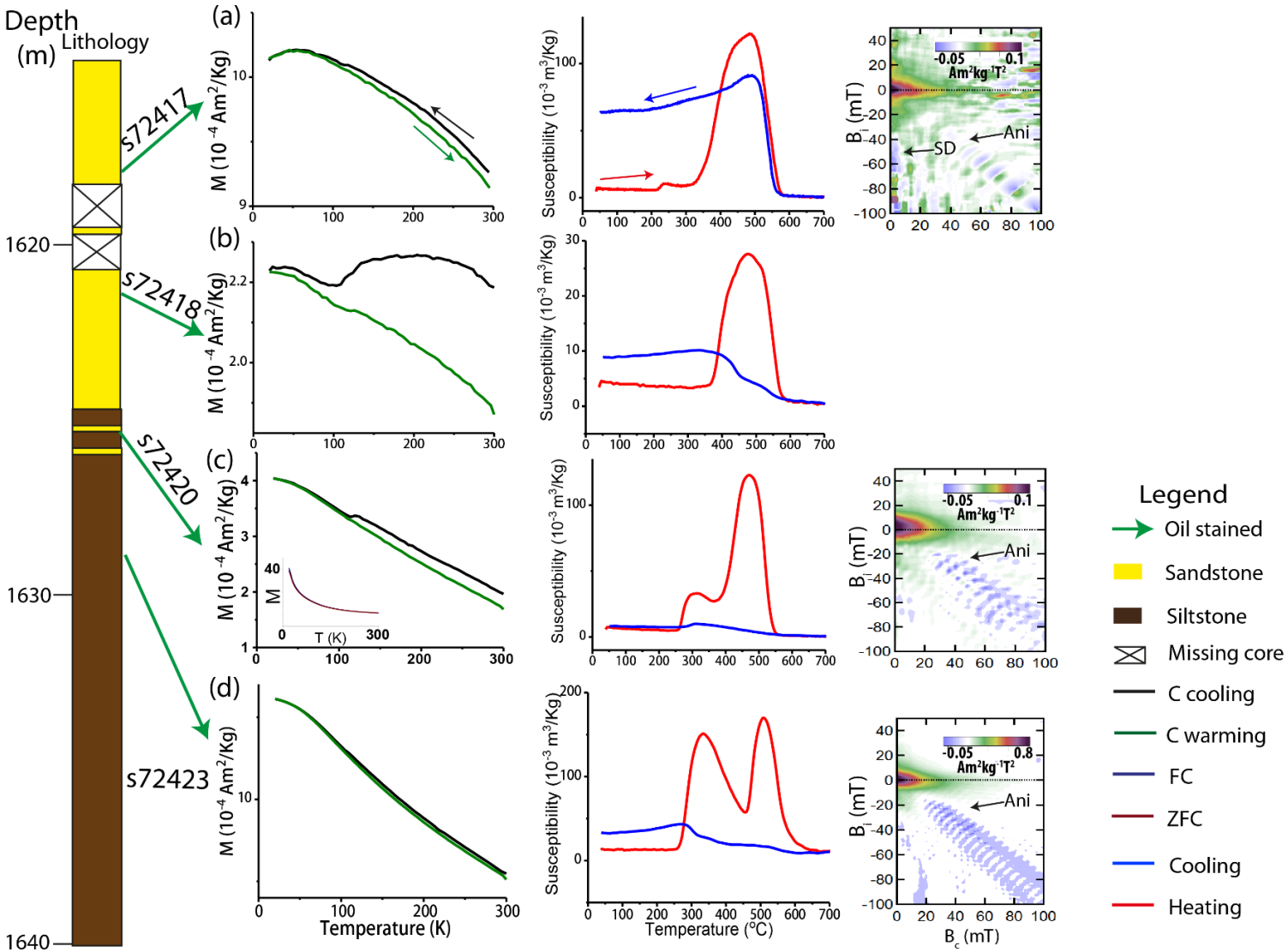


Figure 5.13 Representative samples from well 21/24-03 showing an abundance of Iron sulphides relative to siderite a) LT and HT experiments suggests the presence of iron sulphides and magnetite. The FORC diagram suggests the presence of SP and SD grains. b) LT and HT experiments suggest the presence maghemite and iron sulphides. c) LT and HT experiments suggest the presence of iron sulphides and magnetic. FORC diagram suggests the presence SD grains with vortex structure or multiaxial anisotropy. d) LT and HT experiments suggest the presence iron sulphides. FORC diagram suggests the presence of SP greigite and SD grains with vortex structure or multiaxial anisotropy. VARIFORC parameters (Egli, 2013) for smoothing FORCs are $s_{c,0} = 2$, $s_{c,1} = 3$, $s_{b,0} = 3$, $s_{b,1} = 3$, and $\lambda_c = \lambda_b = 0.1$, , measuring time= 200 ms. Samples were heated in argon for susceptibility measurements. Ani = Multiaxial anisotropy or single vortex structure, SD = Single domain.

The increase in remanence on cooling in samples s63651, s65302, s65294, s65297 (Figure 5.9 a, Figure 5.10 a, Figure 5.11 a & c respectively) suggests the presence of goethite or titanohematite (Rochette and Fillion, 1989; Sprain et al., 2016). A goethite test (Guyodo et al., 2006) was carried out to confirm the presence of goethite; the test implemented was as follows:

- Samples were heated from RT to 400 K in the MPMS in zero field.
- At 400 K a field of 5T was applied and the sample cooled to RT. This induces a thermoremanence in goethite (Banerjee, 1970).
- The samples were then removed from the MPMS and AF (alternating field) demagnetised with a peak field of 200 mT. This eliminated the contribution of low coercivity minerals like magnetite *etc.* (Dunlop and Özdemir, 1997).
- The sample was placed in the MPMS and the remanent magnetisation measured as the sample was cooled from RT to 20 K in zero field; this process was labelled thermoremanent magnetization LT demagnetisation (TRM LTD).
- The behaviour of remaining remanent magnetisation was measured as the sample was heated to 400 K in zero field. This is labelled “re-warming curve”. All the remanence carried by goethite should be lost at its Néel temperature of about 400 K (Banerjee, 1970).
- Subsequently the remanent magnetisation was measured as the sample was cooled to 20 K in zero field, this is labelled LT demagnetisation (LTD). This should show no remanence in the absence of other high-coercivity phases.

Goethite tests were carried out on an oil stained sample (s72399) from well 21/25-A1 and a water wet sample (s63605) from well 21/25-04 (Figure 5.14). The drop in remanence at RT suggests some of the remanence is carried by goethite, but the continued increase in remanence on cooling (LTD curve in Figure 5.14 a and b) suggests titanohematite is also present (Sprain et al., 2016). S72399 (Figure 5.14 a) has a 29 % drop in remanence (M goethite) at RT while s63605 (Figure 5.14 b) has a 18 % drop in remanence at RT, which is proportional to the amount of goethite in the sample (Guyodo et al., 2006).

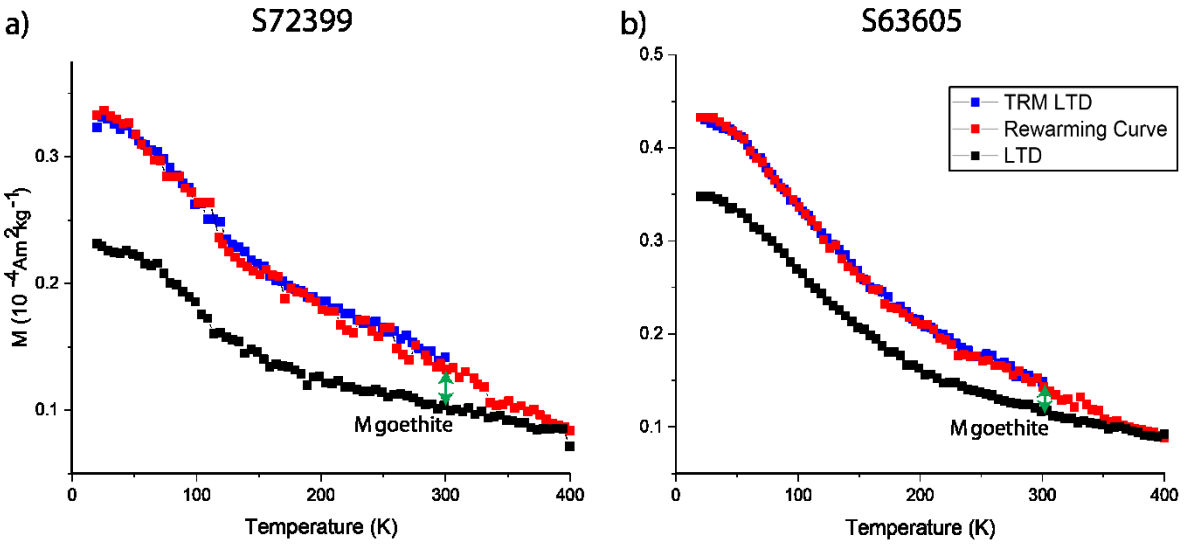


Figure 5.14. A goethite test on samples a) s72399 from well 21/25-A1 and b) s63605 from well 21/25-04. The drop-in remanence at 300 K suggests some of the remanence in the sample is carried by goethite. M goethite is the percentage drop in remanence at room temperature.

No Besnus transition was observed in any of the samples analysed; this suggests there is no monoclinic pyrrhotite in any of the samples, but other iron sulphides such as pyrite, hexagonal pyrrhotite and greigite maybe present (Rochette et al., 1990; Dekkers et al., 2000; Chang et al., 2009; Horng, 2018; Horng and Roberts, 2018a). The absence of a lambda transition in any of the HT-susceptibility experiments suggests lack of hexagonal pyrrhotite also (Dunlop and Özdemir, 1997). Pyrite was identified in some sample's HT-susceptibility behaviour (Figure 5.15a). On heating the samples, the susceptibility is very low from room temperature until about 400°C where the susceptibility rapidly increases, and a sharp drop is noticed around 570 °C suggesting alteration of pyrite to magnetite; on cooling from 700 °C the susceptibility rapidly increases between 350 °C to values much higher that the susceptibility during heating indicating the formation of new pyrrhotite phases. Similar behaviour to this was observed when natural pyrite obtained from Imperial College's mineral repository was heated (Figure 5.15b).

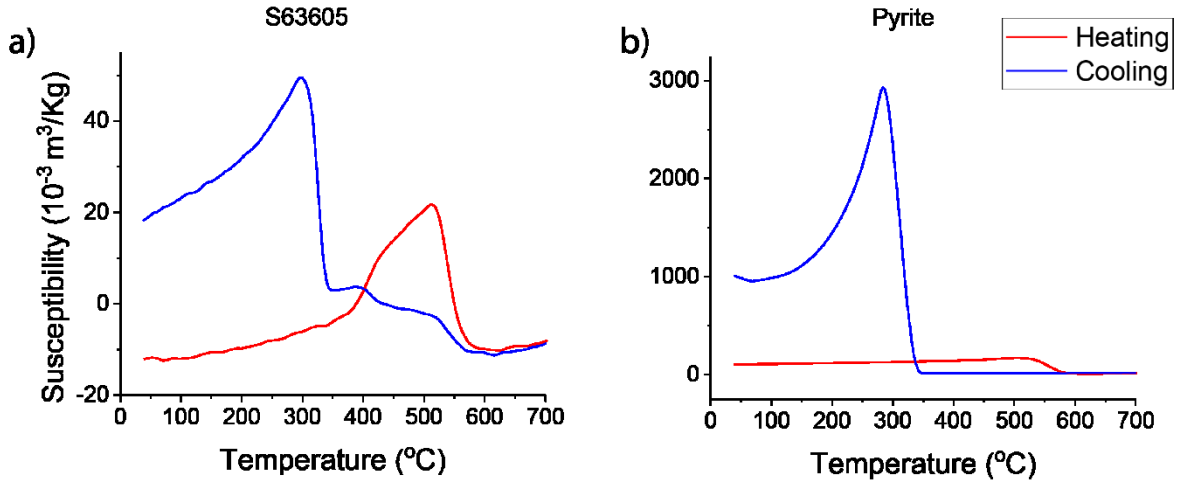


Figure 5.15. HT-susceptibility heating and cooling in argon for a) s63605 from well 21/25-04 in CNS, and b) natural pyrite from Imperial College mineral repository

Greigite can be identified during heating by its thermal decomposition between 200 400 °C (Chang et al., 2008; Bol'shakov and Dolotov, 2011). Different greigite samples typically portray different HT-susceptibility heating and cooling behaviours. Some of the behaviours observed in literature are described below:

- A noticeable drop in susceptibility on heating in the range 350 – 450 °C, e.g. s63651, s65310, s72413 and s72423 (Figure 5.9a, Figure 5.11b, Figure 5.12d and Figure 5.13d respectively) (Bol'shakov and Dolotov, 2011; Roberts et al., 2011).
- Kinks in susceptibility on heating accompanied by a noticeable increase in susceptibility 250- 450 °C e.g. s72412 and s72417 (Figure 5.12c and Figure 5.13d respectively) (Reynolds et al., 1994; Dekkers et al., 2000).
- Increase in susceptibility on heating between 350 and 450 °C accompanied by a lower susceptibility on cooling until the temperature of the noticeable increase in susceptibility on heating e.g. s65300, s72412 and s72418 (Figure 5.11d, Figure 5.12c and Figure 5.13b respectively). This relationship is also noticed in thermomagnetic curves for magnetic extracts from s65311 (Figure 5.16c, its high-temperature susceptibility data suggests the presence greigite as shown in Figure 5.16a)

The last HT susceptibility heating and cooling behaviour has not been attributed to greigite in previous literature. To test this, thermomagnetic curves were measure for magnetic extracts of samples s65311 and s65328 (Figure 5.16 a-b). The resulting thermomagnetic heating and

cooling behaviours (Figure 5.16 c-d) have been observed in natural and synthetic greigite samples (Dekkers et al., 2000; Roberts et al., 2011).

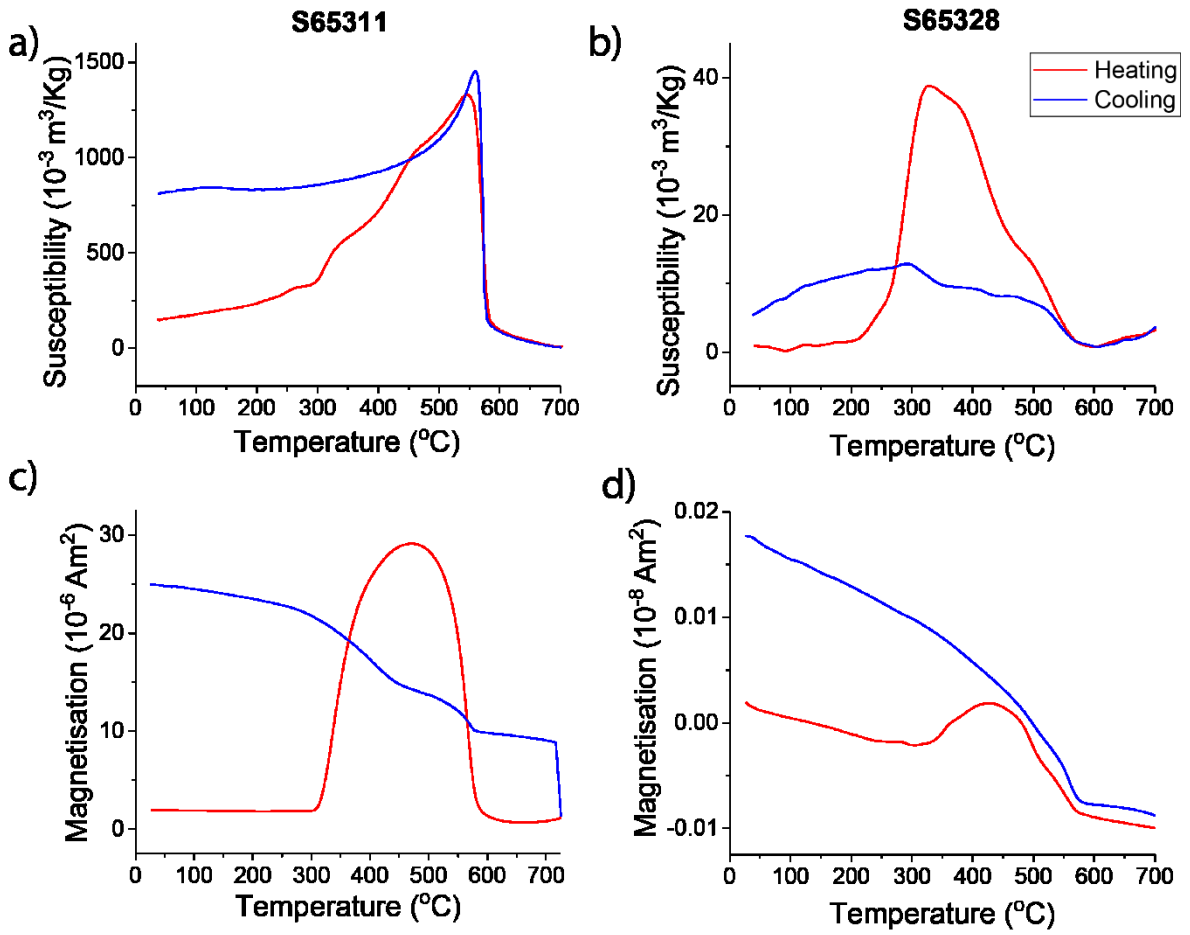


Figure 5.16. (a-b) HT susceptibility curves with heating in argon, compared with thermomagnetic curves heated in vacuum at 100 mT (c-d) for sample s65311 from well21/28a-08 and S65328 for well 21/27-04. Both samples are oiled stained sandstone. Note the increase in magnetisation at 720 °C on cooling in s65311 (c) is due to the MPMS delaying to cool down the sample after the maximum temperature was reached. All curves suggest the presence of greigite.

To confirm the presence of greigite SEM imaging (Figure 5.17) was carried out on extracted and non-extracted samples suspected to contain greigite. SEM Images of monoclinic pyrrhotite appear needle like, hexagonal pyrrhotite crystals have a hexagonal structure, greigite is typically cubic and pyrite crystals can either be cubic or euhedral (Horng and Roberts, 2006; Roberts, 2015). No crystal structure akin to monoclinic or hexagonal pyrrhotite was observed in the SEM images. This does not rule out their presence as the SEM images only represent a small sample volume. EDX analysis of the crystals in Figure 5.17a-c, identified iron and sulphur grains, which are likely (the EDX was not calibrated for this) 40 nm to 170nm greigite or pyrite grains (Figure 5.17a). Figure 5.17b shows two fused euhedral pyrite framboids with a mixture of 500 nm to 1.5 µm sized pyrite grains. These framboids are likely

formed after the pyritization of greigite framboids (Wilkin and Barnes, 1997; Hunger and Benning, 2007) (Figure 5.17b). The framboids also appear to be flanked by smaller (< 100 nm) greigite grains (Figure 5.17b). The elongated framboid shown in Figure 5.17c is made up of 30 – 100 nm sized greigite particles. The SEM imaging also showed evidence for microbial activity in s65311 and s65328 (Figure 5.17d-e).

FORC diagrams for most of the samples suggest the presence of thermally relaxing SD particles (Roberts et al., 2006; Chang et al., 2009; Roberts et al., 2018b) as shown in s65297, s72410, s72412 and s72413 (Figure 5.11c and Figure 5.12b-d). The presence of SD grains was identified by a peaked FORC distribution on the $B_i = 0$ axis or areas of negative values adjacent to the vertical axis (Roberts et al., 2000; Lascu et al., 2015) as shown in s65301, s72412, s72413, s72417 and s72420 (Figure 5.11b, Figure 5.12c-d, Figure 5.13a and c). Samples with multiaxial anisotropy were identified by the steeply dipping negative region to the right of the B_u axis (Harrison and Lascu, 2014; Valdez-Grijalva and Muxworthy, 2019) as seen in s65301, s72412, s72420 and s72423 (Figure 5.11b, Figure 5.12c, Figure 5.13c and d). This feature may also be due to SD vortex behaviour (Lascu et al., 2018; Valdez-Grijalva et al., 2018a). FORC diagrams for some samples have contours that diverge away from the origin, which suggest the presence of PSD grains (Roberts et al., 2000; Roberts et al., 2017) as seen in s65294 and s72417 (Figure 5.11a and Figure 5.13a).

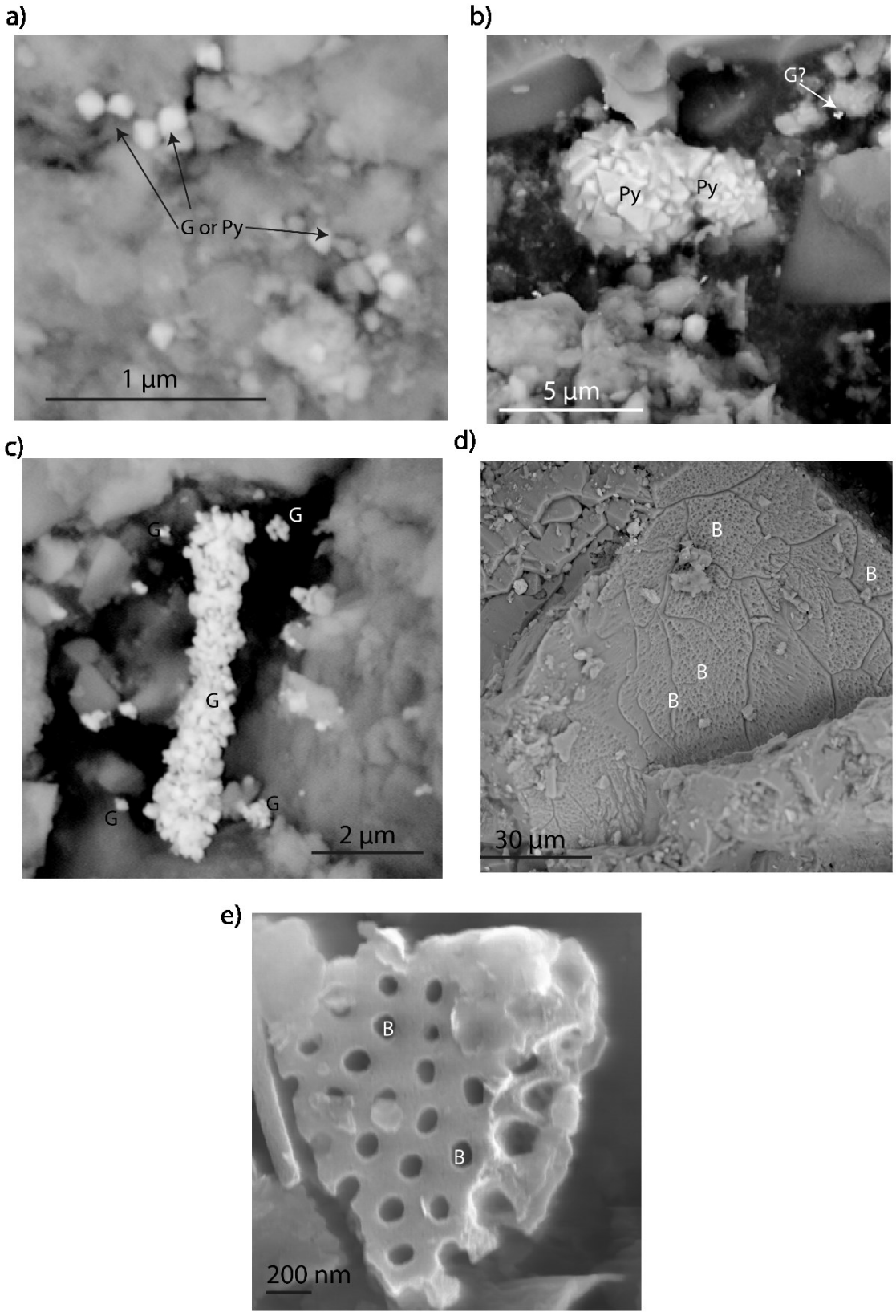


Figure 5.17. SEM Images showing a) Greigite (G) or pyrite (Py) crystals in s65329 b) Two fused coarse-grained euhedral pyrite framboids surrounded by possibly smaller cubic greigite crystals in s65328 c) likely elongated greigite framboid in s65311 d) evidence of bioturbation in s63594 highlighted with a "B", and e) evidence for bioturbation in s65328, also highlighted with a "B". Images a-c are backscattered electron images obtained with a Phenom SEM while images d-e are backscattered electron images obtained with a Leo SEM.

5.3.2.2 Background Sample Behaviour

Extracted aliphatic fractions from water-wet samples s70402, s70403 and s70404 were analysed in the GC-MS for compound identification. Oil-stained sandstones from reservoirs charged by type II source rocks in the UK can have aliphatic contents ranging from 39-48% (Barnard and Bastow, 1991; Emmerton, 2013). The flat response of the aliphatic mass chromatograph and the lack of lack of biomarkers (Figure 5.18) suggests there is no evidence of oil in the samples (Tyson, 2006). These results suggest the rock magnetic experiments carried out on the dry core sample represent a true background sample.

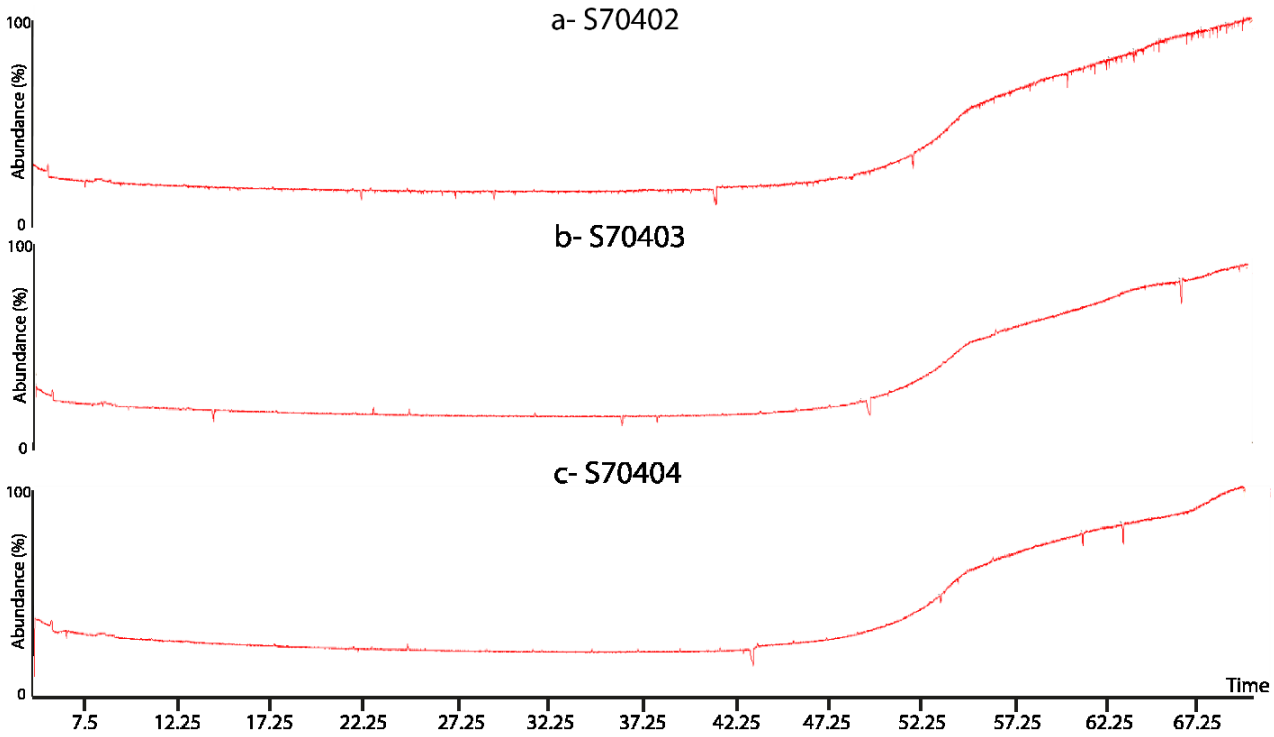


Figure 5.18. Mass chromatograph of aliphatic hydrocarbon fractions in samples from dry well core 21/28b-07 a) s70402, b) s70403, c) s70404.

Mean M_s, M_{rs}, H_c and susceptibility values for well 21/28b-07 are shown in Table 5.1. The M_s, M_{rs}, and susceptibility values are typically lower than the values measured in the oil well samples (Table 5.1, Figure 5.5, Figure 5.6 and Figure 5.7). LT and HT magnetic experiments were carried out on core samples to identify the magnetic minerals present in the sandstones prior to impregnation with oil. The results are shown in Figure 5.19. The heating and cooling susceptibility behaviour of s70402 and s70403 (Figure 5.19a-b) is likely due to the presence of magnetite rich samples and is supported by the LT cycling warming and cooling curves (Verwey, 1939). The spread on the vertical axis in the FORC diagram for s70402 (Figure 5.19a)

suggests some of the magnetite grains are MD (Roberts et al., 2000). The heating and cooling susceptibility in behaviour s70404 (Figure 5.19c) is similar to that of s72392 and s63654 (Figure 5.9b and c) suggesting a siderite rich sample. An increase in remanence on cooling in all the samples (Figure 5.19) suggests the presence of goethite or titanohematite (Rochette and Fillion, 1989; Guyodo et al., 2006; Sprain et al., 2016).

A low-temperature transition was observed at ~ 100 K for s70402 and s70403 (Figure 5.19a-b) this type of behaviour has been noticed in samples that contained biogenic extracellular magnetite (BM) (Chang et al., 2016). This is partly supported by the FORC diagram for s70403 (Figure 5.19b) which has a narrow positive distribution extending from B_c= 0-80 mT axis, this type of FORC distribution has been observed in SP biogenic magnetite (Roberts et al., 2012; Heslop et al., 2014; Chang et al., 2016). A subtle drop in remanence at around 40 K (LT experiment in Figure 5.19b) may be caused by the presence of monoclinic pyrrhotite (BT), which could also give rise to the FORC distribution observed (FORC diagram in Figure 5.19b) (Rochette et al., 1990; Roberts et al., 2000). There was no evidence for the presence of greigite in any of the dry-well samples. The dry-well cuttings were not considered as they were contaminated by drilling mud; heating such mud leads to the precipitation of iron sulphides and iron oxides (Cairanne et al., 2004; Aubourg and Pozzi, 2010).

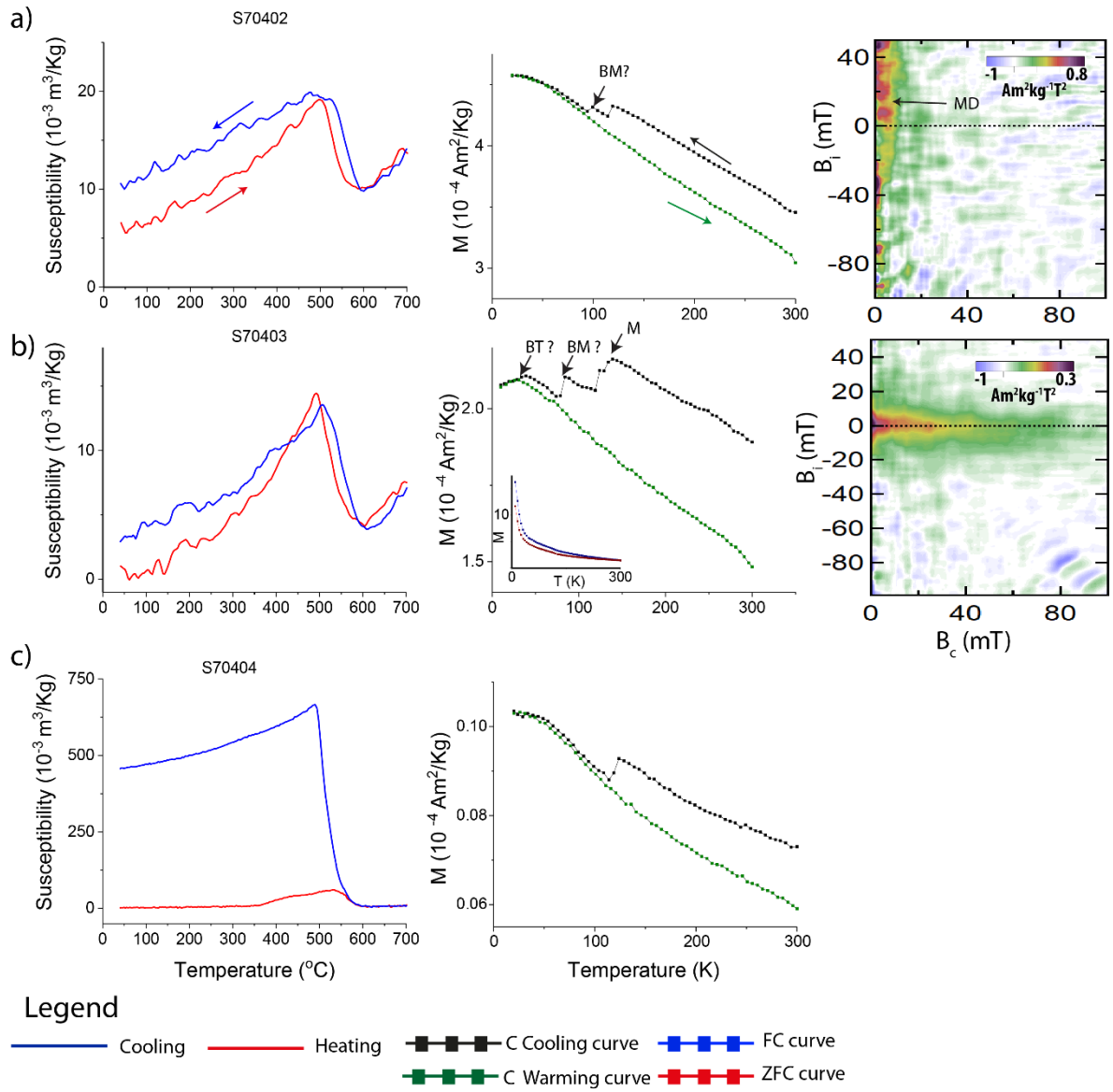


Figure 5.19. Samples from dry well 21/28b-07 a) s70402- LT and HT experiments suggests the presence of magnetite with a MD grain size b) s70403- LT experiments suggest the presence of magnetite and possibly monoclinic pyrrhotite and biogenic magnetite. The FORC diagram suggests the presence of a high H_c phase and c) s70404- LT and HT experiments suggest the presence of magnetite and siderite. VARIFORC parameters (Egli, 2013) for smoothing FORCs are $s_{c,0} = 3$, $s_{c,1} = 3$, $s_{b,0} = 4$, $s_{b,1} = 3$ and $\lambda_c = \lambda_b = 0.1$, measuring time= 200 ms. HT susceptibility measurements were heated in argon. BT - Besnus transition, BM - biogenic magnetite and M - magnetite, and MD – Multidomain.

5.4 Discussion

Rock magnetic experiments were carried out to identify differences between the various sample types (oil-stained sandstone, water wet sandstone, sandstone in the gas cap and siltstones) and differences along the hydrocarbon migration pathway. Measured M_s and M_{rs} (Figure 5.5) were similar for the different sample types within a well and showed no noticeable variation along the migration pathway. H_c values (Table 5.1 and Figure 5.6) appear to be relatively higher in wells charged laterally compared to the measured values in wells charged vertically. The measured susceptibility appears to be relatively higher in siltstone samples.

HT and LT experiments identified the presence of magnetite, maghemite, titanohematite, goethite, siderite, pyrite and greigite in the samples from oil wells. Magnetite, titanohematite, goethite, siderite and monoclinic pyrrhotite were observed in the dry well samples. Importantly, an increasing abundance of iron sulphides was noticed along the lateral hydrocarbon migration path (east to west).

5.4.1 Variations in coercivity and susceptibility along the migration pathway

The coercivity of the core samples in wells that were charged vertically are < 15 mT, e.g., wells 21/25-04 and 21/25-A1 (Figure 5.6a-b). Previous studies have attributed these low coercivity magnetic phases in hydrocarbon reducing environments to the presence of authigenic magnetite (Costanzo-Alvarez et al., 2000; Guzmán et al., 2011). These magnetite particles are very fined grained as most of the samples in wells 21/25-04 and 21/25-A1 have χ_{FD}> 10 % (Figure 5.8 a-b). Relatively higher H_c observed in wells charged laterally; wells 21/29a-06, 21/28a-04, 21/28a-08 and 21/27-04 (Figure 5.6 c-g) are likely due to the increased abundance of iron sulphides (predominantly greigite). The χ_{FD} also suggests these greigite grains are very fine (Figure 5.8 c-g). This is also supported by the SP greigite signature noticed in the FORC diagrams of core samples from well charged laterally e.g. s72412, s72413 (Figure 5.5 c-d).

Susceptibility of the siltstone samples appears to be generally higher than the other sample types as seen in wells 21/29a-06, 21/28a-04 and 21/27-04 (Figure 5.7 c, e and g). This is likely caused by the presence of relatively bigger grains in the siltstone samples as they generally

have FDF less than 15% (Figure 5.8). It is unclear whether the bigger grains are detrital or authigenic. The susceptibility of the siltstones generally increases along the migration pathway (Figure 5.7). It is possible that the reducing conditions generated by the hydrocarbons along with varying diagenetic conditions along the migration pathway (e.g. temperature and pressure) could result in an increase in the susceptibility of the siltstones (Machel and Burton, 1991a;1991b; Burton et al., 1993; Guzmán et al., 2011). This increase could also represent an increase in the abundance of bigger grained detrital magnetic minerals along the migration pathway (Liu et al., 2006). No such correlation is noticed when the oil-stained sandstones and the water wet sandstones are analysed (Figure 5.20). Their susceptibility values are generally lower than 10^{-3} m^3kg^{-1}.

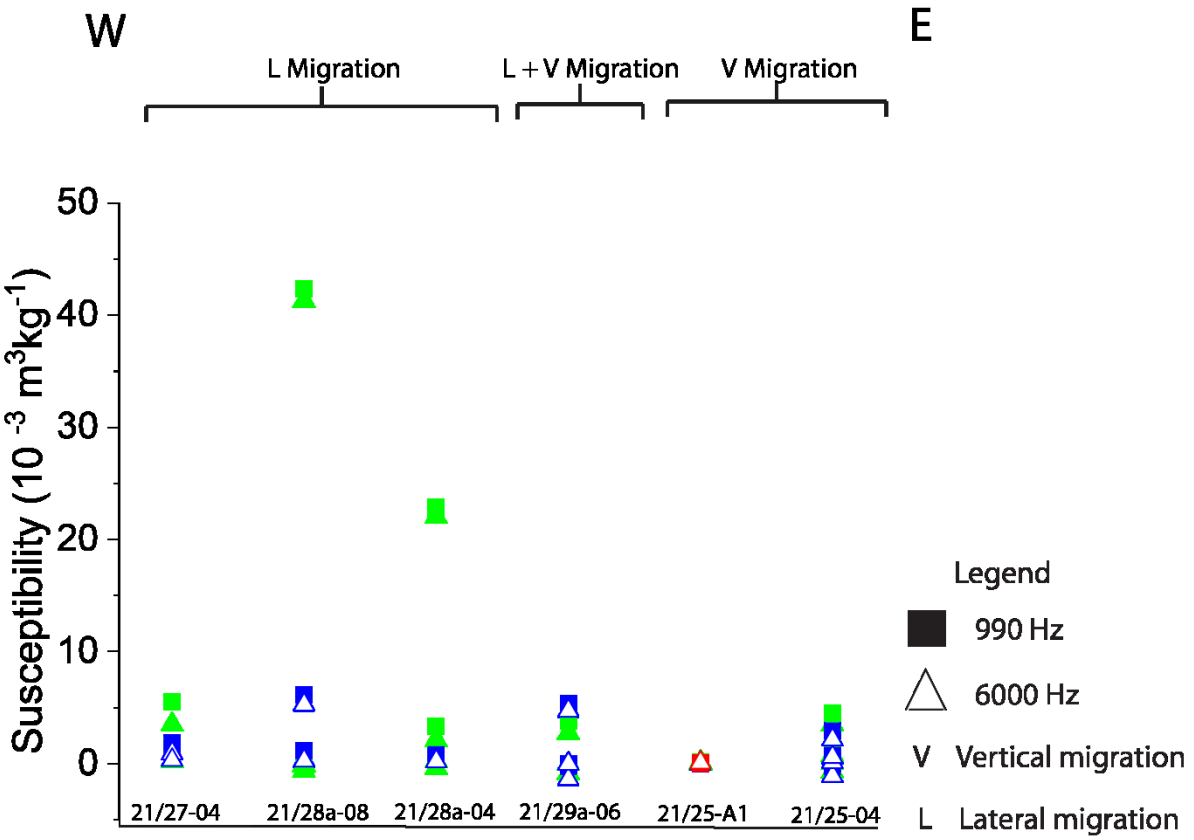


Figure 5.20. Plot comparing the susceptibility values measured at 990 and 6000 Hz in oil stained sandstones (green), water wet sandstones (blue), and sandstones in the gas cap (red) Wells are arranged from east to west with predominantly vertical migration in the east and lateral migration in the west. Note: high susceptibility values observed at the hydrocarbon contacts are not shown in the plot.

5.4.2 Origin of Background and Source Signal

5.4.2.1 Origin of Titanohematite and Goethite

All the background samples obtained from the dry well core (Figure 5.19) along with some samples from the oil well (e.g. s63651, s65302, s65297, s72410 and s724200; Figure 5.9a, Figure 5.10a, Figure 5.11c, Figure 5.12b and Figure 5.13c) showed an increase in remanence on cooling. The goethite test carried out on some of the samples (Figure 5.14) suggests the increase in remanence on cooling is caused by the presence of titanohematite and goethite. These two minerals have never been observed in studies carried out on samples from or near hydrocarbon wells, so they have been classed as background magnetic signal, i.e., not due to the reducing environment caused by hydrocarbons.

Detrital titanohematite is most likely derived from the mechanical weathering of the parent rock (Marshall and Cox, 1972). Goethite in the samples can either be detrital or authigenic. Detrital goethite can be derived from the weathering of primary iron-bearing minerals (Dunlop and Özdemir, 1997). As the core samples are stored in air, oxidation of the iron sulphides present in the samples can lead to the precipitation of authigenic goethite (Rochette and Fillion, 1989; Mycroft et al., 1995).

5.4.2.2 Origin of Magnetite and Maghemite

Magnetite was present in almost all the oil well and dry well core samples (Figure 5.9, Figure 5.10, Figure 5.11, Figure 5.12 and Figure 5.19). Biogenic magnetite was only observed in the dry well core samples s70402 and s70403 (Figure 5.19a-b), suggesting microbial activity in the east end of the section. The occurrence of magnetite in the dry-well core samples suggest it is detrital, but it can also be authigenic as studies have shown it to be precipitated in the reducing conditions generated by hydrocarbons (Benthien and Elmore, 1987; Elmore et al., 1987; Elmore and Crawford, 1990; Machel and Burton, 1991a;1991b; Burton et al., 1993; Machel, 1995; Emmerton et al., 2012). FORC diagrams suggests the detrital magnetite are larger MD grains, e.g., s70402 (Figure 5.19), while the authigenic magnetite grains are most likely thermally relaxing SD grains (s72409; Figure 5.12 a). Similar characterisations have been made in other studies (Elmore et al., 1993a; Liu et al., 2006). Maghemite seen in samples s72392, s65305, s65307 and s65300 (Figure 5.9b, Figure 5.10b-c and Figure 5.11d

respectively) is most likely a product of the oxidation of detrital or authigenic magnetite (Özdemir and Dunlop, 2010).

5.4.2.3 Origin of Siderite

In common with magnetite, siderite was observed in the oil-well core samples (e.g. S72392, s65302, s65307 and s65297; Figure 5.9 a, Figure 5.10 a-b and Figure 5.11 c respectively) and in one dry well core sample (s70404; Figure 5.19 c). Siderite is typically of authigenic origin in a sedimentary setting and is often found as a diagenetic cementing agent (Ellwood et al., 1986; Ellwood et al., 1988; Frederichs et al., 2003). Diagenetic changes in temperature or increase in total inorganic carbon or bacteria reduction of Fe^{2+} can lead to the precipitation of siderite in the dry wells (Ellwood et al., 1988; Machel and Burton, 1991b). The reducing environment generated by hydrocarbon also likely promotes the replacement of hematite and magnetite by siderite in the oil wells (Machel and Burton, 1991a; Machel, 1995; Liu et al., 2006; Emmerton et al., 2012).

5.4.2.4 Origin of Greigite

Greigite was only identified in the oil wells as seen in samples s63651, s65310, s72413 and s72423 (Figure 5.9a, Figure 5.11b, Figure 5.12d and Figure 5.13d respectively). This is not a surprise as studies by Reynolds et al. (1990) and Mena and Walther (2012) have linked the presence of iron sulphides to the migration of hydrocarbons. Reasons for possible precipitation of greigite in the oil wells are described below:

- Abubakar et al. (2015) demonstrated that source rocks in the oil kitchen can precipitate SP and stable SD greigite (< 100 nm). Greigite can form complexes within the oil and such particles are small enough to pass through the pore throat of the shales, chalk and sandstones (Mallon and Swarbrick, 2008a; Nealson, 2009).
- Diagenetic changes, e.g., increase in total sulphur, caused by hydrocarbon in the reservoir could lead to the precipitation of greigite or the replacement of magnetite, hematite or siderite by greigite (Burton et al., 1993; Machel, 1995; Emmerton et al., 2012).
- Anaerobic biodegradation by sulphate reducing bacteria generates reduced sulphur (HS^- and H_2S) which reacts with dissolved Fe^{2+} (from replacement or dissolution of

magnetite or hematite) to form diagenetic greigite (Reynolds et al., 1990; Machel and Burton, 1991a).

Minerals observed in all the samples are grouped into background or source signal in Table 5.2. Source signal is a group relating to minerals precipitated due to the reducing conditions generated by hydrocarbons while the background signal is related to minerals that are not precipitated due to the hydrocarbons.

Table 5.2. Groups of magnetic minerals belong to background and source signals. Background signals are minerals that are likely present prior to the invasion of oil, while the source signal refers to minerals precipitated or introduced after the charging of the well by oil.

Magnetic Mineral	Detrital	Authigenic	Background or source signal
Titanohematite	✓		Background
Goethite	✓	✓	Background
Magnetite	✓	✓	Could be both
Maghemite		✓	Oxidation product of magnetite
Siderite		✓	Could be both
Greigite		✓	Source

5.4.3 Variation of Magnetic Minerals along the Fill Spill Chain

Titanohematite and goethite are clear background samples as they were noticed in all the background samples (Figure 5.19). Siderite and magnetite were also observed in the background samples s70402, s70403 and s70404 (Figure 5.19), but it is thought they can also be precipitated due to the diagenetic conditions created by hydrocarbons (Machel and Burton, 1991b; Burton et al., 1993; Emmerton et al., 2012). Greigite was only observed in oil well samples (Figure 5.9 - Figure 5.13). In the oil wells, there was evidence for the presence in magnetite in all the samples, but the abundance of siderite relative to iron sulphides varied from sample to sample and from well to well. These observations have led me to classify the samples into five types of behaviour:

1. Siderite-rich samples: This class consists of samples were the LT or HT experiments confirm the presence of siderite and no evidence for Iron sulphides are noticed in the HT susceptibility heating and cooling behaviour e.g. s63654, s63656 and s65303 (Figure 5.9c-d and Figure 5.10b).
2. Siderite-rich samples with some iron sulphides: This class consist of samples where the LT experiments confirm the presence of siderite and the HT susceptibility on heating suggests the presence of iron sulphides (predominantly greigite in this case). The susceptibility on cooling also shows a Hopkinson like peak at ~ 570 °C with the susceptibility on cooling much higher than the susceptibility on heating (> 100% increase in susceptibility). This is seen in s63651 and s65307 (Figure 5.9a and Figure 5.10c).
3. Iron-sulphide-rich samples with some siderite: This class consist of samples where the HT susceptibility on heating suggests the presence of iron sulphides (predominantly greigite in this case), but the susceptibility on cooling curve shows a Hopkinson like peak at ~ 570 °C. The susceptibility cooling curve is usually as high as or less than the susceptibility on heating curve which is likely hints at the presence of some siderite in the sample. This is seen in S65308 and s65297 (Figure 5.10d and Figure 5.11c).
4. Iron-sulphide-rich samples: This class consists of samples with HT susceptibility on heating and cooling behaviour like s72410, s72412, s72413, s72418, s72420, s72423 and s63605 (Figure 5.12b-d Figure 5.13b-d and Figure 5.15a).
5. Magnetite-rich sample: This class consists of samples with a nearly reversible HT susceptibility curve e.g. s72409, s70402 and s70403 (Figure 5.12a and Figure 5.19a-b).

To aid visualisation of the data, each well sample is placed in one of the five classes above. The abundant mineral in that well is determined by the majority sample class. For example, Siderite is the abundant mineral in well 21/29a-08 (Figure 5.9), the samples in well 21/28a-04 (Figure 5.10) show an almost even abundance of siderite and iron sulphides with possibly a bit more siderite, whereas the samples in well 21/28a-03 (Figure 5.11) show an almost even abundance of siderite and iron sulphides with possibly a bit more iron sulphides. Greigite is the abundant mineral in wells 21/27a-06 and 21/24-03 (Figure 5.12 and Figure 5.13).

Variations in abundance of siderite and greigite are noticed along the migration pathway and within the different sample types:

- In the oil stained samples (Figure 5.21) siderite is abundant in the east where vertical migration is predominant and becomes less abundant as the abundance of iron sulphides increases to west where the wells are charged laterally.
- In the water wet samples (Figure 5.22) siderite is the most abundant mineral. No obvious change in abundance of mineral was noticed.
- The siltstone samples (Figure 5.23) are similar to the oil stained sandstones and show an increase in the abundance of iron sulphides to the west.
- Figure 5.24 shows the variation in abundance of siderite and iron sulphides in all the samples from well to well which mirrors the variations noticed in the oil stained sandstones. This is not a surprise as most of the samples sampled in a well are the oil stained sandstones (> 75%).

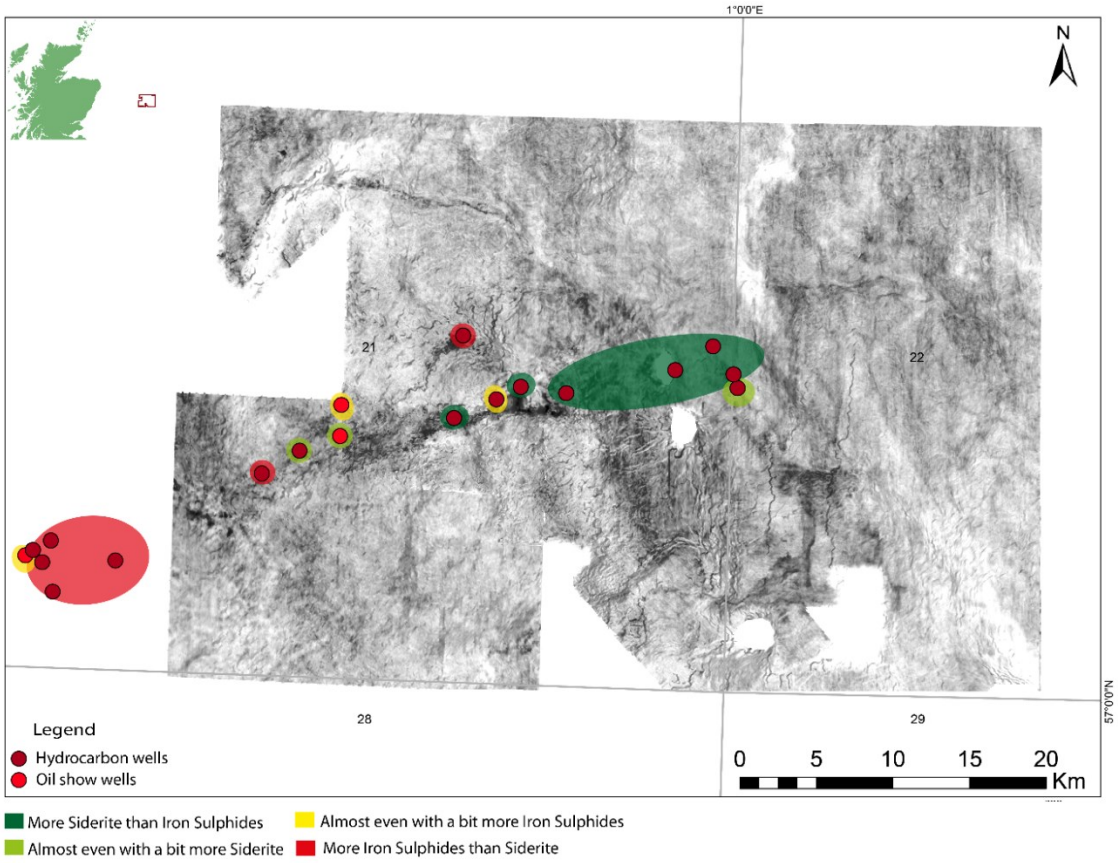


Figure 5.21. Distribution of siderite and iron sulphides (predominantly greigite) in **oil-stained sandstones** in the Tay fan. Areas with predominantly one behaviour are grouped together in coloured ellipses. The abundance of iron sulphides increases along the lateral migration pathway. Background image is RMS amplitude map of Tay Fan. Insert shows the location of the map.

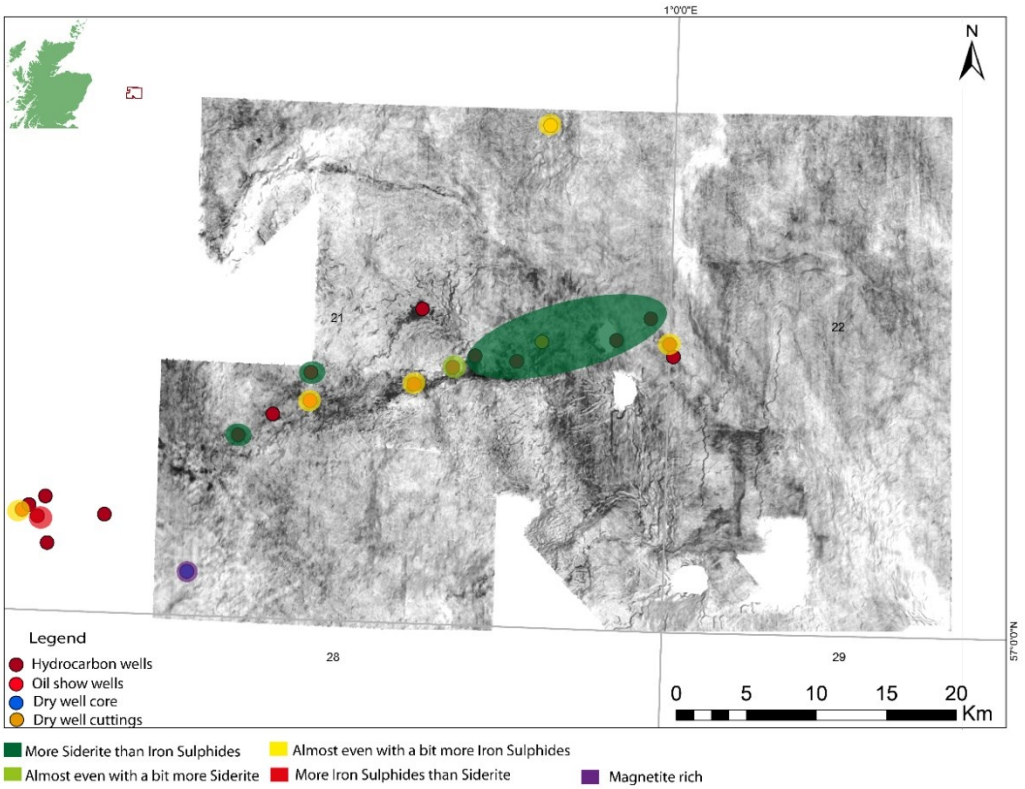


Figure 5.22. Distribution of siderite and iron sulphides (predominantly greigite) in **water-wet sandstones** in the Tay fan. Siderite is the most abundant mineral in the water wet sandstones. Background image is RMS amplitude map of Tay Fan. Insert shows the location of the map.

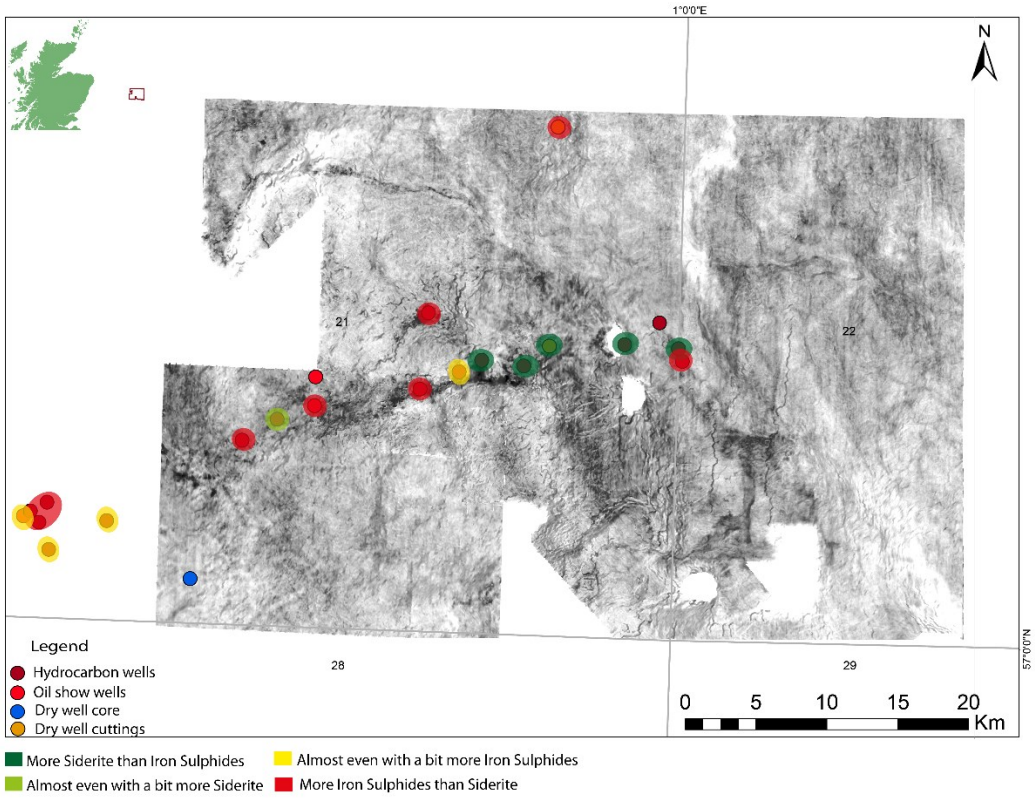


Figure 5.23. Distribution of siderite and iron sulphides (predominantly greigite) in the **siltstones** in the Tay fan. The abundance of iron sulphides increases along the lateral migration pathway and the siltstones are generally iron sulphide rich. Background image is RMS amplitude map of Tay Fan. Insert shows the location of the map.

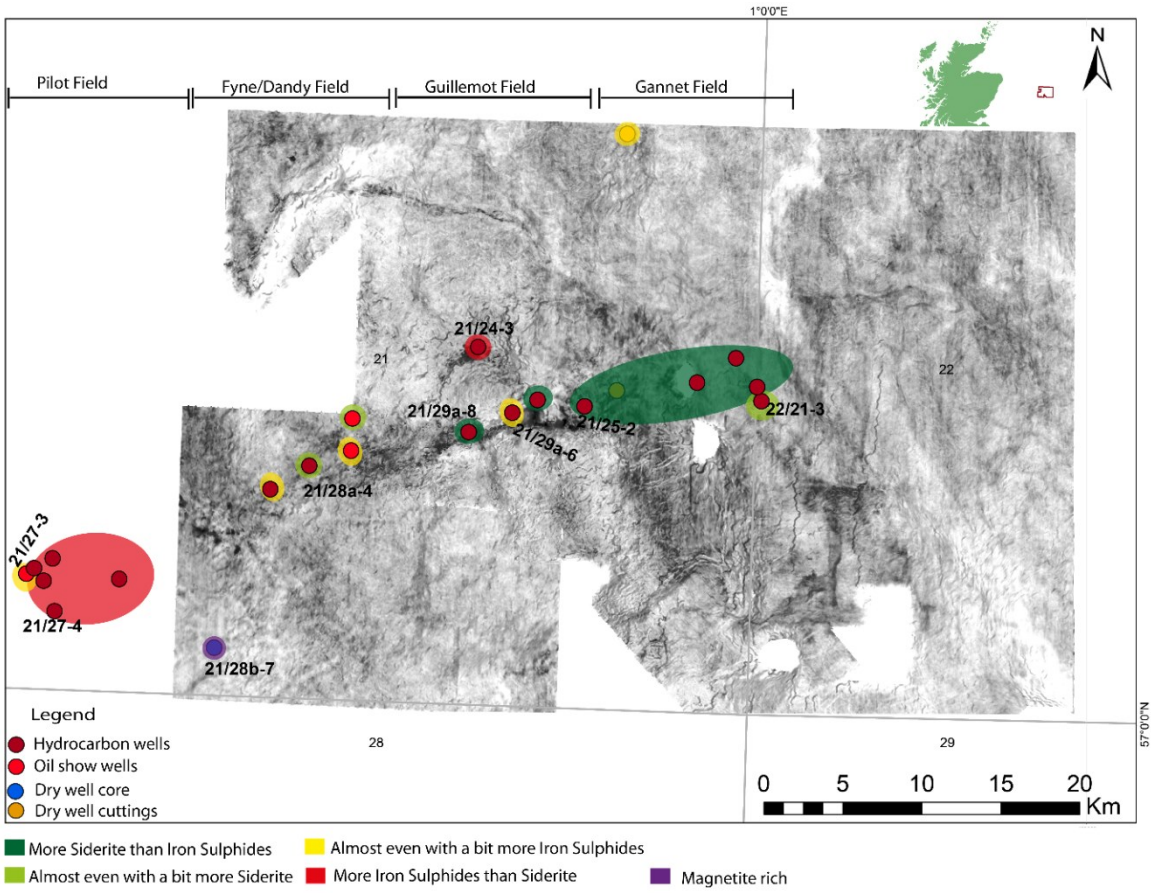


Figure 5.24 Distribution of siderite and iron sulphides (predominantly greigite) in **all the core samples** (average of Figure 5.21 to Figure 5.23) in the Tay fan. The abundance of iron sulphides increases along the lateral migration pathway. Some well names are included are reference. Background image is RMS amplitude map of Tay Fan.Insert shows the location of the map. Note: 21/27-03 is a well with evidence for oil.

Well 21/27-03 shows a mixture of greigite and siderite signals as opposed to the greigite rich signal seen in other wells of the Pilot field (Figure 5.24). This well is classed as an oil show well; it was not deemed productive as most of the oil accumulated has likely leaked to the surface or moved to another trap leaving behind residual oil with some greigite grains.

5.4.4 Limitations to magnetic data interpretation

The magnetic data suggests the increasing presence of iron sulphide (predominantly greigite) from east to west (Figure 5.24). However, in this section I have greatly simplified the magnetic signal. This may have limitations and possible sources of errors in this interpretation are discussed below:

1. Sample size: As the Tertiary sandstones are very friable some wells have missing core sections (e.g. Figure 5.1) while some wells only had a short core section (< 25 m of recovered core a few cases). In addition to that some wells had very thin sandstone

layers interbedded with thicker shales and siltstones (e.g.21/28a-04). This affected a number of samples collected in a few wells (e.g. 21/25-02, 21/27a-04 and 21/27a-06). With a bigger sample size, the interpretation of the dominant mineralogy at some of the wells may change.

2. Magnetic experiments: Some of the techniques used to determine magnetic mineralogy such as SEM and low-temperature experiments only used a very small portion of the sample collected at a depth interval (< 0.2 g). It is possible that the mineralogy observed in the sample portion may not be representative of the magnetic minerals present within the whole depth interval. In some cases, repeat measurements on fresh sample portions were carried to verify the results, because of time and availability of equipment this was not carried out on every sample.
3. Abundance of magnetic minerals in sample: The abundance of magnetic minerals in the samples were very low, this made it difficult to identify the minerals present in the samples. Only a handful of techniques were used to determine mineralogy (FORC diagrams, LT and HT experiments); XRD and Mossbauer Spectroscopy were unsuccessful. If other methods had been successful, the results would have strengthened the argument for the presence of greigite in the sample.

5.5 Conclusions

Rock magnetic measurements were carried out to determine the morphology, mineralogy and size of the magnetic minerals present in samples from oil wells and a dry well sample in the Tay fan of the Central North Sea. The following observations were made:

1. Measured mass-dependent susceptibility, M_s and M_{rs} and H_c were similar for the oil-stained sandstone, water-wet sandstone and sandstone in the gas cap, but the siltstone samples had generally higher mass-dependent values (Figure 5.5, Figure 5.6 and Figure 5.7). The susceptibility, M_s and M_{rs} are generally lower in the dry well samples (Figure 5.19).
2. Calculated χ_{FD} suggested the presence of SP grains in the oil stained sandstone, water wet sandstone, sandstone in the gas cap and relatively bigger grains in the siltstone

(Figure 5.8). This latter observation hints at the presence of detrital minerals in the siltstone.

3. No variation in measured susceptibility, M_s or M_{rs} was observed along the migration pathway (E-W in Figure 5.5 and Figure 5.7) but an increase in H_c was noticed from E-W (Figure 5.6). This suggests the presence of authigenic SP magnetite in the east and SP greigite in the west.
4. HT and LT experiments identified the presence of magnetite, maghemite, titanohematite, goethite, siderite, pyrite and greigite in the samples from oil wells (Figure 5.9, Figure 5.10, Figure 5.11, Figure 5.12 and Figure 5.13) while magnetite, biogenic magnetite, titanohematite, goethite, siderite and possibly monoclinic pyrrhotite were observed in samples from the dry well (Figure 5.19).
5. Titanohematite and goethite were classed as background signals while greigite was classed as a source signal. Magnetite and siderite could be either a background or source signal (Table 5.2).
6. FORC diagrams suggested the presence of SP, SD and PSD grains in the oil well samples (Figure 5.9, Figure 5.10, Figure 5.11, Figure 5.12 and Figure 5.13), while the dry well contained only SP and MD signals (Figure 5.19).
7. Magnetite was present in most samples, but variations in the abundance of siderite and greigite was observed (Figure 5.9, Figure 5.10, Figure 5.11, Figure 5.12 and Figure 5.13).
8. Synthesising the results showed the abundance of siderite in the east and the abundance of greigite in the west with a zone of mixing in the middle (Figure 5.24).

3D petroleum systems modelling of migration into the Tay SM in Chapter 4 (Figure 4.14), suggests vertical migration is prominent in the east (Gannet Field), while a mixture of vertical and lateral migration in the centre (Guillemot Field) and lateral migration to be prominent in the west (Fyne/Dandy to Pilot Field). The change in charging mechanisms from east to the west corresponded to the change in magnetic signal from a siderite rich signal in the east to a greigite rich signal in the west (Figure 5.24). The reasons for the correlation between the magnetic signal and the charging mechanism is addressed in Chapter 6.

Chapter 6

Is there a Magnetic Proxy for Hydrocarbon Migration?

In this chapter I relate the primary findings in the petroleum systems modelling in Chapter 4 to the magnetic data in Chapter 5. The findings in Chapter 4 were in part influenced by the results in Chapter 5, as discussed below.

6.1 Identifying a Proxy for Hydrocarbon Migration

In Figure 6.1, the magnetic results are summarised with respect to a 2D section through the 3D model (Figure. 4.9). The results suggest a dominant siderite signal in the east, which decreases westward, becoming increasingly dominated by greigite. At first glance the siderite signal can be attributed to vertical migration while the greigite signal can be attributed to lateral migration. This initial observation helped in building of the 3D model. The initial 3D model had no accumulation of oil in the wells located in the west. Well 21/29a-08 is in the west but has a dominant siderite signal unlike the surrounding wells that have a mixture of siderite and greigite (Figure 5.24) suggesting the well could be charged (vertically) similarly to the well in the east. The 3D data was reassessed, large scale injectites were observed in the west (Figure 4.3) and included in the basin model. This led to the successful charging of the wells in the west (Figure 6.1).

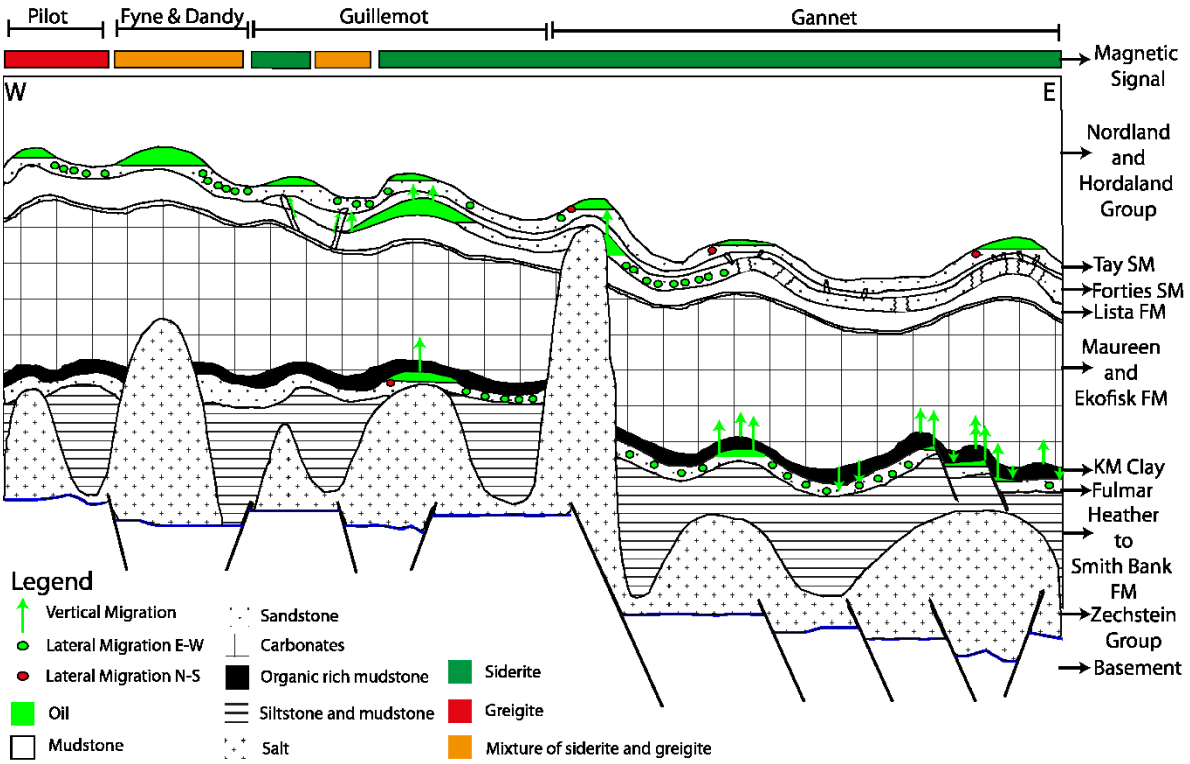


Figure 6.1. Schematic of the magnetic results plotted on a 2D slice of the 3D model shown in Figure 4.9. This figure shows the siderite rich signal in areas dominated with vertical migration and an increasing presence of greigite along the lateral migration pathway. Diagram is not drawn to scale.

The 3D model suggests well 21/24-03 was charged both laterally and vertically in its history (Figures 4.14 and 4.15), but it is dominated by a greigite signal (Figure 5.24). This suggests the correlation of a siderite or greigite dominant signal to vertical or lateral migration pathways might be coincidental. The reason for the change in magnetic minerals along the migration pathway is not immediately obvious. The purpose of this section is to provide mechanisms, which may account for this observed variation. Below I explore two possible mechanisms: (a) Biodegradation and (b) Migration of greigite from the oil kitchen.

(a) Biodegradation

Progressive biodegradation of oil by microbes at temperatures lower than 80 °C results in the removal of saturated hydrocarbons and an increase in the heavy asphaltene and polar oil constituents (Wenger et al., 2002). This decreases the oil quality by increasing the viscosity, sulphur and metal content while reducing its API (American Petroleum Institute) gravity (Miiller et al., 1987; Head et al., 2003). The sulphur combines with hydrogen giving rise to high concentrations of hydrogen sulphide (H_2S), that combines with available iron precipitating SD-SP greigite in the reservoir (Mann et al., 1990). Thermostability phase diagrams calculated for minerals in hydrocarbon reducing environments suggests iron sulphides are stable in high concentrations of sulphur, while iron oxides, i.e., magnetite and hematite are unstable and reduce to iron sulphide phases (Burton et al., 1993; Machel, 1995). These phase diagrams also predict the alteration of magnetite to siderite in relatively lower concentrations of sulphur while hematite alters to pyrite, most likely via greigite (Berner, 1984; Burton et al., 1993).

Volkman et al. (1983) have correlated API gravity to levels of biodegradation using a database of North Sea oils. The results suggested APIs higher than 30^{o} implies the oil is not degraded. APIs between 30° and 22° suggests moderate biodegradation of oil while APIs lower than 22° suggest extensive biodegradation which is considered extreme at values lower than 15° (Barnard and Bastow, 1991). Geochemical data from 25 wells was used to generate a contour plot showing the variation of API gravity in the Tay fan (Figure 6.2).

A siderite dominated signal (Figure 6.1 and Figure 6.2) is observed in wells from the Gannet fields and the Guillemot fields (apart from well 21/29a-06), which have APIs ranging from 40 to 35 ^{o} (Figure 6.2). A reduction in API (24 to 22 ^{o} suggesting moderate biodegradation) seen in the Fyne & Dandy field is accompanied by a signal containing an almost even mixture of a

siderite and greigite (Figure 6.1). A greigite dominated signal (Figure 6.1) in the Pilot Field corresponds to APIs less than 16° (Figure 6.2). A study carried out by Emmerton et al. (2013) from oil fields in Canada, Columbia, Indonesia and the UK linked the presence of MD hematite and magnetite to biodegradation, but my observations suggest the severity of biodegradation (Figure 6.2) is proportional to the abundance of nanometric greigite (Figure 5.24 and Figure 6.1).

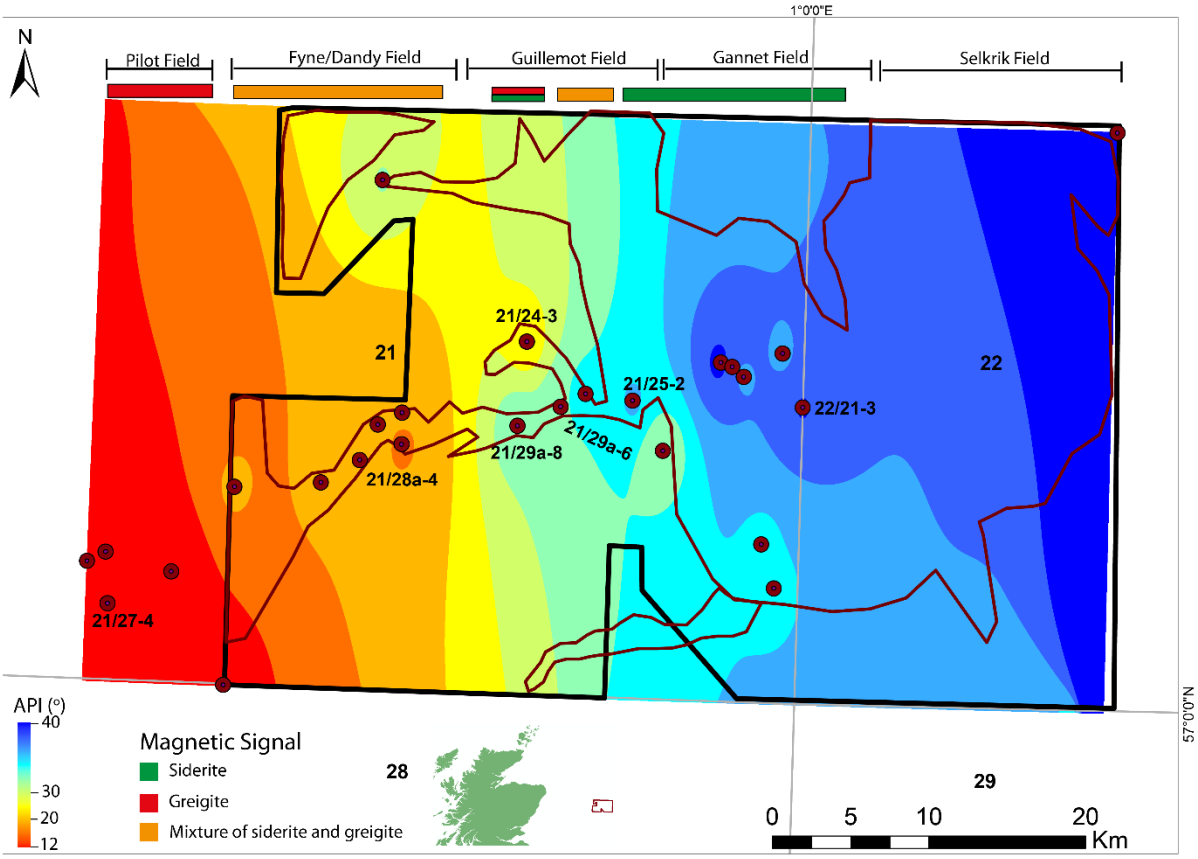


Figure 6.2 Map showing the variation of API gravity in the Tay fan. API generally reduces from east to west. The red line denotes the Tay fan, the black is the 3D data coverage and red circles are the locations of the wells used to generate the contour plot. API data was obtained from purchased geochemical reports from IHS. Some well names are included for referencing. Insert shows the location of the map.

Well 21/29a-08 has a present-day temperature of about 63 °C (Figure 6.3 b), but with an API higher than 30° (Figure 6.2) while well 21/28-04 has a present-day temperature of about 50 °C (Figure 6.3 a), but with an API of about 24° (Figure 6.2). This suggests biodegradation is more common at temperatures < 60 °C; biodegradation has been reported to occur at temperatures up to 80 °C (Miiller et al., 1987). This abnormally high API at the lower temperature is likely due to the high salinity formation water, which is known to limit the biodegradation process (Shelton et al., 2016). Purchased petrophysical reports (from IHS) of wells in the Pilot field show the formation water salinity to be between 65000- 99000 ppm

NaCl. These high levels of salinity are consistent with other measured values of formation water salinity in the Central Graben (Bjørlykke and Gran, 1994).

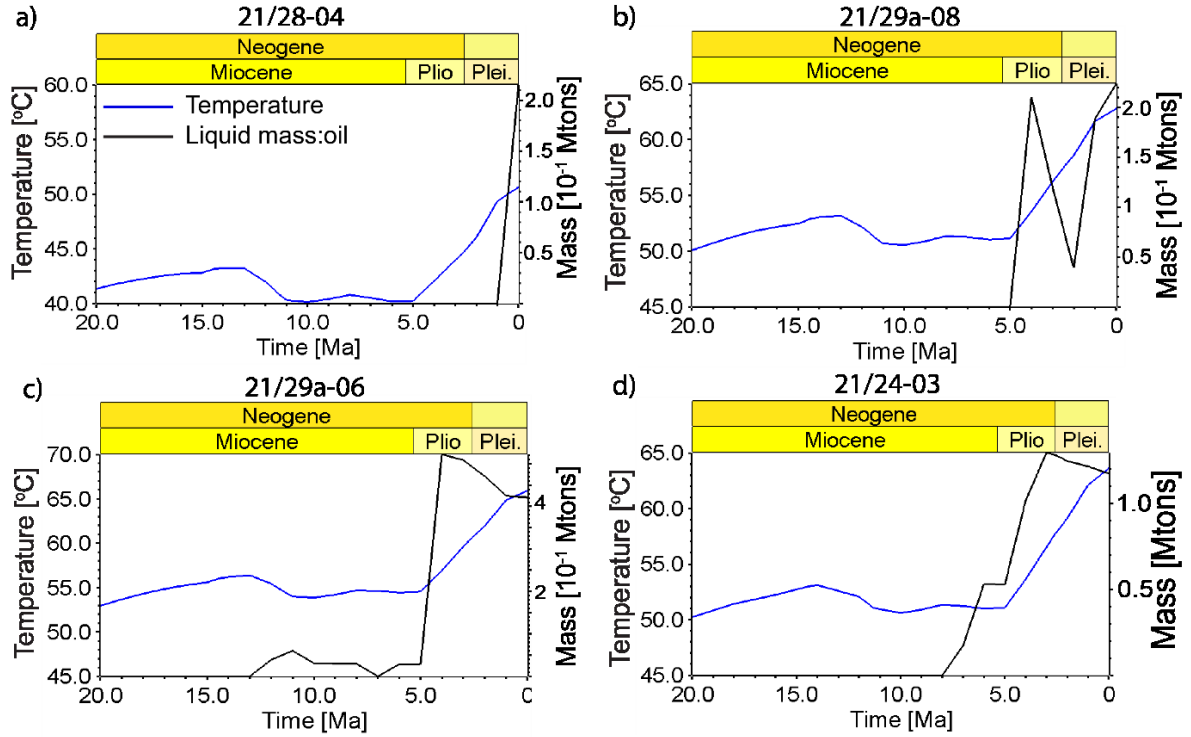


Figure 6.3. Plots of temperature (blue line) and liquid mass of oil (black line) vs time in the top Tay reservoir for wells a) 21/28-04 b) 21/29a-08 c) 21/29a-06 and d) 21/24-03. An increase in liquid mass suggests charging of the well while a reduction indicates loss of oil, because it has moved along the fill spill chain or it has leaked to the surface. Location of the wells are shown in Figure 6.2 and Figure 5.24. Plots are extracts from the PetroMod model shown in Figure 4.9.

Well 21/24-03 has an API of 27° (Figure 6.2) but has a greigite dominated signal (Figure 5.24) as opposed to a mixture of siderite and greigite seen in other samples with moderate biodegradation. The fill history (obtained from PetroMod) of this well (Figure 6.3d) explains the differences observed: Well 21/24-03 was charged at ~8 Ma (black line in Figure 6.3d) when the temperature was < 55 °C (blue line in Figure 6.3 d), low enough for biodegradation and greigite formation, which would have continued until 5 Ma when it was charged with fresh oil and rapid burial caused an increase in temperature. This fresh charging and reduction in biodegradation would have increased the oil quality and the API (Head et al., 2003). However, there was still enough sulphur present to allow greigite to remain stable (Kao et al., 2004). This suggests the presence of greigite could be an indicator of paleo-biodegradation of oil in the reservoir. This may explain why greigite can be present in some high API oil wells, e.g., 21/29a-06 (Figure 5.24). The temperature of well 21/29a-06 was lower than 55 °C (blue line in Figure 6.3c) when it was charged with very little oil at around 13 Ma (black line in Figure

6.3c), which then spilled around 7 Ma followed by fresh charging at 5 Ma (black line in Figure 6.3c) accompanied by a rapid burial and an increase in temperature (blue line in Figure 6.3c). This fill history limited biodegradation and resulted in a magnetic signal containing a mixture of siderite and greigite (Figure 5.24).

(b) Migration of greigite from the oil kitchen

As a source rock gets buried it is usually in the sulphidic diagenetic zone at the onset of oil generation (Berner, 1981). With increasing burial, the source will move into the methanic diagenetic zone, at which point gas rather than oil is expelled. Pyrite and greigite are precipitated in the sulphidic zone while siderite is precipitated in the methanic zone (Roberts, 2015). Abubakar et al. (2015) have shown that < 100 nm sized greigite and magnetite grains are precipitated during the oil generation in the laboratory. These grains form complexes with the oil, which can travel through the carrier bed and within the reservoir as they are smaller than the pore throat of typical sandstones and shales (Mallon and Swarbrick, 2008a; Nealson, 2009). In diagenetic settings, siderite is typically seen as a cementing mineral which over grows pyrite and other sedimentary components, this suggests it is most likely precipitated in the reservoir (Machel and Burton, 1991a; Larrasoaña et al., 2007; Emmerton, 2013).

I propose that the concentration of greigite may be related to thermal maturity of the source rock. Early mature oil would contain a high concentration of greigite and magnetite. As maturity increases the concentration of both minerals reduces to zero at the later stages of maturity when siderite is precipitated during the generation of gas. That is, early mature oil would contain greigite while mid- late mature oil would contain little to no greigite. Magnetite is not considered in this case as it can be both detrital and authigenic in this environment (see Figure 5.19 and Table 5.2).

The fill history constrained by most of the wells shows a reduction of liquid mass of oil after initial charging sometimes followed by an increase in liquid mass, e.g., wells 21/29a-08 and 21/29a-06 (Figure 6.3b-c). This pattern is indicative of a fill to spill lateral migration mechanism with continued filling in some cases. This is sketched in Figure 6.4. Early mature oil containing a high concentration of greigite particles is first introduced to the Fulmar Formation in the east, continued filling would lead to the early mature oil spilling in the west (Figure 6.4a). Early mature oil reaches the Tay SM in the west via vertical migration aided by

injectites, the greigite particles migrate with the oil resulting in a greigite rich signal in the west (Figure 6.4 b). Over time the source rock expels mid-late mature oil with a much lower concentration of greigite, this migrates downwards into the Fulmar FM and then vertically into the Tay SM in the east resulting in a siderite rich signal (Figure 6.4c). Spilling of the mid – late mature oil west in the Tay SM lead to a mixture of early and mid – late mature oil in some traps in the Tay, corresponding to a mixture of siderite and greigite signals where they meet (Figure 6.4d). Well 21/29a-08 has a siderite rich signal in the west (Figure 5.24), this can be explained by the sandstone injectites. The injectites would have transported early mature oil migrating vertically from the Fulmar FM in the west filling traps in the 21/29a-08 area. Eventually more mature oil would migrate vertically into this trap from the Fulmar FM along with mid-late mature oil migrating from the east in the Tay SM displacing majority of the early mature oil west resulting in a siderite rich signal.

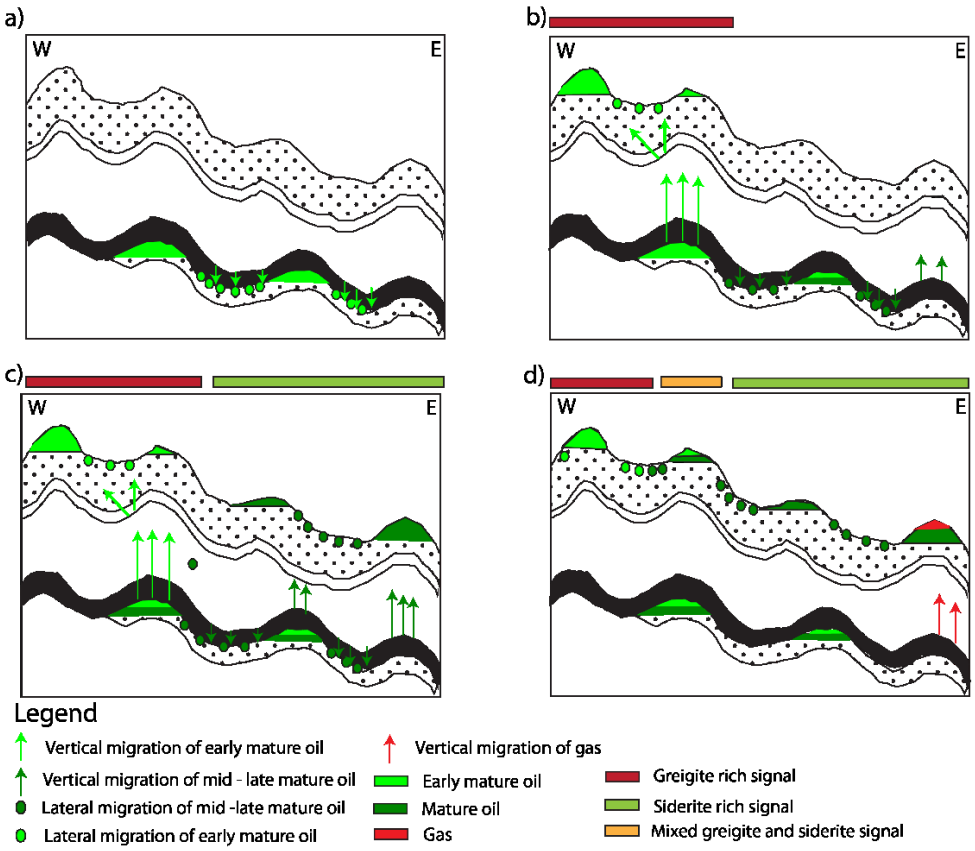


Figure 6.4. Simplified sketch illustrating the time-line (a to d) of magnetic mineral formation, and oil migration and maturity. The total time period is 30 Myrs. Black layer is the Kimmeridge Clay, the dotted layer is the Tay Sandstone member and the white layers are the carrier beds and seal a) downward migration of early mature oil into the Fulmar FM which migrates west b) capillary failure in the west leads to vertical migration of early mature oil into the Tay SM while downwards and upwards migration of mid-late mature oil occurs in the east c) expulsion of more mature oil leads to replacement of early mature oil with mid-late mature oil in the west traps in the Fulmar FM and mid-mature oil in the E traps in the Tay SM. d) continued vertical migration of mid- late mature oil and gas leads to a mixture of early mature oil and mid- late mature oil in some traps in the Tay SM.

To test the model proposed in Figure 6.4, a simulation was carried out in PetroMod 3D to estimate the sequence with which the traps were filled with oil. A pseudo stratigraphic trap was created by turning the facies at the edge of the Fyne and Dandy field to mud resulting in the accumulation of the oil that would have migrated to the Pilot field (Figure 6.5). The results suggest the majority of the early mature oil is accumulated in the Pilot field (Figure 6.5) and well 21/24-03 (blue circle in Figure 6.5) corresponding to the greigite rich signal observed in those locations (Figure 5.24). A discrepancy is noticed in well 21/25-02 (black circle in Figure 6.5); the Petromod 3D model suggests a mixture of early mature oil with more mature oil, but the magnetic signal is siderite rich suggesting mid-late mature oil. However, only 18 m of the Tay SM was cored with 6 m missing, and the sandstones were thin and interbedded with thick mudstone resulting in poor sampling.

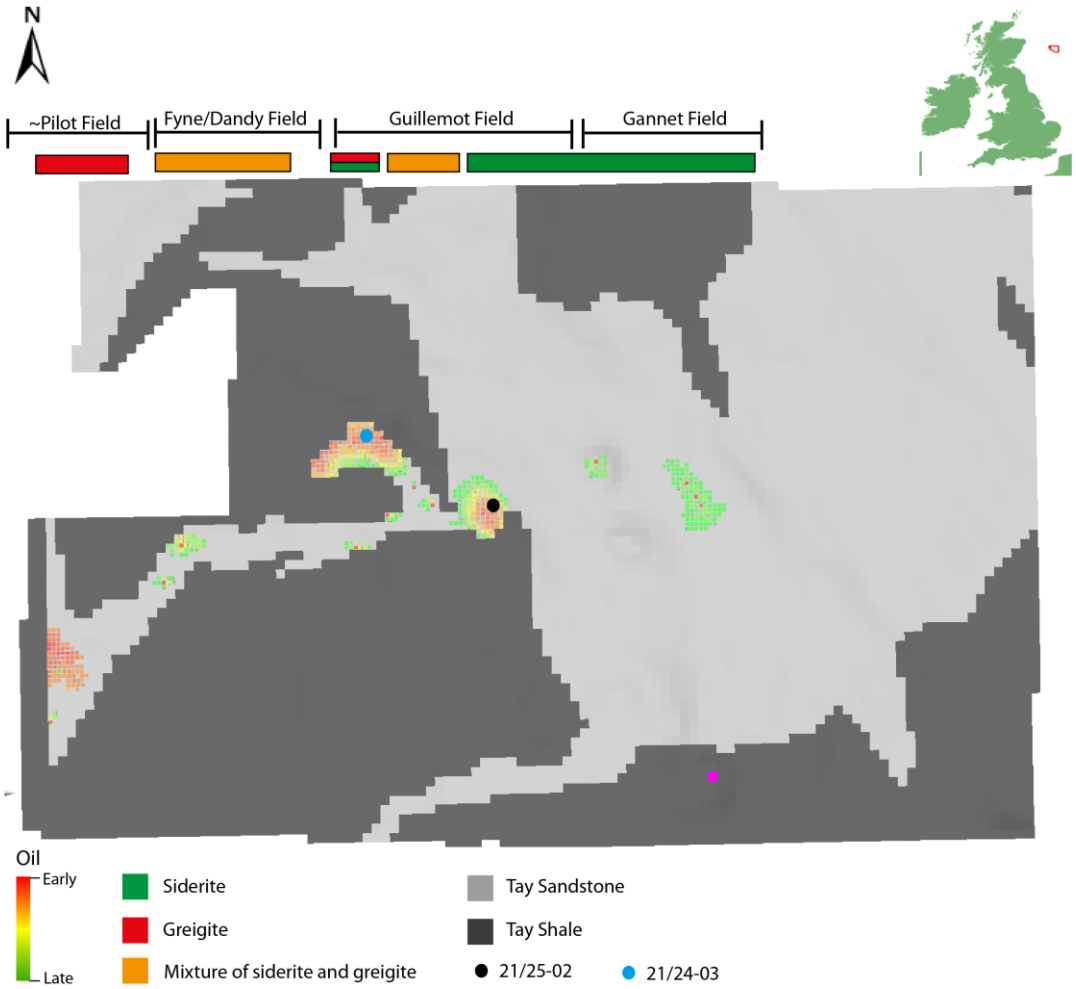


Figure 6.5 Petromod 3D model output highlighting timing of oil formation and its eventual the accumulation. Most of the early mature oil migrated west as predicted in Figure 6.4. Tay sandstone has been greyed out for enhanced visibility. Insert showing location of survey. Note: only the oil accumulations that were sampled in the core store are shown in this image.

Preferred Mechanism

I have proposed two mechanisms for the greigite signal observed in the study area (Figure 5.24). The first proposes an organic mechanism, i.e., a by-product of biodegradation resulting in the precipitation of greigite in the reservoir (Figure 6.2), whilst the second mechanism proposes an inorganic mechanism, i.e. precipitation in the source rock, resulting in the transportation of greigite with the early mature oil to the traps in the west (Figure 6.4).

I believe the first mechanism (Figure 6.2) is the most likely scenario, because of the previously observed direct correlation between biodegradation by sulphate reducing bacteria and the precipitation of iron sulphides (McCabe et al., 1987; Morse et al., 1987; Mann et al., 1990; Sakaguchi et al., 1993); this study finds a clear correlation between low API oil gravities and Iron sulphide rich wells (Figure 6.2). The second mechanism is difficult to verify, because of the lack of geochemical data. The second proposed mechanism simplifies oil mixing and spilling, which is actually lot more complicated and can vary from trap to trap (Wilhelms and Larter, 2004; Zhan et al., 2017).

6.2 Implications for Hydrocarbon Perspectivity

Calibrating Petroleum Systems Models

The clear link between greigite and API gravity in wells (Figure 6.2), could also be a quicker way of determining the severity of biodegradation by measuring susceptibility as a function of temperature. This information can be used in the calibration of PetroMod's estimates for the severity of biodegradation in traps when D+FP migration method is used.

Alternatively, If the model proposed in Figure 6.4 is valid, then this method can be used to calibrate accumulations of early mature oil in a petroleum systems model. This could prove to be a more cost effective and efficient means of estimating oil maturity and/or determining if oils accumulated in different reservoirs are of the same maturity.

Tracking Oil Migration using Aeromagnetic Techniques

High-wave number magnetic anomalies observed over anticlines in oil fields in Alaska have been linked to hydrocarbon seepage (Donovan et al., 1984). I used Petromod 3D to estimate hydrocarbon seepage in the study area (Figure 6.6). As a soft calibration, these seepages were also observed in the seismic data as gas chimneys and bright amplitudes in the overburden.

Hydrocarbon seepage was observed over fields with both a greigite-rich signal (in the west) and a siderite-rich signal (in the east). Siderite is not thought to migrate with the oil, only the nanometric (< 60 nm) magnetite would leak to the surface in the east, whilst in the west nanometric (< 60 nm) greigite and magnetite could both leak to the surface. In a high-resolution aeromagnetic anomaly map this would correspond to a small increase in wave number along the fill spill chain (Figure 6.6). This assumes the magnetic minerals do not alter as they leak to the surface and the background signal of the overburden rocks through, which they migrate has been accurately removed.

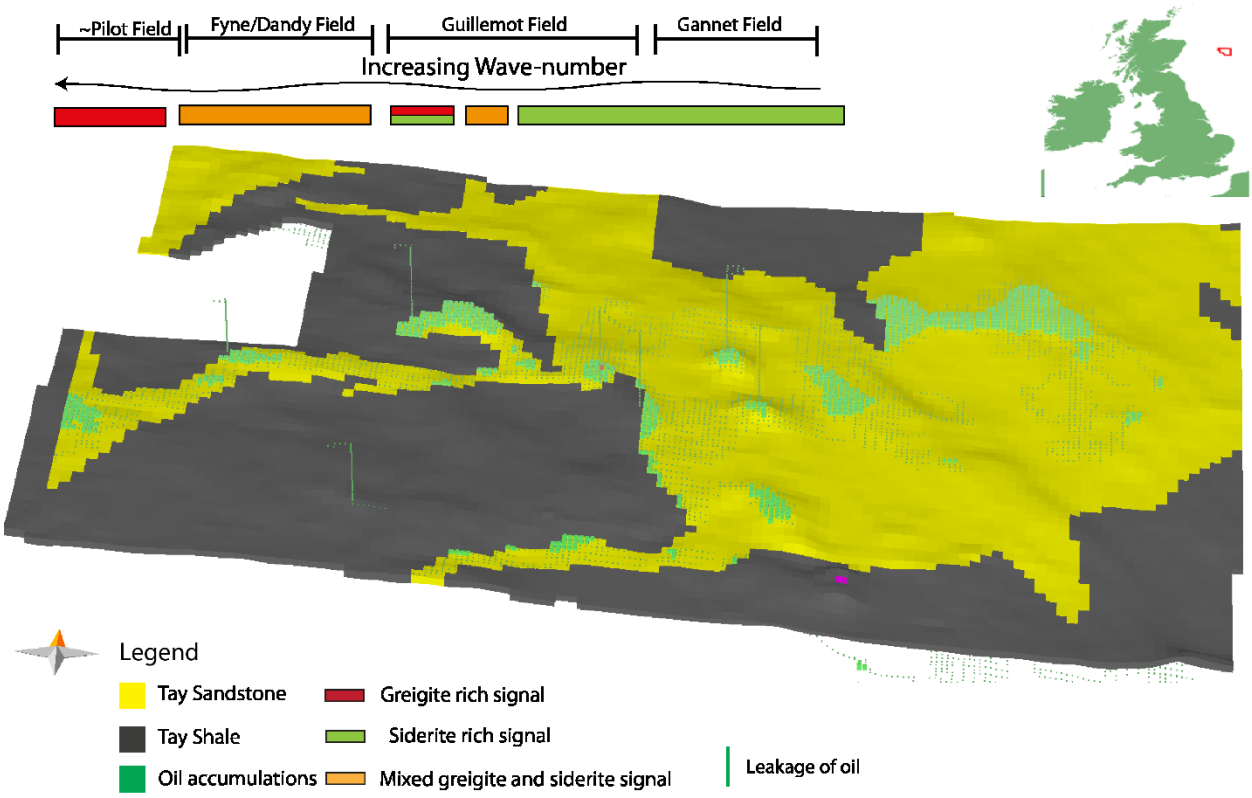


Figure 6.6. PetroMod 3D image showing the locations of oil seepage from 1 Ma to present day. Leakages of oil in the east leads to magnetite leaking to the surface while leakages of oil in the west would lead to magnetite and greigite leaking to surface. This would correspond to an increase in wave number from the east to the west provided the background signal has been accurately subtracted and the minerals do not alter at shallower depths.

6.3 Conclusions

The mineral magnetic data presented in Chapter 5 showed an abundance of siderite in the east, and an abundance of greigite in the west with a zone of mixing in the middle (Figure 5.24 and Figure 6.1). With the aid of the petroleum-systems model described in Chapters 3 and 4, two possible mechanisms are proposed to explain the observation magnetic signals: (a) an organic biodegradation model, and (b) an inorganic migration model.

The organic mechanism proposes the variation observed (Figure 5.24 and Figure 6.1) is caused by an increase in the severity of biodegradation along the migration pathway leading to the precipitation of more iron sulphides (predominantly greigite) in the west (Figure 6.2). The inorganic mechanism suggests greigite is precipitated during early–mature oil generation and expulsion in the east, which has filled and spilled traps until it accumulates in the west (Figure 6.4 and Figure 6.5). The organic mechanism is the most likely scenario, because a clearer trend is noticed between reducing API and an increase in the abundance of iron sulphides, however, the inorganic model cannot be entirely discounted.

It is suggested that these findings could be developed for use in both 2D and 3D petroleum systems model calibration. Leakages predicated by the model (which is common in most basins), coupled with the change in mineralogy along the migration pathway, suggest low-altitude high resolution aeromagnetic surveys may be used to track the migration of oil in basins (Figure 6.6). Additionally, the link between an iron sulphide rich signal and low API gravity oils (Figure 6.2) suggests a quick susceptibility versus temperature measurement to determine the presence of iron sulphides may be an alternative tool for identifying the severity of biodegradation in core samples.

Chapter 7

Identification of magnetic enhancement at hydrocarbon/water contacts.

7.1 Introduction

Hydrocarbon fluid contacts are boundaries that separate hydrocarbon phases from each other and from the formation water (Ahmed, 1989). Identifying the locations of these hydrocarbon fluid contacts is crucial in determining hydrocarbon reserves and production planning.

As source rocks undergo burial, oil is generated and then expelled. The oil usually migrates upwards due to buoyancy, until it escapes at the surface/seabed or is trapped in a reservoir. As burial depth increases, depending on the kerogen type, the source rock can also expel gas which also migrates upwards, but typically at faster rates than oil. If gas reaches the reservoir it will dissolve in the oil, potentially creating a multi-phase system depending on pressure and temperature (Larter and di Primio, 2005). As pressure drops or temperature increases, the gas exsolves from the oil and a gas cap is formed above the oil with the formation water lying below the oil (Ahmed, 1989).

Resistivity wireline logs (Figure 7.1) are a good for identifying oil-water contacts (OWC) and gas-water contacts (GWC), as the resistivity of hydrocarbons are significantly higher than that of water (Rider and Kennedy, 1996). However, as oil and gas have roughly the same resistance, resistivity logs cannot be used to differentiate gas-oil contacts (GOC). To identify GOC (and GWC) contacts, neutron porosity and density wireline logs can be used; gas is less dense than oil or water, and because neutron-derived porosities for gas are significantly under-estimated this provides a clear contrast (known as the “gas effect”) as shown in Figure 7.1 (Rider and Kennedy, 1996). It has been found that hydrocarbon fluid contacts are not always sharp boundaries; they can be gradational with an intermediate transition zone of mixed fluids. Depending on the lateral pressure variation in the reservoir bed, the hydrocarbon fluid contacts can be either flat or tilted (Hubbert, 1953; Dennis et al., 2000). If pressure data, e.g. wireline repeat formation tester (RFT) data, are available an accurate determination of fluid contacts can be made.

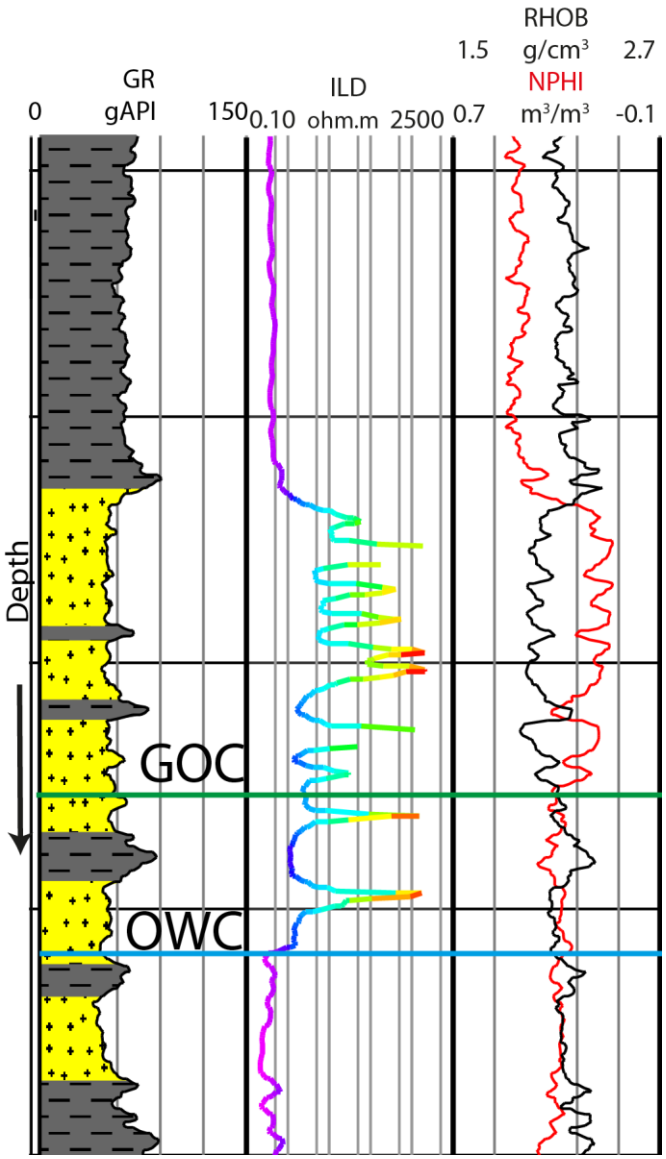


Figure 7.1. Wireline logs for well 21/25-04. GR- gamma ray log, ILD- Deep induction log used to determine formation resistivity, RHOB- density log and NPHI- neutron porosity Log. A decrease in resistivity indicates a change from hydrocarbons to formation water.

I have identified a magnetic enhancement at hydrocarbon-fluid contacts. In this chapter, I show that peaks in magnetic susceptibility, saturation magnetisation and remanent saturation coupled with size of magnetic minerals can be used to determine the hydrocarbon contacts in core samples. These new approaches have the potential to be used in the identification of paleo-hydrocarbon-fluid contacts, which are vital to understanding the fill history of basins. The results of this chapter are to be summited to the journal AAPG Bulletin for publication.

7.2 Methodology

7.2.1 Sample Collection and Magnetic Measurements

Well cores were sampled from the British Geological Survey core repository in Keyworth, UK. Composite logs were used to determine which wells in the study area have penetrated OWCs or GOCs or both: 6 out of the 18 wells selected have cores with a clear OWC, while only 2 wells sample a clear GOC. The composite logs were also used to determine the presence of hydrocarbons in the Tay formation and if the core recovery was successful from the formation. Samples were selected based on geological observations (water wet sandstone, oil stained sandstone, sandstones in gas cap, siltstones and shale). Samples taken were typically 2cm chips. Data from wells 21/25-04, 21/25-A1 and 21/29a-08 (Figure 2.8) are shown in this Chapter.

In addition to the core sections, pure oil samples were obtained from wells 21/29a-8 and the 21/24-2 (Figure 2.8) The oil samples were absorbed in kaolinite clay for magnetic measurements. To purify the kaolinite clay, it was washed in hydrogen peroxide to remove any organic matter and then washed in deionised water and left in an oven at 100 °C for 24 hours. For each sample the mass of the kaolinite clay was measured before (1.98 g per sample) and after oil was added (about 3 g). Approximately, 0.15g of the mixture was used for the LT (low temperature) experiments. The concentration of oil in both samples was ~ 35% by total mass; we subtracted that from the overall signal.

Magnetic measurements were carried out to determine the morphology, mineralogy and size of the magnetic minerals present. The magnetic techniques used in this chapter are described in detail in Section 5.2.2.

7.3 Results

7.3.1 Oil Samples

The following low-temperature experiments were carried out on the samples to identify possible magnetic transitions: (1) Low-temperature demagnetisation: an SIRM was induced in the samples at room-temperature (field = 2.5 T), and then cooled to 10K and back to 300 K in zero-field. This generates two curves called cycling cooling and cycling warming curves; (2) Field cool (FC) – Zero-field cool (ZFC) warming curves: Induce a SIRM at 10 K and warm in zero field to 300 K. In the ZFC scenario the sample is first cooled to 10 K in zero field, in the FC scenario the sample is cooled to 10K in a field a 2.5 T. Cycling cooling/warming and FC/ZFC curves were measured for the blank kaolinite clay, and the oil from wells 21/24-02 and 21/29a-08 (Figure 7.2). The curves for the blank kaolinite clay (Figure 7.2a) are noisy and show no evidence for the presence of any magnetic minerals. In comparison, the signal-to-noise ratio for the oil samples (Figure 7.2b-c) is much higher, i.e., magnetisation is about two orders of magnitude stronger.

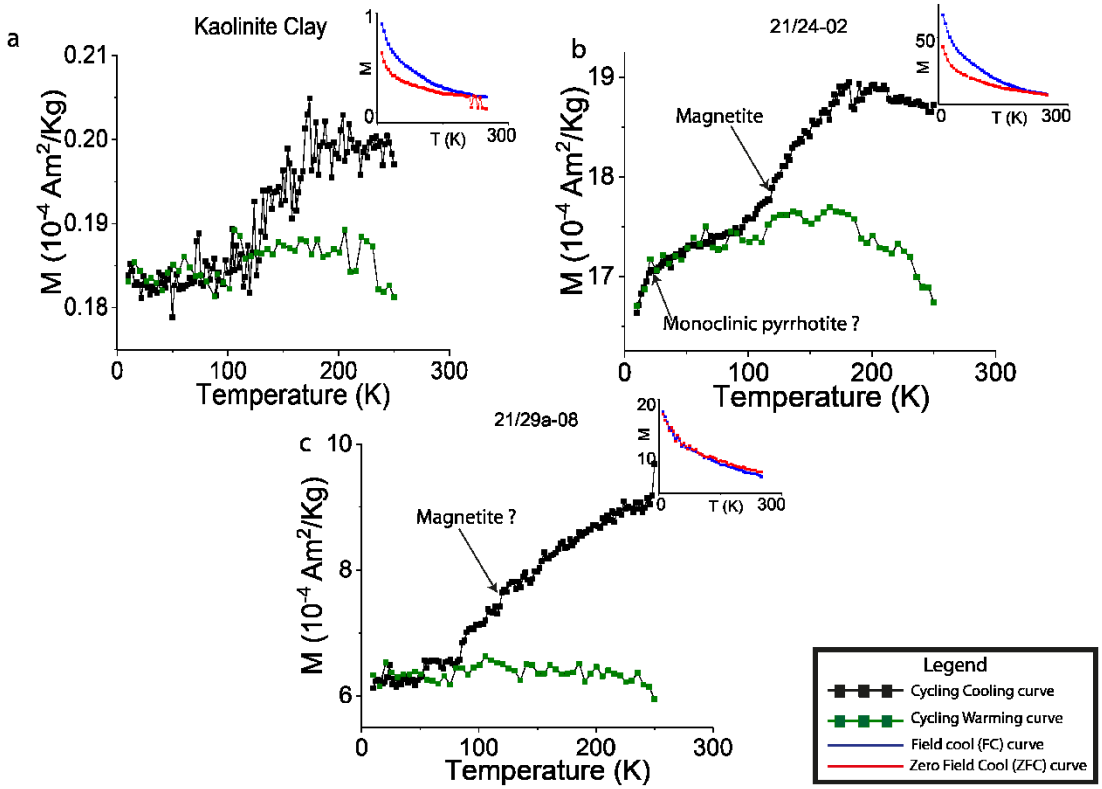


Figure 7.2. Cycling cooling/warming curves and FC/ZFC curves for a) pure Kaolinite clay- noisy signal, b) oil sample from well 21/24-02- cycling and warming curves suggest the presence of magnetite and possibly monoclinic pyrrhotite in the sample. c) oil sample from well 21/29a-08 - cycling cooling and warming curves suggest the presence of magnetite in the sample.

Falls in remanence at around 120 K on the cycling cooling curve suggest the presence of magnetite in both wells (Figure 7.2b-c), while a drop in magnetisation at around 37 K on the cycling cooling curve (Figure 7.2b) could be due to the presence of monoclinic pyrrhotite in well 21/24-02 (Verwey, 1939; Besnus and Meyer, 1964; Dekkers et al., 1989).

7.3.2 Core Samples

Hysteresis loops, FORC diagrams (measured if S/N ratio high enough) and susceptibility were measured for all samples. An increase in M_s, M_{rs} and susceptibility (normalised by mass) were noticed at the hydrocarbon fluid contacts as shown in wells 21/25-04, 21/25-A1 and 21/29a-08 (Figure 7.3). Differences in susceptibility measured at 990 Hz and 6000 Hz observed in samples from wells 21/25-A1 and 21/25-04 (Figure 7.3d and e) suggest the presence of thermally relaxing SD grains, i.e., 25-35 nm in size (Muxworthy, 2001; Mena and Walther, 2012).

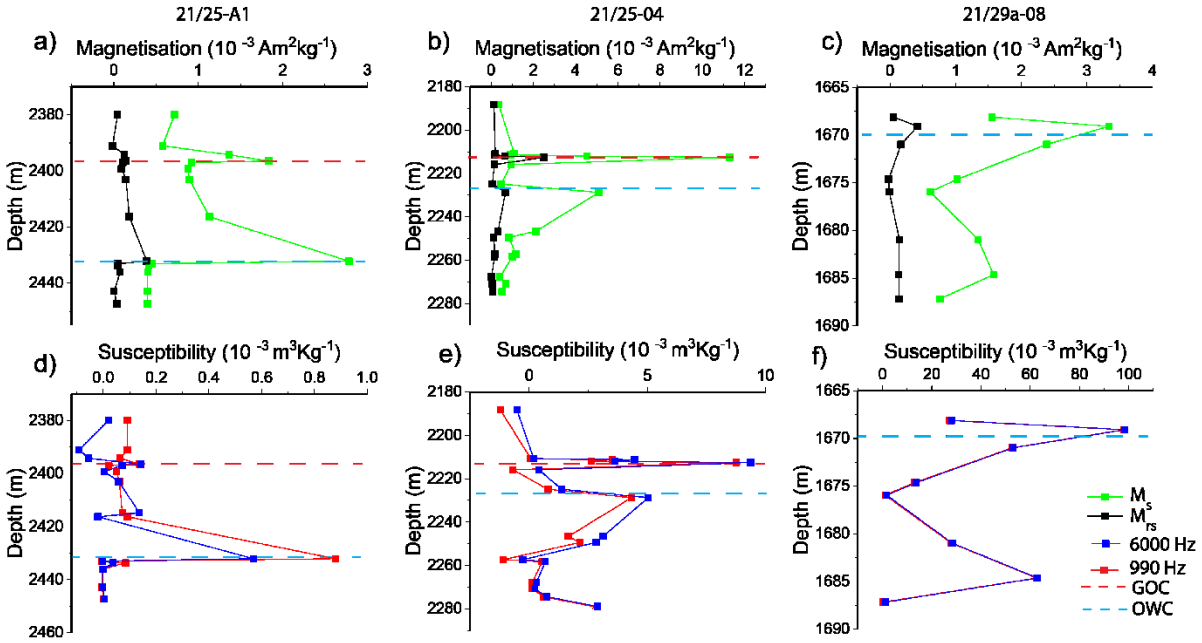


Figure 7.3. M_s (green line), M_{rs} (black line), susceptibility measured at 990 Hz (red line) and 6000 Hz (blue line) for samples from wells 21/25-A1 (a and d), 21/25-04 (b and e) and 21/29a-09 (c and f). Distinct peaks are noticed at the GOC (red dashed line) and OWC (blue dashed line). GOC and OWC depths were obtained from wireline logs. All depths are below mean sea level. Measured hysteresis parameters for other wells are shown in Appendix 4.

The LT experiments, HT (high temperature) experiments and FORC diagrams for wells 21/25-04 and 21/25-A1 are shown in Figure 7.4 and Figure 7.5 respectively.

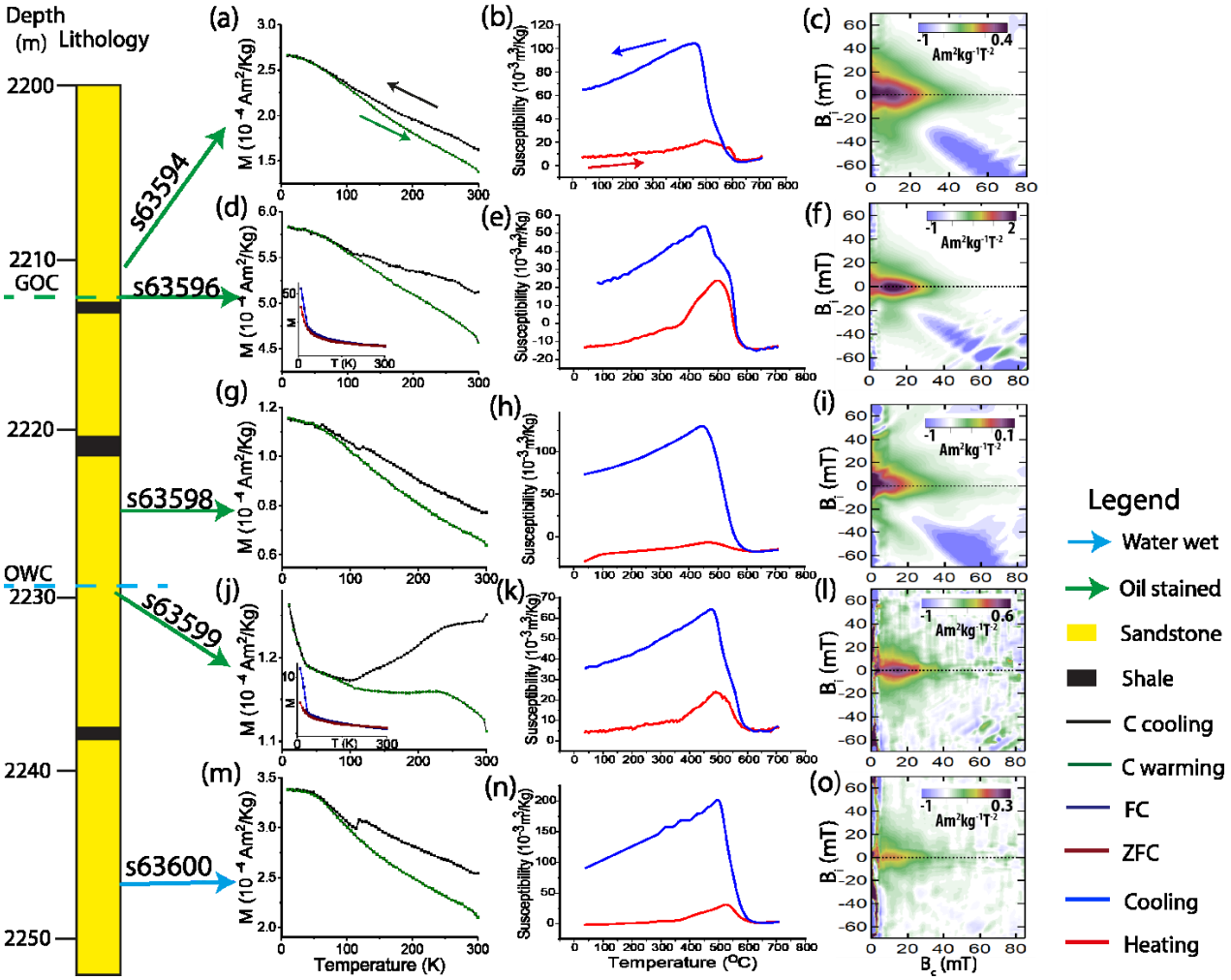


Figure 7.4. LT experiments (cycling cooling, cycling warming, FC and ZFC), HT susceptibility experiments and FORC diagrams for samples in well 21/25-04. S63594; a) LT experiments suggest the presence of titanohematite or goethite and magnetite, b) HT experiment suggests a siderite rich sample and c) FORC diagram suggests a mixture of SP grains with multi axial anisotropy or a vortex structure and PSD grains. S63596 at the GOC; d) LT experiments suggest the presence of titanohematite or goethite and magnetite, e) HT experiment suggests a siderite rich sample with some iron sulphides and f) FORC diagram suggests a mixture of SD grains with multi axial anisotropy or vortex structure and PSD grains. S63598; g) LT experiments suggest the presence of titanohematite or goethite and magnetite, h) HT experiment suggests a siderite rich sample and i) FORC diagram suggests a mixture of SP grains with multi axial anisotropy or a vortex structure and PSD grains. S63599 at the OWC; j) LT experiments suggest the presence of hematite, siderite and magnetite, k) HT experiment suggests a siderite rich sample and l) FORC diagram suggests the presence of SD grains. S63600; m) LT experiments suggest the presence of titanohematite or goethite and magnetite, n) HT experiment suggests a siderite rich sample and o) FORC diagram suggests the presence of SP grains. VARIFORC parameter (Egli, 2013) for FORC smoothing are $s_{c,0}$ = 1.2, $s_{c,1}$ = 3, $s_{b,0}$ = 3, $s_{b,1}$ = 5, and λ_c = 1 λ_b = 1. For the HT susceptibility measurements, the samples were heated in argon.

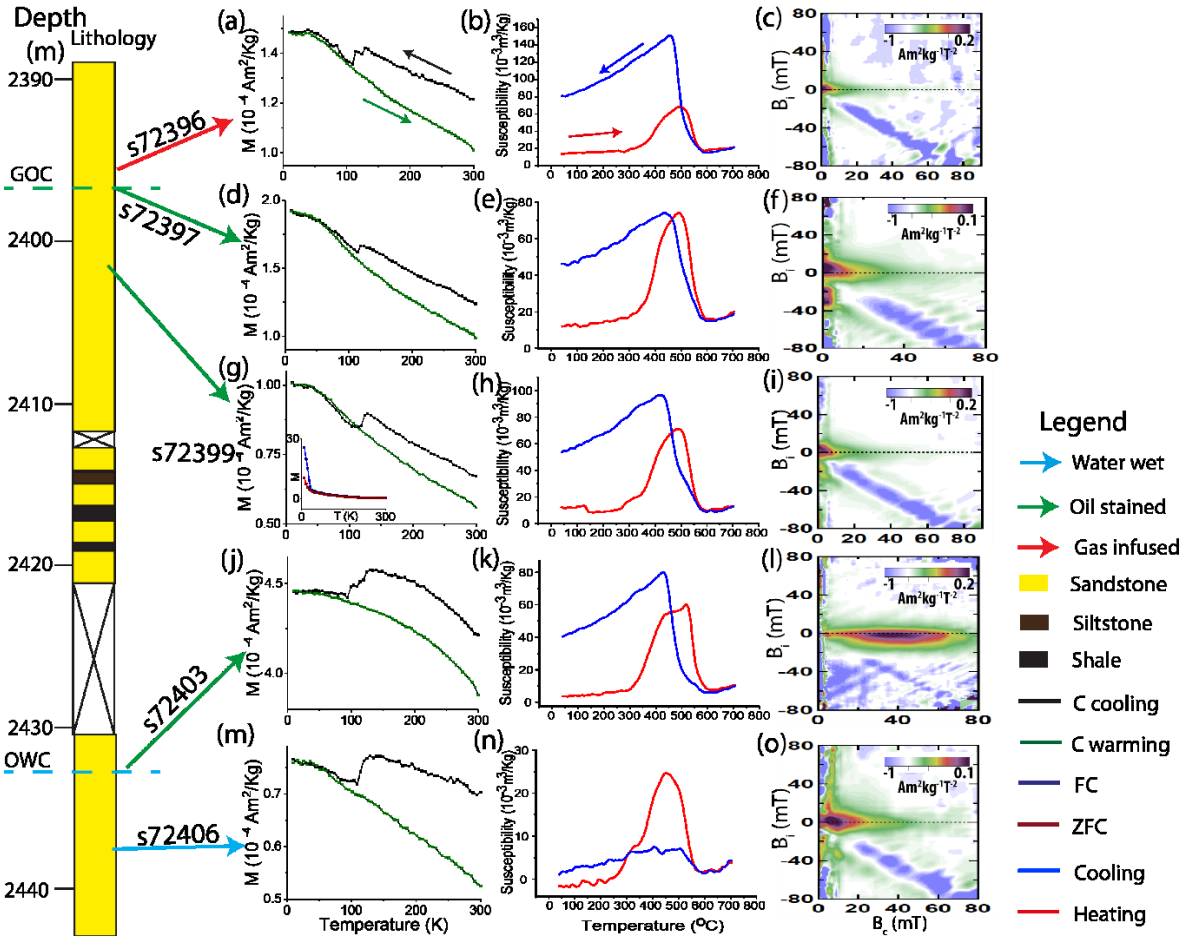


Figure 7.5 LT experiments (cycling cooling, cycling warming, FC and ZFC), HT susceptibility experiments and FORC diagrams for samples in well 21/25-A1. S72396; a) LT experiments suggest the presence of titanohematite or goethite and magnetite, b) HT experiment suggests a siderite rich sample and c) FORC diagram suggests the presence of SP grains with multi axial anisotropy or a vortex structure. S72397 at the GOC; d) LT experiments suggest the presence of titanohematite or goethite and magnetite, e) HT experiment suggests a mixture of siderite and iron sulphides and f) FORC diagram suggests a mixture of SP and SD grains with multi axial anisotropy or vortex structure. S72399; g) LT experiments suggest the presence of titanohematite or goethite, siderite and magnetite, h) HT experiment suggests the presence of siderite and iron sulphides and i) FORC diagram suggests the presence of SP grains with multi axial anisotropy or vortex structure. S72403 at the OWC; j) LT experiments suggest the presence of titanohematite or goethite and magnetite, k) HT experiment suggests the presence of siderite and iron sulphides and l) FORC diagram suggests the presence of SD greigite grains. S72406; m) LT experiments suggest the presence of titanohematite or goethite and magnetite, n) HT experiment suggests an iron sulphide rich sample and o) FORC diagram suggests the presence of SP grains. VARIFORC parameter (Egli, 2013) for FORC smoothing are $s_{c,0}$ = 1.2, $s_{c,1}$ = 3, $s_{b,0}$ = 3, $s_{b,1}$ = 5, and λ_c = 1 λ_b = 1. For the HT susceptibility measurements, the samples were heated in argon.

The LT experiments identified the presence of magnetite (decrease in remanence at about 120 K) in all the samples (Figure 7.4 and Figure 7.5). The increase in remanence on cooling in samples like s63594, s63600, s73397 and s72399 (Figure 7.4a and m and Figure 7.5d and g respectively) suggests the presence of goethite or titanohematite (Rochette and Fillion, 1989; Guyodo et al., 2006; Sprain et al., 2016). RT-SIRM cooling and warming curves also identified the presence of hematite (drop in remanence at about 250 K) in a few samples, e.g., s63599 (Figure 7.4j). This was expected as hematite is often replaced or dissolved in diagenetic settings caused by hydrocarbons (Machel and Burton, 1991b).

No Besnus transition was detected in any of the LT curves measured, indicating there is no monoclinic pyrrhotite in the samples, but other iron sulphides such as hexagonal pyrrhotite or greigite maybe present as they have no low temperature transition (Chang et al., 2009; Horng, 2018). The absence of a lambda transition in the HT-susceptibility experiments suggests a lack of hexagonal pyrrhotite in the samples (Dunlop and Özdemir, 1997). Greigite is typically unstable during heating with thermal decomposition from 200- 400 ^{o}C (Chang et al., 2008; Bol'shakov and Dolotov, 2011). Its presence in samples is inferred from the HT-susceptibility heating and cooling behaviours; kinks in susceptibility on heating between 200 and 400 ^{o}C e.g. s72399, s7203 and s72406 (Figure 7.5h, k and n respectively) have been attributed to the presence of greigite (Reynolds et al., 1994; Dekkers et al., 2000).

Siderite is paramagnetic at room temperature, but in the presence of a field it acquires a large thermal remanence on cooling below its Néel temperature (~37 K) (Jacobs, 1963; Frederichs et al., 2003). A noticeable drop in remanence between 10 and 40 K in the FC experiment was used to identify the presence of siderite as shown in samples s63599 and s72399 (Figure 7.4j and Figure 7.5g). In the absence of FC and ZFC curves, the heating and cooling behaviour of susceptibility was used to identify siderite. When heating in argon siderite alters to magnetite above 400 ^{o}C and on cooling a rapid increase in susceptibility at 580 ^{o}C accompanied by a Hopkinson like peak is observed suggesting the formation of SP magnetite (Housen et al., 1996). This behaviour was noticed in samples s63594, s63596, s63598, s63599, s63600, s72396, s72397, s72399 and s72403 (Figure 7.4 b, e, h, k, n and Figure 7.5b, e, h and k).

FORC diagrams with a vertical spread of concentric contoured peaks on the B_i=0 axis suggest the presence of interacting SD particles (Roberts et al., 2000). Such behaviour is observed at

the hydrocarbon fluid contacts seen in s63594, s63599 (Figure 7.4f and i). FORC diagrams with a contoured peak below the B_i=0 axis are indicative of SD greigite (Horng, 2018); this was observed in one well (21/25-A1) at the OWC (sample s72403; Figure 7.5l). FORC diagrams for some samples have contours that diverge away from the origin, which suggest the presence of PSD grains (Roberts et al., 2000; Roberts et al., 2017) as seen in s63594, s63596 and s63598 (Figure 7.4c, f and i). FORC diagrams also suggest the presence of thermally relaxing (superparamagnetic-SP) SD particles (Roberts et al., 2006; Chang et al., 2009; Roberts et al., 2018b) above and below the hydrocarbon fluid contact as seen in samples s63594, s63598, s63600, s72396, s72399 and s72406 (Figure 7.4c, i and o and Figs. 8c, i and o). Samples with multiaxial anisotropy were identified by the steeply dipping negative region to the right of the B_u axis (Harrison and Lascu, 2014; Valdez-Grijalva and Muxworthy, 2019) (Figure 7.4c, f and i and Figure 7.5c, f, i, l and o). This feature may also be due to SD vortex behaviour (Lascu et al., 2018; Valdez-Grijalva et al., 2018a).

SEM images on magnetic extracts showed a variety of grain sizes and iron-phase mineralogy. Framboids were found in samples such as s63598 (Figure 7.6a). EDX analysis of the framboid in Figure 7.6, identified iron and sulphur grains, which are likely (the EDX was not calibrated for this) a mixture of 1-2 µm sized pyrite grains and smaller < 100 nm greigite grains. Bigger magnetite and pyrite grains (3-5 µm sized) were found as well, e.g., s63597 (Figure 7.6b); the bigger magnetite grains are likely responsible for the PSD behaviour noticed in s63594, s63596 and s63598 (Figure 7.4c, f and i). EDX confirmed the presence of iron oxide minerals, which are most likely magnetite grains ranging from 50-350 nm in size (Figure 7.6c-d).

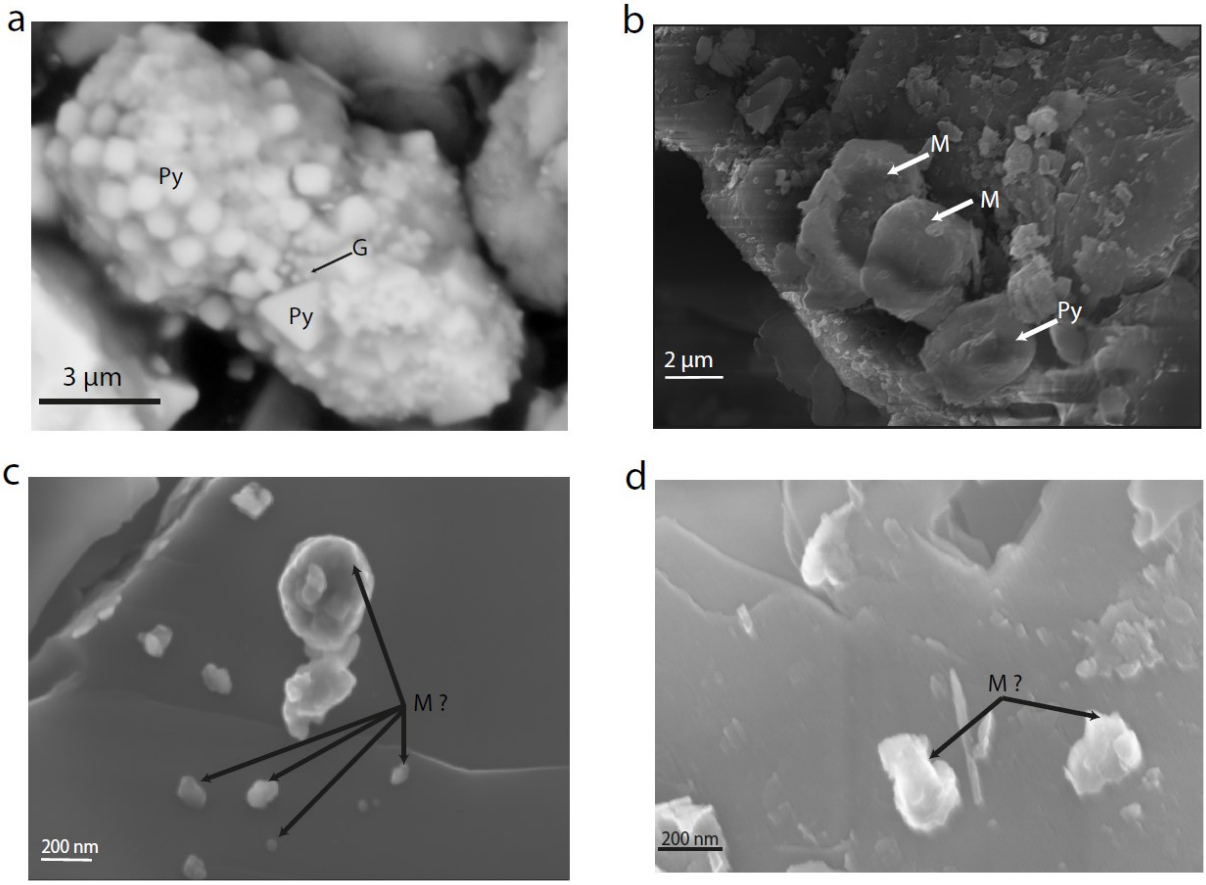


Figure 7.6 SEM images on the Phenom desktop SEM a) s63597 EDX confirms FeS Framboid. SEM images on the LEO SEM; b and c) s63598 from well 21/25-04, and d) s63600 from well 21/25-04. Py- pyrite, M- magnetite and G- greigite.

7.4 Discussion

Peaks in saturation magnetisation, remanent saturation magnetisation and susceptibility have been noticed at the hydrocarbon fluid contacts (Figure 7.3). FORC diagrams from samples at the hydrocarbon fluid contacts (Figure 7.4f and l and Figure 7.5l respectively) suggest the presence of stable SD grains, i.e., ~50-100 nm. FORC diagrams from samples above and below the hydrocarbon contacts suggest the presence of smaller thermally relaxing SD grains (SP) and PSD grains (Figure 7.4c, i and o and Figure 7.5c, i and o). LT and HT experiments confirmed the presence of magnetite, greigite, siderite, hematite, titanohematite and goethite in the samples (Figure 7.4 and 7.5). Only magnetite was observed in the oil-well samples with possibly monoclinic pyrrhotite also present.

7.4.1 Can magnetic minerals be carried in the oil?

The oil samples from wells 21/24-02 and 21/29a-08 (Figure 7.2b-c) have magnetisations that are two orders of magnitude higher than the kaolinite clay sample (Figure 7.2a) and contain magnetite (identified by its Verwey transition at ~ 120 K). This suggests the magnetic minerals can form complexes within the oil that can be transported from the source rock to the reservoir provided they are small enough to fit through the pore throats of the carrier beds. The presence of framboids, e.g., s63597 (Figure 7.6a), suggests the diagenetic conditions caused by the oil could lead to the precipitation of magnetic and non-magnetic minerals in the reservoir that are too large to be transported (Wilkin and Barnes, 1997; Lin et al., 2016).

The drop in remanence at ~37 K on the cycling cooling curve in oil sample 21/24-02 (Figure 7.2b) is typically indicative of monoclinic pyrrhotite, but the ZFC and FC curves (insert in Figure 7.2b) do not support this argument (Kind et al., 2013). Additionally, monoclinic pyrrhotite was not observed under the SEM in any of the measured core samples. It is usually considered to be detrital in origin as it is thought to grow too slowly in sediments to be a diagenetic product (Horng and Roberts, 2006; Roberts, 2015; Horng and Roberts, 2018b). Monoclinic pyrrhotite is therefore unlikely to be the cause of the reduction in remanence observed at around 37 K in oil sample 21/24-02 (cycling cooling curve in Figure 7.2b). It is unclear which mineral is responsible for this.

Surprisingly there was no evidence for siderite in any of the measurements from the two oil samples (Figure 7.2) even though it was found in the core samples e.g. s63599 (Figure 7.4j). Siderite is typically authigenic in origin and has been observed in hydrocarbon reducing environments (Burton et al., 1993; Machel, 1995; Larrasoaña et al., 2007; Emmerton et al., 2012; Roberts, 2015). It is possible that siderite is precipitated in the reservoir and the grains are bigger than the minimum pore throat of sandstone (2µm) or that it acts as a cementing agent (Nealson, 2009; Roberts, 2015). Therefore, it is not extracted along with the oil.

7.4.2 Are the magnetic minerals authigenic, detrital or do they migrate?

Abubakar et al. (2015) showed that magnetic minerals are formed in a mature source rock. They concluded that the vast majority of these minerals were < 60 nm and have the potential

to be transported, though this may have been a result of the duration of the lab experiments; in nature the minerals might be larger.

The magnetic minerals in the core samples are likely to be a mixture of authigenic, detrital and transported minerals. It is difficult to determine which of these categories the magnetic minerals in the core samples belong to. The source rock in this area is a mudstone (Kimmeridge Clay) which typically has pore throat sizes ranging from 5 nm to 100 nm while most sandstone reservoirs typically have 2- 20 µm pore throat sizes (Nealson, 2009). Magnetic minerals that migrate with the oil from the source rock must be less than 100 nm as the oil also passes through layers of shale. This suggests that the < 100 nm grains which are responsible for the SP and SD FORC signatures observed in our samples, e.g. s63596, s72396 and s72403 (Figure 7.4 f, Figure 7.5 c and l) could have been transported from the source rock while the > 150 nm grains are either detrital or authigenic. The framboids, pyrite and siderite are authigenic, while the > 1 µm magnetite grains and titanohematite are most likely detrital. Similar observations have been made by Liu et al. (2006).

7.4.3 Unravelling the magnetic signature: End-member analysis.

For two of the wells in the area, the FORC diagrams were analysed using principal-component analysis (PCA) to help understand variance in FORC distributions as a function of depth and to help identify possible end-members (EM) (Harrison et al. (2018). To do this we used version 3.06 of the FORCinel software package (Harrison and Feinberg, 2008).

Ten samples from well 21/25-04 (Figure 7.4) were selected for FORC-PCA; 95% of the variance were defined by two EMs. EM1 accounted for 90% of the variance while EM2 accounts for 5% of the variance. The data is plotted in the principal component plane in Figure 7.7a. The two components identified (Figure 7.7c and b) are represented by thermally relaxing SD particles (EM1) and SD particles with multi-axial anisotropy or vortex behaviour (EM2). PSD behaviour is observed in both EMs. The depth variation of the two components identified are shown in Figure 7.7d. FORC-PCA for well 21/25-04 (Figure 7.7d) showed a noticeable increase in proportion of SD particles (EM2) at the GOC and OWC. This is also accompanied by a reduction in the proportion of thermally relaxing SD particles (EM1) at the GOC and an increase in proportion of EM1 at the OWC.

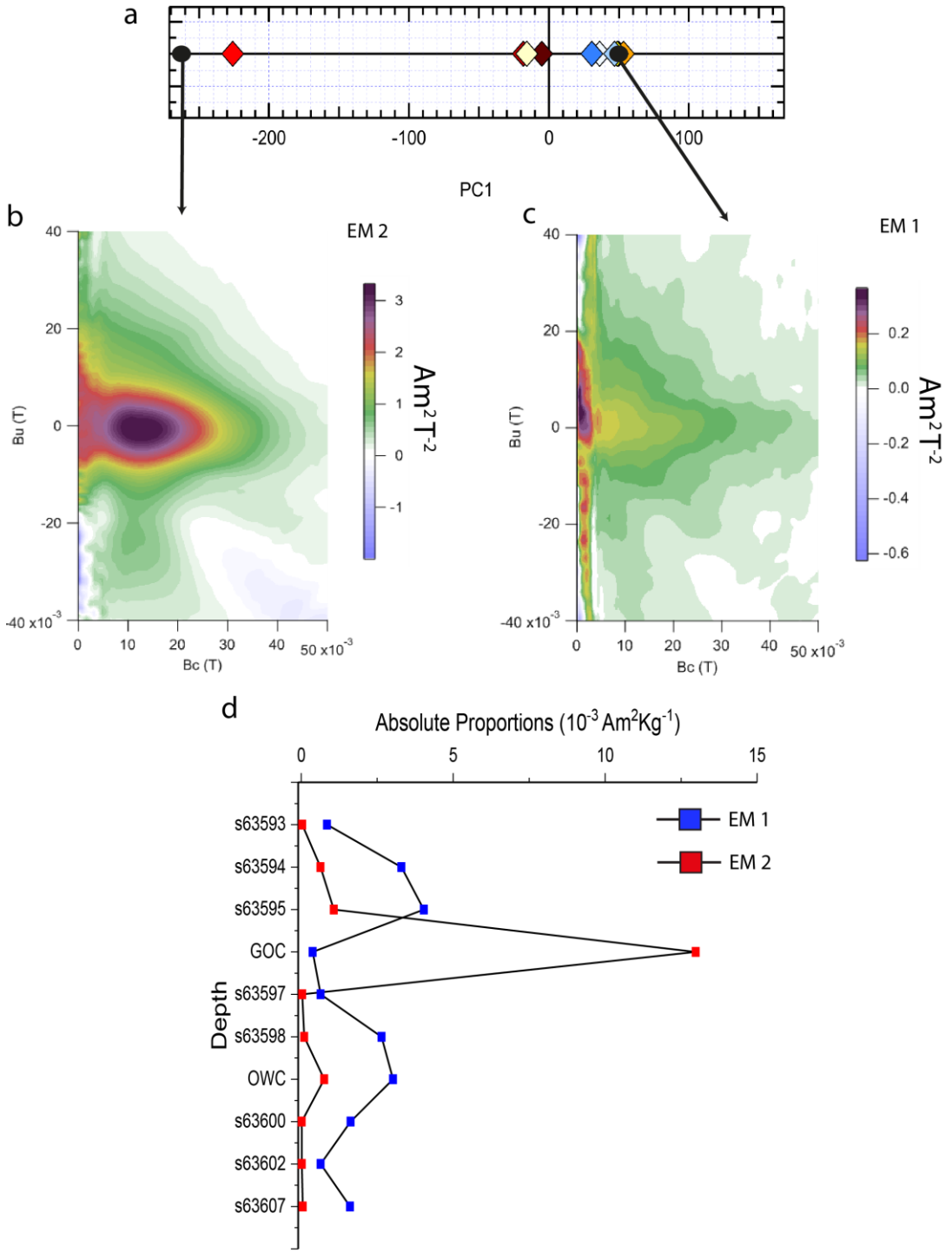


Figure 7.7. FORC-PCA for well 21/25-04. a) principal-component space, b) end member 2 represents SD particles with multi axial anisotropy, c) end member 1 represents thermally relaxing SD particles and d) proportions of EM1 and EM2 as a function of depth showing an increase in proportion of EM2 at the GOC and OWC. VARIFORC parameter (Egli, 2013) for FORC PCA smoothing are $s_{c,0}$ = 1.2, $s_{c,1}$ = 3, $s_{b,0}$ = 3, $s_{b,1}$ = 5, and λ_c = 1 λ_b = 1.

FORC-PCA was also carried out on 12 samples in well 21/25-A1, the variance in the data was defined by three EMs (Figure 7.8 a). For well 21/25-A1, EM1 accounts of 50% of the variance while EM2 accounts for 45% of the variance and EM3 accounts for 2% of the variance. The three components identified (Figure 7.8b-d) are represented by thermally relaxing SD

particles (EM1), thermally relaxing SD particles with multi-axial anisotropy or vortex behaviour (EM2) and stable SD greigite particles (EM3). The proportions of these end members are shown in Figure 11e. Peaks in the proportions of EM3 are found at the OWC and GOC (Fig, 11 e). The proportion of EM1 and EM2 decreases at the OWC. At the GOC, a drop in EM1 is accompanied by an increase in EM2. EM1 is more prominent below the GOC and OWC.

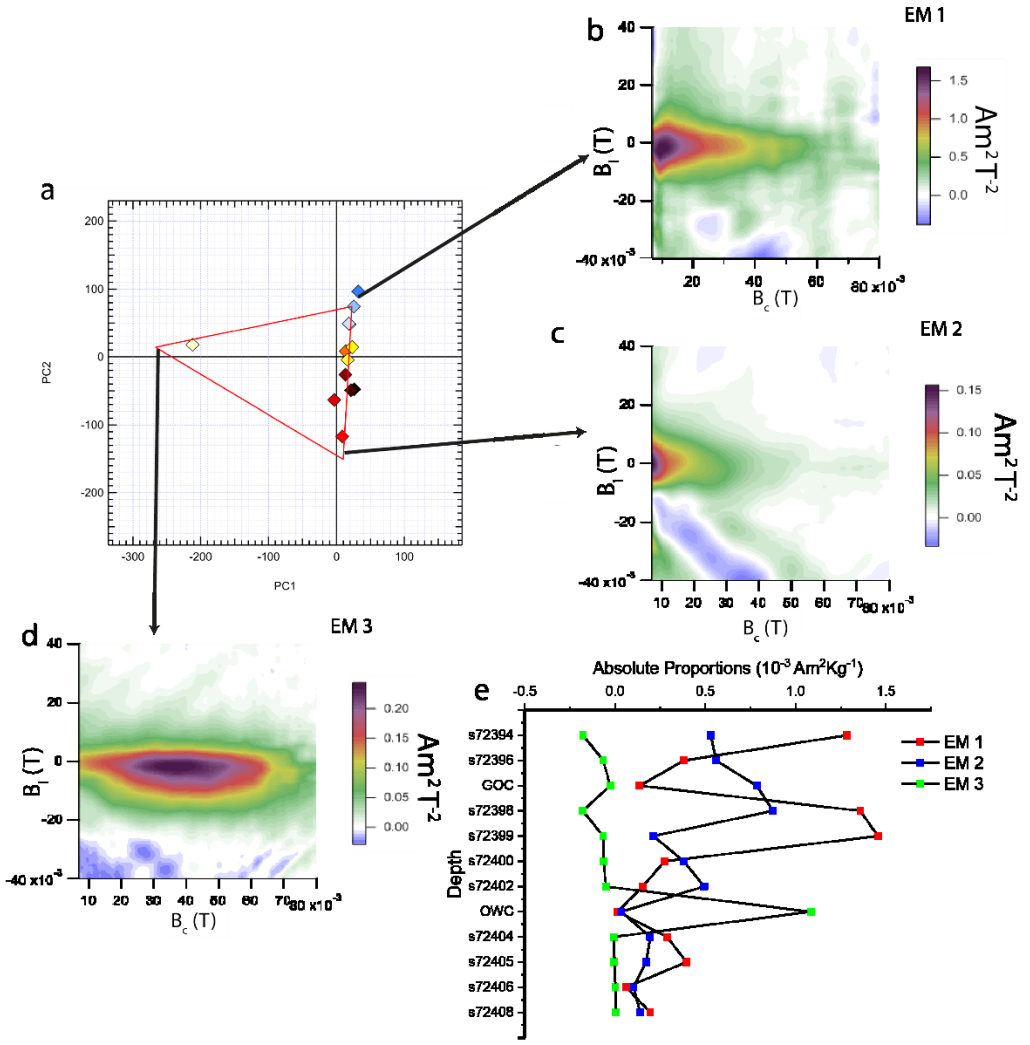


Figure 7.8. FORC-PCA for well 21/25-A1. a) principal component plane, b) end member 1- thermally relaxing SD particles, c) end member 2- thermally relaxing SD particles with multi axial anisotropy, d) end member 3- stable SD greigite particles and e) proportions of EM1, EM2 and EM3 as a function of depth showing an increase in proportion of EM3 at the GOC and OWC. VARIFORC parameter (Egli, 2013) for FORC PCA smoothing are $s_{c,0}$ = 1.2, $s_{c,1}$ = 3, $s_{b,0}$ = 3, $s_{b,1}$ = 5, and λ_c = 0 λ_b = 0.

These SD grains identified at the hydrocarbon contacts can either be magnetite as seen in well 21/25-04 (EM2, Figure 7.7b) or greigite as seen in well 21/25-A1 (EM3, Figure 7.8d). FORC-PCA aids in the interpretation of the data as it was able to pick out trends that go unnoticed in FORC diagrams if they were just compared by mere observation. For example,

the FORC diagram at the GOC for well 21/25/A1 showed no SD signal (Figure 7.5f) but the PCA was able to identify a relative increase in SD particle proportions at the GOC (Figure 7.8e). The proportion of these SD particles is roughly proportional to the M_s, M_{rs} and susceptibility; the highest M_s, M_{rs} and susceptibility values are noticed at the GOC in well 21/25-04 (Figure 7.3b and e). This also corresponds to the highest proportion of SD particles (Figure 7.7 d) and is consistent with the highest M_s, M_{rs} and susceptibility values measured at the OWC in well 21/25-A1 (Figure 7.3a and d), again showing the highest SD proportions (Figure 7.8e).

7.4.4 Magnetic enhancement at the hydrocarbon-fluid contacts

FORC-PCA demonstrates the increased abundance of stable SD material at the GOC and OWC (Figure 7.7d and Figure 7.8e). This increased abundance of larger SD grains at the hydrocarbon fluid contacts is most likely due to changes in diagenetic conditions. Here, I discuss two possible mechanisms for the enhancement: (1) thermodynamic, and (2) biological.

(1)Thermodyanamic model: Burton et al. (1993) calculated thermodynamic stability diagrams for iron bearing mineral at temperatures (50- 200 ^{o}C) and pressures (1-600 bar) similar to what is expected in Tay SM reservoirs. All the minerals identified in our samples are represented in the thermodynamic stability diagrams of Burton et al. (1993) apart from greigite (Figure 7.8l); at the time the importance of greigite was not appreciated, and was not included in their models. It is now thought, that the conditions in the reservoir can ensure the stability of greigite: A high concentration of reactive iron along with a low supply of organic carbon is needed to preserve greigite (Kao et al., 2004). Wells 21/25-04 and 21/25-A1 have API (American Petroleum Institute) gravity oils ranging from 40^{o} to 38^{o} API, which is indicative of sweet crude oil with low sulphur content, and has been argued to prevent greigite from altering to pyrite (Wenger et al., 2002; Roberts and Weaver, 2005). I suggest the thermodynamic stability diagrams in the reservoir include a region for greigite between the pyrrhotite and pyrite regions (Sack and Ebel, 2006). It is possible that subtle diagenetic changes in total dissolved sulphur, total dissolved iron or total dissolved inorganic carbon at the top of the oil column and at the oil-water interface could favour the precipitation of SD greigite or magnetite at the hydrocarbon contacts. A model for the formation of magnetic minerals in the reservoir is shown in Figure 7.9. SD grains are likely precipitated at the top of the oil column during early reservoir filling (Figure 7.9a). This continues until the spill point is

reached and a stable OWC is formed, which kick starts the formation of SD grains at the OWC (Figure 7.9b). This continues as long as the trapping mechanism is unperturbed by geological processes, e.g., regional tilting, halokinesis or compression. The reservoir receives a gas charge, the gas initially dissolves in the oil and the precipitation of SD grains continues at the top of the oil column and at the OWC (Figure 7.9c). A change in pressure, temperature or late gas charge results in the formation of a gas cap which displaces the oil and pushes the SD grains down the accumulation resulting in a concentration of SD grains at the GOC (Figure 7.9d).

(2) Biological mechanism: Biodegradation maybe responsible for the precipitation of SD magnetic minerals at the hydrocarbon contacts. Biodegradation of hydrocarbons can occur during early reservoir filling or at the oil water interface in temperatures less than 80 ^{o}C (Head et al., 2003; Larter et al., 2003). Depending on the bacteria, SD magnetite or greigite may be produced. Bacteria such as GS-15 can produce fined grained extracellular magnetite via oxidation of certain hydrocarbons in an anaerobic environment while sulphate reducing bacteria such as prokaryotes generate high concentrations of hydrogen sulphide (H_2S) which combines with iron to produce fine grained greigite (Lovley et al., 1987; Mann et al., 1990). Wells 21/25-04 and 21/25-A1 are interpreted to have been cooler than 80 ^{o}C at the onset of reservoir filling before rapid burial caused an increase in temperature (Figure 7.10). It is possible that limited biodegradation would have occurred at the top of the oil column during trap filling and at the OWC resulting in precipitation of SD magnetite or greigite at the contacts prior to burial.

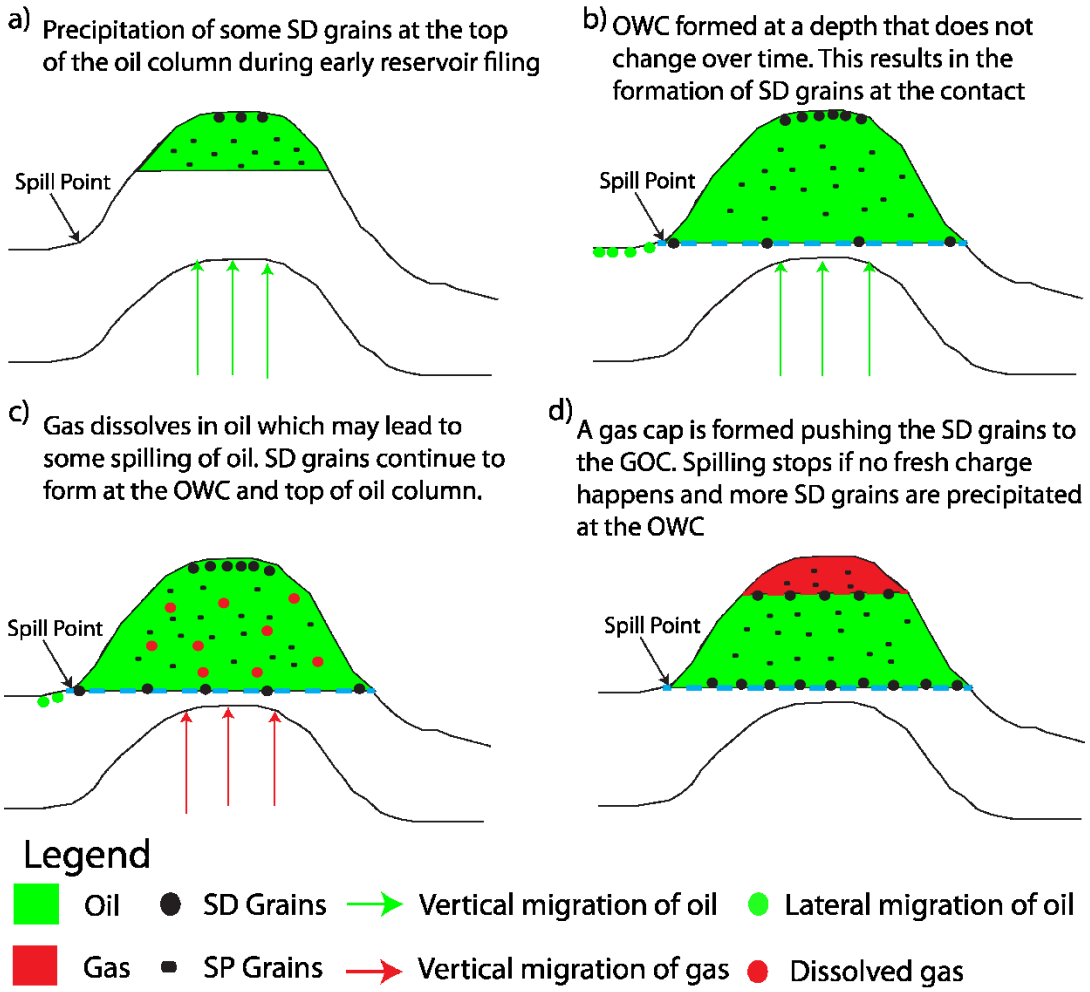


Figure 7.9 A schematic detailing the formation of SD grains at the GOC and OWC: a) formation of SD grains at the top of the oil during early reservoir filling, b) oil has filled to the spill point and the precipitation of SD grains occur at a stable OWC, c) the reservoir is charged with gas which dissolves in the oil, and the OWC is still stable which results in continued precipitation of SD grains, and d) a gas cap is formed displacing oil and the SD grains formed at the top of the oil column down to the GOC.

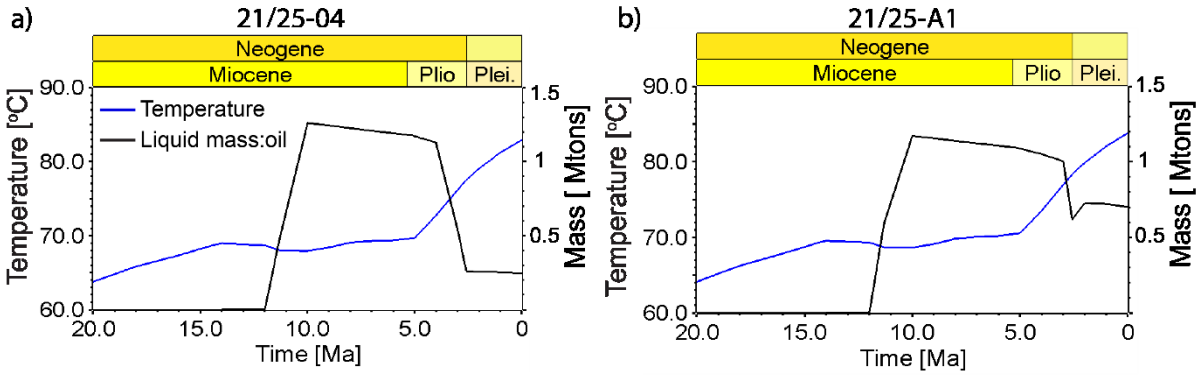


Figure 7.10. Plots of temperature (blue line) and liquid mass of oil (black line) vs time in the top Tay reservoir for wells a) 21/25-04 b) 21/25-A1. An increase in liquid mass suggests charging of the well while a reduction indicates loss of oil, because it has moved along the fill spill chain or it has leaked to the surface. Plots are extracts from the PetroMod model shown in Figure 4.9.

A schematic showing the variation of grain sizes of magnetic minerals precipitated due to the diagenetic environment caused by hydrocarbons is shown in Figure 7.11. This observation could be used to identify both the OWC and GOC when conventional methods are unreliable. Given that most of the magnetic minerals should remain in the host rock after hydrocarbon leakage, this technique has the potential to identify paleo-hydrocarbon contacts; either flat or tilted due to structuration. Identification of paleo-hydrocarbon contacts can provide information on the filling history of a series of fields within a basin which can help calibrate petroleum systems models.

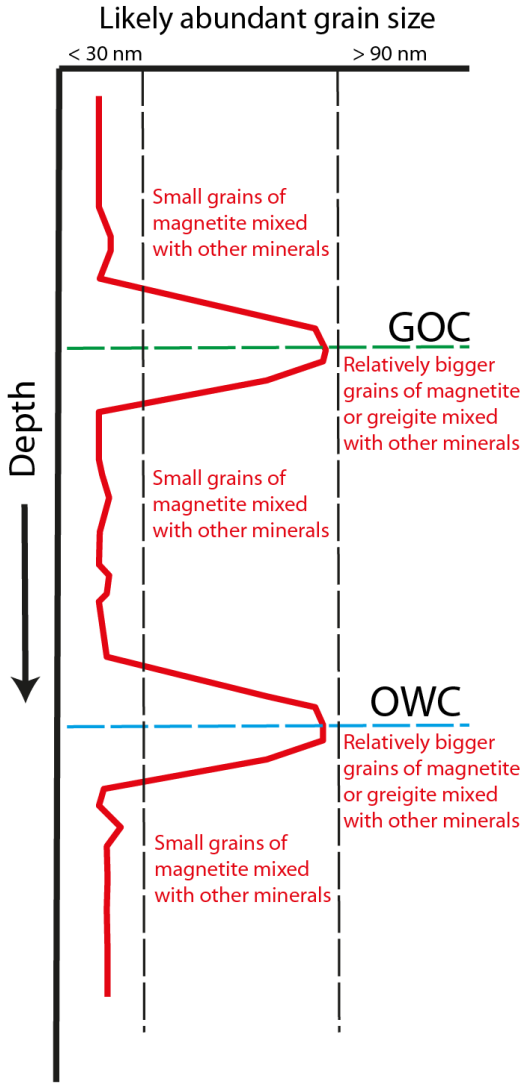


Figure 7.11. A schematic of the authigenic ferromagnetic magnetic mineral grain sizes as a function of depth within the reservoir.

7.5 Conclusions

A peak in measured magnetic susceptibility, saturation magnetisation and remanent saturation magnetisation values have been observed at both the GOC and OWC in Tay Formation oilfields (Figure 7.3). FORC-PCA showed these peaks to be due to an increase in the proportion of single domain magnetite or greigite at the hydrocarbon fluid contacts (Figure 7.7, 7.8 and 7.11). Subtle diagenetic changes at the top of the oil column and at the oil water interface are likely to be responsible for the observed anomalies at the GOC and OWC (Figure 7.9). Biodegradation during early filling of the reservoir and at the OWC are likely be the direct cause of, or enhancement of the signal at the hydrocarbon fluid contacts. This observation is of importance to the oil industry as the presence of paleo- hydrocarbon fluid contacts can be identified by carrying out quick magnetic susceptibility measurements on whole core samples from dry wells. This would give information on the filling history of a basin or could be used in the calibration of petroleum systems model in both frontier and mature basins. This new method can importantly be used on core samples from hydrocarbon wells where conventional methods failed to identify the GOC or OWC.

Chapter 8

Conclusions

The Western Central Graben of the North Sea has proven to be an excellent laboratory for this study. Good core coverage, available 3D seismic data and a relatively well constrained geology with reservoirs and one source system has led to the development of 2D and 3D petroleum system and basin models. These models and results from rock magnetic experiments on core samples have been used to identify a possible magnetic proxy for hydrocarbon migration and new ways to calibrate petroleum systems models.

8.1 Petroleum Systems and Basin Modelling

In Chapters 3 and 4, 2D and 3D petroleum systems modelling was carried out in the study area (Western Central Graben) to understand the processes responsible for oil migration from mature Jurassic source rocks in the east charging anticlinal traps in the Tertiary Tay Sandstone Member in the west.

Significant oil generation in the Kimmeridge Clay started in the Late Cretaceous consistent with earlier estimates made by Barnard and Bastow (1991). The model predicts the source rock (Kimmeridge Clay) to be immature over the majority of the study area and only mature for oil generation in the east and late mature for oil/early mature for gas at the far eastern edge of the study area. Expulsion of oil and gas occurred in the Oligocene in areas with transformation ratios (TR) greater than 20 %. The initial expulsion of oil was downward into the Fulmar FM in synclines followed by vertical migration from the anticlinal highs. Oil accumulated in the Fulmar FM exceeded capillary entry pressure which led to leakage of oil to the Tertiary Strata. Vertical migration into the Tertiary Strata is not restricted to the east as the Fulmar FM and marls of the Cromer Knoll Group can act as lateral carriers of oil to the west; areas of vertical migration into the Tertiary Strata in the west typically correspond to oil accumulations in the Fulmar FM.

Oil reached the Tertiary Strata during the Miocene, with the salt ridges and diapirs aiding vertical migration into the Forties and Tay SM (sandstone member). This study stresses the importance of the injectites for migration into the Tay SM; without the injectites no long-distance lateral migration is noticed in the Tay SM and most of the oil accumulates in the underlying Forties SM.

3D Modelling predicts vertical migration as the charging mechanism for the Gannet Field, a mixture of vertical and lateral migration as the charging mechanism for the Guillemot Field and lateral migration as the charging mechanism for the Fyne/Dandy and Pilot Fields. Long distance lateral migration of at least 30 km is needed to charge the Pilot Field in the far west of the study area supporting claims by Cayley (1987) and Kubala et al. (2003).

Temperature data show a progressive decrease in temperature along the migration pathway to the west (Gannet to pilot Field) correlating with a reduction in oil API gravity due to biodegradation. Note, biodegradation occurs at lower temperatures than expected because of the high formation water salinity which is reported to retard biodegradation (Shelton et al., 2016).

8.1.1 Future Research- Basin Modelling

The petroleum systems model presented in this thesis could be improved by including the Pilot Field in the far west and the extension of the oil kitchen to the east. Including the rest of the oil kitchen is needed for two reasons: (1) it would mean an initial TOC < 8 % may be enough to charge the Tertiary Strata, and (2) it would introduce gas to the model which may alter the location of oil accumulations and migration of oil. The model could also be improved by interpreting the top Fulmar FM as including this may alter the migration of oil into the Tertiary Strata.

Initial TOC has been assumed to be uniform, but this is not the case in nature where the TOC would vary laterally and vertically. To accurately model hydrocarbon generation and expulsion, the Schmoker (1981) formula could be used to convert gamma ray wireline log values to present day TOCs, which can be inverted to obtain initial TOCs (Hantschel and Kauerauf, 2009).Alternatively the Passey et al. (1990) method can be used to estimate present day TOC from Porosity and resistivity logs. Accurately determining initial TOC would lead to more a constrained filling of the traps and discrepancies where the model predicts oil accumulation in the Forties SM would likely not occur (Figure 4.9 b),

8.2 Identifying a Magnetic Proxy for Hydrocarbon Migration

Mineral magnetic techniques were used to characterise the core samples from the Tay SM in Chapter 5. Mass-dependent susceptibility, M_s, M_{rs}, and H_c were similar for the oil stained sandstone, water-wet sandstone, sandstone in the gas cap, but the siltstone samples had generally higher mass-dependent values. No consistent variation in M_s and M_{rs} was noticed along the migration pathway (E-W), but H_c increases from east to west suggesting the increasing presence of iron sulphides.

Low-temperature and high-temperature experiments were carried out to determine the magnetic mineralogy of the samples. Magnetite, maghemite, titanohematite, goethite, siderite, pyrite and greigite were observed in the samples from the hydrocarbon wells while magnetite, biogenic magnetite, titanohematite, goethite, siderite and possibly monoclinic pyrrhotite were observed in the dry wells. Comparing the oil-well samples to the dry-well samples suggest titanohematite and goethite are background signals (detrital), magnetite and siderite could be either a background or source signal (authigenic), while greigite is a source signal (Table 5.2). The presence of greigite in only the hydrocarbon wells is no surprise as the precipitation of iron sulphides has been previously linked to the presence of hydrocarbons (Reynolds et al., 1990; Reynolds et al., 1991; Costanzo-Alvarez et al., 2000; Mena and Walther, 2012). Superparamagnetic and single-domain grains have been assumed to be authigenic or transported from source, while larger pseudo-single-domain and multidomain grains are thought to be detrital in origin in agreement with Liu et al. (2006).

Synthesising all the results in Chapter 5 shows a siderite-rich signal in the east and an increase in the abundance of iron sulphides (predominantly greigite) along the migration pathway to the west. A zone of mixed iron sulphides and siderite signals was observed in the middle. Petroleum systems modelling and available geochemical reports were used to identify reasons for the change in magnetic mineralogy along the migration pathway. Two mechanisms are proposed: (1) an organic, and (2) an inorganic mechanism. The organic mechanism suggests biodegradation by anaerobic sulphate reducing bacteria would lead to the precipitation of greigite in the west. The inorganic mechanism suggests greigite grains are

precipitated during generation and expulsion of early mature oil which, progressively fills and spills traps forming oil accumulations in the west. The organic mechanism is the mostly likely scenario as a link between low API gravity oils and high greigite abundance is observed, but it is possible that the inorganic mechanism may enhance the abundant greigite signal observed in the west. These observations suggest rock magnetic techniques may be an effective and efficient method for identifying severity of biodegradation and/or determining oil maturity in core samples. This could be used to help calibrate petroleum systems models leading to a better understanding of hydrocarbon migration and improved exploration performance. Hydrocarbon seepages observed on seismic and predicted in the model in the east and west of the study area suggest high resolution aeromagnetic surveys may be a tool for tracking hydrocarbon migration.

8.2.1 Future Research- Magnetic Proxy

This study represents an important step towards identifying a magnetic proxy for hydrocarbon migration. However, some questions about the exact mechanism responsible for the change in mineralogy along the migration pathway have yet to be fully addressed. To verify and identify a universal proxy the following experiments can be carried out:

1. Scanning electron microscope observation identified greigite and pyrite to be the dominant iron sulphide phase in the oil stained samples. Other techniques such as synchrotron XRD or measuring H_c as a function of temperature (from room temperature down to 20 K) could be carried out to verify the presence or absence of monoclinic pyrrhotite or hexagonal pyrrhotite in the samples (Horng, 2018; Horng and Roberts, 2018a).
2. This study could be extended by including wells that were not sampled in the southern Tay channel of the study area. This channel is charged vertically in the east and laterally in the west with a reduction in API gravity to the east. The lateral migration occurs over a shorter distance than the one observed in this study and the channel is likely charged by the early mature oil. This would be ideal to test if the change in magnetic mineralogy is due to biodegradation.

3. Repeating this study in an area with long distance lateral migration, adequate oil maturity data and no biodegradation would test the inorganic mechanism proposed.
4. Repeating this study in an area sourced by a different kerogen type, e.g., lacustrine source rock responsible for the hydrocarbon charge in the Beatrice Field, may result in a different magnetic response.

8.3 A New Magnetic Technique for Identifying Hydrocarbon Fluid Contacts

In Chapter 7 peaks in measured mass-dependent susceptibility, M_s and M_{rs} were observed at the Gas-Oil Contact (GOC) and Oil-Water Contacts (OWC). These peaks have been attributed to the presence of SD grains or either magnetite or greigite at both contacts. Diagenetic changes at the top of the oil column and at the oil water interface is the likely mechanism for the precipitation of SD grains at the GOC and OWC. Alternatively, biodegradation at the top of the oil column during early reservoir filling or at the oil water interface could lead to the precipitation of extracellular or intracellular magnetite/greigite at the contacts. These observations suggest a quick susceptibility measurement can be carried out on both hydrocarbon bearing and dry well cores to identify the presence of a paleo- hydrocarbon fluid contact. This provides information on the filling history from basin to field scale, which could be used to calibrate petroleum systems model. This new method could also be used on core samples from hydrocarbon wells were conventional methods fail to identify the GOC or OWC. The observation that paleo fluid contacts existed in fields often tilted since charging would also assist in understanding fill/spill history of fields and future exploration potential for the spilt oil. Examples from the onshore UK would include Wytch Farm in Dorset and Welton in Lincolnshire (Bowman et al., 1993; Steventon and Bowman, 2016).

8.3.1 Future Research- Fluid Contacts

This experiment should be repeated in a well with no biodegradation to find out if this enhancement at the OWC and GWC is impacted by biodegradation. To further understand the reason for the precipitation of single-domain greigite or magnetite at the hydrocarbon fluid contacts, thermostability diagrams similar to the ones calculated by Burton et al. (1993)

should be generated to identify the conditions needed for single-domain magnetite or greigite to be stable at the top of the oil column and at the oil water interface. This should be tested in fields with a tilted OWC such as Welton and Wytch Farm. Both fields have 3D seismic data with an abundance of wells so this observation can be used to map the tilted OWC. Carbonate reservoirs should also be studied to see if this phenomenon is exclusive to clastic reservoirs.

List of References

Abubakar, R., Muxworthy, A. R., Sephton, M. A., Southern, P., Watson, J. S., Fraser, A. J., and Almeida, T. P., 2015, Formation of magnetic minerals in hydrocarbon-generation conditions: Marine and Petroleum Geology, v. 68, Part A, p. 509-519.doi:10.1016/j.marpetgeo.2015.10.003.

Abubakar, R., 2016, Mapping petroleum migration pathways using magnetics, geochemistry and seismic mapping. Case study: Wessex Basin, southern England, UK PhD: Imperial College London.

Ahmadi, Z., Sawyers, M., Kenyon-Roberts, S., Stanworth, C., Kugler, K., Kristensen, J., and Fugelli, E., 2003, Paleocene in The Millennium Atlas: Petroleum Geology of the Central and Northern North Sea. : Evans, D, Graham, C, Armour, A, and Bathurst, P (editors and co-ordinators). The Geological Society of London, p. 235-259. doi:10.1017/S0016756803218124.

Ahmed, T. H., 1989, Hydrocarbon phase behavior, Volume volume 2, Gulf Pub. Co., p. 36.doi:13960/t9283vf99.

Al-Balushi, A. N., Neumaier, M., Fraser, A. J., and Jackson, C. A.-L., 2016, The impact of the Messinian salinity crisis on the petroleum system of the Eastern Mediterranean: a critical assessment using 2D petroleum system modelling, v. 22, no. 4, p. 357-379.doi:10.1144/petgeo2016-054.

Aldana, M., Costanzo-Alvarez, V., and Díaz, M., 2003, Magnetic and mineralogical studies to characterize oil reservoirs in Venezuela: The Leading Edge, v. 22, no. 6, p. 526-529.doi:10.1190/1.1587674.

Allen, P. A., and Allen, J. R., 1991, Basin Analysis: Principles and Applications, Blackwell Pub,

Anderton, R., 1993, Sedimentation and basin evolution in the Paleogene of the Northern North Sea and Faeroe–Shetland basins: Geological Society, London, Petroleum Geology Conference series, v.4, no.1, p.31-31. doi:10.1144/0040031.

Armstrong, L., Ten Have, A., and Johnson, H., 1987, The geology of the Gannet fields, central North Sea, UK sector: Petroleum geology of north-west Europe: London, Graham and Trotman, p. 533-548

Aubourg, C., Pozzi, J. P., Janots, D., and Sahraoui, L., 2008, Imprinting chemical remanent magnetization in claystones at 95 °C: Earth and Planetary Science Letters, v. 272, no. 1–2, p. 172-180.doi:10.1016/j.epsl.2008.04.038.

Aubourg, C., and Pozzi, J.-P., 2010, Toward a new <250°C pyrrhotite–magnetite geothermometer for claystones: Earth and Planetary Science Letters, v. 294, no. 1, p. 47-57.doi:10.1016/j.epsl.2010.02.045.

Aubourg, C., Pozzi, J., and Kars, M., 2012, Burial, claystones remagnetization and some consequences for magnetostratigraphy: Geological Society, London v. 371, p. 181-188 doi:10.1144/SP371.4.

Baerg, J. R., 1991, Traveltime in media with linear velocity-depth functions: Consortium for Research in Elastic Wave Exploration Seismology Research Report, v. 27, p. 461-466

Banerjee, S. K., 1970, Origin of thermoremanence in goethite: Earth and Planetary Science Letters, v. 8, no. 3, p. 197-201.doi:10.1016/0012-821X(70)90175-5.

Baniasad, A., Rabbani, A., Sachse, V. F., Littke, R., Moallemi, S. A., and Soleimany, B., 2016, 2D basin modeling study of the Binak Trough, northwestern Persian Gulf, Iran: Marine and Petroleum Geology, v. 77, p. 882-897.doi:10.1016/j.marpetgeo.2016.07.025.

Banner, J., Chatellier, J., Feurer, J., and Neuhaus, D., 1992, Guillemot D: a successful appraisal through alternative interpretation: Geological Society, London, Special Publications, v. 67, no. 1, p. 129-149.doi:10.1144/GSL.SP.1992.067.01.06.

Barnard, P. C., and Bastow, M. A., 1991, Hydrocarbon generation, migration, alteration, entrapment and mixing in the Central and Northern North Sea: Geological Society, London, Special Publications,v.59,no.1,p.167-190. doi:10.1144/gsl.sp.1991.059.01.12.

Barton, P., and Wood, R., 1984, Tectonic evolution of the North Sea basin: crustal stretching and subsidence: Geophysical Journal of the Royal Astronomical Society, v. 79, no. 3, p. 987-1022.doi:10.1111/j.1365-246X.1984.tb02880.x.

Baur, F., and Katz, B., 2018, Some practical guidance for petroleum migration modeling: MarineandPetroleumGeology,v.93,p.409421.doi:/10.1016/j.marpetgeo.2018.03.003.

Benthien, R. H., and Elmore, R. D., 1987, Origin of magnetization in the Phosphoria Formation at Sheep Mountain, Wyoming: A possible relationship with hydrocarbons: Geophysical Research Letters, v. 14, no. 4, p. 323-326.doi:10.1029/GL014i004p00323.

Berner, R. A., 1981, A new geochemical classification of sedimentary environments: Journal of Sedimentary Research, v. 51, no. 2, p. 359-365.doi:10.1306/212F7C7F-2B24-11D7-8648000102C1865D.

-, 1984, Sedimentary pyrite formation: An update: Geochimica et Cosmochimica Acta, v. 48, no. 4, p. 605-615.doi:10.1016/0016-7037(84)90089-9.

Besnus, M., and Meyer, A., Nouvelles données expérimentales sur le magnétisme de la pyrrhotine naturelle, *in* Proceedings Proc. Int. Conf. Mag, Nottingham, 1964, Volume 20, p. 507-511

Bjørlykke, K., and Gran, K., 1994, Salinity variations in North Sea formation waters: implications for large-scale fluid movements: Marine and Petroleum Geology, v. 11, no. 1, p. 5-9.doi:10.1016/0264-8172(94)90003-5.

Bol'shakov, V. A., and Dolotov, A. V., 2011, The curie temperature of the natural greigite (a new interpretation of the thermomagnetic data): Doklady Earth Sciences, v. 440, no. 2, p. 1431-1434.doi:10.1134/s1028334x11100114.

Bose, S., Hochella, M. F., Gorby, Y. A., Kennedy, D. W., McCready, D. E., Madden, A. S., and Lower, B. H., 2009, Bioreduction of hematite nanoparticles by the dissimilatory iron reducing bacterium Shewanella oneidensis MR-1: Geochimica et Cosmochimica Acta, v. 73, no. 4, p. 962-976.doi:10.1016/j.gca.2008.11.031.

Bowman, M. B. J., McClure, N. M., and Wilkinson, D. W., 1993, Wytch Farm oilfield: deterministic reservoir description of the Triassic Sherwood Sandstone: Geological Society, London, Petroleum Geology Conference series, v. 4, no. 1, p. 1513-1517.doi:10.1144/0041513.

Brown, A., Davies, M., Nicholson, H., and Gane, B. R., 1999, The Machar Field, Unlocking the Potential of a North Sea Chalk Field, Offshore Europe Oil and Gas Exhibition and Conference: Aberdeen, United Kingdom, Society of Petroleum Engineers, p. 13.

Brown, D., Gross, G. A., and Sawicki, J. A., 1995, A review of the microbial geochemistry of banded iron-formations: The Canadian Mineralogist, v. 33, no. 6, p. 1321-1333

Burton, B. P., Robinson, P., McEnroe, S. A., Fabian, K., and Ballaran, T. B., 2008, A low-temperature phase diagram for ilmenite-rich compositions in the system Fe2O3-

FeTiO3: American Mineralogist, v. 93, no. 8-9, p. 1260-1272.doi:10.2138/am.2008.2690.

Burton, E. A., Machel, H. G., and Qi, J., 1993, Thermodynamic Constraints on Anomalous Magnetization in Shallow and Deep Hydrocarbon Seepage Environments: Applications of Paleomagnetism to Sedimentary Geology p. 193-207.doi:10.2110/pec.93.49.0193.

Butler, R. F., 1992, Paleomagnetism: Magnetic Domains to Geologic Terranes, Blackwell Scientific Publications.doi:10.3997/2214-4609.201801750

Cairanne, G., Aubourg, C., Pozzi, J.-P., Moreau, M.-G., Decamps, T., and Marolleau, G., 2004, Laboratory chemical remanent magnetization in a natural claystone: a record of two magnetic polarities: Geophysical Journal International, v. 159, no. 3, p. 909-916.doi:10.1111/j.1365-246X.2004.02439.x.

Cayley, G., 1987, Hydrocarbon migration in the central North Sea: Petroleum geology of north west Europe: London,Graham and Trotman, p. 549-555

Centrica,2013,RelinquishmentReport.https://itportal.decc.gov.uk/web_files/relinqs/P233.pdf.

Chang, L., Roberts, A. P., Tang, Y., Rainford, B. D., Muxworthy, A. R., and Chen, Q., 2008, Fundamental magnetic parameters from pure synthetic greigite (Fe3S4): Journal of Geophysical Research: Solid Earth, v. 113, no. B6, p. 1-20.doi:10.1029/2007JB005502.

Chang, L., Roberts, A. P., Rowan, C. J., Tang, Y., Pruner, P., Chen, Q., and Horng, C.-S., 2009, Low-temperature magnetic properties of greigite (Fe3S4): Geochemistry, Geophysics, Geosystems, v. 10, no. 1, p. 1-14.doi:10.1029/2008GC002276.

Chang, L., Roberts, A. P., Williams, W., Fitz Gerald, J. D., Larrasoaña, J. C., Jovane, L., and Muxworthy, A. R., 2012, Giant magnetofossils and hyperthermal events: Earth and Planetary Science Letters, v. 351-352, p. 258-269.doi:10.1016/j.epsl.2012.07.031.

Chang, L., Vasiliev, I., van Baak, C., Krijgsman, W., Dekkers, M. J., Roberts, A. P., Gerald, J. D. F., van Hoesel, A., and Winklhofer, M., 2014, Identification and environmental interpretation of diagenetic and biogenic greigite in sediments: A lesson from the Messinian Black Sea: Geochemistry, Geophysics, Geosystems, v. 15, no. 9, p. 3612-3627.doi:10.1002/2014GC005411.

Chang, L., Heslop, D., Roberts, A. P., Rey, D., and Mohamed, K. J., 2016, Discrimination of biogenic and detrital magnetite through a double Verwey transition temperature: Journal of Geophysical Research: Solid Earth, v. 121, no. 1, p. 3-14.doi:10.1002/2015JB012485.

Chaudhuri, S. K., Lack, J. G., and Coates, J. D., 2001, Biogenic Magnetite Formation through Anaerobic Biooxidation of Fe(II): Applied and Environmental Microbiology, v. 67, no. 6, p. 2844-2848.doi:10.1128/AEM.67.6.2844-2848.2001

Cornford, C., 1990, Source rocks and hydrocarbons of the North Sea. In: Glennie K. W. (ed) Introduction to the Petroleum Geology of the North Sea, Third edition. , Blackwell Scientific Publications, Oxford, p. 294-351.doi:10.1002/9781444313413.ch11.

Costanzo-Alvarez, V., Aldana, M., Aristeguieta, O., Marcano, M. C., and Aconcha, E., 2000, Study of magnetic contrasts in the Guafita oil field (south-western Venezuela): Physics and Chemistry of the Earth, Part A: Solid Earth and Geodesy, v. 25, no. 5, p. 437-445.doi:10.1016/S1464-1895(00)00068-5.

Darcy, H., 1856, Les fontaines publiques de la ville de Dijon: exposition et application, Victor Dalmont, 647 p

Day, R., Fuller, M., and Schmidt, V. A., 1977, Hysteresis properties of titanomagnetites: Grain-size and compositional dependence: Physics of the Earth and Planetary Interiors, v. 13, no. 4, p. 260-267.doi:10.1016/0031-9201(77)90108-X.

Dearing, J. A., Dann, R. J. L., Hay, K., Lees, J. A., Loveland, P. J., Maher, B. A., and O'Grady, K., 1996, Frequency-dependent susceptibility measurements of environmental materials: Geophysical Journal International, v. 124, no. 1, p. 228-240.doi:10.1111/j.1365-246X.1996.tb06366.x.

Dekkers, M. J., 1989a, Magnetic Properties of Natural Goethite—II. TRM Behaviour During Thermal and Alternating Field Demagnetization and Low-Temperature Treatment: Geophysical Journal International, v. 97, no. 2, p. 341-355.doi:10.1111/j.1365-246X.1989.tb00505.x.

-, 1989b, Magnetic properties of natural pyrrhotite. II. High- and low-temperature behaviour of Jrs and TRM as function of grain size: Physics of the Earth and Planetary Interiors, v. 57, no. 3, p. 266-283.doi:10.1016/0031-9201(89)90116-7.

Dekkers, M. J., Mattéi, J. L., Fillion, G., and Rochette, P., 1989, Grain-size dependence of the magnetic behavior of pyrrhotite during its low-temperature transition at 34 K: Geophysical Research Letters, v. 16, no. 8, p. 855-858.doi:10.1029/GL016i008p00855.

Dekkers, M. J., Passier, H. F., and Schoonen, M. A. A., 2000, Magnetic properties of hydrothermally synthesized greigite (Fe3S4)—II. High- and low-temperature characteristics: Geophysical Journal International, v. 141, no. 3, p. 809-819.doi:10.1046/j.1365-246x.2000.00129.x.

Den Hartog Jager, D., Giles, M. R., and Griffiths, G. R., 1993, Evolution of Paleogene submarine fans of the North Sea in space and time: Geological Society, London, Petroleum Geology Conference series, v. 4, p. 59-71.doi:10.1144/0040059.

Dennis, H., Baillie, J., Holt, T., and Wessel-Berg, D., 2000, Hydrodynamic activity and tilted oil-water contacts in the North Sea, *in* Ofstad, K., Kittilsen, J. E., and Alexander-Marrack, P., eds., Norwegian Petroleum Society Special Publications, Volume 9, Elsevier, p. 171-185.doi:10.1016/S0928-8937(00)80016-8.

di Primio, R., and Horsfield, B., 2006, From petroleum-type organofacies to hydrocarbon phase prediction: AAPG Bulletin, v. 90, no. 7, p. 1031-1058.doi:10.1306/02140605129.

Díaz, M., Aldana, M., Costanzo-Alvarez, V., Silva, P., and Pérez, A., 2000, EPR and magnetic susceptibility studies in well samples from some Venezuelan oil fields: Physics and Chemistry of the Earth, Part A: Solid Earth and Geodesy, v. 25, no. 5, p. 447-453.doi:10.1016/S1464-1895(00)00069-7.

Donovan, T. J., Hendricks, J. D., Roberts, A. A., and Eliason, P. T., 1984, Low-altitude aeromagnetic reconnaissance for petroleum in the Arctic National Wildlife Refuge, Alaska: Geophysics, v. 49, no. 8, p. 1338-1353.doi:10.1190/1.1441760.

Doré, A., Lundin, E., Jensen, L., Birkeland, Ø., Eliassen, P., and Fichler, C., 1999, Principal tectonic events in the evolution of the northwest European Atlantic margin: Geological society, London, petroleum geology conference series, v. 5, no. 1, p. 41-61.doi:10.1144/0050041.

Dunlop, D. J., 1981, The rock magnetism of fine particles: Physics of the Earth and Planetary Interiors, v. 26, no. 1, p. 1-26.doi:10.1016/0031-9201(81)90093-5.

Dunlop, D. J., and Özdemir, Ö., 1997, Rock Magnetism:Fundamentals and Frontier, Cambridge University Press.doi:10.1017/CBO9780511612794

Egli, R., 2013, VARIFORC: An optimized protocol for calculating non-regular first-order reversal curve (FORC) diagrams: Global and Planetary Change, v. 110, p. 302-320.doi:10.1016/j.gloplacha.2013.08.003.

Eldrett, J., Tripsanas, E., Davis, C., McKie, T., Vieira, M., Osterloff, P., and Sandison, T., 2015, Sedimentological evolution of Sele Formation deep-marine depositional systems of the Central North Sea: Geological Society, London, Special Publications, v. 403, no. 1, p. 63-98.doi:10.1144/sp403.9.

Ellwood, B. B., Balsam, W., Burkart, B., Long, G. J., and Buhl, M. L., 1986, Anomalous magnetic properties in rocks containing the mineral siderite: Paleomagnetic implications: Journal of Geophysical Research: Solid Earth, v. 91, no. B12, p. 12779-12790.doi:10.1029/JB091iB12p12779.

Ellwood, B. B., Chrzanowski, T. H., Hrouda, F., Long, G. J., and Buhl, M. L., 1988, Siderite formation in anoxic deep-sea sediments: A synergetic bacteria controlled process with improtant implications in paleomagnetism: Geology, v. 16, no. 11, p. 980-982.doi:10.1130/0091-7613(1988)016<0980:SFIADS>2.3.CO;2.

Elmore, R. D., Engel, M. H., Crawford, L., Nick, K., Imbus, S., and Sofer, Z., 1987, Evidence for a relationship between hydrocarbons and authigenic magnetite: Nature, v. 325, no. 6103, p. 428-430.doi:10.1038/325428a0.

Elmore, R. D., and Crawford, L., 1990, Remanence in authigenic magnetite: Testing the hydrocarbon-magnetite hypothesis: Journal of Geophysical Research: Solid Earth, v. 95, no. B4, p. 4539-4549.doi:10.1029/JB095iB04p04539.

Elmore, R. D., Imbus, S., Engel, M. H., and Fruit, D., 1993a, Hydrocarbons and magnetizations in magnetite: SEPM, v. No.49, p. 181-191.doi:10.2110/pec.93.49.0181.

Elmore, R. D., London, D., Bagley, D., Fruit, D., and Gao, G., 1993b, Remagnetization by basinal fluids: Testing the hypothesis in the Viola limestone, southern Oklahoma: J. Geophys. Res, v. 98, no. B4, p. 6237-6254.doi:10.1029/92JB02577.

Elmore, R. D., Kelley, J., Evans, M., and Lewchuk, M. T., 2001, Remagnetization and orogenic fluids: testing the hypothesis in the central Appalachians: Geophysical Journal International, v. 144, no. 3, p. 568-576.doi:10.1046/j.0956-540X.2000.01349.x.

Elmore, R. D., Muxworthy, A. R., and Aldana , M., 2012, Remagnetization and chemical alteration of sedimentary rocks: Geological Society, London, v. 371, p. 1–21.doi:10.1144/SP371.15.

Emmerton, S., Muxworthy, A. R., and Sephton, M. A., 2012, Magnetic characterization of oil sands at Osmington Mills and Mupe Bay, Wessex Basin, UK: Geological Society, London, Special Publications, v. 371, no. 1, p. 189-198.doi:10.1144/sp371.6.

Emmerton, S., Muxworthy, A. R., Sephton, M. A., Aldana, M., Costanzo-Alvarez, V., Bayona, G., and Williams, W., 2013, Correlating biodegradation to magnetization in oil bearing sedimentary rocks: Geochimica et Cosmochimica Acta, v. 112, p. 146-165.doi:10.1016/j.gca.2013.03.008.

Emmerton, S. A., 2013, Investigating the relationship between magnetisation and oil geochemistry PhD: Imperial College London, 329 p.

Erratt, D., Thomas, G. M., and Wall, G. R. T., 1999, The evolution of the Central North Sea Rift: Geological Society, London, Petroleum Geology Conference series, v. 5, p. 63-82.doi:10.1144/0050063.

Evans, M., and Heller, F., 2003, Environmental magnetism: principles and applications of enviromagnetics, Academic press, 1-299 p.doi:10.1002/jqs.858

Fisher, Q. J., and Knipe, R. J., 2001, The permeability of faults within siliciclastic petroleum reservoirs of the North Sea and Norwegian Continental Shelf: Marine and Petroleum Geology, v. 18, no. 10, p. 1063-1081.doi:10.1016/S0264-8172(01)00042-3.

Foote, R. S., 1984, Significance of near-surface magnetic anomalies: Unconventional Methods in Exploration for Petroleum and Natural Gas. Institute for Study of Earth and Man, Southern Methodist University, Dallas, p. 12-24.doi:10024495022.

Franke, C., Thiry, M., Gomez-Gras, D., Jelenska, M., Kadzialko-Hofmokl, M., Lagroix, F., Parcerisa, D., Spassov, S., Szuszkiewicz, A., and Turniak, K., Paleomagnetic age constrains and magnetomineralogic implications for the Triassic paleosurface in Europe, *in* Proceedings Geophysical Research Abstracts2010, Volume 12, p. 787-821

Fraser, S., Robinson, A., Johnson, H., Underhill, J., Kadolsky, D., Connell, R., Johannessen, P., and Ravnås, R., 2003, Upper Jurassic in The Millennium Atlas: Petroleum Geology of the Central and Northern North Sea. : Evans, D, Graham, C, Armour, A, and Bathurst, P (editors and co-ordinators).The Geological Society of London, p. 157-189.doi:10.1017/S0016756803218124.

Frederichs, T., von Dobeneck, T., Bleil, U., and Dekkers, M. J., 2003, Towards the identification of siderite, rhodochrosite, and vivianite in sediments by their low-temperature magnetic properties: Physics and Chemistry of the Earth, Parts A/B/C, v. 28, no. 16–19, p. 669-679.doi:10.1016/S1474-7065(03)00121-9.

Glennie, K., Higham, J., and Stemmerik, L., 2003, The Permian in The Millennium Atlas: petroleum geology of the central and northern North Sea: Evans, D, Graham, C, Armour, A, and Bathurst, P (editors and co-ordinators).The Geological Society of London, p. 91-103.doi:10.1017/S0016756803218124.

González, F., Aldana, M., Costanzo-Álvarez, V., Díaz, M., and Romero, I., 2002, An integrated rock magnetic and EPR study in soil samples from a hydrocarbon prospective area: Physics and Chemistry of the Earth, Parts A/B/C, v. 27, no. 25–31, p. 1311-1317.doi:10.1016/S1474-7065(02)00125-0.

Gowers, M. B., and Sæbøe, A., 1985, On the structural evolution of the Central Trough in the Norwegian and Danish sectors of the North Sea: Marine and Petroleum Geology, v. 2, no. 4, p. 298-318.doi:10.1016/0264-8172(85)90026-1.

Guyodo, Y., LaPara, T. M., Anschutz, A. J., Penn, R. L., Banerjee, S. K., Geiss, C. E., and Zanner, W., 2006, Rock magnetic, chemical and bacterial community analysis of a modern soil from Nebraska: Earth and Planetary Science Letters, v. 251, no. 1, p. 168-178.doi:10.1016/j.epsl.2006.09.005.

Guzmán, O., Costanzo-Álvarez, V., Aldana, M., and Díaz, M., 2011, Study of magnetic contrasts applied to hydrocarbon exploration in the Maturín Sub-Basin (eastern Venezuela): Studia Geophysica et Geodaetica, v. 55, no. 2, p. 359-376.doi:10.1007/s11200-011-0020-7.

Hancock, J. M., 1990, Cretaceous in Glennie K. W. (ed) Introduction to the Petroleum Geology of the North Sea, Third edition. , Blackwell Scientific Publications, Oxford, p. 255-270 doi:7097116.

Hantschel, T., Kauerauf, A. I., and Wygrala, B., 2000, Finite element analysis and ray tracing modeling of petroleum migration: Marine and Petroleum Geology, v. 17, no. 7, p. 815-820.doi:10.1016/S0264-8172(99)00061-6.

Hantschel, T., and Kauerauf, A. I., 2009, Fundamentals of basin and petroleum systems modeling, Springer Science & Business Media, 471 p.doi:10.1007/978-3-540-72318-9

Harding, R., and Huuse, M., 2015, Salt on the move: Multi stage evolution of salt diapirs in the Netherlands North Sea: Marine and Petroleum Geology, v. 61, p. 39-55.doi:10.1016/j.marpetgeo.2014.12.003.

Harrison, R. J., and Feinberg, J. M., 2008, FORCinel: An improved algorithm for calculating first-order reversal curve distributions using locally weighted regression smoothing: Geochemistry, Geophysics, Geosystems, v.9,no.5,p.1-11.doi:10.1029/2008GC001987.

Harrison, R. J., and Lascu, I., 2014, FORCulator: A micromagnetic tool for simulating first-order reversal curve diagrams: Geochemistry, Geophysics, Geosystems, v. 15, no. 12, p. 4671-4691.doi:10.1002/2014GC005582.

Harrison, R. J., Muraszko, J., Heslop, D., Lascu, I., Muxworthy, A. R., and Roberts, A. P., 2018, An Improved Algorithm for Unmixing First-Order Reversal Curve Diagrams Using Principal Component Analysis: Geochemistry, Geophysics, Geosystems, v. 19, no. 5, p. 1595-1610.doi:10.1029/2018GC007511.

Head, I. M., Jones, D. M., and Larter, S. R., 2003, Biological activity in the deep subsurface and the origin of heavy oil: Nature, v. 426, p. 344.doi:10.1038/nature02134.

Heslop, D., Roberts, A. P., and Chang, L., 2014, Characterizing magnetofossils from first-order reversal curve (FORC) central ridge signatures, v. 15, no. 6, p. 2170-2179.doi:10.1002/2014GC005291.

Hodgson, N. A., Farnsworth, J., and Fraser, A. J., 1992, Salt-related tectonics, sedimentation and hydrocarbon plays in the Central Graben, North Sea, UKCS: Geological Society, London, Special Publications, v. 67, no. 1, p. 31-63.doi:10.1144/gsl.sp.1992.067.01.03.

Horng, C.-S., and Roberts, A. P., 2006, Authigenic or detrital origin of pyrrhotite in sediments?: Resolving a paleomagnetic conundrum: Earth and Planetary Science Letters, v. 241, no. 3, p. 750-762.doi:10.1016/j.epsl.2005.11.008.

Horng, C.-S., 2018, Unusual Magnetic Properties of Sedimentary Pyrrhotite in Methane Seepage Sediments: Comparison With Metamorphic Pyrrhotite and Sedimentary Greigite: Journal of Geophysical Research: Solid Earth, no. 123, p. 4601-4617.doi:10.1002/2017JB015262.

Horng, C.-S., and Roberts, A. P., 2018a, The low-temperature Besnus magnetic transition: Signals due to monoclinic and hexagonal pyrrhotite: Geochemistry, Geophysics, Geosystems, v. 19, p. 1-20.doi:10.1029/2017GC007394.

Horng, C.-S., and Roberts, A. P., 2018b, The low-temperature Besnus magnetic transition: Signals due to monoclinic and hexagonal pyrrhotite: Geochemistry, Geophysics, Geosystems, v. 0, no. ja.doi:10.1029/2017GC007394.

Housen, B. A., Banerjee, S. K., and Moskowitz, B. M., 1996, Low-temperature magnetic properties of siderite and magnetite in marine sediments: Geophysical Research Letters, v. 23, no. 20, p. 2843-2846.doi:10.1029/96GL01197.

Hubbert, M. K., 1953, Entrapment of petroleum under hydrodynamic conditions: AAPG Bulletin, v. 37, no. 8, p. 1954-2026

Hubbert, M. K., 1956, Darcy's law and the field equations of the flow of underground fluids: Trans. AIME, v. 207, no. 7, p. 222-239.doi:10.1080/02626665709493062.

Hunger, S., and Benning, L. G., 2007, Greigite: a true intermediate on the polysulfide pathway to pyrite: Geochemical transactions, v. 8, p. 1-20.doi:10.1186/1467-4866-8-1.

Husmo, T., Hamar, G., Høiland, O., Johannessen, E., Rømuld, A., Spencer, A., and Titterton, R., 2003, Lower and Middle Jurassic in The Millennium Atlas: petroleum geology of the central and northern North Sea: Evans, D, Graham, C, Armour, A, and Bathurst, P

(editors and co-ordinators).(London: The Geological Society of London), p. 129–155.doi:10.1017/S0016756803218124.

Huuse, M., and Cartwright, J., 2004, Sandstone intrusions - Reservoirs and fluid conduits through sealing sequences, Proceedings of EAGE Conference: Faults and Top Seals: Montpellier, France, p. 1-10.

Huuse, M., Cartwright, J. A., Gras, R., and Hurst, A., 2005, Kilometre-scale sandstone intrusions in the Eocene of the Outer Moray Firth (UK North Sea): migration paths, reservoirs and potential drilling hazards: Petroleum Geology: North-West Europe and Global Perspectives—Proceedings of the 6th Petroleum Geology Conference.doi:10.1144/0061577.

Irwin, H., 1979, On an environmental model for the type Kimmeridge Clay: Nature 279, p. 819-820.doi:10.1038/279819a0.

Isaksen, G. H., 2004, Central North Sea hydrocarbon systems: Generation, migration, entrapment, and thermal degradation of oil and gas: AAPG bulletin, v. 88, no. 11, p. 1545-1572.doi:10.1306/06300403048.

Jackson, C. A.-L., 2007, The Geometry, distribution, and development of clastic injections in slope systems: Seismic examples from the Upper Cretaceous Kyrre Formation, Mly Slope, Norwegian Margin, in A. Hurst and J. Cartwright, eds., Sand injectites: Implications for hydrocarbon exploration and production: AAPG Memoir v. 87, p. 37-48.doi:10.1306/1209848M873254.

Jackson, C. A. L., Huuse, M., and Barber, G. P., 2011, Geometry of winglike clastic intrusions adjacent to a deep-water channel complex: Implications for hydrocarbon exploration and production: AAPG Bulletin, v. 95, no. 4, p. 559-584.doi:10.1306/09131009157.

Jacobs, I. S., 1963, Metamagnetism of Siderite (FeCO3): Journal of Applied Physics, v. 34, no. 4, p. 1106-1107.doi:10.1063/1.1729389

Jarvie, D. M., 2012, Shale resource systems for oil and gas: Part 2—Shale-oil resource systems, in J. A. Breyer, ed., Shale reservoirs—Giant resources for the 21st century: AAPG Memoir, v. 97, no. 69-87.doi:10.1306/13321447M973489.

Johnson, H. D., MacKay, T. A., and Stewart, D. J., 1986, The Fulmar Oil-field (Central North Sea): geological aspects of its discovery, appraisal and development: Marine and Petroleum Geology, v. 3, no. 2, p. 99-125.doi:10.1016/0264-8172(86)90023-1.

Johnson, R. J. E., Van Der Voo, R., and Lowrie, W., 1984, Paleomagnetism and late diagenesis of Jurassic carbonates from the Jura Mountains, Switzerland and France: GSA Bulletin, v. 95, no. 4, p. 478-488.doi:10.1130/0016-7606(1984)95.

Jones, E., Jones, R., Ebdon, C., Ewen, D., Milner, P., Plunkett, J., Hudson, G., Slater, P., Ross, J., and Kubala, M., 2003, Eocene in The millennium atlas: Petroleum geology of the central and northern North Sea: Evans, D, Graham, C, Armour, A, and Bathurst, P (editors and co-ordinators).The Geological Society of London, p. 261-278 doi:10.1017/S0016756803218124.

Kao, S.-J., Horng, C.-S., Roberts, A. P., and Liu, K.-K., 2004, Carbon–sulfur–iron relationships in sedimentary rocks from southwestern Taiwan: influence of geochemical environment on greigite and pyrrhotite formation: Chemical Geology, v. 203, no. 1, p. 153-168.doi:10.1016/j.chemgeo.2003.09.007.

Kars, M., Aubourg, C., Labaume, P., Berquó, T., and Cavailhes, T., 2014, Burial diagenesis of magnetic minerals: new insights from the Grès d'Annot transect (SE France): Minerals Engineering, v. 4, no. 3, p. 667-689.doi:10.3390/min4030667.

Kennedy, L. P., 1981, Self Reversed Thermoremanent Magnetization in a Late Brunhes Dacite Pumice: Journal of geomagnetism and geoelectricity, v. 33, no. 8, p. 429-448.doi:10.5636/jgg.33.429.

Kilgore, B., and Elmore, R. D., 1989, A study of the relationship between hydrocarbon migration and the precipitation of authigenic magnetic minerals in the Triassic Chugwater Formation, southern Montana: Geological Society of America Bulletin, v. 101, no. 10, p. 1280-1288.doi:10.1130/0016-7606(1989)101<1280:asotrb>2.3.co;2.

Kilhams, B., Hartley, A., Huuse, M., and Davis, C., 2012, Characterizing the Paleocene turbidites of the North Sea: the Mey Sandstone Member, Lista Formation, UK Central Graben: Petroleum Geoscience, v. 18, no. 3, p. 337-354.doi:10.1144/1354-079311-054.

Kind, J., Gehring, A. U., García-Rubio, I., Charilaou, M., Nowaczyk, N. R., and Löffler, J. F., 2013, Domain-wall dynamics in 4C pyrrhotite at low temperature: Geophysical Journal International, v. 195, no. 1, p. 192-199.doi:10.1093/gji/ggt262.

Knox, R., and Holloway, S., 1992, 1. Paleogene of the central and northern North Sea: In: Lithostratigraphic nomenclature of the UK North Sea. British Geological Survey, Nottingham, p. 1-127

Koša, E., 2007, Differential subsidence driving the formation of mounded stratigraphy in deep-water sediments; Palaeocene, central North Sea: Marine and Petroleum Geology, v. 24, no. 10, p. 632-652.doi:10.1016/j.marpetgeo.2007.04.001.

Kubala, M., Bastow, M., Thompson, S., Scotchman, I., and Oygard, K., 2003, Geothermal regime, petroleum generation and migration in The Millennium Atlas: Petroleum Geology of the Central and Northern North Sea. Geological Society, London: Evans, D, Graham, C, Armour, A, and Bathurst, P (editors and co-ordinators).(London: The Geological Society of London), p. 289-215.doi:10.1017/S0016756803218124.

Kuhn, O., Smith, S. W., Van Noort, K., and Loiseau, B., 2003, The Fulmar Field, Blocks 30/16, 30/11b, UK North Sea: Geological Society, London, Memoirs, v. 20, no. 1, p. 563-585.doi:10.1144/GSL.MEM.2003.020.01.46.

Larrasoaña, J. C., Roberts, A. P., Musgrave, R. J., Gràcia, E., Piñero, E., Vega, M., and Martínez-Ruiz, F., 2007, Diagenetic formation of greigite and pyrrhotite in gas hydrate marine sedimentary systems: Earth and Planetary Science Letters, v. 261, no. 3, p. 350-366.doi:10.1016/j.epsl.2007.06.032.

Larter, S., Wilhelms, A., Head, I., Koopmans, M., Aplin, A., Di Primio, R., Zwach, C., Erdmann, M., and Telnaes, N., 2003, The controls on the composition of biodegraded oils in the deep subsurface—part 1: biodegradation rates in petroleum reservoirs: Organic Geochemistry, v. 34, no. 4, p. 601-613.doi:10.1016/S0146-6380(02)00240-1.

Larter, S., and di Primio, R., 2005, Effects of biodegradation on oil and gas field PVT properties and the origin of oil rimmed gas accumulations: Organic Geochemistry, v. 36, no. 2, p. 299-310.doi:10.1016/j.orggeochem.2004.07.015.

Lascu, I., J., H. R., Li, Y., Muraszko, J. R., Channell, J. E. T., Piotrowski, A. M., and Hodell, D. A., 2015, Magnetic unmixing of first-order reversal curve diagrams using principal component analysis: Geochemistry, Geophysics, Geosystems, v. 16, no. 9, p. 2900-2915.doi:10.1002/2015GC005909.

Lascu, I., Einsle, J. F., Ball, M. R., and Harrison, R. J., 2018, The Vortex State in Geologic Materials: A Micromagnetic Perspective: Journal of Geophysical Research: Solid Earth, no. 123, p. 1-20.doi:10.1029/2018JB015909.

Leach, D. L., Bradley, D., Lewchuk, M. T., Symons, D. T., de Marsily, G., and Brannon, J. J. M. D., 2001, Mississippi Valley-type lead–zinc deposits through geological time: implications from recent age-dating research, v. 36, no. 8, p. 711-740.doi:10.1007/s001260100208.

Leeder, M. R., 1983, Lithospheric stretching and North Sea Jurassic clastic sourcelands: Nature, v. 305, no. 5934, p. 510-514.doi:10.1038/305510a0.

Lewchuk, M. T., and Symons, D. T. A., 1995, Age and duration of Mississippi Valley–type ore-mineralizing events: Geology, v. 23, no. 3, p. 233-236.10.1130/0091-7613(1995)023<0233:AADOMV>2.3.CO;2 %J Geology.

Lin, Q., Wang, J., Algeo, T. J., Sun, F., and Lin, R., 2016, Enhanced framboidal pyrite formation related to anaerobic oxidation of methane in the sulfate-methane transition zone of the northern South China Sea: Marine Geology, v. 379, p. 100-108.doi:10.1016/j.margeo.2016.05.016.

Liu, Q., Liu, Q., Chan, L., Yang, T., Xia, X., and Cheng, T., 2006, Magnetic enhancement caused by hydrocarbon migration in the Mawangmiao Oil Field, Jianghan Basin, China: Journal of Petroleum Science and Engineering, v. 53, no. 1–2, p. 25-33.doi:10.1016/j.petrol.2006.01.010.

Loucks, V., and Elmore, R. D., 1986, Absolute dating of dedolomitization and the origin of magnetization in the Cambrian Morgan Creek Limestone, central Texas: GSA Bulletin, v. 97, no. 4, p. 486-496.doi:10.1130/0016-7606(1986)97.

Lovley, D. R., Stolz, J. F., Nord, G. L., and Phillips, E. J., 1987, Anaerobic production of magnetite by a dissimilatory iron-reducing microorganism: Nature, v. 330, no. 6145, p. 252-254.doi:10.1038/330252a0.

Lynn, G. J., Bacciotti, M., Van Bergen, P. F., and Gray, K. R., 2015, Depositional controls on fluid flow in the Gannet A Field: Geological Society, London, Special Publications, v. 403, no. 1, p. 381-398.doi:10.1144/sp403.2.

Machel, H. G., and Burton, E. A., 1991a, Chemical and microbial processes causing anomalous magnetization in environments affected by hydrocarbon seepage: Geophysics, v. 56, no. 5, p. 598-605.doi:10.1190/1.1443076.

-, 1991b, Causes and spatial distribution of anomalous magnetization in hydrocarbon seepage environments (1): AAPG Bulletin, v. 75, no. 12, p. 1864-1876.doi:10.1306/0C9B2A5B-1710-11D7-8645000102C1865D.

Machel, H. G., 1995, Magnetic mineral assemblages and magnetic contrasts in diagenetic environments with implications for studies of palaeomagnetism, hydrocarbon migration and exploration: Geological Society, London, Special Publications, v. 98, no. 1, p. 9-29.doi:10.1144/GSL.SP.1995.098.01.02.

Magot, M., Ollivier, B., Patel, B. K. C., and Leeuwenhoek, J. A. v., 2000, Microbiology of petroleum reservoirs, v. 77, no. 2, p. 103-116.doi:10.1023/a:1002434330514.

Mallon, A. J., and Swarbrick, R. E., 2008a, Diagenetic characteristics of low permeability, non-reservoir chalks from the Central North Sea: Marine and Petroleum Geology, v. 25, no. 10, p. 1097-1108.doi:10.1016/j.marpetgeo.2007.12.001.

Mallon, A. J., and Swarbrick, R. E., 2008b, How should permeability be measured in fine-grained lithologies? Evidence from the chalk: Geofluids, v. 8, no. 1, p. 35-45.doi:10.1111/j.1468-8123.2007.00203.x.

Mann, S., Sparks, N. H. C., Frankel, R. B., Bazylinski, D. A., and Jannasch, H. W., 1990, Biomineralization of ferrimagnetic greigite (Fe3S4) and iron pyrite (FeS2) in a magnetotactic bacterium: Nature, v. 343, p. 258.doi:10.1038/343258a0.

Marshall, M., and Cox, A., 1972, Magnetic changes in pillow basalt due to sea floor weathering, v. 77, no. 32, p. 6459-6469.doi:10.1029/JB077i032p06459.

McCabe, C., Sassen, R., and Saffer, B., 1987, Occurrence of secondary magnetite within biodegraded oil: Geology, v. 15, no. 1, p. 7-10.doi:10.1130/0091-7613(1987)15.

McCabe, C., and Elmore, R. D., 1989, The occurrence and origin of Late Paleozoic remagnetization in the sedimentary rocks of North America: Reviews of Geophysics, v. 27, no. 4, p. 471-494.doi:10.1029/RG027i004p00471.

McCabe, C., Jackson, M., and Saffer, B., 1989, Regional patterns of magnetite authigenesis in the Appalachian Basin: Implications for the mechanism of Late Paleozoic remagnetization: J. Geophys. Res, v. 94, no. B8, p. 10429-10443.doi:10.1029/JB094iB08p10429.

McKie, T., Rose, P. T. S., Hartley, A. J., Jones, D. W., and Armstrong, T. L., 2015, Tertiary deep-marine reservoirs of the North Sea region: an introduction: Geological Society, London, Special Publications, v. 403, no. 1, p. 1-16.doi:10.1144/sp403.12.

Megson, J., and Hardman, R., 2001, Exploration for and development of hydrocarbons in the Chalk of the North Sea: a low permeability system: Petroleum Geoscience, v. 7, no. 1, p. 3-12.doi:10.1144/petgeo.7.1.3.

Mena, M., and Walther, A. M., 2012, Rock magnetic properties of drill cutting from a hydrocarbon exploratory well and their relationship to hydrocarbon presence and petrophysical properties: Geological Society, London, Special Publications, v. 371, p. 217-228.doi:10.1144/sp371.14.

Miiller, D. E., Holba, A. G., and Hughes, W. B., 1987, Effects of Biodegradation on Crude Oils, *in* Meyer, R. F., ed., Exploration for Heavy Crude Oil and Natural Bitumen, American Association of Petroleum Geologists, p. 1-9.doi:10/1306/St25468C11.

Moreau, M. G., Ader, M., and Enkin, R. J., 2005, The magnetization of clay-rich rocks in sedimentary basins: low-temperature experimental formation of magnetic carriers in natural samples: Earth and Planetary Science Letters, v. 230, no. 1–2, p. 193-210.doi:10.1016/j.epsl.2004.11.013.

Morin, F. J., 1950, Magnetic Susceptibility of αFe2O3 and αFe2O3 with Added Titanium: Physical Review, v. 78, no. 6, p. 819-820.doi:10.1103/PhysRev.78.819.2.

Morse, J. W., Millero, F. J., Cornwell, J. C., and Rickard, D., 1987, The chemistry of the hydrogen sulfide and iron sulfide systems in natural waters: Earth-Science Reviews, v. 24, no. 1, p. 1-42.doi:10.1016/0012-8252(87)90046-8.

Mudge, D. C., and Copestake, P., 1992, Revised Lower Palaeogene lithostratigraphy for the Outer Moray Firth, North Sea: Marine and Petroleum Geology, v. 9, no. 1, p. 53-69.doi:10.1016/0264-8172(92)90004-X.

Muxworthy, A., Williams, W., and Heslop, D., 2004, Influence of magnetostatic interactions on first-order-reversal-curve (FORC) diagrams: a micromagnetic approach: Geophysical Journal International, v. 158, no. 3, p. 888-897.doi:10.1111/j.1365-246X.2004.02358.x

Muxworthy, A. R., 2001, Effect of grain interactions on the frequency dependence of magnetic susceptibility: Geophysical Journal International, v. 144, no. 2, p. 441-447.doi:10.1046/j.1365-246x.2001.00342.x.

Mycroft, J. R., Nesbitt, H. W., and Pratt, A. R., 1995, X-ray photoelectron and Auger electron spectroscopy of air-oxidized pyrrhotite: Distribution of oxidized species with depth: Geochimica et Cosmochimica Acta, v. 59, no. 4, p. 721-733.doi:10.1016/0016-7037(94)00352-M.

Nagy, L., 2016, Parallelisation of Micromagnetic Simulations [PhD: University of Edinburgh, 149 p.

Nealson, P. H., 2009, Pore-throat sizes in sandstones, tight sandstones, and shales: AAPG Bulletin, v. 93, no. 3, p. 329-340.doi:10.1306/10240808059.

Oakman, C. D., 2005, The Lower Cretaceous plays of the Central and Northern North Sea: Atlantean drainage models and enhanced hydrocarbon potential Petroleum Geology: North-West Europe and Global Perspectives, *in* Doré, A. G., and Vining, B. A., eds., Proceedings of the 6th Petroleum Geology Conference, Volume 6: London, Geological Society of London, p. 187-198.

Özdemir, Ö., and Dunlop, D. J., 2010, Hallmarks of maghemitization in low-temperature remanence cycling of partially oxidized magnetite nanoparticles: Journal of Geophysical Research: Solid Earth, v. 115, no. B2, p. 1-10.doi:10.1029/2009JB006756.

Ozima, M., Funaki, M., Hamada, N., Aramaki, S., and Fujii, T., 1992, Self-Reversal of Thermo-Remanent Magnetization in Pyroclastics from the 1991 Eruption of Mt. Pinatubo, Philippines: Journal of geomagnetism and geoelectricity, v. 44, no. 10, p. 979-984.doi:10.5636/jgg.44.979.

Pan, Y., Zhu, R., Banerjee, S. K., Gill, J., and Williams, Q., 2000, Rock magnetic properties related to thermal treatment of siderite: Behavior and interpretation: Journal of Geophysical Research: Solid Earth, v. 105, no. B1, p. 783-794.doi:10.1029/1999JB900358.

Pannalal, S. J., Symons, D. T. A., and Sangster, D. F., 2004, Paleomagnetic dating of Upper Mississippi Valley zinc–lead mineralisation, WI, USA: Journal of Applied Geophysics, v. 56, no. 2, p. 135-153.doi:10.1016/j.jappgeo.2004.04.006.

Parsley, A., 1990, North Sea hydrocarbon plays in Glennie K. W. (ed) Introduction to the Petroleum Geology of the North Sea, Third edition. , Blackwell Scientific Publications, Oxford, p. 362-386

Passey, Q., Creaney, S., Kulla, J., Moretti, F., and Stroud, J., 1990, A practical model for organic richness from porosity and resistivity logs: AAPG bulletin, v. 74, no. 12, p. 1777-1794

Pepper, A. S., and Corvi, P. J., 1995, Simple kinetic models of petroleum formation. Part I: oil and gas generation from kerogen: Marine and Petroleum Geology, v. 12, no. 3, p. 291-319.doi:10.1016/0264-8172(95)98381-E.

Pike, C. R., Roberts, A. P., and Verosub, K. L., 1999, Characterizing interactions in fine magnetic particle systems using first order reversal curves, v. 85, no. 9, p. 6660-6667.doi:10.1063/1.370176.

Rattey, R. P., and Hayward, A. B., 1993, Sequence stratigraphy of a failed rift system: the Middle Jurassic to Early Cretaceous basin evolution of the Central and Northern North Sea: Geological Society, London, Petroleum Geology Conference series, v. 4, p. 215-249.doi:10.1144/0040215.

Reynolds, R. L., Fishman, N. S., Wanty, R. B., and Goldhaber, M. B., 1990, Iron sulfide minerals at Cement oil field, Oklahoma: Implications for magnetic detection of oil fields:

Geological Society of America Bulletin, v. 102, no. 3, p. 368-380.doi:10.1130/0016-7606(1990)102<0368:ISMACO>2.3.CO;2.

Reynolds, R. L., Fishman, N. S., and Hudson, M. R., 1991, Sources of aeromagnetic anomalies over Cement oil field (Oklahoma), Simpson oil field (Alaska), and the Wyoming-Idaho-Utah thrust belt: GEOPHYSICS, v. 56, no. 5, p. 606-617.doi:10.1190/1.1443077.

Reynolds, R. L., Tuttle, M. L., Rice, C. A., Fishman, N. S., Karachewski, J. A., and Sherman, D. M., 1994, Magnetization and geochemistry of greigite-bearing Cretaceous strata, North Slope Basin, Alaska: American Journal of Science, v. 294, no. 4, p. 485-528.doi:10.2475/ajs.294.4.485.

Rider, M. H., and Kennedy, M., 1996, The Geological Interpretation of Well Logs, Rider-French.doi:10.1017/S0016756800016162

Roberts, A. P., Pike, C. R., and Verosub, K. L., 2000, First-order reversal curve diagrams: A new tool for characterizing the magnetic properties of natural samples: Journal of Geophysical Research: Solid Earth (1978–2012), v. 105, no. B12, p. 28461-28475.doi:10.1029/2000JB900326

Roberts, A. P., and Weaver, R., 2005, Multiple mechanisms of remagnetization involving sedimentary greigite (Fe3S4): Earth and Planetary Science Letters, v. 231, no. 3, p. 263-277.doi:10.1016/j.epsl.2004.11.024.

Roberts, A. P., Liu, Q., Rowan, C. J., Chang, L., Carvallo, C., Torrent, J., and Horng, C.-S., 2006, Characterization of hematite (α-Fe2O3), goethite (α-FeOOH), greigite (Fe3S4), and pyrrhotite (Fe7S8) using first-order reversal curve diagrams: Journal of Geophysical Research: Solid Earth, v. 111, no. B12, p. 1-16.doi:10.1029/2006JB004715.

Roberts, A. P., Chang, L., Rowan, C. J., Horng, C.-S., and Florindo, F., 2011, Magnetic properties of sedimentary greigite (Fe3S4): An update: Reviews of Geophysics, v. 49, p. 1-46.doi:10.1029/2010RG000336.

Roberts, A. P., Chang, L., Heslop, D., Florindo, F., and Larrasoaña, J. C., 2012, Searching for single domain magnetite in the “pseudo-single-domain” sedimentary haystack: Implications of biogenic magnetite preservation for sediment magnetism and relative paleointensity determinations, v. 117, no. B8.doi:10.1029/2012JB009412.

Roberts, A. P., Heslop, D., Zhao, X., and Pike, C. R., 2014, Understanding fine magnetic particle systems through use of first-order reversal curve diagrams: Reviews of Geophysics, v. 52, no. 4, p. 557-602.doi:10.1002/2014RG000462.

Roberts, A. P., 2015, Magnetic mineral diagenesis: Earth-Science Reviews, v. 151, p. 1-47.doi:10.1016/j.earscirev.2015.09.010.

Roberts, A. P., Almeida, T. P., Church, N. S., Harrison, R. J., Heslop, D., Li, Y., Li, J., Muxworthy, A. R., Williams, W., and Zhao, X., 2017, Resolving the Origin of Pseudo-Single Domain Magnetic Behavior: Journal of Geophysical Research: Solid Earth, v. 122, no. 12, p. 9534-9558.doi:10.1002/2017JB014860.

Roberts, A. P., Tauxe, L., Heslop, D., Zhao, X., and Jiang, Z., 2018a, A Critical Appraisal of the “Day” Diagram, v. 123, no. 4, p. 2618-2644.doi:10.1002/2017JB015247.

Roberts, A. P., Zhao, X., Harrison, R. J., Heslop, D., Muxworthy, A. R., Rowan, C. J., Larrasoaña, J.-C., and Florindo, F., 2018b, Signatures of Reductive Magnetic Mineral Diagenesis From Unmixing of First-Order Reversal Curves: Journal of Geophysical Research: Solid Earth, v. 123, no. 6, p. 4500-4522.doi:10.1029/2018JB015706.

Robertson, J., 2013, Overpressure and Lateral Drainage in the Palaeogene Strata of the Central North Sea, Durham theses, Durham University. Available at Durham E-Theses Online:http://etheses.dur.ac.uk/9452/.

Rochette, P., and Fillion, G., 1989, Field and temperature behavior of remanence in synthetic goethite: Paleomagnetic implications: Geophysical Research Letters, v. 16, no. 8, p. 851-854.doi:10.1029/GL016i008p00851.

Rochette, P., Fillion, G., Mattéi, J.-L., and Dekkers, M. J., 1990, Magnetic transition at 30–34 Kelvin in pyrrhotite: insight into a widespread occurrence of this mineral in rocks: Earth and Planetary Science Letters, v. 98, no. 3, p. 319-328.doi:10.1016/0012-821X(90)90034-U.

Rodrigues Duran, E., di Primio, R., Anka, Z., Stoddart, D., and Horsfield, B., 2013, 3D-basin modelling of the Hammerfest Basin (southwestern Barents Sea): A quantitative assessment of petroleum generation, migration and leakage: Marine and Petroleum Geology, v. 45, p. 281-303.doi:10.1016/j.marpetgeo.2013.04.023.

Rowland, S. J., and Revill, A. T., 1995, Chapter 5 Chromatography in petroleum geochemistry, *in* Adlard, E. R., ed., Journal of Chromatography Library, Volume 56, Elsevier, p. 127-141.doi:10.1016/S0301-4770(08)61284-1.

Rudmin, M., Roberts, A. P., Horng, C.-S., Mazurov, A., Savinova, O., Ruban, A., Kashapov, R., and Veklich, M., 2018, Ferrimagnetic Iron Sulfide Formation and Methane Venting Across the Paleocene-Eocene Thermal Maximum in Shallow Marine Sediments, Ancient West Siberian Sea: Geochemistry, Geophysics, Geosystems, v. 19, no. 1, p. 21-42.doi:10.1002/2017GC007208.

Sack, R. O., and Ebel, D. S., 2006, Thermochemistry of Sulfide Mineral Solutions: Reviews in Mineralogy and Geochemistry, v. 61, no. 1, p. 265-364.doi:10.2138/rmg.2006.61.6.

Saffer, B., and McCabe, C., 1992, Further studies of carbonate remagnetization in the northern Appalachian Basin: J. Geophys. Res, v. 97, no. B4, p. 4331-4348.doi:10.1029/91JB02746.

Sakaguchi, T., Burgess, J. G., and Matsunaga, T., 1993, Magnetite formation by a sulphate-reducing bacterium: Nature, v. 365, no. 6441, p. 47-49.doi:10.1038/365047a0.

Saunders, D., and Terry, S., 1985, Onshore exploration using the new geochemistry and geomorphology: Oil & Gas Journal, v. 83, no. 37, p. 126-130.doi.:10024495046.

Schmoker, J. W., 1981, Determination of organic-matter content of Appalachian Devonian shales from gamma-ray logs: American Association of Petroleum Geologists Bulletin, v. 65, no. 7, p. 1285-1298.doi:10.1306/03B5949A-16D1-11D7-8645000102C1865D.

Schneider, F., and Wolf, S., 2000, Quantitative HC potential evaluation using 3D basin modelling: application to Franklin structure, Central Graben, North Sea, UK: Marine and Petroleum Geology, v. 17, no. 7, p. 841-856.doi:10.1016/S0264-8172(99)00060-4.

Scotchman, I. C., Carr, A. D., and Astin, T. R., 2000, Porefluid evolution in the Kimmeridge Clay Formation of the UK Outer Moray Firth: Journal of Geochemical Exploration, v. 69-70, p. 53-57.doi:10.1016/S0375-6742(00)00044-3.

Shelton, J. L., McIntosh, J. C., Warwick, P. D., and McCray, J. E., 2016, Impact of formation water geochemistry and crude oil biodegradation on microbial methanogenesis: Organic Geochemistry, v. 98, p. 105-117.doi:10.1016/j.orggeochem.2016.05.008.

Sprain, C. J., Feinberg, J. M., Renne, P. R., and Jackson, M., 2016, Importance of titanohematite in detrital remanent magnetizations of strata spanning the Cretaceous-Paleogene

boundary, Hell Creek region, Montana: Geochemistry, Geophysics, Geosystems, v. 17, no. 3, p. 660-678.doi:10.1002/2015GC006191.

Stamatakos, J., Hirt, A. M., and Lowrie, W., 1996, The age and timing of folding in the central Appalachians from paleomagnetic results: Geological Society of America Bulletin, v. 108, no. 7, p. 815-829.doi:10.1130/0016-7606(1996)108.

Steventon, J., and Bowman, M., 2016, An assessment of the Upper Succession and the related secondary reservoirs in the Welton Field, onshore UK: Geological Society, London, Petroleum Geology Conference series, v. 8, no. 1, p. 595-609.doi:10.1144/pgc8.22.

Stewart, S. A., 1999, Seismic interpretation of circular geological structures: Petroleum Geoscience, v. 5, no. 3, p. 273-285.doi:10.1144/petgeo.5.3.273.

Surlyk, F., Dons, T., Clausen, C., and Higham, J., 2003, Upper cretaceous in The Millennium Atlas: Petroleum Geology of the Central and Northern North Sea.: Evans, D, Graham, C, Armour, A, and Bathurst, P (editors and co-ordinators). The Geological Society of London, p. 213-233.doi:10.1017/S0016756803218124.

Swanson, B. W., Munro, R., Sanders, M. W., and Kelly, R., 2000, Application of Novel Technologies in the Design and Engineering of Synthetic-Based Mud Used to Drill and Complete Horizontal, High-Temperature/High-Pressure Wells in the Central North Sea, Marnock Field, IADC/SPE Drilling Conference: New Orleans, Louisiana, Society of Petroleum Engineers, p. 20.

Sylta, Ø., 2004, Hydrocarbon migration modelling and exploration risk: J. Parnell Dokumentet er del av serien Geological Society special publication, v. 144, p. 221-232.doi:/11250/235827.

Symons, D. T. A., Sangster, D. F., and Leach, D. L., 1996, Paleomagnetic Dating of Mississippi Valley-Type Pb-Zn-Ba Deposits

Carbonate-Hosted Lead-Zinc Deposits: 75th Anniversary Volume, *in* Sangster, D. F., ed., Volume 4, Society of Economic Geologists, p. 0.doi:10.5382/sp.04.38.

Symons, D. T. A., Coveney, R. M., Jr., Sangster, D. F., and Pannalal, S. J., 2005, Paleomagnetism of Late Paleozoic Strata and Mineralization in the Tri-State Lead-Zinc Ore District: Economic Geology, v. 100, no. 2, p. 295-309.doi:10.2113/gsecongeo.100.2.295

Tauxe, L., 2010, Essentials of paleomagnetism, Univ. of California Press.doi:10.1029/2011EO190008

Tissot, B., and Welte, D., 1984, Petroleum formation and occurrence: a new approach to oil and gas exploration, Springer Science & Business Media, 1-538 p

Tyson, R., 2006, Peters, K. E., Walters, C. C. & Moldowan, J. M. 2006. The Biomarker Guide. Volume 1: Biomarkers and Isotopes in the Environment and Human History. Volume 2: Biomarkers and Isotopes in Petroleum Exploration and Earth History. Second Edition. (First edition published 1993 by Chevron Texaco.) 1132 pp. total. Cambridge, New York, Melborne: Cambridge University Press. Price £150.00, US $250.00 (hard covers). ISBN 0 521 83763 4: Geological Magazine, v. 143, no. 2, p. 249-250.doi:10.1017/S0016756806212056.

Underhill, J. R., and Partington, M. A., 1993, Jurassic thermal doming and deflation in the North Sea: implications of the sequence stratigraphic evidence: Geological Society, London, Petroleum Geology Conference series, v. 4, p. 337-345.doi:10.1144/0040337.

Vail, P., Mitchum Jr, R., and Thompson III, S., 1977, Seismic Stratigraphy and Global Changes of Sea Level: Part 4. Global Cycles of Relative Changes of Sea Level.: Section 2.

Application of Seismic Reflection Configuration to Stratigraphic Interpretation, p. 83-97.doi:10.1016/0031-0182(86)90004-0.

Valdez-Grijalva, M. A., Muxworthy, A. R., Williams, W., Ó Conbhuí, P., Nagy, L., Roberts, A. P., and Heslop, D., 2018a, Magnetic vortex effects on first-order reversal curve (FORC) diagrams for greigite dispersions: Earth and Planetary Science Letters, v. 501, p. 103-111.doi:10.1016/j.epsl.2018.08.027.

Valdez-Grijalva, M. A., Nagy, L., Muxworthy, A. R., Williams, W., and Fabian, K., 2018b, The magnetic structure and palaeomagnetic recording fidelity of sub-micron greigite (Fe3S4): Earth and Planetary Science Letters, v. 483, p. 76-89.doi:10.1016/j.epsl.2017.12.015.

Valdez-Grijalva, M. A., and Muxworthy, A. R., 2019, First-order reversal curve (FORC) diagrams of nanomagnets with cubic magnetocrystalline anisotropy: A numerical approach: Journal of Magnetism and Magnetic Materials, v. 471, p. 359-364.doi:10.1016/j.jmmm.2018.09.086.

van Dalfsen, W., Doornenbal, J. C., Dortland, S., and Gunnink, J. L., 2006, A comprehensive seismic velocity model for the Netherlands based on lithostratigraphic layers: Netherlands Journal of Geosciences - Geologie en Mijnbouw, v. 85, no. 4, p. 277-292.doi:10.1017/S0016774600023076.

Vasseur, G., Luo, X., Yan, J., Loggia, D., Toussaint, R., and Schmittbuhl, J., 2013, Flow regime associated with vertical secondary migration: Marine and Petroleum Geology, v. 45, p. 150-158.doi:10.1016/j.marpetgeo.2013.04.020.

Verwey, E. J. W., 1939, Electronic Conduction of Magnetite (Fe3O4) and its Transition Point at Low Temperatures: Nature, v. 144, p. 327.doi:10.1038/144327b0.

Volkman, J. K., Alexander, R., Kagi, R. I., and Woodhouse, G. W., 1983, Demethylated hopanes in crude oils and their applications in petroleum geochemistry: Geochimica et Cosmochimica Acta, v. 47, no. 4, p. 785-794.doi:10.1016/0016-7037(83)90112-6.

Weaver, R., Roberts, A. P., and Barker, A. J., 2002, A late diagenetic (syn-folding) magnetization carried by pyrrhotite: implications for paleomagnetic studies from magnetic iron sulphide-bearing sediments: Earth and Planetary Science Letters, v. 200, no. 3, p. 371-386.doi:10.1016/S0012-821X(02)00652-0.

Welte, D. H., and Yalçin, M. N., 1988, Basin modelling—A new comprehensive method in petroleum geology: Organic Geochemistry, v. 13, no. 1, p. 141-151.doi:10.1016/0146-6380(88)90034-4.

Wenger, L. M., Davis, C. L., and Isaksen, G. H., 2002, Multiple Controls on Petroleum Biodegradation and Impact on Oil Quality, v. 5, no. 05, p. 375-383.doi:10.2118/80168-PA.

White, N., and Lovell, B., 1997, Measuring the pulse of a plume with the sedimentary record: Nature, v. 387, no. 6636, p. 888-891.doi:10.1038/43151.

Wilhelms, A., and Larter, S., 2004, Shaken but not always stirred. Impact of petroleum charge mixing on reservoir geochemistry, v. 237, no. 1, p. 27-35.doi:10.1144/GSL.SP.2004.237.01.03.

Wilkin, R. T., and Barnes, H. L., 1997, Formation processes of framboidal pyrite: Geochimica et Cosmochimica Acta, v. 61, no. 2, p. 323-339.doi:10.1016/S0016-7037(96)00320-1.

Wilkinson, D., and Willemsen, J. F., 1983, Invasion percolation: a new form of percolation theory: Journal of Physics A: Mathematical and General, v. 16, no. 14, p. 3365.doi:10.1088/0305-4470/16/14/028/meta.

Wilkinson, J. J., Muxworthy, A. R., Vowles, K., and Niocaill, C. M., 2017, Regional remagnetization of Irish Carboniferous carbonates dates Variscan orogenesis, not Zn-Pb mineralization: Geology, v. 45, no. 8, p. 747-750.doi:10.1130/G39032.1

Wygrala, B., 1989, Integrated study of an oil field in the southern Po basin, northern Italy [PhD]: University of Cologne.

Yilmaz, Ö., 2001, Seismic Data Analysis: Processing, Inversion, and Interpretation of Seismic Data, Society of Exploration Geophysicists, 2065 p.doi:10.1190/1.9781560801580

Zhan, Z.-W., Zou, Y.-R., Pan, C., Sun, J.-N., Lin, X.-H., and Peng, P. a., 2017, Origin, charging, and mixing of crude oils in the Tahe oilfield, Tarim Basin, China: Organic Geochemistry, v. 108, p. 18-29.doi:10.1016/j.orggeochem.2017.03.007.

Zhao, X., Heslop, D., and Roberts, A. P., 2015, A protocol for variable-resolution first-order reversal curve measurements: Geochemistry, Geophysics, Geosystems, v. 16, p. 1364–1377.doi:10.1002/2014GC005680

Appendices

Appendix 1: Seismic Interpretation

1.1 Acquisition and processing parameters

1.2 Synthetics used for interpretation

1.3 Time and depth maps of interpreted surfaces

1.4 Time depth relationships for wells used in the velocity model

Appendix 2: Seismic Interpretation

2.1 Lithology Logs

Appendix 3: Rock Magnetic Experiments

3.1 Hysteresis, FORC, LT experiment and Susceptibility vs Temperature

Appendix 4: Hysteresis parameters

4.1 Measured hysteresis parameters for all wells

Appendix 1

1.1 Acquisition and processing parameters

Acquisition Parameter for TGS's data:

Survey:	**Catcher North DT WiBand Polarcus Adira (Ph 1)/Nadia (Ph 2)**
Acq. contractor:	Polarcus
Field data format:	SEGD
Tape format:	3592
Vessel:	Phase 1 - Adira Phase 2 - Nadia
Line prefix:	MC1203
Year of survey:	2012/2013
Sample rate:	2ms
Record length:	6200ms
Source:	Dual
Source volume:	Phase 1 - 2940cu/in Phase 2 - 2380 cu/in
Source separation:	37.5m
Source depth:	6m
Gun delay:	200ms
SP interval	18.75m (flip/flop)
Cables:	8 x 480 groups
Cable length:	6000m
Cable depth:	15m
Cable separation:	75m
Near channels:	1, 481, 961, 1441, 1921, 2401, 2881, 3361,
Group interval:	12.5m
Nominal fold:	80
Nominal nr offset:	100m
Acquired bin size:	18.75m x 6.25m
Swaths	1 – 2

Processing steps:

- 2Hz 36dB/Oct Debias filter was applied to the data.
- ION-GXT's proprietary "SWDenoise" was used to attenuate acquisition noise.
- A 2-Pass, targeted radial filter was used to eliminate linear noise associated with acquisition.
- A half-Nyquist spatial anti-alias filter was applied with an NMO wrap.
- Short period multiples were effectively removed by short period multiple attenuation (SPMA) followed by a shot domain Tau-P deconvolution prior to velocity picking. A

delayed-start 2DSRME (LP2DSRME) was also applied, to tackle the longer period surface multiple.

- Manual semblance picking on a 1km x 1km grid was performed; the resulting velocity model was used to drive the subsequent Radon demultiple process and as an input for velocity model building.
- ION-GXT's proprietary WiBand™ broadband deghosting technology was applied to the data to remove the source and receiver ghost components from the acquisition scheme. Following this a further Radial filter was applied to the data to target residual low-frequency linear noise.
- Velocity model was built using 2 passes of dense RMO auto-picking and incorporated the top chalk horizon to preserve sharp velocity contrast where necessary in the model.
- Amplitude preserving Pre-Stack Kirchhoff isotropic Time migration was carried out using the final velocity model.
- Residual multiples were attenuated in the post-processing by means of ION-GXT's High Resolution Radon process.
- Residual noise attenuation was then undertaken in the CPD domain, with SWNA and Radfilt.
- The final post-processed gathers was muted with a 36 degree outer and 3 degree inner mute, before stacking.

Information of the acquisition and initial processing is unavailable as this was not done by PGS. Two datasets were merged and QC'd by PGS the processing steps are described below:

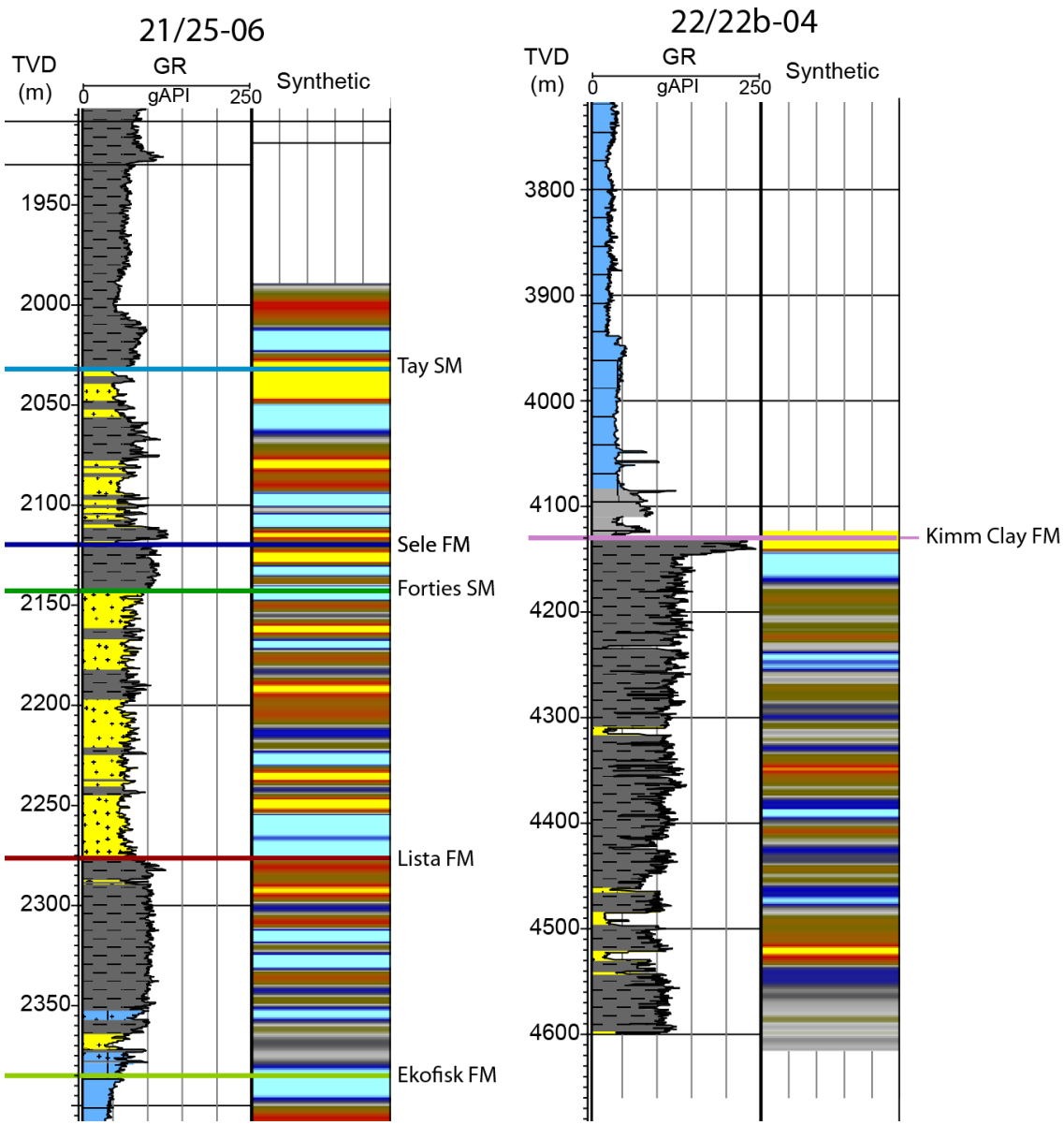
- The data was interpolated to a 12.5 m x 12.5 m bin, then re-binned on to the master grid using a sinc interpolator. The re-binned data was then QC'd by PGS's interactive holoSeis™ QC.
- A mild fx-decon or TVF was applied to remove noise in the deeper section while K-notch filter was applied to clean up any shallow jitter.
- Static analysis was carried out by cross-correlation of an overlapping region, with the lowest possible static being chosen.
- Amplitude analysis was carried out on overlapping data by picking a wide range of CDPs to sample the amplitude range as broadly as possible. The amplitudes were measured over sliding gates of 400 ms, with an overlap of 200 ms, over a time window of 200 - 5500

ms. A match gain curve was then derived by using a 5-point polynomial smoothing filter. Additionally, an AGC scalar was applied using a 1000 ms gate on output to SEG-Y.

- Phase rotations were then checked using full orthogonal interactive holoSeis™ QC.
- Pre-Stack Kirchhoff Time migration was carried out using a derived velocity model.
- Final merge quality was checked by interactive holoSeis™ QC, with spatial QC performed by output of UKOOA datasets and time slices.

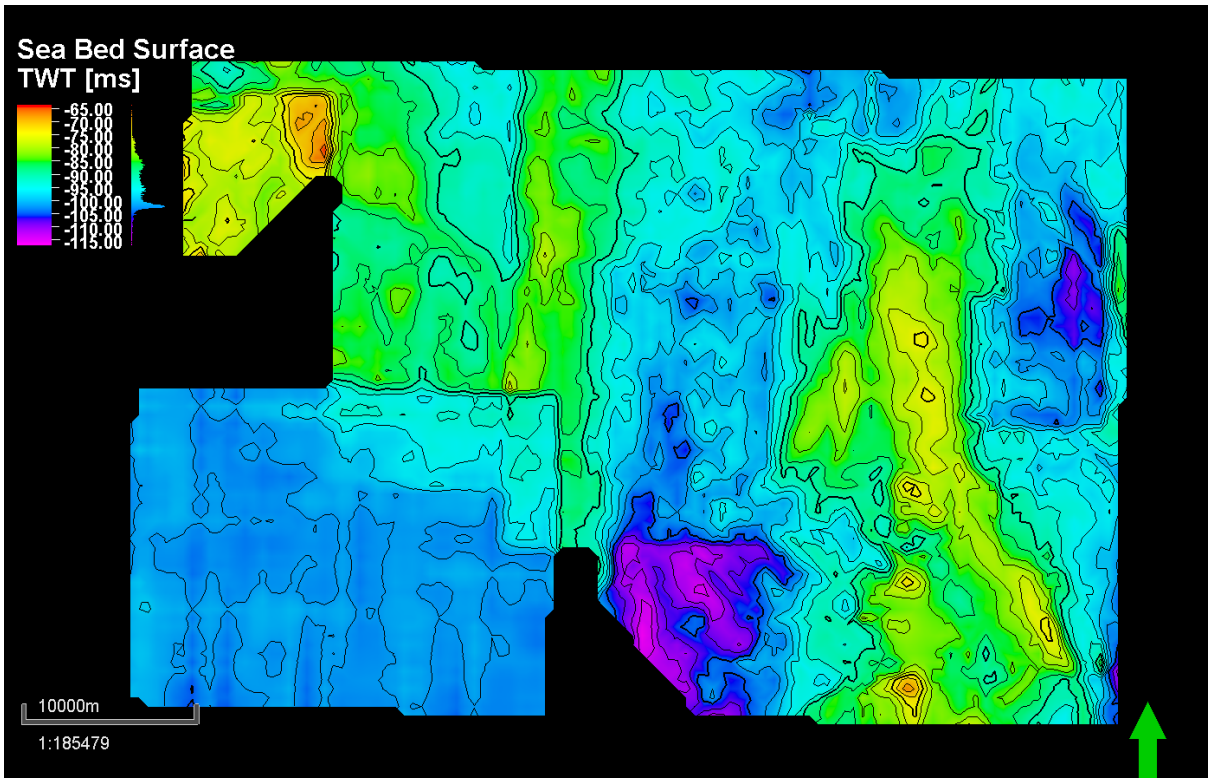
1.2 Synthetics used for interpretation

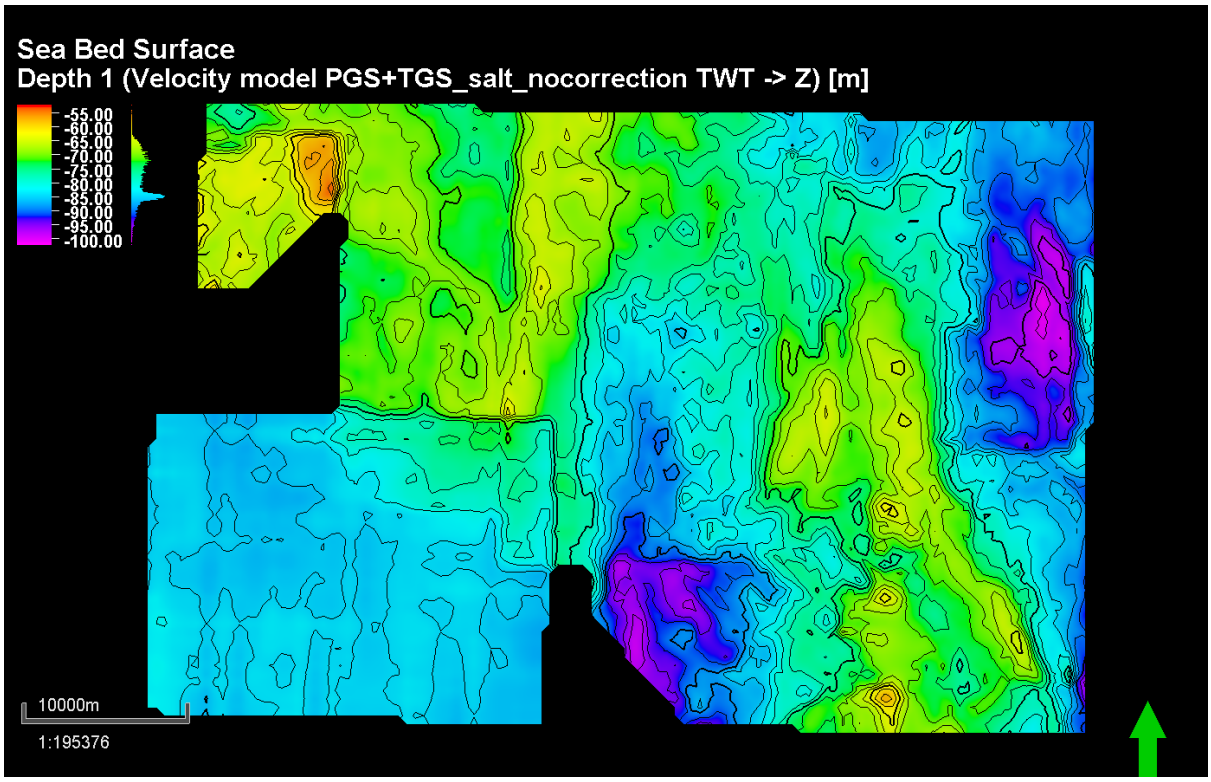
Synthetic generated in petrel using extracted wavelet form the seismic data, sonic and density wireline logs.



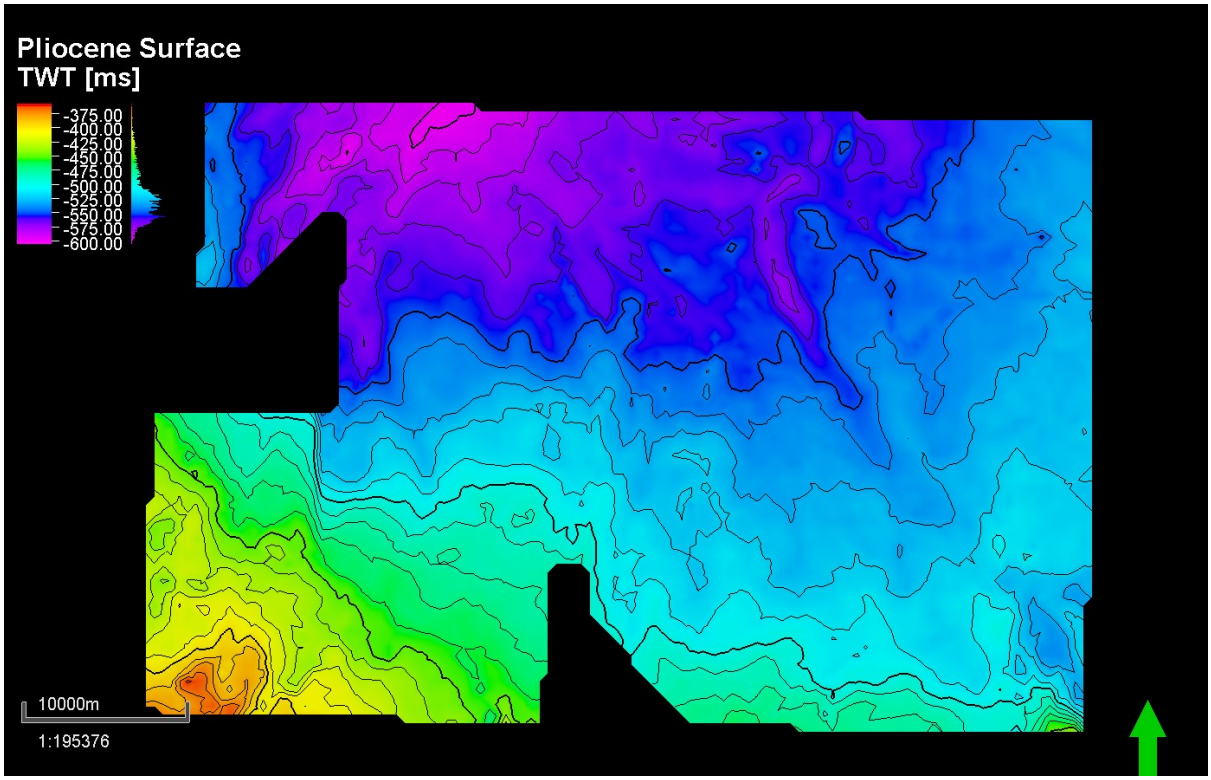
1.3 Time and depth maps of interpreted surfaces

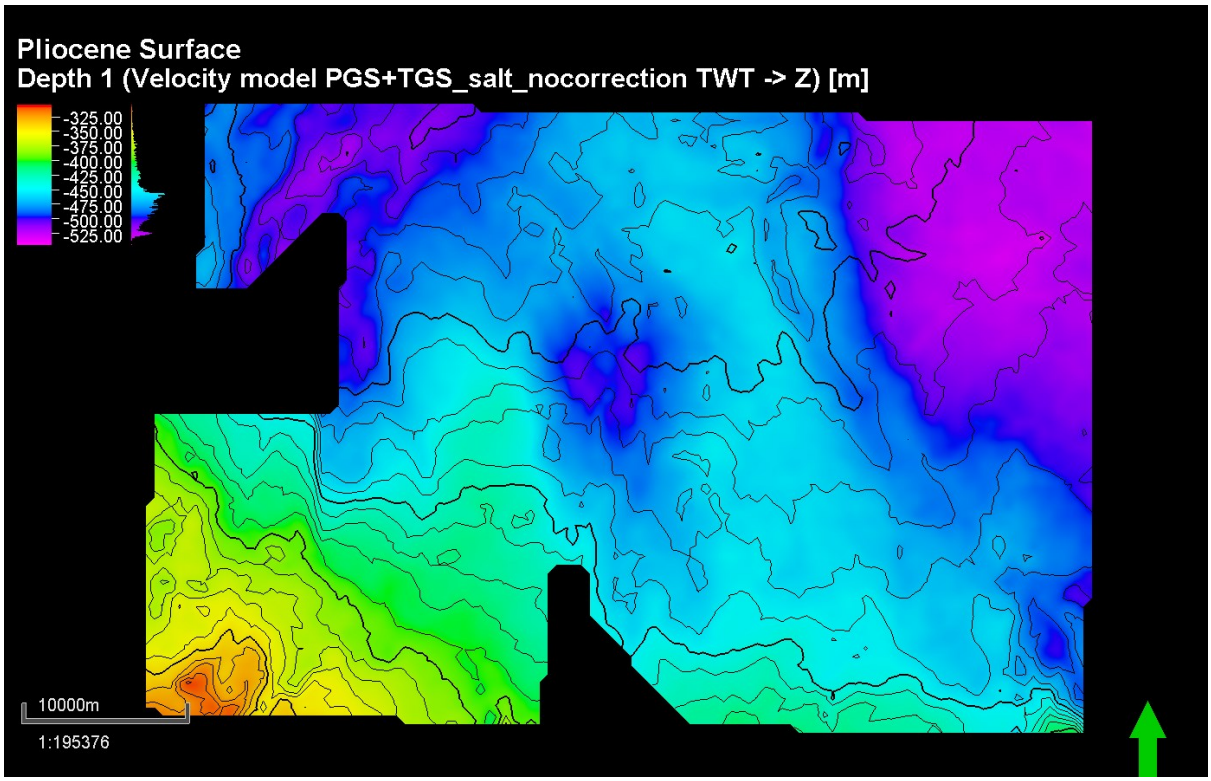
Sea bed Surface



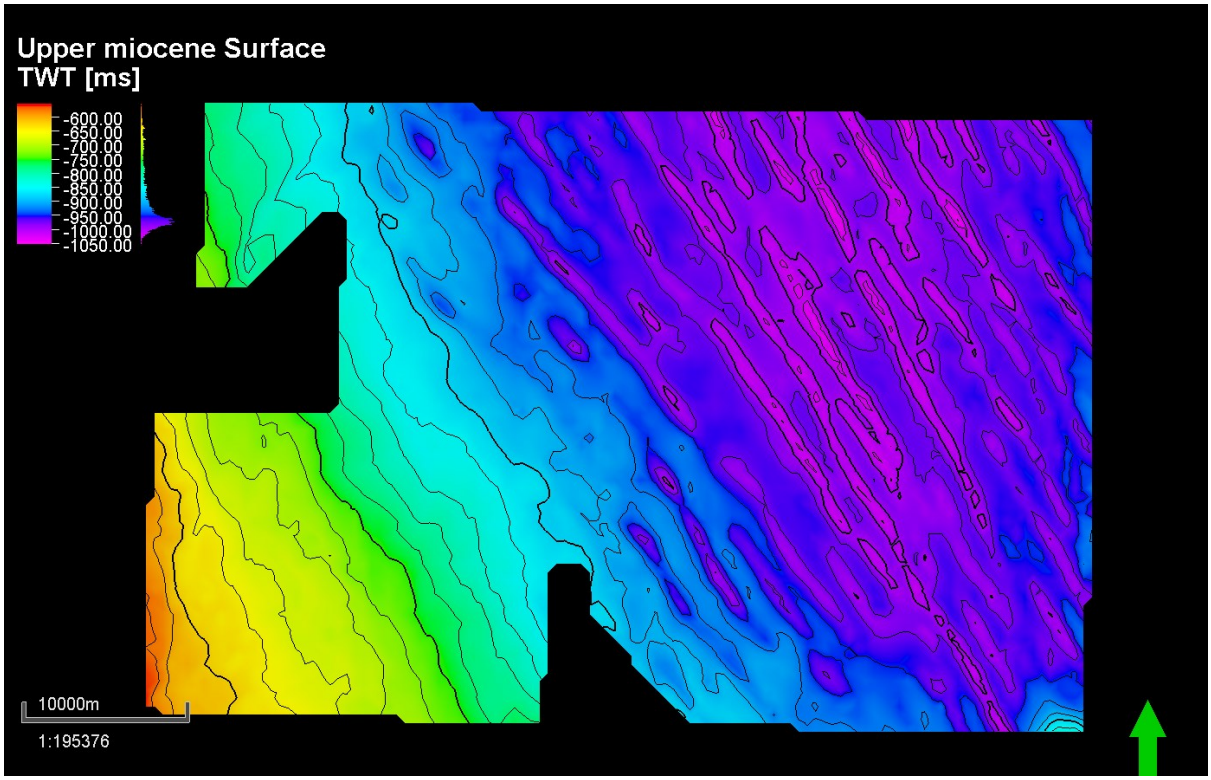


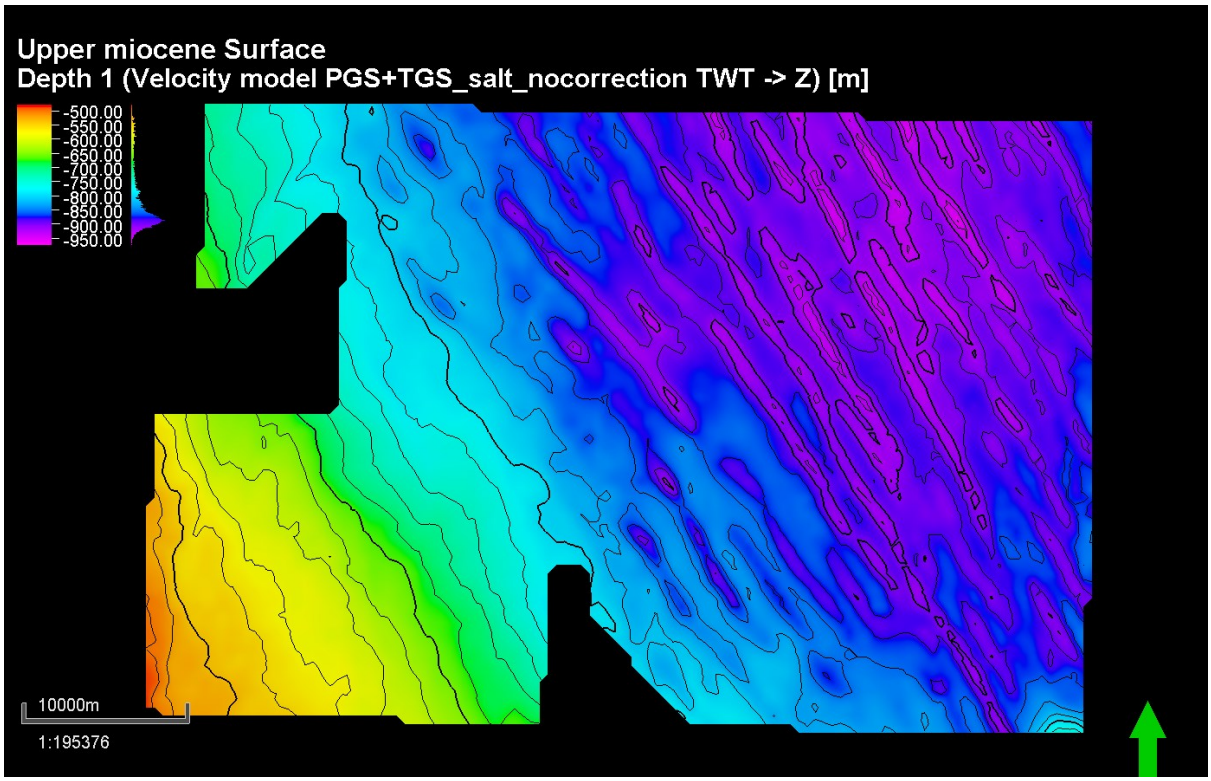
Top Pliocene Surface



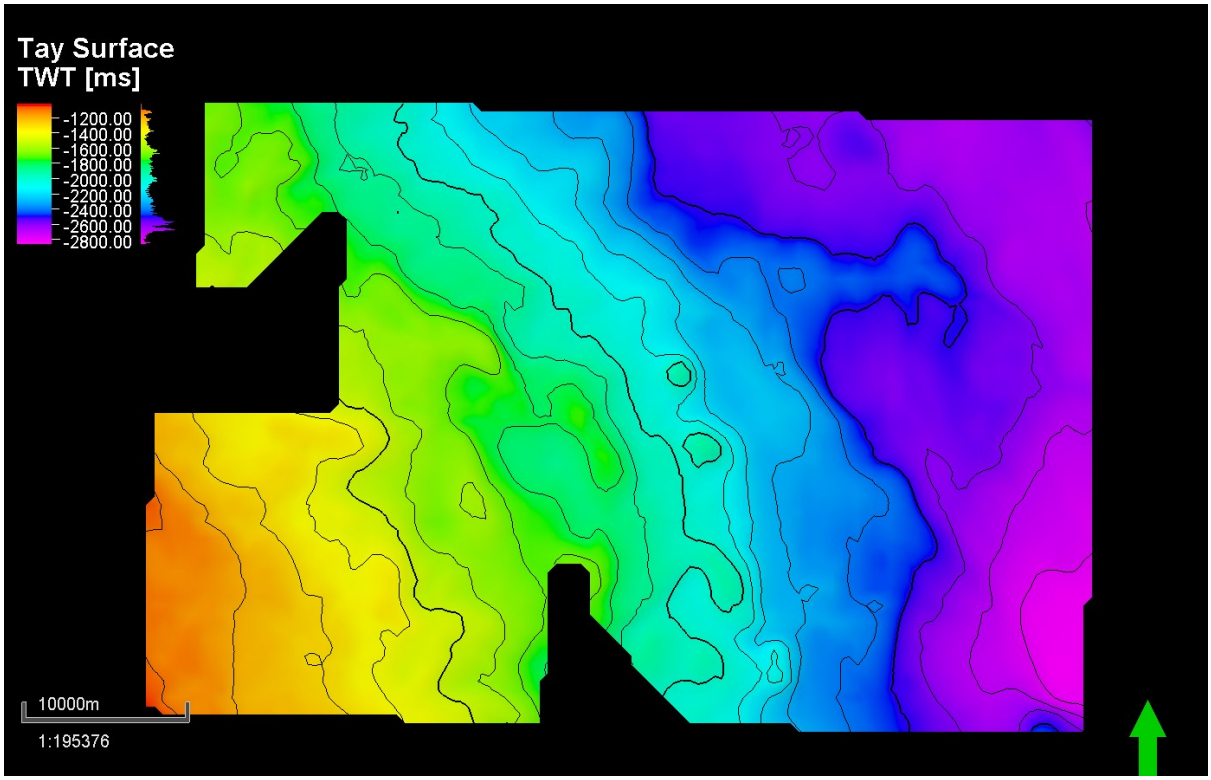


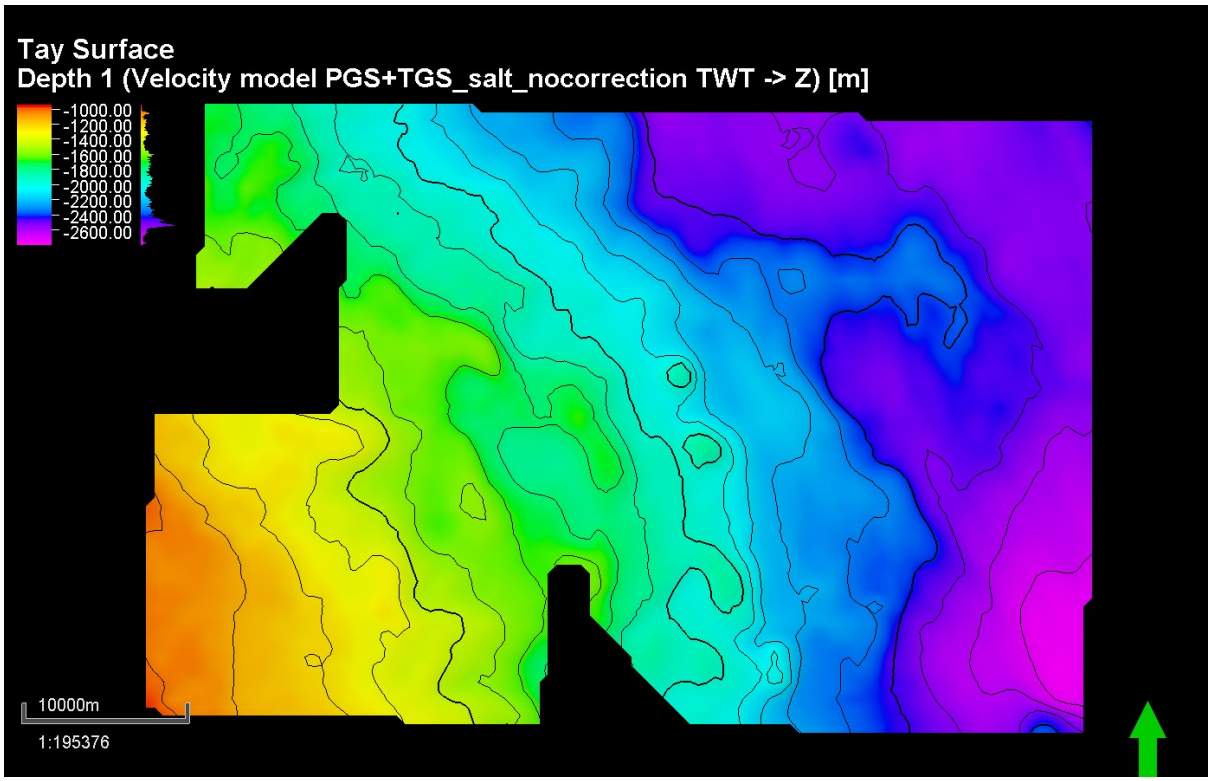
Top Upper Miocene Surface



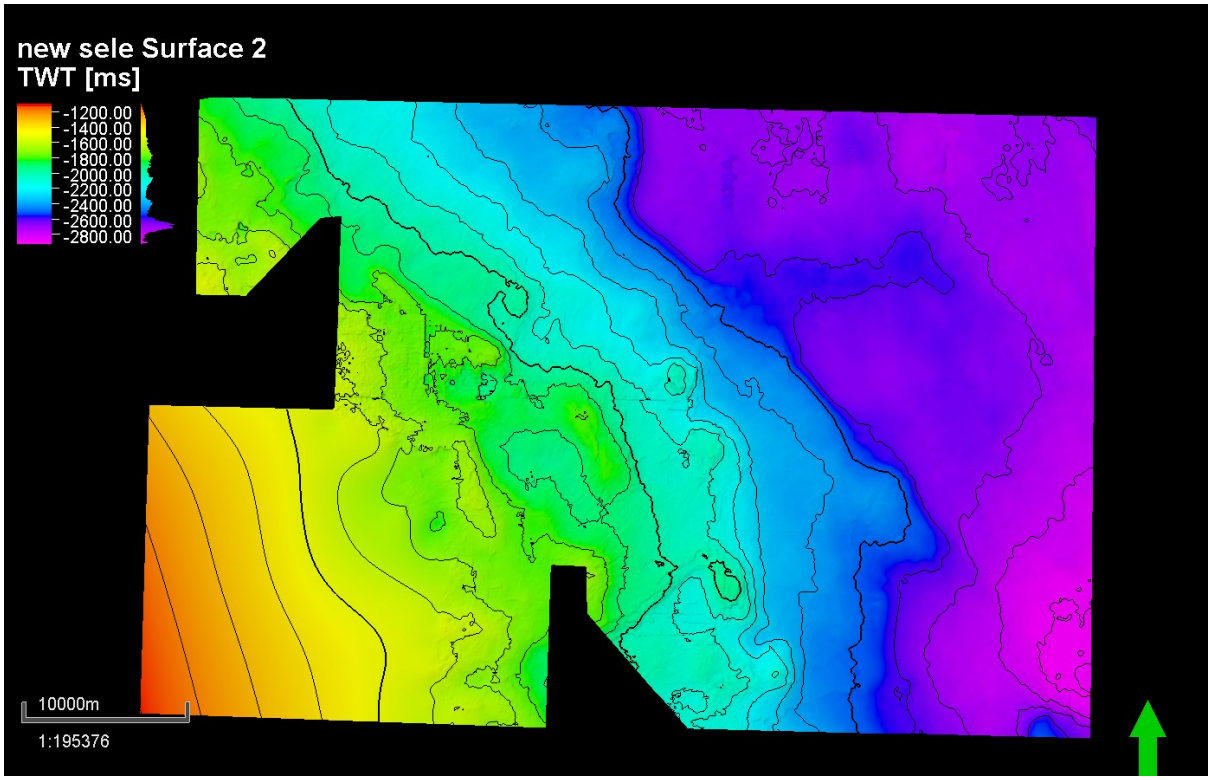


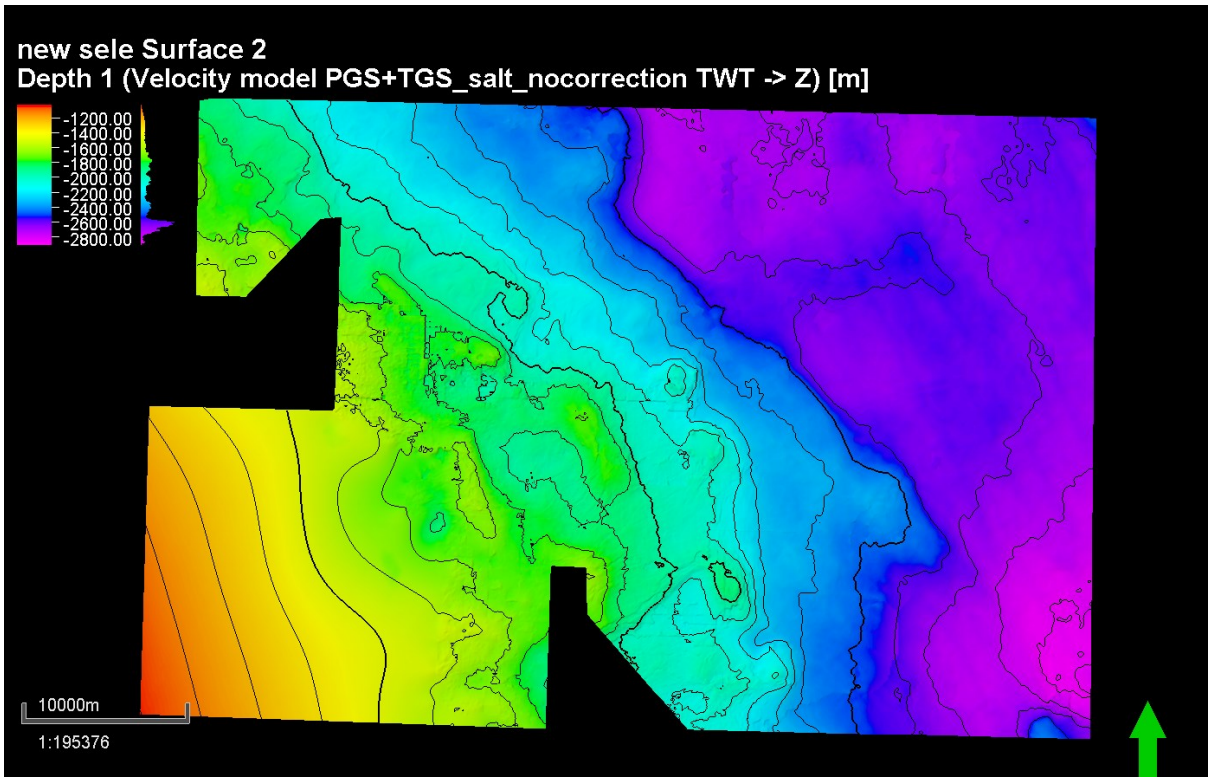
Top Tay SM Surface



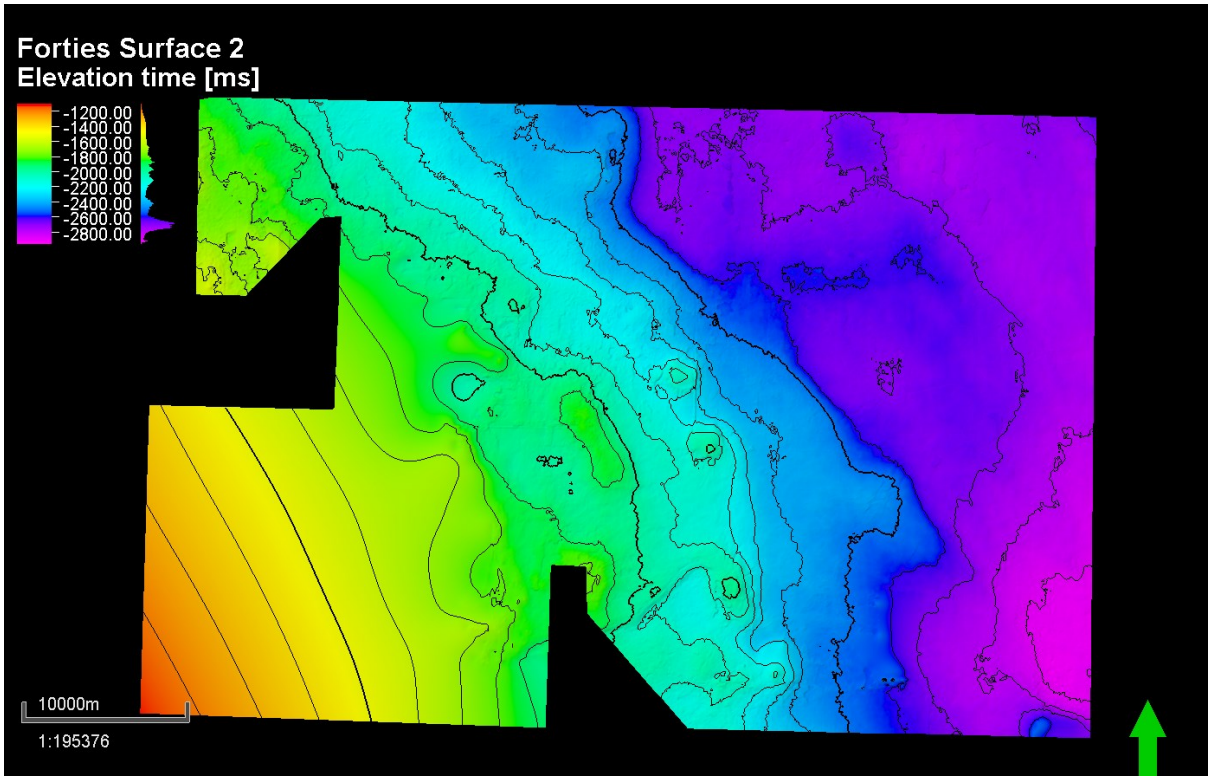


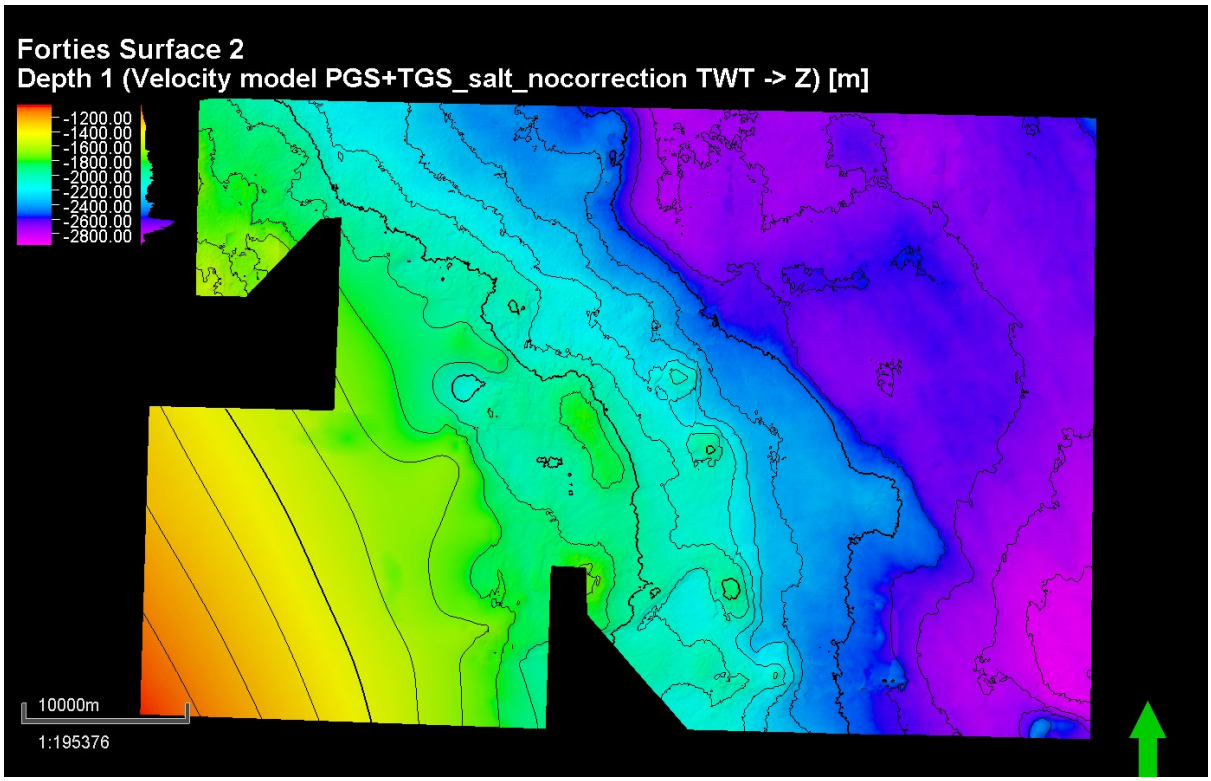
Top Sele FM Surface



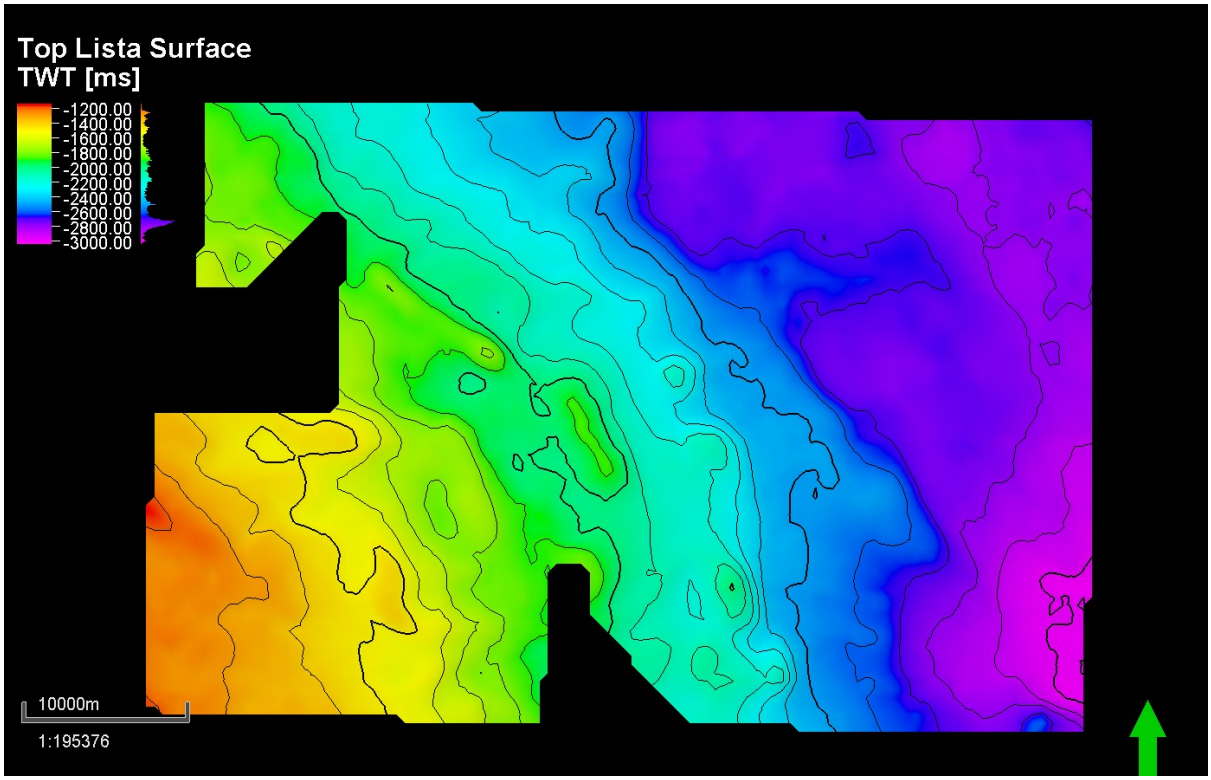


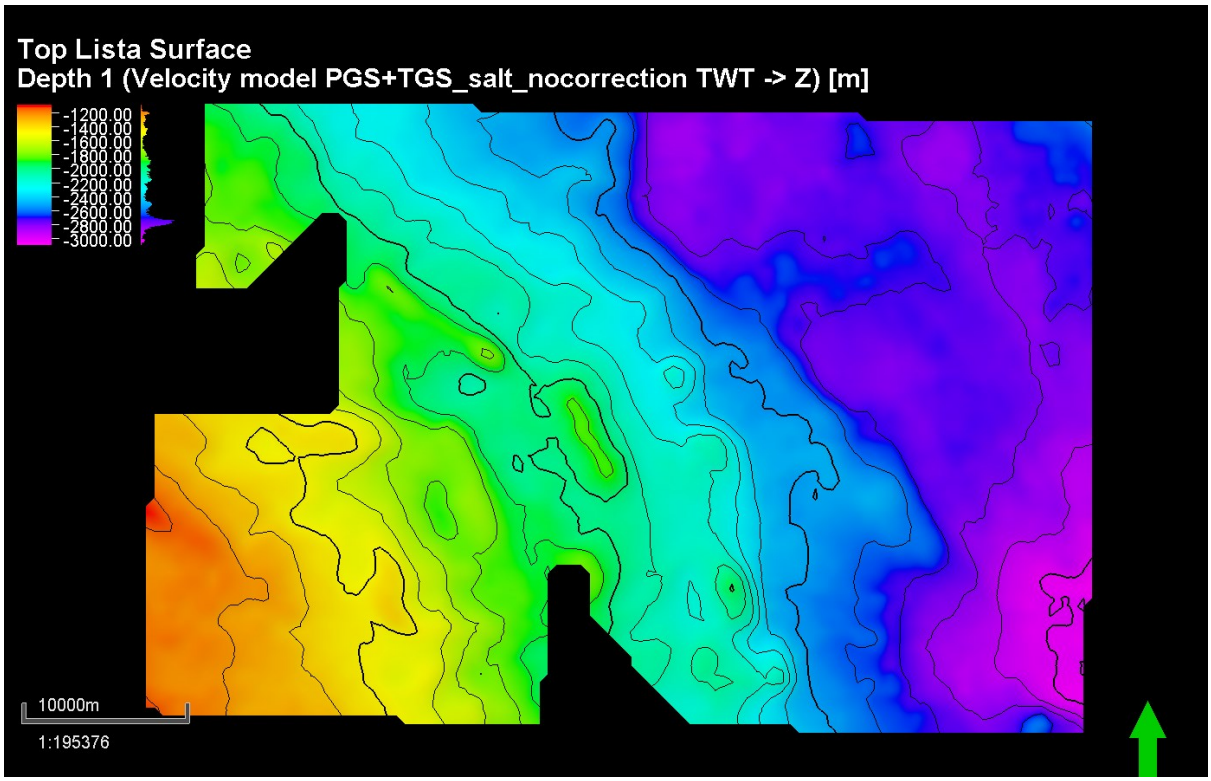
Top Forties SM surface



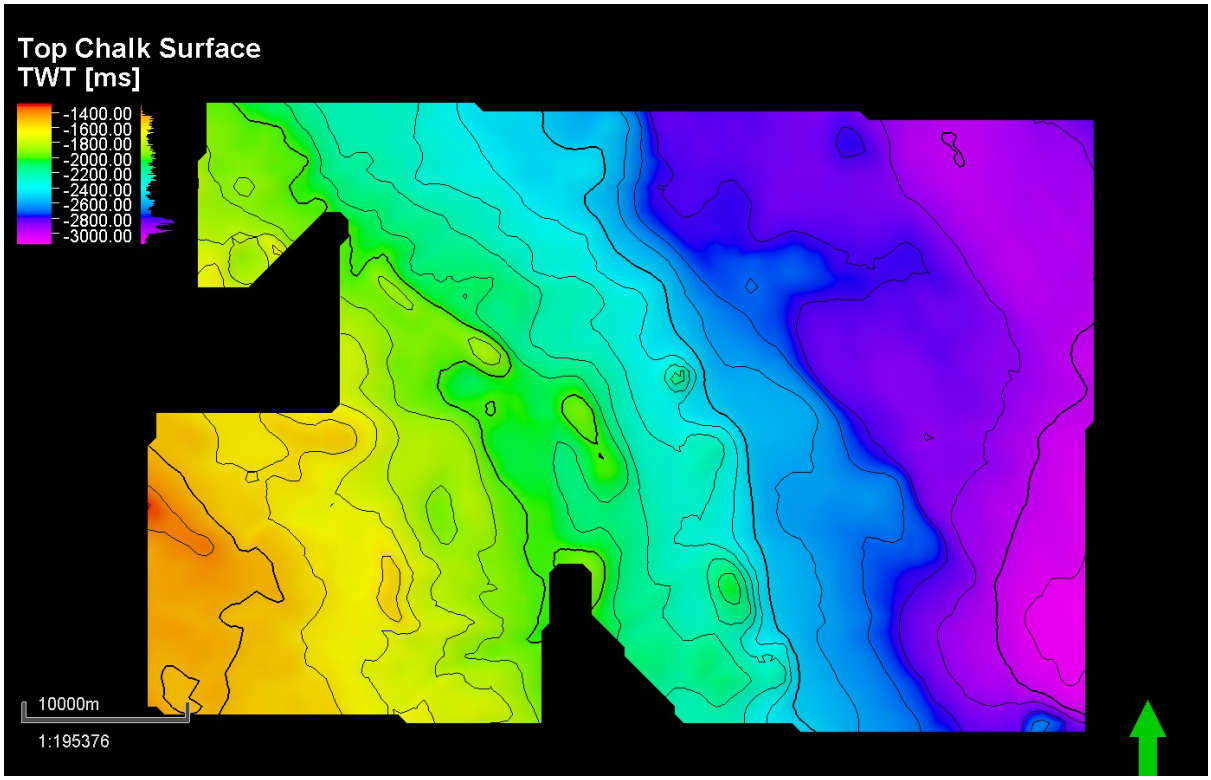


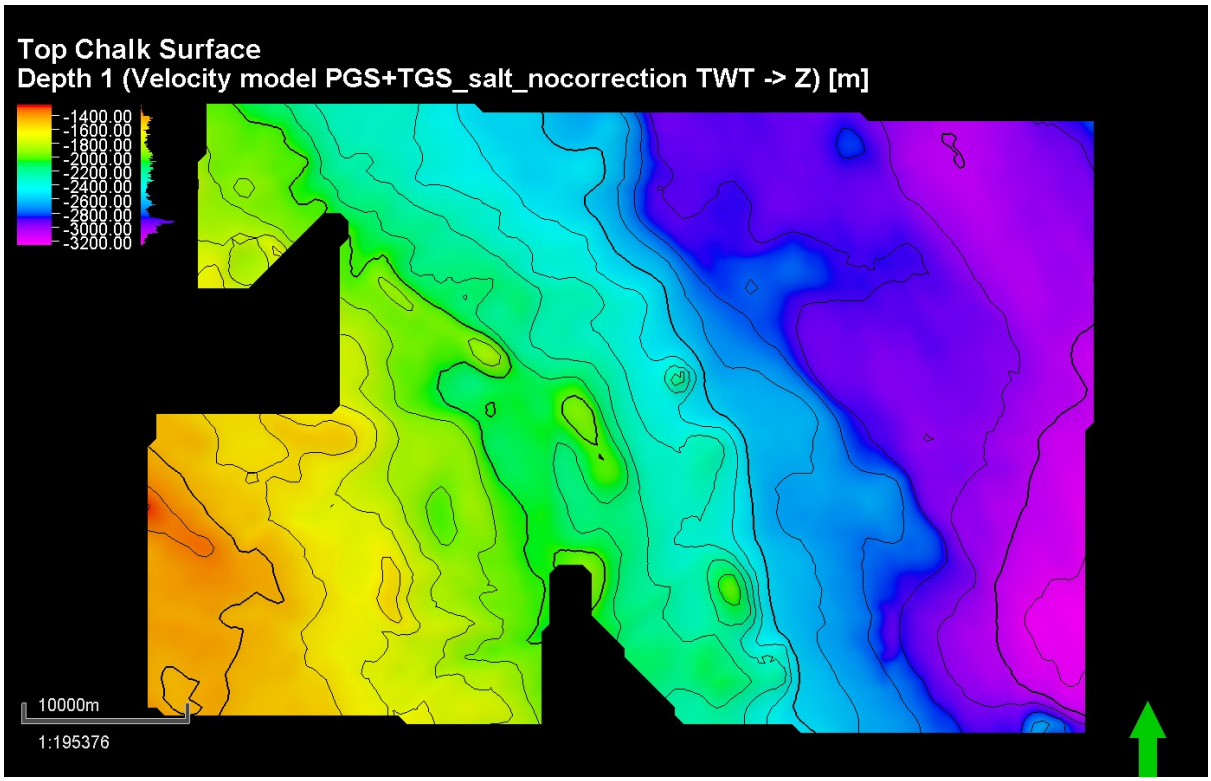
Top Lista FM Surface



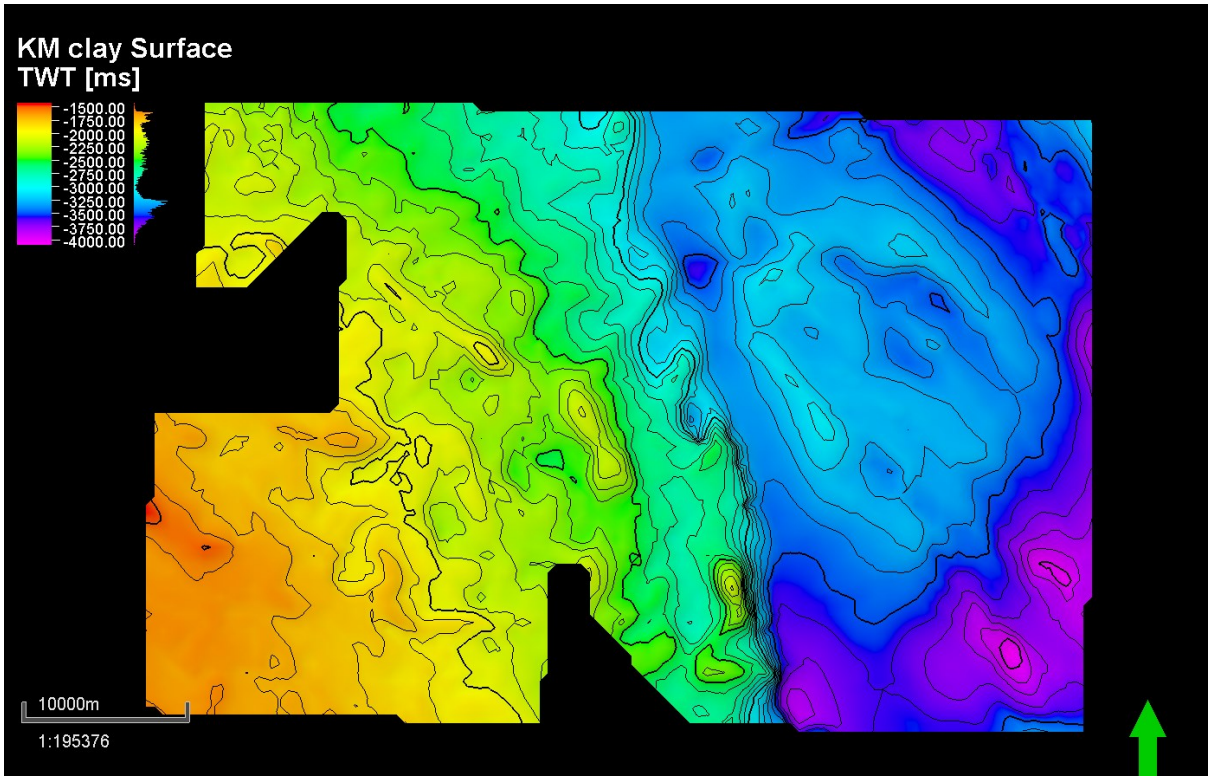


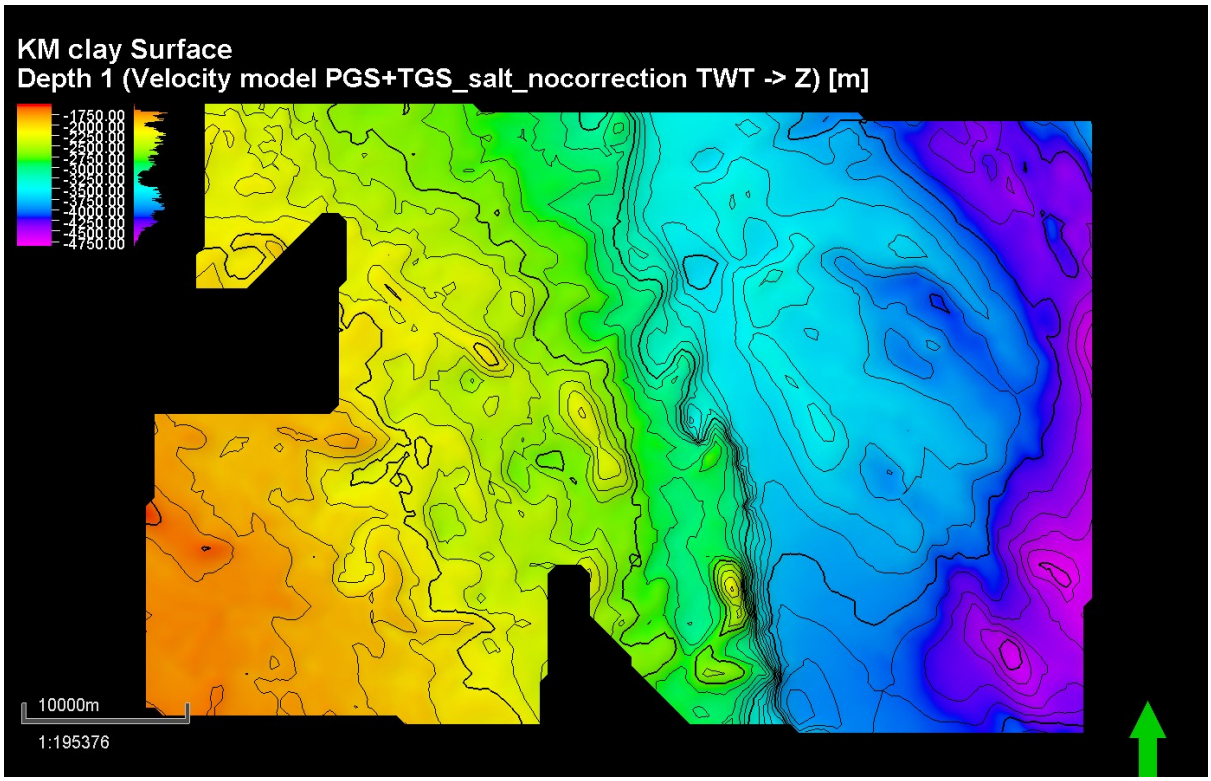
Top Chalk Surface



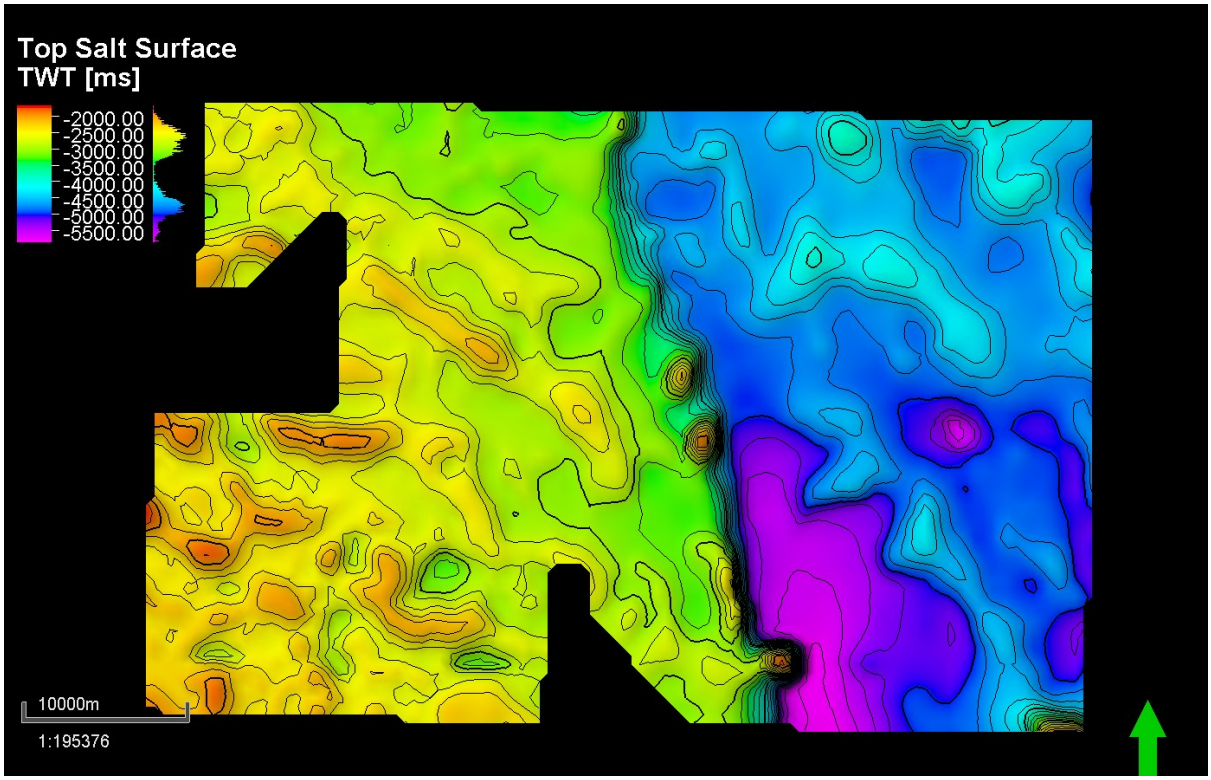


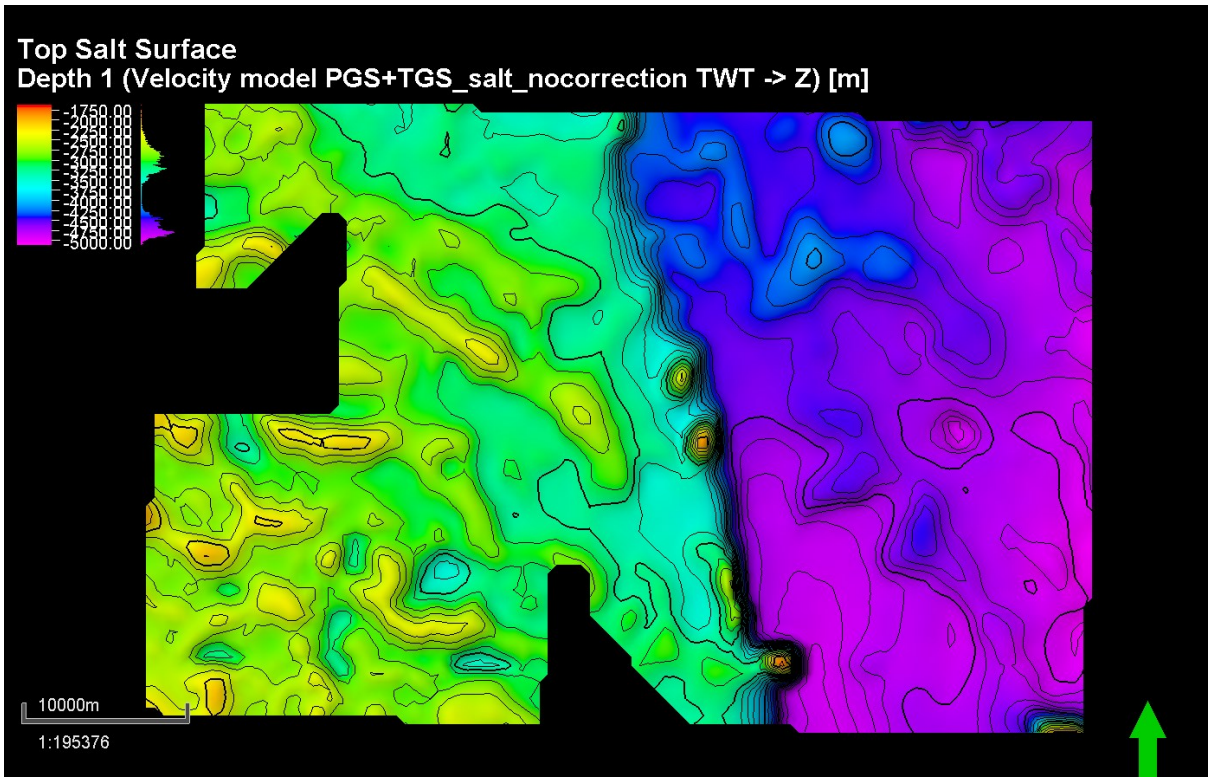
Top Kimm Clay Surface



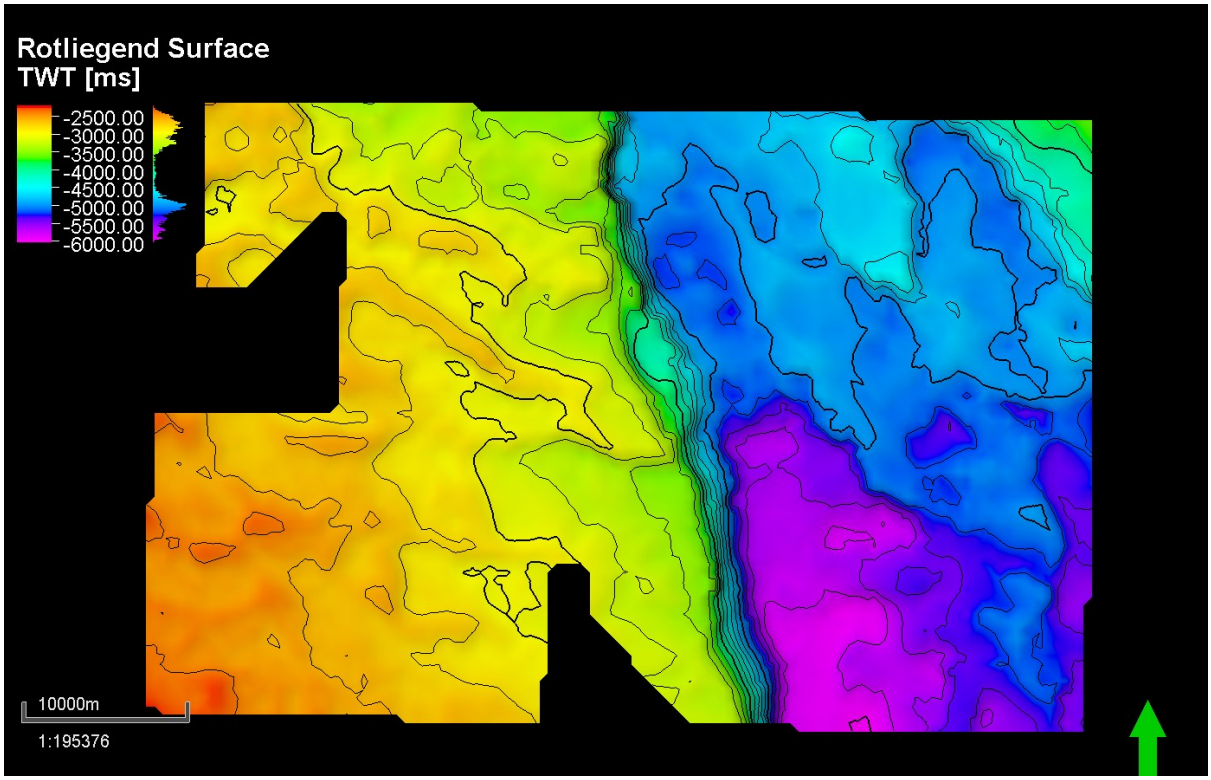


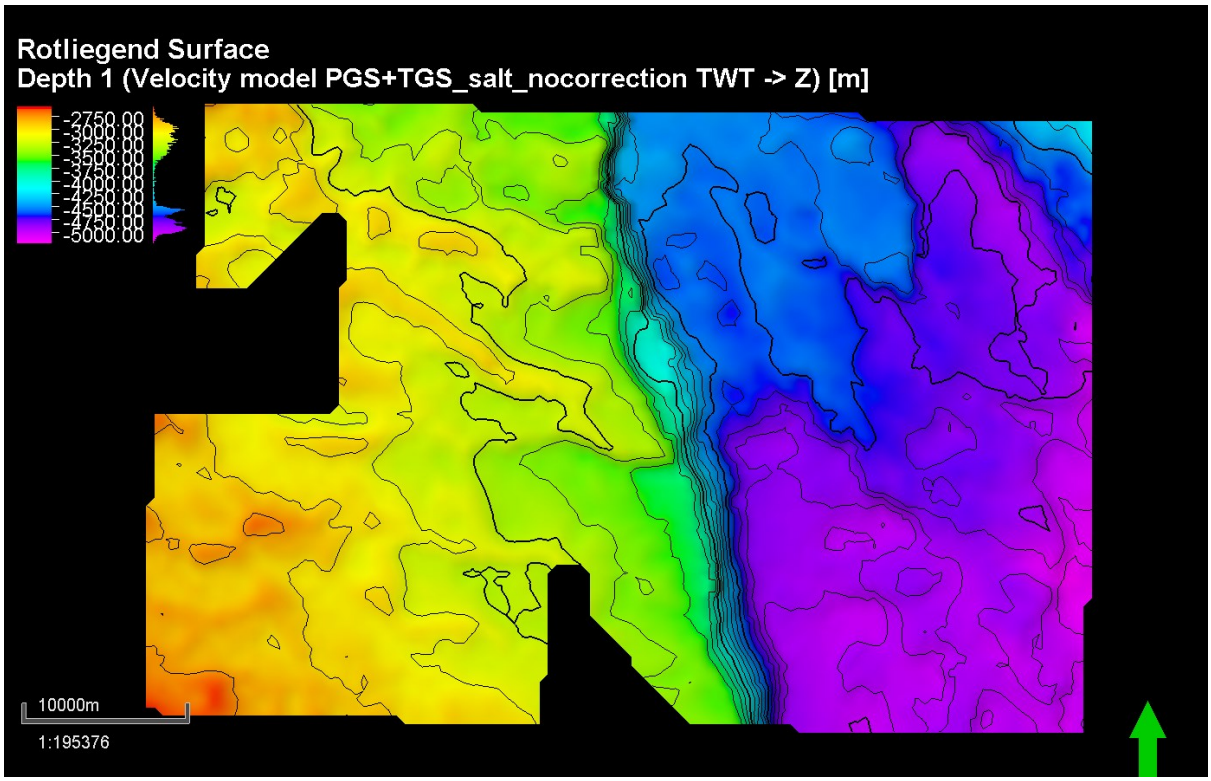
Top Salt Surface





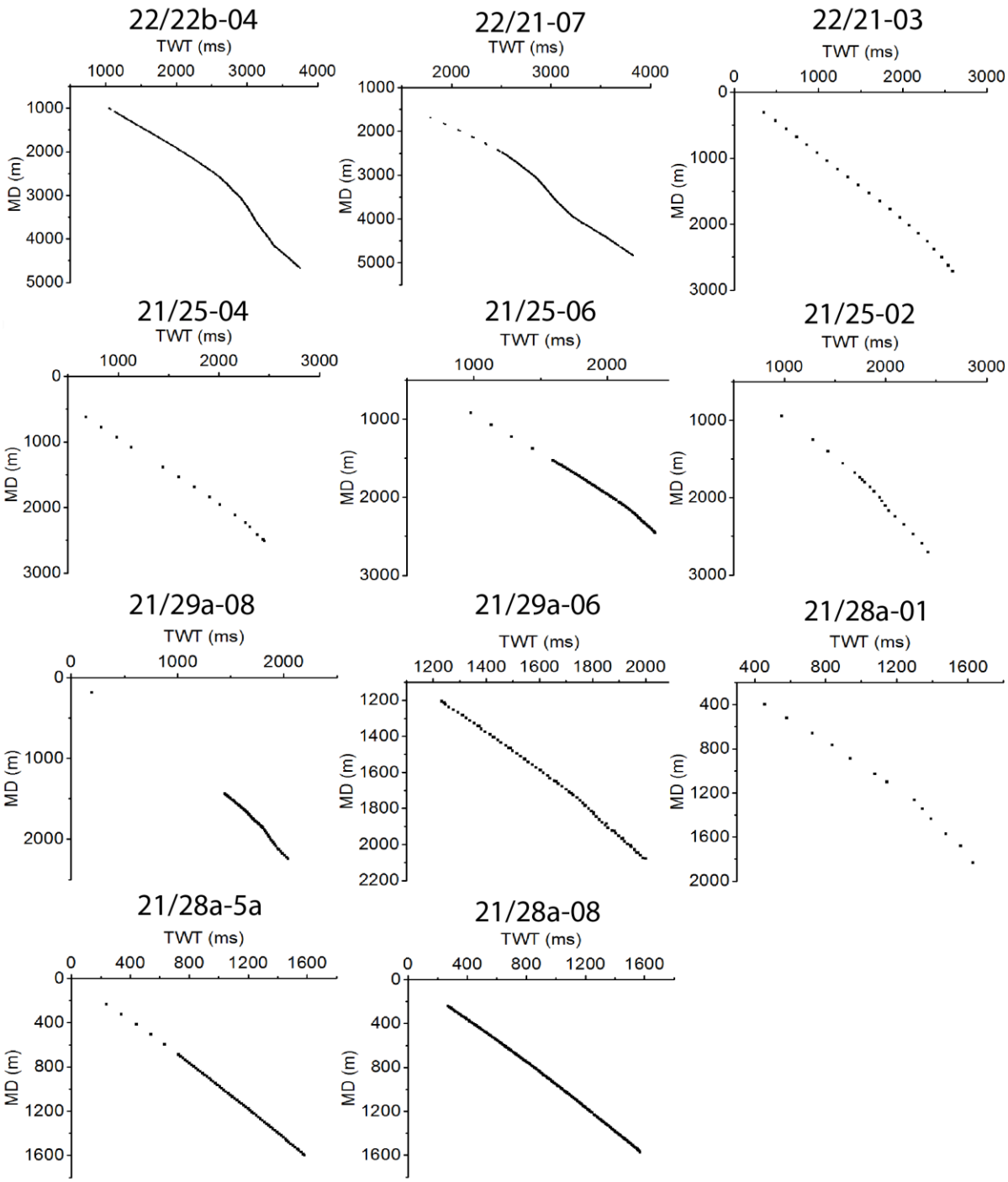
Top Rotliegend Surface





1.4 Time depth relationships for wells used in the velocity model

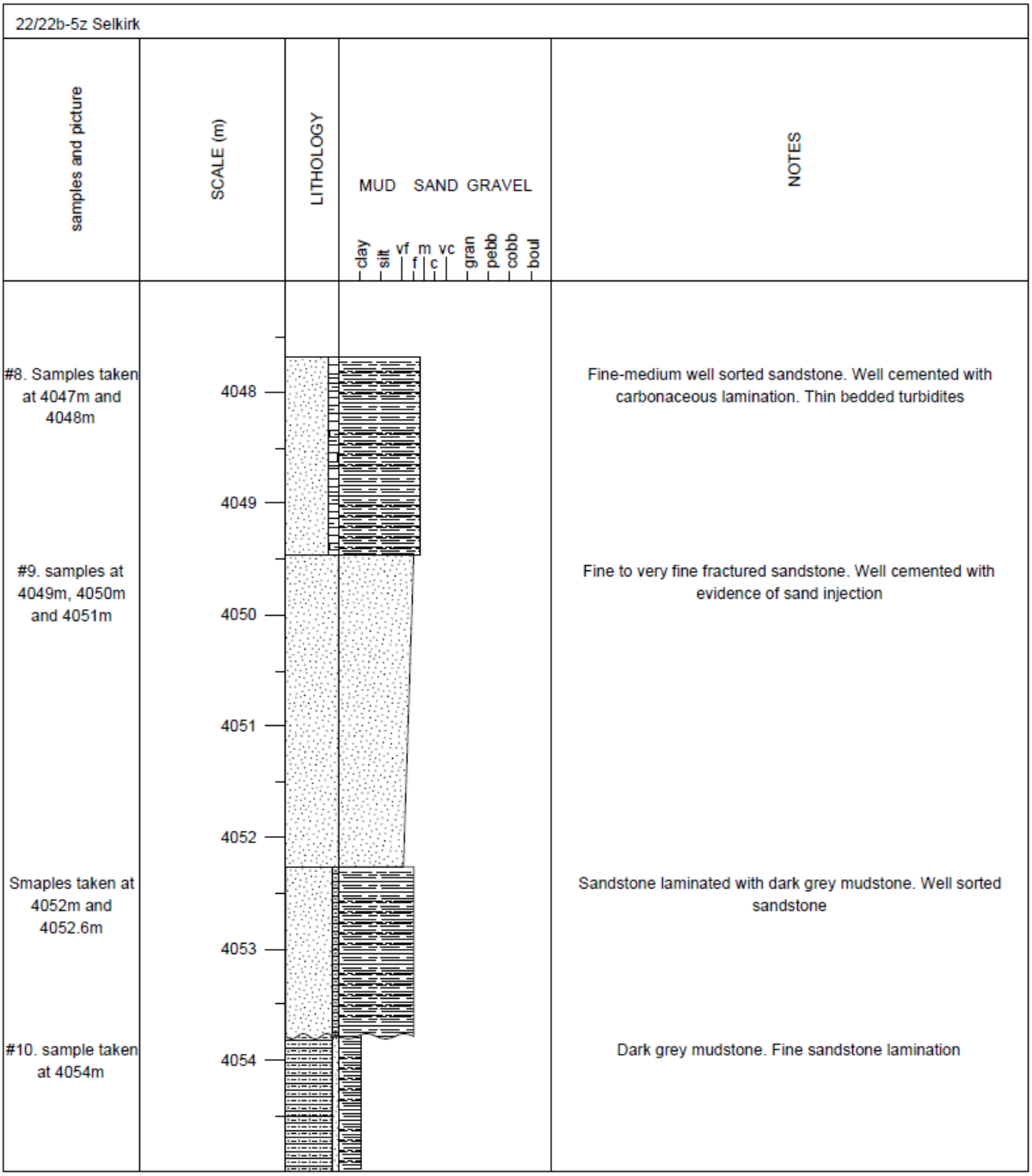
Plots of measured depths (MD) vs two-way travel time (TWT) for wells used to build the velocity model



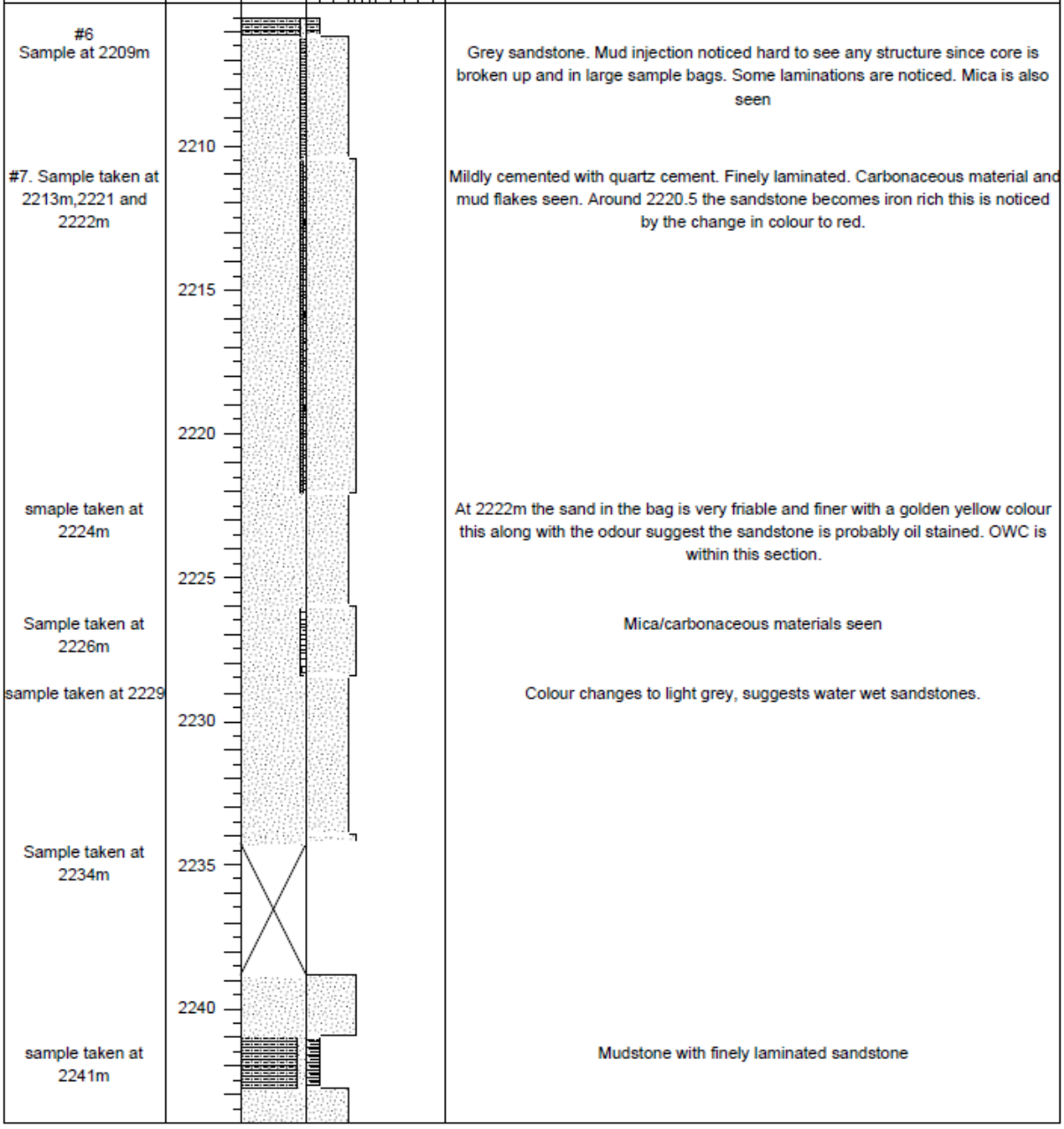
Appendix 2

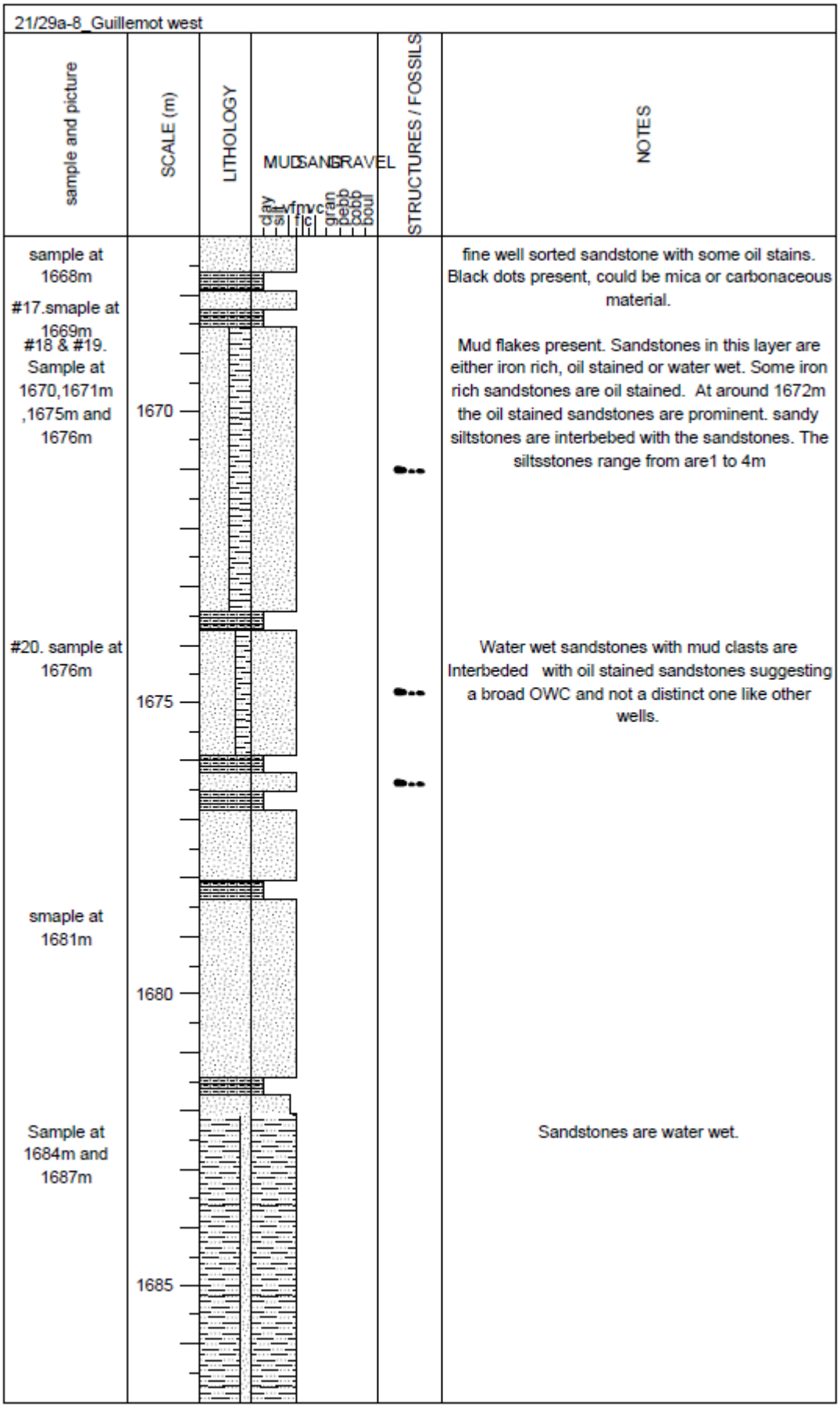
2.1 Lithology Logs

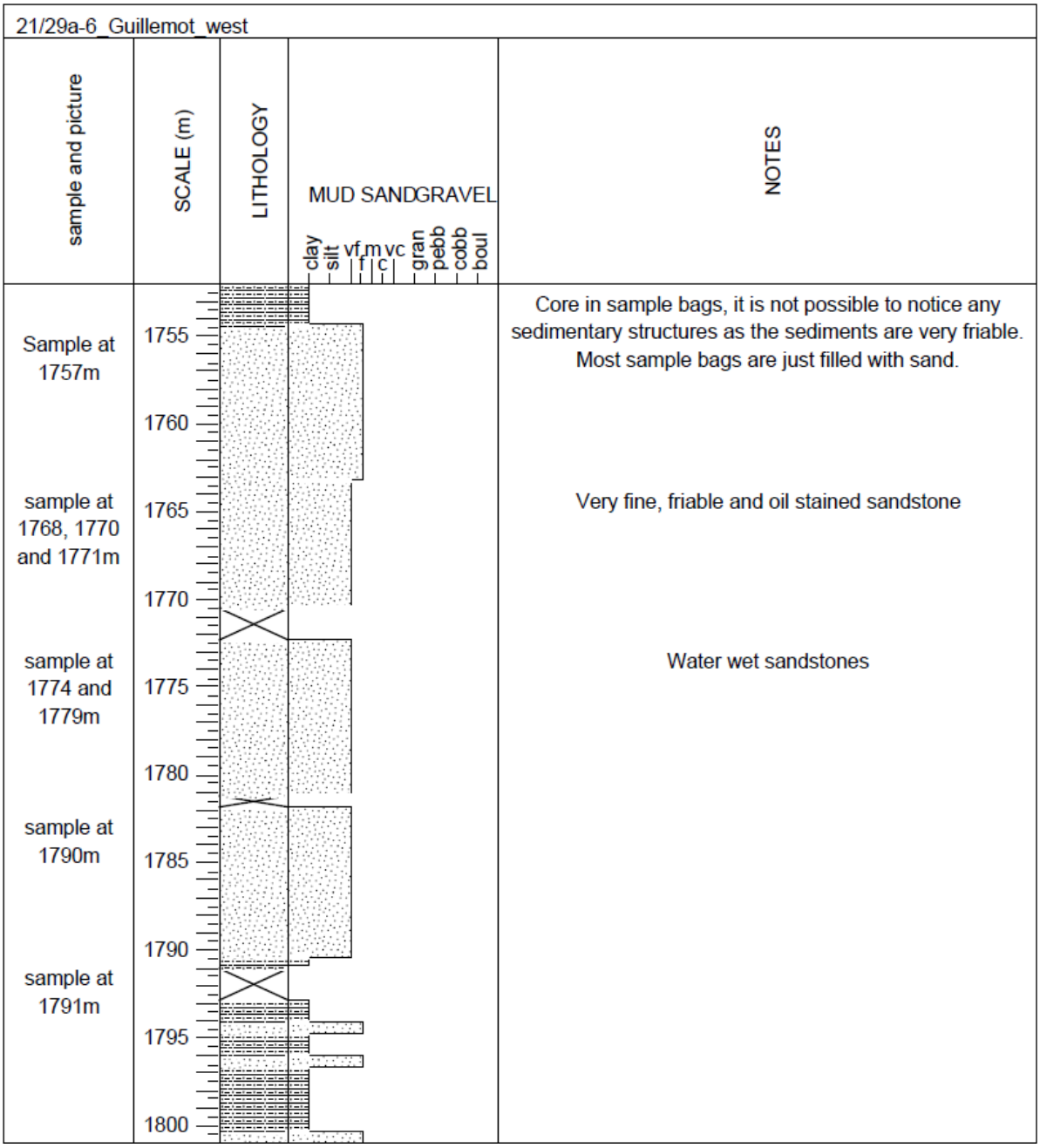
Logs were drawn in the core store at Keyworth, UK and redrawn in Sedlog

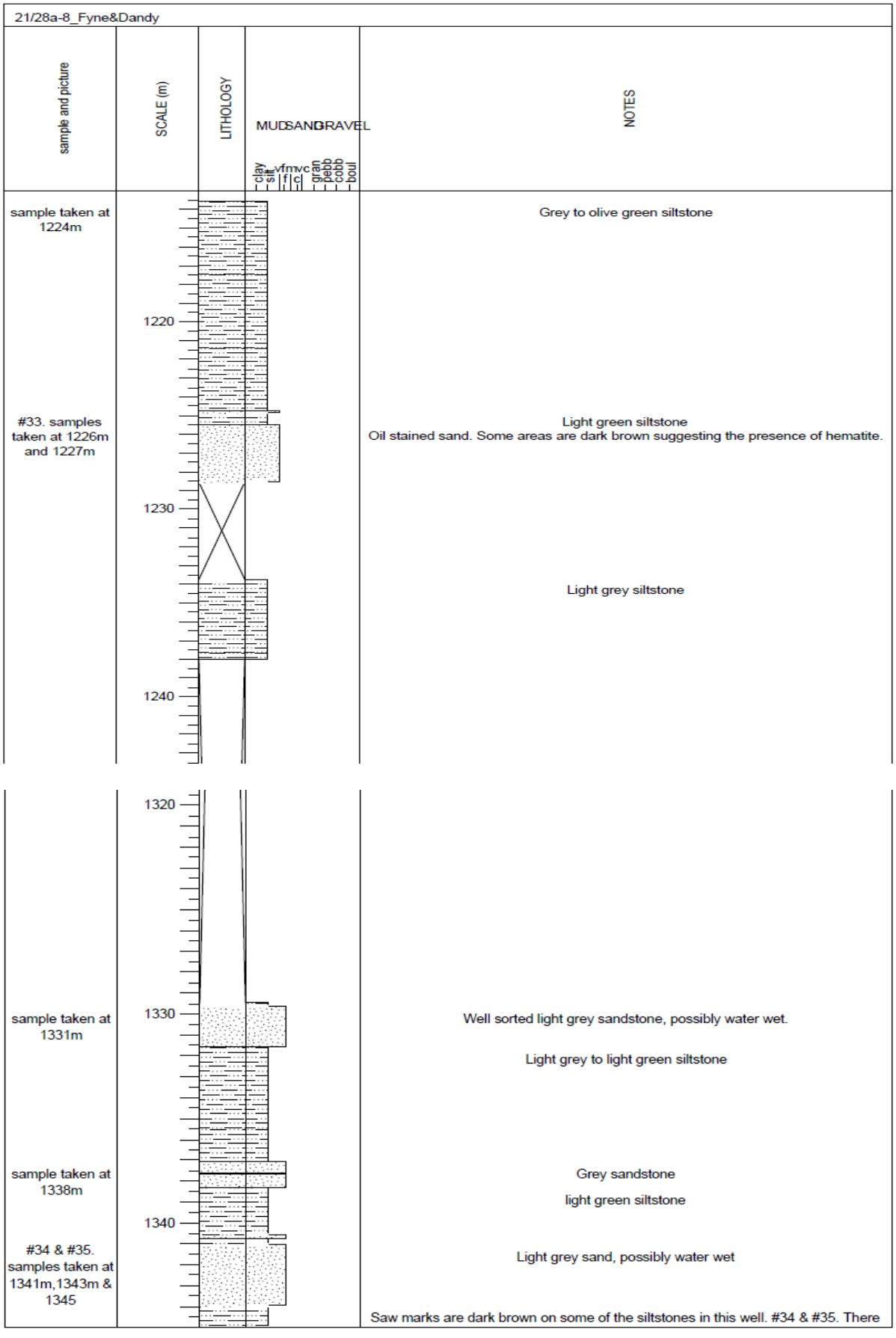


22-21-3_Gannet

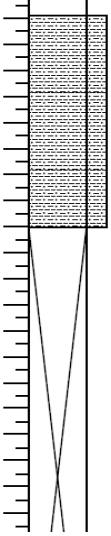
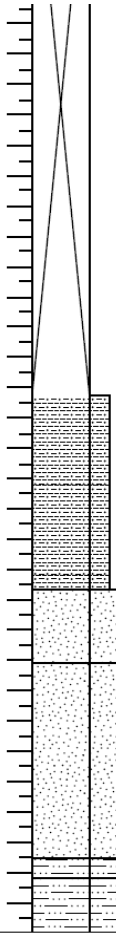


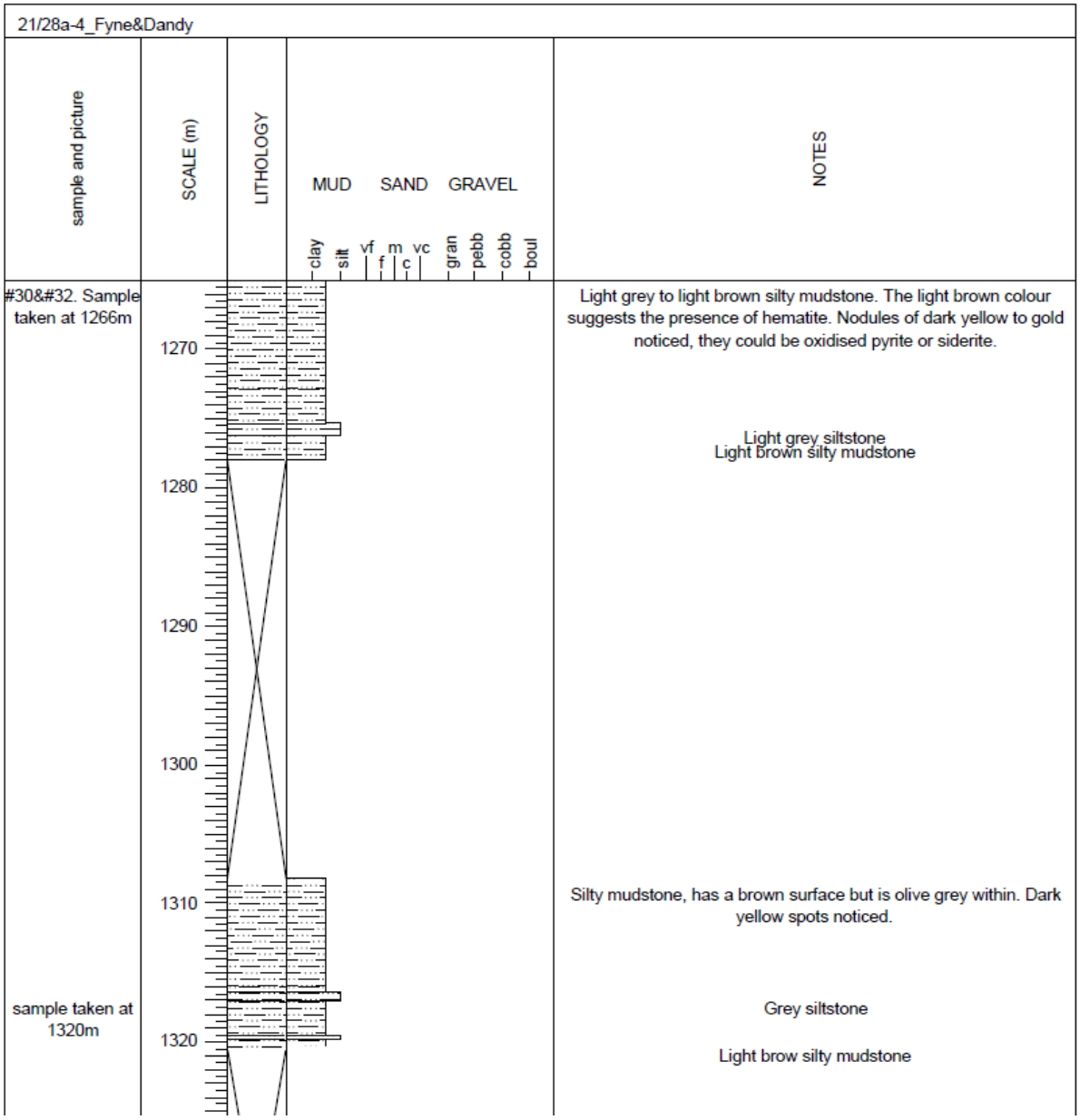

21/29a-8_Guillemot west
sample and picture
SCALE (m)
LITHOLOGY
MUD
SAND
GRAVEL
clay
silt
vf
f
m
c
vc
gran
pebb
cobb
boul
STRUCTURES / FOSSILS
NOTES
sample at 1668m
#17.smaple at 1669m
#18 & #19. Sample at 1670,1671m ,1675m and 1676m
#20. sample at 1676m
smaple at 1681m
Sample at 1684m and 1687m
1670
1675
1680
1685
fine well sorted sandstone with some oil stains. Black dots present, could be mica or carbonaceous material.
Mud flakes present. Sandstones in this layer are either iron rich, oil stained or water wet. Some iron rich sandstones are oil stained. At around 1672m the oil stained sandstones are prominent. sandy siltstones are interbebed with the sandstones. The siltsstones range from are1 to 4m
Water wet sandstones with mud clasts are Interbeded with oil stained sandstones suggesting a broad OWC and not a distinct one like other wells.
Sandstones are water wet.

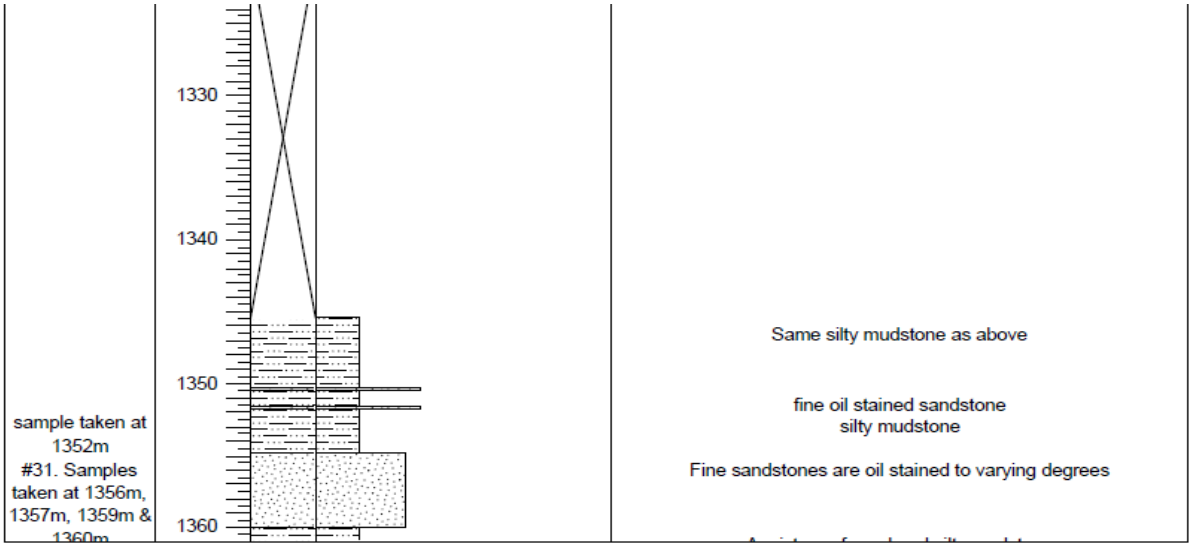

21/29a-6_Guillemot_west
sample and picture
SCALE (m)
LITHOLOGY
MUD SANDGRAVEL
clay
silt
vf
f
m
c
vc
gran
pebb
cobb
boul
NOTES
Sample at 1757m
sample at 1768, 1770 and 1771m
sample at 1774 and 1779m
sample at 1790m
sample at 1791m
1755
1760
1765
1770
1775
1780
1785
1790
1795
1800
Core in sample bags, it is not possible to notice any sedimentary structures as the sediments are very friable. Most sample bags are just filled with sand.
Very fine, friable and oil stained sandstone
Water wet sandstones


21/28a-8_Fyne&Dandy
sample and picture
SCALE (m)
LITHOLOGY
MUD
SAND
GRAVEL
clay
silt
vf
f
m
c
vc
gran
pebb
cobb
boul
NOTES
sample taken at 1224m
Grey to olive green siltstone
1220
#33. samples taken at 1226m and 1227m
Light green siltstone
Oil stained sand. Some areas are dark brown suggesting the presence of hematite.
1230
Light grey siltstone
1240
1320
sample taken at 1331m
1330
Well sorted light grey sandstone, possibly water wet.
Light grey to light green siltstone
sample taken at 1338m
Grey sandstone
light green siltstone
1340
#34 & #35. samples taken at 1341m,1343m & 1345
Light grey sand, possibly water wet
Saw marks are dark brown on some of the siltstones in this well. #34 & #35. There

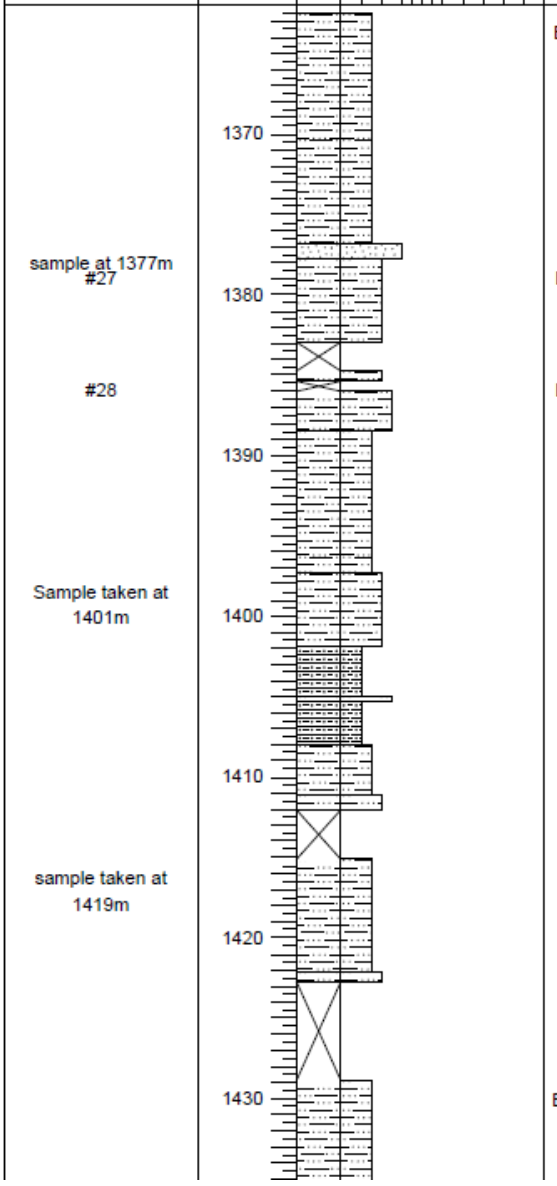
21/28a-5a_Fyne&Dandy

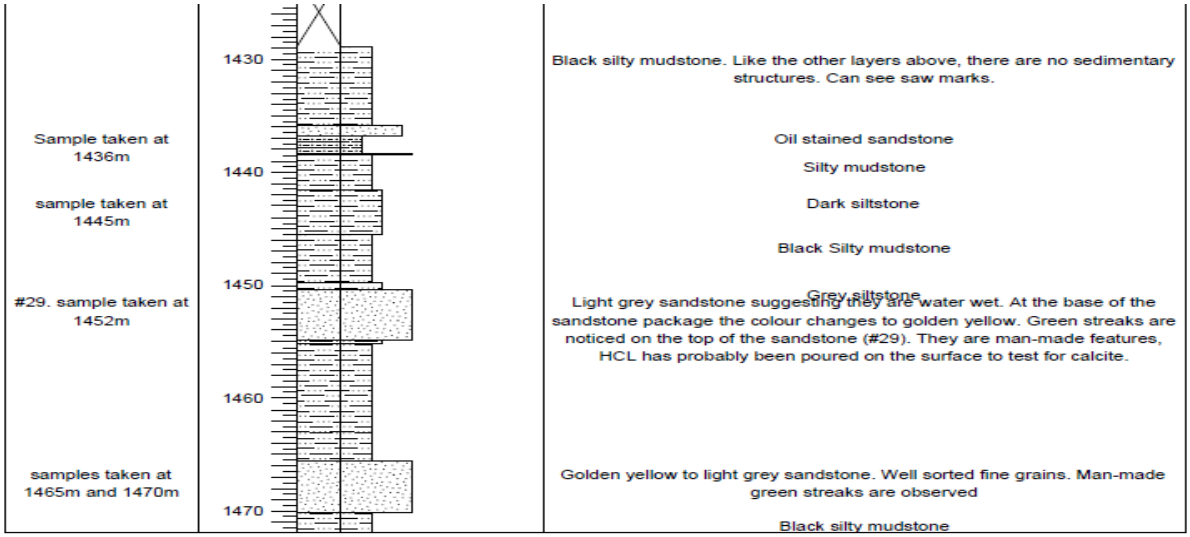
sample and picture	SCALE (m)	LITHOLOGY	MUD SANDGRAVEL (clay, silt, vf, f, m, c, vc, gran, pebb, cobb, boul)	NOTES
#22 &#23	1380			Black mudstones, with dark yellow and green bands. I can see white crystals on the surface of the mudstones. These crystals are probably precipitated from fluids in the mudstone. The crystals could be calcite #22. I can also see mud cracks.
	1390			
	1400			Same mudstone as above
#24. sample at 1414m	1410			Sandstone is mostly oil stained, fine grained and well sorted. Towards the end the sandstones are green. This could suggest the presence of chlorine or glauconite
#25 &#26. Sample taken at 1415m, 1417m, 1418m, 1420m & 1422m	1420			Sandstones are very friable and oil stained to varying degrees. Some golden spots which could be oxidised pyrite or siderite #26. Sample of it taken at 1422m
				Green siltstone. Silty Mudstone

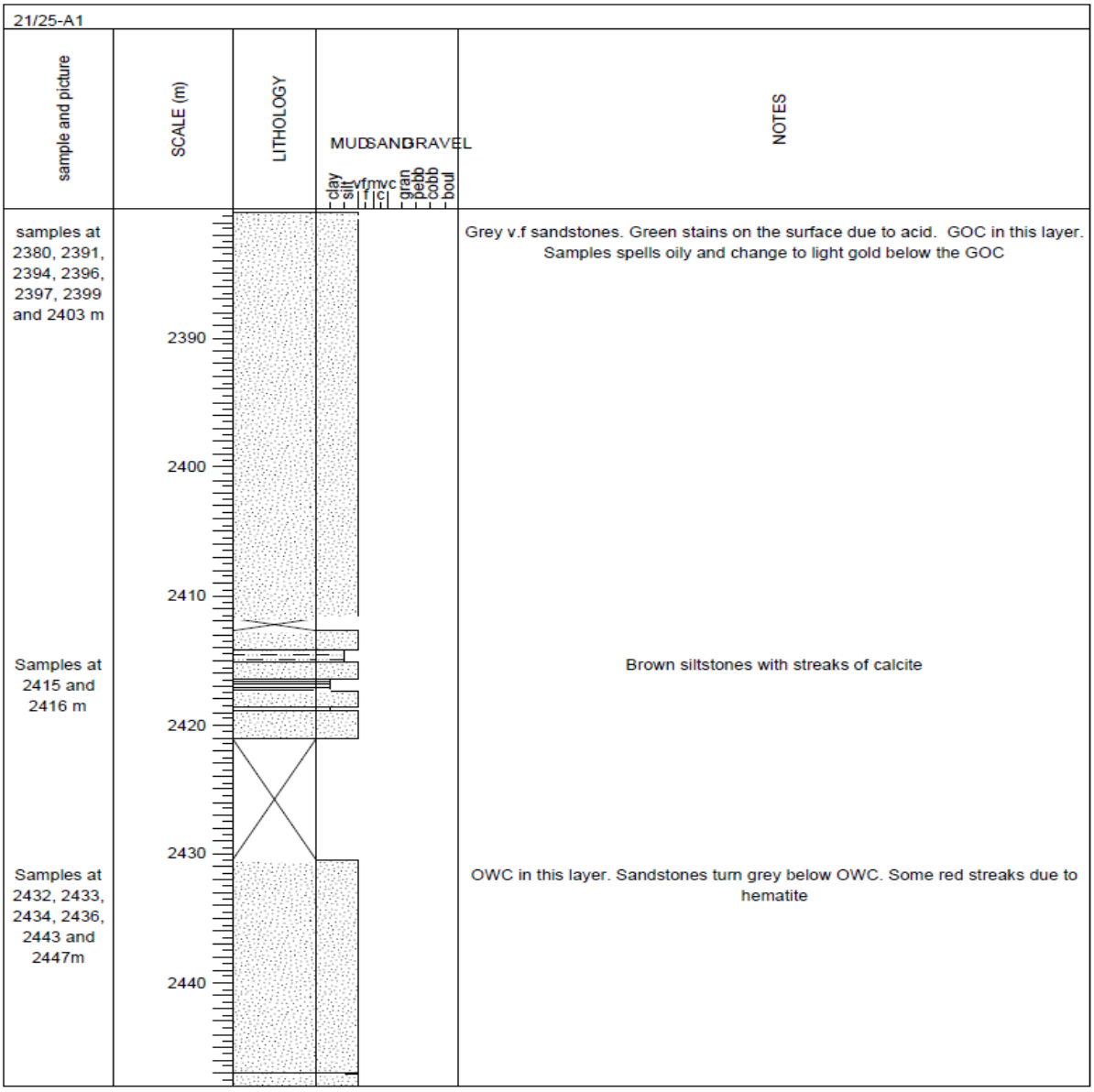

21/28a-4_Fyne&Dandy
sample and picture
SCALE (m)
LITHOLOGY
MUD
SAND
GRAVEL
clay
silt
vf
f
m
c
vc
gran
pebb
cobb
boul
NOTES
#30&#32. Sample taken at 1266m
1270
1280
1290
1300
1310
1320
sample taken at 1320m
Light grey to light brown silty mudstone. The light brown colour suggests the presence of hematite. Nodules of dark yellow to gold noticed, they could be oxidised pyrite or siderite.
Light grey siltstone
Light brown silty mudstone
Silty mudstone, has a brown surface but is olive grey within. Dark yellow spots noticed.
Grey siltstone
Light brow silty mudstone

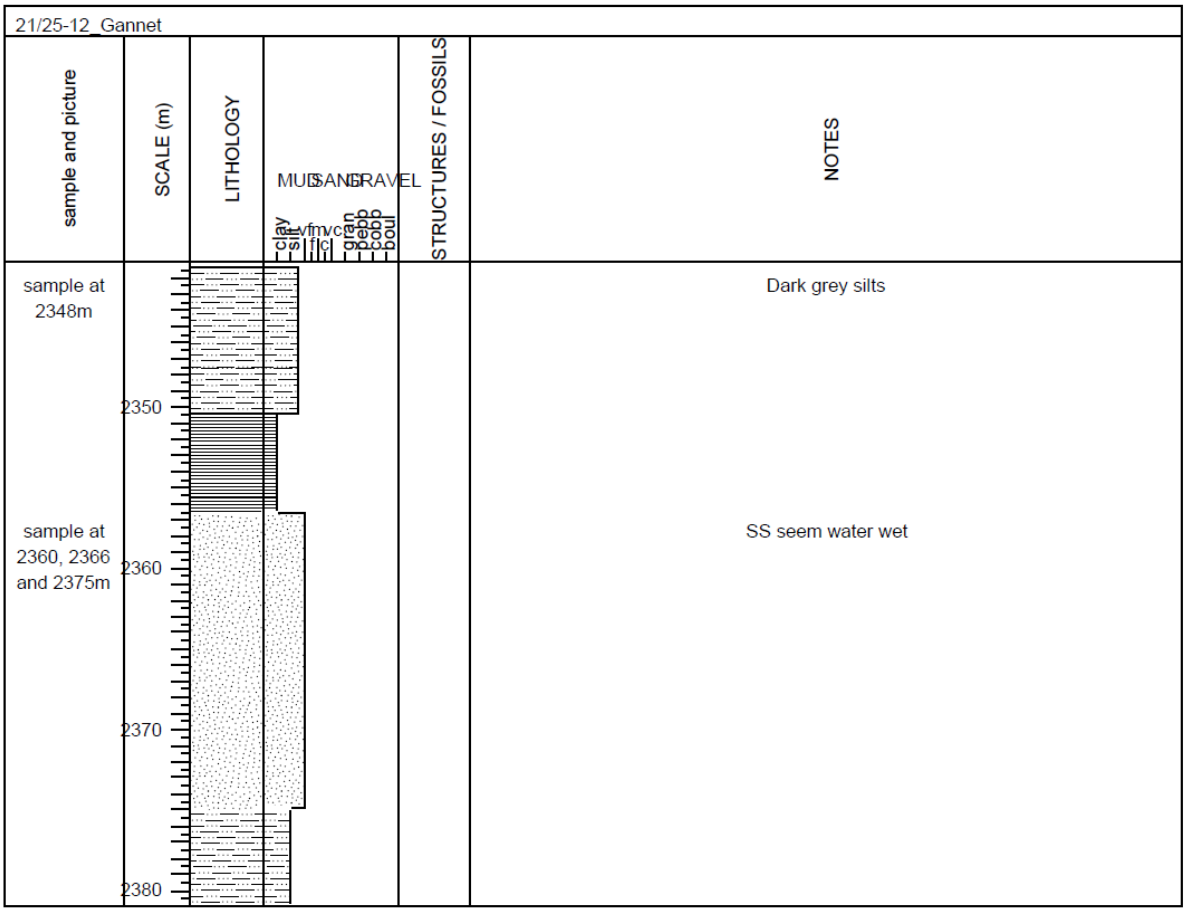

1330
1340
1350
1360
sample taken at 1352m #31. Samples taken at 1356m, 1357m, 1359m & 1360m
Same silty mudstone as above
fine oil stained sandstone
silty mudstone
Fine sandstones are oil stained to varying degrees

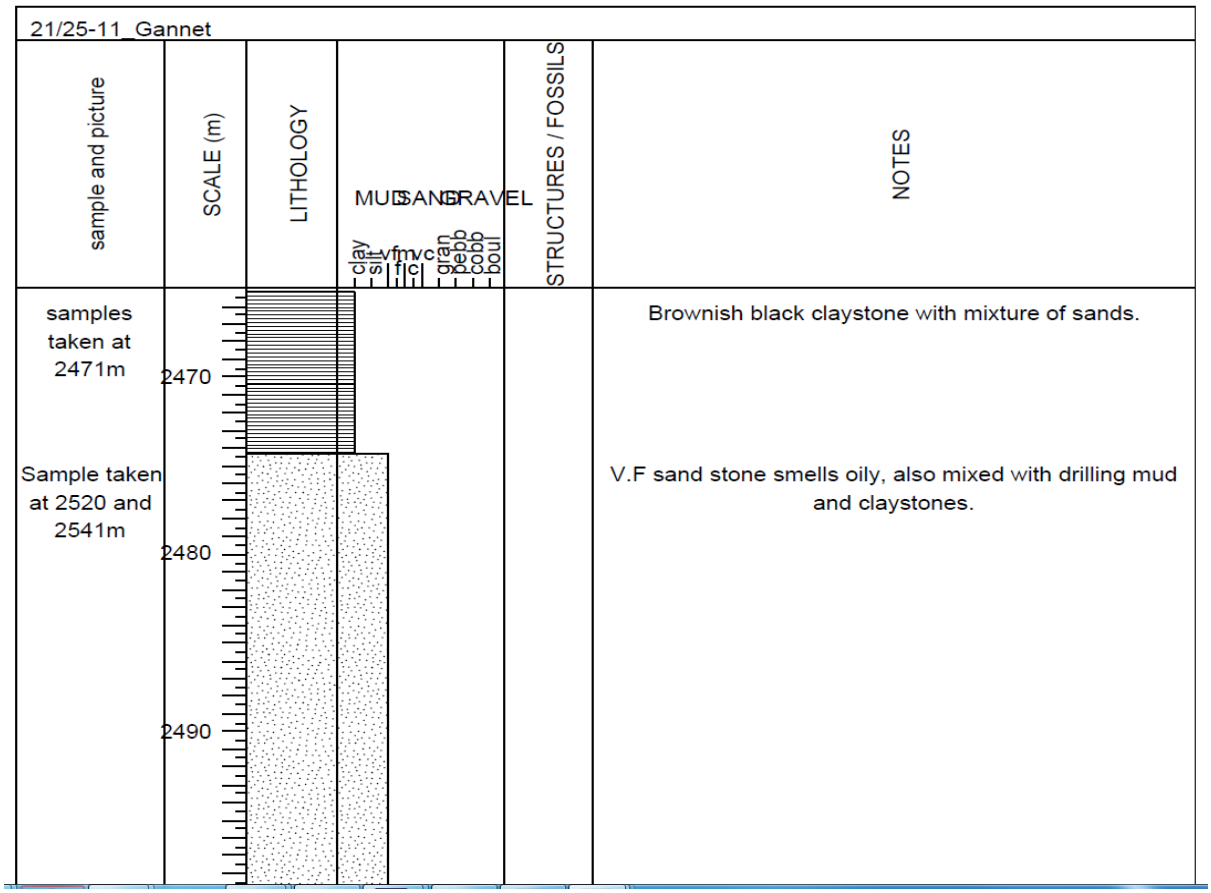
21/28a-3_Fyne & Dandy



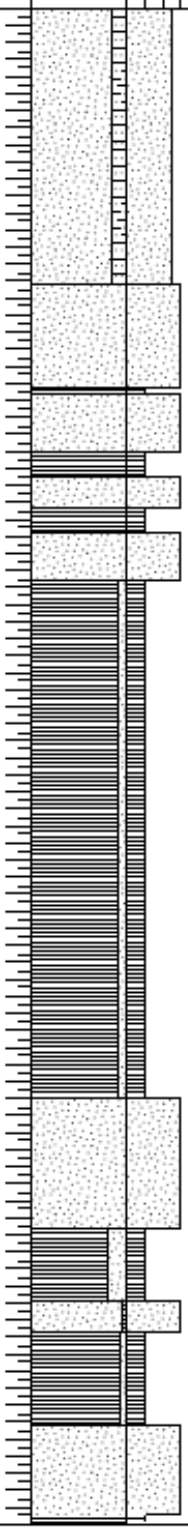

1430
1440
1450
1460
1470
Sample taken at 1436m
sample taken at 1445m
#29. sample taken at 1452m
samples taken at 1465m and 1470m
Black silty mudstone. Like the other layers above, there are no sedimentary structures. Can see saw marks.
Oil stained sandstone
Silty mudstone
Dark siltstone
Black Silty mudstone
Grey siltstone
Light grey sandstone suggesting they are water wet. At the base of the sandstone package the colour changes to golden yellow. Green streaks are noticed on the top of the sandstone (#29). They are man-made features, HCL has probably been poured on the surface to test for calcite.
Golden yellow to light grey sandstone. Well sorted fine grains. Man-made green streaks are observed
Black silty mudstone


21/25-A1
sample and picture
SCALE (m)
LITHOLOGY
MUD
SAND
GRAVEL
clay
silt
vf
f
m
c
vc
gran
peb
cobb
boul
NOTES
samples at 2380, 2391, 2394, 2396, 2397, 2399 and 2403 m
2390
2400
2410
Samples at 2415 and 2416 m
2420
2430
Samples at 2432, 2433, 2434, 2436, 2443 and 2447m
2440
Grey v.f sandstones. Green stains on the surface due to acid. GOC in this layer. Samples spells oily and change to light gold below the GOC
Brown siltstones with streaks of calcite
OWC in this layer. Sandstones turn grey below OWC. Some red streaks due to hematite

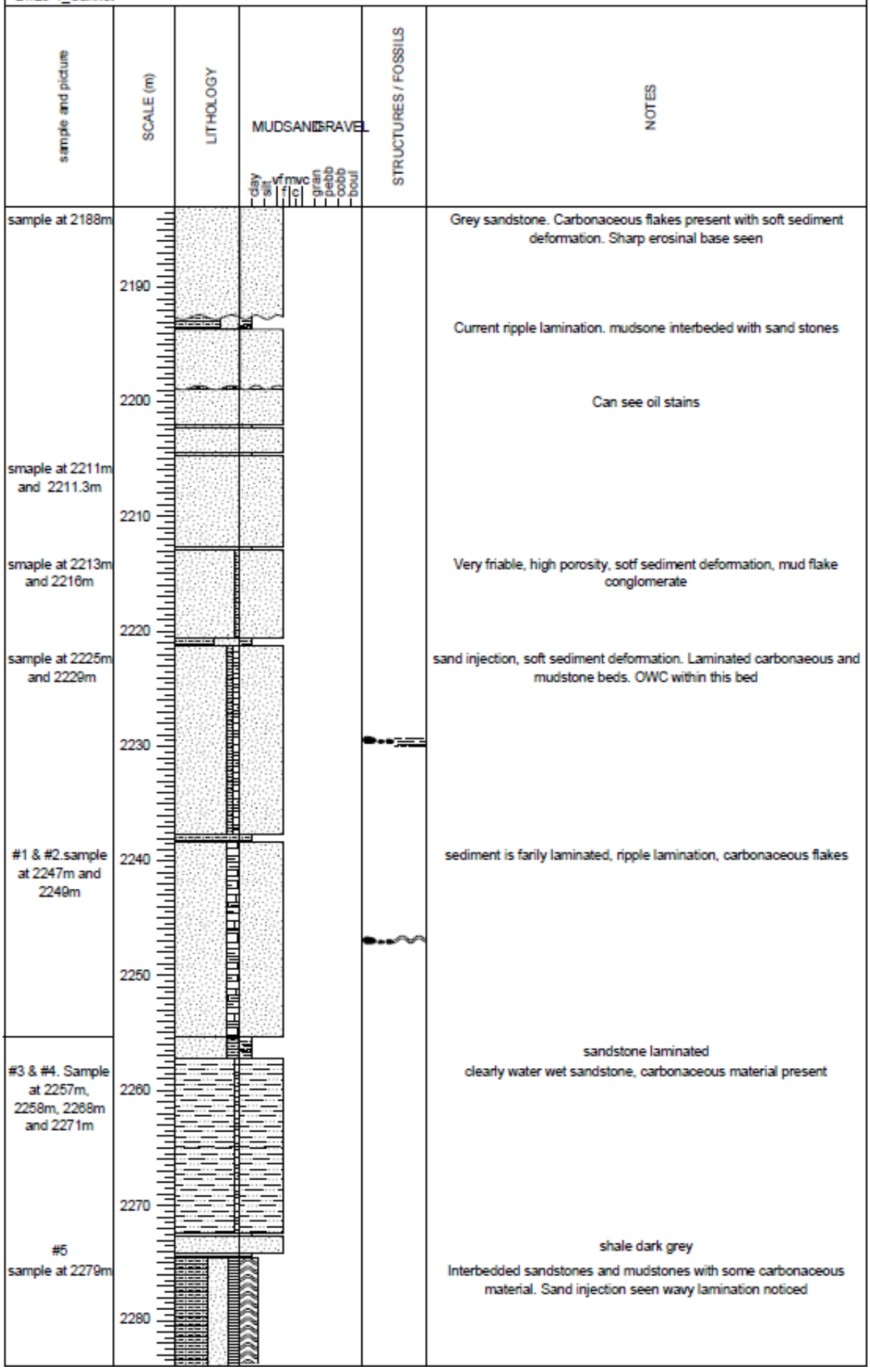

21/25-12_Gannet
sample and picture
SCALE (m)
LITHOLOGY
MUD
SAND
GRAVEL
clay
silt
vf
f
m
c
vc
gran
peb
cobb
boul
STRUCTURES / FOSSILS
NOTES
sample at 2348m
Dark grey silts
2350
sample at 2360, 2366 and 2375m
SS seem water wet
2360
2370
2380


21/25-11_Gannet
sample and picture
SCALE (m)
LITHOLOGY
MUD
SAND
GRAVEL
clay
slt
vf
f
m
c
vc
gran
pebb
cobb
boul
STRUCTURES / FOSSILS
NOTES
samples taken at 2471m
2470
Brownish black claystone with mixture of sands.
Sample taken at 2520 and 2541m
2480
V.F sand stone smells oily, also mixed with drilling mud and claystones.
2490

21/25-6_Gannet

sample and picture	SCALE (m)	LITHOLOGY	MUD SAND GRAVEL (clay, silt, vf, f, m, c, vc, gran, peb, cobb, boul)	NOTES
#11 & #12 sample at 2036m, 2031m, 2034m and 2036m	2030			Paper thin shale with thin beds of sandstone each less than a 40cm.
	2040			Highly porous friable sandstone, well sorted and quartz rich
sample at 2045m				GOC. oil stained friable sandstone
sample at 2047m				
sample at 2048m				still oil stained
Samples at 2051m	2050			
#13a. sample at 2053m				Oil down to
#14. samples at 2056m, 2060m, 2062m, 2063m, 2067m, 2078m, 2079m, 281m, 2082m and 2083m	2060			Colour varies from black to green indicating possible presence of chlorine to red indicating iron rich sediments. About 4 very thin sandstone beds are present.
	2070			
	2080			
#15 & #13b. sample at 2088m				Water wet sandstone, light grey in colour and well sorted
	2090			
sample at 2092m, 2093m,2094m and 2096m				papper thin shale. dark grey. Very thin sandstone bed.
sample at 2097m				
#16	2100			Some very thin sandstone beds
sample 2106m				very friable

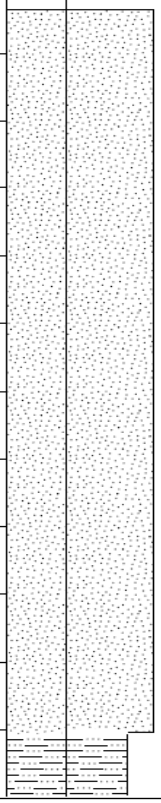
21/25-4_Gannet

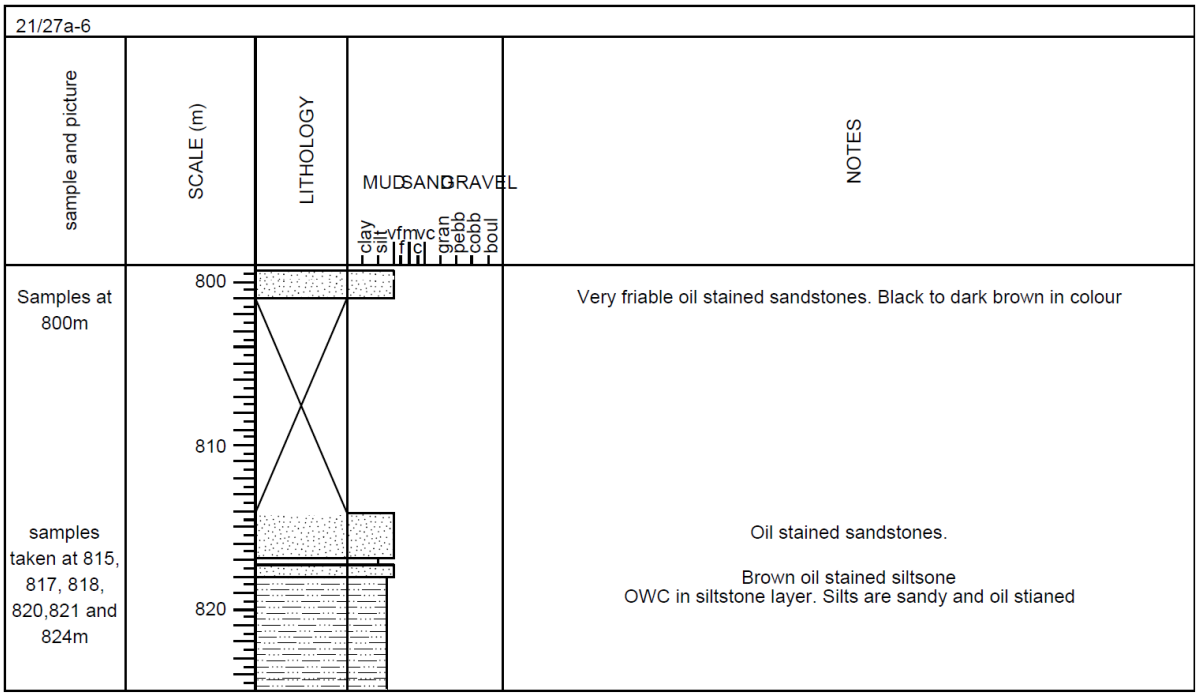


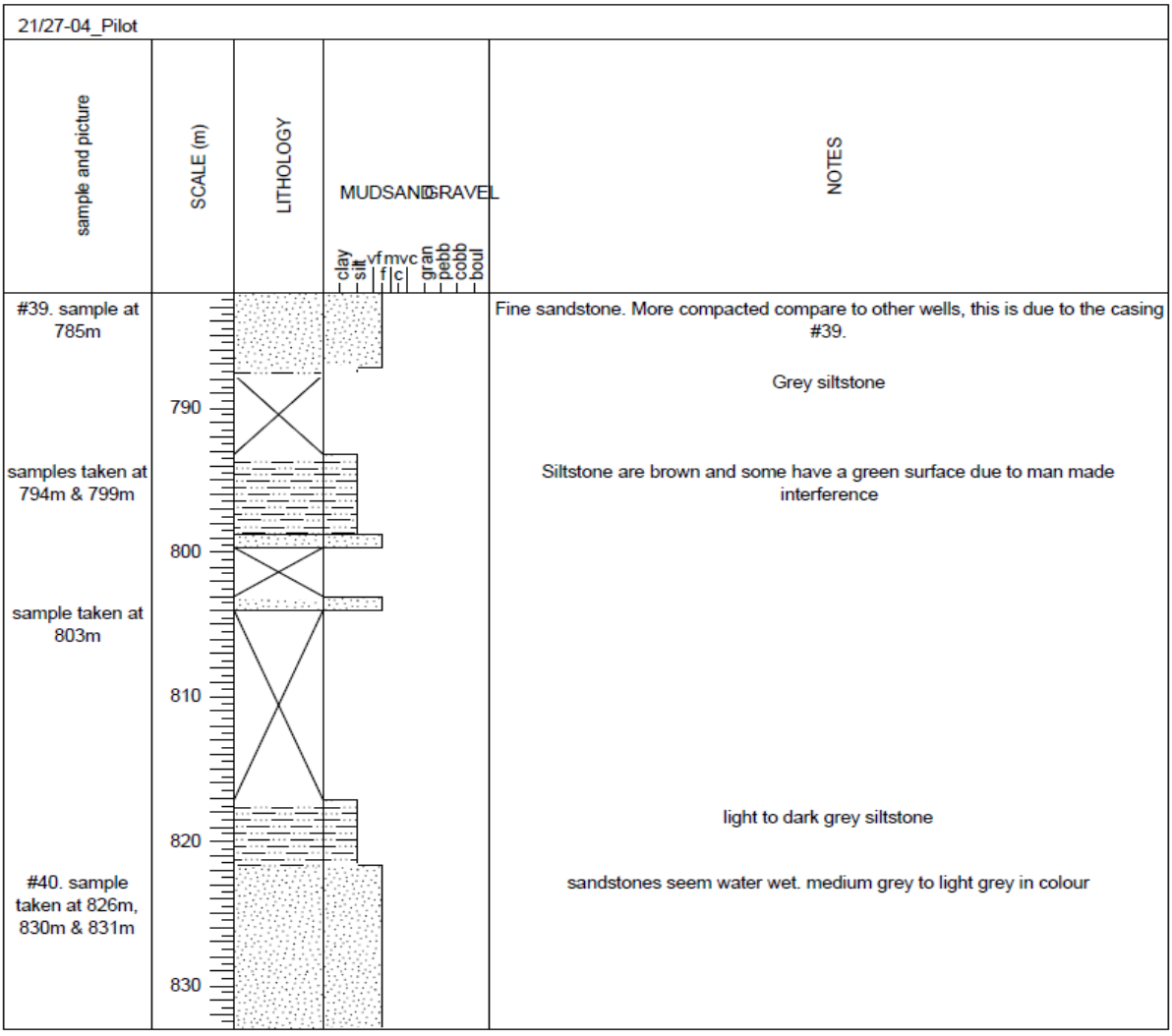
21/25-2_Guillemot

sample and picture	SCALE (m)	LITHOLOGY	MUD SAND GRAVEL (clay, silt, vf, f, m, c, vc, gran, pebb, cobb, boul)	STRUCTURES / FOSSILS	NOTES
sample at 1730					Fine sand, oil stains are present
sample at 1733m and 1734m					Mud clasts and carbonaceous material present
	1735				
sample at 1740m	1740				Sandstone seems water wet
sample at 1744m					Mudstones have carbonaceous streaks. Either red (iron rich) or green (probably chlorine rich)
	1745				
sample at 1749m					Red mudstone, iron rich

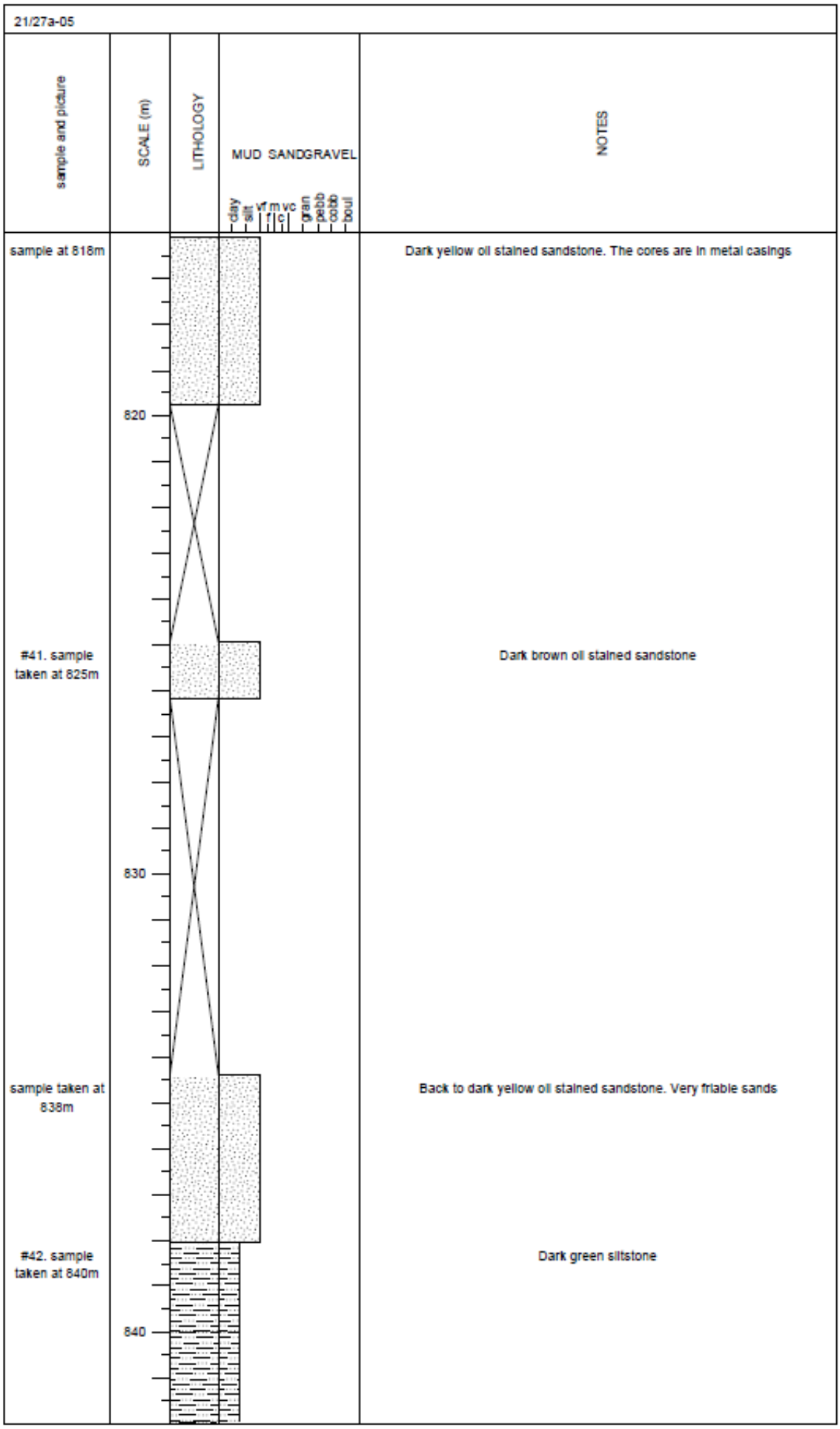
21-28b-7

samples and picture	SCALE (m)	LITHOLOGY	MUD SANDGRAVEL clay silt vf f m c vc gran pebb cobb boul	NOTES
#48 and #49. Samples at 1063, 1066,1067 and 1068m	1064 1065 1066 1067 1068			Fine white sandstones. Seems water wet. Some brownish red patches found on the sandstones (#49). Saw marks are also seen (#48). sandstones get darker towards the next layer
sample taken at 1069m				Brown sandy siltstones. seems oil stained

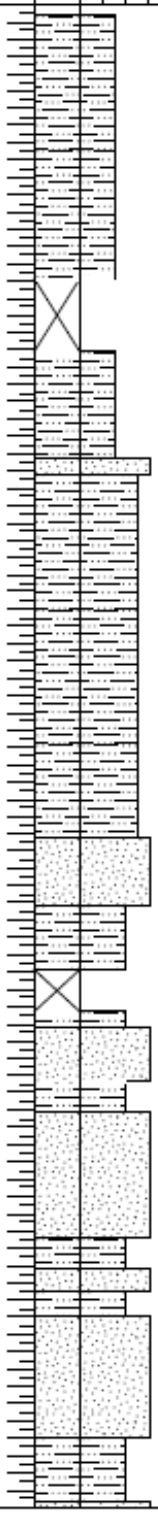

21/27a-6
sample and picture
SCALE (m)
LITHOLOGY
MUD
SAND
GRAVEL
clay
silt
vf
f
m
c
vc
gran
pebb
cobb
boul
NOTES
800
810
820
Samples at 800m
samples taken at 815, 817, 818, 820,821 and 824m
Very friable oil stained sandstones. Black to dark brown in colour
Oil stained sandstones.
Brown oil stained siltsone
OWC in siltstone layer. Silts are sandy and oil stianed


21/27-04_Pilot
sample and picture
SCALE (m)
LITHOLOGY
MUD
SAND
GRAVEL
clay
silt
vf
f
m
c
vc
gran
pebb
cobb
boul
NOTES
790
800
810
820
830
#39. sample at 785m
samples taken at 794m & 799m
sample taken at 803m
#40. sample taken at 826m, 830m & 831m
Fine sandstone. More compacted compare to other wells, this is due to the casing #39.
Grey siltstone
Siltstone are brown and some have a green surface due to man made interference
light to dark grey siltstone
sandstones seem water wet. medium grey to light grey in colour

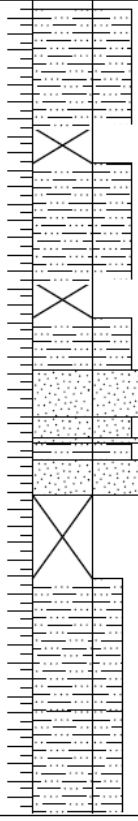
21/27a-05


sample and picture
SCALE (m)
LITHOLOGY
MUD SAND GRAVEL
clay
silt
vf
f
m
c
vc
gran
pebb
cobb
boul
NOTES
sample at 818m
Dark yellow oil stained sandstone. The cores are in metal casings
820
#41. sample taken at 825m
Dark brown oil stained sandstone
830
sample taken at 838m
Back to dark yellow oil stained sandstone. Very friable sands
#42. sample taken at 840m
Dark green siltstone
840

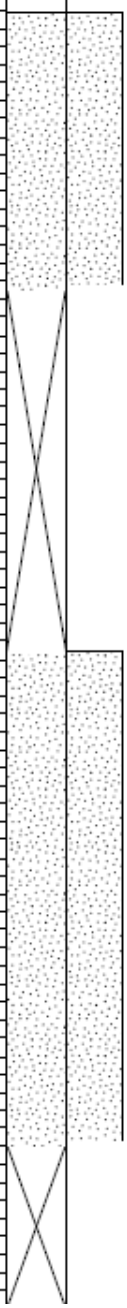
21/27-3_Pilot

sample and picture	SCALE (m)	LITHOLOGY	MUD SANDGRAVEL (clay, silt, vf, f, m, c, vc, gran, pebb, cobb, boul)	NOTES
	770			Dark grey oily silty mudstone. Think dark bands about 20cm which could be hematite #43
	780			
sample at 788m				Same as above. I can see saw marks.Siltstone are stained orange could be siderite or oxidised pyrite
	790			
#43. sample taken at 897m				Thin oil stained sandstone Sandy siltstone. Can see saw marks and man-made green streaks from HCL
	800			
	810			
sample taken at 817m				Sandstone seems water wet
				Oily siltstone
	820			
#44. sample taken at 825m				Oily siltstone Medium grey sandstone
sample taken at 833m	830			Sandstone seems water wet
				Oily siltstone
	840			
sample taken 845m				
	850			

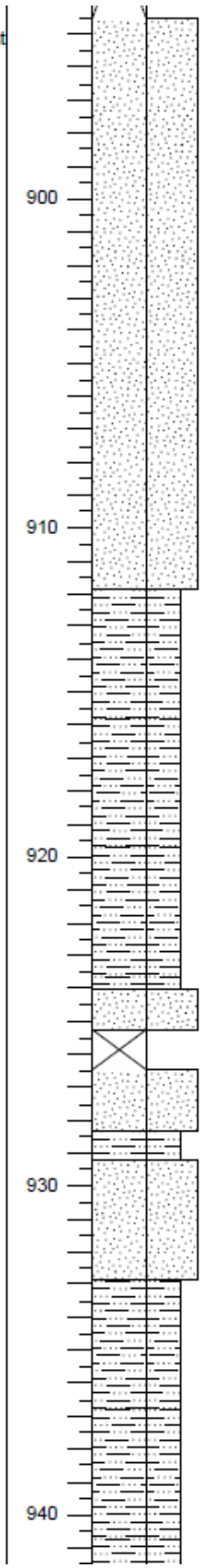
21/27-02_Pilot

sample and picture	SCALE (m)	LITHOLOGY	MUD SAND GRAVEL (clay, silt, vf, f, m, c, gran, pebb, cobb, boul)	NOTES
	840			Grey siltstone with man-made green streak
				Grey siltstone
	850			Dark grey siltstone. Saw marks are present with man-made green streaks on the surface
Sample taken at 854m & 857m				Well sorted lightly oil stained sandstone
				Dark grey siltstone
Sample taken at 860m	860			Light grey sandstone. Smells oily
sample taken at 880m	870			Dark grey siltstone. Smells oily

21/27-1A_Pilot

sample and picture	SCALE (m)	LITHOLOGY	MUD SAND GRAVEL clay silt vf f m c vc gran pebb cobb boul	NOTES
#36. samples taken at 861m, 863m & 865m	860			Well sorted oil stained sand.
	870			
#37. samples taken at 881m & 888m	880			Sandstones are below the OWC but not completely water wet. Some sandstones are mildly oil stained
	890			

Samples taken at 896m & 908m



sandstones are still oil stained

Brown siltstone. saw marks are present. Small light brow spots could suggests the presence of hematite

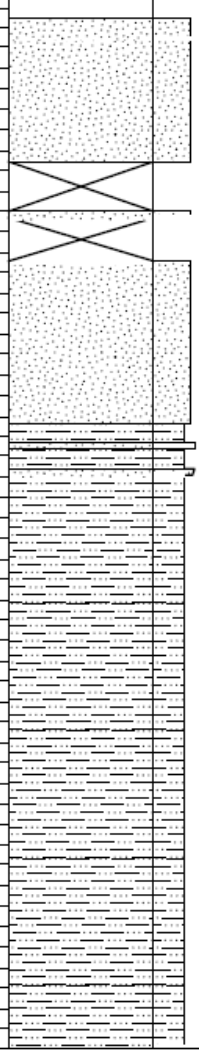
Oil stained sandstone

Light brown siltstone

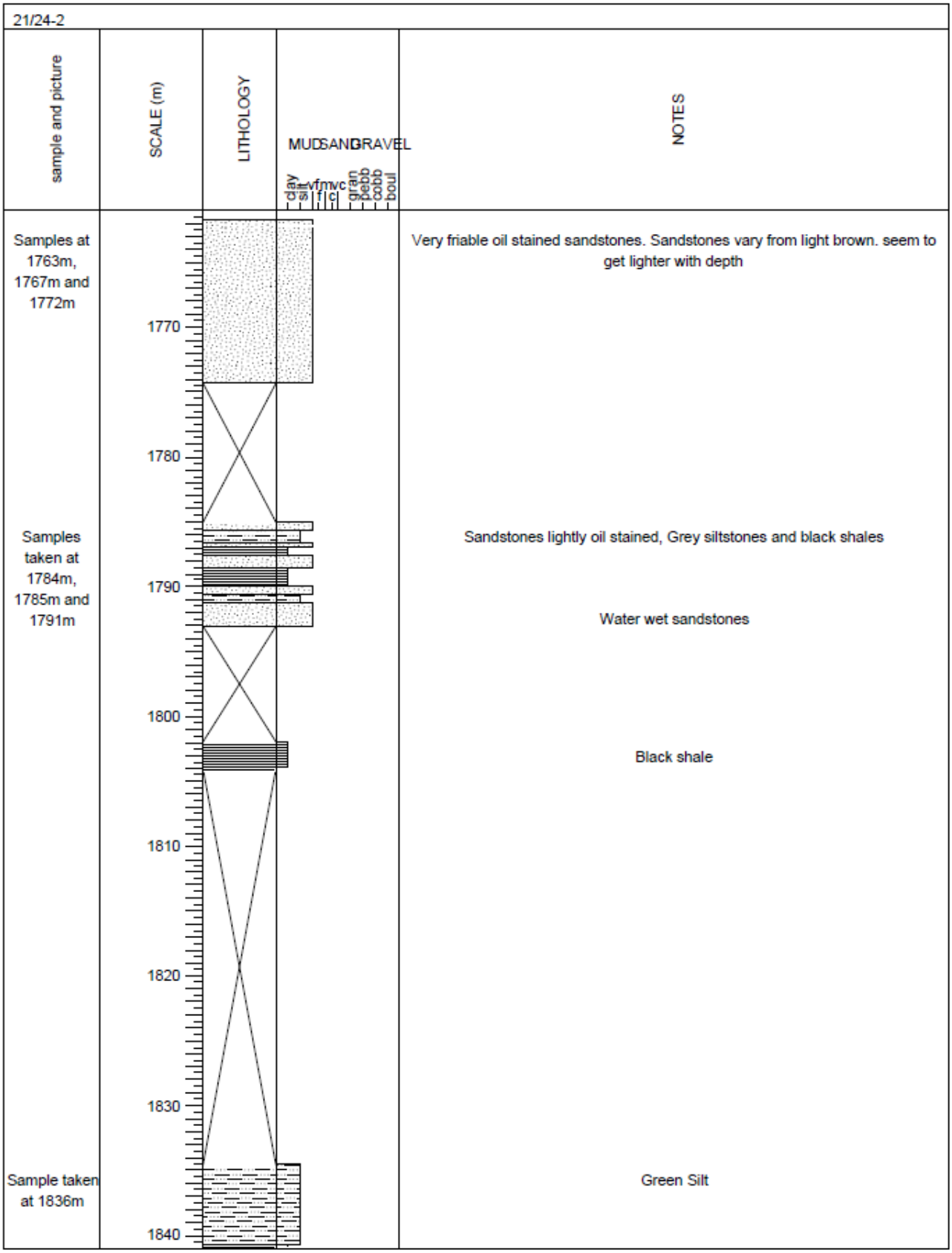
#38. sample taken at 933m

light brown to dark brown to light red siltstone. saw marks are present.

21/24-3

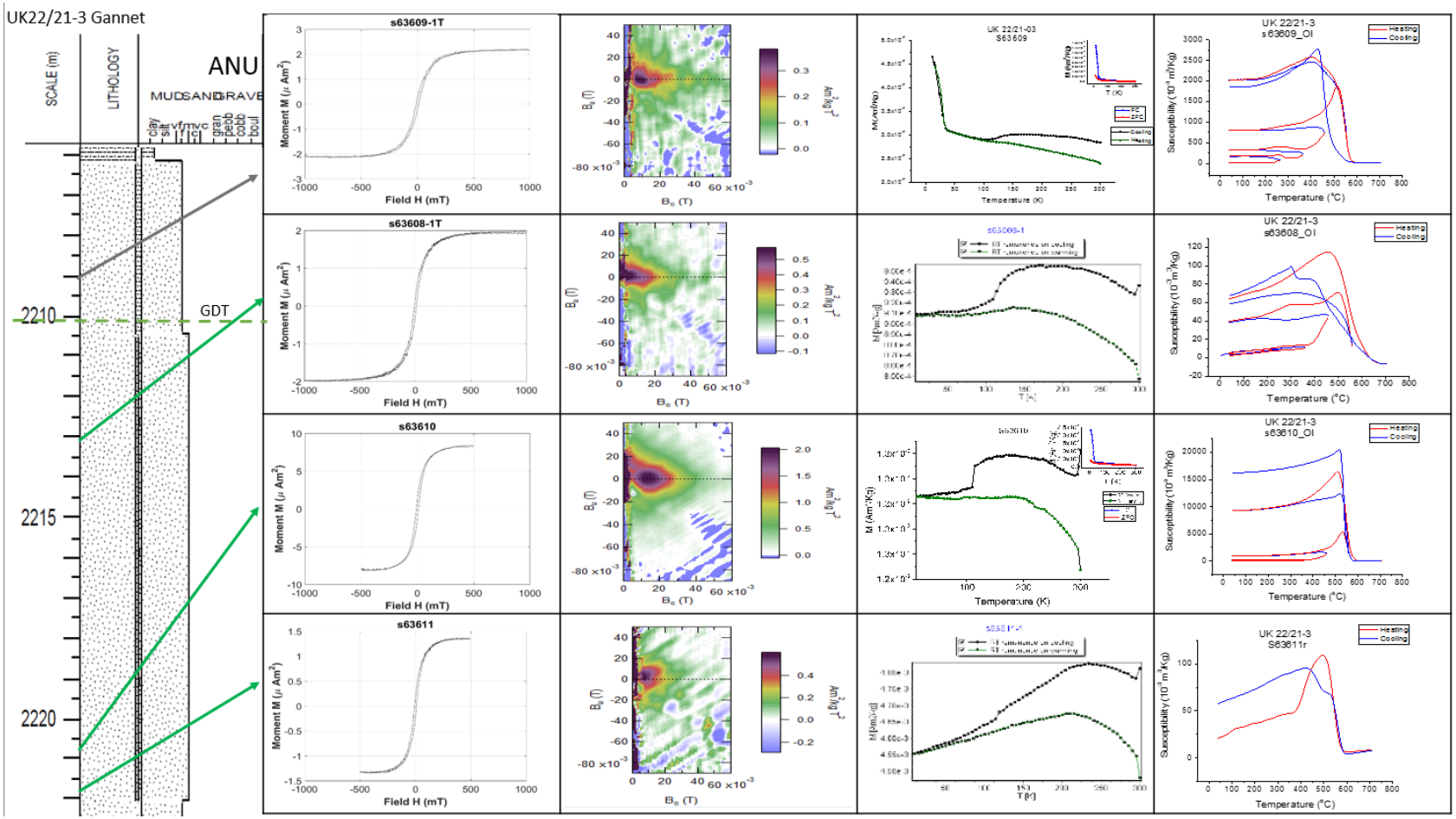
sample and picture	SCALE (m)	LITHOLOGY	NOTES
Samples at 1616m and 1618m	1615 1616 1617 1618 1619 1620 1621 1622 1623 1624 1625 1626 1627 1628 1629 1630 1631 1632 1633 1634 1635 1636 1637 1638 1639		Very friable oil stained sandstones. Sandstones are brown
Samples at 1623m, three samples at 1625m. samples at1626m and 1627m			Oil stained sands OWC in Siltstone layer
Samples taken at 1629 m, 1624 m and 1638 m			Thin dark brown oil stained sandstones which appear to be cemented unlike the sandstones above Light green siltstones with red patches suggesting hematite. pyrite noodles seen from 1661 m

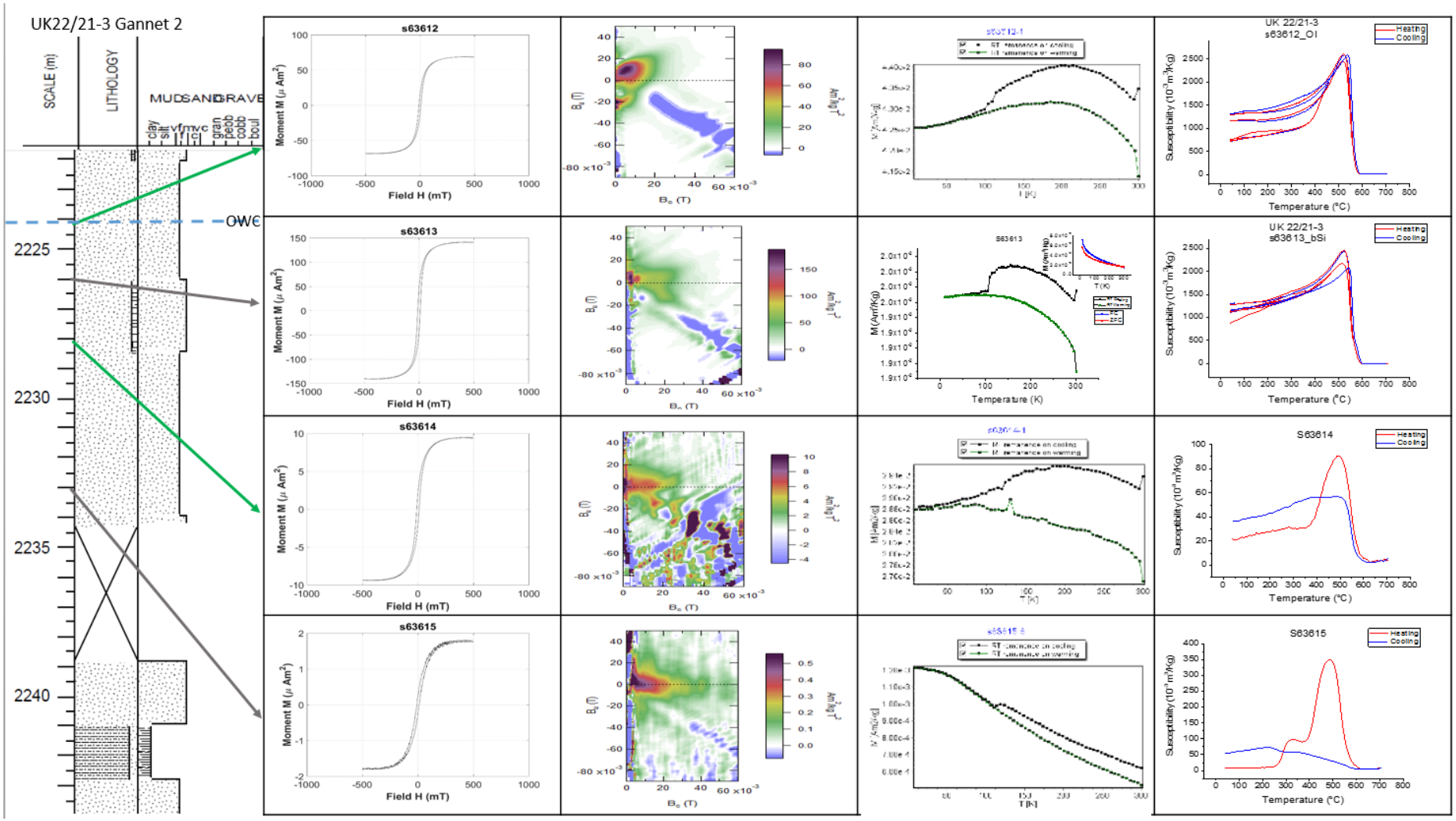
21/24-2


sample and picture
SCALE (m)
LITHOLOGY
MUD
SAND
GRAVEL
clay
silt
vf
f
m
c
vc
gran
pebb
cobb
boul
NOTES
Samples at 1763m, 1767m and 1772m
Very friable oil stained sandstones. Sandstones vary from light brown. seem to get lighter with depth
1770
1780
Samples taken at 1784m, 1785m and 1791m
Sandstones lightly oil stained, Grey siltstones and black shales
1790
Water wet sandstones
1800
Black shale
1810
1820
1830
Sample taken at 1836m
Green Silt
1840

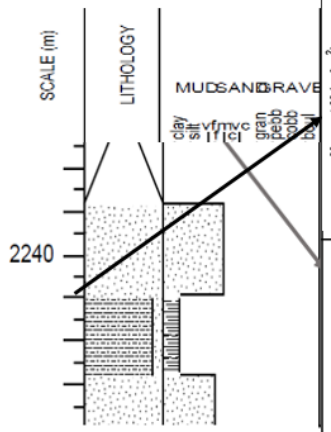
Appendix 3

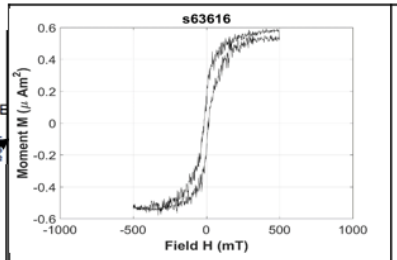
3.1 Hysteresis, FORC, LT experiment and Susceptibility vs Temperature

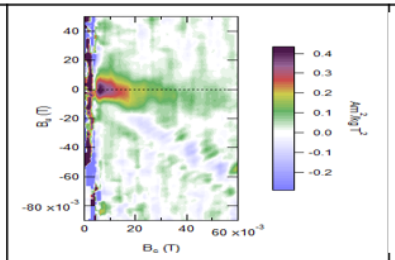


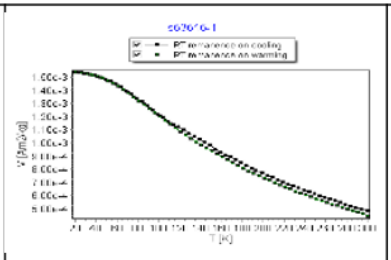

UK22/21-3 Gannet 2
SCALE (m)
LITHOLOGY
MUDSANDGRAVE
clay
silt
vf
f
m
vc
gran
pebb
cobb
boul
OWC
2225
2230
2235
2240
s63612
s63613
s63614
s63615
Moment M (μ Am²)
Field H (mT)
Bc (T)
Temperature (°C)
Susceptibility (10⁻⁸ m³/kg)
UK 22/21-3
s63612_OI
s63613_bSi
Heating
Cooling
S63614
S63615

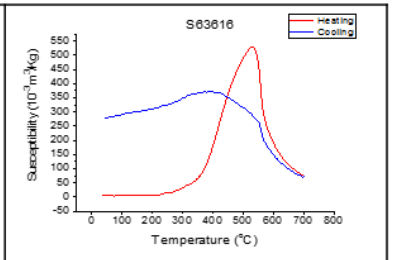
UK22/21-3 Gannet 2

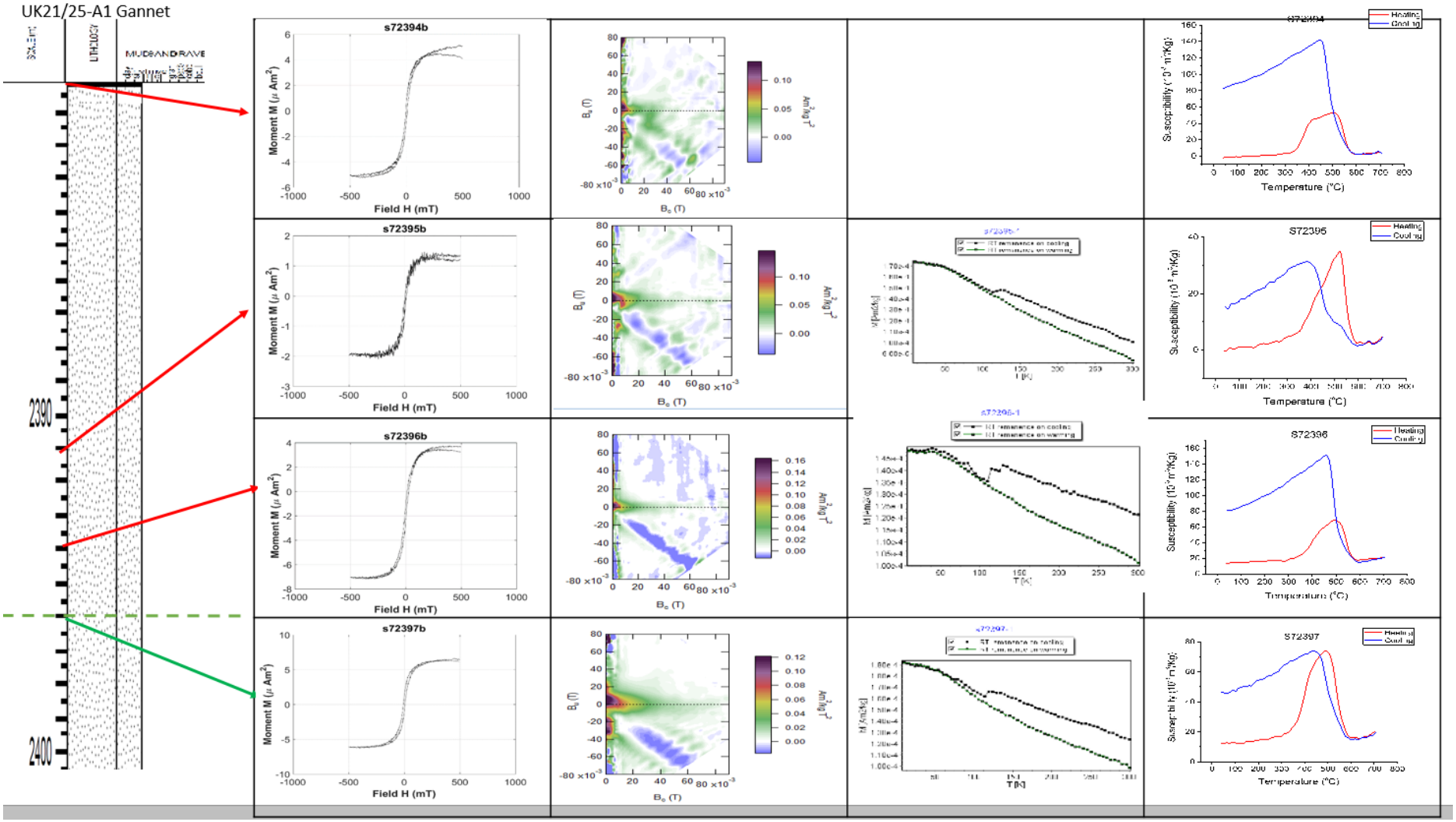


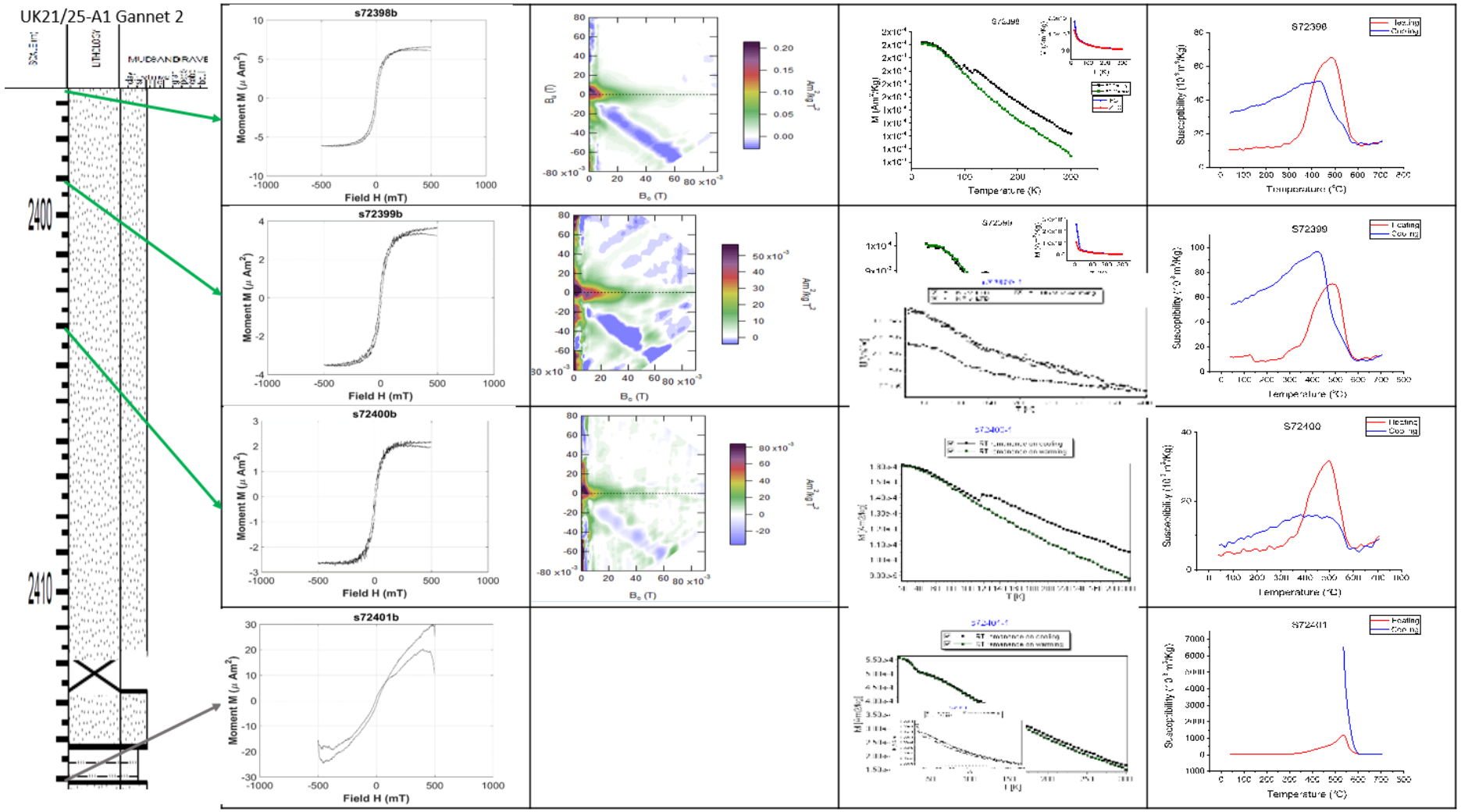


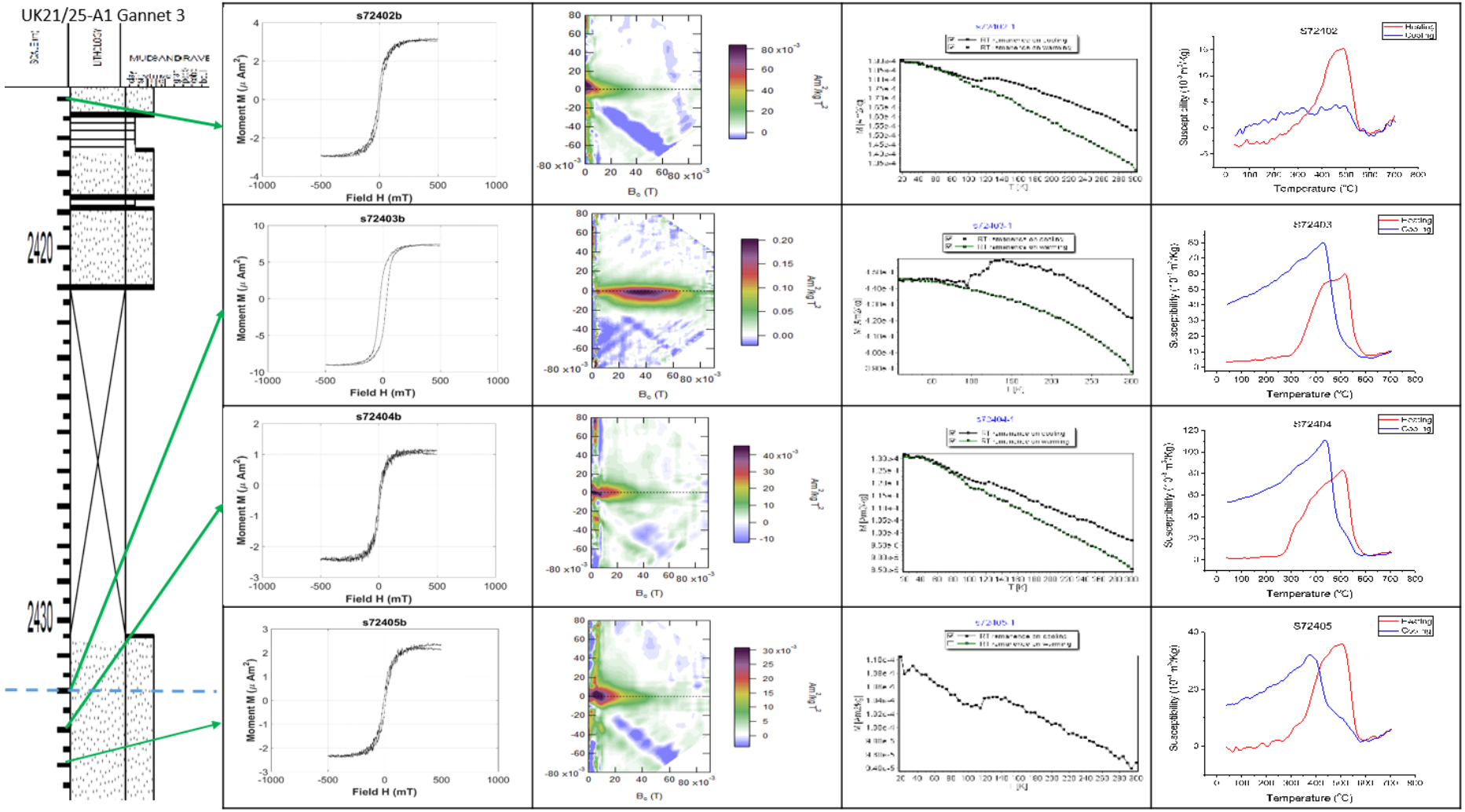


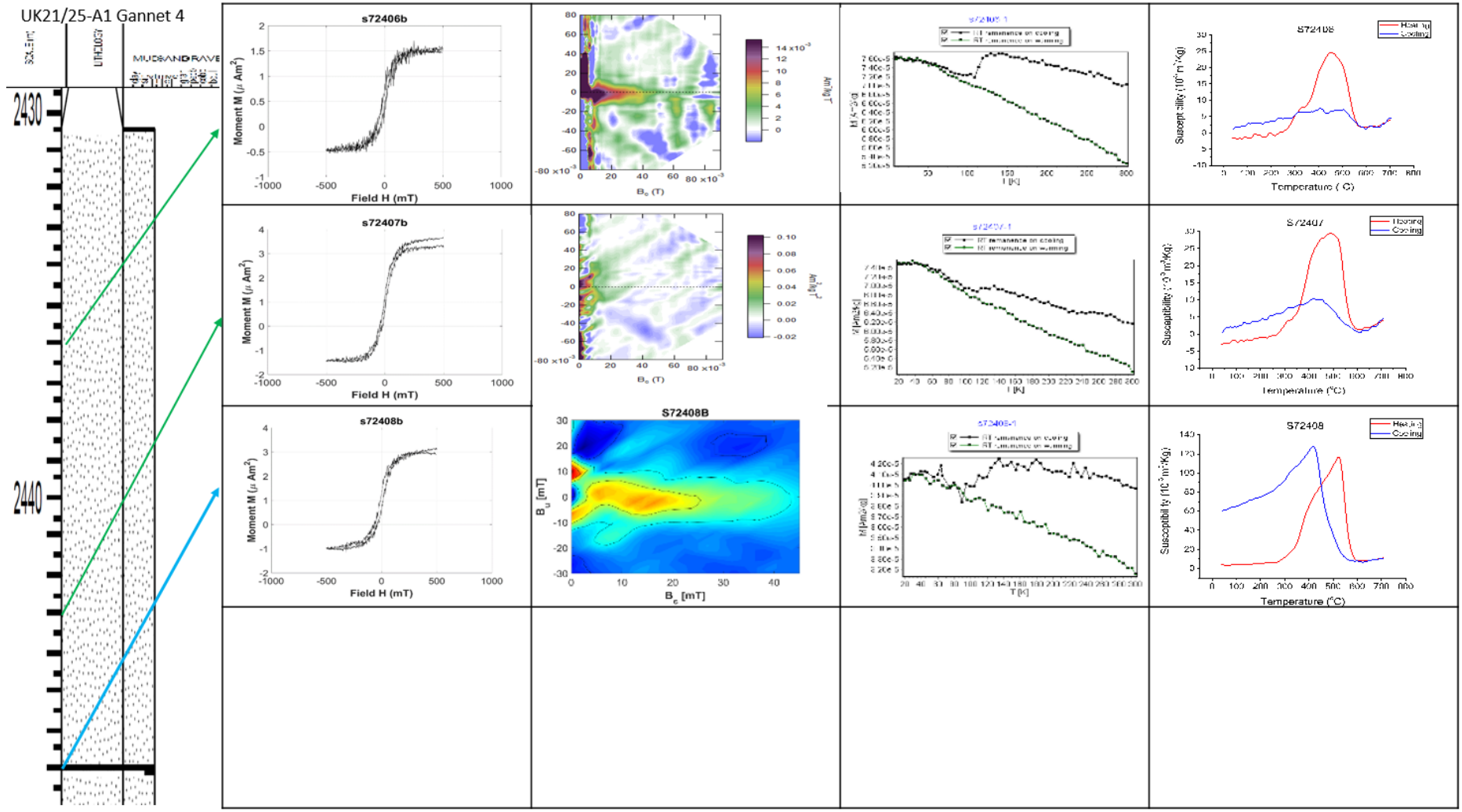


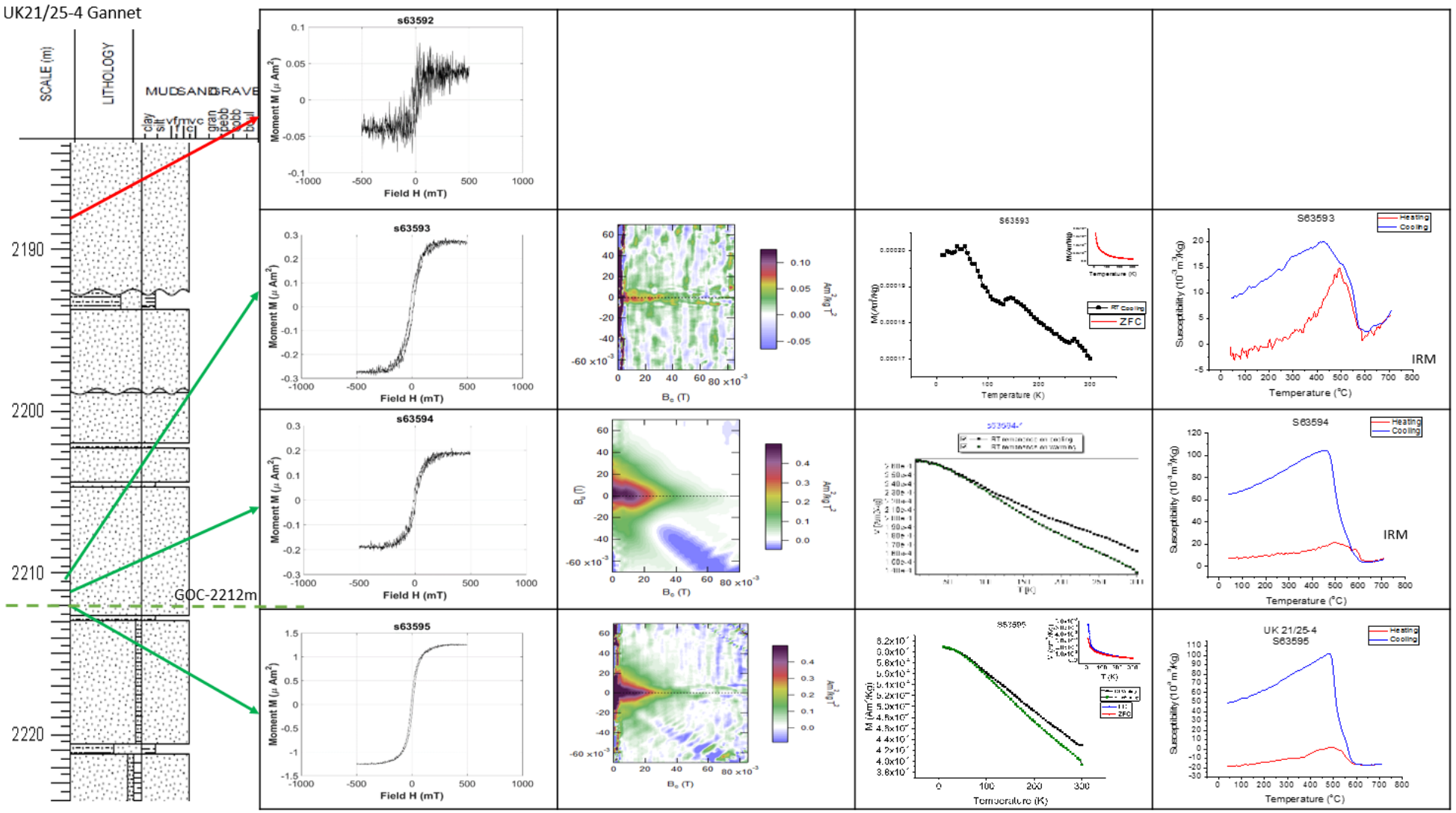


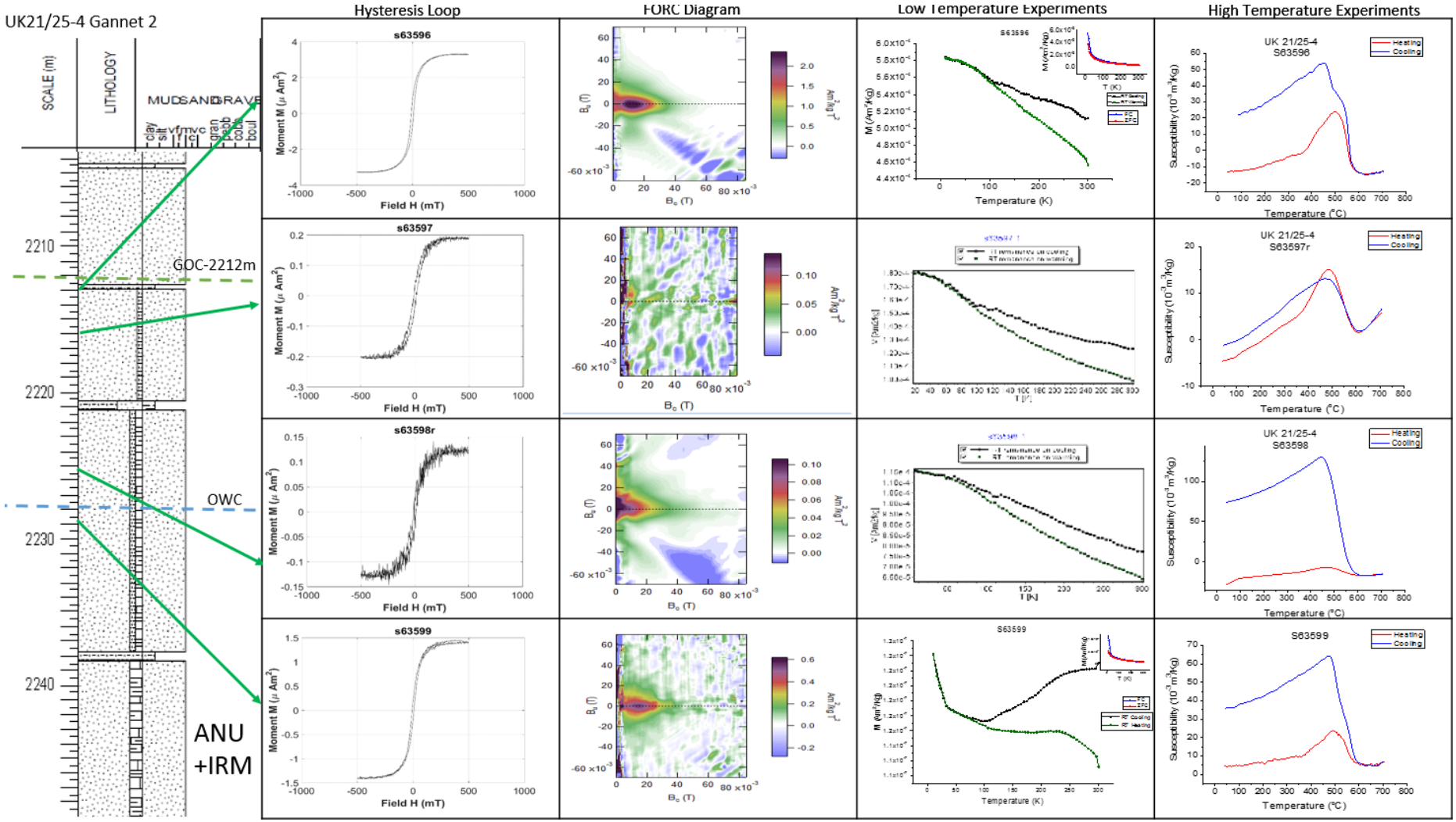

UK21/25-A1 Gannet
MUDSANDRAVE
2390
2400
s72394b
s72395b
s72396b
s72397b
Moment M (μ Am²)
Field H (mT)
Bc (T)
Heating
Cooling
Susceptibility (10⁻⁹ m³/Kg)
Temperature (°C)
S72395
S72396
S72397

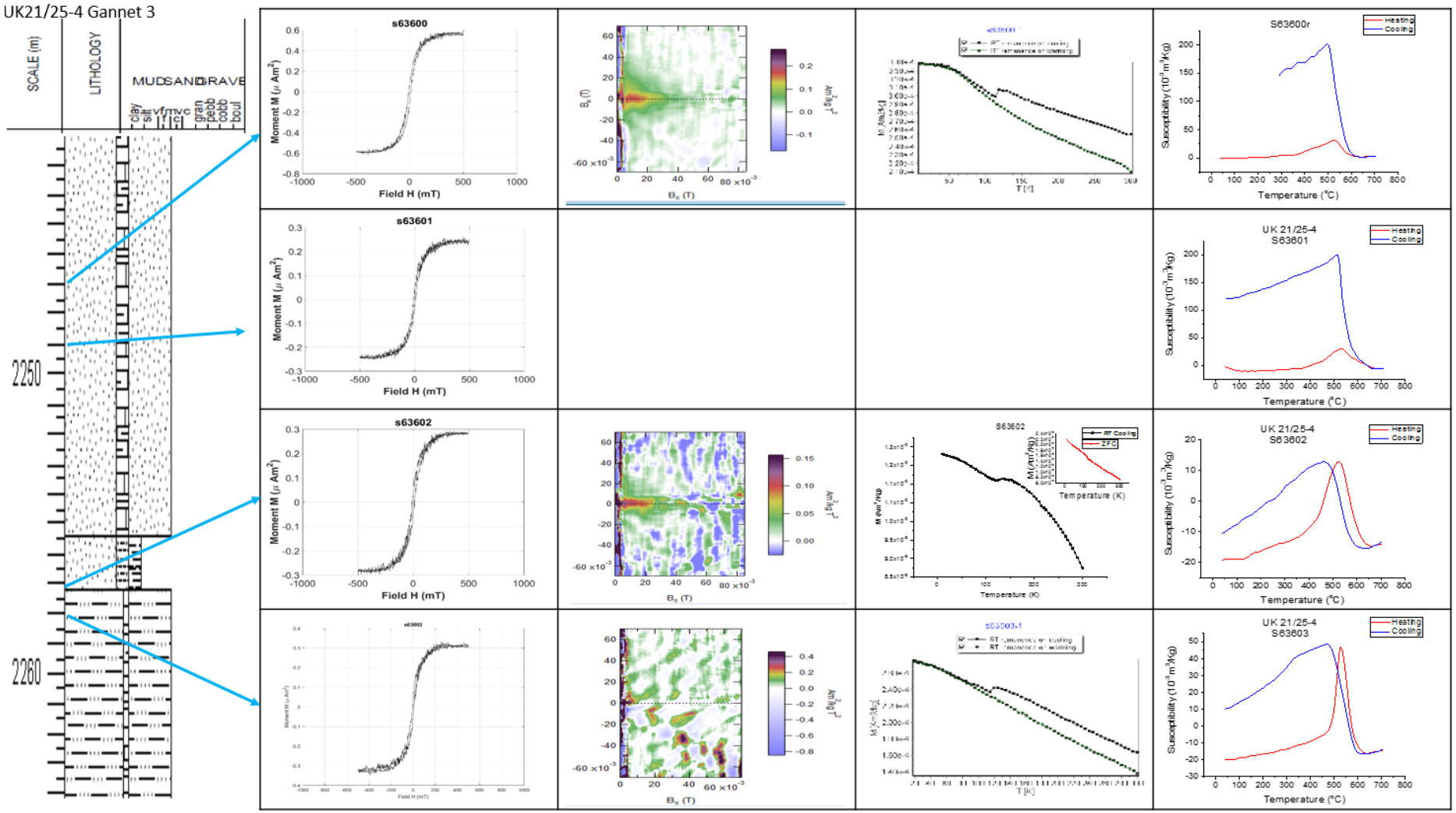

UK21/25-A1 Gannet 2
MUDSANDRAVE
2400
2410
s72398b
s72399b
s72400b
s72401b
Moment M (μ Am²)
Field H (mT)
Bc (T)
Temperature (K)
Temperature (°C)
S72398
S72399
S72400
S72401
Heating
Cooling

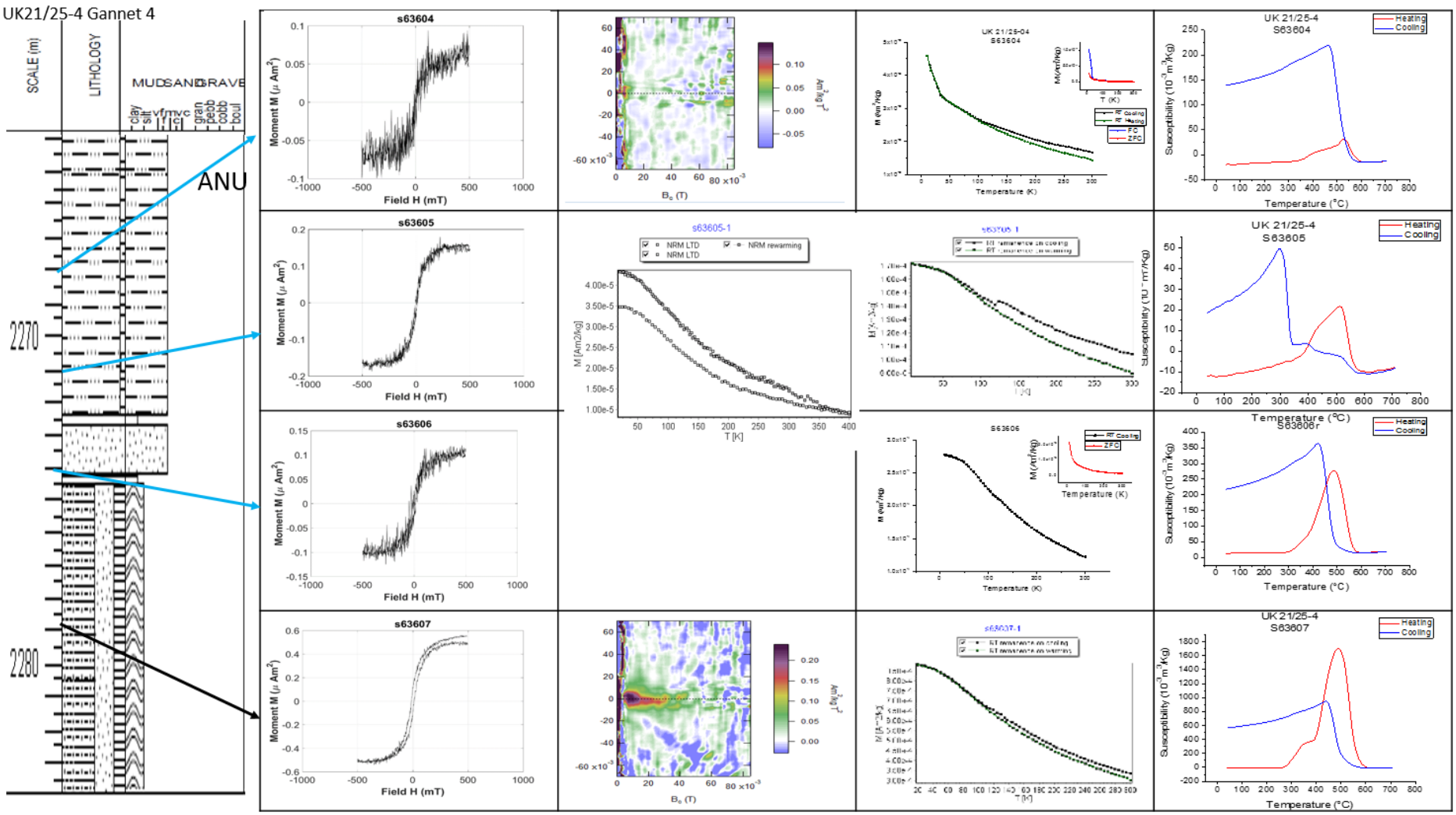

UK21/25-A1 Gannet 3
MUDSANDRAVE
2420
2430
s72402b
s72403b
s72404b
s72405b
Moment M (μ Am²)
Field H (mT)
Bc (T)
S72402
S72403
S72404
S72405
Heating
Cooling
Susceptibility (10⁻⁹ m³/Kg)
Temperature (°C)

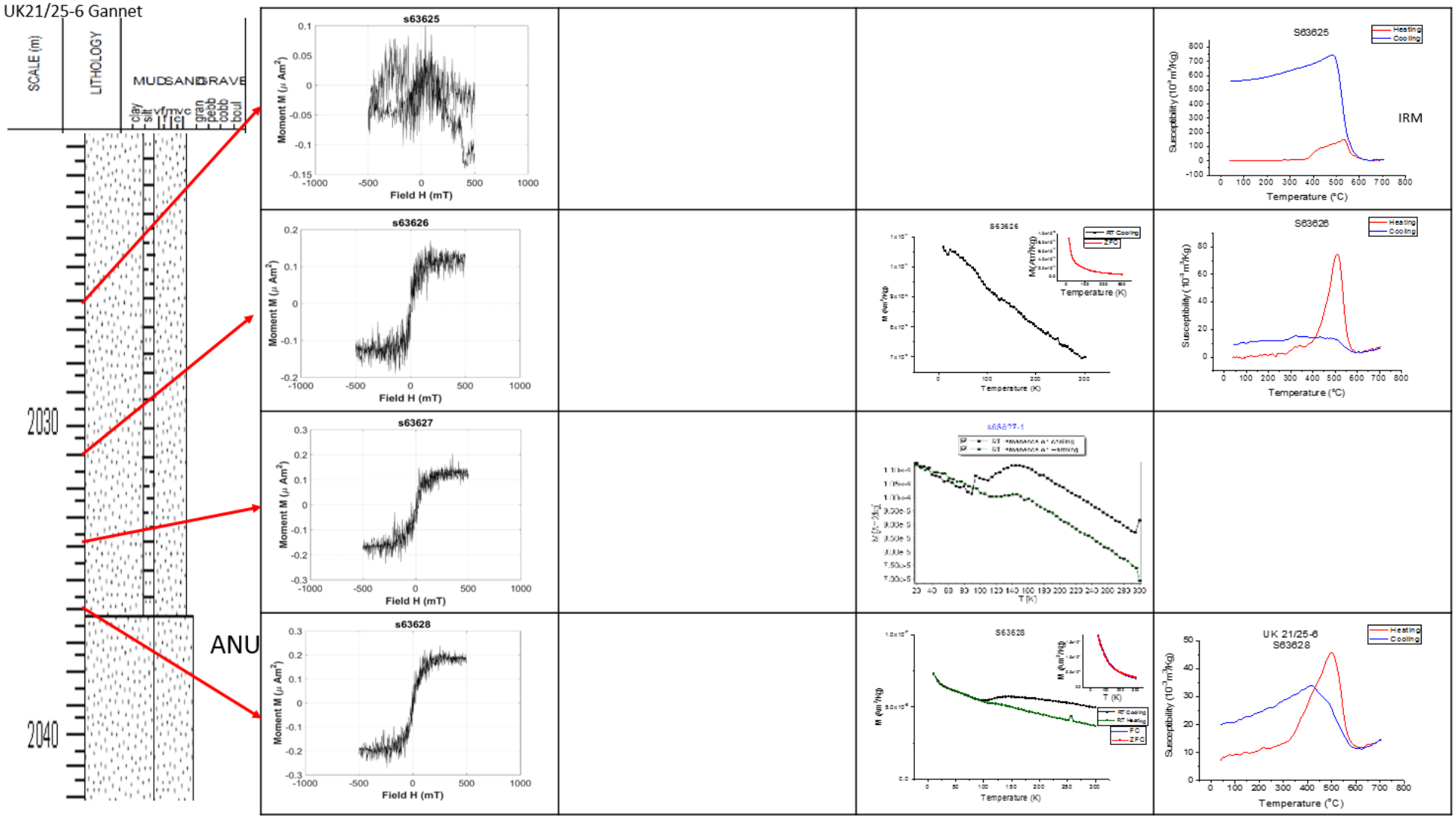

UK21/25-A1 Gannet 4
MUD AND RAVE
2430
2440
s72406b
Moment M (μ Am²)
Field H (mT)
s72407b
Moment M (μ Am²)
Field H (mT)
s72408b
Moment M (μ Am²)
Field H (mT)
S72408B
B_u [mT]
B_c [mT]
S72408
Heating
Cooling
Susceptibility (10⁻⁸ m³/Kg)
Temperature (°C)
S72407
Heating
Cooling
Susceptibility (10⁻⁸ m³/Kg)
Temperature (°C)
S72408
Heating
Cooling
Susceptibility (10⁻⁸ m³/Kg)
Temperature (°C)


UK21/25-4 Gannet
SCALE (m)
LITHOLOGY
MUD
SAND
GRAVE
clay
silt
vf
f
m
c
vc
gran
peeb
cobb
bld
2190
2200
2210
2220
GOC-2212m
s63592
s63593
s63594
s63595
Moment M (μ Am²)
Field H (mT)
Bc (T)
S63593
Temperature (K)
RT Cooling
ZFC
Susceptibility (10⁻⁹ m³/Kg)
Temperature (°C)
Heating
Cooling
IRM
S63594
UK 21/25-4
S63595

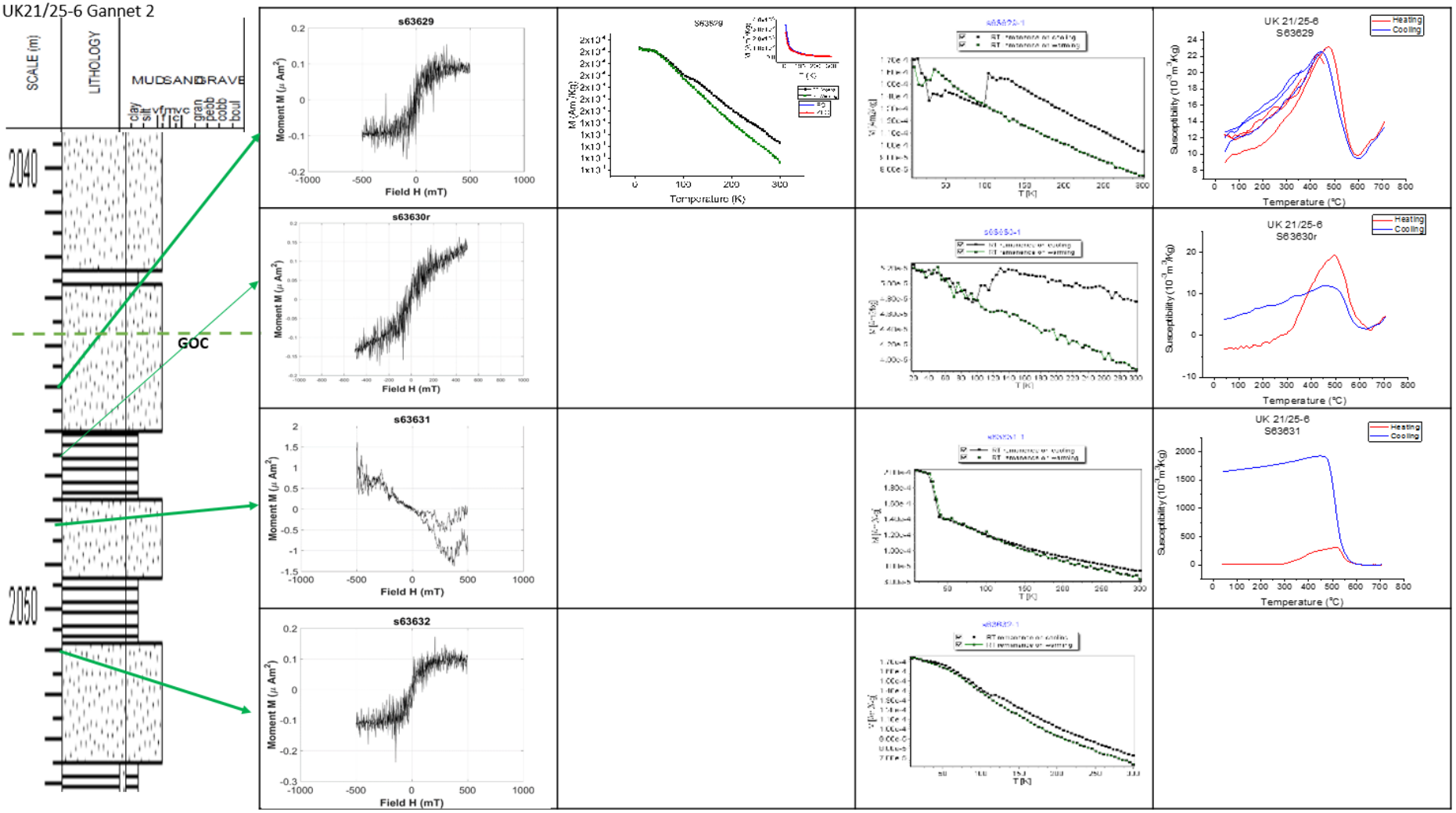

UK21/25-4 Gannet 2
SCALE (m)
LITHOLOGY
MUDSANDGRAVE
clay
2210
GOC-2212m
2220
OWC
2230
2240
ANU
+IRM
Hysteresis Loop
FORC Diagram
Low Temperature Experiments
High Temperature Experiments
s63596
s63597
s63598r
s63599
Moment M (μ Am²)
Field H (mT)
Bc (T)
Temperature (K)
Temperature (°C)
Susceptibility (10⁻⁹ m³/kg)
UK 21/25-4
S63596
S63597r
S63598
S63599
Heating
Cooling

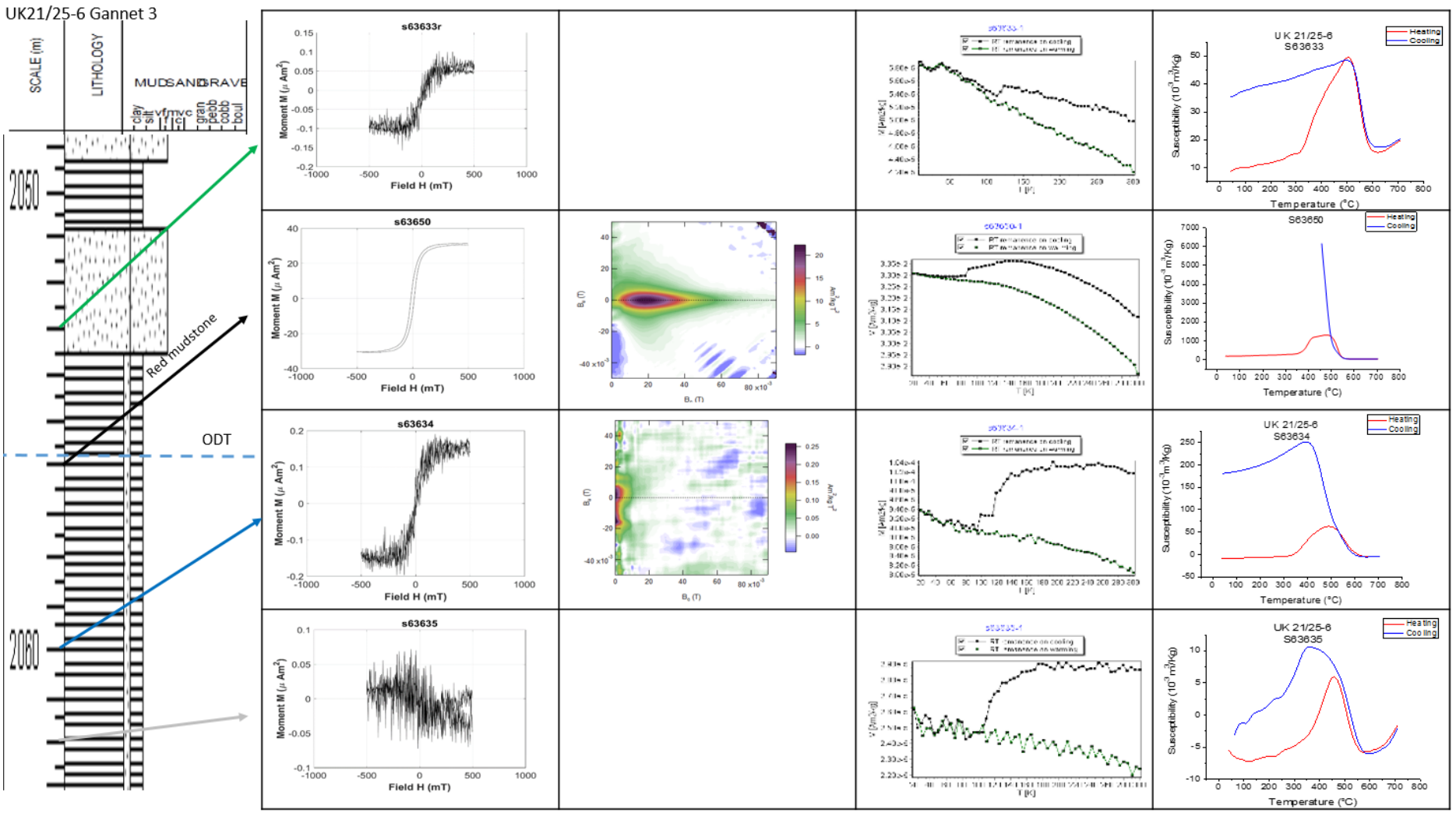

UK21/25-4 Gannet 3
SCALE (m)
LITHOLOGY
MUDSANDGRAVE
clay
silt
vf
mvc
gran
pebb
cobb
boul
2250
2260
s63600
Moment M (μ Am²)
Field H (mT)
Bc (T)
S63600r
Heating
Cooling
Susceptibility (10⁻⁸ m³/kg)
Temperature (°C)
s63601
UK 21/25-4
S63601
s63602
S63602
RT Cooling
ZFC
Temperature (K)
UK 21/25-4
S63602
s63603
UK 21/25-4
S63603

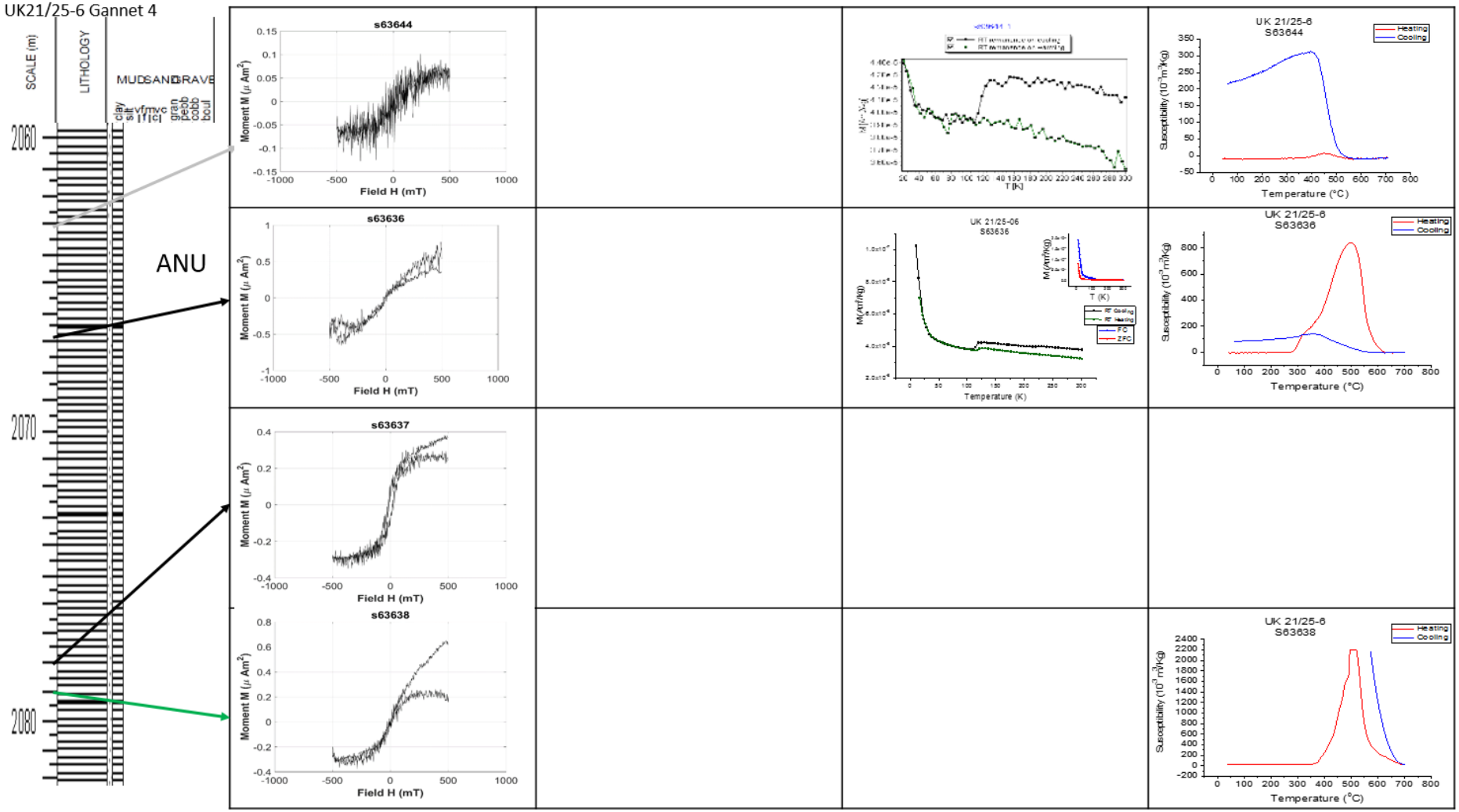

UK21/25-4 Gannet 4
SCALE (m)
LITHOLOGY
MUDSANDGRAVE
clay
sil
vf
f
m
c
vc
gran
peb
cobb
boul
ANU
2270
2280
s63604
Moment M (μ Am²)
Field H (mT)
s63605
s63606
s63607
s63605-1
NRM LTD
NRM rewarming
M [Am2/kg]
T [K]
Bo (T)
UK 21/25-04
S63604
Temperature (K)
Temperature (°C)
FC
ZFC
RT Cooling
RT Heating
UK 21/25-4
S63604
S63605
S63606r
S63607
Heating
Cooling
Susceptibility (10⁻⁸ m³/kg)


UK21/25-6 Gannet
SCALE (m)
LITHOLOGY
MUD
SAND
GRAVE
clay
silt
vf
f
m
c
vc
gran
peob
cobb
boul
2030
2040
ANU
s63625
s63626
s63627
s63628
Moment M (μ Am²)
Field H (mT)
S63625
S63626
S63628
Heating
Cooling
IRM
RT Cooling
ZFC
RT Heating
FC
Susceptibility (10⁻³ m³/kg)
Temperature (°C)
Temperature (K)
T (K)
UK 21/25-6
S63628

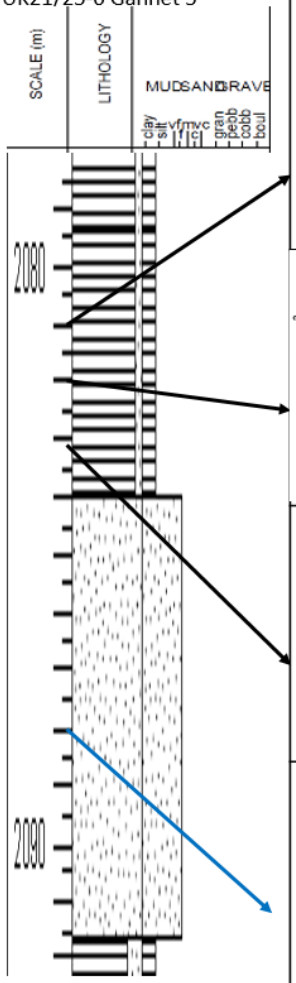
UK21/25-6 Gannet 2

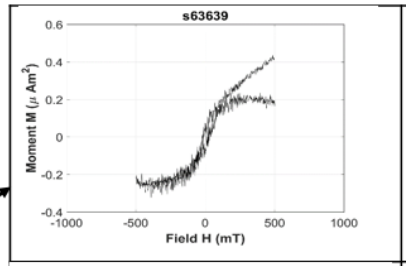


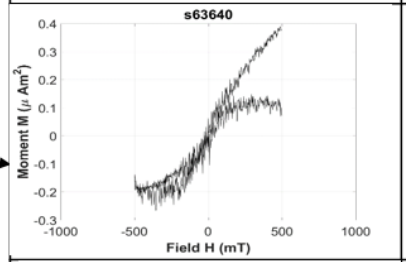

UK21/25-6 Gannet 3
SCALE (m)
LITHOLOGY
MUDSANDGRAVE
clay
silt
vf
f
m
c
vc
gran
peeb
cobb
boul
2050
2060
Red mudstone
ODT
s63633r
Moment M (μ Am²)
Field H (mT)
s63650
s63634
s63635
UK 21/25-6
S63633
S63650
S63634
S63635
Heating
Cooling
Susceptibility (10⁻³ m³/kg)
Temperature (°C)

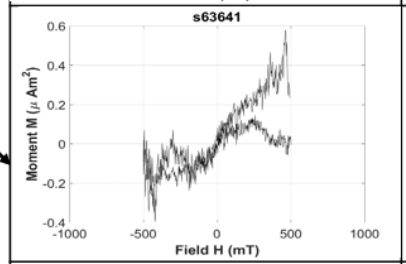

UK21/25-6 Gannet 4
SCALE (m)
LITHOLOGY
MUDSANDGRAVE
clay
slt
vf
f
m
c
vc
gran
pebb
cobb
boul
2060
2070
2080
ANU
s63644
s63636
s63637
s63638
Moment M (μ Am²)
Field H (mT)
UK 21/25-6
S63644
S63636
S63638
Heating
Cooling
Susceptibility (10⁻⁹ m³/kg)
Temperature (°C)
T (K)
Temperature (K)
RT Cooling
RT Heating
FC
ZFC

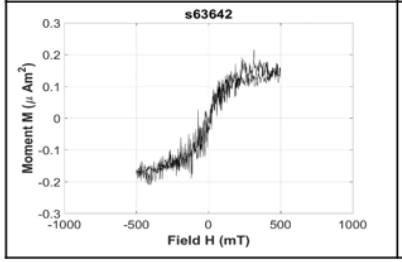
UK21/25-6 Gannet 5

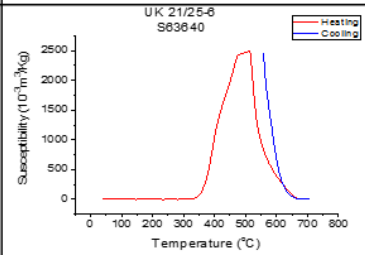


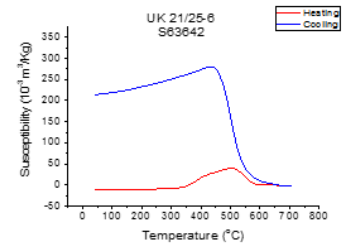


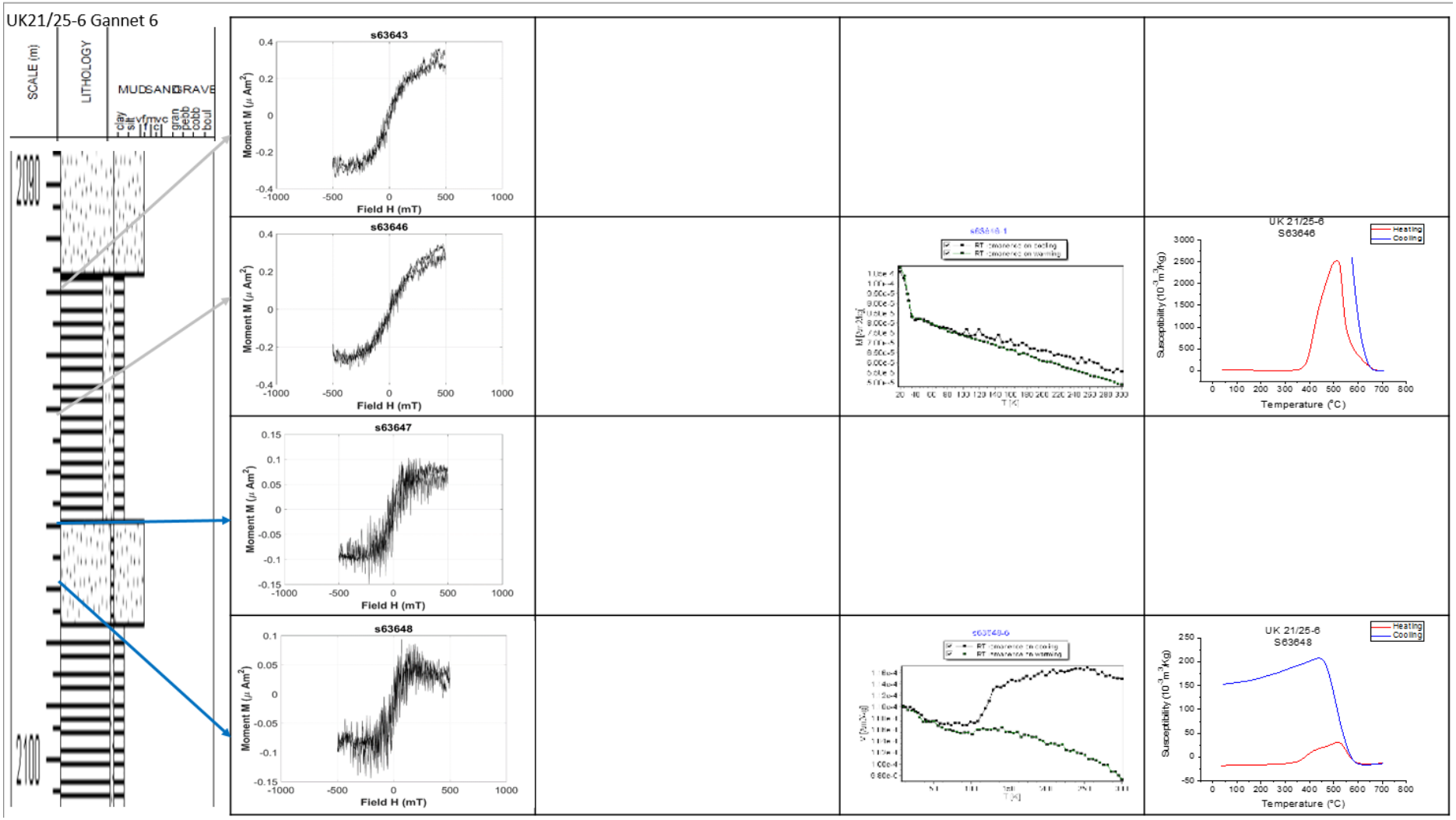


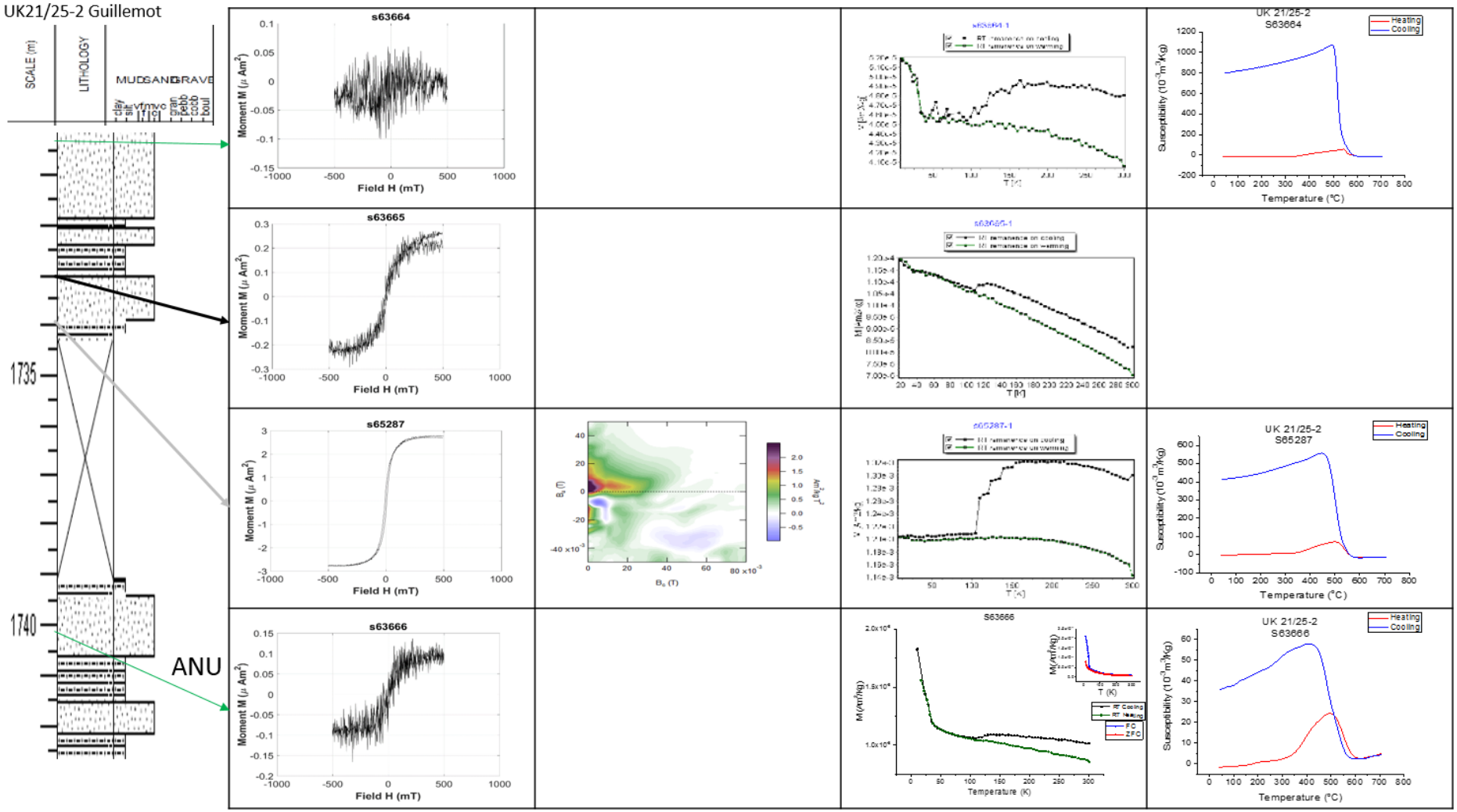




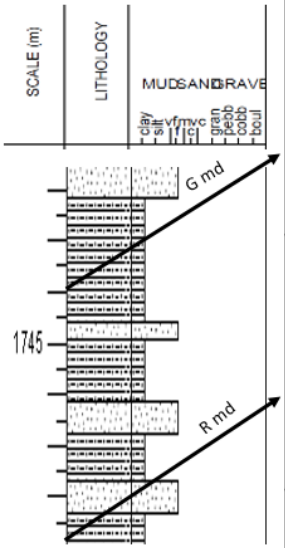


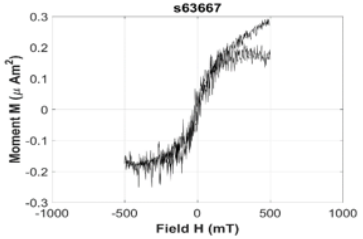


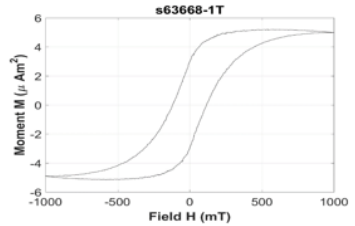

UK21/25-6 Gannet 6
SCALE (m)
LITHOLOGY
MUD
SAND
GRAVE
clay
silt
vf
f
m
c
gran
pebb
cobb
boul
2090
2100
s63643
s63646
s63647
s63648
Moment M (μ Am²)
Field H (mT)
UK 21/25-6
S63646
UK 21/25-6
S63648
Heating
Cooling
Susceptibility (10⁻³ m³/kg)
Temperature (°C)

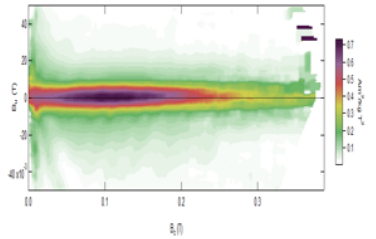

UK21/25-2 Guillemot
SCALE (m)
LITHOLOGY
MUD
SAND
GRAVE
clay
vf
f
m
c
vc
gran
pebb
cobb
boul
1735
1740
ANU
s63664
Moment M (μ Am²)
Field H (mT)
s63665
s65287
s63666
UK 21/25-2
S63664
S65287
S63666
Heating
Cooling
Susceptibility (10⁻⁹ m³/kg)
Temperature (°C)
FC
ZFC
RT Cooling
RT Heating

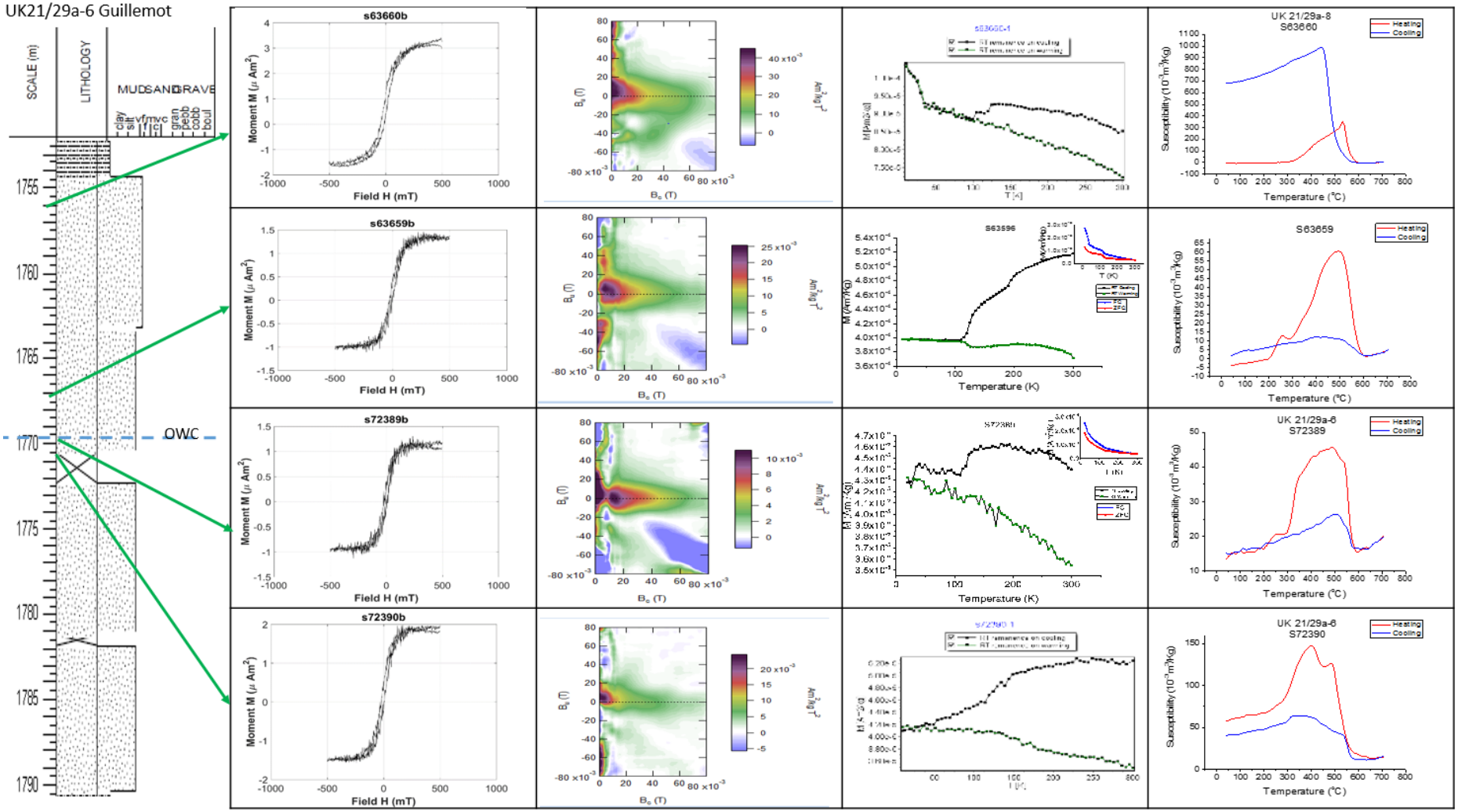
UK21/25-2 Guillemot 2

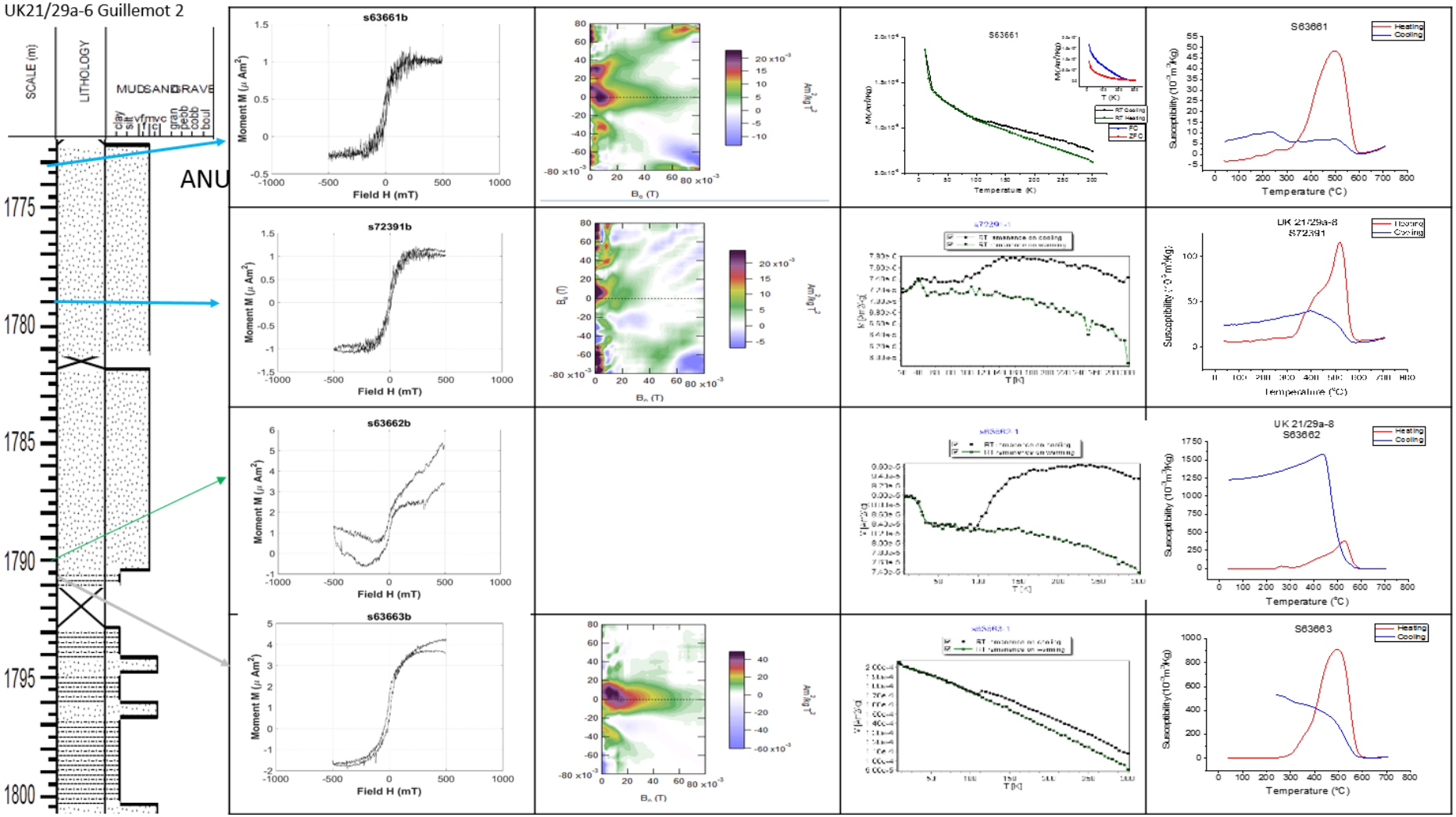


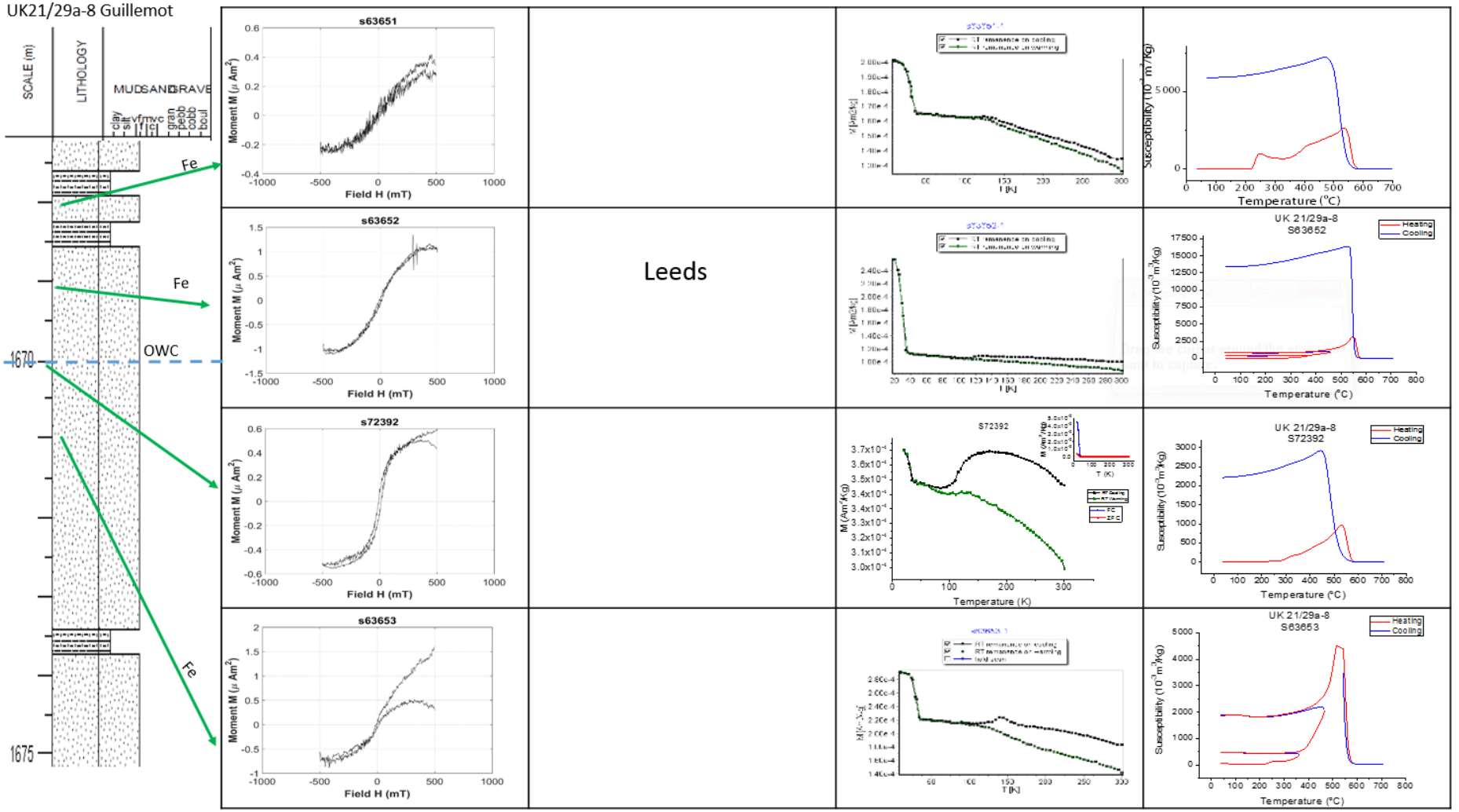




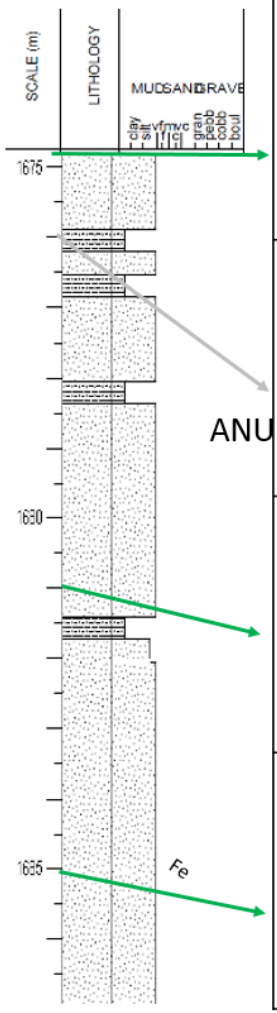



UK21/29a-6 Guillemot
SCALE (m)
LITHOLOGY
MUDSAND
GRAVE
clay
silt
vf
f
m
c
vc
gran
pebb
cobb
boul
1755
1760
1765
OWC
1770
1775
1780
1785
1790
s63660b
s63659b
s72389b
s72390b
Moment M (μ Am²)
Field H (mT)
Bo (T)
T (K)
Temperature (K)
Temperature (°C)
Susceptibility (10⁻⁹m³/kg)
UK 21/29a-8
S63660
S63659
UK 21/29a-6
S72389
S72390
Heating
Cooling
FC
ZFC

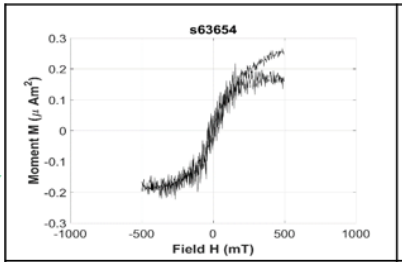

UK21/29a-6 Guillemot 2
SCALE (m)
LITHOLOGY
MUDSAND
GRAVE
clay
silt
vf
f
m
c
vc
gran
pebb
cobb
boul
ANU
1775
1780
1785
1790
1795
1800
s63661b
Moment M (μ Am²)
Field H (mT)
s72391b
s63662b
s63663b
S63661
Heating
Cooling
Susceptibility (10⁻⁹m³/Kg)
Temperature (°C)
UK 21/29a-8
S72391
S63662
S63663
RT cooling
RT heating
FC
ZFC
Temperature (K)

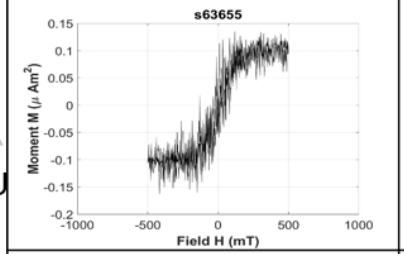

UK21/29a-8 Guillemot
SCALE (m)
LITHOLOGY
MUDSAND
GRAVE
clay
silt
vf
m
vc
cl
gran
pebb
cobb
boul
Fe
Fe
OWC
1670
Fe
1675
s63651
Moment M (μ Am²)
Field H (mT)
s63652
Moment M (μ Am²)
Field H (mT)
s72392
Moment M (μ Am²)
Field H (mT)
s63653
Moment M (μ Am²)
Field H (mT)
Leeds
S72392
Temperature (K)
Susceptibility (10⁻³ m³/Kg)
Temperature (°C)
UK 21/29a-8
S63652
Heating
Cooling
Susceptibility (10⁻³ m³/Kg)
Temperature (°C)
UK 21/29a-8
S72392
Heating
Cooling
Susceptibility (10⁻³ m³/Kg)
Temperature (°C)
UK 21/29a-8
S63653
Heating
Cooling
Susceptibility (10⁻³ m³/Kg)
Temperature (°C)

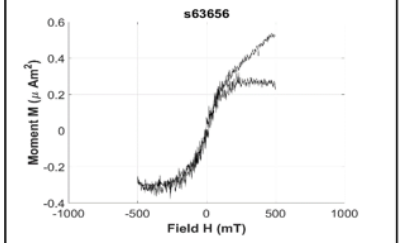
UK21/29a-8 Guillemot 2

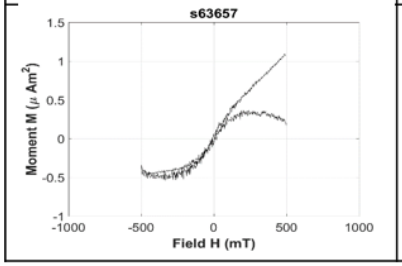


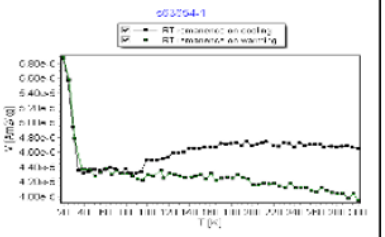
ANU

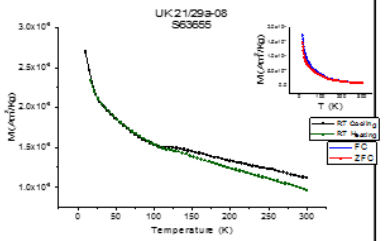


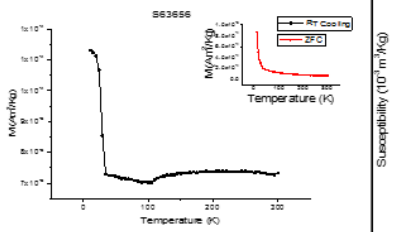


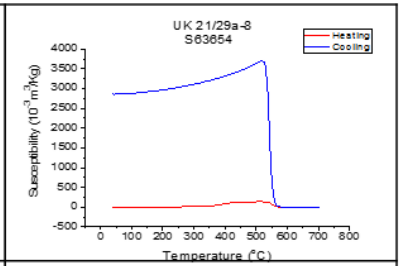


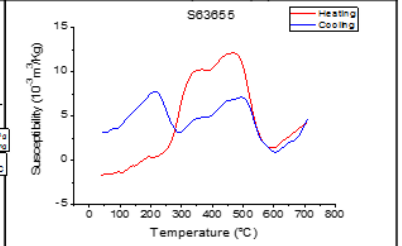


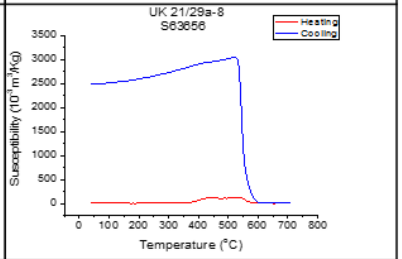


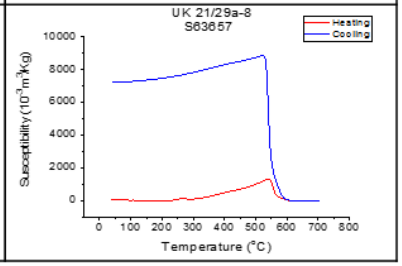




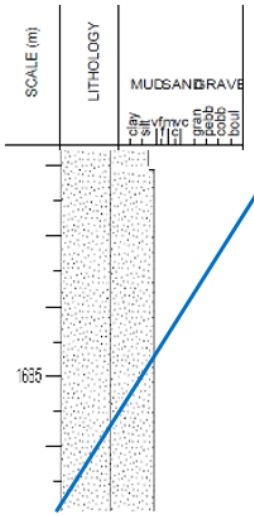


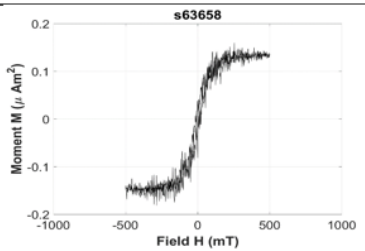
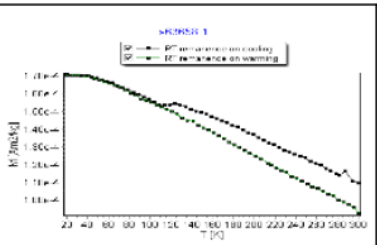
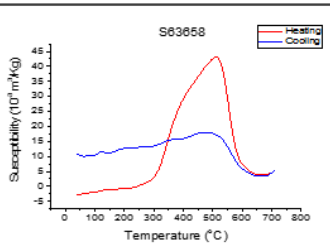




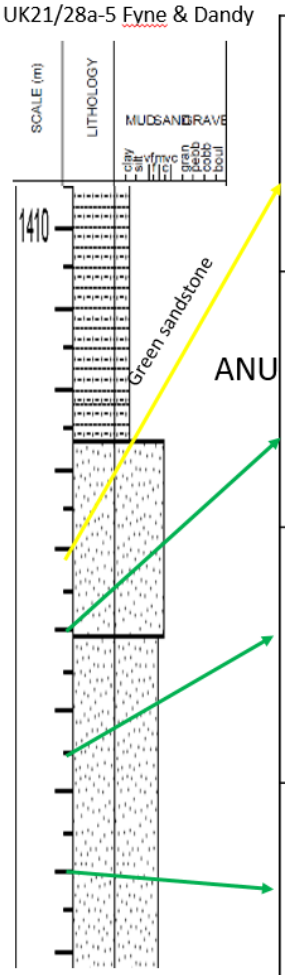


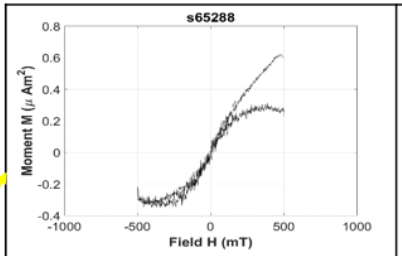
UK21/29a-8 Guillemot 2

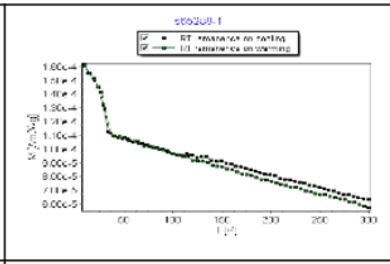


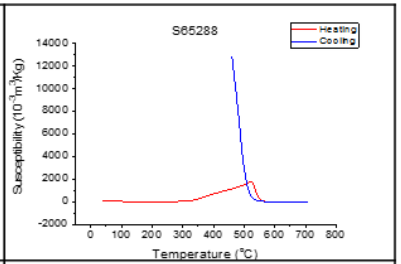
			

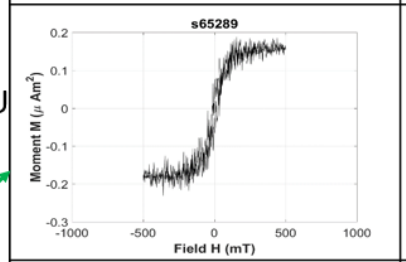
UK21/28a-5 Fyne & Dandy

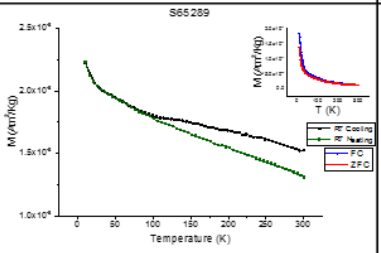


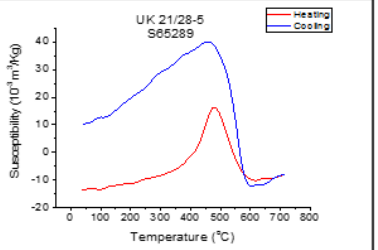


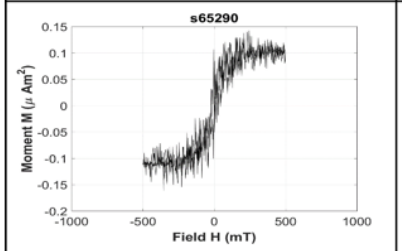


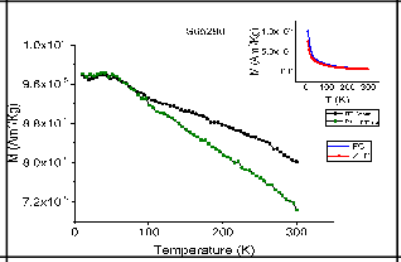


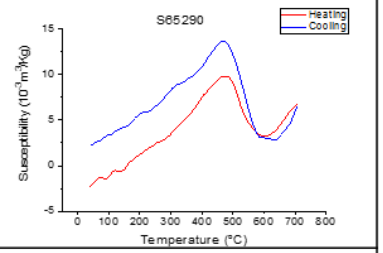


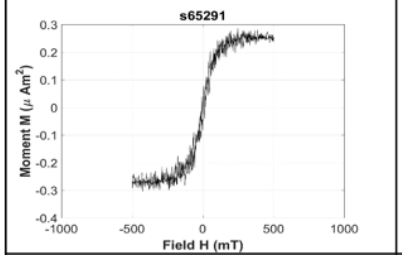


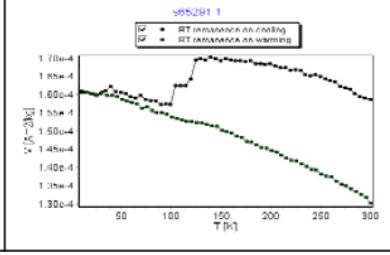


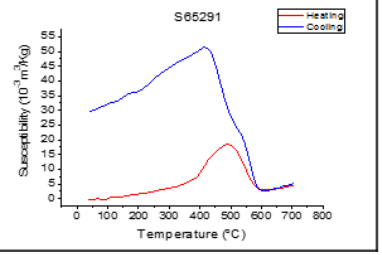


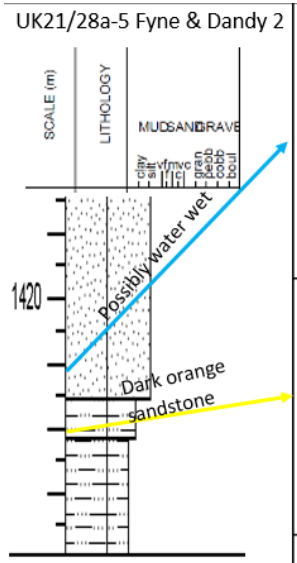


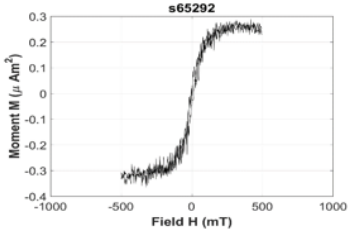


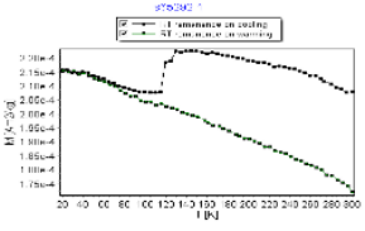


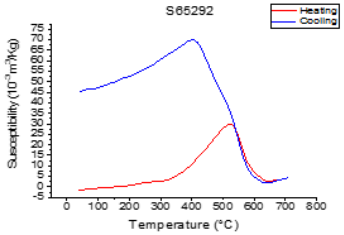


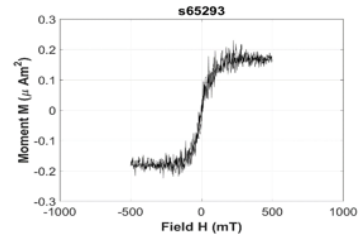


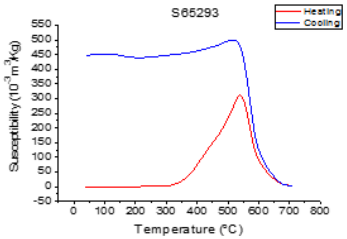

UK21/28a-5 Fyne & Dandy 2
SCALE (m)
LITHOLOGY
MUDSAND
GRAVE
clay
silt
vf
m
vc
fn
cr
gran
pebb
cobb
boul
1420
Possibly water wet
Dark orange sandstone

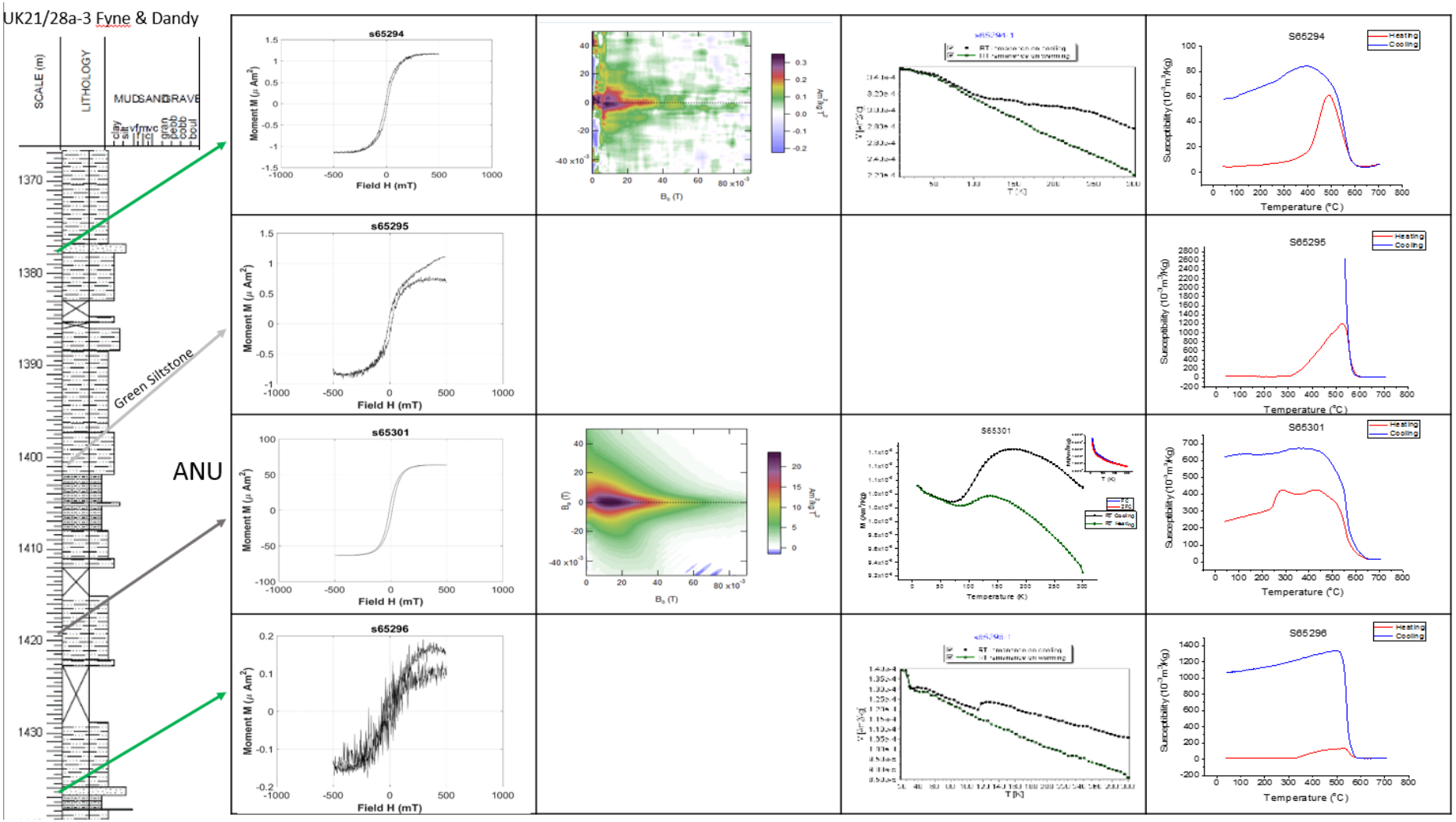

s65292
Moment M (μ Am²)
Field H (mT)

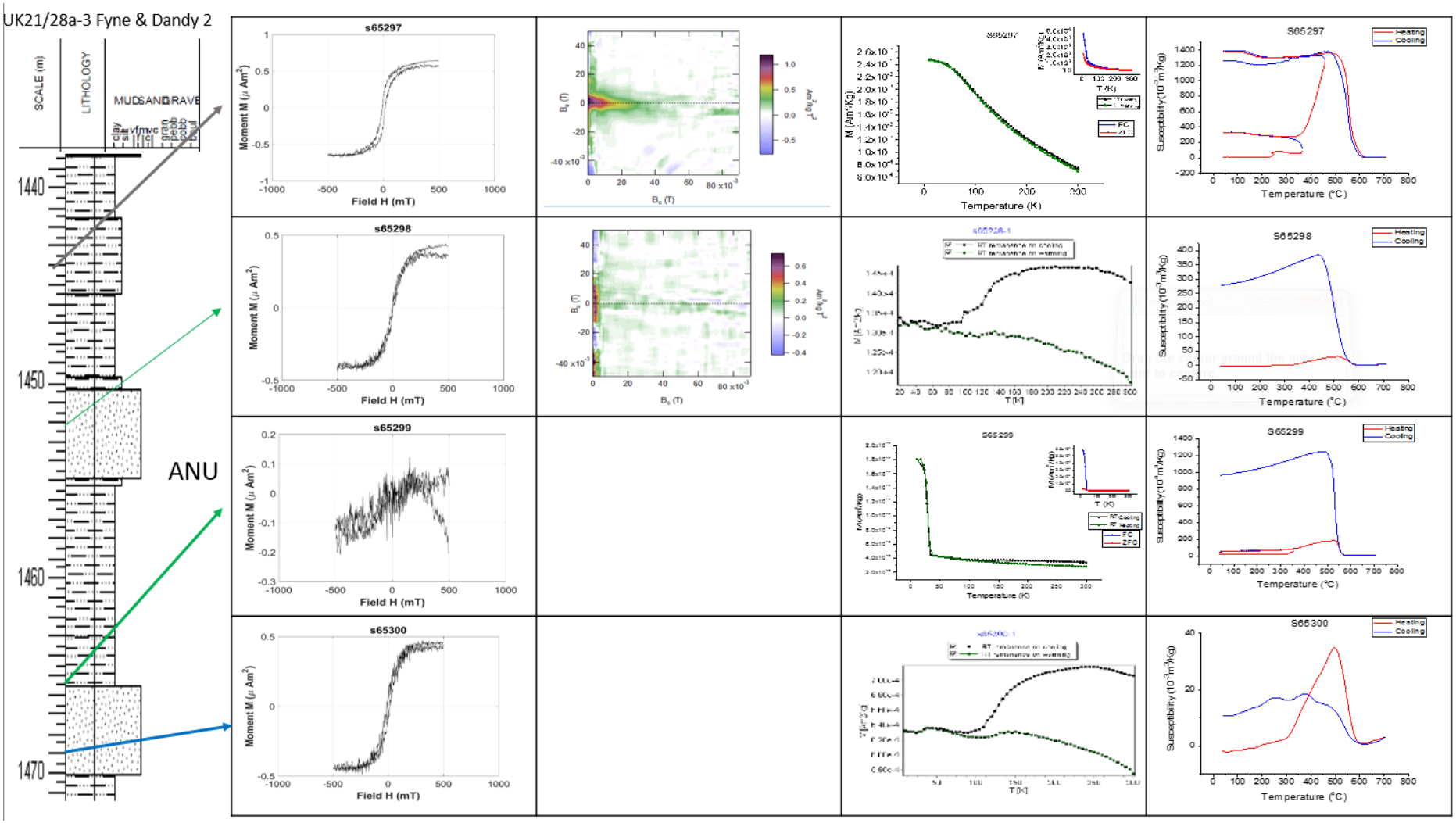



S65292
Heating
Cooling
Susceptibility (10⁻⁸ m³/kg)
Temperature (°C)

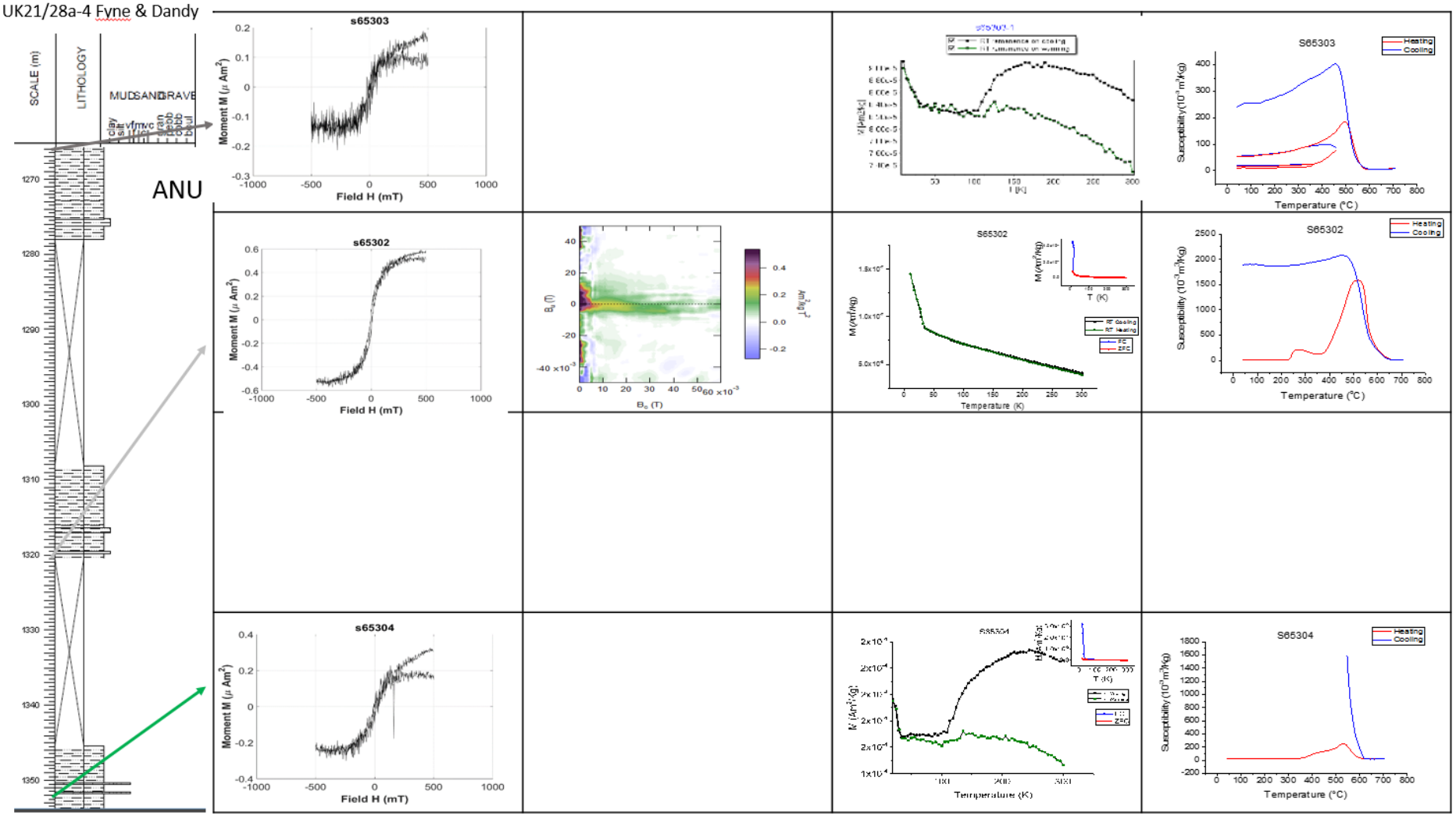

s65293
Moment M (μ Am²)
Field H (mT)


S65293
Heating
Cooling
Susceptibility (10⁻⁸ m³/kg)
Temperature (°C)

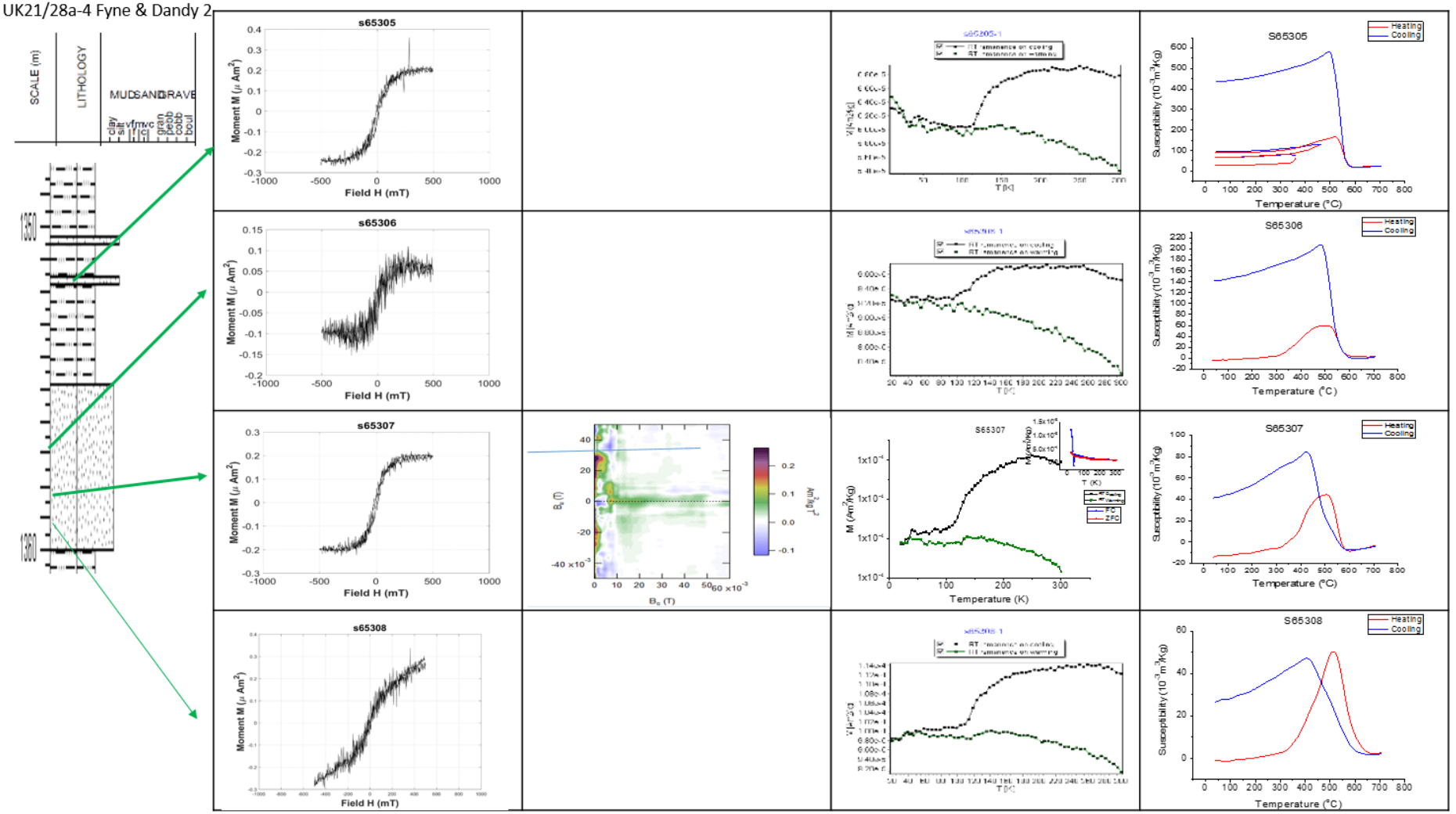

UK21/28a-3 Fyne & Dandy
SCALE (m)
LITHOLOGY
MUD
SAND
GRAVE
clay
vf/fm/c
gran
pebb
cobb
boul
1370
1380
1390
1400
1410
1420
1430
Green Siltstone
ANU
s65294
s65295
s65301
s65296
Moment M (μ Am²)
Field H (mT)
Susceptibility (10⁻⁹m³/kg)
Temperature (°C)
Heating
Cooling
S65294
S65295
S65301
S65296
Temperature (K)


UK21/28a-3 Fyne & Dandy 2
SCALE (m)
LITHOLOGY
MUDSAND
GRAVE
clay
slt
vf
f
m
c
gran
pebb
cobb
boul
1440
1450
1460
1470
ANU
s65297
Moment M (μ Am²)
Field H (mT)
s65298
s65299
s65300
S65297
S65298
S65299
S65300
Heating
Cooling
Susceptibility (10⁻⁸ m³/kg)
Temperature (°C)
Temperature (K)
FC
ZFC

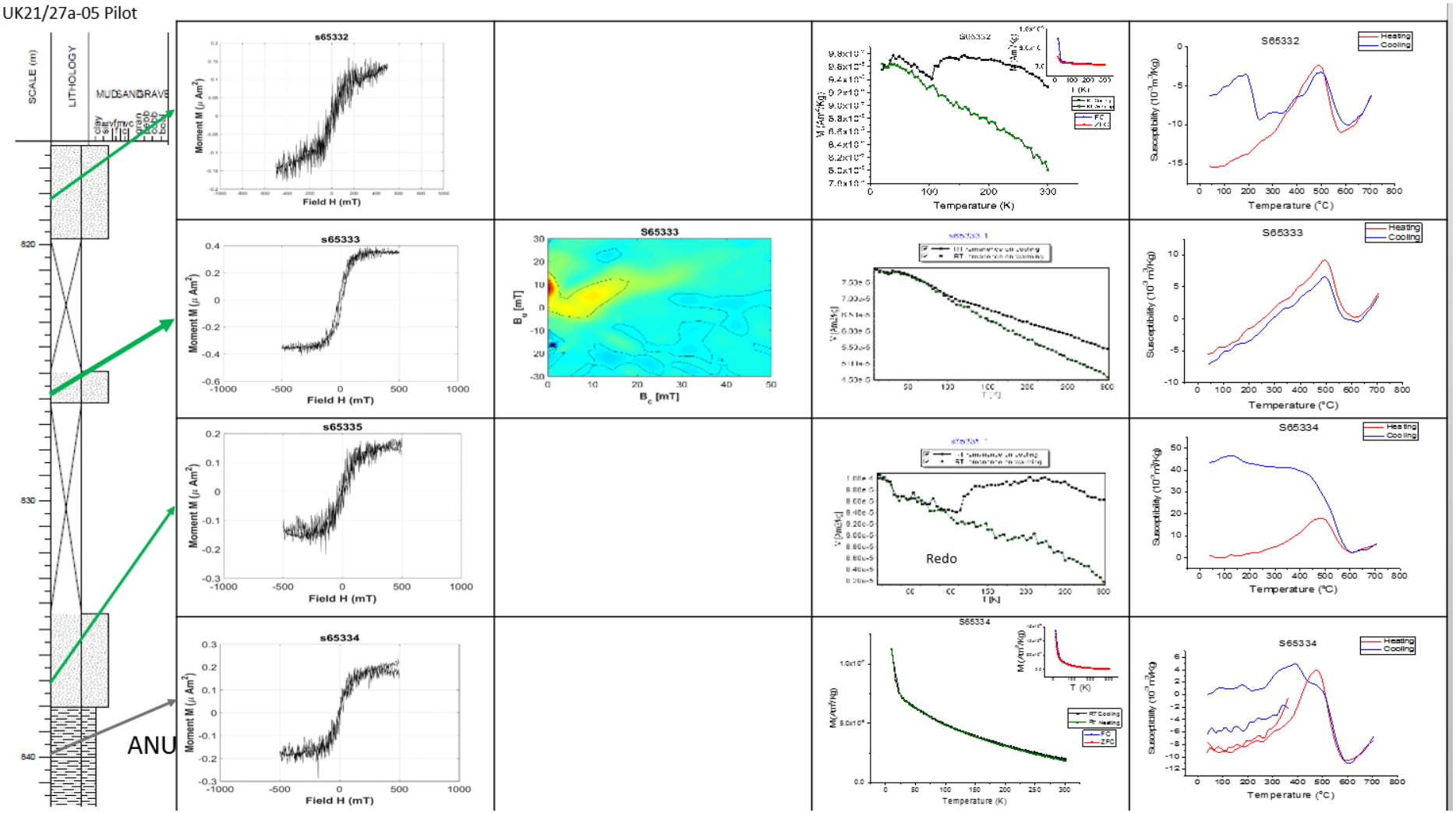
UK21/28a-4 Fyne & Dandy



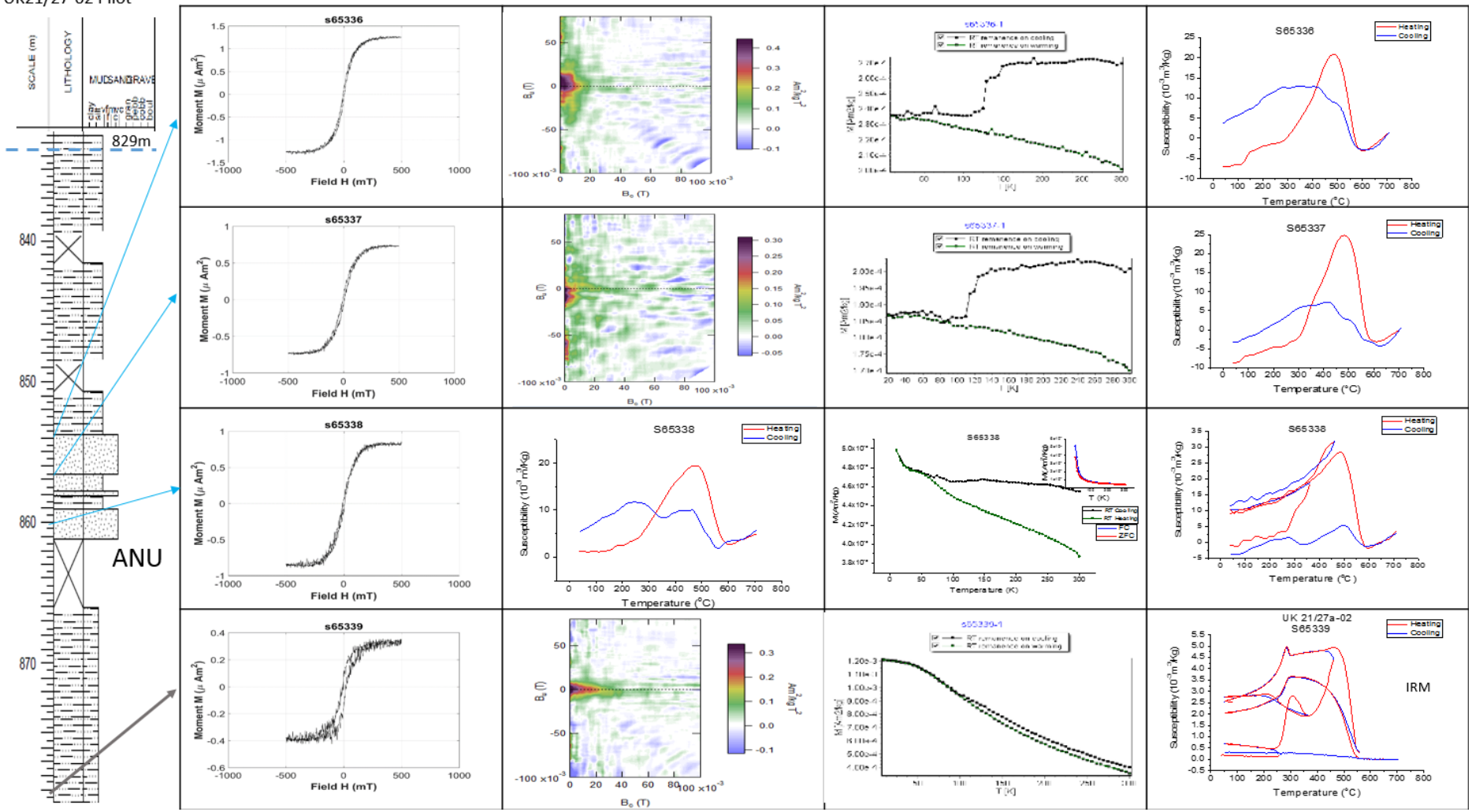
UK21/28a-4 Fyne & Dandy 2



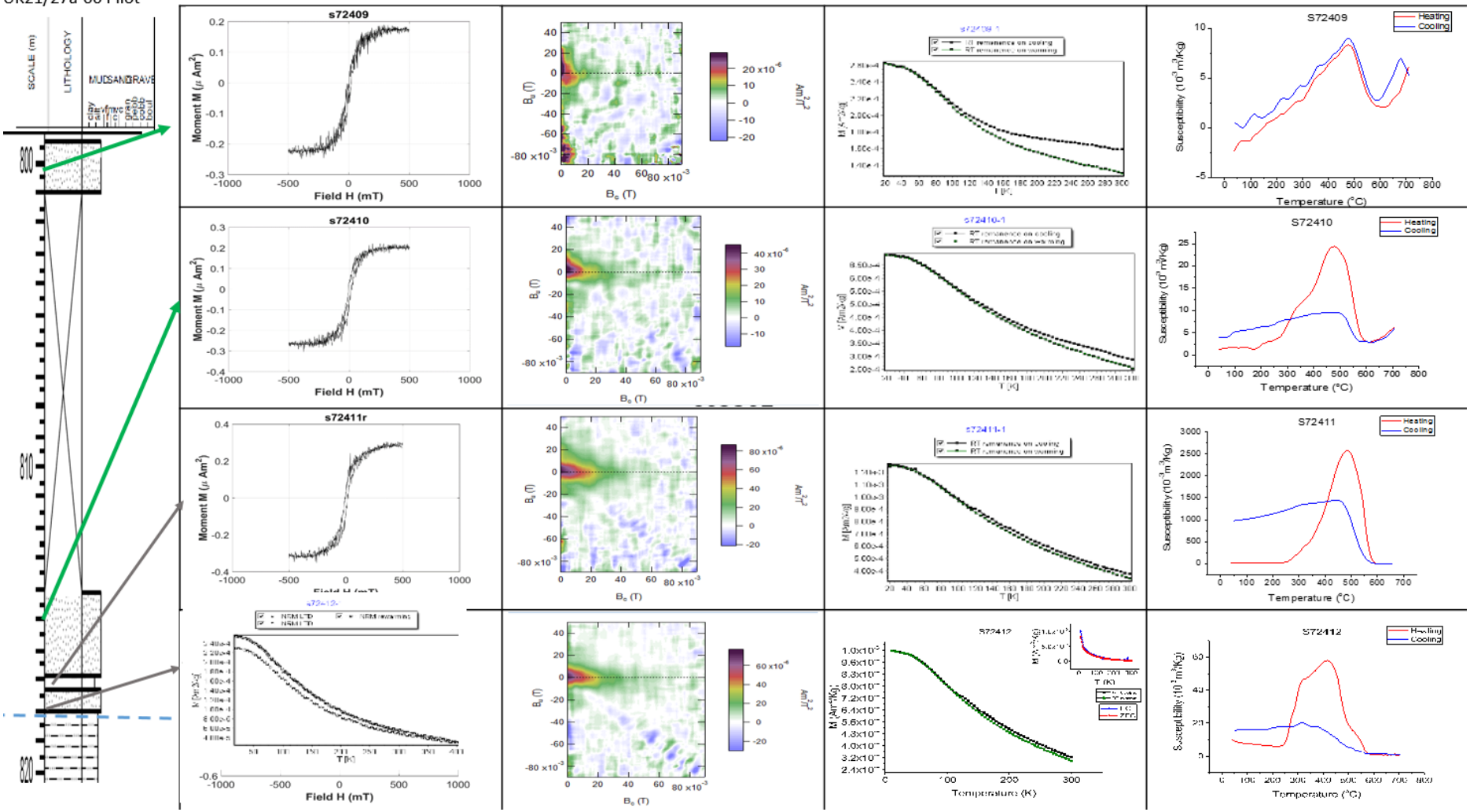
UK21/27a-05 Pilot



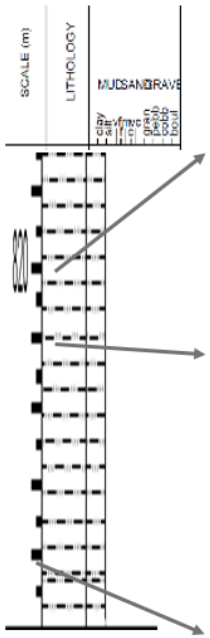
UK21/27-02 Pilot

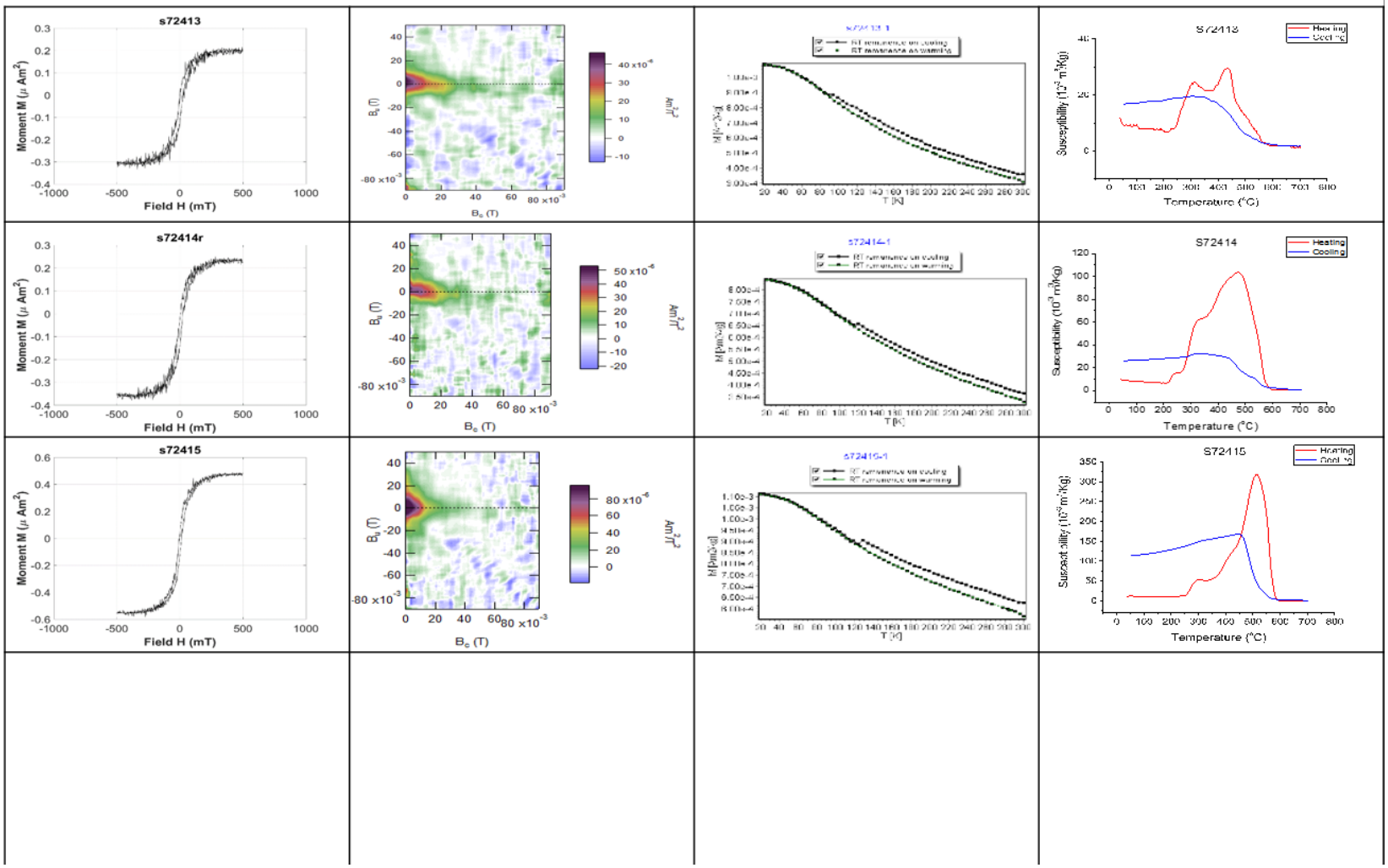


UK21/27a-06 Pilot

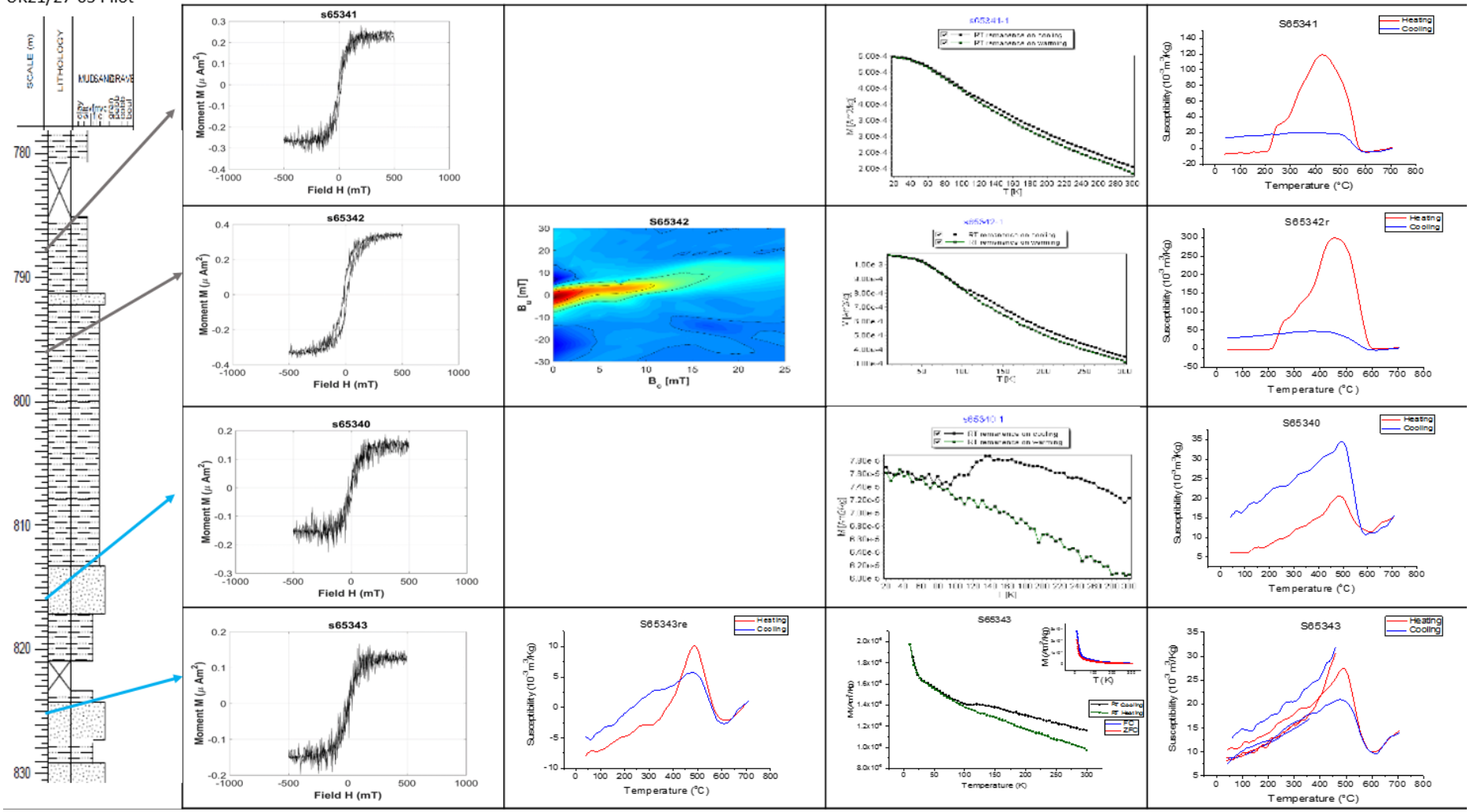


UK21/27a-06 Pilot 2

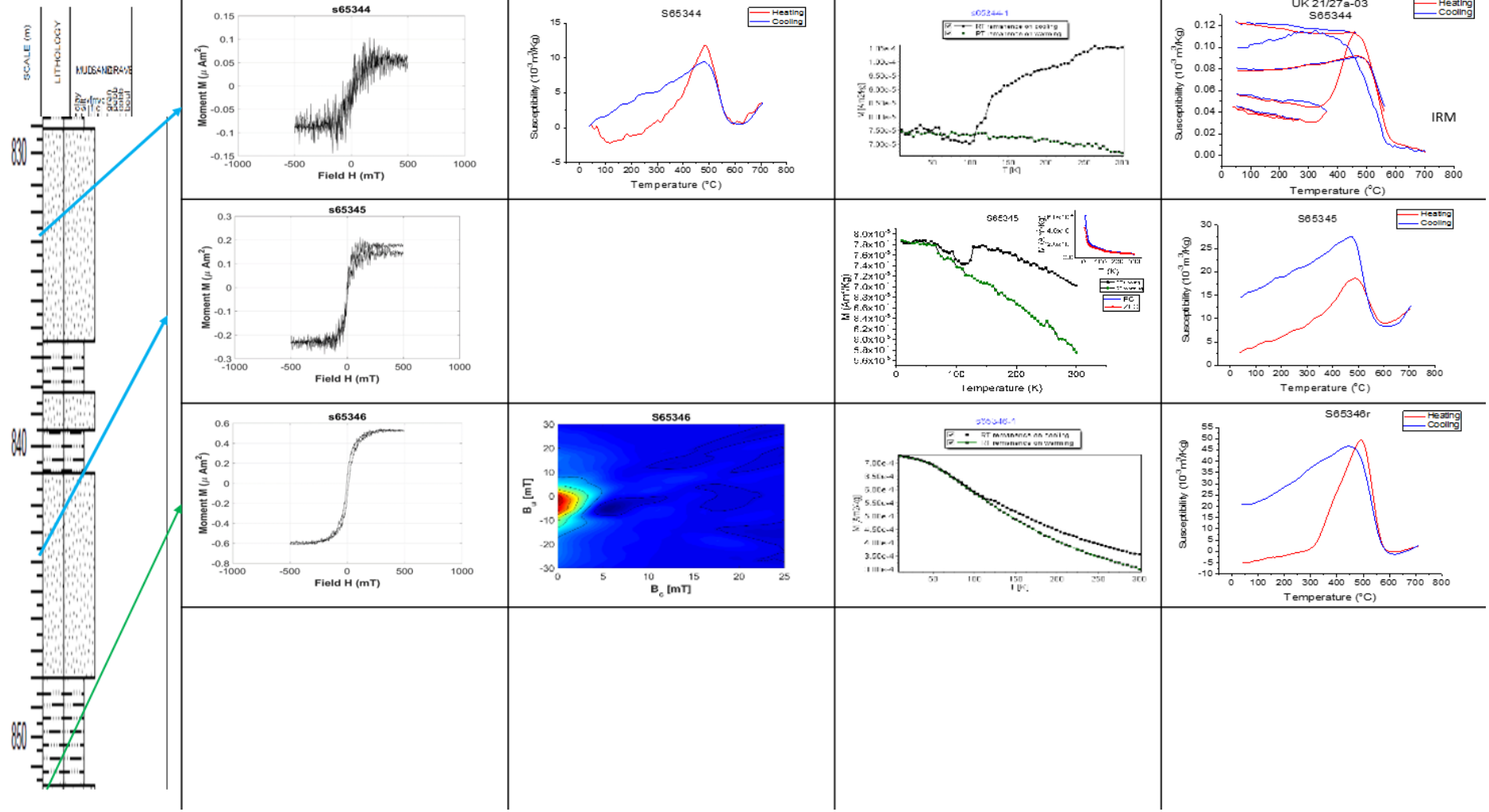


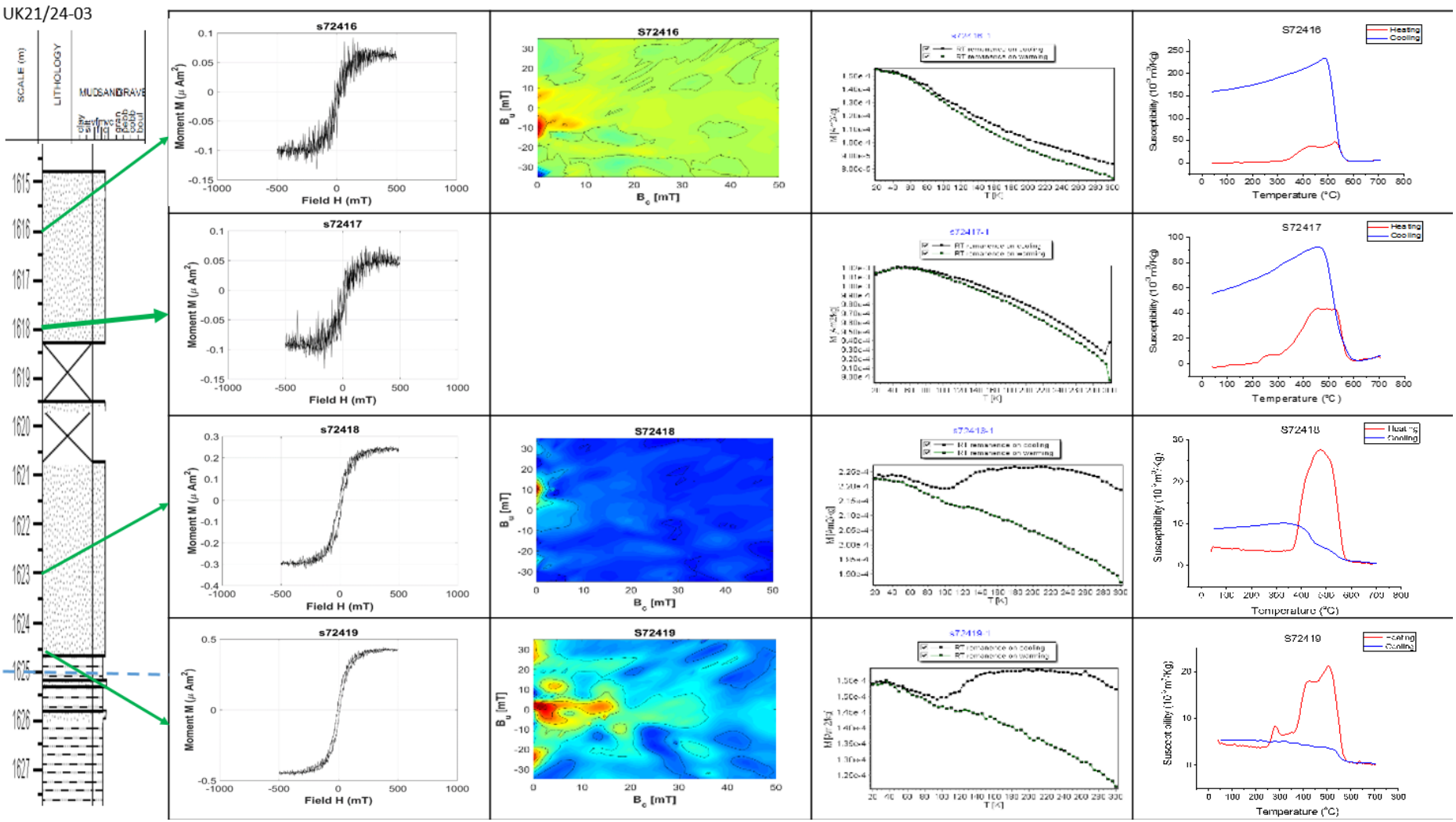


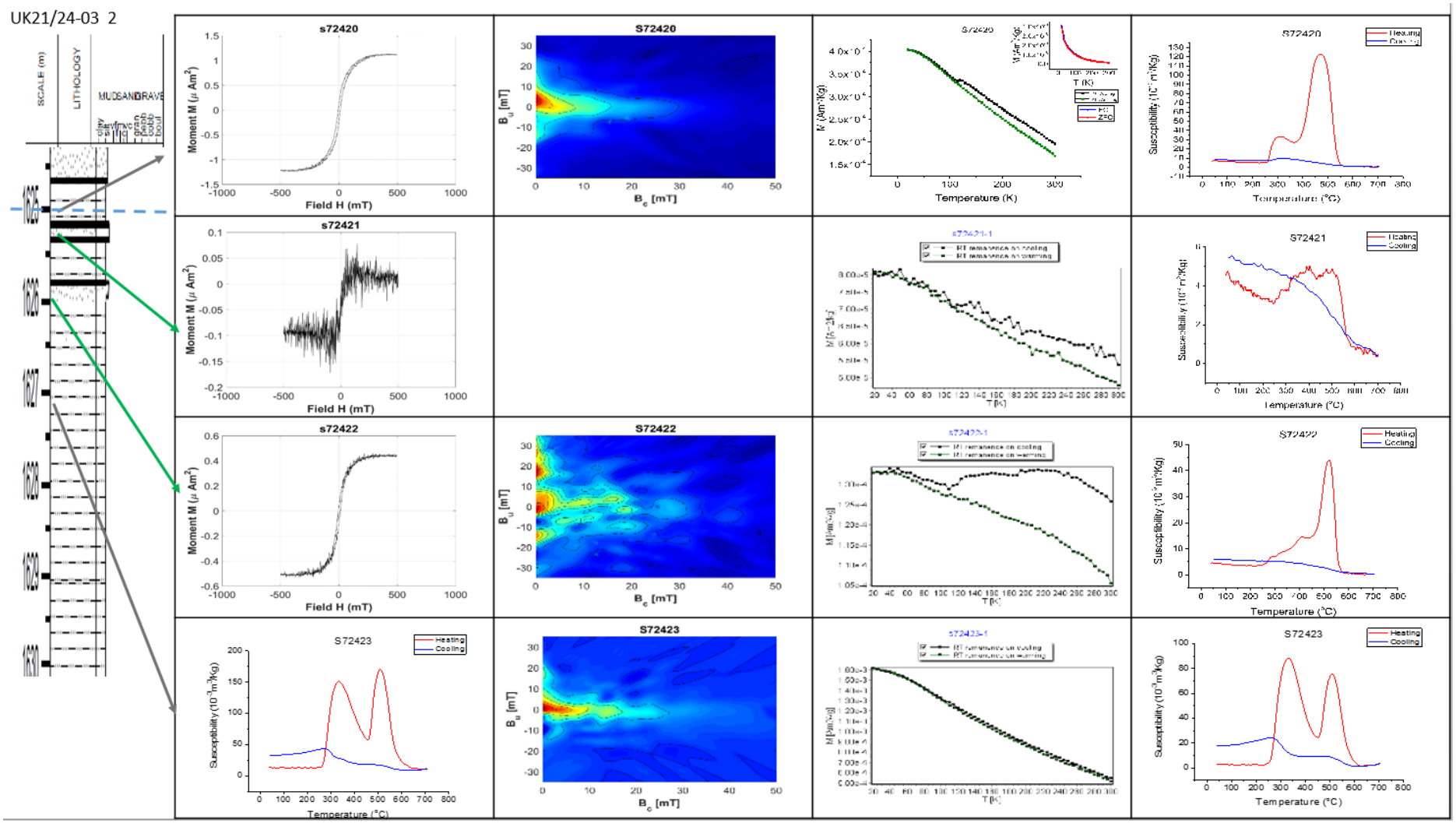
UK21/27-03 Pilot



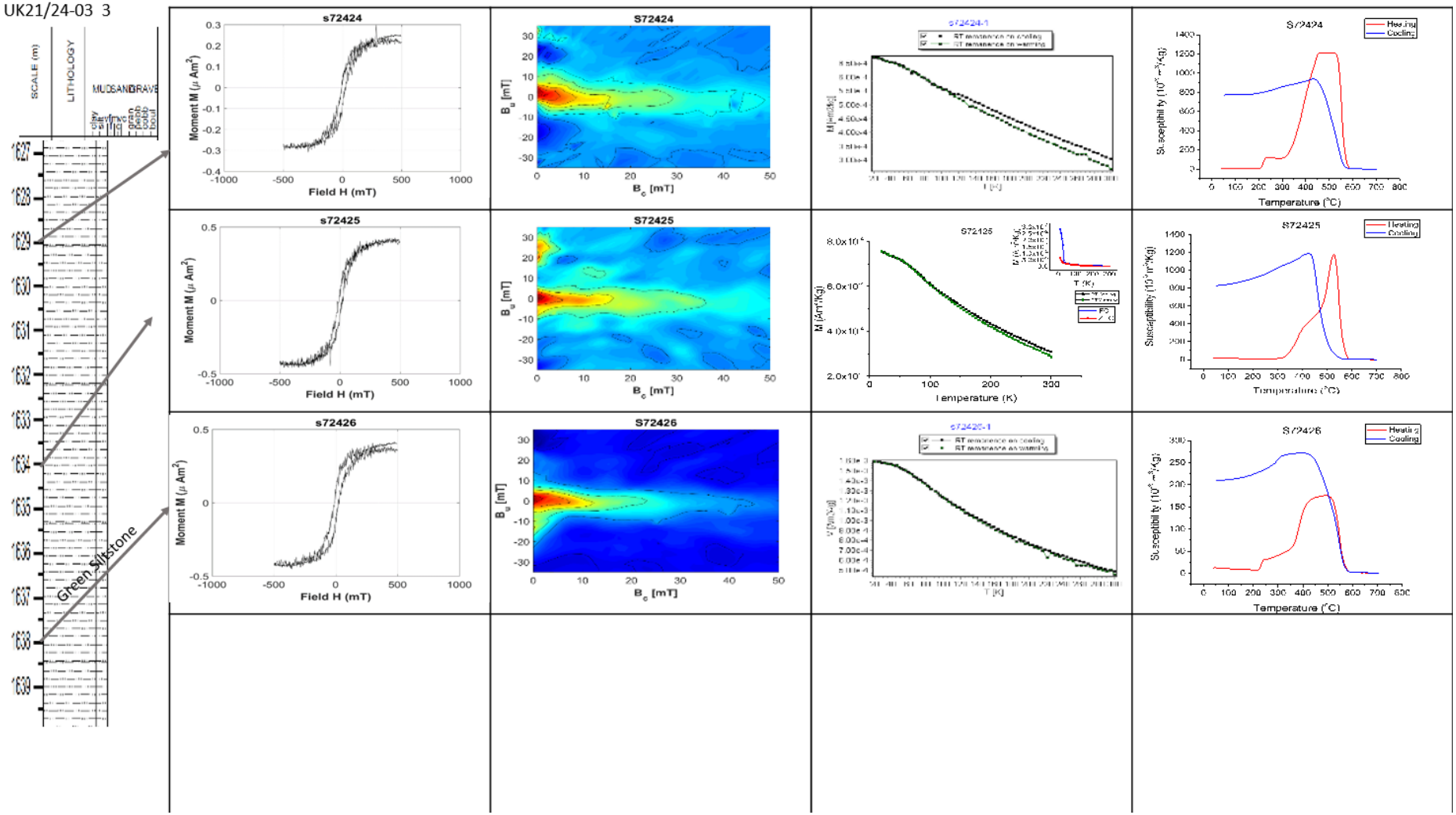
UK21/27-03 Pilot 2

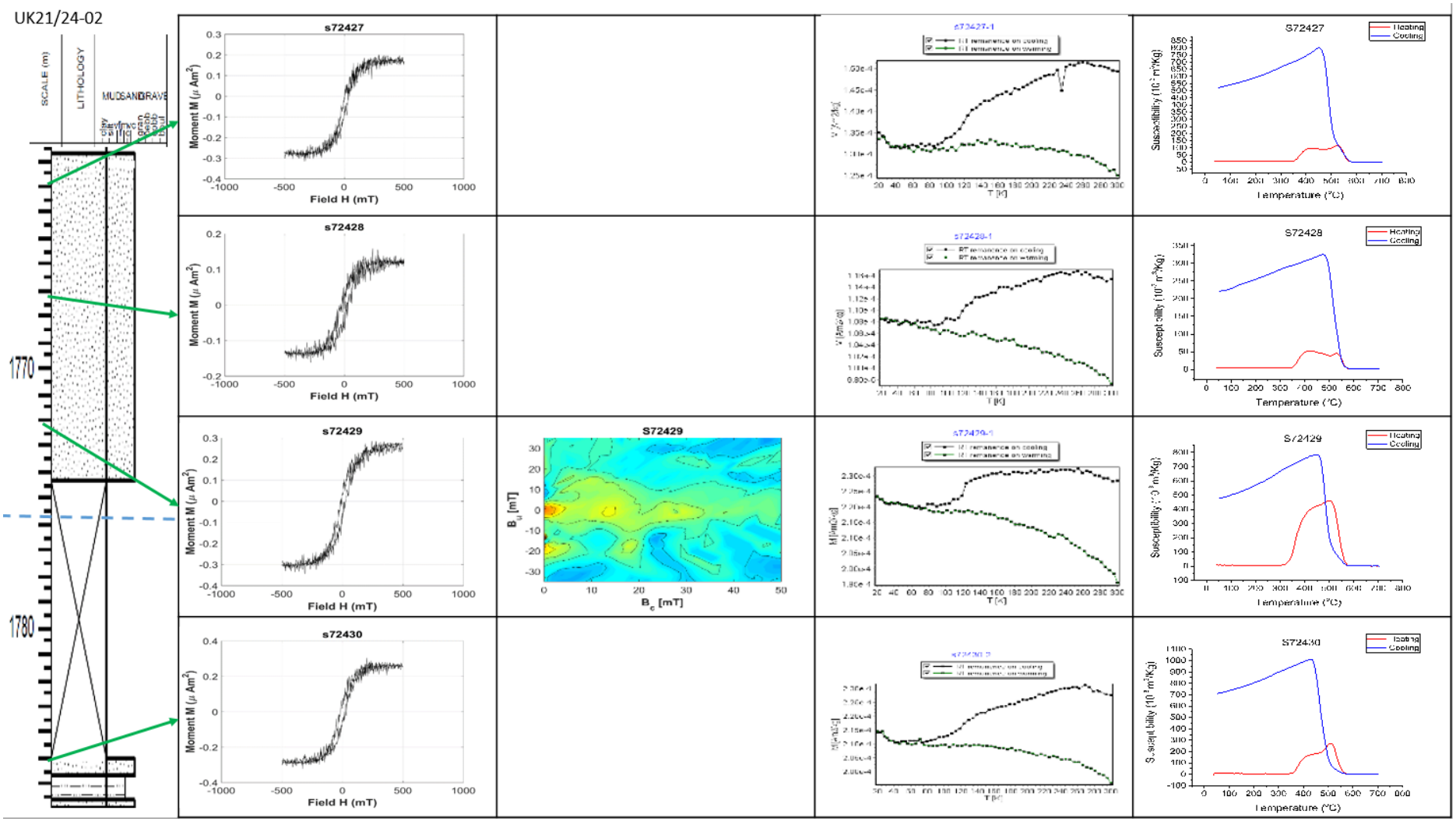


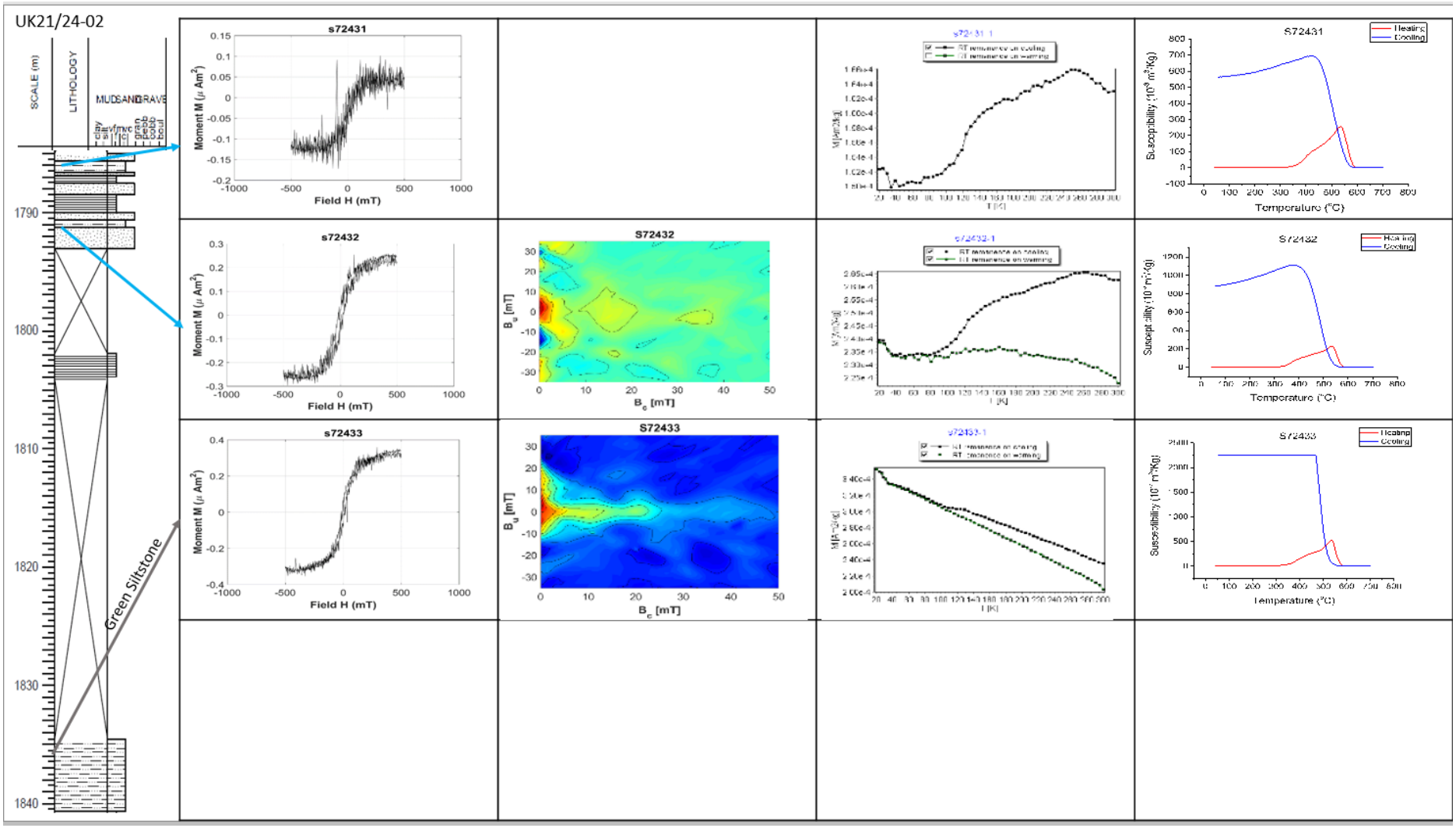

UK21/24-03
SCALE (m)
LITHOLOGY
MUD
SAND
GRAVEL
clay
silt
sand
granule
pebble
cobble
boulder
1615
1616
1617
1618
1619
1620
1621
1622
1623
1624
1625
1626
1627
s72416
Moment M (μ Am²)
Field H (mT)
S72416
B_u [mT]
B_c [mT]
S72416
Heating
Cooling
Susceptibility (10⁻⁸ m³/kg)
Temperature (°C)
s72417
Moment M (μ Am²)
Field H (mT)
S72417
Heating
Cooling
Susceptibility (10⁻⁸ m³/kg)
Temperature (°C)
s72418
Moment M (μ Am²)
Field H (mT)
S72418
B_u [mT]
B_c [mT]
S72418
Heating
Cooling
Susceptibility (10⁻⁸ m³/kg)
Temperature (°C)
s72419
Moment M (μ Am²)
Field H (mT)
S72419
B_u [mT]
B_c [mT]
S72419
Heating
Cooling
Susceptibility (10⁻⁸ m³/kg)
Temperature (°C)


UK21/24-03 2
SCALE (m)
LITHOLOGY
MUDSANDGRAVE
s72420
S72420
s72421
s72422
S72422
S72423
Moment M (μ Am²)
Field H (mT)
Temperature (K)
Temperature (°C)
Heating
Cooling

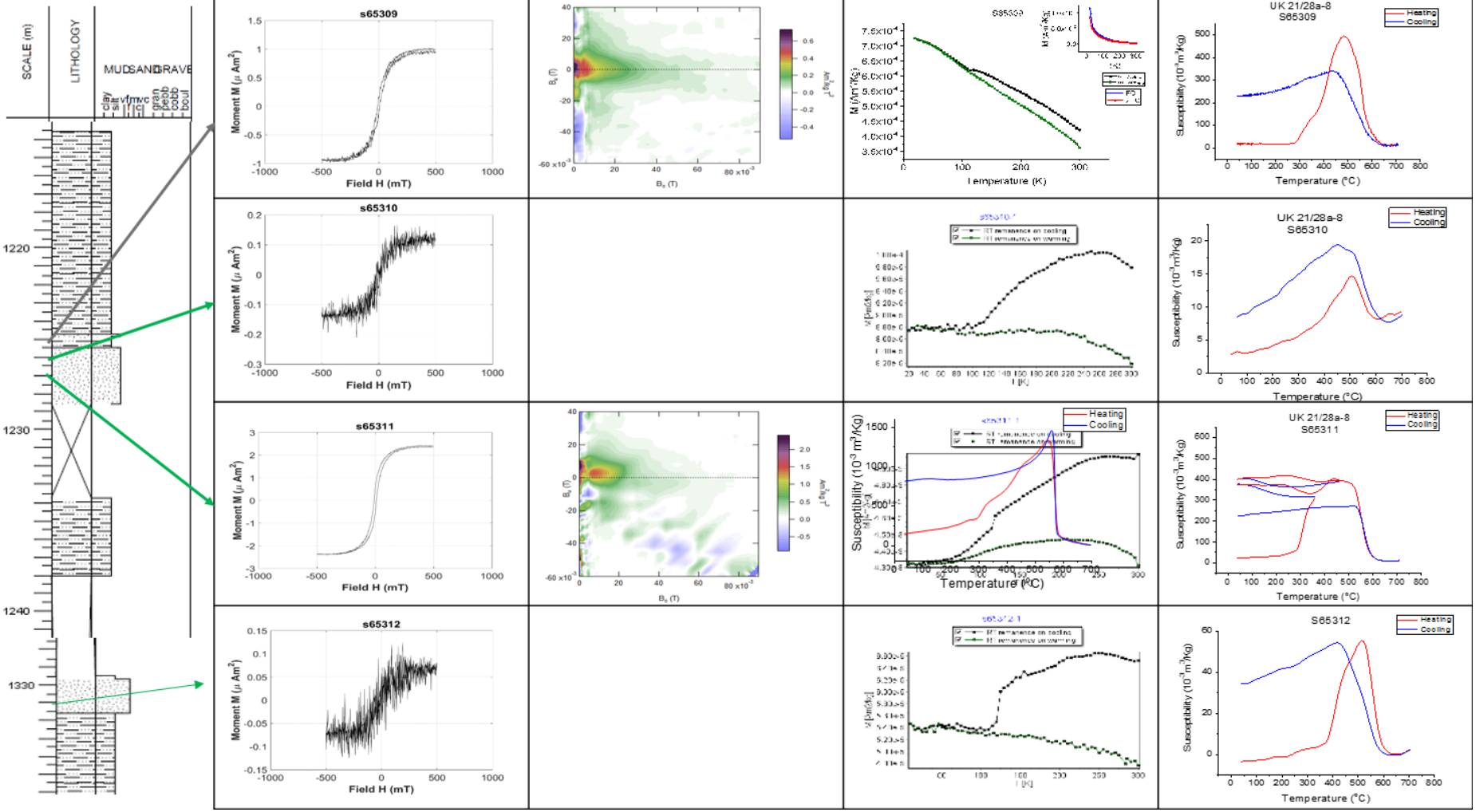
UK21/24-03 3


SCALE (m)
LITHOLOGY
MUDSANDGRAVE
clay
silt
vfc
fc
mc
gran
pebb
cobb
boul
627
628
629
630
631
632
633
634
635
636
637
638
639
Green Siltstone
s72424
Moment M (μ Am²)
Field H (mT)
S72424
B_u [mT]
B_c [mT]
S72424-1
RT remanence on cooling
RT remanence on warming
T [K]
S72424
Heating
Cooling
Susceptibility (10⁻⁸ m³/Kg)
Temperature (°C)
s72425
Moment M (μ Am²)
Field H (mT)
S72425
B_u [mT]
B_c [mT]
S72425
M (Am²/Kg)
Temperature (K)
T (K)
FC
ZFC
S72425
Heating
Cooling
Susceptibility (10⁻⁸ m³/Kg)
Temperature (°C)
s72426
Moment M (μ Am²)
Field H (mT)
S72426
B_u [mT]
B_c [mT]
S72426-1
RT remanence on cooling
RT remanence on warming
T [K]
S72426
Heating
Cooling
Susceptibility (10⁻⁸ m³/Kg)
Temperature (°C)

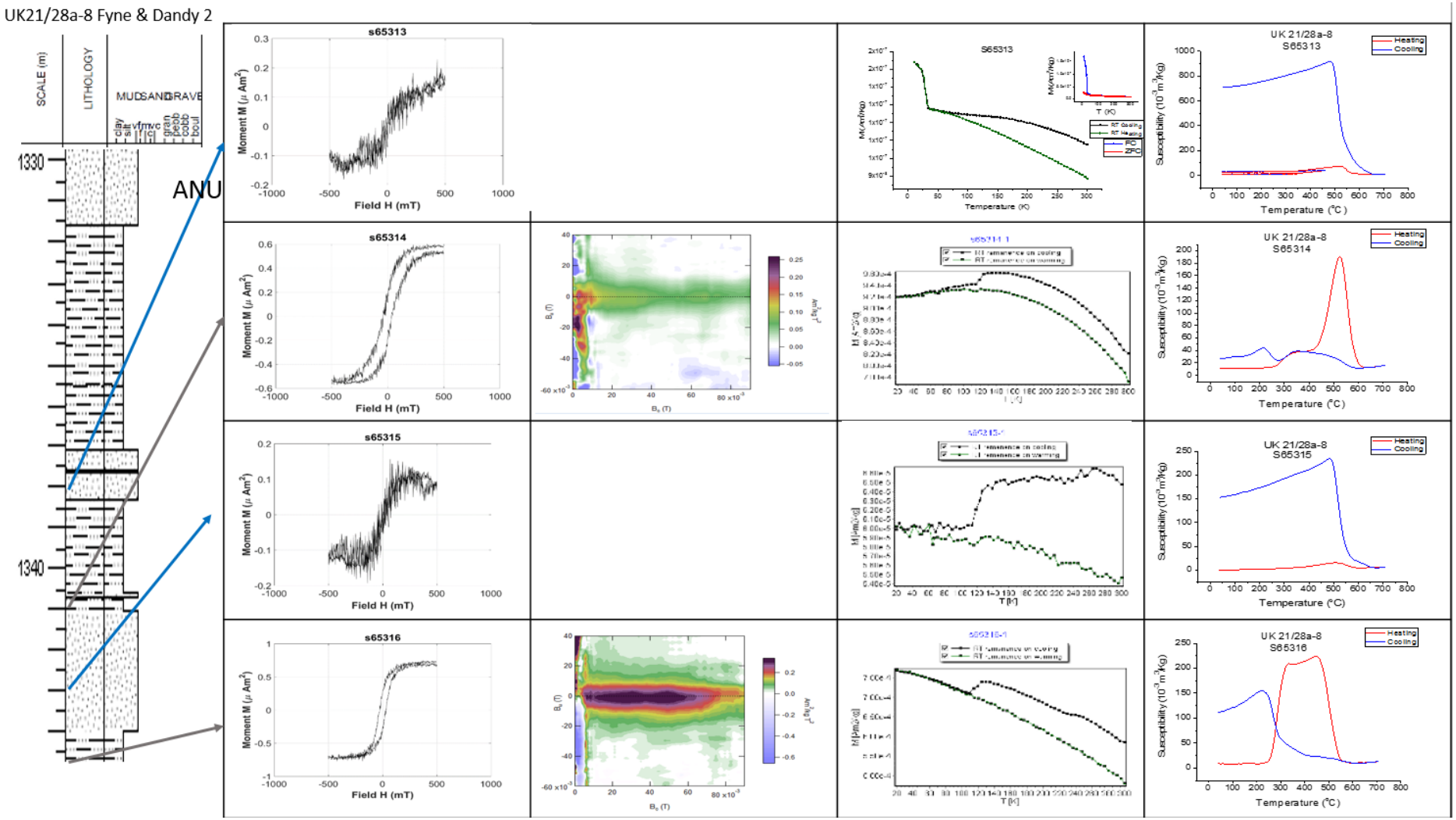

UK21/24-02
SCALE (m)
LITHOLOGY
MUDSANDGRAVE
1770
1780
s72427
Moment M (μ Am²)
Field H (mT)
s72428
s72429
s72430
S72429
B_u [mT]
B_c [mT]
T [K]
S72427
S72428
S72429
S72430
Heating
Cooling
Temperature (°C)

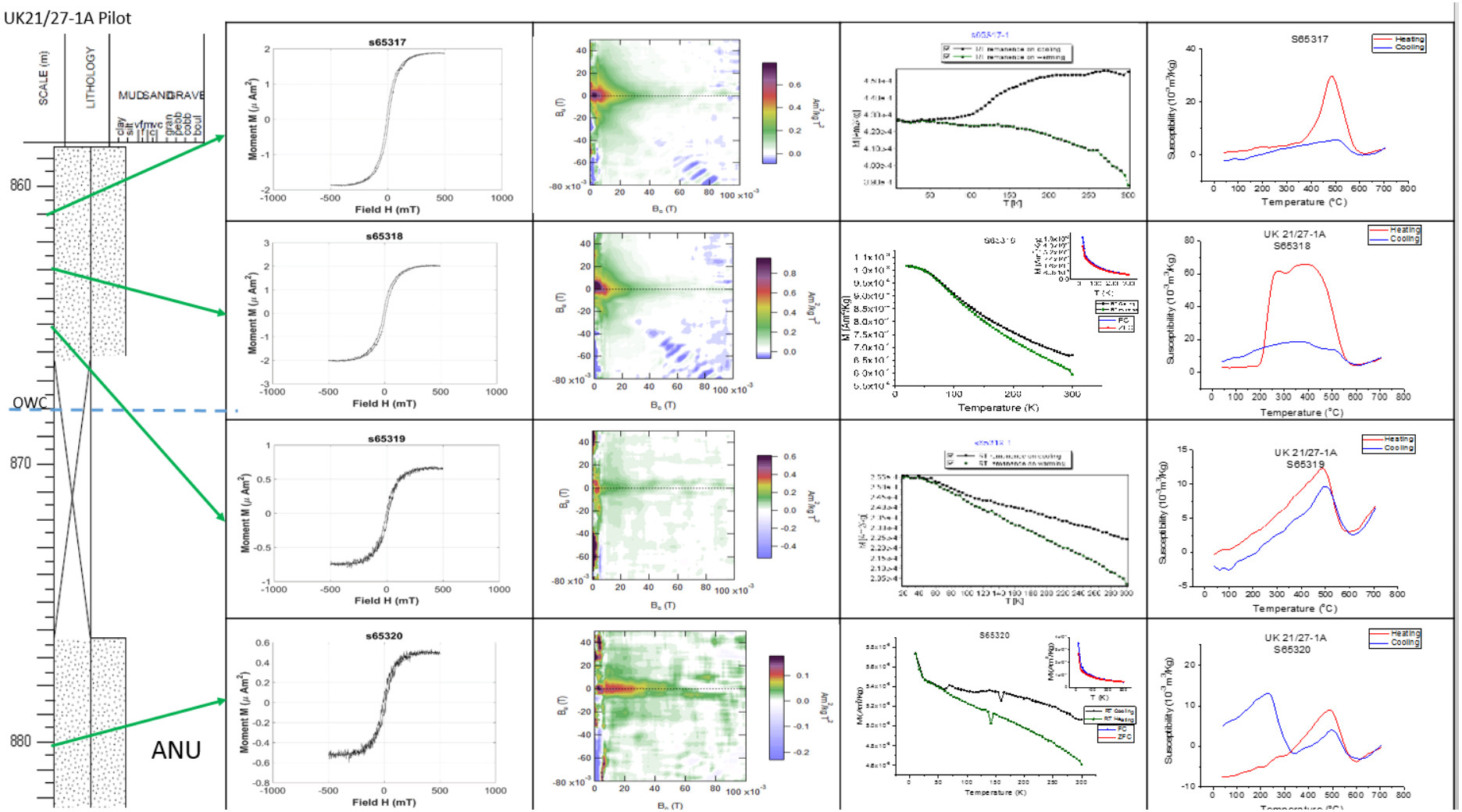

UK21/24-02
SCALE (m)
LITHOLOGY
MUDSAND
GRAVE
clay
silt
vf
f
m
c
gran
pebb
cobb
boul
1790
1800
1810
1820
1830
1840
Green Siltstone
s72431
Moment M (μ Am²)
Field H (mT)
S72432
B_u [mT]
B_c [mT]
s72433
S72431
S72432
S72433
Heating
Cooling
Susceptibility (10⁻⁹ m³/Kg)
Temperature (°C)

UK21/28a-8 Fyne & Dandy

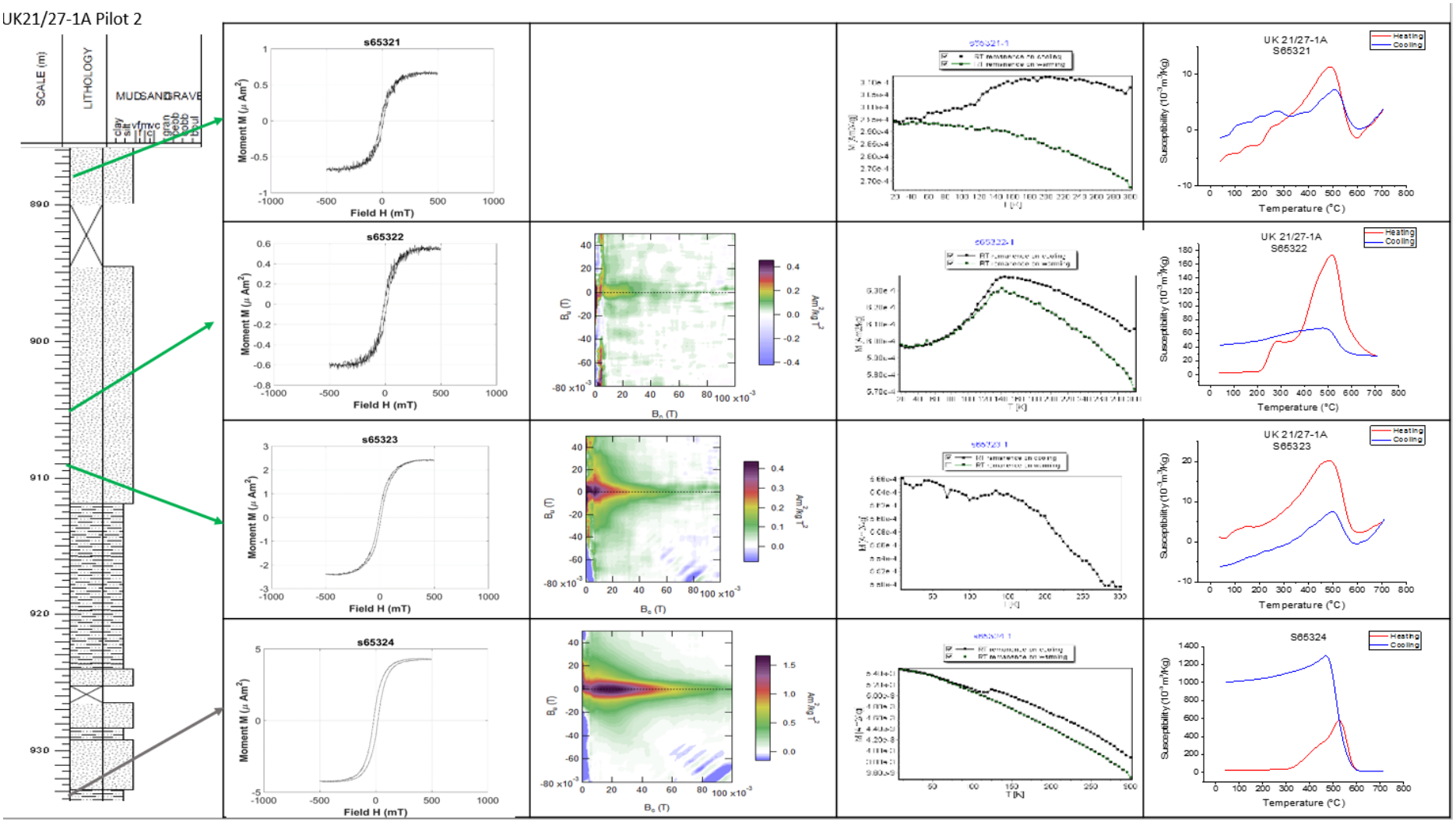


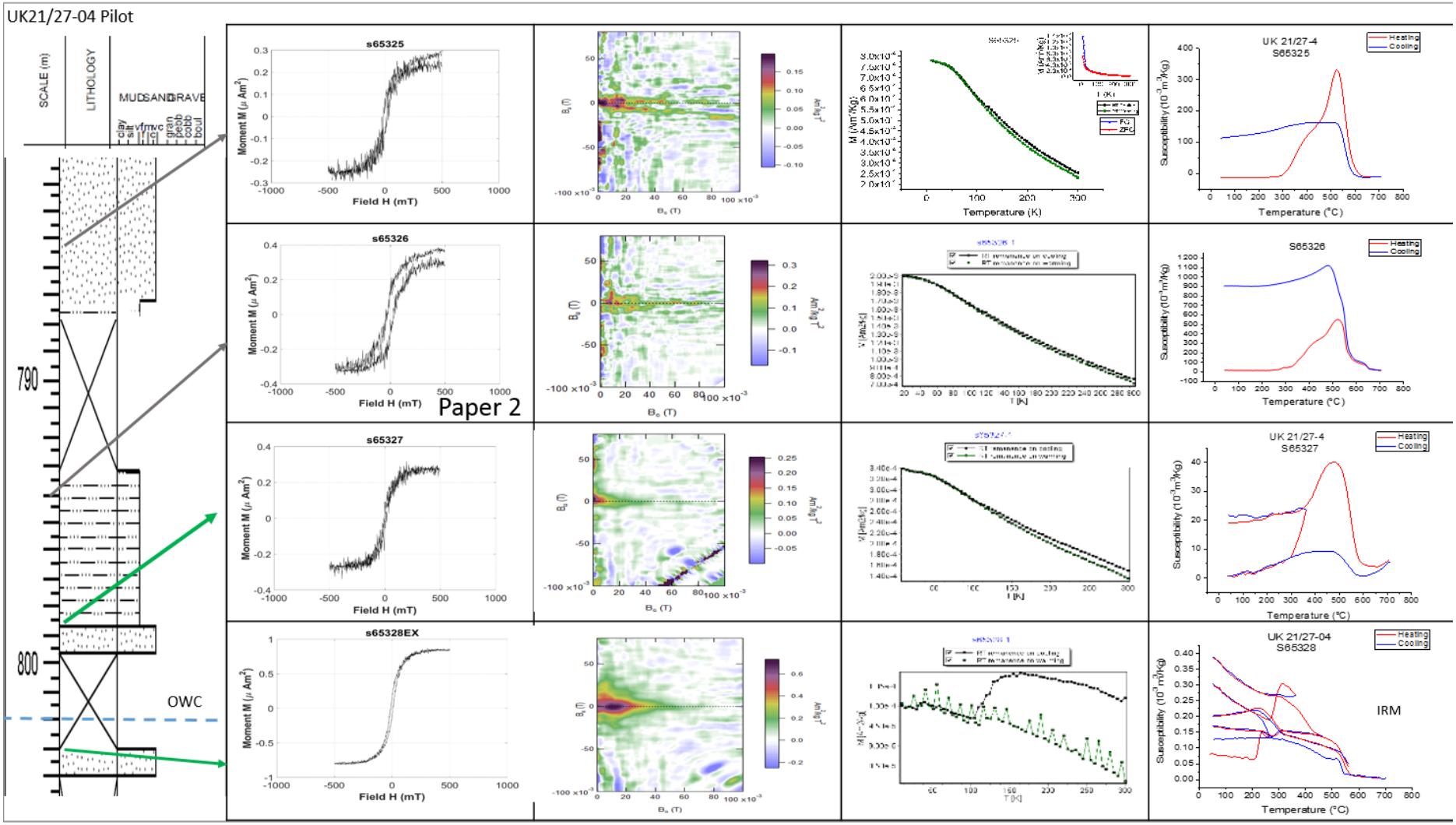
UK21/28a-8 Fyne & Dandy 2



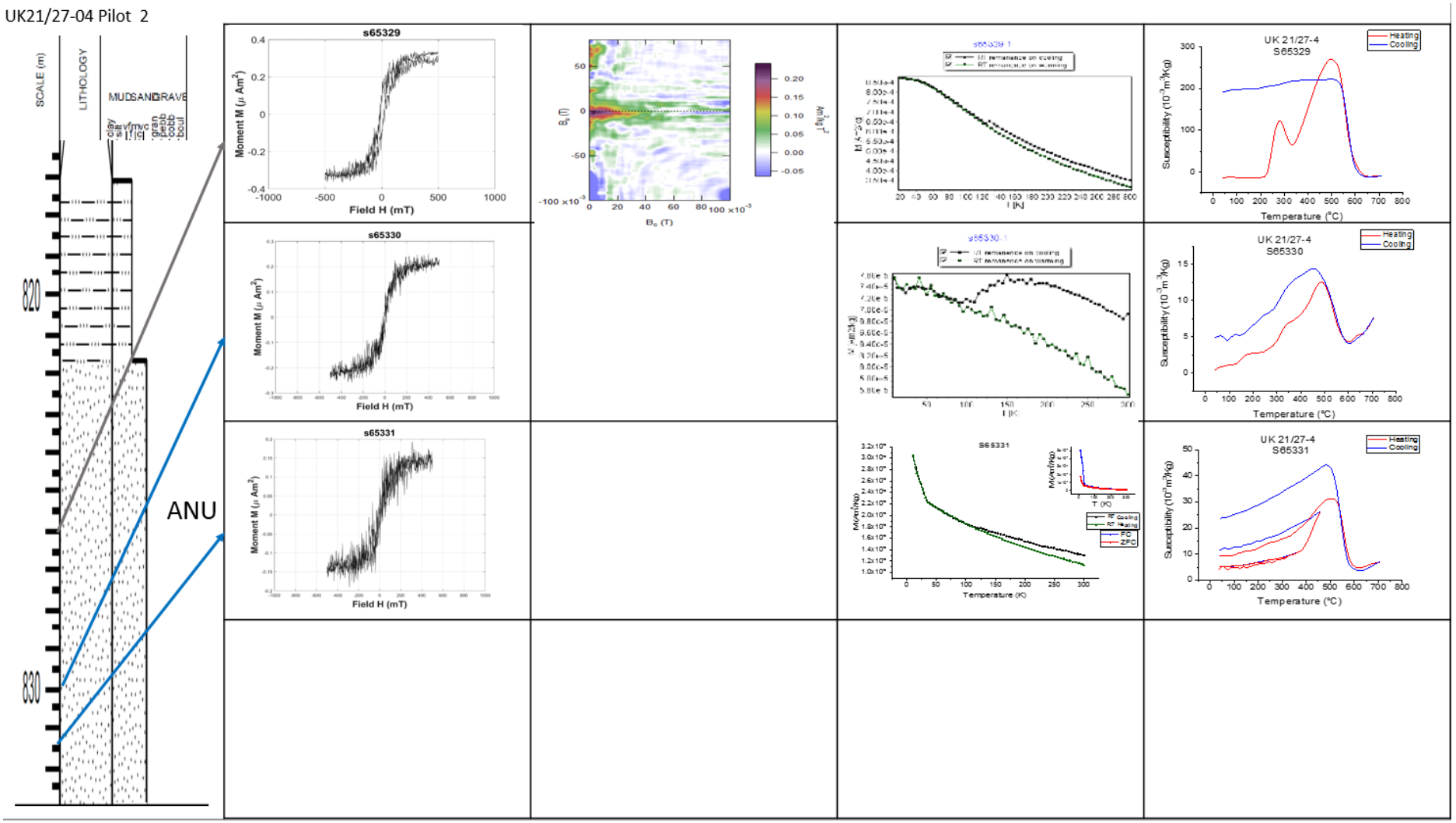

UK21/27-1A Pilot
SCALE (m)
LITHOLOGY
MUDSANDGRAVE
clay
sil
vf
f
m
c
gran
pebb
cobb
boul
860
OWC
870
880
ANU
s65317
s65318
s65319
s65320
Moment M (μ Am²)
Field H (mT)
Bc (T)
Temperature (K)
T (K)
Temperature (°C)
Susceptibility (10⁻⁸ m³/kg)
Heating
Cooling
UK 21/27-1A
S65317
S65318
S65319
S65320
FC
ZFC

UK21/27-1A Pilot 2



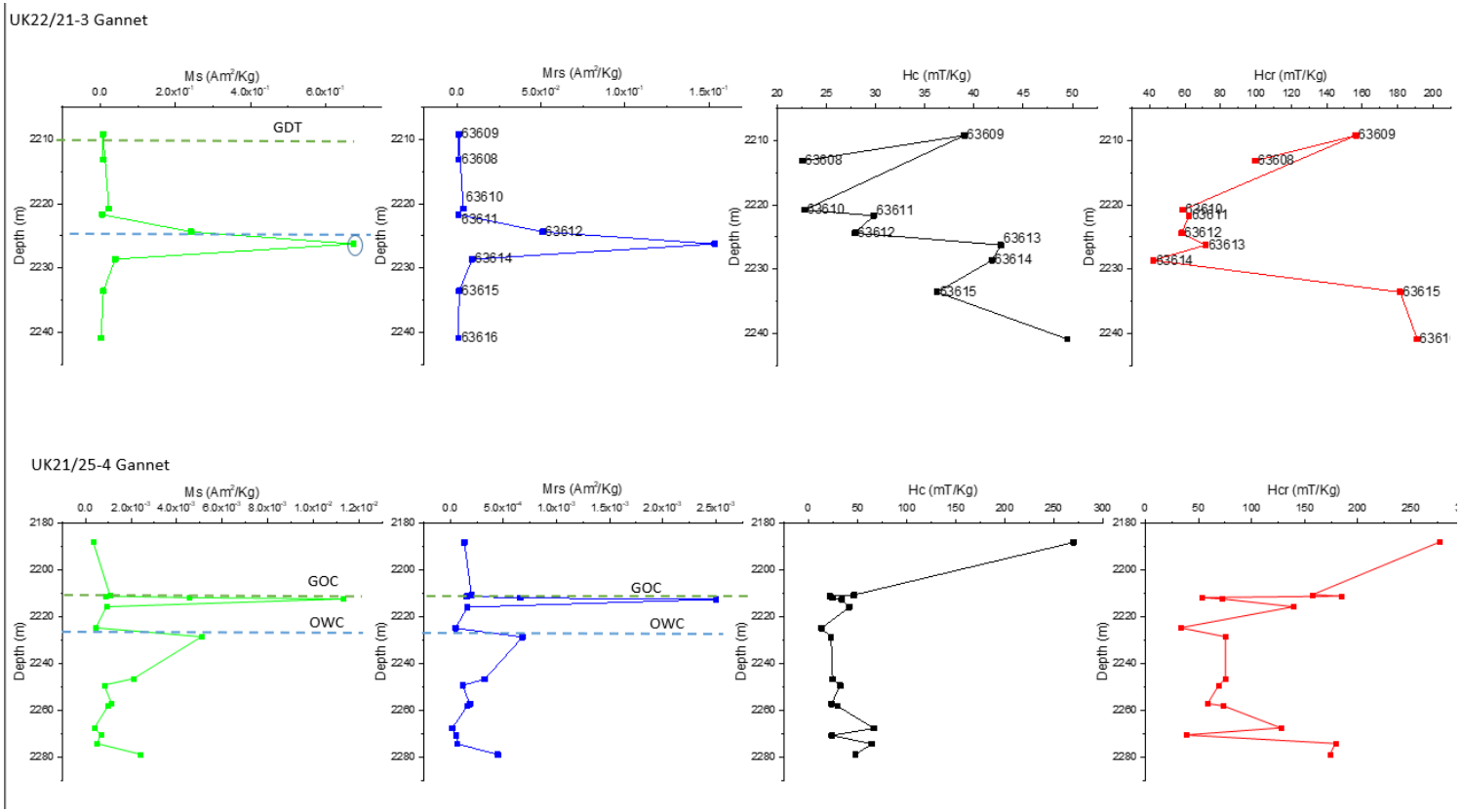

UK21/27-04 Pilot
SCALE (m)
LITHOLOGY
MUDSANDGRAVE
790
800
OWC
s65325
s65326
s65327
s65328EX
Moment M (μ Am²)
Field H (mT)
Paper 2
Temperature (K)
Temperature (°C)
Susceptibility (10⁻³ m³/kg)
Heating
Cooling
UK 21/27-4
S65325
S65326
UK 21/27-4
S65327
UK 21/27-04
S65328
IRM

UK21/27-04 Pilot 2

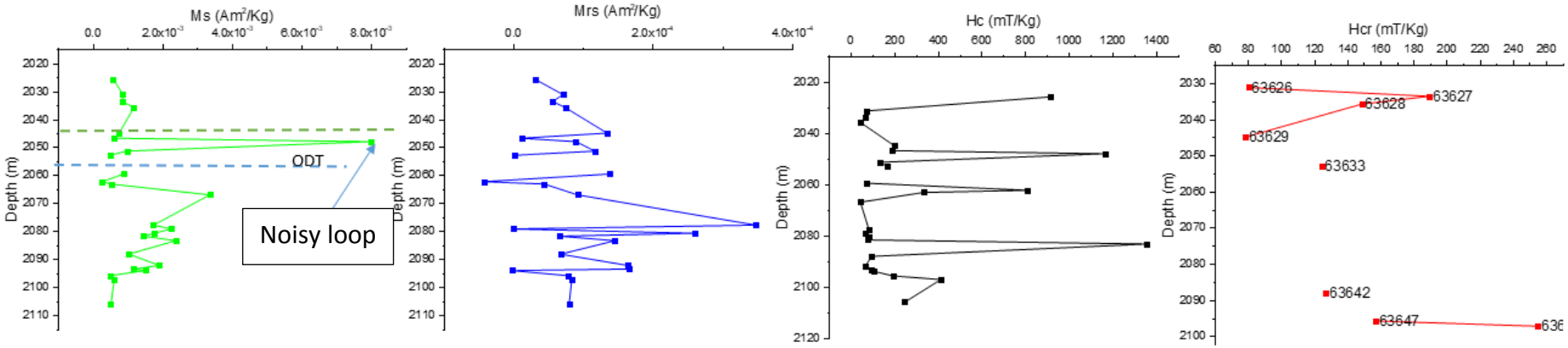


Appendix 4

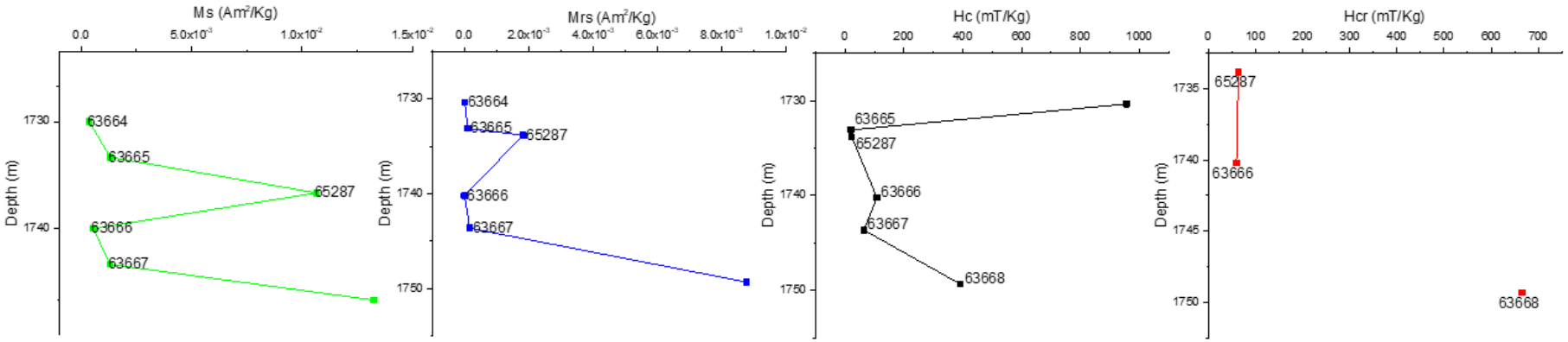
4.1 Measured hysteresis parameters for all wells, with gas and oil water contacts highlighted. The contacts were identified using composite logs.



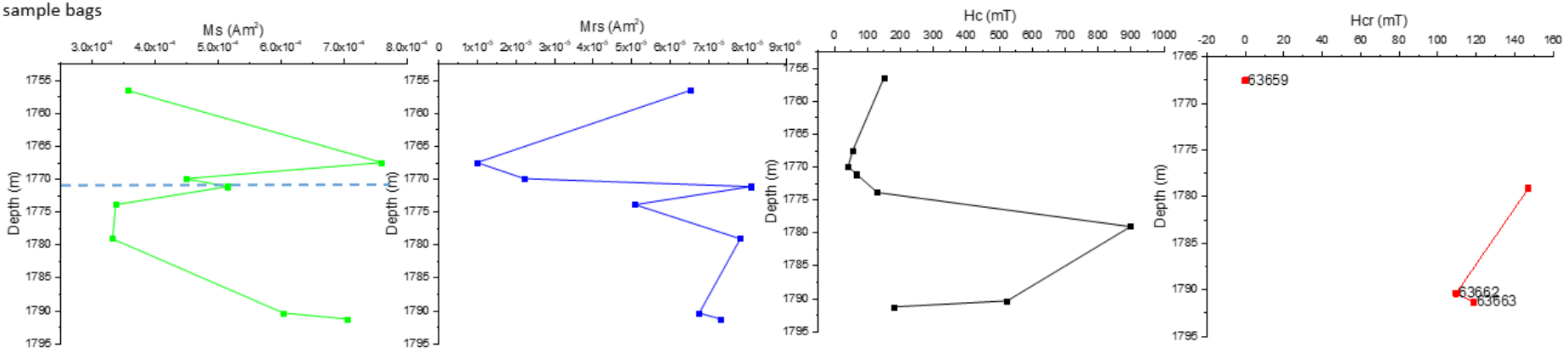
UK21/25-6 Gannet



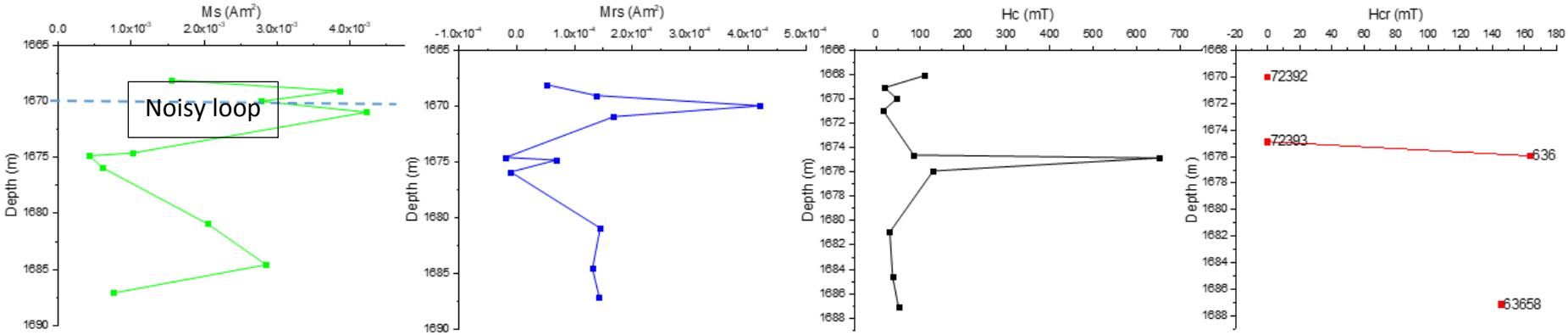
UK21/25-2 Guillemot



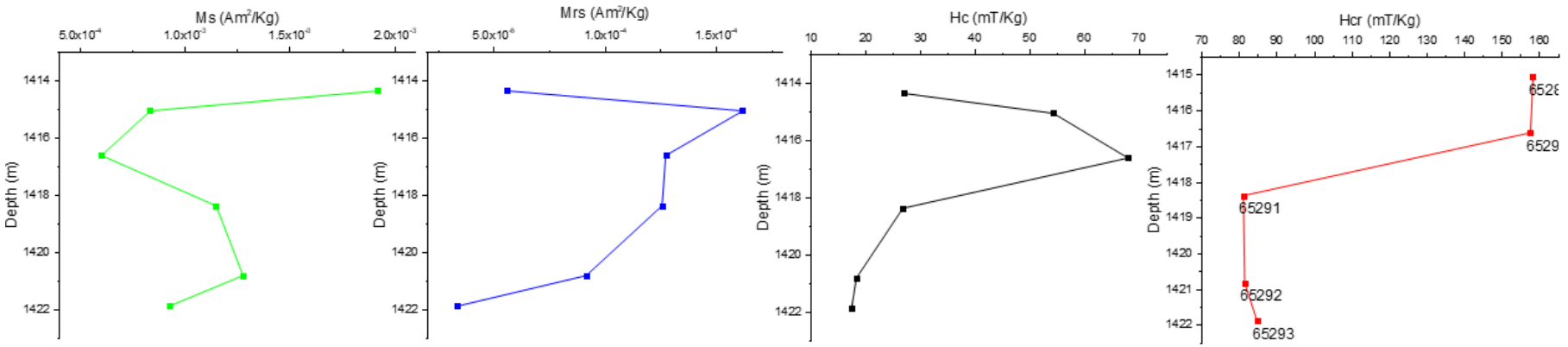
UK21/29a-6 Guillemot- all in sample bags



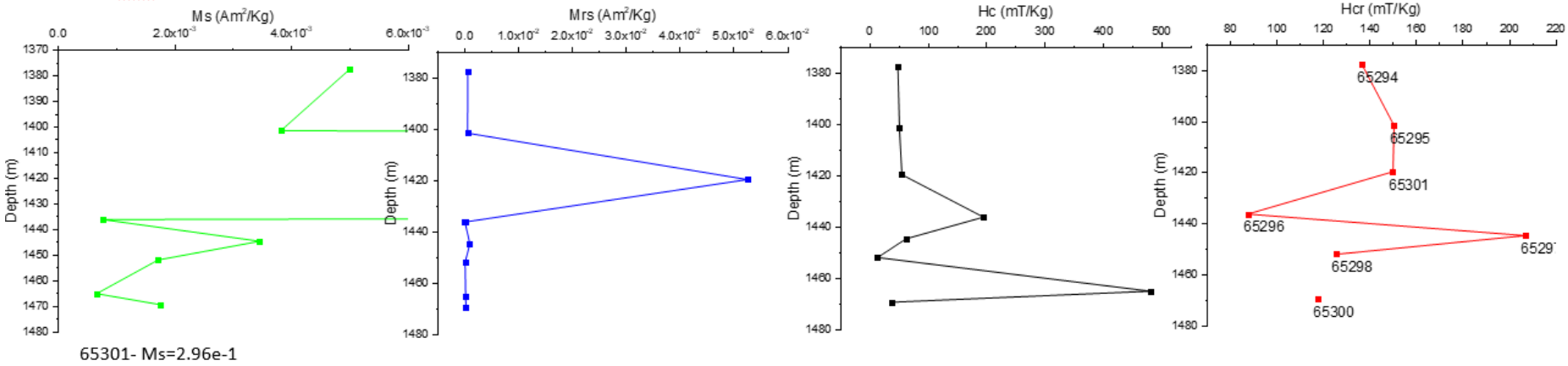
UK21/29a-8 Guillemot- Fe rich



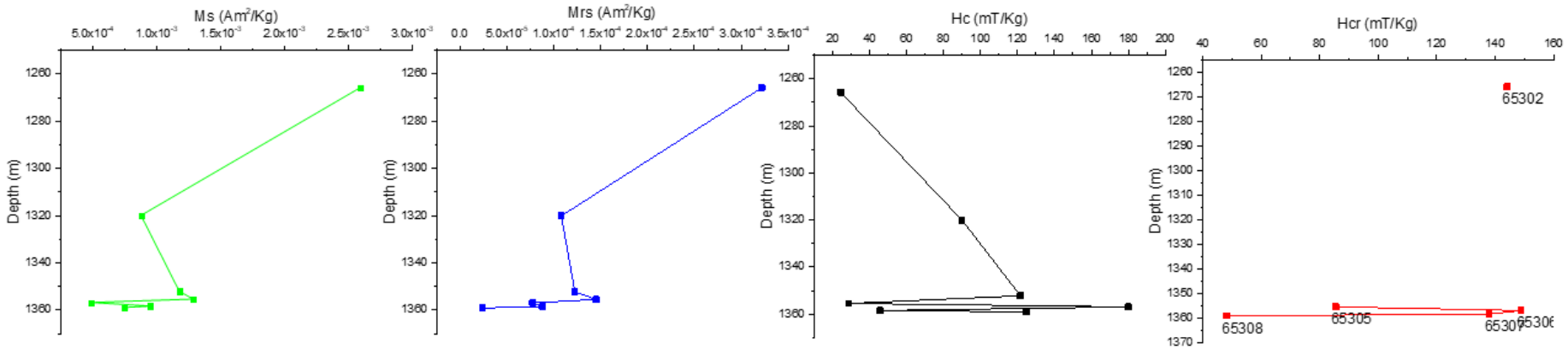
UK21/28a-5 Fyne & Dandy



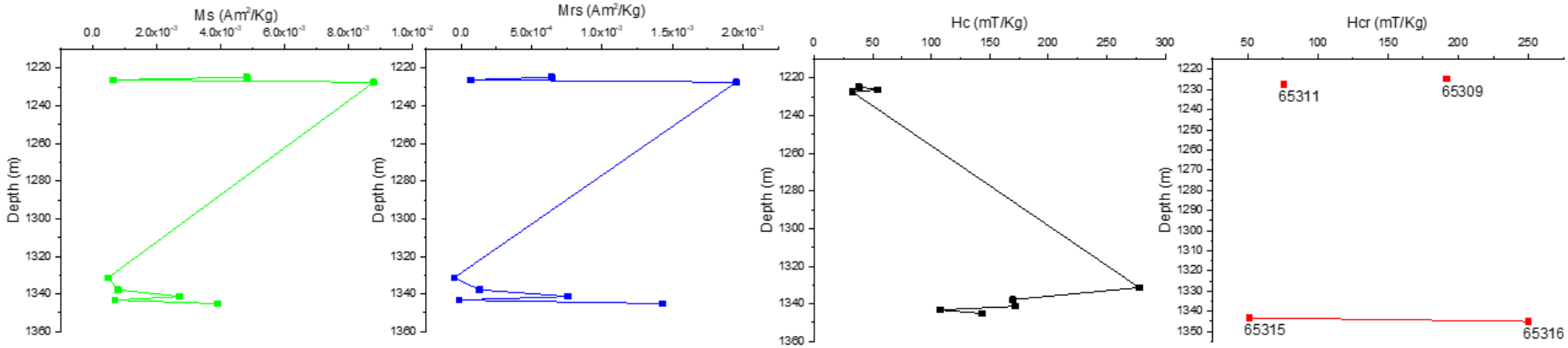
UK21/28a-3 Fyne & Dandy



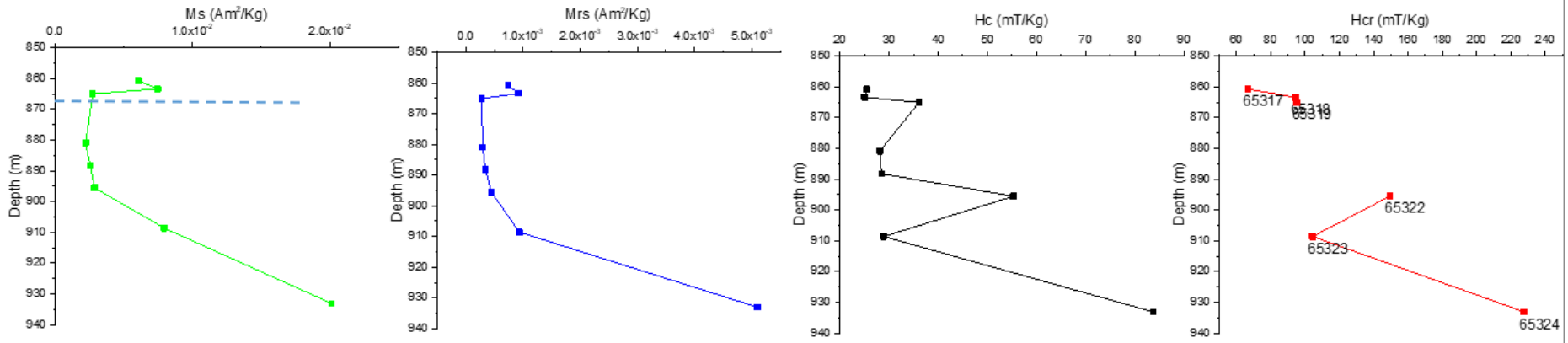
UK21/28a-4 Fyne & Dandy



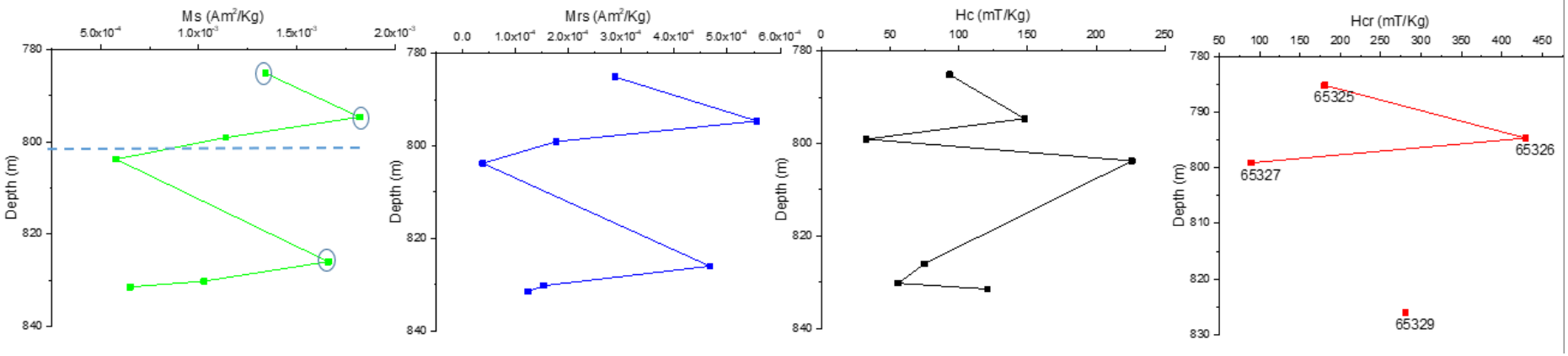
UK21/28a-8 Fyne & Dandy



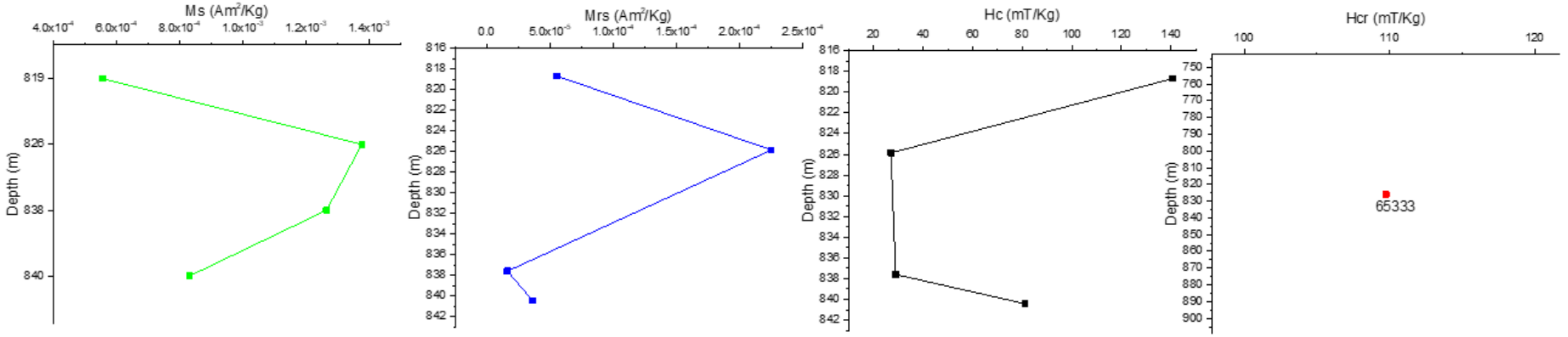
UK21/27-1A Pilot



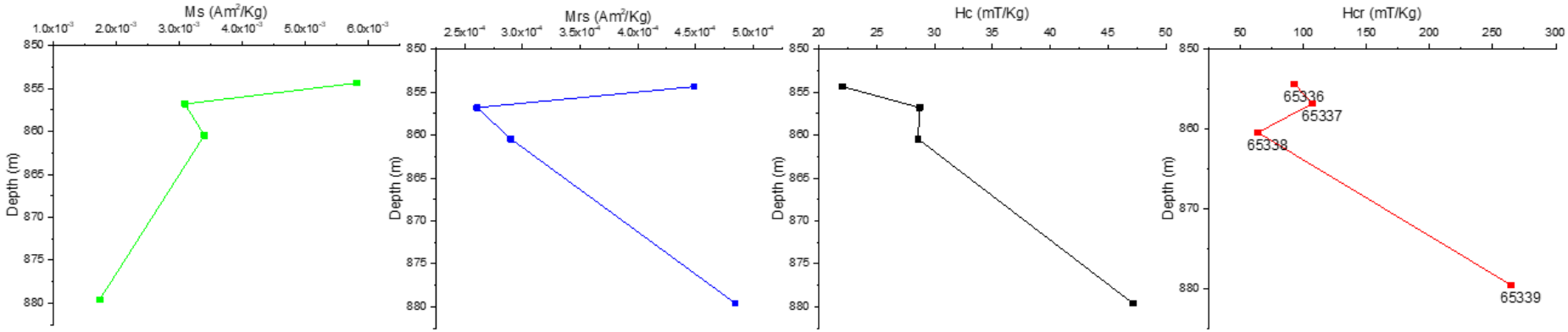
UK21/27-04 Pilot



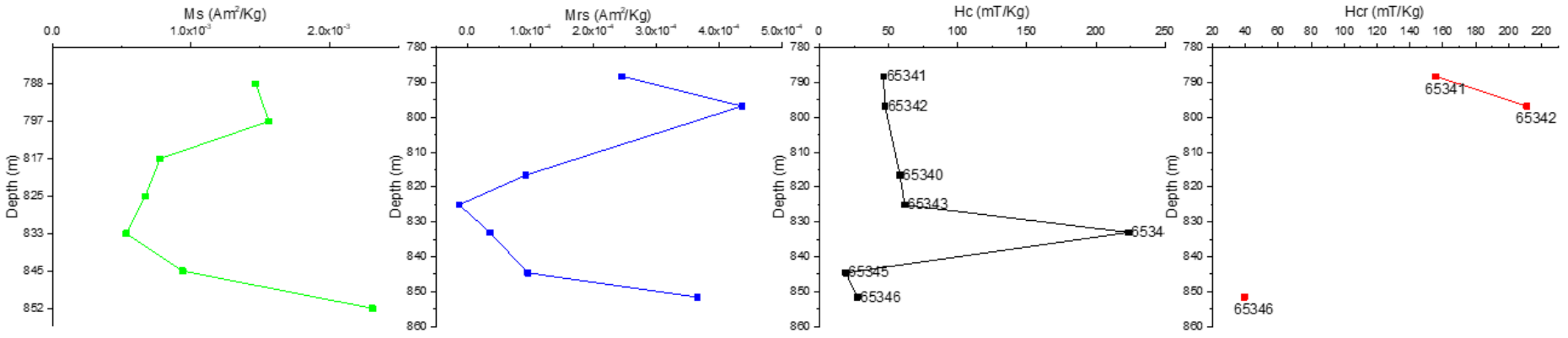
UK21/27a-05 Pilot



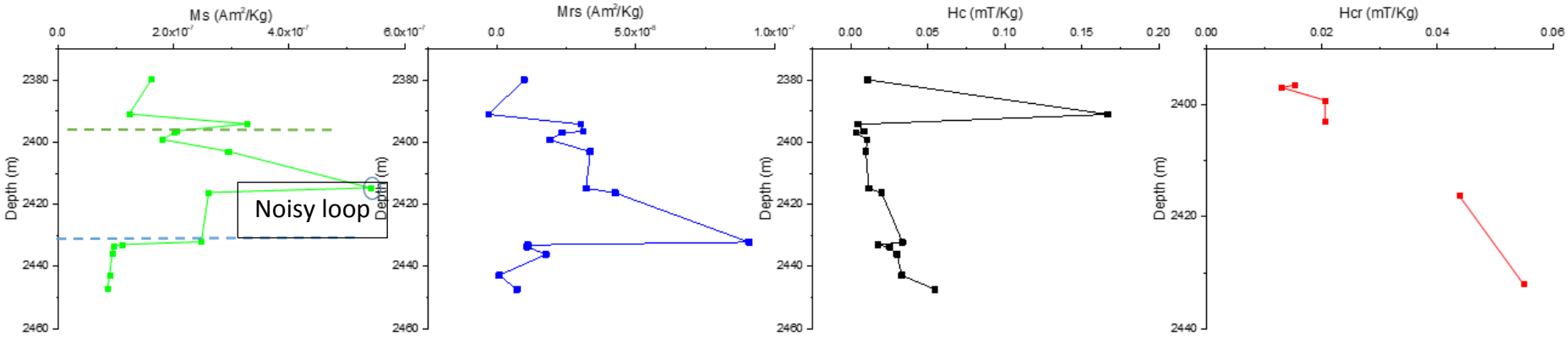
UK21/27-02 Pilot



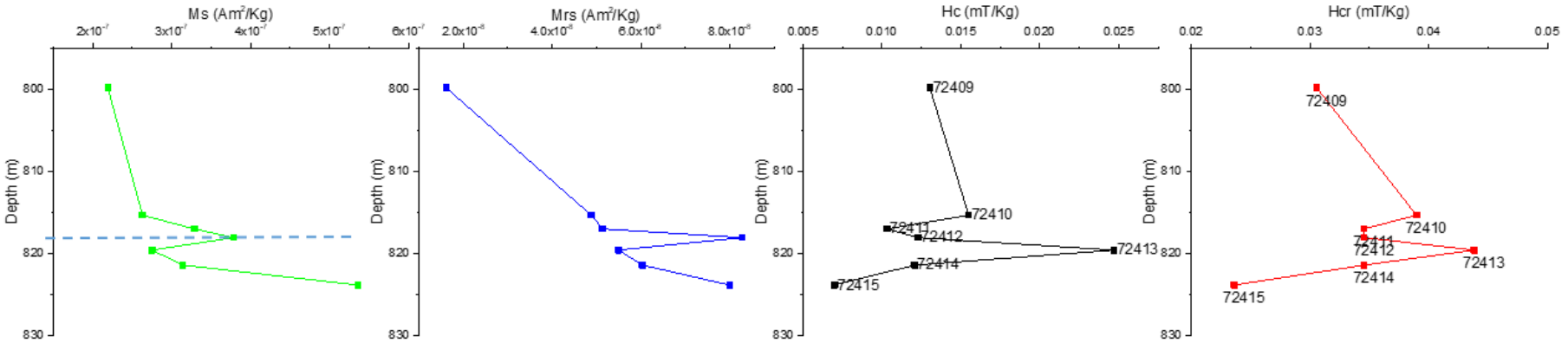
UK21/27-03 Pilot



UK21/25-A1 Gannet



UK21/27a-06 Pilot



UK21/24-03

